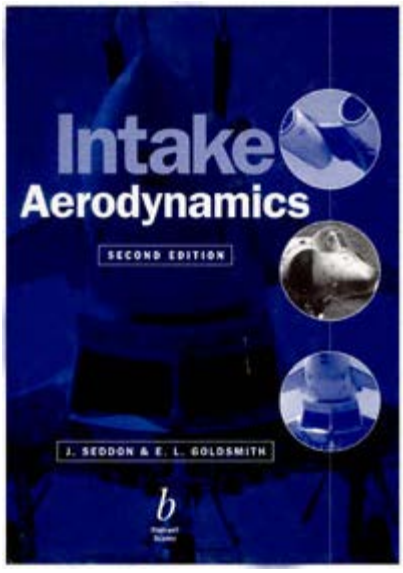

title:	Intake Aerodynamics
author:	Shedon, J.
publisher:	Blackwell Publishing Ltd.
isbn10 | asin:	0632049634
print isbn13:	9780632049639
ebook isbn13:	9780632061624
language:	English
subject	Jet engines--Air intakes--Design and construction, Gas dynamics.
publication date:	1999
lcc:	TL709.5.I5I58 1999eb
ddc:	629.134/353
subject:	Jet engines--Air intakes--Design and construction, Gas dynamics.

Intake Aerodynamics

Second Edition

J. Seddon PhD, DSc, CEng, CFF, FRAeS
E.L. Goldsmith MSc(Eng), DIC, CEng, FRAeS

revised by
E.L. Goldsmith

Blackwell Science Ltd
Editorial Offices:
Osney Mead, Oxford OX2 0EL
25 John Street, London WC1N 2BL
23 Ainslie Place, Edinburgh EH3 6AJ
350 Main Street, Malden MA 02148 5018, USA
54 University Street, Carlton Victoria 3053, Australia
10, rue Casimir Delavigne 75006 Paris, France

Other Editorial Offices:

Blackwell Wissenschafts-Verlag GmbH
Kurfürstendamm 57
10707 Berlin, Germany

Blackwell Science KK
MG Kodenmacho Building
7 10 Kodenmacho Nihombashi
Chuo-ku, Tokyo 104, Japan

First published 1985
Second edition 1999

Set in 10/13 pt Times
by DP Photosetting, Aylesbury, Bucks
Printed and bound in the United Kingdom by
MPG Books Ltd, Bodmin, Cornwall

DISTRIBUTORS

Marston Book Services Ltd
PO Box 269
Abingdon
Oxon OX14 4YN
(*Orders:* Tel: 01235 465500
Fax: 01235 465555)

USA
Blackwell Science, Inc.
Commerce Place
350 Main Street
Malden, MA 02148 5018
(*Orders:* Tel: 800 759 6102
781 388 8250

Fax: 781 388 8255)

Canada
Login Brothers Book Company
324 Saulteaux Crescent
Winnipeg, Manitoba R3J 3T2
(*Orders:* Tel: 204 837 2987
Fax: 204 837 3116)

Australia
Blackwell Science Pty Ltd
54 University Street
Carlton, Victoria 3053
(*Orders:* Tel: 03 9347 0300
Fax: 03 9347 5001)

A catalogue record for this title is available
from the British Library
ISBN 0 632 04963 4
Library of Congress
Cataloging-in-Publication data
is available

For further information on
Blackwell Science, visit our website:
www.blackwell-science.com

Contents

Foreword to the First Edition

Since the advent of the jet engine rapid developments in airframe and engine performance have presented the air intake designer with many new challenges. For example, maintaining good quality intake flow for the Harrier in conventional flight, through transition and down to the hover; combining the requirements of transonic manoeuvrability and sustained Mach 2 flight for the Tornado; or reconciling the conflicting needs of Concorde for efficient supersonic cruise performance and carefree engine handling in other flight conditions. The future looks no less challenging with prospects of military designs involving ultra high incidence manoeuvring capability; supersonic VSTOL; contrarotating unducted fan installations; second generation supersonic transports and air breathing missiles and space launchers.

The subject of intake aerodynamics, therefore, has been and will remain of primary importance to the aerospace industry, in which progress depends on combining fundamental research and practical development in a way that the authors clearly understand.

John Seddon and Laurie Goldsmith are both international authorities in the field and, between them, combining some seventy-five years of experience of intake aerodynamics, could not be better qualified to write this book. In their research they have had to probe the fundamentals of the subject and to elucidate important considerations as they have arisen, for example, spillage drag, shock oscillation, dynamic distortion and swirl. At the same time they have between them headed up the Royal Aircraft Establishment's advice to industry throughout the entire history of jet propulsion and in varying degrees have been associated with every British jet aircraft development. In addition they have been consulted by overseas manufacturers.

Now the authors have assembled their extensive knowledge and experience in this book, which as a comprehensive and practical appraisal of intake aerodynamics, is the first of its kind. The subject matter is well digested and excellently presented, and the authors have combined an easily understood treatment of the basic ideas and concepts employed in intake aerodynamics with discussion of the more specialised aspects of the subject.

This book will prove invaluable both to the newcomer to the subject and to the specialist alike and can be recommended to young aerospace engineers and to the not so young as a refresher and reference text. I am sure it will prove to be of great service to academic centres and research organisations as well as to design and development departments in industry.

J.T. STAMPER, MA, FENG, HON FRAES
TECHNICAL DIRECTOR
BRITISH AEROSPACE PLC

Preface

The title of the book calls for a small apology to readers across the Atlantic. It is surprising perhaps but true, that in a field of technology which over the years has seen much valuable exchange and collaboration between countries, the English-speaking nations have persisted in using different names for the main topic. In Britain the object of our attention is an *intake:* in the United States it is an *inlet.* After due consideration, home loyalty has prevailed and the traditional British terminology has been retained.

The subject of intake aerodynamics has developed since the Second World War in parallel with the development of the jet engine itself, taking over, however, a good deal of background initially from earlier experience on the aerodynamics of cooling systems for piston-engined aircraft. The advent of supersonic flight in the late 1940s led to a burgeoning of research on intakes, around a central theme of the efficiency of shock-wave systems. Practical limits to what could be achieved were evaluated, based on necessary compromises between the requirements of internal and external flows. More recently the effects of aircraft attitude and local flow fields have been brought in and much attention has been given to the aspects of airflow compatibility between intake and engine. The subject has never been lacking in interest to research workers and major surprises have emerged at roughly decade frequency.

In the 1940s and 1950s there was the discovery of the phenomenon of intake shock oscillation at superonic speeds and the realisation of the increasing importance, again principally at supersonic speeds, of the drag due to flow spillage in front of the intake. Shock oscillation has become known widely by the American term 'buzz', but in the nomenclature associated with intake drag disparate terms for the same thing pre-entry drag, the British, and additive drag, the American still coexist to this day.

In the late 1960s the significance of dynamic distortion became apparent, while in the late 1970s a problem to emerge unexpectedly was that of swirl, restricted to certain types of intake but occurring at both subsonic and supersonic speeds. None of these problems has 'gone away' and all are treated in this book.

Some explanation may be offered for the lack of previous textbooks on the subject. The air intake stands in a position of linking the aircraft and

engine in a continuum of aerodynamics, but intake aerodynamics as a subject differs from the corresponding subjects on either side in an important respect. Whereas both airframe aerodynamics and compressor aerodynamics are based heavily on the lift function and less on that of drag, with the intake the reverse is true. Loss of total pressure is the form taken by the drag function in the internal flow and in the external flow it is basically the drag which has to be evaluated and used to effect a final compromise in design. This almost entire emphasis on drag leads to a subject much influenced by the behaviour of the turbulent boundary layer and hence heavily weighted on the experimental side. Because, moreover, the boundary layer is usually operating in a significantly adverse pressure gradient, flow separation is rarely far away and, unlike the situation in classical wing aerodynamics, say, where the occurrence of separation is generally taken to mark a limit of operation, an intake is often required to operate satisfactorily in separated flow regimes. Thus from a practical aspect, exact theories are rarely available and the designer looks rather to empirical generalisations, the applicability of which may become questionable as more evidence is accumulated.

The book is the first of its kind and it aims to cover *ab initio* the aerodynamics of both subsonic and supersonic intakes in real flows and to demonstrate continuity through the transonic range. This applies particularly to the behaviour of the turbulent boundary layer in adverse pressure gradients. Although internal and external flows are treated in the context of both civil and military applications, an area excluded is that of aerodynamic interference between the engine nacelle and the rest of the airframe. At subsonic speeds, particularly approaching Mach 1.0, interference forces exist between the nacelle, its support strut and the adjacent wing or fuselage. This usually increases the drag and often modifies lift and moment characteristics. At supersonic speeds the problem of impingement of intake shock waves on wing or body must be considered. In suitable conditions, favourable interference is a possibility, at least in principle. The subject of interference is difficult to quantify, however, except in terms of specific situations: moreover it calls generally for consideration of the total engine nacelle rather than simply the intake and this in turn involves the aerodynamics of afterbody and nozzle flows, a subject area that is outside the present one.

In the arrangement of the book, the first eight chapters are concerned with internal flow (the flow to the engine, considered from initial free stream conditions) and the general progression is from subsonic through transonic to supersonic. Next the topic of external drag is treated. This would logically divide similarly into a number of chapters dealing with various aspects. Owing however to a close interplay amongst most of the items, it was decided that continuity combined with cross-linking could best

be achieved by keeping the subject within the bounds of a single chapter, in which however the succession of subsonic, transonic and supersonic is broadly preserved. After establishing in this way the principles of internal and external performance, which can henceforward be referred to whenever required, the book turns to consideration of other aspects which go into a practical compromise design: these are concerned with flow quality (distortion, swirl and buzz), with engine and intake matching and with incidence effects, which have grown in importance in recent times. Finally, Chapter 14 describes some unusual concepts of intake design that have cropped up over the years and Chapter 15 discusses the techniques of wind tunnel testing and analysis which apply specially to intakes.

The emphasis throughout the book is firstly on understanding the fluid mechanics of the process of decelerating the air from free-stream to engine-face velocity. Secondly, it is on the condition of that air on reaching the compressor of the engine and thirdly on the external drag of the outer shape of the intake in the immediate vicinity of the inlet plane.

The object of this second edition is to clarify the explanation and presentation of all these aspects, especially where computational and experimental evidence has become available since the early 1980s, the time of writing of the first edition. Thus Chapters 4 and 9 have been extensively revised; smaller revisions have been made to Chapters 13 and 15 and minor additions to Chapters 3 and 14. Throughout the book the opportunity has been taken to improve the majority of the diagrams and to update the photographs.

Acknowledgements.

Parts of Chapters 2, 4 and 9 are a fresh presentation of material contained in a paper entitled 'Air intakes for aircraft gas turbines', published in the Journal of the Royal Aeronautical Society, October 1952. We acknowledge the Society's permission to extract freely from that material and, in particular, to reproduce Figs 2.3, 2.5, 2.10, 2.13, 2.16, 4.32, 4.33, 4.34, 9.7 and 9.8.

We acknowledge similarly the permission of H.M. Stationery Office to quote from Crown Copyright papers (ARC R & M and unpublished RAE reports) and in particular to reproduce Figs 3.2, 3.3, 3.9, 3.10, 3.11,3.12, 5.31, 8.18 and 8.19.

Much use has been made of American data, published and unpublished. In this context we are greatly indebted to NASA for permission to reproduce Figs 5.7, 5.9, 5.10, 5.22, 6.15, 6.16, 6.17, 7.8, 7.12, 8.14, 8.16, 8.17, 9.40, 11.7, 11.9, 11.11, 13.6, 13.7, 13.8, 14.13, 14.14, 14.28, 14.29 and 14.30; to the AIAA for Figs 11.4, 11.5, 12.8, 12.9, 12.12, 13.1, 13.4, 13.9, 14.16 and 14.27; and to the Marquardt Corporation for Fig. 10.7.

Our thanks are expressed also to AGARD and the authors concerned for permission to reproduce Figs 11.2, 11.6, 11.10, 13.32, 13.34, 13.36, 15.4 and 15.27; to ARL (Melbourne) for Figs 10.3,10.4 and 13.35; to ONERA (Paris) for Figs 8.12 and 8.13; to British Aerospace for Figs 2.1, 2.2 and 14.24; and to Engineering Sciences Data Unit (ESDU) for Figs 9.22 9.25.

If other sources are involved, the failure to acknowledge them specifically is not intentional and our thanks are hereby conveyed.

The book is published with the permission of the UK Ministry of Defence.

J.S.
E.L.G

Notation List

A general list is given, followed by lists special to individual chapters. Some symbols are used in more than one context, where this can be done without confusion. In a small number of cases the same quantity is defined by different symbols in different chapters (for example, I and L are both used to define geometric lengths) as the context appears favourable. The use of numerical suffixes for stations in a flow and of shorthand suffixes such as 'max' and 'spill' is so ephemeral in the one case and so obvious in the other as not to require their inclusion in these lists.

General

p static pressure

P total pressure

r density

T temperature

R gas constant

g ratio of specific heats, taken as 1.4 for numerical purposes

V velocity of flow

a velocity of sound

M Mach number, V/a

q dynamic pressure, $\frac{1}{2}\rho V^2$

A area of cross section

*A** sonic area

m mass flow, r*AV*

*C*p static pressure coefficient, (*p* *p*¥)/*q*¥

hs total-pressure efficiency, compressible flow (little used)

hs*i* incompressible-flow form of hs (much used)

hp total-pressure ratio (most-used definition of efficiency)

hR 'ram' efficiency (used only for one illustration in Chapter 3)

[Any of these four definitions can be referred to loosely as 'intake pressure recovery']

S aircraft surface area ahead of entry 'wetted' by internal flow

g perimetric length of cross section, whole or partial

*C*f, *C*F	friction coefficient, local or mean
J	position ratio, S/A or kS/A
I	duct integral
µ	inverse flow ratio, Ac/A¥
d	boundary layer thickness (also flow turning angle, see below)
d*	boundary layer displacement thickness
q	boundary layer momentum thickness (also lip position angle, see below)
H	form parameter, d*/q
Hi	form parameter for incompressible flow
n	reciprocal of index for boundary-layer profile power law
d	flow turning angle (wedge angle or cone semi-angle)
b	oblique-shock angle relative to incident flow direction
q	lip-position angle
bD	value of b or q when oblique shock is on cowl lip
h*e*, h*o*	cowl-lip external ('outer') angle relative to duct axis
h*i*	cowl-lip internal angle relative to duct axis
h*v*	cowl-lip included angle
h	height dimension representing cross-section area A in two-dimensional flow
CR	contraction ratio, (highlight area) ÷ (throat area)
X	engine thrust
D	intake drag
t	shorthand for factor (1 + (g 1)M2/2)

Suffixes

o	stagnation values of flow quantities other than pressure
¥	free-stream conditions (station 'at infinity' in flow)
c	conditions at entry (gross entry area enclosed by cowl lip)
f	conditions at nominal engine face (end of intake duct)
e	conditions at duct exit
i	net flow area at entry
t	duct throat (normally just inside entry)

a	relates to approach length
d	relates to duct length
s	relates to shock system
i	relates to shock and boundary-layer interaction (Chapters 3, 8)
L	relates to local flow conditions (Chapters 13, 15)

Prefix	
D	change in a quantity (usually DP, loss of total pressure)
Chapter 1	
cp	specific heat at constant pressure
cv	specific heat at constant volume
k	constant in relation P = kqf
K	constant in relation (DX/X) = K (DP/P¥)
Chapter 2	
l	length of streamtube in direction of flow
F	friction force on elementary length of streamtube
k	empirical factor in approach loss
a	effective cone angle
*R*eff	effective Reynolds number
d	station of duct immediately before sudden enlargement
N	number of propeller blades
t	representative thickness of blade section
r	representative radius of blade section
L	projecting length of spinner and hub
P, *Q*, *R*	points on flow characteristic of twin intake
P', *S*	points on static pressure characteristic of twin intake
Chapter 3	
d	boundary layer thickness
l	length of streamtube in direction of flow
Cpm, *C*ps	minimum and actual rise in pressure-coefficient for flow separation
Q	flow factor in interaction-loss formula
G	geometric factor in interaction-loss formula
F, Y	Mach number functions in interaction-loss formula
*A*q	effective boundary layer ingestion area, based on momentum thickness
*R*q	Reynolds number based on momentum thickness

*A*h	duct area at half length
l	perimeter factor gc/ga
u	velocity in boundary layer

Suffixes

p	relates to length over which pressure rise acts

s relates to separated flow conditions

u undisturbed

Chapter 4

AR subsonic diffuser area ratio *A*f/*A*t

CR contraction ratio *A*c/*A*t

*D*f, *R* duct diameter/radius at final section of the subsonic diffuser

*D*maxcowl maximum diameter

*L*f, *L* subsonic diffuser length

e internal cowl lip radius

a/b ellipse major to minor axis ratio

D engine face distortion $\left[=\frac{P_{\max}-P_{\min}}{P_{\text{mean}}}\right]$

Suffixes

t intake throat (i.e. minimum area) section

c capture plane

lip associated with losses emanating from the cowl lip under surface

f engine face (gross)

s separated flow

Chapter 5

*L*N, *l*n geometric dimensions ahead of entry (Fig. 5.6b)

n number of shocks in a general system

r, f radial and angular coordinates in Prandtl Meyer expansion

x, *y* linear coordinates in Prandtl Meyer expansion

μ Mach angle, sin 1 1/M

v turning angle in expansion

K constant in Prandtl Meyer flow, function of g

a, *b*, *c*zones behind shock intersection point

L distance of detached shock ahead of entry, measured to point where outer shock crosses stagnation streamline

r distance out from axis of flow

bs	slope of shock hyperbola at sonic point
*A*s	area of flow section between sonic point and cowl lip
ls	inclination of streamline at sonic point on shock
lda, ldt	angle of shock detachment from lip at free stream Mach number for axisymmetric and two-dimensional flow respectively
B, *C*	Mach number functions in expression for *L*
*L*i	distance of shock intersection point ahead of entry
*L*N	distance of tip of compression surface ahead of entry

Suffixes

w	conditions behind a normal shock
s	conditions behind a total compression system
i	quantities relating to total flow turning in oblique-shock compression

Chapter 6

c	limiting contraction ratio for internal compression

Chapter 7

*M*n	Mach number ahead of normal shock
*A*n	net flow area ahead of normal shock
*A*i	net flow area at entry
r	radial distance from axis of duct
f	angle of lip overhang relative to shoulder of compression surface
*A*s	pre-entry wetted surface area of compression system

Chapter 8

h	bleed efficiency
h	bleed or diverter height
f	a momentum integral across the boundary layer
l	denotes outer edge of boundary layer
m	mass flow in boundary layer
en	suffix for bleed entry
ex	suffix for bleed exit

Chapter 9

Cx	internal thrust coefficient
CD	drag coefficient
*C*f	flat-plate friction coefficient
l, *x*	cowl length to maximum section
d, *D*	cowl diameter
r	lip radius
F	thrust force on cowl exterior
*M*D	drag-rise Mach number

*D*DF	maximum disturbed-flow drag
*D*NS	maximum normal-shock drag
a, b	coefficients in definition of spillage drag
*L*max	stand-off distance of bow shock ahead of bluff body

x, *r*	cylindrical coordinates
u, *v*	axial and radial velocities
f	velocity potential
*u*p, *v*p	perturbation velocities
b	$\sqrt{M^2 - 1}$
r	body radius
h	cone semi-angle
h0	initial angle of cowl external surface
*U*1, *T*	functions of x in quasi-cylinder approximations
n	power index for Willis and Randall cowl profiles
K	empirical factor for blunt-lipped cowl drag
Suffixes	
f	friction drag
p	pressure drag
o	pressure drag at full flow
m	maximum section of cowl
w	conditions behind normal shock
pre	upstream of cowl entry plane
stag, *s*	stagnation point or line
c	capture plane
Chapter 10	
*f*1, *f*2	functions of Pi/pi
Chapter 11	
DC(q)	distortion coefficient based on q deg. sector
*P*q	mean total pressure in q deg. sector
	alternative distortion coefficients
*K*A2, *K*q, *K*rad, *K*DA, *K*DM	
b	weighting factor
n	number of rings of pitot tubes

m	number of pitots per ring
U	mainstream velocity round a duct bend
U'	reduced velocity, as in boundary layer
R	radius of bend
DCpbt2	difference in pressure coefficient between bottom and top of duct after second bend

Chapter 12

N	engine rpm
*m*E	intake flow to engine
*m*B	intake flow to bleed
*p*v	pressure in ramp void
*p*B	pressure in bleed chamber
n	suffix for nozzle quantities in ramjet

Chapter 13

LN, *LW*	geometric dimensions ahead of entry (Fig. 13.23)

Suffixes

a	values at incidence
D	values corresponding to oblique shock on lip

Chapter 14

x, *y*, *z*	axes defined (Fig. 14.3) for bump intake
K, q	dimensions relating to construction of bump intake (Fig. 14.3)
l	volume of vaporised liquid for isothermal compression
a	volume of air for isothermal compression
Suffix l	refers to vaporised liquid

Chapter 15

R, *r*	duct/cowl radius
*C*d, *C*D	nozzle discharge coefficient
*K*f, *K*v	calibration factors in flow-ratio evaluation
a.	angle of incidence
b	angle of sideslip
q	inclination of duct axis to body axis in incidence plane
l	inclination of duct axis to body axis in yaw plane
Y	angle of cant of duct exit in incidence
g	angle of cant of duct exit in yaw plane
L	lift
M	pitching moment

Y	sideforce
N	yawing moment
d, e	moment arms
$f1(Me)$	function of Me in internal drag
Q	non-dimensional flow coefficient

Suffixes

d section in constant-area duct after mixing to uniform flow

v venturi section for accurate measurement in duct

i individual pitot tube in rake

List of Abbreviations

AGARD	Advisory Group for Aeronautical Research and Development (Paris, France)
AIAA	American Institute for Aeronautics and Aerospace (New York, USA)
ARA	Aircraft Research Association (Bedford, England)
ARC	Aeronautical Research Council (London, England, disbanded 1980)
ARL	Aeronautical Research Laboratories (Melbourne, Australia)
ASME	American Society of Mechanical Engineers
BAC	British Aircraft Corporation (now part of BAe)
BAe	British Aerospace
Caltech CIT	California Institute of Technology (Pasadena, USA)
DLRFB	Deutsche Luft-und Raumfahrt Forschungsbericht (Portz-Wahn, W. Germany)
ESDU	Engineering Sciences Data Unit (London, England)
IAF	International Astronautical Federation (Paris, France)
ICAS	International Congress of Aerospace Sciences
MIT	Massachusetts Institute of Technology (Boston, USA)
NACA	National Advisory Committee for Aeronautics (now NASA)
NAI	Nanjing Aeronautical Institute (Nanjing, China)
NASA	National Aeronautics and Space Administration (Washington DC, USA)
NGTE	National Gas Turbine Establishment (now DERA UK Defence Evaluation and Research Agency)
ONERA	Office National d'Etudes et de Recherches Aerospatiales (Paris, France)
RAE	Royal Aircraft Establishment (now DERA UK Defence Evaluation and Research Agency, Farnborough and Bedford, England)
RAeS	Royal Aeronautical Society (London, England)
UK	United Kingdom
USA	United States of America

USCEC University of Southern California Engineering Centre (Los Angeles, USA)

V/STOL Vertical and (or) Short Take-off and Landing

Chapter 1
Introduction

1.1
Useful Flow Relationships

We begin by setting out some standard flow relationships of which use is made from time to time throughout the book. This will serve also to introduce the notation adopted for the more commonly used quantities. No attempt is made to derive the equations from first principles; such derivations are to be found in a number of standard accounts, as for example that by Liepmann and Roshko (1957).

Air is assumed to be a perfect gas and therefore to obey the gas law:

$$p/\rho = RT \qquad (1.1)$$

in which p is the static pressure, r is the density and T is the absolute temperature. R is the gas constant, equal to the difference between specific heats at constant pressure and constant volume, that is

$$R = c_p - c_v = c_p(\gamma - 1)/\gamma \qquad (1.2)$$

where g is the ratio of specific heats, *cp/cv*.

For isentropic flow, steady in time, Bernoulli's equation applies along a streamline:

$$\int \frac{\mathrm{d}p}{\rho} + \frac{1}{2}V^2 = \text{constant} \qquad (1.3)$$

where V is the flow velocity. If a number of streamlines forming a stream tube or a total flow field have the same initial conditions of pressure and velocity conditions 'at upstream infinity' Bernoulli's equation applies to the whole stream tube or flow field so long as the flow remains isentropic. For incompressible flow in the case of air an approximation only but a very useful one the density r is constant and Equation (1.3) takes the well-known form:

$$p + \rho V^2/2 = \text{constant} \qquad (1.4)$$

Defining stagnation or *total* conditions at any point in the flow as the conditions that would be obtained if the flow there were brought to rest isentropically, the total pressure P is given by the constant in Equation (1.3) or (1.4).

The adiabatic law, valid for isentropic flow, relates pressure and density in the form:

$$p/\rho^{\gamma} = \text{constant} \qquad (1.5)$$

This allows integration of the Bernoulli equation to give

$$\frac{\gamma}{(\gamma-1)}\frac{p}{\rho}+\frac{1}{2}V^2 = \text{constant} = \frac{\gamma}{(\gamma-1)}\cdot\frac{\mathrm{P}}{\rho_0} \qquad (1.6)$$

where the suffix zero is used to denote stagnation conditions (this convention is applied to all quantities other than total pressure P, which as defined above requires no suffix).

Use of the adiabatic law leads also to a definition of the velocity of the sound, a, namely

$$a^2 = dp/d\rho = \gamma p/\rho \qquad (1.7)$$

Then if M is written for Mach number (= V/a) and q is written for dynamic pressure (= rV2/2), we have

$$M^2 = V^2/a^2 = \rho V^2/\gamma p \qquad (1.8)$$

whence

$$q/p = \gamma M^2/2 \qquad (1.9)$$

Manipulating Equation (1.6) gives

$$p\left(1+\frac{\gamma-1}{2}\frac{\rho V^2}{\gamma p}\right) = P\rho/\rho_0 = P(p/P)^{1/\gamma}$$

so that

$$1+\frac{\gamma-1}{2}M^2 = (P/p)^{(\gamma-1)/\gamma}$$

or

$$P/p = \left(1+\frac{\gamma-1}{2}M^2\right)^{\gamma/(\gamma-1)} \qquad (1.10)$$

Corresponding expressions, differing only in the power index, follow for the total to static ratios of density, temperature and sonic speed. Two other formulae of particular interest are, firstly

$$(P-p)/q = \left(\frac{P}{p}-1\right)/\frac{1}{2}\,\gamma M^2 \qquad (1.11)$$

which follows directly from Equation (1.9) and secondly, writing A for flow cross-sectional area and A^* for the area corresponding to sonic conditions.

$$\frac{A}{A^*} = \frac{1}{M}\left[\frac{2}{\gamma+1}\left(1+\frac{\gamma-1}{2}M^2\right)\right]^{(\gamma+1)/2(\gamma-1)} \qquad (1.12)$$

Equations (1.3) to (1.12) are all for isentropic flow. The Mach number functions expressed in Equations (1.9) to (1.12) are to be found in numerical tabulations for compressible flow, for example that by the ARC (1952).

1.2 Incompressible Flow.

Air is a compressible fluid, it may nevertheless be treated as incompressible when the velocity is small compared with the speed of sound. To do so has a number of advantages: it is valuable for illustrative purposes because of the simple forms taken by flow relationships, it is fundamental to low-speed wind-tunnel testing and it is a satisfactory basis for the assessment of many practical subsonic intakes. We shall make considerable use, therefore, of the assumption of incompressible flow, particularly in Chapter 2 which deals exclusively with intakes for subsonic aircraft.

It is important, however, to remember that incompressible airflow is only an approximation to the true airflow, an approximation which becomes exact only when the Mach number is zero. Probably the most useful property of incompressible flow is that expressed in Equation (1.4), namely that the dynamic pressure q is the simple difference between total pressure P and static pressure p. The divergence of this relationship from reality is expressed in equation 1.11: it amounts to about 6% at Mach 0.5, 17% at Mach 0.8 and 28% at Mach 1.0.

Formulae in compressible flow tend to be complicated even when defining simple quantities such as, for example, the pressure coefficient at a point. It is sometimes useful to be able to check the consistency of such formulae with their counterparts in incompressible flow. Now the assumption of incompressible flow implies that Mach number is effectively zero, even though velocity is not: these two statements are mutually

consistent only if the speed of sound, and therefore g, are assumed to be infinite see Equation 1.8. Hence a formula in compressible flow is converted to its incompressible flow counterpart by putting *M* equal to zero and g equal to infinity, remembering that the product g *M*2 is finite and non-zero and, by Equation 1.9, converts directly to velocity and pressure. A simple example, not involving Mach number explicitly, is provided by the compressible form of Bernoulli's Equation 1.6 which, on putting g = ¥ (infinity) converts immediately to the incompressible form at Equation 1.4.

1.3 Momentum Theorem

Use will be made from time to time of the momentum theorem, which is a statement of Newton's Second Law of Motion adapted to a continuum fluid. It may be stated thus: in steady flow the flux of momentum through a closed surface bounding a definite volume of fluid is equal to the resultant of the pressure integral over the bounding surface and the forces exerted by the fluid on any bodies within it. Three sets of terms are involved, momentum flux terms of the form $\int \rho V^2 \, dA$ (d*A* being an element of area of the bounding surface resolved in a streamwise direction), pressure integrals of the form $\int p \, dA$ and body forces *F*, say. The respective signs can be seen by reference to Fig. 1.1. Where flow is entering the bounding surface, the momentum term corresponds to a force in the same direction while the pressure term corresponds to a force opposing the flow direction. The converse applies where flow is leaving the surface. If the resultant force on an enclosed body (or bodies) is reckoned positive downstream, then the theorem states that

$$\int_B \rho V^2 dA = -\int_B p dA + F$$

or

$$F = \int_B (p + \rho V^2) \, dA \qquad (1.13)$$

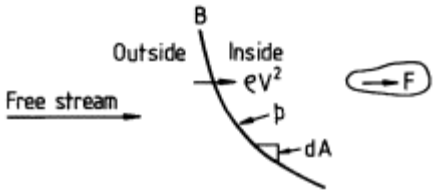

Figure 1.1
Section of bounding surface
B for momentum theorem.

This is the general form of relationship between the three sets of terms. The quantity in brackets is sometimes referred to as the *total momentum.*

The bounding surface must lie wholly within the fluid. It may be chosen in different ways; for instance it may be made to coincide with part of the surface of a body and thereby isolate the pressure integral on that part; or it may be selected in such a way that the pressures on the surfaces are known so that either the force *F* is directly determinable or the level of outgoing momentum can be found.

The theorem is true for dissipative systems, that is where there is a loss of total pressure between the flow entering the bounding surface and leaving it. Equally of course the theorem is applicable to systems involving total pressure gain, as will be seen in considering definitions of engine thrust (Chapter 9). For a derivation of the momentum theorem from first principles, reference may be made to standard accounts such as that of Liepmann and Roshko (*loc. cit.*). A more detailed description, illustrated in the context of engine thrust, has been given by Küchemann and Weber (1953).

1.4
The Aerodynamic Duct Concept

The problem of air intake design is to ensure that an aircraft engine is properly supplied with air under all conditions of aircraft operation and that the aptitude of the airframe is not unduly impaired in the process. To see the nature of this problem in aerodynamic terms, we introduce the concept of an aerodynamic duct, illustrated in Fig. 1.2. The duct 'captures' a certain streamtube of air, thus dividing the airstream into an internal flow and an external low, as indicated. The internal flow has the positive duty of feeding the engine; to the external flow falls the task of preserving the good aerodynamics of the airframe. The basic shape of the duct is important: since an engine requires to take in its air at a moderate subsonic speed, that is at a speed lower than the principal aircraft flying speed (whether the latter is subsonic or supersonic), the front part of the duct, or intake proper, is in the form of a diffuser, increasing in area from the entry to a position representing the engine face. The rear part of the duct is then convergent, simulating in essence the engine nozzle system.

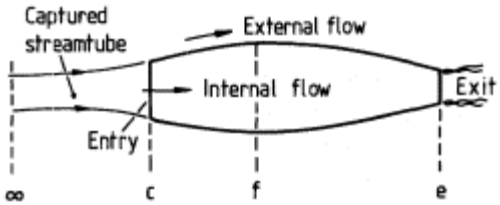

Figure 1.2
Aerodynamic duct in an airstream.

Principal stations in the flow are indicated in Fig. 1.2; these are as used throughout the book. Station ¥ is in the undisturbed flow, or free stream, ahead of the duct, station c is at the duct entry, station f is at the engine-face position and station e is at the duct exit. The internal cross-sectional area at station f, *A*f, is fixed by the engine size; entry area *A*c is a first item of choice for the intake designer. Further such items relate to the shapes to be put on to the walls of the duct both internally and externally. All these items will vary with the type of aircraft, location of the engine, whether the aircraft is subsonic or supersonic and so on.

In some respects the aerodynamic duct is an annular analogue of the 'two-dimensional' aircraft wing, the internal and external surfaces of the duct corresponding respectively to the lower and upper surfaces of the wing. We shall find the analogy useful in the development of our subject: one obvious area is in the design of supercritical cowl profiles for high subsonic aircraft (Chapter 9), where the methods used are essentially annular developments of those devised for supercritical wings. For the most part, however, the specialised use to which the duct internal flow is put necessitates that in the intake problem the internal and external flows are given separate consideration and are brought together only in the process of determining a final design compromise.

1.5 Flow Quantity through an Aerodynamic Duct

Given an aerodynamic duct in a uniform airstream, a basic question is: how much flow goes through the duct and what controls this? Is the flow quantity determined by the size of entry (*A*c), the maximum area (*A*f), the size of exit (*A*e) or details of the engine when installed? Experience shows that the answers have not always been well appreciated.

We consider first the empty duct in a subsonic stream. In one-dimensional flow terms, continuity of mass flow demands that:

$$\rho_\infty V_\infty A_\infty = \rho_c V_c A_c = \rho_f V_f A_f = \rho_e V_e A_e \qquad (1.14)$$

The considerations are simplified if we first assume incompressible flow. Then r is constant and the continuity relations become

$$V_\infty A_\infty = V_c A_c = V_f A_f = V_e A_e \qquad (1.15)$$

Writing

$$P_\infty - p_e = (P_\infty - P_e) + (P_e - p_e), \qquad (1.16)$$

the second term on the right is, by Bernoulli's theorem, the dynamic pressure at exit, *q*e; while the first term on the right represents the change in

total pressure of the internal flow D*P*, say, which for convenience will be reckoned positively as a loss, that is when *P*e is lower than *P*¥. Dividing Equation (1.16) throughout by *q*¥ and rearranging, leads to:

$$q_e/q_\infty = (P_\infty - p_e)/q_\infty - \Delta P/q_\infty = 1 - (p_e - p_\infty)/q_\infty - \Delta P/q_\infty \quad (1.17)$$

The second term on the right is the static pressure coefficient at exit, *Cpe* say. We make an assumption corresponding to that of the Joukowski condition for wings, namely that the flow leaves the duct trailing edge smoothly: it follows that the static pressures are equal in the internal and external flows on the two sides of the edge. Now the external static pressure is not known, and in practice would depend on the details of a particular installation, but general considerations of streamlining imply a pressure not greatly different from that of the free stream at infinity, so the value of *Cpe* may be expected to be small in comparison with unity. Next, concerning the last term in Equation (1.17), the loss of total pressure in the duct will depend on internal velocity in something like a *V*2 proportionality. For the present approximation we assume D*P* to be a constant *k* times *q*f (chosen because station f relates to a fixed area in the duct), which can then be written as *kq*e *times* (*A*e/*A*f)2 from Equation (1.15). Equation (1.17) now becomes

$$(1 + kA_e^2/A_f^2)q_e/q_\infty = 1 - C_{pe} \quad (1.18)$$

from which the throughflow, expressed by the capture stream tube area *A*¥ and using 1.15 is given as

$$A_\infty/A_e = V_e/V_\infty = (q_e/q_\infty)^{\frac{1}{2}} = [(1 - C_{pe})/(1 + kA_e^2/A_f^2)]^{\frac{1}{2}} \quad (1.19)$$

Equation 1.19 shows that for incompressible conditions the flow quantity through the empty duct is determined primarily by the exit area *A*e. In particular there is no dependence on entry area: the flow at entry adapts to the value determined by the exit. A larger entry would take the same flow quantity at a lower velocity; conversely a smaller entry would take the same flow quantity at a higher velocity.

If the exit area is assumed to be varied by some means, for example by a translating plug, the characteristic of flow quantity in terms of exit area is of the form shown in Fig. 1.3. For small *A*c, the term *kA*e2/*A*f2 is necessarily small, the slope of the curve near the origin is therefore approximately (1 *Cp*e)1/2 which itself is not greatly different from unity, so the duct captures a streamtube area approximately equal to the exit area. As *A*e increases, the loss term *kA*e2/*A*f2 becomes progressively more significant and if the process of increasing *A*e could be continued indefinitely without affecting in

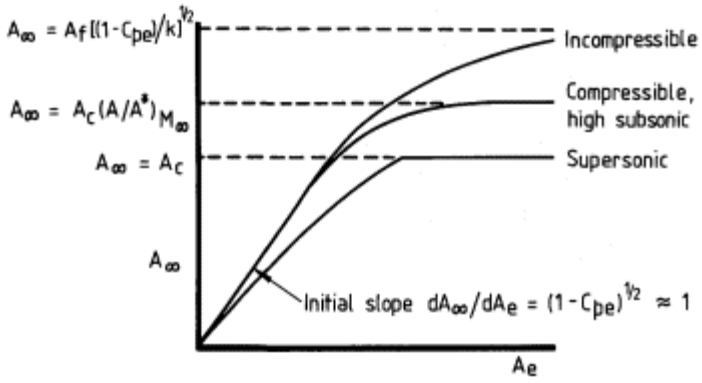

Figure 1.3
Types of variation of capture area with exit area.

a major way the values of either *k* or *Cp*e (in practice there would be limitations to this) the flow quantity would ultimately be limited by the loss term, the formal asymptotic value from Equation (1.19) being

$$A_\infty = A_f \left[(1 - C_{pe})/k\right]^{\frac{1}{2}} \qquad (1.20)$$

The foregoing arguments may be applied to compressible subsonic flow, with results which up to a point are different only in degree, not in kind, from those for incompressible flow. The exit area *A*e is again the principal determinant of flow quantity, for a range of values of capture area *A*¥ from zero to the entry area *A*c and somewhat above. Once the capture area is greater than entry area, however, the flow has to accelerate from free stream into the entry; a point will be reached therefore when the Mach number at entry becomes unity, so that the entry is choked and can accept no further increase. Clearly this occurs when the ratio *A*¥/*A*c is equal to the sonic area ratio *A/A** see Equation 1.12 corresponding to the particular free stream Mach number. A limit of this kind is indicated in principle in Fig. 1.3.

When the main stream is supersonic both the exit pressure and the loss term require fundamental reconsideration; the former may be complicated by the existence of a shock system at the duct exit, with which would be associated a difference between internal and external static pressures, while the loss term must now include an allowance for shock loss in the intake. A primary dependence of *A*¥ upon *A*e remains for small flows, the slope d*A*¥/d*A*e however being reduce *ab initio.* Also for this case it can be shown that the capture area cannot exceed the entry area, so the cut-off in flow quantity is a stage more severe than for compressible subsonic flow. These features are shown in a typical curve included in Fig. 1.3.

In general then, the flow quantity through an aerodynamic duct, without engine, is expressible in the form

$$A_\infty = \text{fn.}(A_e, \Delta P), \qquad (1.21)$$

the exit area *A*e being the primary parameter at least over a certain range. With an engine installed the essential difference is that a temperature term must be included, so that

$$A_\infty = \text{fn.}(A_e, \Delta P, \Delta T) \qquad (1.22)$$

Note also that in this condition D*P* may represent an increase in total pressure overall rather than a loss as previously. Again the exit area is the primary control, at least for small flows, though the control exercised by the engine, and expressed within D*P* and D*T*, may be a more influential factor than the loss term alone in the case of the empty duct.

1.6
Intake Pressure Recovery

In high-speed flight an air intake is a form of compressor; it accepts air initially at free stream Mach number and pressure and converts it to lower Mach number and correspondingly higher pressure, as required by the engine. The process is illustrated in pressure terms in Fig. 1.4. Static pressure, initially *p*¥, rises to a value *p*f; total pressure, initially *P*¥, falls to a value *P*f. If the flow at station c is uniform, *p*f and *P*f are related to the Mach number *M*f by Equation (1.10).

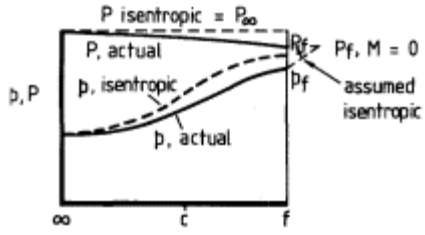

Figure 1.4
Process of intake pressure recovery.

The most natural definition of efficiency for the process is

$$\eta_\sigma = \frac{\text{Work done in compression}}{\text{Kinetic energy available}} \qquad (1.23)$$

which, for compressible flow, would be

$$\eta_\sigma = \sigma\left[\left(\frac{p_f}{p_\infty}\right)^{(\gamma-1)/\gamma} - 1\right] \Big/ \frac{\gamma-1}{2}(M_\infty{}^2 - M_f{}^2) \qquad (1.24)$$

Sensitivity to a particular value of *M*f is avoided by assuming that from the state reached at station f the compression is continued isentropically to zero velocity see Fig. 1.4 so that *p*f becomes equal to *P*f and the denominator in Equation (1.23) represents the total kinetic energy initially available. This yields a definition in terms of the total pressure achieved and the free stream conditions, viz.

$$\eta_\sigma = \left[\left(\frac{P_f}{p_\infty}\right)^{(\gamma-1)/\gamma} - 1\right] \Big/ \frac{\gamma-1}{2} M_\infty{}^2 \qquad (1.25)$$

For incompressible flow the expression reduces to

$$\eta_{\sigma i} = (P_f - p_\infty)/q_\infty \qquad (1.26)$$

which is a convenient and useful definition for low-speed work.

At high free-stream speeds, and particularly for supersonic flow, a more convenient measure of efficiency than Equation (1.25) is the simple total pressure ratio:

$$\eta_p = P_f/P_\infty \qquad (1.27)$$

The correlation between definitions (1.25) and (1.27) is given by:

$$\left(1 + \frac{\gamma-1}{2} M_\infty{}^2\right) \eta_p{}^{(\gamma-1)/\gamma} = 1 + \frac{\gamma-1}{2} M_\infty{}^2 \eta_\sigma \qquad (1.28)$$

This relationship is illustrated in Fig. 1.5. It is seen that as *M*¥ tends to zero, the value of h*p* tends to 1.0 for all values of hs .h*P* is thus a non-discriminating, hence impracticable, form for use with incompressible flow.

In summary, whilst Equation (1.25) expresses a formally correct measure of efficiency, in practice it is more convenient to use either Equation (1.26) or Equation (1.27), the former if working in terms of incompressible flow and the latter at all other times. This is the method adopted throughout the book. The efficiency as defined by either equation is termed the *pressure recovery* of the intake.

A shortfall in efficiency emerges as a loss of total pressure from the free stream value. If the loss is denoted by D*P* we have

$$\eta_{\sigma i} = 1 - \Delta P/q_\infty \qquad (1.29)$$

and

$$\eta_P = 1 - \Delta P/P_\infty \qquad (1.30)$$

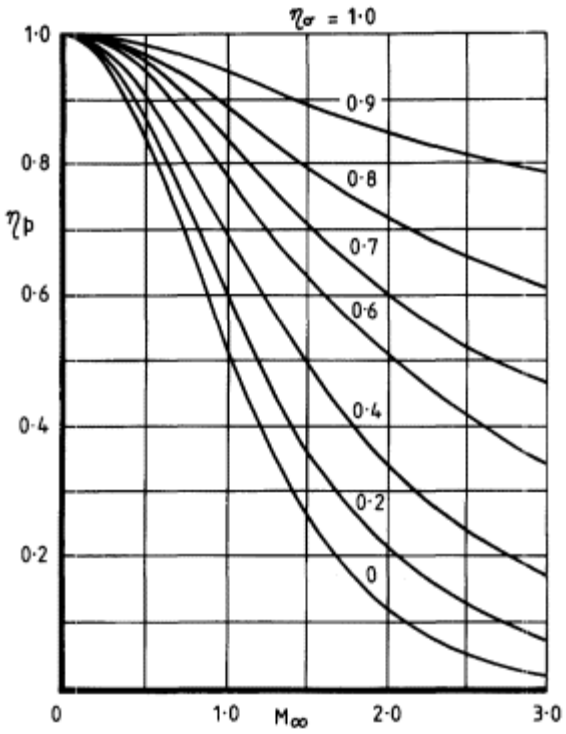

Figure 1.5
Relationship between hs and hp.

The effect of pressure recovery on engine thrust depends on the characteristics of the engine. It is assumed usually that loss of total pressure in the intake is translatable directly to loss of engine thrust by a relationship of the form:

$$\Delta X/X = K.\Delta P/P_\infty \qquad (1.31)$$

where X is written for thrust and K is a factor the value of which depends on the type of engine but is greater than unity and generally closer to 1.5. On this basis the conversion factor in incompressible flow terms depends on free stream Mach number in the form:

$$\Delta X/X = K(q_\infty/P_\infty).\Delta P/q_\infty \qquad (1.32)$$

Rounded values of $q¥/P¥$ are 0.15 for Mach 0.5, 0.29 for Mach 0.8 and 0.37 for Mach 1.0. A rough and ready approximation to Equation (1.32), adequate for most practical purposes in the range of flight speeds Mach 0.5 to 1.0, is:

$$\Delta X/X = 0.35KM_{\infty}.\Delta P/q_{\infty} \qquad (1.33)$$

Loss of total pressure can occur in any of three ways:

(a) by friction on the walls of the duct and on any external surface which is wetted by flow going into the duct;

(b) from turbulent mixing, associated with flow separation or near-separation;

(c) in shock waves.

The potential significance of source (b) is a feature to be noted in the subject of intake aerodynamics. Since the internal flow is normally being retarded as has been described, boundary layers in the duct and on forward surfaces are all subjected to adverse pressure gradients, which is the classical condition for the creation of flow separation and turbulent mixing. Going further, the interaction of a boundary layer and a shock wave is a particularly severe form of the same flow situation. Historically, most of the development problems of practical intakes have been attributable in one way or another to the behaviour of the boundary layer in this hostile environment. Boundary layer effects are therefore given considerable attention in the present treatment of the subject.

1.7
Intake Drag:
Compromise in Design.

A practical intake design involves many compromises, one of which is that between pressure recovery and intake drag. Pressure recovery, as has been stated, has a determining effect upon engine thrust, which latter in fluid-mechanical terms may be defined descriptively as the resultant force in the direction of flight produced on the aerodynamic duct system by the internal flow. Intake drag correspondingly is the resultant force, opposing the direction of flight, produced on the aerodynamic duct system by the external flow. A number of qualifications are to be noted:

(a) There are several ways in which the thrust of an engine, as installed in an aircraft, may arguably be defined. The more important of these are discussed in Chapter 9. The choice is a matter of convenience but the point to be noted here is that the definition of drag must correspond to that of thrust, so that all air forces on the aircraft, internal and external, are accounted for once and once only. It will be shown in Chapter 9 that the generally accepted definition of thrust leads to the inclusion of an important term in the intake drag known as *pre-entry drag* in U.S. terminology *additive drag.*

(b) In many installations, such as where intakes are located on the sides of an aircraft fuselage or in the wing roots, the capture stream tube may be in contact with an external surface ahead of the entry, creating a boundary layer which then passes wholly or partially into the intake. Degradation of total pressure occurring in this way has a direct effect on pressure recovery, hence on engine thrust, and so is part of the internal flow account. If, however, the air thus wetting a forward surface is diverted from the intake by a bleed duct or other device, accounting for the loss of total pressure becomes a part of total drag. Bleed drag is an item to which attention is given in Chapter 8.

(c) Whilst it is of course total aircraft drag which in steady level flight balances engine thrust, this book is concerned only with drag items which are special to the intake problem: these are pre-entry drag, bleed drag and cowl drag. Cowl drag is the pressure drag created on the cowling around the intake the external shaping of the fore part of the aerodynamic duct which is a function both of its shape and of its relation to the capture streamtube.

(d) In wind-tunnel model testing the engine is not usually represented: the internal flow undergoes only a loss of total pressure corresponding to the pressure recovery assessment. This is in effect an *internal drag* of the model and must be assessed as such in order to deduce the relevant *external drag* from a measurement of total drag force on the model (as is discussed in Section 15.4.2). Internal drag is calculated from pressure measurements by an application of the momentum theorem.

An initial glimpse can be obtained at this stage of the general nature of the compromise problem between pressure recovery and drag. Fig. 1.6 illustrates this by showing typical (though hypothetical) variations of Mach number of the internal flow, one-dimensional flow being assumed, in its progress from station ¥ to station f. Three kinds of intake, in simple aerodynamic-duct form, are used for the illustration, these being appropriate to flight Mach numbers around 0.8, 1.4 and 2.0 successively. It is assumed that the Mach number required at engine face is the same, around 0.4, for all cases. The following points are to be noted:

(1) For subsonic design, an entry area intermediate between *A*¥ (known from the engine flow requirement) and *A*f is chosen: this produces a smooth deceleration of flow from *M*¥ to *M*f. In the absence of an external wetted surface see point (b) above the compression up to station c will be 100% efficient: this argues in favour of a large entry area restricting the amount of internal diffusion, station c to station f, to a safe minimum; but the need to have a well-faired cowl giving low drag imposes a restriction on the size of entry that can be used. If an

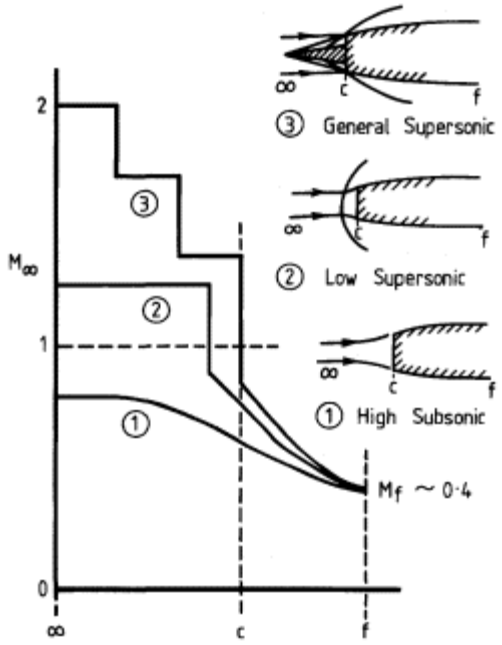

Figure 1.6
Nature of flow retardation for subsonic,
transonic and supersonic intakes.

external wetted surface is present, a still smaller entry area will normally be needed in order to reduce the amount of deceleration hence the strength of adverse pressure gradient associated with it.

(2) At supersonic speeds low enough for a normal-shock system to be used (this situation is developed in Chapter 5), the normal shock provides a first stage of flow retardation and compression. The choice of entry area determines the shock position ahead of the entry and the amount of (subsonic) compression taking place between shock and entry must be restricted in order to avoid high pre-entry drag. A choice of *A*c equal to *A*¥ would allow the shock to stand across the entry face, thereby eliminating pre-entry drag, but the problem of internal subsonic diffusion is thereby made more difficult than with a larger entry.

(3) A more common form of supersonic intake, typified by the Mach 2 design, has a staged supersonic compression involving oblique shocks and a weak terminal normal shock (see Chapter 5). Entry area *A*c is now chosen to be equal, or very nearly equal, to the capture area *A*¥ in order to restrict both pre-entry drag and cowl drag. This intake therefore probably has the most acute problem of the three as concerns the internal subsonic diffusion. By and large the difficulty of

achieving a satisfactory compromise between pressure recovery and drag increases as M_∞ increases.

In the last few paragraphs we have begun to touch on a number of subjects which require to be developed properly in an orderly succession. Also it needs to be recognised that the pressure recovery and drag compromise is only one of several aspects which have to be studied in the process of designing an efficient modern air intake. It is time therefore to proceed to a systematic and detailed consideration of all these aspects.

References

ARC (1952) *A selection of tables for use in calculations of compressible airflow.* Oxford: Clarendon Press.

Fabri, J. (ed.) (1958) *Air intake problems in supersonic propulsion.* AGARDograph 27, Pergamon Press Ltd.

Hermann, R. (1956) *Supersonic inlet diffusers and introduction to internal aerodynamics.* Minneapolis Honeywell Regulator Company, Minnesota, USA and Toronto, Canada.

Küchemann, D. and Weber, J. (1953) *Aerodynamics of Propulsion.* New York: McGraw-Hill.

Liepmann, H.W. and Roshko, A. (1957) *Elements of Gasdynamics.* New York: John Wiley; London: Chapman and Hall.

Chapter 2
Pressure Recovery of Subsonic Intakes

2.1
Introduction

Intakes on subsonic aircraft divide broadly into two categories, those for 'podded' installations and those for 'integrated' installations. Broadly again, though not necessarily, these relate to transport aircraft (civil or military) and combat aircraft respectively. With a podded installation, as on say the Airbus A340 (Fig 2.1), the internal flow has the shortest and most direct route possible to the engine and its pressure recovery is almost one hundred per cent. A problem of shock waves may exist if the internal shaping of the cowl is such as to induce local supersonic velocity, and this is discussed in Chapter 4. Generally though, the significant problems of this type of installation relate to the external flow and concern the external cowl shaping and how it merges either to the aircraft wing or fuselage. External aerodynamics are treated in Chapter 9.

With an integrated installation, however, as on the British Aerospace Harrier (Fig. 2.2), the internal flow problems of the intake are of more dominant concern, owing to (a) the duct being longer, usually containing bends and shape changes and (b) the presence of aircraft surface ahead of the intake, wetted by the internal flow. In the present chapter the problem of pressure recovery is approached from this more complex side. Based on the study of wind-tunnel model results, an approximate theory is devised to take into account the effects of (a) and (b) above. Suitable presentation of the characteristics enables ready assessment to be made of the extent to which a particular design shows the undesirable effects of flow separation. Special cases, to which the theory can be applied only with some addition or modification, are described. A particular problem of flow stability with twin intakes is discussed and a section on helicopter intakes is included. In order to facilitate the presentation of essential fluid dynamical characteristics, the terms of incompressible flow are used throughout.

Figure 2.1
Airbus A340.

Figure 2.2
British Aerospace Harrier GR7 in hovering flight with its auxiliary air intakes open.

2.2
Collected Data

The approach to a formula for intake loss is based on a collection of wind-tunnel and flight data presented in Fig. 2.3. Three categories of intake are shown, firstly direct or fully-ducted intakes, secondly intakes for plenum-chamber installations and thirdly intakes for propeller-turbine engines. It is obvious that the two latter categories have special features which set them apart from the direct intakes. These are each discussed separately later in the chapter. What is equally clear, however, is that for all three categories a major factor in determining pressure recovery is the degree to which aircraft wetted surface S in the diagram is present ahead of the intake. This is the basis of the treatment which follows.

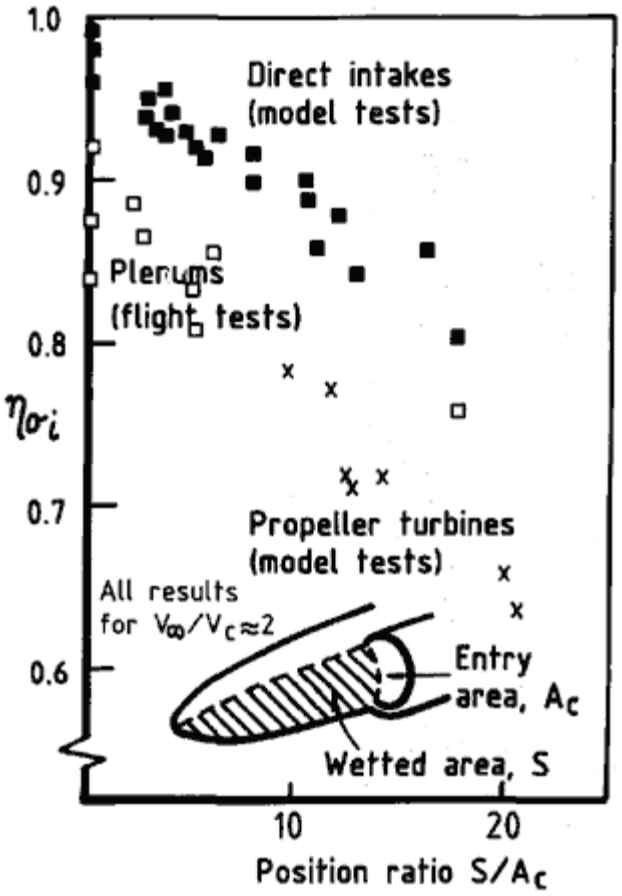

Figure 2.3
Collected data on pressure
recovery of subsonic intakes.

The definition of wetted area S is liable to be somewhat imprecise, since streamline patterns ahead of an intake are not usually known with precision. For practical purposes, however, it is sufficient to adopt the following definitions: for an intake on the side of the fuselage, S is taken to be the surface area between generators carried from the ends of the entry where it meets the surface to the foremost point of the fuselage nose: for an intake on the wing, S is taken to be the surface area between chordwise lines from the ends of the entry to the leading edge. For an intake in the wing root the two definitions have to be combined in as practical a manner as possible.

2.3
Approximate Theory of Friction Loss.

The following analysis was first given by Seddon (1952). It is assumed that for direct intakes, flow separations can be removed by careful design and wind tunnel tests, at least for the principal design condition, the high speed cruise. Therefore loss of total pressure is caused essentially by friction on the walls of the duct and on the approach.

We need to relate the friction force at any position to a change in total pressure. Figure 2.4 illustrates the flow in a streamtube with viscosity on the whole or part of the boundary. Inclination of the boundary of the streamtube to its axis is assumed small. F is the frictional force on an element of the boundary, that is on an area $g\,\mathrm{d}\ell$ where g is the local perimeter length along which the friction force is applied this may or may not be the complete perimeter at that station. F is therefore equal to $q\,C_f\,g\,\mathrm{d}\ell$, in which q is the local dynamic pressure, $\frac{1}{2}\rho V^2$, and Cf is the local friction coefficient.

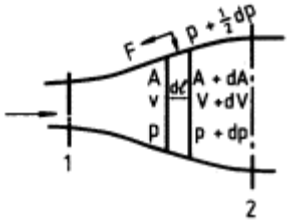

Figure 2.4
Streamtube with boundary viscosity.

Applying the momentum theorem to the streamtube element of initial area A gives:

$$\rho AV(V + \mathrm{d}V - V) = pA + \left(p + \frac{1}{2}\mathrm{d}p\right)\mathrm{d}A - (p + \mathrm{d}p)(A + \mathrm{d}A) - F \qquad (2.1)$$

whence

$$\rho AV\ \mathrm{d}V = -A\ \mathrm{d}p - F \qquad (2.2)$$

or

$$\mathrm{d}\left(p + \frac{1}{2}\ \rho \mathrm{V}^2\right) = -F/A \qquad (2.3)$$

that is to say

$$\mathrm{d}P = -F/A \qquad (2.4)$$

So if D*P* is written for the loss of total pressure, reckoned positively between stations 1 and 2 of the streamtube, we have

$$\Delta P = \int_1^2 F/A = \int_1^2 qC_f \frac{g}{A}\, d\ell \qquad (2.5)$$

Nondimensionally and using continuity (*AV* = *A*1 *V*1)

$$\frac{\Delta P}{q_1} = \int_1^2 \frac{q}{q_1} C_f \frac{g}{A}\, d\ell = \int_1^2 \left(\frac{A_1}{A}\right)^2 C_f \frac{g}{A}\, d\ell \qquad (2.6)$$

Therefore here we have an approximate expression for the loss of total pressure along a streamtube bounded wholly or partly by a solid surface, approximate because the assumption has been built in of uniform conditions of pressure and velocity at each station, that is to say of instantaneous mixing. The assumption, together with others to be made, is justified only by results.

Consider now the flow into an intake, represented diagrammatically in Fig. 2.5. The approach runs from $\ell = 0$ to ℓ_c, the duct from ℓ_c to ℓ_f.

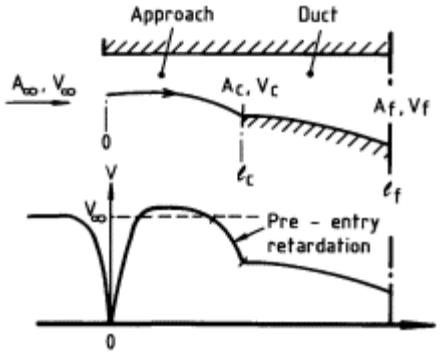

Figure 2.5
Representation of internal flow
with external wetted surface.

Referring the loss in total pressure to the dynamic pressure at entry, the formula at Equation (2.6) gives for the total intake:

$$\frac{\Delta P}{q_c} = \int_0^{\ell_f} \left(\frac{A_c}{A}\right)^2 C_f \frac{g}{A}\, d\ell \qquad (2.7)$$

which may be expressed as the sum of approach loss and duct loss, where

$$\text{Approach loss} = \frac{\Delta P_a}{q_c} = \int_0^{\ell_c} \left(\frac{A_c}{A}\right)^2 C_f \frac{g}{A}\, d\ell \qquad (2.8)$$

$$\text{Duct loss} = \frac{\Delta P_d}{q_c} = \int_{\ell_c}^{\ell_f} \left(\frac{A_c}{A}\right)^2 C_f \frac{g}{A}\, d\ell \qquad (2.9)$$

The two components are evaluated along different lines. On the approach surface the velocity varies in some such way as that indicated in the diagram. Since it is known from experimental evidence that the pre-entry retardation takes place in a short distance ahead of the entry and since also the effects of a stagnation region near the fuselage nose or wing leading edge and a region of excess velocity on the shoulder will tend to cancel, it follows that the situation on the approach may be approximated by the assumption of a constant velocity close to *V*¥. We may then write

$$\frac{\Delta P_a}{q_c} = \int_0^{\ell_c} kC_f \left(\frac{A_c}{A_\infty}\right)^3 \frac{g}{A_c}\, d\ell$$

$$= C_{Fa} \cdot \left(\frac{A_c}{A_\infty}\right)^3 k \frac{S}{A_c} \qquad (2.10)$$

where *C*F,a is the overall friction coefficient of the approach, *A*c/*A*¥ is the inverse of the intake flow ratio and S, which equals $\int g\, d\ell$, is the wetted surface area illustrated in Fig. 2.3. *k* is an empirical factor with a value close to 1.0, which can be taken to incorporate both the difference from *V*¥ of the assumed constant approach velocity and also any extent to which boundary layer on the approach may be diverted around the ends of the intake. Experience shows that *k* = 0.8 is a sufficiently good approximation for many practical cases. The factor *kS/A*c will be termed the *corrected position ratio* and represented by the symbol *J*. We have then for the approach loss

$$\frac{\Delta P_a}{q_c} = JC_{Fa} \left(\frac{A_c}{A_\infty}\right)^3 \qquad (2.11)$$

To evaluate the duct loss we consider first the implications of an experiment by H.B. Squire (1947). Squire measured the total-pressure loss in a series of conical diffusers of varying cone angle and found that while the average velocity decreased as cone angle increased, the *effective* overall friction coefficient increased owing to distortion of the boundary-layer profile in the adverse pressure gradient of the diffuser. Figure 2.6 gives a curve derived from Squire's results, expressing the effective friction coefficient in terms of the friction coefficient for a flat plate at the same Reynolds number, plotted as a function of cone angle. The Reynolds number is based on cone entry diameter.

Adapting this result to the intake duct, considered as a diffuser of arbitrary section shape and area variation, it is assumed that an effective

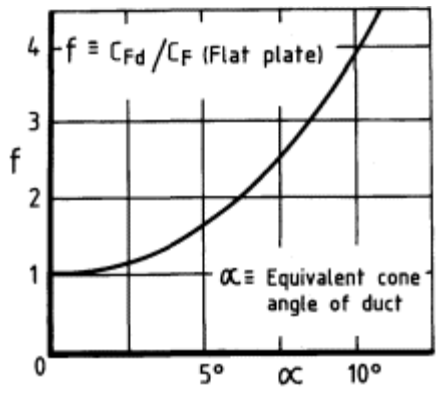

Figure 2.6
Effective friction coefficient in duct
deduced from experiments of Squire.

overall friction coefficient CFd can be defined as for the conical diffuser and is determined from Fig. 2.6 by taking a to be the equivalent cone angle of the duct, given by

$$\tan\frac{\alpha}{2}=\frac{2(g_c A_f - g_f A_c)}{g_c g_f(\ell_f-\ell_c)} \qquad (2.12)$$

and Reynolds number for the equivalent flat plate to be defined in terms of the hydraulic diameter at entry, so that

$$R_{eff}=\frac{4A_c}{g_c}\cdot\frac{V_c}{\nu} \qquad (2.13)$$

Then the duct loss from Equation (2.9) becomes

$$\frac{\Delta P_d}{q_c}=C_{Fd}\cdot\int_{\ell_c}^{\ell_f}\left(\frac{A_c}{A}\right)^2\frac{g}{A}\,d\ell = IC_{Fd} \qquad (2.14)$$

where

$$I=\int_{\ell_c}^{\ell_f}\left(\frac{A_c}{A}\right)^2\frac{g}{A}\,d\ell \qquad (2.15)$$

and is a purely geometrical function, readily evaluated for a duct of known shape. It will be referred to as the *duct integral.*

Summing up therefore, the total loss for a fully ducted intake emerges in the form

$$\frac{\Delta P}{q_c}=IC_{Fd}+JC_{Fa}\cdot\mu^3 \qquad (2.16)$$

in which the parameters *I* and *J* define the geometry of the duct and its approach, *C*Fd and *C*Fa are the respective effective friction coefficients and the symbol μ is now written for the inverse flow ration *A*c/*A*¥.

2.4
Examination of μ3 Variation

From the conditions for which it was derived, illustrated in Fig. 2.5, the loss formula at Equation (2.16) might be expected to apply for any flow ratio which involves pre-entry retardation, that is to say for values of *A*¥/*A*c between zero and 1.0. This means values of μ from 1.0 to infinity. In this context it is useful to examine a series of experimental results for wing leading-edge intakes at various angles of sweep: these are shown in Fig. 2.7 where it is seen that the loss calculated by Equation (2.16) agrees well with the experimental points for each sweepback angle. The μ3 variation is well substantiated for $\mu > 1$ and is seen to hold also for the few measurements made below $\mu = 1$, except in the extreme case of 52° sweepback. Here an upturn of the experimental variation marks the onset of additional loss from flow separation inside the outer lip of the entry as the approaching streamtube contracts in area corresponding to $\mu < 1$, that is *A*¥ > *A*c. This additional loss reaches a maximum in the ground running condition, $\mu = 0$, when the engine is being run at zero forward speed of the aircraft as at the start of take-off. Lip separation loss is discussed more fully, in Chapter 4; for the present we note that some upturn of the loss characteristic as μ decreases towards zero is an invariable feature of practical intakes.

For the calculations of Fig. 2.7 it has been necessary to vary the value of the empirical constant *k* as shown; and this requires explanation. Firstly, it is observed with a swept intake that the region of pre-entry retardation extends to the plane at which the duct first becomes fully closed: this plane therefore, namely the transverse plane at the rearmost point of the lip, is the effective entry plane. One result is that in the series shown the duct integral *I* decreases with increase of sweepback. A second consequence is that as sweepback is decreased, a progressively larger proportion of the pre-entry retardation occurs ahead of the sweptback surfaces, which is allowed for in the loss formula by decreasing the value of *k* approximately linearly with sweepback angle. The values of *k* tabulated in Fig. 2.7 represent for each case a compound between a fixed value 0.8 for the body contribution and a varying value for the contribution of the swept surfaces.

Normally the design point for high speed level flight, determined by sizing of the entry, lies in a range of μ values between about 1.4 and 2.0. We have seen that the μ3 variation can be well upheld in this range, implying that the losses are in fact purely those associated with boundary layer development. That this may not always be the case, however, is demon-

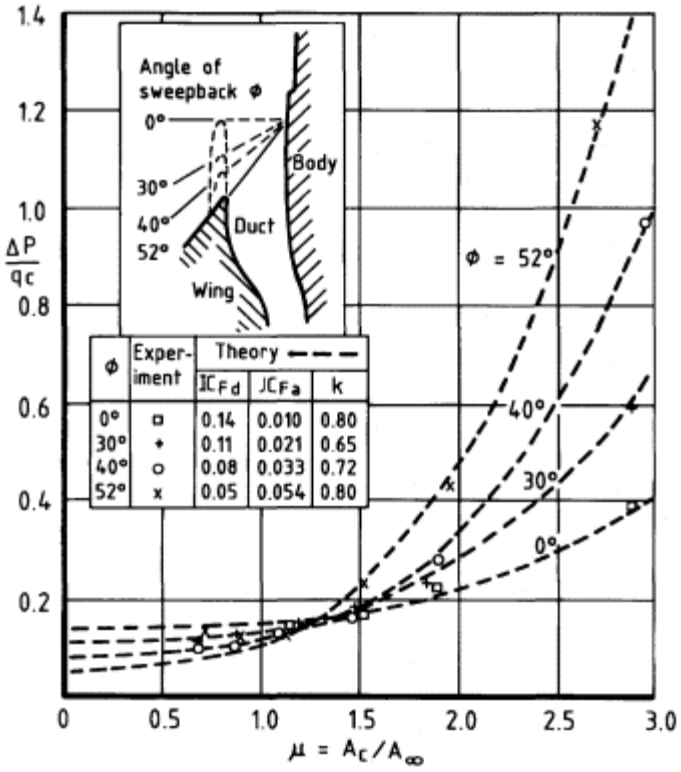

Φ	Experiment	Theory JC_{Fd}	JC_{Fa}	k
0°	□	0.14	0.010	0.80
30°	+	0.11	0.021	0.65
40°	○	0.08	0.033	0.72
52°	×	0.05	0.054	0.80

Figure 2.7
Loss in leading-edge intakes at various angles of sweep.

strated by a further series of tests made with the 52° swept intake and illustrated in Fig. 2.8. Here the body was replaced by a flat plate which could be clamped to the wing at various spanwise displacements from the inner sidewall of the intake. The length of plate forward of the wing leading edge was such as to give a boundary layer thickness at the leading edge position equal to one-eighth of the intake width a fairly extreme representation of body length, dictated by conditions of the experiment.

The results show that with the plate far removed spanwise from the intake, losses were given by the $\mu 3$ formula but departures from this occurred at increasingly low values of μ as the plate was brought closer to the intake wall. The departures were due to the occurrence of flow separation from the plate under the influence of the adverse pressure gradient accompanying pre-entry retardation. Put another way round these results illustrate a general principle, namely that with a subsonic intake having an external wetted surface (the approach), flow separation occurs above a certain value of μ, caused by the adverse pressure gradient accompanying pre-entry retardation, and the critical value of μ for this

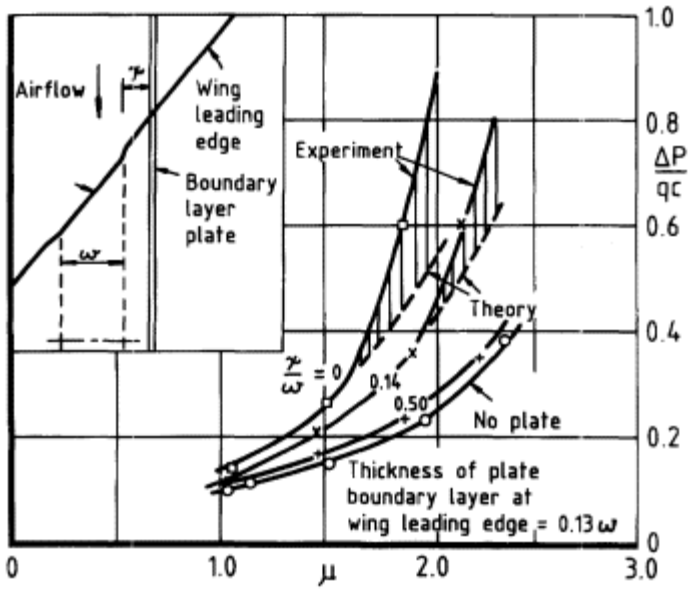

Figure 2.8
Illustration of pre-entry flow separation.

occurrence decreases with increase of the corrected position ratio. This important general result is the starting point for a study of transonic effects described in the next chapter, which in turn leads to significant results for supersonic intakes.

Some independent checks of the $\mu 3$ formula have been given by Küchemann (1953). One such, from a test by P. Ruden, is reproduced in Fig. 2.9. A thin flat plate was placed in the plane of symmetry of a two-dimensional intake, extending forward of the entry, thereby forming an approach surface. Results are shown for various extension lengths ℓ_1. They demonstrate that for values of μ around 2.5, for which the intake was designed, the measured and calculated results agree well. Some evidence of flow separation from the plate at high values of μ is seen in Fig. 2.9, similar to that in Fig. 2.8. Below $\mu = 2.5$ the additional 'ground running' loss described in Fig. 2.7 comes in early owing to the entry lips being sharp. This sharp-lipped profile is referred to again later in the context of external cowl design (Chapter 9).

A further check applied by Küchemann relates to the extent to which intake three-dimensionality affects the corrected position ratio. Defining intake aspect ratio as the span of the entry parallel to the wetted external surface divided by the height of entry normal to that surface, Küchemann quotes the case of an intake of aspect ratio 7.5 for which it was found that a value $k = 0.8$ defined the corrected position ratio satisfactorily for values of μ between 1.0 and 2.0 but for $\mu > 2$ a progressive reduction in k was required

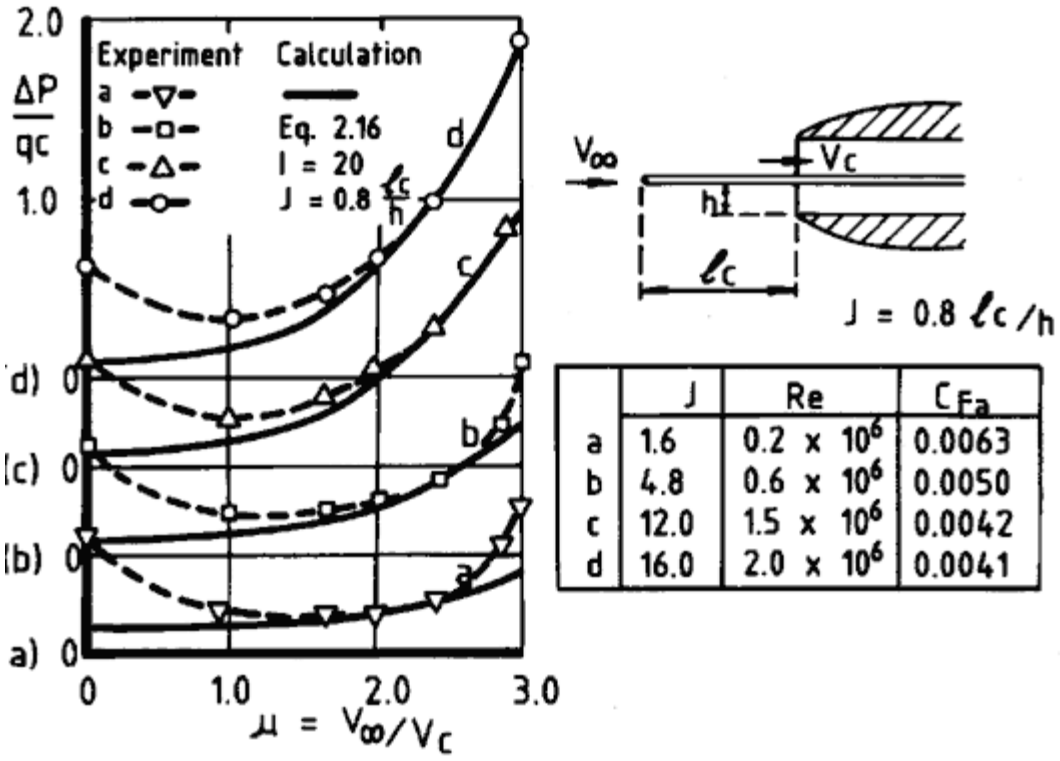

	J	Re	C_{Fa}
a	1.6	0.2 x 10^6	0.0063
b	4.8	0.6 x 10^6	0.0050
c	12.0	1.5 x 10^6	0.0042
d	16.0	2.0 x 10^6	0.0041

Figure 2.9
Comparison of Equation 2.16 with experimental results by Ruden.

(approximately $k = 0.7$ at $\mu = 2.5$ and 0.6 at $\mu = 3.0$). Clearly aspect ratio is not the only determining factor (body radius and entry shape are among others) but in default of specific evidence, such as that of the swept intake quoted earlier, it is best to assume that the value $k = 0.8$ applies adequately across the intake working range.

2.5
Pressure Recovery Characteristics

When the loss formula at Equation (2.16) is applied to the working range of an intake, a full presentation of pressure recovery characteristics takes the form shown in Fig. 2.10. Several points are involved, as follows:

(1) Use of the parameter μ as abscissa in preference to the direct flow ratio $A¥/Ac$ ($= 1/\mu$) enables the ground running characteristic ($\mu = 0$) to be examined on an equivalent basis with the flight performance. This can be valuable for ensuring that no unexpected fluid mechanical effects are present. The technique is practicable only for subsonic intakes.

(2) A comparison of measured loss coefficient with that calculated from Equation (2.16) reveals the extent of lip separation at low speeds and that of pre-entry separation at high speeds.

(3) Use of the entry dynamic head qc for non-dimensionalising the total-pressure loss is analytically convenient since it is relevant to both of the separate treatments of approach loss and duct loss. In terms of practical design, however, a different basis is needed in view of the fact

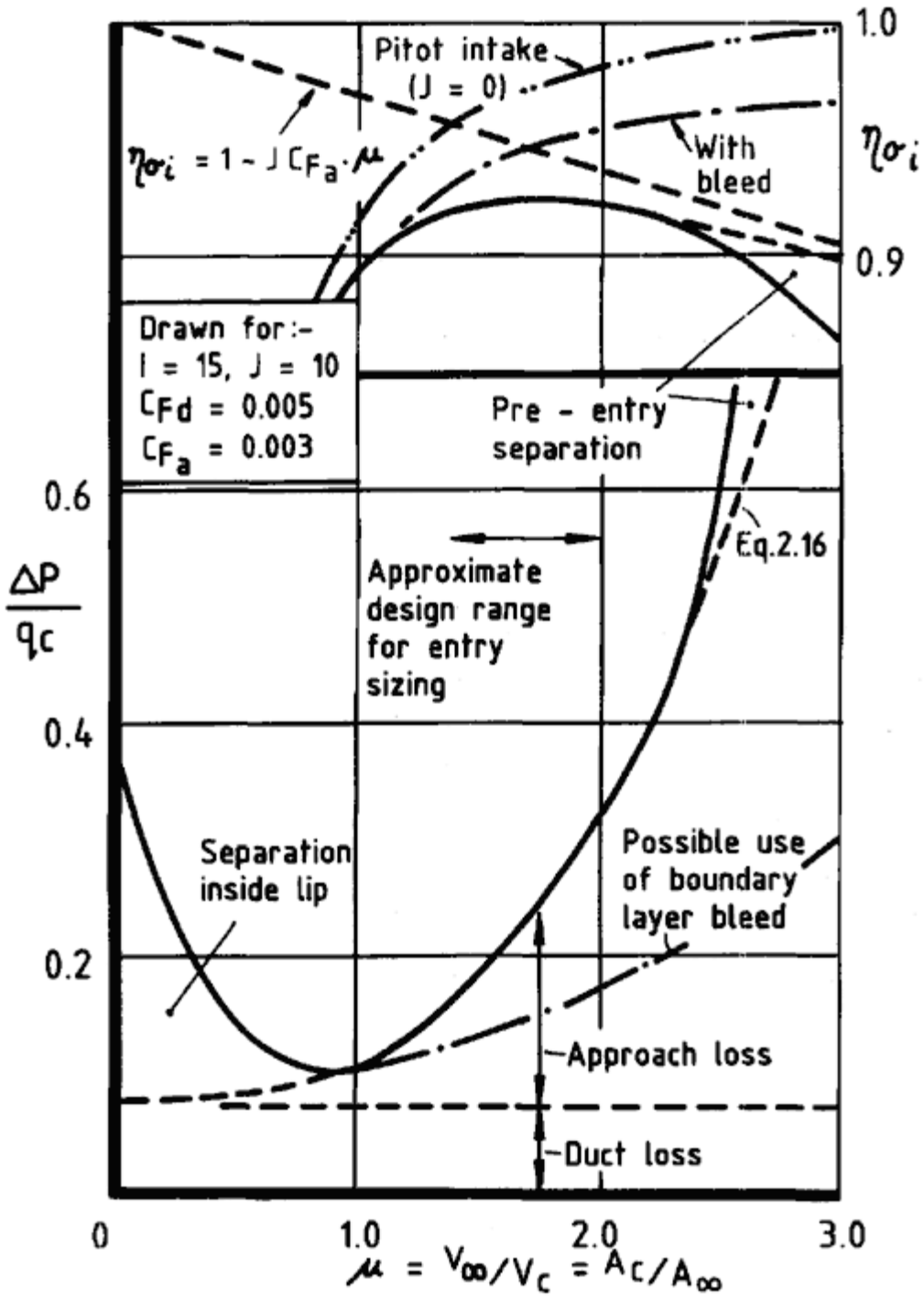

Figure 2.10
Loss and recovery characteristics for subsonic intakes.

that the entry area is an exploitable variable. When considering the high-speed design point it is usual to express the loss in terms of free-stream dynamic head and make use of the recovery factor hsi defined in Chapter 1. From Equation (2.16) and using continuity we have

$$\frac{\Delta P}{q_\infty} = IC_{Fd}\left(\frac{A_\infty}{A_c}\right)^2 + JC_{Fa}\left(\frac{A_c}{A_\infty}\right) = \frac{IC_{Fd}}{\mu^2} + JC_{Fa}\,\mu \qquad (2.17)$$

so that

$$\eta_{\sigma i} = 1 - \frac{\Delta P}{q_\infty} = 1 - \frac{IC_{Fd}}{\mu^2} - JC_{Fa} \cdot \mu \qquad (2.18)$$

< previous page page_27 next page >

(4) The recovery factor hsi is plotted in the upper half of Fig. 2.10. If there were no approach surface, this characteristic would tend to the value 1.0 as μ increased to infinity: the intake would then have no throughflow and would be a pitot tube registering free stream total pressure. More generally, if the loss characteristic follows the $\mu 3$ formula, hsi tends to the line 1 $J\,C$Fa.μ as indicated. This implies hsi passing through an optimum which, other considerations permitting, will be the design point target. For given values of I, J and the friction coefficients, the optimum hsi occurs when $\mu 3$ equals $2IC$Fd/JCFa, that is at the flow ratio

$$\frac{A_\infty}{A_c} = \frac{1}{\mu} = \left[\frac{JC_{Fd}}{2IC_{Fd}}\right]^{\frac{1}{3}} \qquad (2.19)$$

With the specimen values used in the diagram, this optimum flow ratio is 0.585 (or μ = 1.71). Entry size is normally chosen to give a design flow ratio in the range 0.5 to 0.8, values toward the higher end being needed the higher the corrected position ration J, as indicated by the formula in Equation (2.19). In practice a change of entry area involves changes in the geometrical parameters I and J as well as in the design point value of μ, so that a total reassessment has to be made.

(5) Approach loss, as we have seen, is the result of natural boundary layer development on the approach surface. It can be reduced below the values given by Equation (2.16) only if measures are taken to divert the boundary layer in some way from the intake. One such measure, for example, might be the use of a lip which stands the entry off from the approach surface in a manner as illustrated for the body boundary layer in Fig. 2.7. Another possible measure is the use of a suction slot or *boundary layer bleed.* Any such device if deployed successfully will lead to a reduce loss characteristic and an improved pressure recovery as indicated in Fig. 2.10. At the same time there is a necessary penalty in aircraft drag which should be taken into account. Boundary layer bleeds have increased importance at supersonic speeds: their use across the spectrum of intake design is discussed in Chapter 8.

(6) A form of intake which achieves a measure of diversion of the approach boundary layer is the NACA submerged intake devised by Frick, Davis, Randall and Mossman (1945). Distinctive features of this type, illustrated in Fig. 2.11, are (i) the entry is submerged within the general contour of a fuselage or wing and is approached by way of a long, gently-sloping ramp; (ii) the ramp is narrow at its commencement and has divergent sharp-edge sidewalls leading to the spanwise extremities of the entry. The action of this ingenious design is that the divergent sidewalls, cutting across the lines of flow, set up a vortex

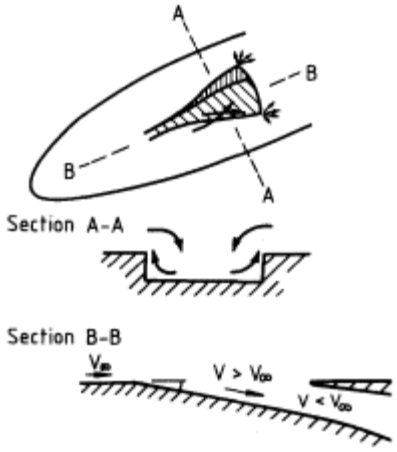

Figure 2.11
NACA submerged intake
(illustrative diagram).

motion which sweeps the ramp boundary layer sideways and carries a proportion of it past the ends of the entry and out into the external stream. Thus the ramp arrangement works as a form of boundary layer diverter, reducing the effective position ratio of the intake. Results can sometimes be enhanced by the addition of small ridges along the divergent sidewalls, increasing their effective height, and also by increasing the sidewall divergence to allow for slots at the ends of the entry, easing the passage of the boundary layer.

Success of the NACA submerged intake in application depends on practical considerations of layout, such as space to run the ramp at a sufficiently small angle (about 7º appears to be optimum) and on having some indication of the extent to which the boundary layer diverted from the intake adds to the drag of the aircraft. Because velocity, or Mach number, on the initial part of the ramp is higher than that of the free stream (see Fig. 2.11) the design is unsuitable for supersonic speeds and probably for high subsonic speeds also, except in the context of small auxiliary intakes.

2.6
Plenum Chambers

Referring back to the data collection in Fig. 2.3, we consider next the special feature of plenum chamber installations. In the early days of jet propulsion these installations were appropriate to the then current engines which had front and rear inlets to centrifugal compressors. Although practically all jet engines now have axial compressors, the following analysis of the effect of

installing an engine downstream of a sudden enlargement in duct cross-section is still of interest.

The aircraft intake feeds directly into a plenum chamber. A typical layout is represented pictorially in Fig. 2.12. Practical space restrictions invariably dictate that (a) it is not possible to diffuse efficiently in the intake duct up to the full cross-sectional area of the plenum chamber, so that there is necessarily a sudden enlargement in area at the end of the duct, (b) velocities within the chamber itself are by no means negligible. So far as overall efficiency is concerned, there may of course be compensatory effects within the engine but we are dealing here only with pressure recovery up to the engine inlets.

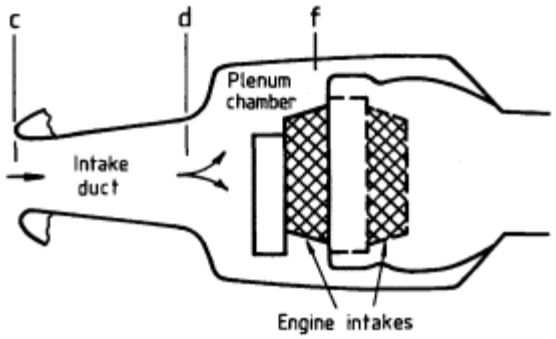

Figure 2.12
Plenum chamber installation.

Considering first the effect of the sudden enlargement, under uniform flow conditions in the duct this may be calculated readily by use of the momentum theorem. In Fig. 2.12, station f represents the enlarged cross-sectional area and station d the end of the duct proper, that is the start of the sudden enlargement. The pressure on the front wall of the chamber is pd and the momentum theorem determines that

$$(p_f - p_d)A_f + \rho V_d A_d (V_f - V_d) = 0 \qquad (2.20)$$

Dividing throughout by *q*d and replacing velocity ratios by area ratios from continuity leads to

$$\frac{(p_f - p_d)}{q_d} = 2\frac{A_d}{A_f}\left(1 - \frac{A_d}{A_f}\right) \qquad (2.21)$$

The loss of total pressure is, by definition,

$$\Delta P = (p_d + q_d) - (p_f + q_f) = (q_d - q_f) - (p_f - p_d) \qquad (2.22)$$

so that from (2.21),

$$\frac{\Delta P}{q_d} = 1 - \left(\frac{A_d}{A_f}\right)^2 - 2\frac{A_d}{A_f}\left(1 - \frac{A_d}{A_f}\right)$$

$$= \left(1 - \frac{A_d}{A_f}\right)^2 \qquad (2.23)$$

This is a general result for loss at a sudden enlargement with initially uniform flow. In the present real situation (Fig. 2.12) it has to be recognised that the flow at station d is not uniform but is characterised by a core of velocity higher than the mean, surrounded by a boundary layer which has developed in the adverse pressure gradient of the intake duct and may be close to separation. In an extreme case the flow may have separated in the duct before reaching station d. If the loss at Equation (2.23) is expressed in terms of the dynamic head at duct entry *q*c, giving

$$\frac{\Delta P}{q_c} = \left(\frac{A_c}{A_d}\right)^2 \left(1 - \frac{A_d}{A_f}\right)^2 \qquad (2.24)$$

it is readily seen that a modest reduction in *effective* area *A*d results in a large increase in the theoretical loss at enlargement. Thus, for example, with *A*d = 2 *A*c and *A*f = 4 *A*d, a 20% reduction in effective *A*d increases D*P*/*q*c by 78%.

The effect on total pressure loss of the second practical aspect mentioned, that of non-negligible velocities in the plenum chamber, is not generally quantifiable owing to the complex nature of blockages formed by the engine combustion chambers, accessories and pipework.

In Fig. 2.13 the flight test results of Fig. 2.3 have been plotted in a form suitable for comparison with the theoretical sudden enlargement loss. Friction losses in the intake duct have been subtracted according to Equation (2.16) and the residue is plotted against (1/*A*d)2 for constant airflow conditions. It is seen that the high additional losses experienced in the practical cases, ranging from 10% to 70% of free stream dynamic pressure, follow a similar general trend to the theoretical loss and are roughly speaking twice as great, a factor which the foregoing arguments show to be not unlikely.

The analysis shows that where plenum chamber loss is severe, the only effective measure is to increase the area of the intake duct at discharge, which probably means increasing the duct area throughout its length. This was done successfully in an experimental programme carried out by Rolls-Royce on the Meteor aircraft, some flight test results from which are shown in Fig. 2.14.

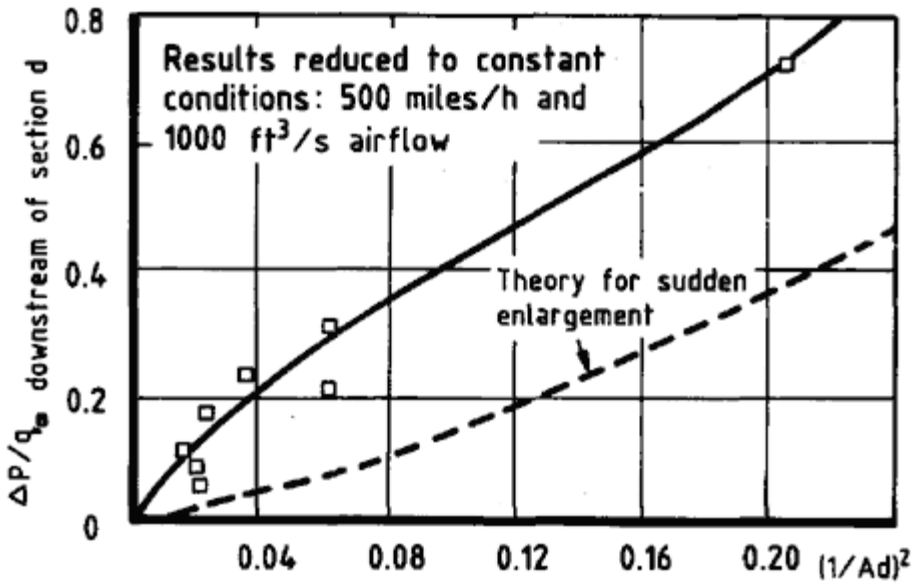

Figure 2.13
Collected data on plenum chamber loss from flight tests.

Although plenum chamber intakes are unlikely contenders for future jet aircraft installations, the general character of the results described is, however, of intrinsic interest and may also have practical relevance to other ducted systems involving sudden enlargements.

2.7
Propeller Turbines

A third category featured in the data collection of Fig. 2.3 is that of the propeller turbine intake. The interest is more than historical since propeller-turbine engines come under re-examination from time to time because of their potentially good fuel economy. The historically conventional arrangement is that of an annular intake located directly behind the propeller (Fig. 2.15). The data collection of Fig. 2.3 brings out the following features:

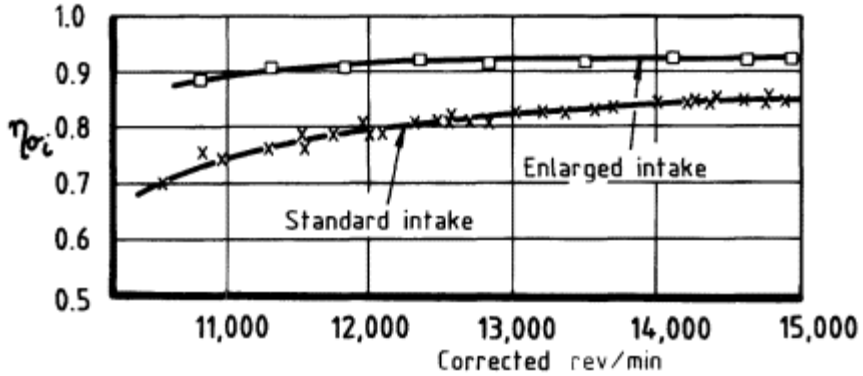

Figure 2.14
Flight results on Meteor with standard and enlarged intakes.

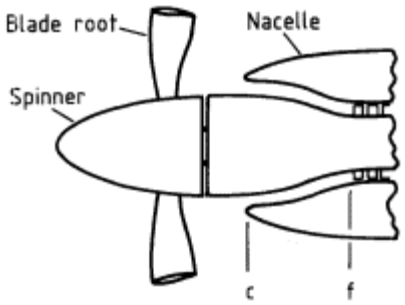

Figure 2.15
Propeller turbine intake.

(1) position ratio tends to be high and has the usual detrimental effect (it is calculated in this case on the total surface area of the spinner and fixed hub projecting forward of the annular entry);

(2) there is a large additional loss as compared with direct intakes, some 15% of free stream dynamic head at typical model Reynolds numbers.

Wind tunnel tests show that the additional loss is attributable to the presence of the propeller blade roots ahead of the intake. The flow over the roots, which are virtually non-lifting, is complicated in character because of the large thickness/chord ratio of the sections and the action of centrifugal forces on the boundary layer. A rough rule for estimating the blade root loss is

$$\frac{\Delta P_b}{q_\infty} = 0.6\,\frac{Nt}{2\pi r} \qquad (2.25)$$

in which N is the number of blades and t and r are respectively the profile thickness and radius of rotation of a representative root section, the latter being taken as the estimated mid-section relative to the intake airflow at the blade roots. Blade root loss DPb has then to be added to approach loss DPa and duct loss DPd to give the total intake loss.

The value of the empirical coefficient in Equation (2.25) is insensitive to changes in root thickness/chord over a considerable range. As a result there is little advantage to be gained from flared roots in which low thickness/ chord is obtained by increasing the chord. Blade development in the direction of producing thinner roots is a surer way of reducing the total-pressure loss.

An interesting phenomenon observed with the annular intake is that when pre-entry flow separation occurs it does so in localised patches rather than uniformly round the circumference. In other words there is a limiting

value of μ (the inverse flow ratio as previously used) above which circumferentially uniform flow cannot exist. The limit, as determined by wind-tunnel tests, is expressible by the approximate formula

$$\mu_{\text{lim}} = 1 + 1.8\,\frac{A}{LR} \qquad (2.26)$$

where A is the annular entry area, L is the length of projecting spinner and hub and R is its maximum radius. A breakdown of uniformity in the intake has a potentially detrimental effect both on total-pressure recovery and also on engine compatibility (see Chapter 11). The avoidance of pre-entry separation is therefore more important with an annular intake than with other forms so far discussed. The phenomenon is akin to that of flow inequality in twin intake systems, which is described in the next section of the present chapter.

An aerodynamically efficient propeller turbine intake can be achieved by use of a ducted spinner (Fig. 2.16). In a typical situation, several improvements are obtained. Choice of a suitably large entry area allows a major reduction in velocity over the blade roots. Minimum cylindrical roots are encased in fairings of low thickness/chord which form the structural members supporting the spinner cowl. The intake itself is converted into near pitot type (i.e. low position ratio) and the high design value of μ (following from the large entry area) implies by virtue of Equation (2.17) a low duct loss. In Fig. 2.16, wind tunnels results for a conventional annular intake with exposed blade roots and a ducted spinner designed for the same engine are compared. The advantage of the latter, at comparative design points, is 19% in hsi. The principal disadvantages of a ducted spinner are its weight and the difficulty of providing a satisfactory anti-icing system.

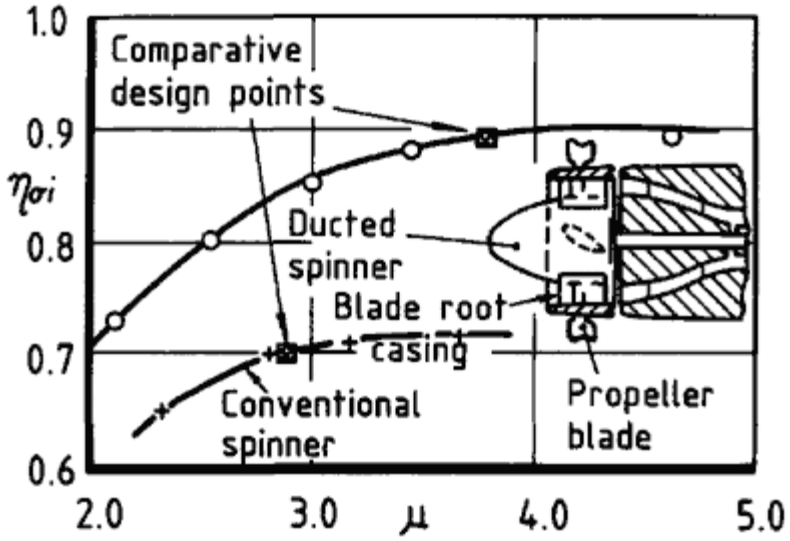

Figure 2.16
Ducted spinner for propeller turbine intake.

2.8
Flow Stability in Twin Intakes.

The term 'twin intakes' refers to a pair of intakes, for example in the wing roots or on the two sides of a fuselage, feeding a single engine via a common section of duct or a plenum chamber. Such a system has been known to cause aircraft vibration, accompanied by noise known as intake 'banging', during a high-speed dive or when throttling back the engine in level flight.

Wind tunnel tests have shown that as the intake mean flow ratio is reduced by some form of exit control, a critical point is reached below which unequal flows develop in the two intakes. On one side the flow begins to increase again while on the other side it falls rapidly to zero and even becomes negative. The asymmetry usually persists down to zero net flow, so that with the exit closed there remains a considerable inflow into one intake and a corresponding outflow from the other.

The phenomenon was first described by Martin and Holzhauser (1951) who showed it to be associated with a pressure recovery characteristic (in this case *static* rather than *total* pressure) in which a decrease of flow is accompanied by a decrease of pressure. If a small disturbance occurs from a steady state of equal flows in the two ducts, the movement of pressure in the section where the ducts join is such as to increase the magnitude of the disturbance. Thus the initial steady state is unstable and the flows in the two ducts diverge until a stable condition is reached in which the static pressures on the two sides are once more equal but one flow has increased above the critical value and the other has decreased accordingly. The mean total pressure corresponding to this new equilibrium state is generally lower than that for the initial state. The net result, as it affects the engine, is that as flow ratio is decreased through the critical value, the intake pressure recovery falls suddenly and, probably more significantly, the velocity distribution into the engine suffers a marked deterioration. Moreover if the flow oscillates between the two sides, as may reasonably be expected in unsteady flight conditions near the critical value, this may account for rapid pressure changes the banging effect and aircraft vibration.

The crucial condition, that of the 'unstable' pressure characteristic of the intake, is typical of an intake with high approach loss. It has been seen, for example in Fig. 2.10, that the total-pressure efficiency of such an intake has a maximum value; at μ values above the maximum (that is, at lower flow ratios) the characteristic is of the unstable kind. An illustration in terms of static pressure will help: also for this purpose it is convenient to use the direct flow ratio *A*¥/*A*c as abscissa in preference to the inverse ration μ. Fig. 2.17 shows results from wind tunnel tests of a pair of wing-root intakes. In the upper part of the diagram are plotted the variations of both total and

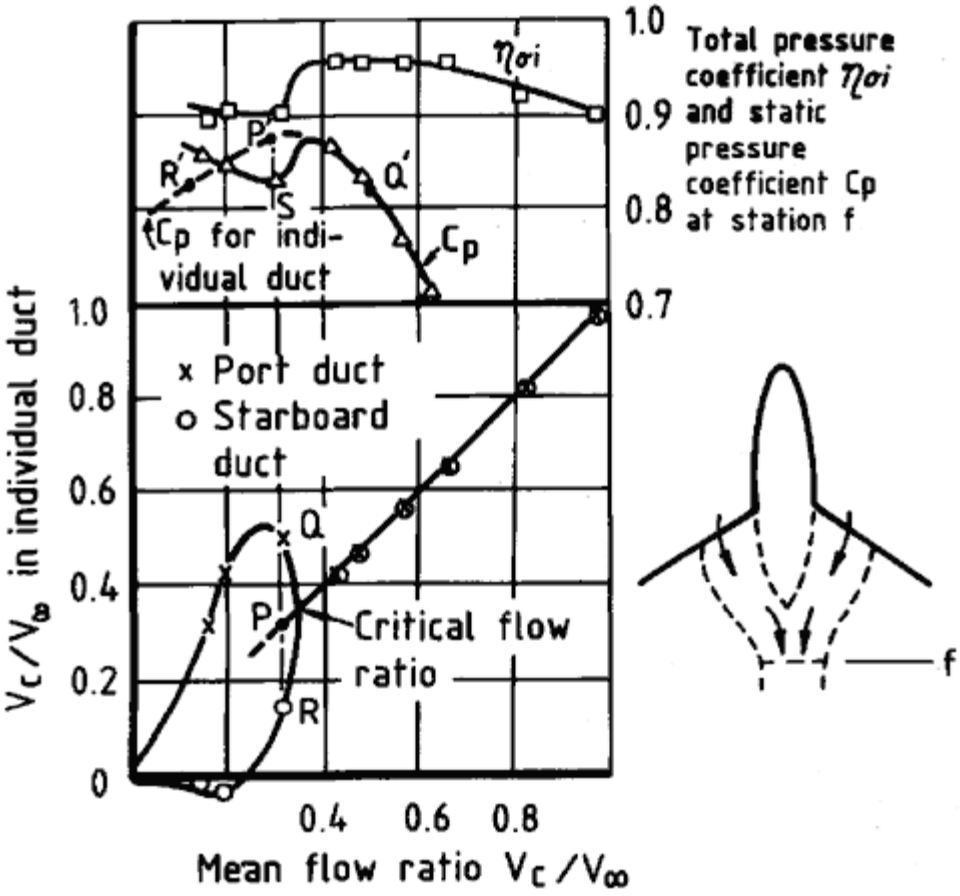

Figure 2.17
Wind tunnel results on flow in twin intakes.

static pressure at the junction of the two ducts (this was a smooth merging with no change in total cross-sectional area). The characteristics of an individual duct tested singly are shown dotted. In the lower part of the diagram the flow ratio measured for each duct of the paired system is plotted against the mean flow ratio of the pair.

Occurrence of a critical flow ratio, below which the flows in the two ducts diverge rapidly, is clearly shown. The critical value in this case is *A*¥/*Ac* = 0.34 and corresponds to the peak of the static pressure characteristic of the single duct. Both total and static pressure recovery of the twin system fall suddenly as mean flow is decreased through the critical. The situation just below critical is illustrated by means of marked points: a mean flow ratio 0.31 is obtained, not with equal flows as at *P* (static pressure at *P*') but with flows 0.48 as at *Q* in the port duct and 0.14 as at *R* in the starboard duct, the static pressure then being that at *S*, the same as for points *Q* and *R* in an individual duct.

From Equation (2.18) and Bernoulli's relationship between total and static pressure, it is readily seen that the static pressure coefficient *Cp* at station f (the duct junction, equivalent to engine-face position) is given by

$$C_p = \frac{p_f - p_\infty}{q_\infty} = 1 - \left[IC_{Fd} + \left(\frac{A_c}{A_f}\right)^2 \right] \left(\frac{A_\infty}{A_c}\right)^2 - JC_{Fa}\,\frac{A_c}{A_\infty} \qquad (2.27)$$

Maximum *Cp* according to this expression occurs when

$$\left(\frac{A_\infty}{A_c}\right)^3 = JC_{Fa}/2\left[IC_{Fd} + \left(\frac{A_c}{A_f}\right)^2\right] \qquad (2.28)$$

which, by inclusion of the term (*A*c/*A*f)2, is a flow ratio somewhat lower than that for maximum hsi. Factors which, by increasing this ratio, are conducive to the onset of flow inequality and the practical consequences thereof are:

(1) a high value of the corrected position ratio *J*; in a practical case this may call for the application of boundary layer suction or some other form of diverter;

(2) low *A*c/*A*f: a plenum chamber arrangement would therefore be particularly suspect.

Experience shows that if the dividing wall between the two ducts can be carried right to the face of the engine, the pressure equalizing function is transferred downstream to the compressor exit and the instability may thereby be prevented from developing.

2.9
Helicopter Intakes

Although the flight speeds of helicopters are usually much lower than those of fixed-wing aircraft, gas-turbine engines have nevertheless been adopted generally for helicopter propulsion. It is pertinent, therefore, to consider to what extent the air intakes for helicopters conform aerodynamically to their fixed-wing counterparts and wherein lie any essential differences.

The first point to be recognised is that the helicopter has its own set of priorities within the flight regime; in particular the intake must work well in prolonged hover, where loss of engine power needs to be kept to a strict minimum. By comparison, the loss of a small amount of thrust in cruise because of intake deficiency may not be highly important. A consequence of this situation, taking into account also the desired airspeed at entry to the engine, is that the intake is normally designed to have a contraction in area between entry and engine face. This greatly assists the achievement of low loss in the hover (see the section on ground running, Chapter 4), so that the intake loss characteristic, expressed as in Fig. 2.10, exhibits little or none of the upward turn towards zero forward speed which is characteristic of fixed-geometry intakes on fixed-wing aircraft.

A second determining factor is that the helicopter engine generally requires to be protected against ingestion of some or all of the many types of foreign matter which characterize its varied operational environments

ice, hail, sand, salt spray, birds, ground debris and others. Protection in some degree can be built into the engine design but to the extent to which this is not done, any protection needed must be provided by the intake. This consideration often dominates the intake design to the detriment of pressure recovery in the cruise. One measure frequently adopted is to use a sideways-facing intake, which provides a degree of protection by inertial separation of the foreign matter but gives of course a low pressure recovery at cruise.

Types of protection device which may be fitted either alternatively or additionally to a sideways-facing intake include, according to a review by Brammer and Rabone (1980), electrical surface heaters, wire mesh guards, solid deflectors and filter packs. For a particular operational role of the helicopter, adequate protection can normally be ensured. Comprehensive protection schemes are more difficult and generally require a combination of devices: such a combination might consist, for example, of a sideways-facing intake fitted with a filter pack at entry and backed up by an engine-incorporated particle separator.

Other practical factors operate in determining the intake layout and detail design. Engines mounted aft of the rotor axis require normally the use of side intakes (forward- or sideways-facing) incorporated with the fuselage superstructure and hence taking in aircraft boundary layer. The aft engine layout also results in the drive shaft to the gearbox an item of large diameter in relation to intake size having to pass longitudinally through the duct. The need to preserve ready access to any part of the transmission system can impose restrictions on intake shape and mode of construction. In some cases the outcome of all the practical considerations is an installation of plenum-chamber type.

It is seen from the foregoing that in aerodynamic terms the principal kinds of intake to be found on helicopters are (1) the pitot type, (2) the forward-facing side intake, (3) the sideways-facing intake and (4) the plenum chamber installation, which may be associated with any one of the other three forms. In all cases the loss characteristic, expressed as in Fig. 2.10 (lower part), is a minimum in the hover ($\mu = 0$) but the extent of increase with forward speed varies greatly among the types. This is best seen by comparing typical pressure recoveries as in Fig. 2.10 (upper part) which is done in Fig. 2.18 for the four intake types without protection devices. The pitot and side intake types have characteristics similar to their counterparts for fixed-wing aircraft. For the plenum-chamber installation assumed in this case to be used together with a forward-facing side intake the additional deficit in pressure recovery depends critically on internal details and can only be shown in principle, but it may be expected to decrease with increase of μ, emphasizing the need to use as large an entry size as possible.

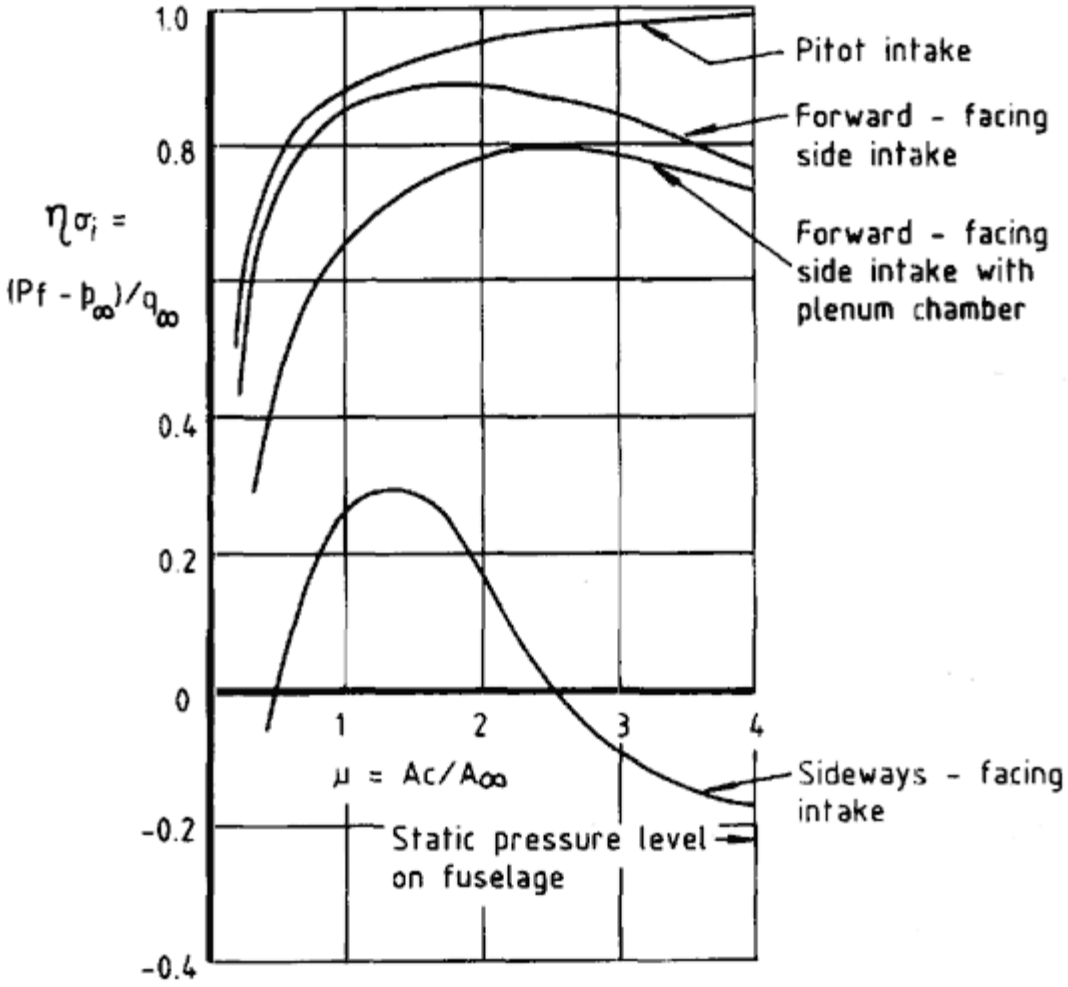

Figure 2.18
Typical pressure recoveries of helicopter intakes.

The sideways-facing intake can be expected to reach a maximum pressure recovery of only 30% or thereabouts, this at a moderate value of μ only, corresponding to a flight speed significantly lower than for normal cruise. As μ increases thereafter the pressure recovery falls progressively to zero and below, tending ultimately, as μ tends to infinity (i.e. zero flow into the intake), to a static pressure level, shown in the example as 0.2 in pressure coefficient, corresponding to the position of the entry on the surface of the vehicle. The poor recovery of this intake is accepted, as we have seen, as a price to be paid for its value as an inertial separator of foreign matter.

The fitting of mechanical protection devices of the types described earlier results in additional normally large degradation in the pressure recovery of whichever type of intake is used. Owing to the wide variety of detail designs, no generalisation is possible individual schemes need to be checked out in the wind tunnel or by other means.

References

Brammer, P.A.H. and Rabone, D.J. (1980) 'Intake design with particular reference to ice protection and particle separators'. AGARD CP 302.

Frick, C., Davis, W.F., Randall and Mossman, E.A. (1945) 'An experimental investigation of NACA submerged duct entrances'. NACA ACR 5120.

Küchemann, D. and Weber, J. (1953) *Aerodynamics of Propulsion.* New York: McGraw-Hill.

Martin and Holzhauser (1950) 'Analysis of factors influencing the stability characteristics of symmetrical twin-intake air induction systems'. NACA TN 2049.

Seddon, J. (1952) 'Air intakes for aircraft gas turbines'. *J. R.Ae.S.*

Squire, H.B. (1947) 'Experiments on conical diffusers'. RAE Aero 2216.

Chapter 3
Transonic Effects in Pre-Entry Flow

In transonic flow, which we may loosely define as the range of free-stream Mach numbers from 0.8 to 1.4, notable changes occur in the pattern of flow into the general intake with forward external surface, as considered in Chapter 2. It is important to appreciate the nature of these changes, not only for their significance within the Mach number range in question but also for their implications in relation to intake design at higher Mach numbers.

3.1 First Expectations

Figure 3.1(a) shows the basic flow pattern under consideration; this is as discussed in Chapter 2 and as might be expected to apply without change of principle up to free-stream Mach number unity. Above $M¥ = 1$ the pre-entry retardation, given one-dimensional flow, would be expected to commence with a normal shock wave, taking the flow to subsonic Mach number, after which further retardation could take place as before. This basic pattern for supersonic speeds is shown in Fig. 3.1(b).

The total-pressure losses to be expected *a priori* are therefore the friction losses on the approach and in the duct, as derived in Chapter 2 but corrected for compressibility effects, together with the loss in the normal shock, this last applying only when the free stream is supersonic. For the friction losses, since the equation of continuity within the streamtube is now

$$\rho A V = \text{constant}. \qquad (3.1)$$

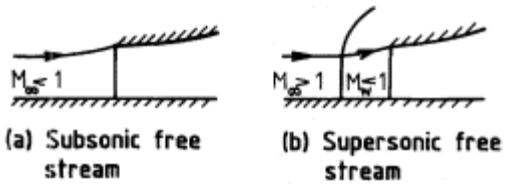

Figure 3.1
Flow patterns of intake with forward external surface first expectation for transonic speeds.

Equation (2.6) modifies to

$$\frac{\Delta P}{q_1} = \int_1^2 \frac{q}{q_1} C_f \frac{g}{A} \, d\ell = \int_1^2 \frac{\rho_1 A_1^2}{\rho A^2} C_f \frac{g}{A} \, d\ell \qquad (3.2)$$

Following the division into approach loss and duct loss, an approximation which allows the order of magnitude of changes to be established is to assume that on the approach r is equal to r¥ and within the duct, r is equal to rc. The first of these equalities obviously fails, in the supersonic case, in the region between the shock and the entry but this distance is assumed to be small in relation to the total approach length, or if not then the whole approach loss is itself small. The second equality is simply a recognition that the flow within the duct is wholly subsonic and virtually incompressible. To this degree of approximation the intake friction loss takes the form

$$\frac{\Delta P}{q_c} = IC_{Fd} + JC_{Fa} \frac{\rho_c}{\rho_\infty} \left(\frac{A_c}{A_\infty} \right)^3 \qquad (3.3)$$

or alternatively

$$\frac{\Delta P}{q_\infty} = IC_{Fd} \frac{\rho_\infty}{\rho_c} \left(\frac{A_\infty}{A_c} \right)^2 + JC_{Fa} \left(\frac{A_c}{A_\infty} \right) \qquad (3.4)$$

In terms of q¥ therefore, since rc is greater than r¥, the friction loss decreases somewhat with increase of compressibility. The change is not one of first magnitude.

Flow through a shock wave is not isentropic but undergoes a loss of total pressure. For a normal shock, the analytical form for the total pressure ratio, going from supersonic Mach number $M1$ (in the present case M¥) to the corresponding subsonic Mach number $M2$ (shown in Fig. 3.1(b) as Mw) is

$$\frac{P_2}{P_1} = \left[\frac{M_1^2}{1 + \frac{\gamma-1}{\gamma+1} (M_1^2 - 1)} \right]^{\gamma/(\gamma-1)} \times \left[\frac{1}{1 + \frac{2\gamma}{\gamma+1} (M_1^2 - 1)} \right]^{1/(\gamma-1)} \qquad (3.5)$$

Values of this ratio, as a function of the argument of $M1$, are normally to be found in compressible-flow tables.

Judging, therefore, from the flow patterns in Fig. 3.1, intake loss for the general transonic case would be expected as a first approximation to be the sum of three components thus:

$$\Delta P = \Delta P_d + \Delta P_a + \Delta P_s \qquad (3.6)$$

in which D*P*d and D*P*a are the duct and approach friction losses as given in Equation (3.4) and *P*s is the shock loss (supersonic speeds only) given from Equation (3.5) by

$$\frac{\Delta P}{P_\infty} = 1 - \frac{P_2}{P_1} \qquad (3.7)$$

At this stage, and generally from here onwards, it is convenient to express pressure and pressure loss in terms of the absolute total pressure *P*¥, for which purpose the friction losses expressed in Equation (3.4) in terms of *q*¥ need to be converted by the use of the relationship from Equations (1.9) and (1.10):

$$\frac{P}{q} = \frac{2}{\gamma M^2}\left(1 + \frac{\gamma - 1}{2}M^2\right)^{\gamma/(\gamma-1)} \qquad (3.8)$$

values for which are normally derivable from compressible flow tables.

3.2
Experiments of Davis *et al*..

That the first expectation described above leads to results which are far from the truth was demonstrated by the outcome of some experiments by Davis *et al.* (1948) of the Ames Laboratory of NACA. Wind tunnel tests were made at low supersonic speed of a research model fuselage with side intakes enclosing various percentages of the body circumference. A comparison between the measured pressure recoveries and those estimated according to Equation (3.6) is made in Table 3.1.

Table 3.1 Comparison of pressure recoveries measured by Davis *et al.* (*M* = 1.4) with those calculated from Equation (3.6)

Enclosure (%)	37	61	100
Measured *P*/*P*¥	0.79	0.75	0.65
Calculated losses:			
D*P*d/*P*¥	0.02	0.02	0.02
D*P*a/*P*¥	0.03	0.05	0.07
D*P*s/*P*¥	0.04	0.04	0.04
Total	0.09	0.11	0.13
Calculated *P*/*P*¥	0.91	0.89	0.87

The very large discrepancy the measured losses being between twice and three times the calculated ones makes it clear that the flow models of Fig. 3.1 are inadequate and that a major source of total-pressure loss exists in addition to those postulated. Such a loss can occur only as the result of large scale turbulence associated with flow separation.

3.3
The Real Nature of Pre-Entry Flow

The manner in which pre-entry flow in the presence of a boundary layer develops through the transonic range is illustrated in Figs. 3.2 and 3.3, which relate to wind-tunnel tests by Seddon and Haverty (1954) on model intakes of various shapes mounted on a flat plate, with a turbulent boundary layer of variable, controllable thickness. Fig. 3.2 shows Mach number profiles in the entry plane, taken normal to the plate in the centre of the intake span, for two of several test Mach numbers used. At (a), the profiles for free stream Mach number 0.51, virtually incompressible flow, are shown. When the flow ratio *Ac*/*A*¥ is 1.0, there is no pressure gradient in the pre-entry flow and the profile at entry shows the same boundary layer on the plate as with intake removed. Reducing the flow ratio imposes a pre-entry pressure gradient, the boundary layer at entry thickens and distorts in profile until, at a flow ratio 0.66, the thickness is about twice the original value and the profile is approximately linear. When the flow ratio is reduced beyond this critical value the boundary layer separates this is shown by the appearance of a dead water region at the base of the entry. Progressive reduction of flow ratio now corresponds to a forward movement of the separation point in the pre-entry field, the height of the dead water region at entry

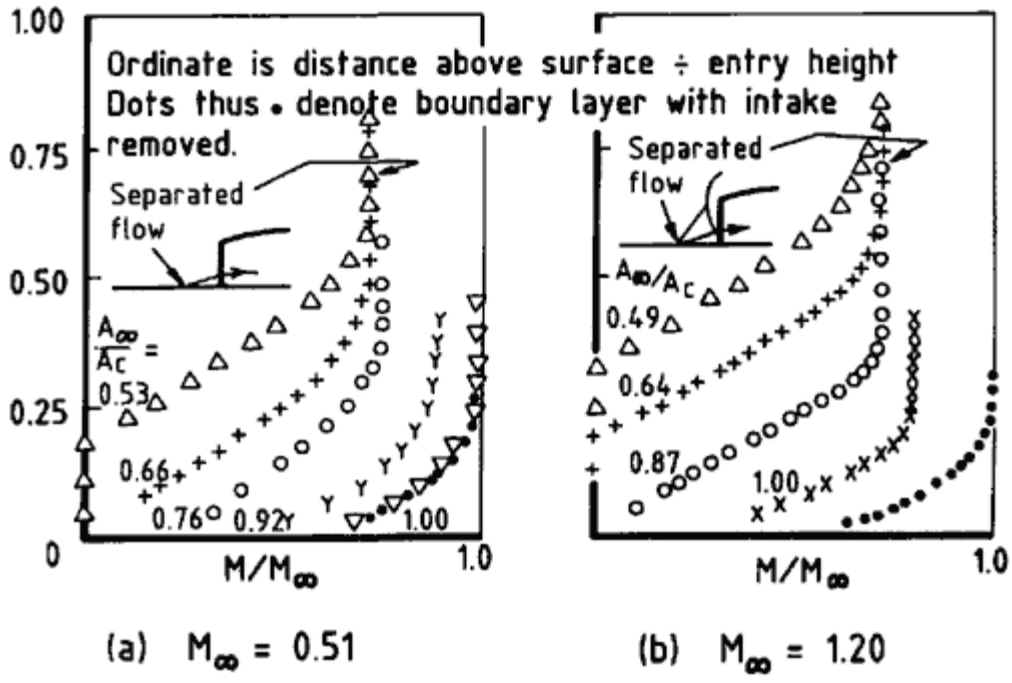

Figure 3.2
Mach number profiles in entry plane (Seddon and Haverty).

increasing, the static pressure at entry remaining constant at the critical or separation value and the Mach number in the entry outside the separated layer being correspondingly fixed.

The profiles for free stream Mach number 1.20 (Fig. 3.2(b)) exhibit essentially similar characteristics but with the two important differences that, (a) at flow ratio 1.0 a normal shock sits across the entry plane, hence the profile, while showing an unchanged boundary layer thickness, corresponds to the subsonic Mach number behind the normal shock, (2) the critical flow ratio for boundary layer separation is now much higher (0.87) than for the lower free-stream Mach number.

This last point is the crucial one: it is demonstrated effectively by plotting entry static pressure as a function of flow ratio for each test Mach number, as is done in Fig. 3.3. At each Mach number, the point of initial separation as flow ratio is reduced is indicated by the levelling off of static pressure and the locus of these points, or separation boundary, is seen to move to higher flow ratios as the Mach number increases. Above $M = 1$ the movement is rapid, such that at approximately 1.3 free stream Mach number, separation occurs at all flow ratios. This is to say that a normal shock at that (or any higher) Mach number is sufficient in itself to cause boundary layer separation.

Separation of the boundary layer, because it involves a sudden change in flow direction at the surface, is characterized by a bifurcation of the shock. This is clearly seen in the two schlieren photographs for Mach 1.34 (less clearly for Mach 1.05 where the shock is weak) and contrasts clearly with the non-bifurcated shock for Mach 1.20 at flow ratio 1.0. The basic characteristics of the interaction of a normal shock and a turbulent boundary layer are discussed more fully later in the chapter.

3.4
Pressure Coefficient at Separation

In studying the interactions between turbulent boundary layers and oblique shock waves, Gadd (1953) obtained an expression for the pressure coefficient at separation. The derivation is based on the assumption that the separation pressure is that pressure which is just sufficient to bring to rest, without friction, the fluid at the 'knee' of the normal turbulent velocity profile. Writing the pressure coefficient as Cpm, referred to free stream conditions (M¥) before the pressure rise, Gadd's formula is

$$C_{pm} = \frac{2}{\gamma M_\infty{}^2}\left[\left(\frac{1+\frac{\gamma+1}{2}M_\infty{}^2}{1+0.64\,\frac{\gamma-1}{2}M_\infty{}^2}\right)^{\gamma/(\gamma-1)} - 1\right] \qquad (3.9)$$

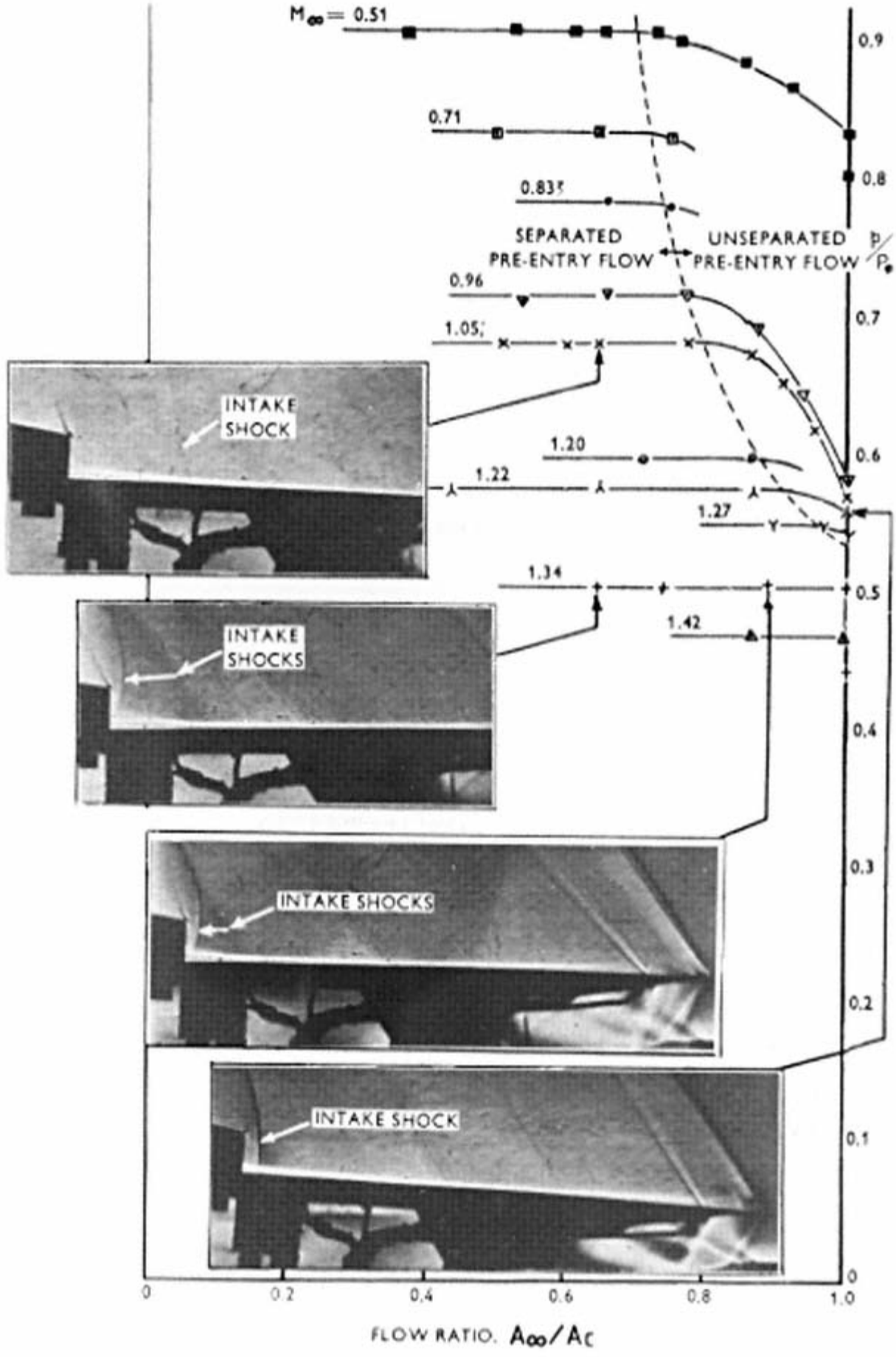
$M_\infty = 0.51$
0.71
0.835
SEPARATED PRE-ENTRY FLOW
UNSEPARATED PRE-ENTRY FLOW
p/p_0
0.96
1.05
1.20
1.22
1.27
1.34
1.42
INTAKE SHOCK
INTAKE SHOCKS
INTAKE SHOCKS
INTAKE SHOCK
0.9
0.8
0.7
0.6
0.5
0.4
0.3
0.2
0.1
0
0
0.2
0.4
0.6
0.8
1.0
FLOW RATIO, A_∞/A_C

Figure 3.3

Variations of entry static pressure with flow ratio.

The study was made at Mach numbers 1.5 and above but the expression is formally valid for all Mach numbers, including subsonic ones. The value for incompressible flow, for example, obtained as described in Chapter 1 by putting $M¥$ equal to zero and g equal to infinity, is

$$(C_{pm})_{\text{incompressible}} = 0.36 \qquad (3.10)$$

The expression may be taken as applying to a boundary layer passing through a sudden pressure jump, or infinite pressure gradient. In a finite pressure gradient, some energy is entrained into the boundary layer from the main stream in the distance over which the gradient acts. As the boundary layer distorts, the friction at the surface falls towards zero and hence an energy surplus is available for increasing the pressure rise. Using this argument, an empirical correction on the Gadd formula can be deduced in order to determine the pressure coefficient for separation in the intake pre-entry flow.

The energy fed into the boundary layer by entrainment may be assumed to be proportional to the initial free stream dynamic pressure and to the increase in momentum thickness which would occur normally, i.e. without pressure gradient, in the streamwise length over which the gradient acts. If that length is ℓ_p and q is written for momentum thickness, we have

$$\text{Energy fed in} \propto q_\infty \cdot \ell_p \frac{d\theta}{d\ell} \qquad (3.11)$$

A proportion of this energy is considered to be distributed over the boundary layer thickness to increase the static pressure rise. The thickness at separation, for given initial and final profile forms, is proportional to the thickness, ds, say, that an undisturbed layer would have at the separation position. Hence the additional pressure rise takes the form

$$\Delta C_p \propto \frac{\ell_p}{\delta_s} \frac{d\theta}{d\ell} \qquad (3.12)$$

Using incompressible flow relationships which, while not strictly true for compressible flow, are sufficiently approximate for this empirical approach, we write

$$\theta_s \propto \delta_s \qquad (3.13)$$

and, for the turbulent layer with 1/7 power velocity profile,

$$\frac{d\theta}{d\ell} \propto R_\theta{}^{-\frac{1}{4}} \qquad (3.14)$$

We then obtain

$$\Delta C_P \propto \frac{\ell_p}{\theta_s} \cdot R_\theta{}^{-\frac{1}{4}} \qquad (3.15)$$

In the experiments discussed in Section 3.3, different boundary layer thicknesses were produced artificially by applying roughness near the

leading edge of the plate and were calibrated by pressure measurement leading directly to the evaluation of momentum thickness qs. The distance ℓ_p could be ascertained from pressure measurements on the plate surface. Thus the expression $\ell_p R_\theta^{-\frac{1}{4}}/\theta_s$ could be evaluated for each set of observations and compared with D*Cp*, the difference between the pressure rise to separation *Cps*, and that given by the Gadd formula, *Cpm*. The comparisons are found to justify a single constant of proportionality for all boundary layers (turbulent profile), all entry shapes and all Mach numbers, both subsonic and supersonic, in the ranges covered. The result is

$$\Delta C_p = 0.012 \frac{\ell_p}{\theta_s} \cdot R_\theta^{-\frac{1}{4}} \qquad (3.16)$$

and the pressure rise to separation is given as

$$C_{ps} = C_{pm} + 0.012 \frac{\ell_p}{\theta_s} R_\theta^{-\frac{1}{4}} \qquad (3.17)$$

The measure of agreement is shown in Fig. 3.4 and is seen to be well inside the level of changes produced by different boundary layers and different Mach numbers.

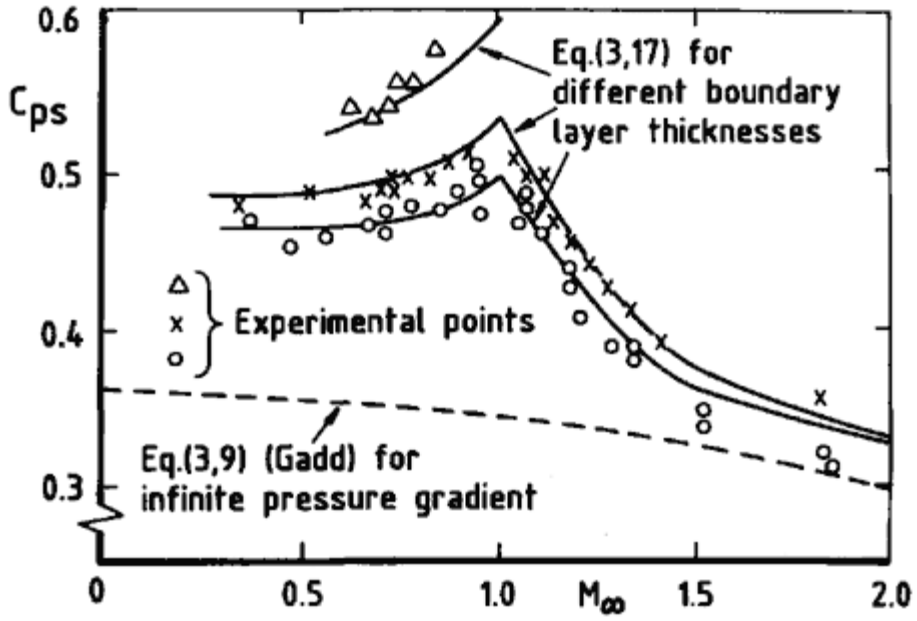

Figure 3.4
Pressure rise to separation of turbulent
boundary layer in adverse pressure gradient.

It may be noted that the flow as now established for flow ratios below the separation boundary, culminating in a condition of zero intake flow, is analogous to the flow approaching a solid step, where similar separation occurs. Beastall and Eggink (1950), in a study of step flow (Mach numbers 1.86 and 2.48), gave the pressure *p*s in the angle of the step as

$$\frac{p_s}{p_\infty} = 1 + \frac{M_\infty^2}{4} \qquad (3.18)$$

This is equivalent to a pressure coefficient

$$C_{ps} = \frac{1}{2\gamma} = 0.36 \qquad (3.19)$$

which is in fair agreement with results in Fig. 3.4 at $M = 1.83$.

The length *lp* in Equation (3.17) may be written in terms of the overall pressure rise and equivalent linear pressure gradient, thus:

$$\ell_p = C_{ps} \Big/ \frac{dC_p}{d\ell} \qquad (3.20)$$

Substituting and rearranging gives

$$C_{ps} = C_{pm} \Big/ \left[1 - 0.012\left(\theta_s \frac{dC_p}{d\ell} R_\theta^{\frac{1}{4}}\right)^{-1}\right] \qquad (3.21)$$

Equation (3.21) expresses the pressure coefficient at separation of the turbulent boundary layer in terms of the undisturbed momentum thickness and the imposed pressure gradient, together with Reynolds number and Mach number. The equation is believed to have a degree of validity wider than that of the present context. It is to be noted that the product $\theta\,(dC_p/d\ell)R_\theta^{\frac{1}{4}}$ is effectively the parameter G used by Prandtl in discussing the basic mechanics of the turbulent boundary layer in accelerated and decelerated flows.

For the case of a real air intake, if ℓ_s is the length of naturally turbulent layer up to the separation point, ℓ_s may be substituted for qs by using

$$\theta \propto \ell R_\theta^{-\frac{1}{4}} \qquad (3.22)$$

so the proportionality (3.15) becomes simply

$$\Delta C_p \propto \frac{\ell_p}{\ell_s} \qquad (3.23)$$

and the 'Prandtl' parameter in Equation (3.21) becomes $\ell_s\,(dC_p/d\ell)$. At a given flow ratio the pressure rise length ℓ_p is a function of Mach number and a characteristic dimension of the entry. For an effectively two-dimensional entry with the long dimension parallel to the external surface, the characteristic dimension is twice the entry height: in general for an arbitrary entry shape we use the hydraulic radius of the entry and its reflection in the external surface (Fig. 3.5), namely

$$\frac{2 \times 2A_c}{2(g_c - g_a)} \text{ or } \frac{2A_c}{g_c - g_a}$$

$$\text{or } \frac{2A_c}{g_a(\lambda - 1)} \text{ where } \lambda = \frac{g_c}{g_a}$$

To the extent to which the geometrical function and the Mach number function are separable probably true below $M\infty = 1$, less accurate above we therefore have, from Equation (3.23),

$$\Delta C_p = \frac{A_c}{\ell_s g_a(\lambda - 1)} \cdot f(M_\infty)$$

$$= \frac{1}{J(\lambda - 1)} f(M_\infty) \qquad (3.24)$$

where J is the corrected position ratio as used in Chapter 2. Hence the separation pressure is

$$C_{ps} = C_{pm} + f(M_\infty)/J(\lambda - 1) \qquad (3.25)$$

Using the function of Mach number which can be derived from the experiments of Section 3.3, curves of Cps against Mach number can be plotted for an arbitrary series of values of J(l 1). If an overplot is then made of curves of Cp at entry for constant values of flow ratio $A\infty/Ac$, assuming uniform, unseparated flow (in this plot the points at $M\infty = 0$ are values of incompressible Cp,

$$C_{pi} = 1 - \left(\frac{A_\infty}{A_c}\right) \qquad (3.26)$$

while the curve for $A\infty/Ac = 1.0$ consists of the zero axis for $M\infty = 0$ to 1.0 and for $M\infty > 1.0$ the static pressure coefficient behind a normal shock)

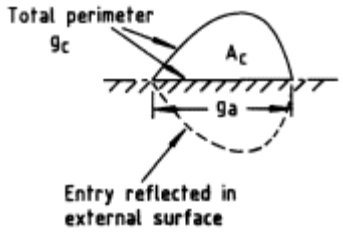

Figure 3.5
Definition of hydraulic radius of entry.

intersection points between the two families define critical flow ratios for separation for the particular combinations of $M¥$ and $J(l \quad 1)$.

Emerging from this analysis is the chart shown at Fig. 3.6 for readily obtaining a first estimate of critical flow ratio in a given situation. In the example indicated by arrowed dotted lines, an intake with $J(l \quad 1) = 23$, operating at $M¥ = 1.1$, would experience pre-entry separation for flow ratios 0.85 and below. For incompressible flow, combining Equations (3.25) and (3.26) leads to

$$\left(\frac{A_\infty}{A_c}\right)_{\text{crit}} = [0.64 - f(0)/J(\lambda - 1)]^{\frac{1}{2}} \qquad (3.27)$$

this has values between 0.8 [$J(l \quad 1) = ¥$] and zero [$J(l \quad 1)$ £ 5]. In fine detail the subsonic part of the chart is liable to be more accurate than the supersonic part, but in any case the principal feature above $M¥ = 1.0$ is the rapidity with which the unseparated flow range is reduced as $M¥$ increases, finally disappearing at around $M¥ = 1.3$.

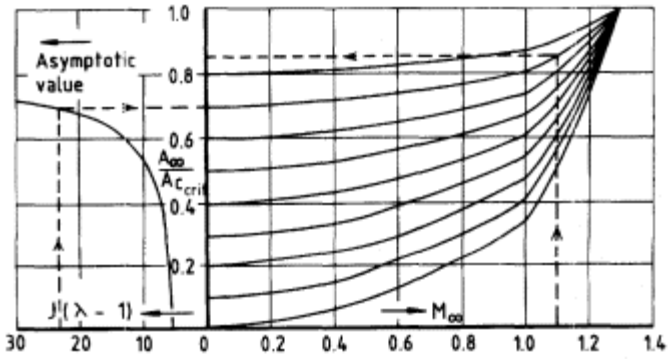

Figure 3.6
Critical flow ratio for pre-entry separation.

3.5
Effect of Separation on Intake Pressure Recovery

The nature of pre-entry flow at transonic speeds having been elucidated, it remains to determine the effect with which this flow has on intake pressure recovery. Clearly with flow separation playing a prominent part, losses in total pressure from turbulent mixing of the flow downstream of separation are to be expected. We continue to assume at this stage that no boundary layer bleed or other form of diverter is provided. Should this not be the case, fresh considerations are needed; these are discussed in later chapters. It is desirable in any event however, that the basic situation be appreciated, both for its intrinsic significance and in order to be able to

decide whether some form of boundary layer removal is required in a given case.

The overall situation from incompressible-flow speeds and through the transonic range is portrayed in Fig. 3.7 for a typical configuration taken from the experiments of Section 3.3. The presentation is made in terms of a 'ram efficiency' defined as

$$\eta_R = (P_f - p_\infty)/(P_\infty - p_\infty) \qquad (3.28)$$

*P*f being the total pressure at equivalent engine face position station f of the standard aerodynamic duct (Section 1.4). hR is not identical with hs of Equation (1.27) but serves the same purpose of linking low- and high-speed results and for incompressible flow the two coincide. The plot (curve A) is of peak pressure recovery at each test Mach number *M*¥, so that at all points the flow pattern is that corresponding to a cruise condition (flow ratio £ 1.0).

The situation revealed is precisely of a kind to confirm and account for the results obtained by Davis *et al.*, as described earlier. Whereas at incompressible-flow speeds the frictional forces account in full for the loss of total pressure, at test Mach number 1.4 the frictional forces and a normal shock loss account together for only about half the total loss. The remainder comes from the interaction of boundary layer and adverse pressure gradient, including the shock wave at supersonic speeds, and may be termed an interaction loss. This, it is seen, develops progressively through the transonic speed range as the flow separation boundary encroaches on the

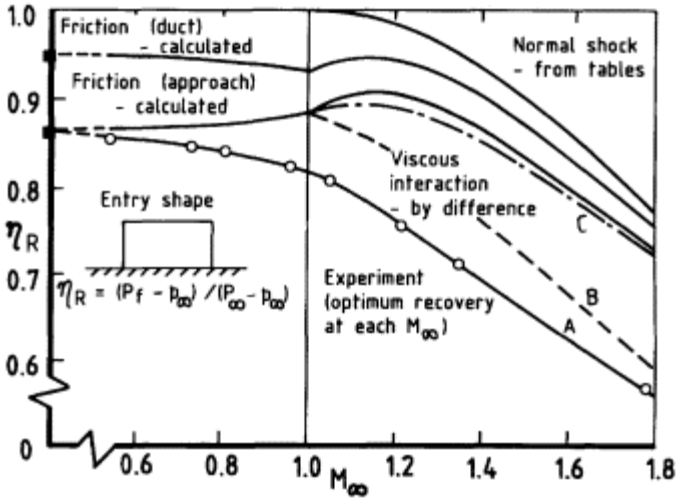

Figure 3.7
Breakdown of loss for intake with external surface at subsonic and supersonic speeds.

working range of flow ratio in the manner already described. The following further points are to be noted:

(a) Pre-entry separation at supersonic speeds is characterized by the bifurcation of the shock, as was seen in Fig. 3.3. The loss of total pressure through the shock system itself, outside the boundary layer, is thereby changed, in fact reduced, as compared with the normal shock. In certain circumstances (see for example Chapter 8) it is necessary to isolate this change in the accounting. For the present analysis, however, it is convenient and sufficient to treat the shock loss as coming still from a normal shock and include the change in shock loss as part of the interaction loss.

(b) In Fig. 3.7, if curves such as curve A for different amounts of the boundary layer capture (represented by the position ratio *J* or alternatively by a factor based on boundary layer momentum thickness) are extrapolated to zero boundary layer, the curve arrived at is the broken curve B. This result indicates that the interaction loss comprises two components, one dependent upon boundary layer capture and existing at both subsonic and supersonic speeds, the other in effect independent of the degree of boundary layer (so long as a boundary layer, however thin, is actually present) and existing at supersonic speeds only. There is a clear connection here with a conclusion partly drawn previously, that the tendency of a shock wave to distort a boundary layer towards separation is independent of the initial boundary layer thickness and a shock wave above Mach 1.3, approximately, is sufficient to separate a turbulent boundary layer, however thin. Use is made of this two-component nature of the interaction in deriving an empirical loss formula.

(c) Generally, in a practical intake, the flow undergoes a net pressure rise inside the duct, the engine face area *A*f being greater than the entry area *A*c. A situation in which adverse pressure gradients, other than the shock wave, would be avoided is with *A*f equal to (or less than) *A*c and flow ration *A*¥/*A*c equal to 1.0. A test result for such an artificial case is shown by the chain-dotted curve C and it is seen that in these circumstances the interaction loss, even supersonically, is small. This result is also used in the empirical generalisation which follows.

Although the behaviour of a turbulent boundary layer in an adverse pressure gradient and at a shock wave interaction is now well understood and theoretical methods are available for treating the flow in isolation, including the effects of separation (see next Section), the ideas have not so far been widely incorporated into aerodynamic design methods. For the present situation, however, using the experimental results of Section 3.3, an

empirical generalisation can be made which has stood the test of checking by independent experiment. The total intake loss is expressed as

$$\Delta P = \Delta P_a + \Delta P_d + \Delta P_s + \Delta P_i \qquad (3.29)$$

where the first two terms are as before, D*P*s is the normal shock loss and D*P*i is the interaction loss, principally from turbulent mixing in the flow but including the change from deformation of the shock. The factors of which account has to be taken in an expression for D*P*i are:

(i) Flow ratio. Normally this would be defined as *A*¥/*A*c; however, the ultimate loss at engine face includes the effects of both external and internal pressure gradients and for that reason an overall ratio *A*¥/*A*f is preferable.

(ii) Boundary layer capture. Either the position ratio *J* or an area ratio based on momentum thickness of the external boundary layer may be used. In the latter case an area *A*q is defined as qga, q being the momentum thickness of the undisturbed layer at entry position, and the capture ratio is then *A*q/*A*c.

(iii) Duct shape parameter. In addition to the factor of duct area increase, *A*f/*A*c, the rate at which this increase takes place in the early part of the duct has an important bearing. If increase in duct area immediately behind the external interaction can be avoided, better still if a contraction in area can be provided, the loss-producing development of turbulent mixing is reduced. To allow for this a further parameter *A*h/*A*c is included, *A*h being the area at half duct length.

With these incorporations, a complete analysis of the results of the experiments of Section 3.3. leads to the conclusion that the interaction loss in the system of a forward-facing intake with external boundary layer may be determined from the formula

$$\frac{\Delta P_i}{P_\infty} = Q\left(G\frac{A_\theta}{A_c}\Phi + \Psi\right) \qquad (3.30)$$

In this, *Q* is the flow factor, defined by

$$Q = 1 - \left(\frac{A_\infty}{A_f}\right)^3 \qquad (3.31)$$

G is a geometrical factor, defined by

$$G = \frac{4A_h - 3A_c}{A_f} \qquad (3.32)$$

and the effect of free-stream Mach number is represented by functions F and Y, given in Fig. 3.8. The two-fold representation follows the conclusion drawn at Note (b) on page 53: F may be termed the boundary layer function and Y the shock function.

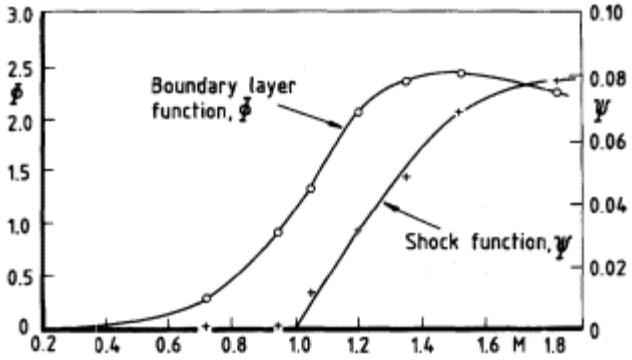

Figure 3.8
Functions F, Y that determine viscous interaction loss.

Independent checks of the formula at Equation (3.30) have been made by free flight tests on a model consisting of a pair of semi-elliptical side intakes on a cylindrical fuselage with ogival nose. Two models were flown, of identical design but with different flow ratios. Figure 3.9 shows that in both cases a large interaction loss was present and that agreement is good between the experimental results and calculations based on Equations (3.29) and (3.30). The interaction loss formula is considered, therefore, to be generally valid for forward-facing (i.e. normal shock type) intakes with

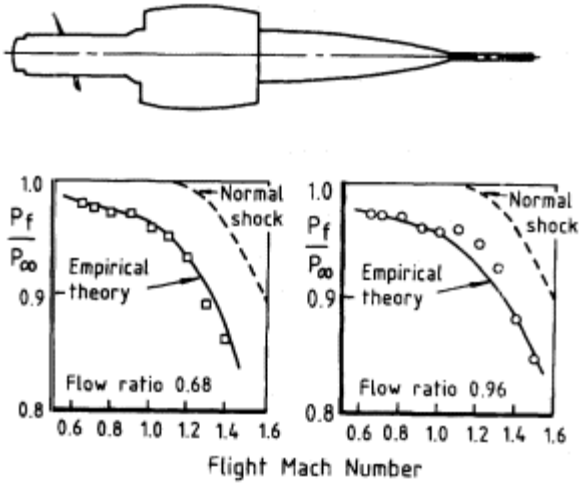

Figure 3.9
Check of interaction loss theory by free flight model test.

external boundary layer. It may also be applied (Chapter 7) to supersonic intakes with external compression. In this context, checks with wind-tunnel results have shown that the formula provides a reasonable first approximation; its chief deficiency is a lack of provision for the duct curvature which is normally required in such cases to restore the flow to axial direction following a supersonic compression.

If a boundary layer bleed is used in a practical case, then since the primary purpose of a bleed is to counteract the interaction loss by preventing or at least controlling flow separation, the chief use of the formula at Equation (3.30) is to provide an estimate of how much loss of total pressure has been saved.

3.6 Basics of Normal Shock and Turbulent Boundary-Layer Interaction

In the foregoing treatment, emphasis has been placed on the behaviour of the boundary layer in adverse pressure gradients and in particular on the consequences of its interaction with the shock wave when the free stream is supersonic. We now give a more detailed account of the physical nature of flow at and downstream of the interaction of a turbulent boundary layer and a normal shock wave. This has implications not only in the present context but also in connection with the flow capture and loss characteristics of fully supersonic intakes, spillage drag, the design of boundary layer bleeds and the onset of intake flow instability or 'buzz', all of which are matters to be discussed in later chapters.

Experimental studies of the interaction, in two dimensions and at Mach numbers high enough for the shock wave to cause a measurable degree of flow separation, have been made by a number of workers, with general agreement on the broad characteristics. The description which follows is taken mainly from an experiment of Seddon (1960) made at the California Institute of Technology; reference should also be made to work by Vidal *et al.* (1973), Kooi (1975), Mateer *et al.* (1976) and East (1976).

The way in which a turbulent boundary layer interacts with a strong normal shock constitutes an interesting phenomenon, not least because of the large degree of accommodation which each component makes in the final system. Each component sinks its identity in the whole: the shock is (in part) no longer a normal shock and the boundary layer is (for the time being) no longer a boundary layer. The pressure rise in the shock being too great for the inner layers of the boundary layer to surmount, some flow is driven back upstream and becomes the eddy flow of a separation zone. The general flow turns away from the surface, i.e. 'separates', to circumnavigate this and that in turn generates an inclined shock as in the supersonic flow over a wedge. This is accommodated by a bifurcation in the lower part of

the incident shock, as is seen in the schlieren photograph in Fig. 3.10. The total flow thus divides into three regions, which are indicated in the illustrative drawing at Fig. 3.11:

(1) an outer, or mainstream, flow passing through the residual normal shock;

(2) an intermediate layer, in which the flow passes through the bifurcated shock system and is therefore at different total pressure from the outer flow;

(3) the viscous layer, including the separation zone.

A solution to the flow depends upon conditions of pressure and velocity appropriate to the different regions being simultaneously satisfied.

Because of the difference in total pressure, velocities downstream of the shock system are higher in the intermediate layer than in the outer region. On the common boundary this difference is reconciled through a vortex sheet which emanates from the shock bifurcation point and allows the static pressure to be continuous across the boundary. The vortex sheet is clearly visible in Fig. 3.10 and is remarkably persistent: in the Caltech experiment it was plainly observable at 60 initial boundary layer thicknesses downstream, which represented the full range of the experiment.

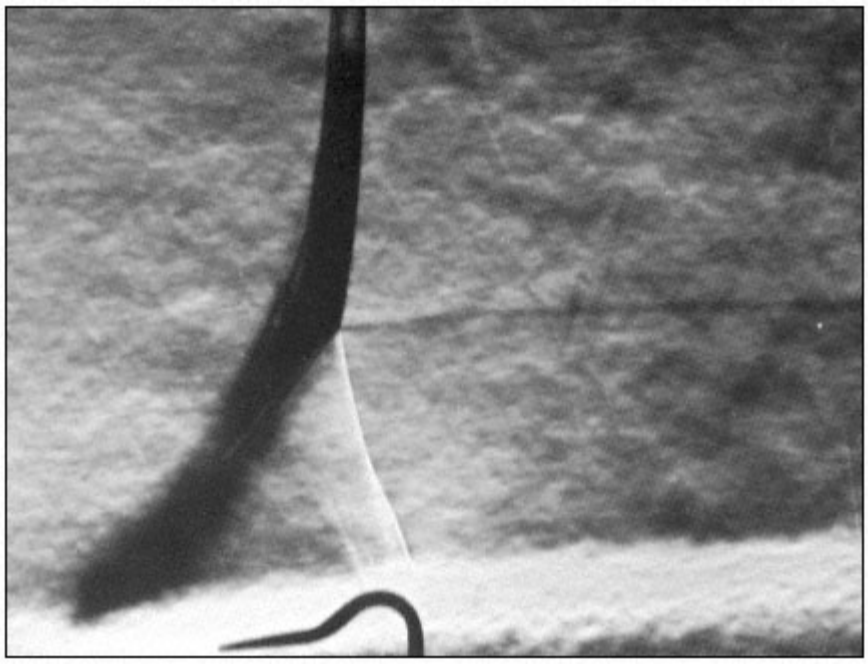

Figure 3.10
Interaction of normal shock and turbulent boundary layer (Seddon).

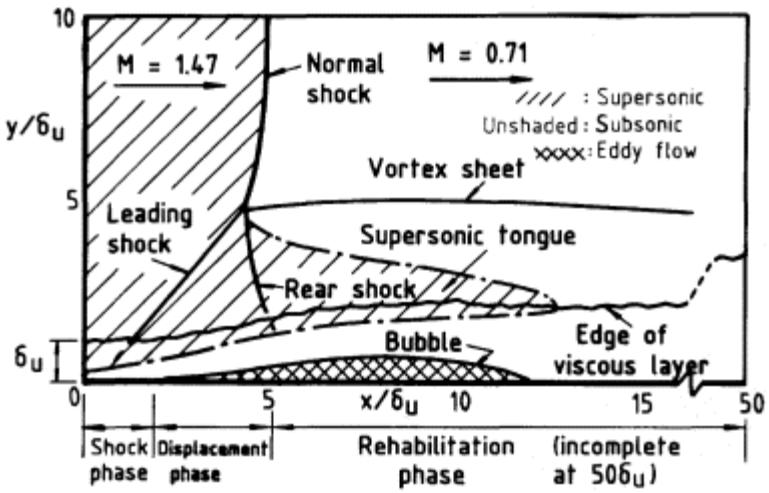

Figure 3.11
Features of flow in interaction of normal shock
and turbulent boundary layer (illustrative sketch).

In the outer layer the velocity behind the shock is subsonic, as befits a normal shock, even though the shock becomes a little inclined approaching the bifurcation point. In the intermediate layer the velocity increases progressively from the vortex sheet to the edge of the boundary layer and may become supersonic. The Caltech experiment revealed the presence of a supersonic 'tongue', extending a considerable way downstream of the rear shock as shown in the diagram. A similar tongue was observed by Mateer and by East, but Vidal and Kooi, experimenting at lower (though not greatly so) free-stream Mach numbers, observed only subsonic velocities in this region. The flow in the intermediate layer, having turned away from the surface at the leading shock, turns partly back at the rear shock and is then accommodated between the vortex sheet and the edge of the viscous layer.

Turning now to the viscous layer itself, the streamwise distribution of static pressure along the surface and Mach number at the edge of the layer are characteristically as shown in Fig. 3.12. The pressure rises sharply to the separation point, where there is a discontinuity in curvature; thereafter a much slower rise takes place towards the normal shock value which appertains to the outer flow. These changes are reflected in the Mach number distribution. In the Caltech experiment, with free-stream Mach number 1.47, the measured pressure ratio at separation was 1.48, with which a value 1.49 calculated from Gadd's formula, Equation (3.9), compares well. A selection of velocity profiles through the layer is given in Fig. 3.13. This reveals the existence of a region of reversed flow (between profiles 2 and 7), which forms the lower part of a separation bubble, shown more clearly in Fig. 3.14. A clear distinction is also revealed in Fig. 3.13 between

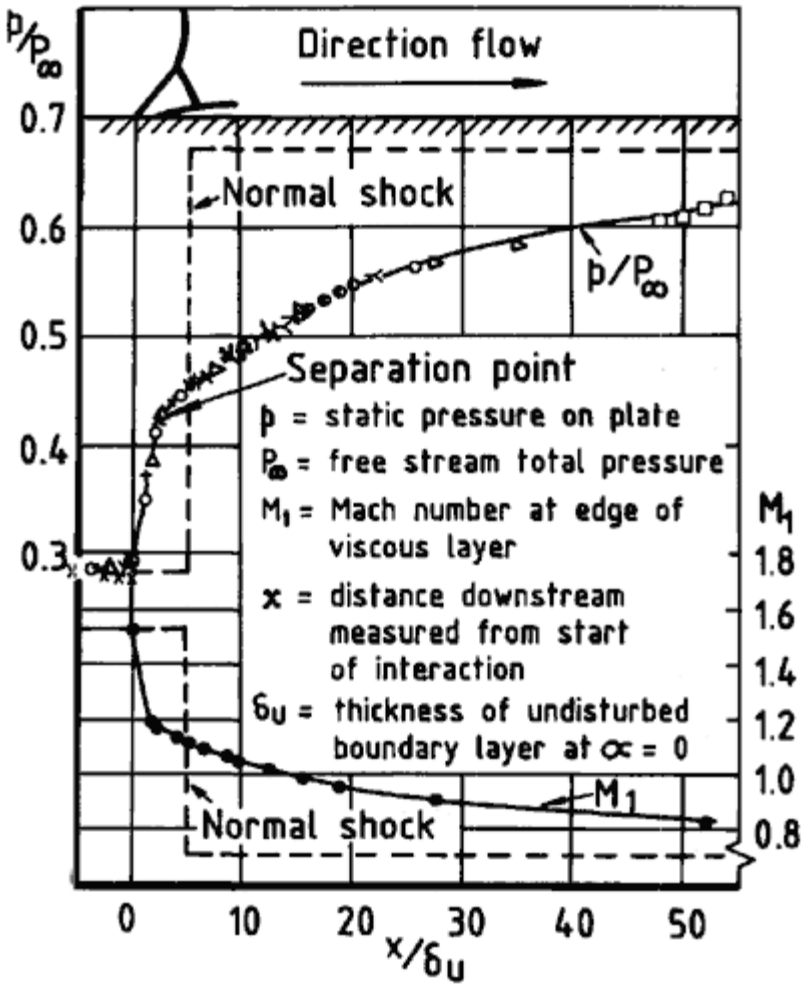

Figure 3.12
Surface pressure distribution and Mach numbers outside viscous layer in interaction of normal shock and turbulent boundary layer.

the profile at separation (profile 2), occurring under the impulsive influence of the strong pressure rise from the shock, and that at reattachment (profile 7), occurring naturally, almost incidentally, in the rehabilitating flow downstream.

Variation of the standard boundary layer parameters is as indicated in Fig. 3.15. Overall thickness of the viscous layer increases rapidly as the flow is torn from the surface and thereafter grows at about twice the normal rate. Entrained mass flow increases more slowly at first but subsequently adopts a similar trend. All the mean flow parameters are well predicted by the theory of East *et al.* (1977), which is a development of the lag entrainment method of Green (1972).

It is of interest to note that over the later part of the interaction, the momentum thickness of the viscous layer has values between three and four times that of the initial boundary layer. Transferring to the air intake context, this suggests an interaction loss equal to three or four times the external friction loss, which is very much as shown for the shock component alone in the example at Fig. 3.7 and as would be given by the Y term in Equation (3.30) for a value of *Q* corresponding to a flow pattern such as those in the two middle photographs of Fig. 3.4. As the formula at Equation (3.30) indicates, the total effect in an intake situation depends additionally

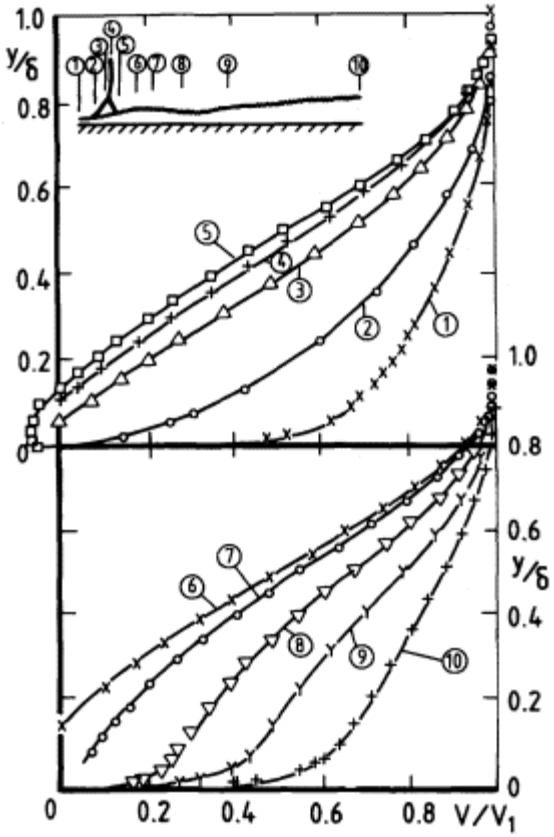

Figure 3.13
Non-dimensional velocity profiles.

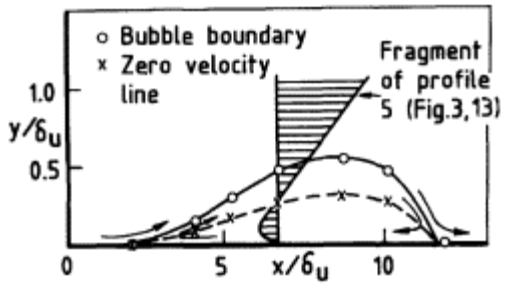

Figure 3.14
Detail of separation bubble.

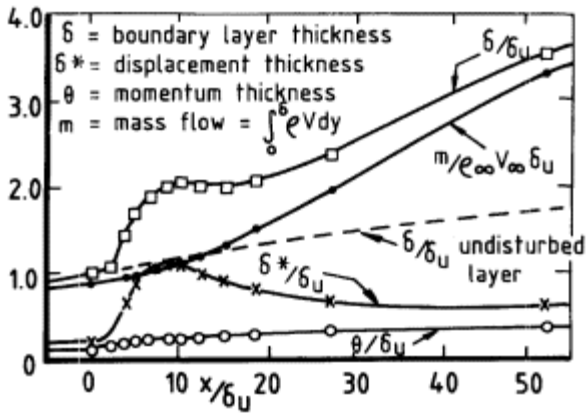

Figure 3.15
Boundary layer parameters.

upon flow ratio and duct shape, in other words upon the way in which additional surfaces constrain the flow.

In Fig. 3.16 are shown two examples of interaction flows with additional constraints, not conceived in the air intake context but having some similarity with it. In example (a), a second plate, parallel to the boundary layer plate, has been brought up to the normal shock in the outer flow. There is now a continuity condition to be satisfied in the outer flow beneath the second plate, which involves the vortex sheet taking up a slightly different position from that in the basic unconstrained interaction. The change produces a more extensive supersonic flow in the intermediate layer but the flow in the viscous layer is not significantly affected. In example (b) the second plate has been brought closer to the boundary layer plate and the flow between them has been adjusted (by means of a rearward control not shown) so that the shock system is pushed forward of the second plate leading edge. The second plate is now operating in the intermediate layer. It is seen that the scale of the interaction has been significantly increased, as judged for example by the height of the shock bifurcation point above the boundary layer plate. A further change is that the intermediate layer below the second plate now contains a train of shocks and expansions.

3.7
Effect of Bifurcated Shock on Intake Performance.

The bifurcated shock resulting from normal shock and boundary layer interaction can have a wholly beneficial effect on the pressure recovery of a pitot intake when mounted on a sufficiently high boundary layer diverter. The two-shock recovery equivalent to a 10° wedge compression surface resulting from the boundary layer deflection progressively

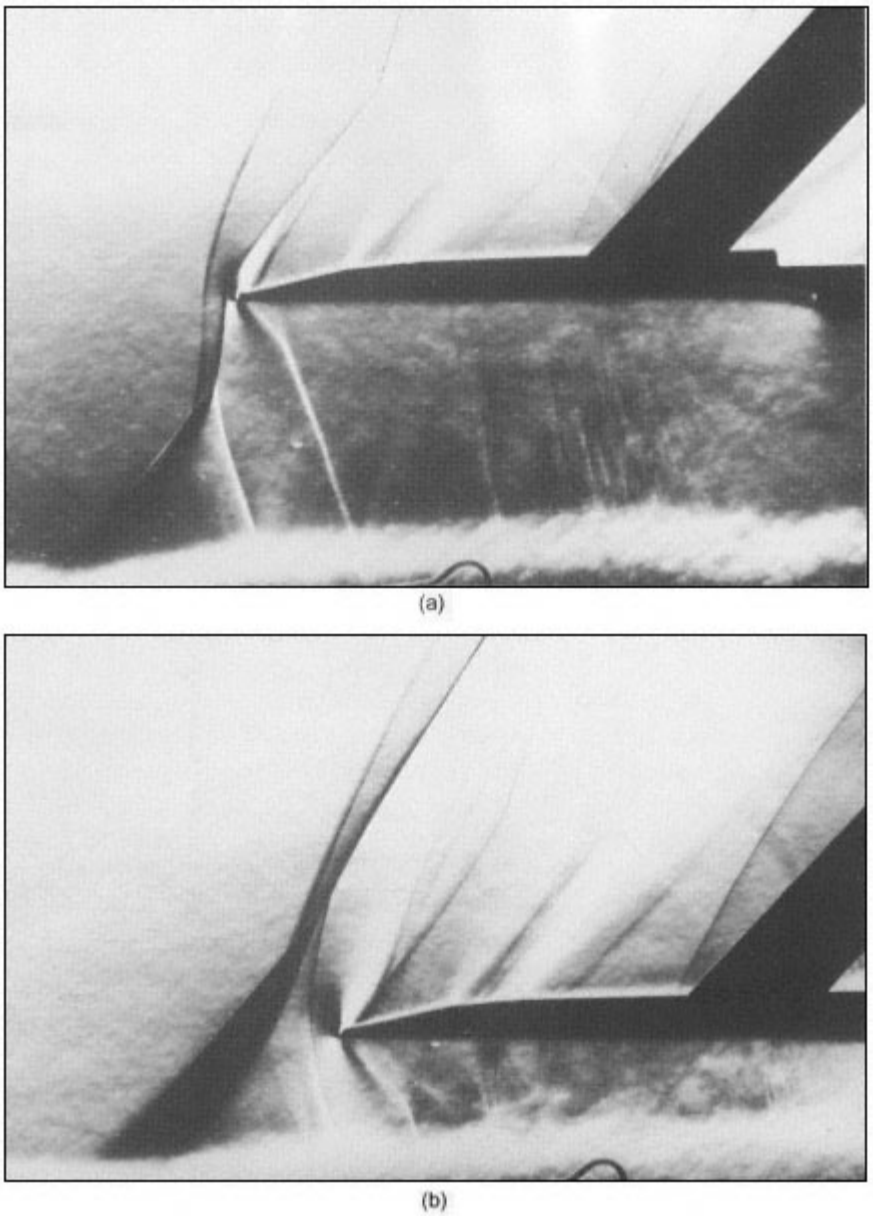

Figure 3.16
Shock and boundary layer interaction with additional constraints.

encompasses the whole of the ingested intake flow as flow ratio is reduced from the maximum value of capture flow. However, eventually this theoretical advantage of the two-shock pattern is increasingly overtaken (unless the diverter height is inordinately high) by the adverse effect of body boundary layer ingestion. This happens if the flow remains stable,

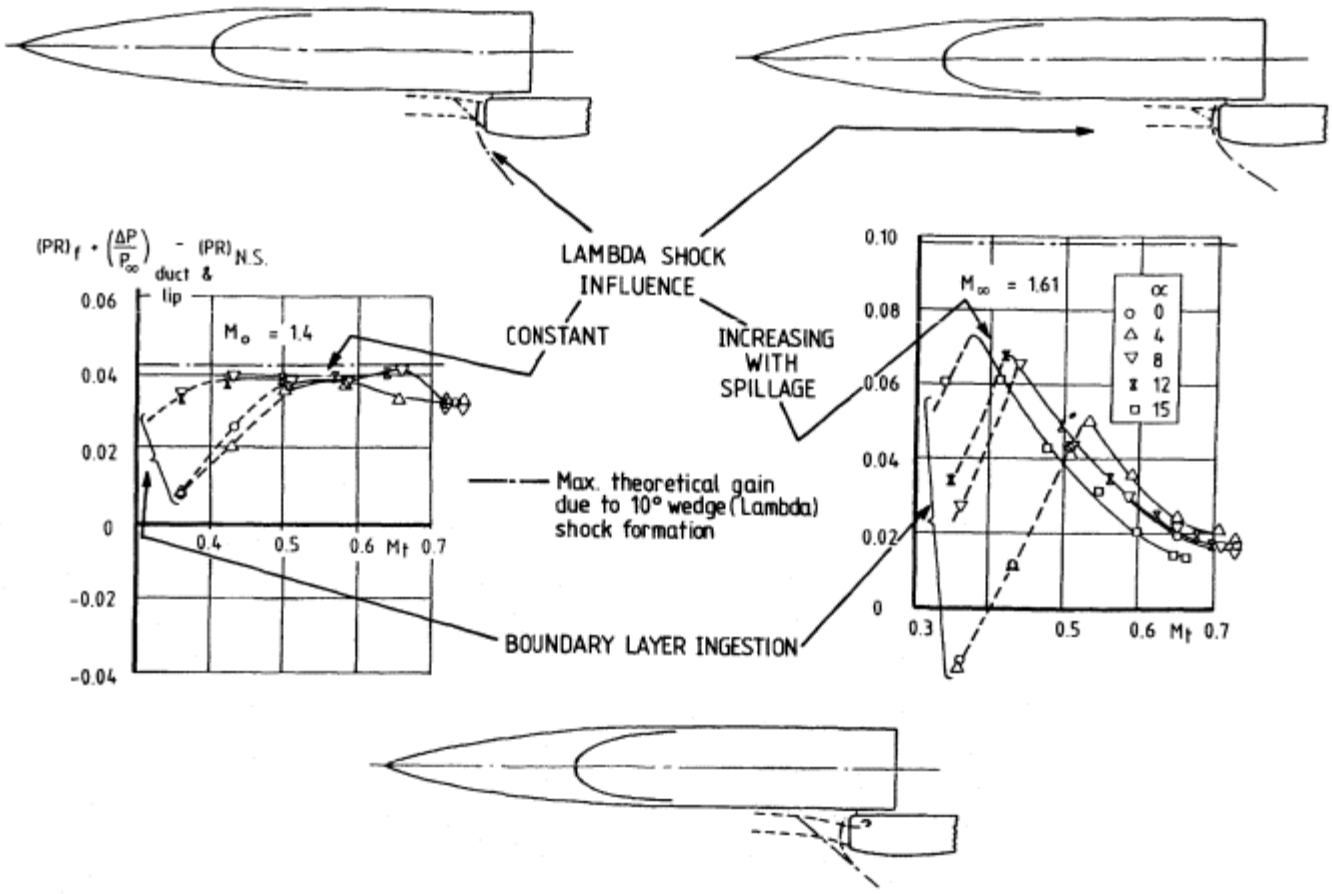

Figure 3.17
Normal shock interaction effects for a pitot on a diverter.

which is not always the case (depending on free-stream Mach number and amount of flow spillage).

The measured gain in recovery relative to normal shock recovery is shown in Fig. 3.17 at $M¥$ = 1.4 and 1.6 as a function of throat Mach number (spillage) compared with the theoretical gain from the two-shock recovery. The measured gain is derived by adding a duct and lip loss (obtained at subsonic speeds) to the measured pressure recovery and subtracting the theoretical normal shock recovery. As can be seen at $M¥$ = 1.4, the two-shock recovery appears to influence the whole of the intake flow even at the smallest spillage condition (higher Mt). At $M¥$ = 1.6 the smaller shock wave angle of the 10° separated flow ramp results in only a small part of the ingested intake flow being influenced by the two-shock pattern at high Mt values, but the effect progresses rapidly as spillage increases until some ingestion of the separated body boundary layer commences at values of Mt below 0.4 0.5. An exploration of this gain in performance over normal shock recovery values is manifested in the step-bleed intake discussed in Section 14.4.1.

References

Beastall, D. and Eggink (1950) 'Some experiments on breakaway in supersonic flow', Parts I & II. RAE TN Aero 2041 and 2061.

Davis, W.F. and Edwards, S.S. (1948) 'Experimental investigation at supersonic speeds of an inlet enclosing 37.2% of the maximum circumference of the forebody'. NACA RM A8E04.

Davis, W.F. and Goldstein, D.L. (1948) 'Experimental investigation at supersonic speeds of an inlet enclosing 61% of the maximum circumference of the forebody'. NACA RM A7J27.

East, L.F. (1976) 'The application of a laser anemometer to the investigation of shock-wave-boundary-layer interactions'. AGARD CP 193, Paper 5.

East, L.F., Smith, P.D. and Merryman, P.J. (1977) 'Prediction of the development of separated turbulent boundary layers by the lag-entrainment method'. RAE TR 77046.

Gadd, G.E. (1953) 'A semi-empirical theory for interactions between turbulent boundary layers and shock waves strong enough to cause separation'. ARC 15543.

Green, J.E., Weeks, D.J. and Brooman, J.W.F. (1973) 'Prediction of turbulent boundary layers and wakes in compressible flow by a lag-entrainment method'. ARC R & M 3791.

Kooi, J.W. (1975) 'Experiment on transonic shock-wave boundary layer interaction'. AGARD CP 168, Paper 30.

Mateer, G.G., Brosh, A. and Viegas, J.R. (1976) 'A normal shock wave turbulent boundary layer interaction at transonic speeds'. AIAA Paper 76-161.

Seddon, J. (1960) 'The flow produced by interaction of a turbulent boundary layer

with a normal shock wave of strength sufficient to cause separation'. ARC R & M 3502.

Seddon, J. (1970) 'Boundary-layer interaction effects in intakes with particular reference to those designed for dual subsonic and supersonic performance'. ARC, R & M no. 3565.

Seddon, J. and Haverty, L. (1954) 'Experiments at Mach numbers from 0.5 to 1.8 on side intakes of normal-shock type without boundary layer control'. Pt. I: 'The nature of pre-entry flow and its effect on pressure recovery'. RAE TN Aero 2329, ARC 17398.

Vidal, R.J., Wittliff, C.E., Catlin, P.A. and Sheen, B.H. (1973) 'Reynolds number effects on the shock wave turbulent boundary layer interaction at transonic speeds'. AIAA 73 661.

Chapter 4
Lip Separation and Transonic Throat Flow

4.1
Introduction

In this chapter the flow within the duct is considered in greater detail with particular attention to the influence that compressibility and the effects of separation at the capture plane have on the subsequent flow downstream. The intake and duct are taken to be in isolation, i.e. there is no approach surface upstream of the capture plane as in Chapters 2 and 3, and most of the data is taken from tests on axisymmetric intakes.

Relevant features of the duct as shown in Fig. 4.1 are (1) a leading edge or 'highlight' area *A*c, (2) a minimum or throat area *A*t some small distance downstream of the capture plane, and (3) the diffusing duct leading to a representative engine face area *A*f. A pressure recovery or loss characteristic such as those shown in Figs. 1.4 and 2.10 give a good general guide to the aerodynamics of an intake, but they are necessarily confusing as they 'integrate' the effects of simultaneous variation of two important flow parameters. These are, for a given relative throughflow *A*¥/*A*c, the position of the stagnation or dividing streamline (between internal and external flow) at the cowl lip and the value of the mean Mach number at the throat of the intake *M*t. The dividing streamline position controls the possibility of

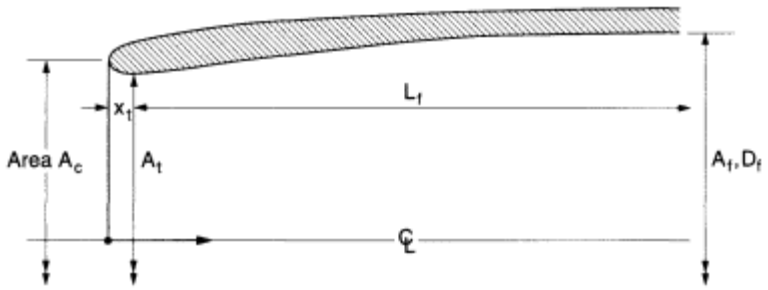

Figure 4.1
Cowl, lip and duct nomenclature.

lip separation, and compressibility effects in the duct are primarily controlled by the value of *M*t. The variation of free-stream Mach number *per se* has no effect except through its influence on the value of *A*¥/*A*t (at low rather than high forward speeds) for a given value of *M*t. Fig. 4.2 shows the interrelationship between the familiar pressure recovery *P*f/*P*¥ versus flow *A*¥/*A*c characteristic and *M*t and *M*¥.

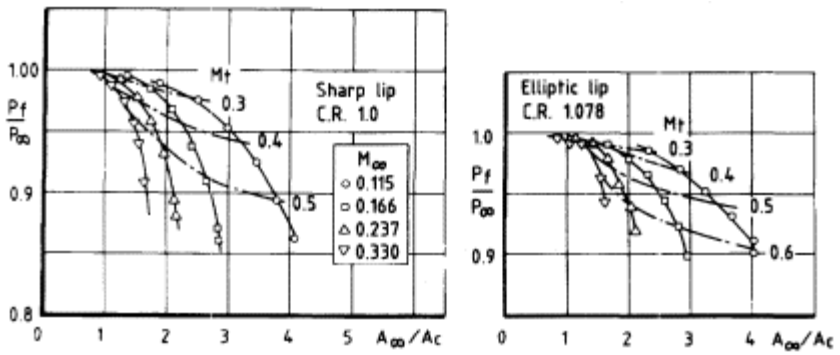

Figure 4.2
Pressure recovery characteristics for axisymmetric pitot intakes with sharp lip and elliptic lip.

4.2
The Subsonic Diffuser

We start by considering the flow in the diffusing duct in isolation. In Chapter 2 the data of Squire for incompressible flow in straight conical diffusers was sufficient. However, in aircraft designs the duct often changes cross-sectional shape and curves usually in an S-bend shape longitudinally. In addition, where available length is restricted, recommended rates of diffusion and/or wall curvature to avoid local flow separation may have to be exceeded. The losses accrued in these situations exceed those derived from simple skin friction estimations and have to be evaluated either from a suction test of the duct fitted with a bellmouth entry or increasingly from a computer program based on the Navier Stokes equations.

One example from measurements in Fig. 4.3 shows how the initial relatively short duct total pressure loss is increased as duct length is increased due to a higher skin friction loss and then is further increased by duct curving and change of cross-sectional shape. It also shows the very considerable increase due to compressibility as mean throat Mach number *M*t (derived on a one-dimensional basis from mass flow measurements) exceeds 0.6 0.7. Local Mach numbers at the wall surface near the throat are often transonic under these circumstances. In particular, the S-duct flow may include some small areas of separated flow followed by reattachment that are not always detected from wall surface static pressure measure-

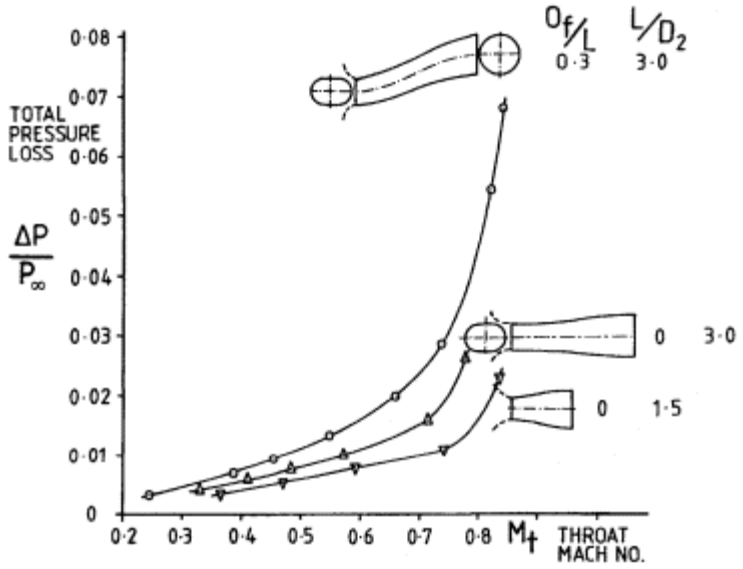

Figure 4.3
Basic duct loss.

ments. Because of the pressure gradient that exists between inner and outer walls due to centrifugal forces, the boundary layer from the outside of the first bend moves towards the inside and as a result some swirl is generated at the engine face. (This is considered in more detail in Chapter 11.)

If the duct cross-section is shaped so that velocity is increased at the outer wall and decreased at the inner wall, the pressure gradient between the walls can be reduced. The extent of any separation can then be reduced without changing mean flow velocity. The effect of this Gerlach shaping is shown in Fig. 4.4.

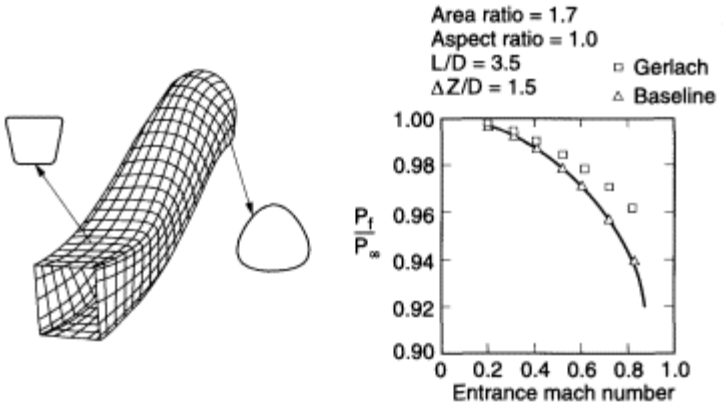

Figure 4.4
Gerlach area shaping.

Results from another systematic series of duct tests are shown in Fig. 4.5. These ducts have a constant length, a constant radius final bend in front of the engine face, and a common area distribution. As the first bend is usually the primary source of engine face total pressure loss and increase in flow distortion, the series of ducts successively decreases the extent of the first bend by decreasing the amount of the initial turning and replacing the turning by canting the entry plane. This results in considerable reduction in total pressure loss and delay in *M*t above which the loss becomes increasingly high. Finally, to put some practical perspective to duct loss, Fig. 4.6 shows the variation of some aircraft duct losses with throat Mach number.

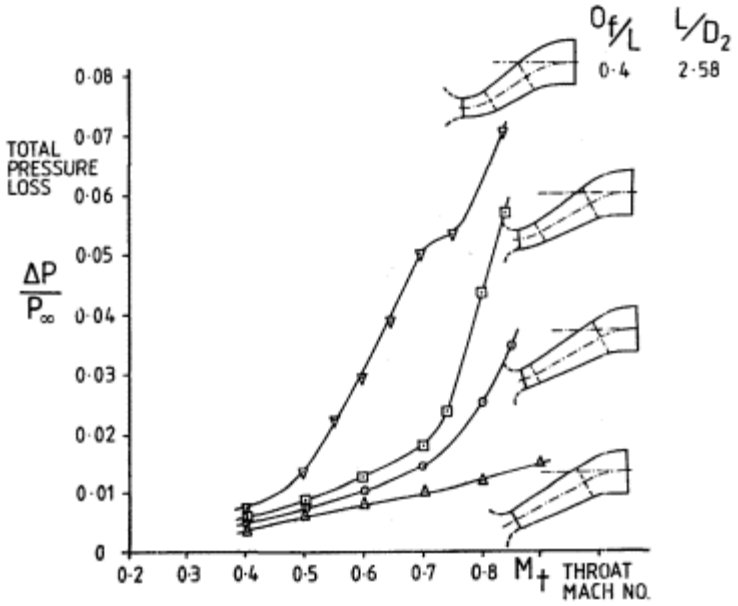

Figure 4.5
Basic duct loss for S-bend duct
due to changes in first bend shape.

Both active and passive methods of boundary layer control can be used to enhance diffuser performance. Active control entails either blowing or sucking the boundary layer and its most important applications are considered in Chapters 8 and 14. Probably the most successful method of passive control is in the form of small aerofoil-shaped generators placed perpendicular to the duct surface. To minimise separation they should be placed just upstream of the separated flow region. However, as shown in Fig. 4.7, their effect is often not very large.

Attention should be drawn to the large amount of systematic suction tests either with a bellmouth at entry or sometimes in tests with a connected pipe

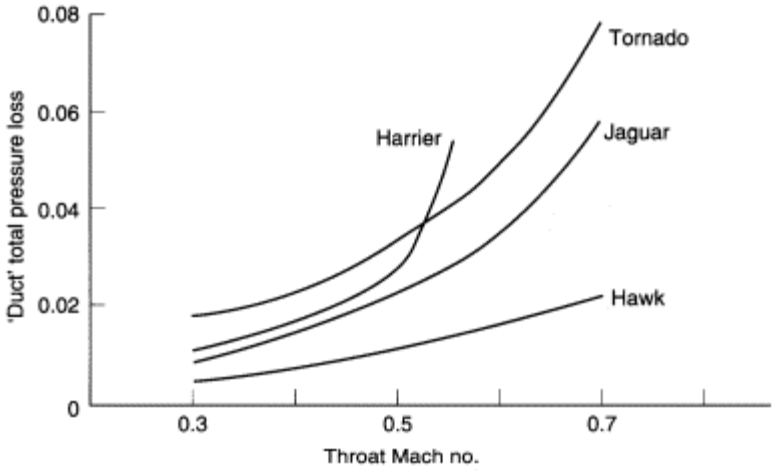

Figure 4.6
Some aircraft duct skin friction losses.

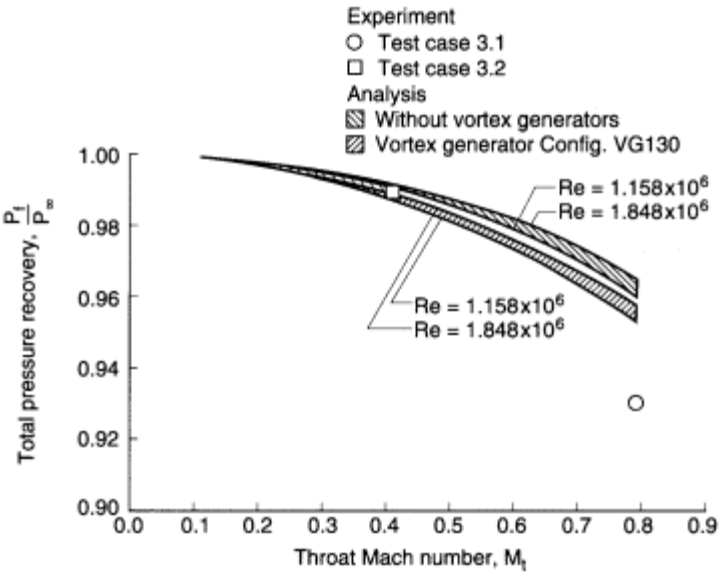

Figure 4.7
Effect of vortex flow control on engine face total pressure recovery for the RAE2129 intake duct.

upstream of the diffuser made in the 1950s and 1960s, e.g. Kline *et al.* (1959), Fox and Kline (1962), Cocanower *et al.* (1965) and Sovran and Klomp (1967), and more recently with more obvious aeronautical application by Lee and Boedicker (1985) and Tindell, (1987).

4.3
Combination of Intake and Subsonic Diffuser.

Although it was stated in the last section that duct skin friction loss is usually obtained from a static bellmouth test, essentially the same result is derived from measurements in a duct plus intake in a free-stream flow provided that the free-stream streamtube is always smaller than the capture area, i.e. *A*¥/*A*c < 1.0. Then, necessarily, the stagnation streamline is always on the underside of the cowl lip. If this is the case, the loss of total pressure in the intake and duct can only be due to skin friction and it can be shown that, typically, for a pitot intake the loss is only a function of the one-dimensional throat Mach number *M*t at all free-stream Mach numbers from 0.6 to 2.0. *M*t is obtained from

$$\left(\frac{A}{A^*}\right)_t = \frac{\left(\frac{A}{A^*}\right)_\infty \times \frac{P_t}{P_\infty}}{(A_\infty/A_c) \times (A_c/A_t)} \qquad (4.1)$$

where *P*t/*P*¥ = 1.0 at subsonic speeds and *P*t/*P*¥ is the normal shock value (*P*t/*P*¥)NS at supersonic speeds. A typical plot of loss, defined as

$$\frac{\Delta P}{P_\infty} = 1 - (P_f/P_\infty) \text{ at subsonic speeds}$$

and

$$= \left(\frac{P}{P_\infty}\right)_{NS} - (P_f/P_\infty) \text{ at supersonic speeds,}$$

is shown in Fig. 4.8 where it is compared with a bellmouth test result. Many more examples of this type of correlation for a range of intake lip shapes and diffuser shapes are shown in Goldsmith (1990).

As free-stream Mach number reduces below about 0.6 and flow rates are increased, the capture streamtube will begin to grow larger than the capture area, and the dividing streamline will then stagnate on the outside of the cowl. When this occurs, potential flow calculations (see Section 4.4.1) show that very high velocities develop around the highlight area of the cowl lip as shown in Fig. 4.9. The real flow will not then be able to sustain the high

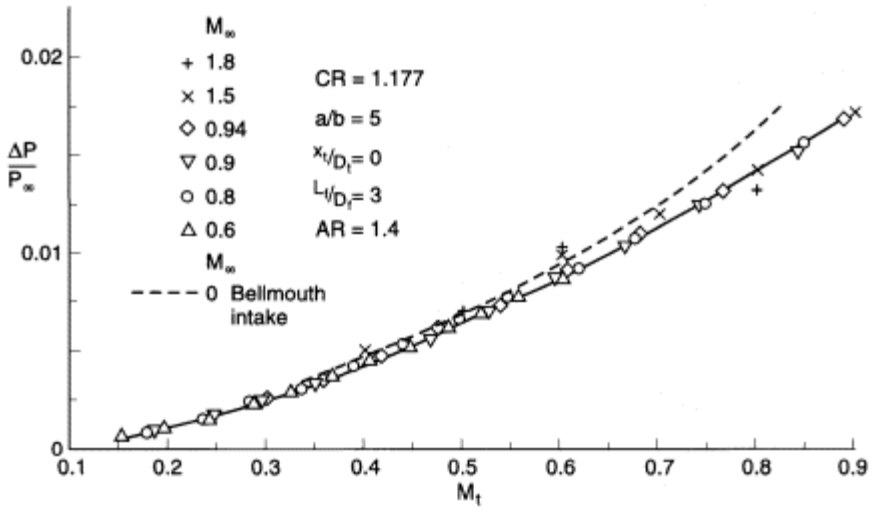

Figure 4.8
Comparison of duct skin friction loss from free-stream pitot intake tests and measurements with a static bellmouth entry.

adverse pressure gradients that follow high supersonic peak velocities and the flow will separate from the undersurface of the cowl in the highlight region. Total pressure loss will then begin to increase as *M*t increases at a much higher rate than for the bellmouth intake due to turbulent mixing following the flow separation.

Calculated peak Mach numbers correlate well with the inverse flow ratio *A*c/*A*¥, for varying *M*¥ (Fig. 4.10), as also does the lip suction force, integrated between the stagnation point and the throat (Fig. 4.11). For the static condition in particular, calculated peak Mach numbers correlate with minimum radius of curvature of the lip, as shown in Fig. 4.12. However, the most important factor influencing the magnitude of this loss and the capture ratio at which it first appears is the intake contraction ratio *CR* = *A*t/*A*c. Use of a sharp lip ensures that the loss increases rapidly as soon as flow ratio exceeds unity and the stagnation point moves to the outside of the cowl. With an elliptic or circular arc lip shape, attached flow around the lip is possible for a range of flow ratios, in this instance from 1.0 to 2.0 (for $M < 0.6$) before separation occurs (Fig. 4.13).

It is convenient to call this loss a lip loss as its magnitude is primarily dependent on lip contraction ratio and to separate it from diffuser skin friction loss. By assuming that lip loss,

$$\left(\frac{\Delta P}{P_\infty}\right)_{\text{lip}} = \frac{\Delta P_f}{P_\infty} - \left(\frac{\Delta P}{P_\infty}\right)_{\text{SF}} \qquad (4.2)$$

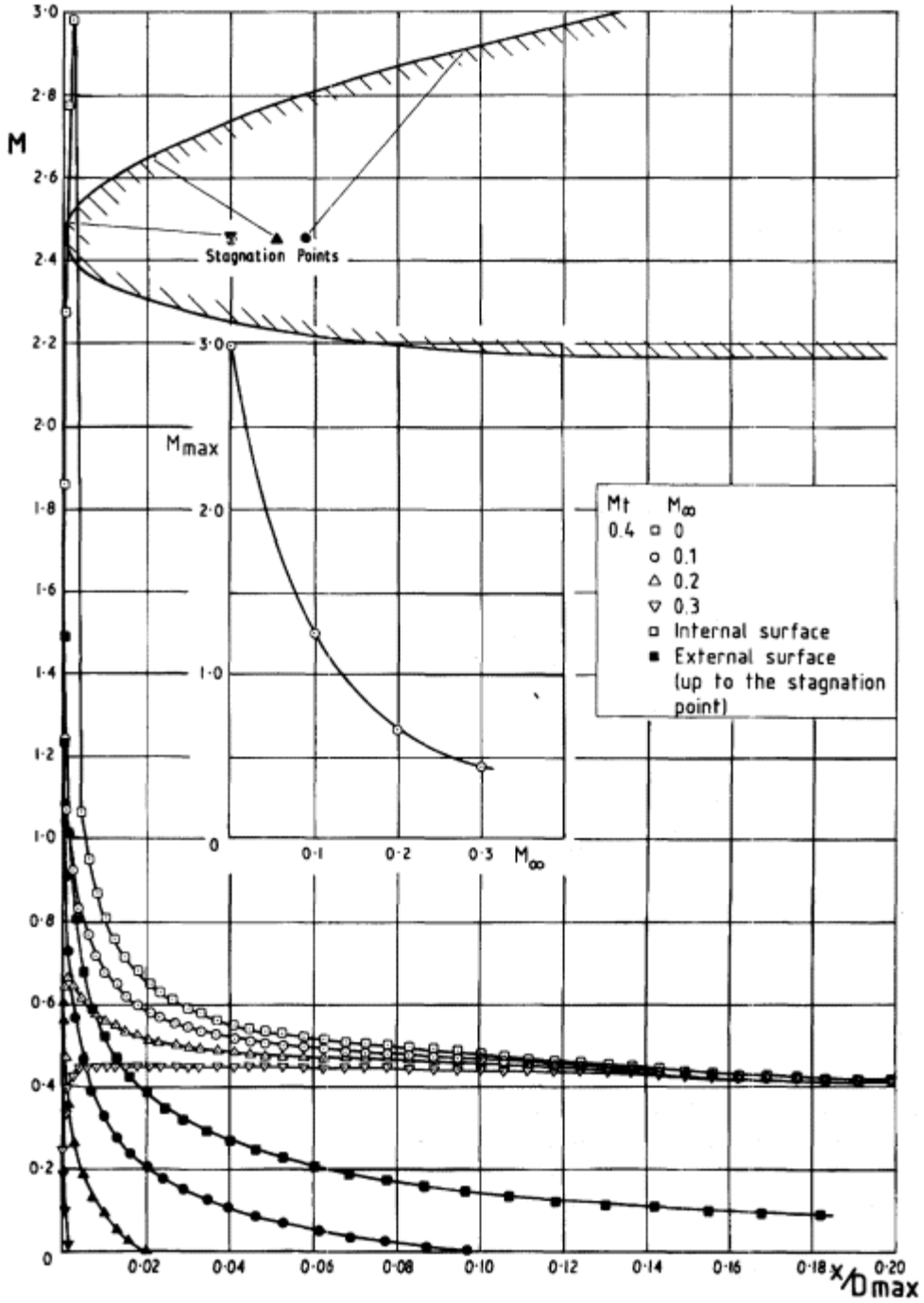

Figure 4.9
Effect of forward speed on lip surface Mach number distribution (ellipse ratio a/b = 5, contraction ratio = 1.15).

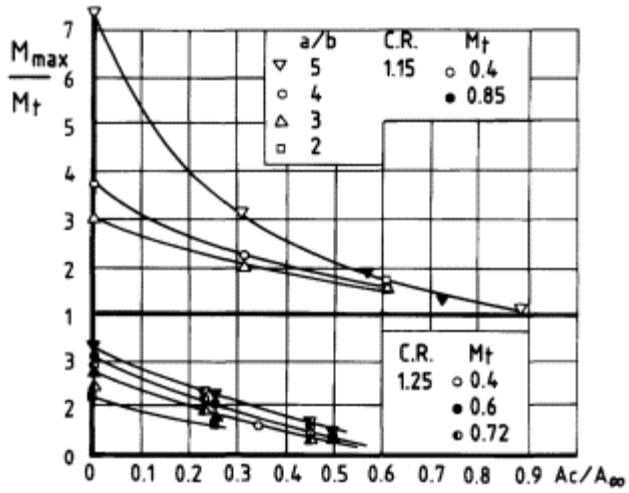

Figure 4.10
Correlation of maximum supervelocity with inverse capture ratio.

is independent of the diffuser geometry, it can be applied to other configurations having the same lip geometry but differing in diffuser length, area ratio and (to a certain degree) area distribution. This latter assumption will undoubtedly be increasingly invalid (particularly at high values of *M*t) if the lip loss data is applied to ducts that have an appreciably higher rate of diffusion than those for which the data shown apply. It is also convenient to plot lip loss versus inverse capture ratio *A*c/*A*¥ so that the loss under static conditions (*A*¥/*A*c = ¥) can be presented. This lip loss, together with an

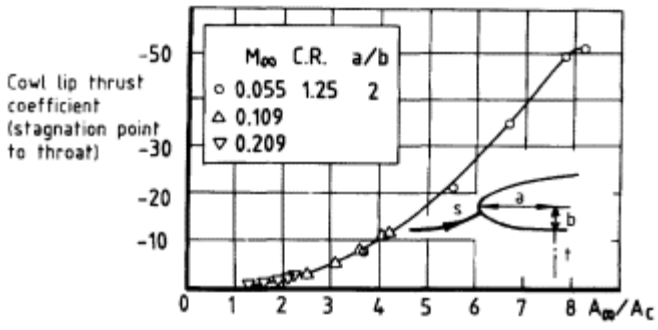

Figure 4.11
Correlation of cowl lip thrust coefficient with capture ratio.

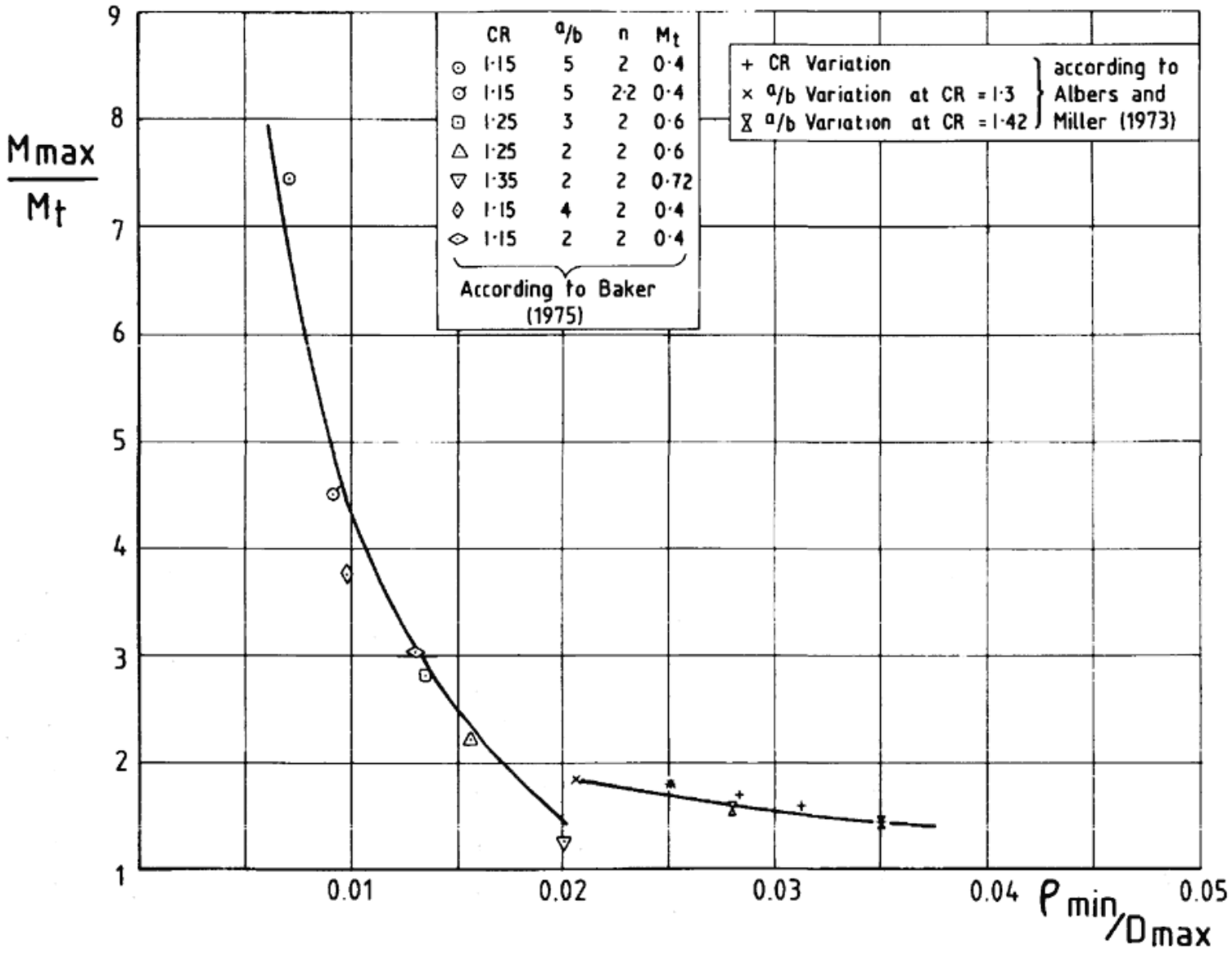

Figure 4.12
Correlation of maximum supervelocity with minimum value of radius of curvature of cowl lip at static conditions.

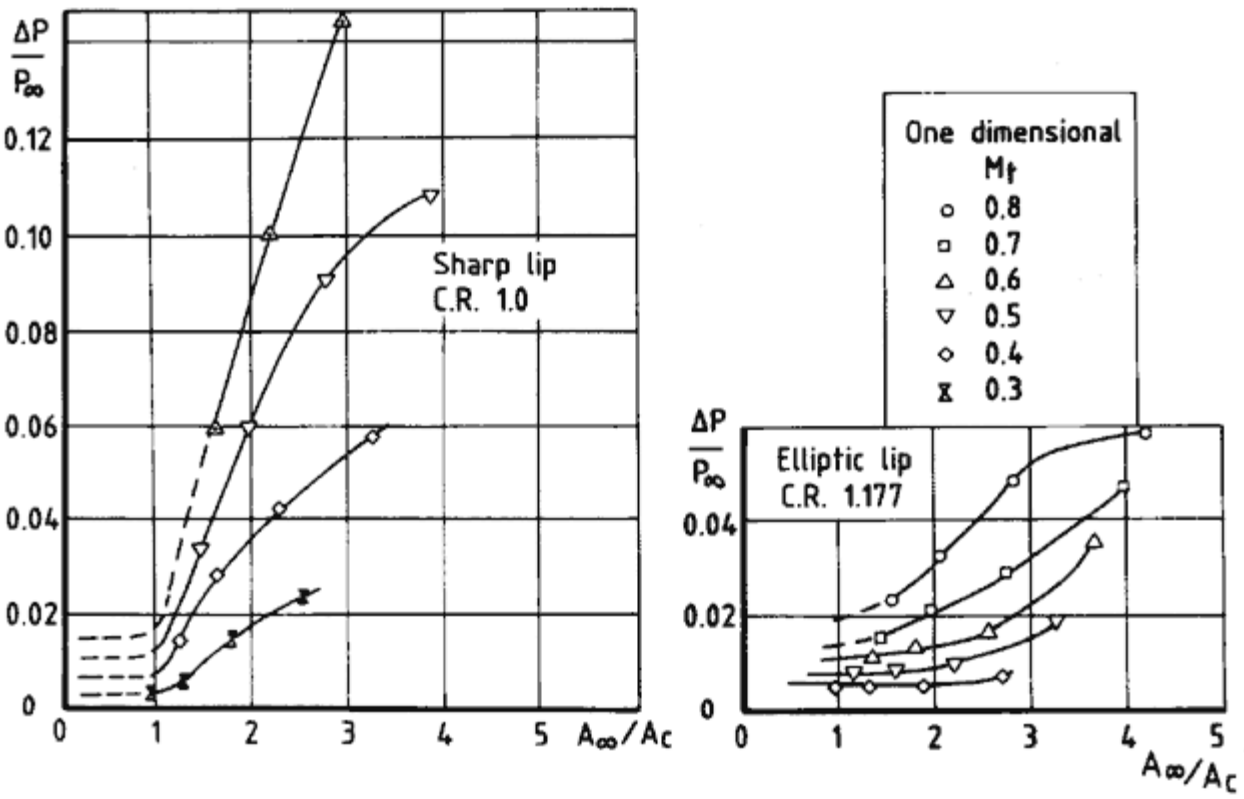

Figure 4.13
Influence of throat Mach number and capture flow ratio on total pressure loss.

engine face flow distortion parameter *D* (see Chapter 11 for a full discussion on engine face distortion), is shown in Fig. 4.14.

As incidence is increased from zero, separation of the internal flow in the region of the windward lip will eventually occur whether the intake streamtube is smaller or larger than the capture area. However, below about 10° incidence the loss curve of Fig. 4.8 will apply if *A*¥/*A*c is less than 1.0. The loss variation above 10° incidence will be discussed in greater detail in Chapter 13.

4.4
Methods of Calculation of Total Pressure Loss with Attached Flow at Entry

A review of the fundamental equations, and of the simplifications and assumptions that are used to make these equations form into computational programs, is given by Anderson and Towne in Chapter 9 of Goldsmith and Seddon (1993). Potential flow, Euler, parabolized Navier Stokes and time-averaged Navier Stokes analyses will now all be considered briefly.

With rapidly increasing computer power and more sophisticated programs becoming available all the time, this section can only illustrate a small amount of the success of tried and tested calculation methods. We will

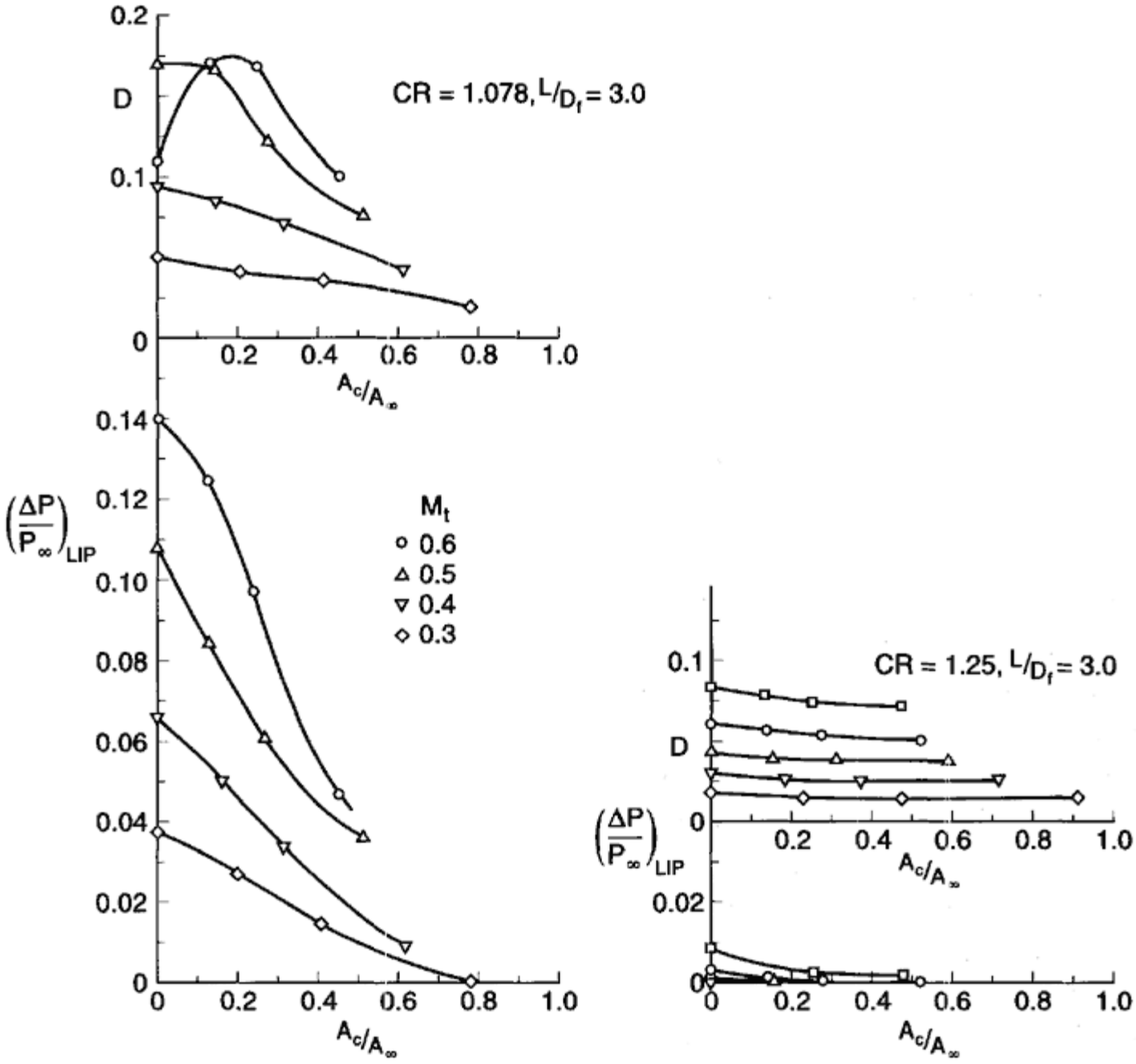

Figure 4.14
Variation of engine face distortion and lip loss with inverse capture ratio for two lip contraction ratios.

make the elementary distinctions that (a) potential flow methods can deal with free-stream Mach numbers up to 1.3 or 1.4 because normal shock losses up to these Mach numbers are small. If they are used in straight ducts with conservative rates of diffusion and no flow separation, they can be combined with boundary layer methods to produce more realistic results. (b) Euler flow methods can deal with non-isentropic flows and therefore can be used at supersonic free-stream Mach numbers, and they also can be combined with boundary layer methods with the same limitations as above. (c) Any duct shapes which lead to three-dimensional flows, e.g. straight ducts at high incidence or S-shaped ducts with or without changing cross-section shape, have to be dealt with by using some form of the Navier Stokes equations.

4.4.1
Straight Ducts

Several methods of evaluating the compressible potential flow equations for axisymmetric cowls and ducts were published in the 1970s, the distinctions between them being mainly in computing techniques resulting from the adoption of different coordinate meshes. One of the first published methods was by Arlinger (1975) which uses a sequence of conformal mappings and a final coordinate stretching, so that the whole flowfield is mapped to a rectangular domain in which the full potential flow equation in rectilinear coordinates can be solved. Chen and Caughey (1979) use a boundary-conforming coordinate system generated by a sequence of conformal and shearing transformations. Reyhner (1977) solves the full potential equations in a cylindrical coordinate system and tackles the difficult interpolations needed to treat accurately the surface boundary conditions.

The method most used in the UK was that due to Baker (1975): this replaces the full potential equation by a finite-difference approximation using a non-orthogonal mesh. Although the use of curvilinear coordinates involves extra terms, the generality of the scheme allows flexibility and the ability to deal with complex geometries. The representation of the coordinate mesh is shown in Fig. 4.15. The coordinates are defined by simple analytical expressions, which are chosen to ensure that the body surface and the axis of symmetry each lie along a coordinate line; this permits boundary conditions on the body surface and along the axis to be applied accurately. The method assumes isentropic flow but predicts the presence of shock waves and in doing so violates the continuity equation by not allowing for entropy increase. Little error is introduced, however, unless the shock Mach number exceeds about 1.3 1.4. This method was used to produce Figs. 4.9 4.12.

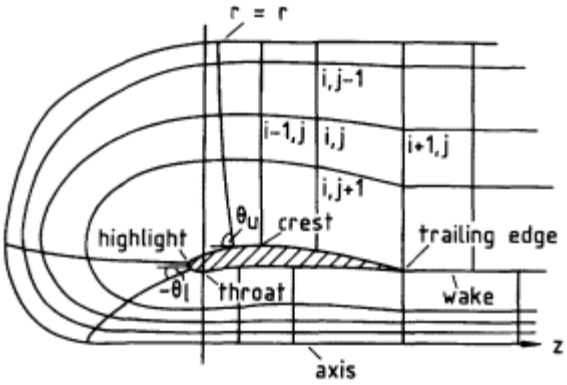

Figure 4.15
Coordinate mesh for potential flow calculations (Baker).

An improved version of the Baker method using finite volume rather than finite difference approximations was devised by Peace (1984a,b). A boundary layer prediction method was developed by Johnston (1984) and was coupled to the Peace inviscid potential flow solution. This boundary solution uses a Thwaites (1948) method for the initial laminar boundary layer and the Green (1973) integral method for the following turbulent portion. The calculated inviscid pressures determine the boundary layer calculation and the displacement surface, in the form of transpiration velocities, reacts on the inviscid calculation in the conventional direct coupling approach. Laminar separation and reattachment is modelled using the Horton (1969) method, but turbulent separation is not.

Addition of the boundary layer improves duct flow prediction accuracy mainly by the increase in duct velocity for a given flow ratio because the duct cross-sectional area has been effectively reduced. The calculated boundary layer parameters at the engine face are used in conjunction with an assumed power law for the mean velocity profile in the boundary layer to obtain a predicted total pressure distribution at the engine face together with an integrated total pressure loss.

An example at $M¥ = 0.94$ (Fig. 4.16) illustrates typically the improvement in agreement between measured and calculated duct surface Mach number distribution when the boundary layer addition is made, and also the agreement for boundary layer profile at the engine face and the total pressure loss. At low speeds, however, the agreement between calculated and measured values of surface Mach number distribution is less satisfactory (Fig. 4.17). In this case the capture ratios are always in excess of unity and this results in an abrupt adverse pressure gradient between highlight and throat, which if it does not separate the boundary layer results in a severe thickening downstream of the throat. The agreement does, however, improve rapidly as throat Mach number is lowered and the adverse pressure gradient is reduced.

At supersonic free-stream Mach numbers a numerical solution of the Euler equations developed at British Aerospace (Doe *et al.*, 1986) has been used to predict inviscid surface Mach number distributions and, coupled with the ARA boundary layer methods, to produce again engine face total pressure values. At $M¥ = 1.5$, Fig. 4.18 shows that the measured values are very sensitive to the mass flow ratio chosen for comparison. At the higher flow ratio the intake is obviously operating very slightly 'supercritically' (this term and related ones are defined in the following chapter) and as a result, although the normal shock at the free-stream Mach number is accurately predicted, the small additional 'supercritical' shock loss shown in the measured total pressure distinctions is not. For all other conditions of flow the agreement on surface distributions and engine face total pressure is very good.

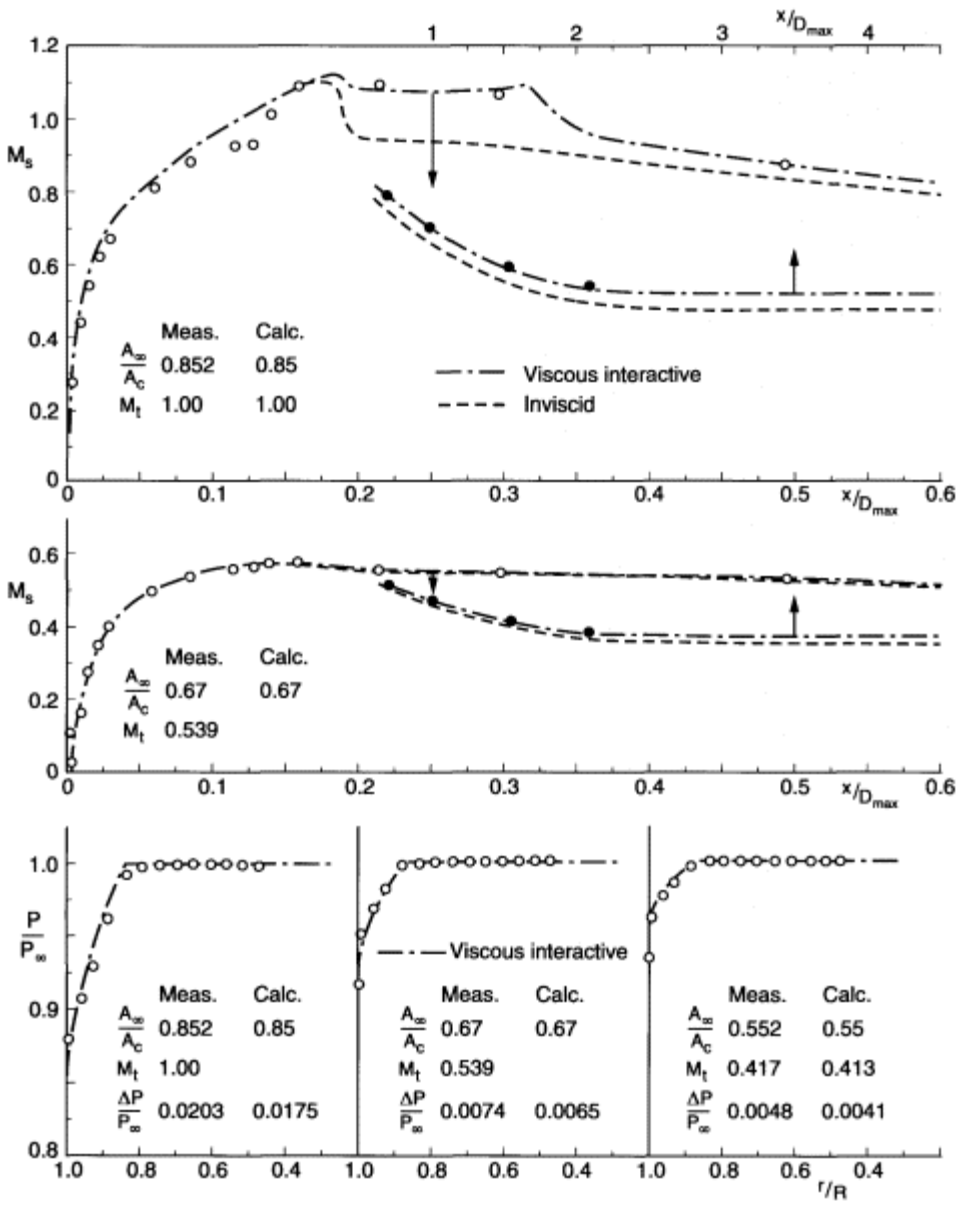

Figure 4.16
Comparison of measured surface Mach number and total pressure distributions with predictions based on potential flow (Peace) with and without boundary layer interaction.

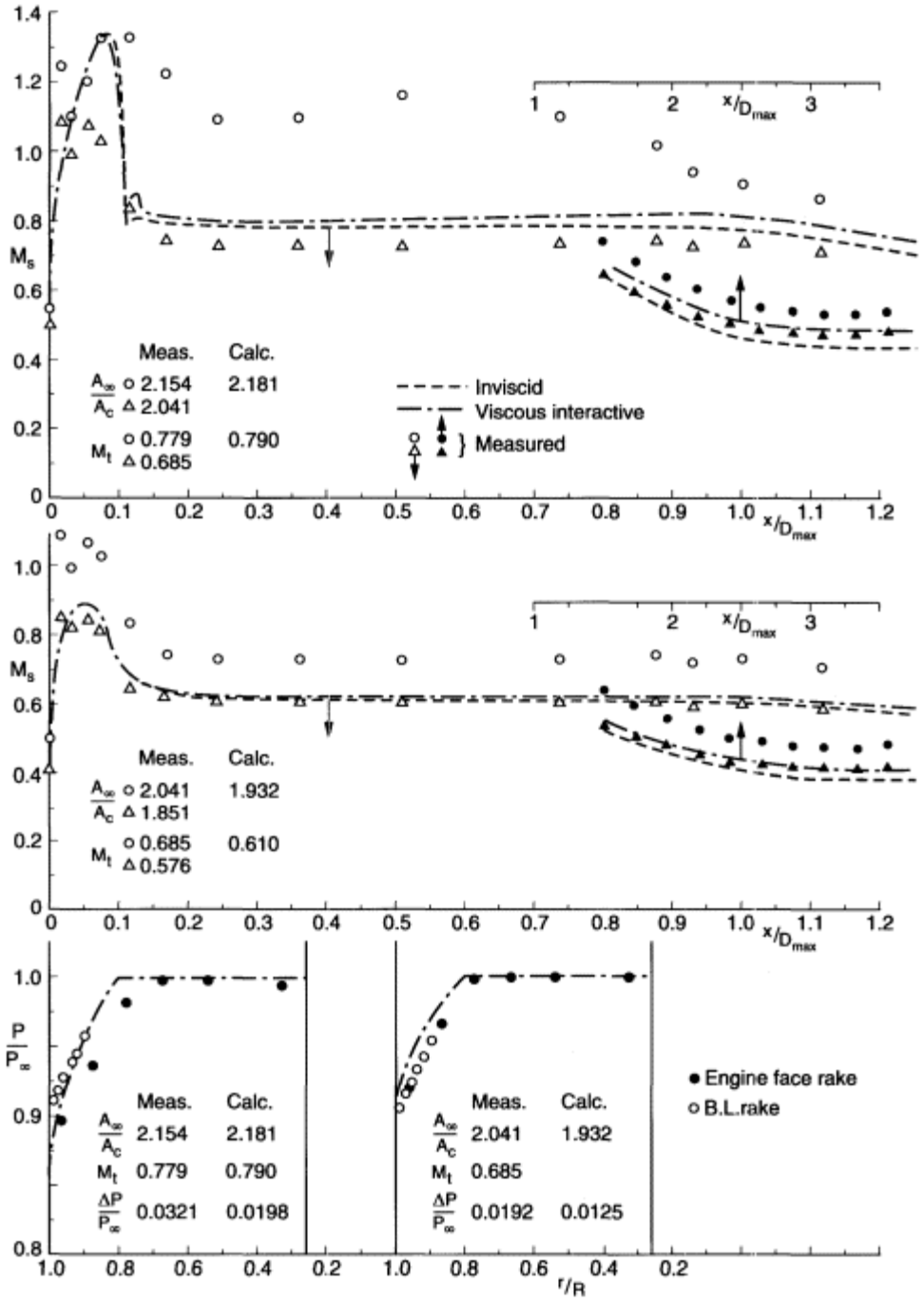

Figure 4.17
Comparison of calculated and measured internal
surface Mach numbers and engine face total pressures.

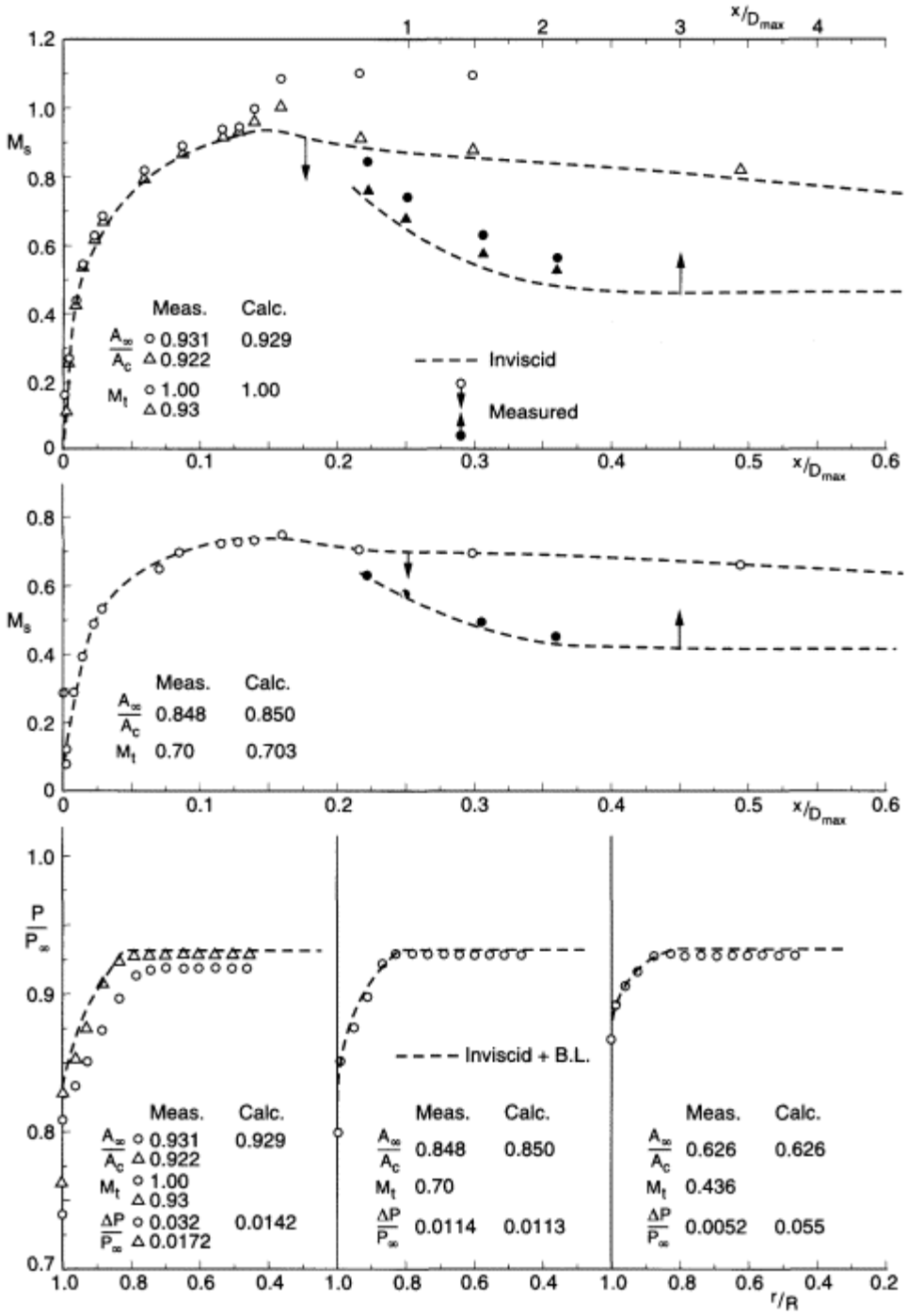

Figure 4.18
Comparison of calculated and measured internal surface Mach numbers and engine face total pressures at M¥ = 1.5, a = 0°.

4.4.2
S-Bend Ducts

Anderson and Towne (1981) have studied S-duct flows extensively using computer programs based on the parabolized Navier Stokes (PNS) equations. The program is known widely as the NASA (Lewis) PEPSI-G program, and a relevant comparison of calculated and measure results is shown in Fig. 4.19. A further example of the power and efficiency of these solutions is contained in some detail in Anderson and Towne's Chapter 9 of Goldsmith and Seddon (1993). In this instance, areas of separated flow were identified. A computing procedure was used to deal with small regions of separated flow, and results with and without the placement of vortex generators in a duct are compared to PNS solutions which incorporate modelling of the aerodynamics of the vortex generators in Anderson *et al.* (1992).

In all these examples the computational methods depend on either measurements or assumptions for the state of the flow at the entrance to the duct. In bellmouth suction tests these measurements are usually absent as the initial boundary layer is so thin. In a more demanding study of calculation methods, a particular blunt-lipped S-duct at a free-stream Mach number of 0.21 was studied using three different computer programs in Chapter 3 of Fluid Dynamics Panel Working Group 13 (1991). Two methods are based on the Navier Stokes equations. The results labelled NS1 are from a program emanating from British Aerospace (Doe *et al.*, 1986) and use an implicit pressure correction method for the Reynolds-average Navier Stokes equations. The standard K e model is used to represent turbulence with a wall function in the near-wall region which implies constant shear stress and no streamwise pressure gradient. The results labelled NS2 use the Dornier IKARUS three-dimensional Navier Stokes code. This is an explicit finite volume code as proposed by Jameson *et al.* (1981). A fully turbulent boundary layer was assumed with a thin-layer approximation and the Baldwin and Lomax (1978) turbulence model. Largely for comparison purposes, and possibly for its better representation of the flow field around the cowl lip, entry plane and throat area, an inviscid program (EU) based on the Euler equations and developed at the ARA was included.

Tabulated results at two engine face conditions for the NS1 and NS2 programs are compared in Table 4.1. Comparison of wall static pressures along the duct for all these programs for port and starboard and top and bottom generators for both flow conditions are shown in Figs. 4.20 and 4.21.

4.5
Influence of Factors Other Than Contraction Ratio

Although contraction ratio is the most important parameter in discussing lip loss in this chapter, there is also an influence of lip shape and initial

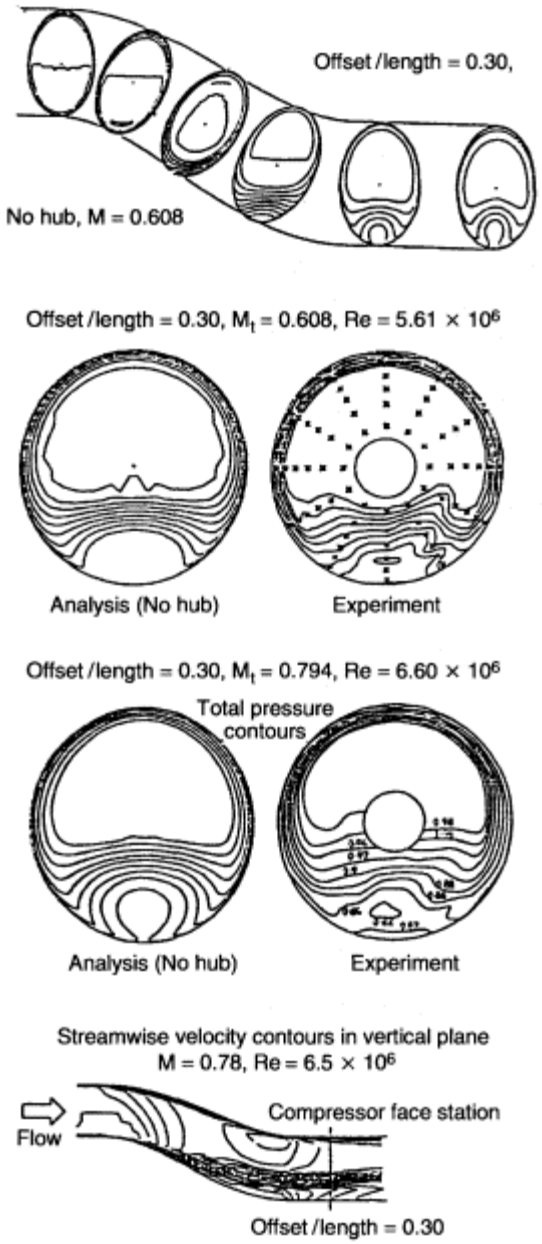

Figure 4.19
Comparison of measured and calculated
(PNS, Anderson) flow contours in an S-duct.

Table 4.1 Test conditions and comparative results

Flight Mach number	M¥	= 0.210	Flight Mach number	M¥	= 0.210
Throat Mach number	Mt	= 0.794	Throat Mach number	Mt	= 0.412
'Non-dimensional' weight flow	WATf	$= 0.311 \frac{in^2\sqrt{^\circ K}}{sec}$	'Non-dimensional' weight flow	WATf	$= 0.197 \frac{in^2\sqrt{K}}{sec}$
Compressor face Mach number	Mf	= 0.536	Compressor face Mach number	Mf	= 0.304
Pressure recovery	PR	= 0.928	Pressure recovery	PR	= 0.9897
Capture flow ratio	A¥/Ac	= 2.173	Capture flow ratio	A¥/Ac	= 1.457

Results from	Pressure recovery	Engine face mean static pressure	DCA60
Experiment	0.92798	0.725	0.398
NS1	0.89000	0.757	0.417
NS2 (non-weighted)	0.88781 (non-weighted) 0.92063	0.729	0.884

Results from	Pressure recovery	Engine face mean static pressure	DCA60
Experiment	0.98974	0.922	0.226
NS1	0.96822	0.926	1.724
NS2 (non-weighted)	0.99180	0.949	0.157

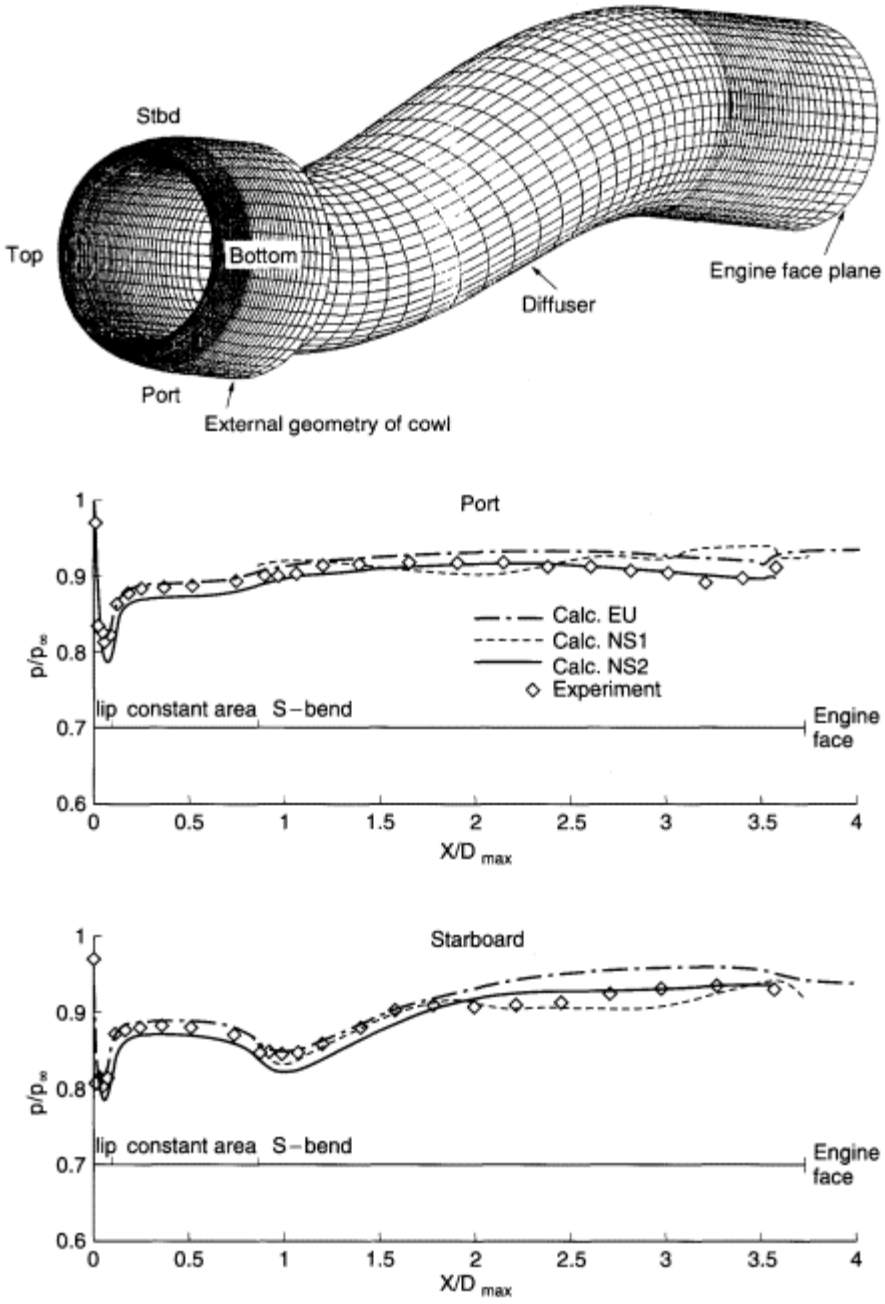

Figure 4.20
Comparison of S-duct port and starboard wall static pressure distributions, measured and calculated by several methods.

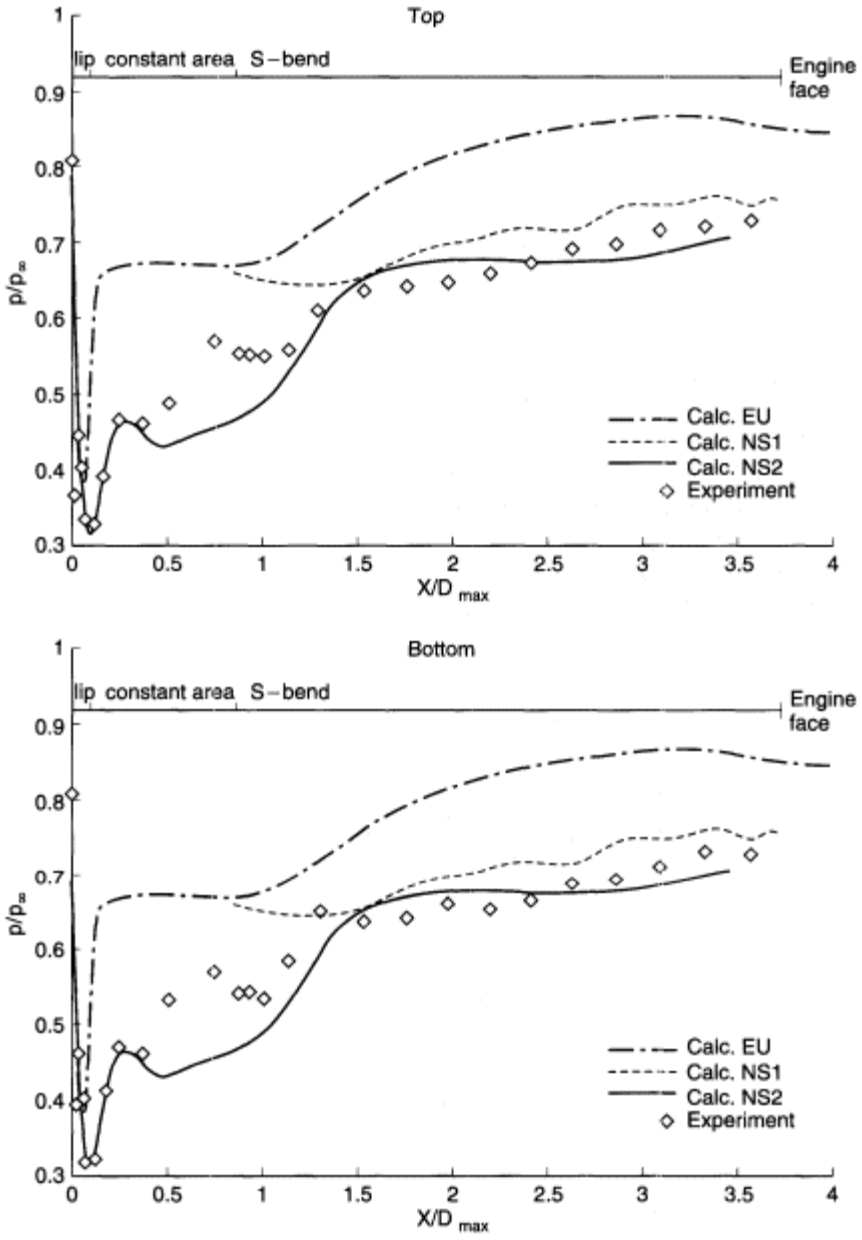

Figure 4.21
Comparison of S-duct top and bottom wall static pressure distributions, measured and calculated by several methods.

shape of the subsonic diffuser. The lower lip losses consequent on using circular arc lips in comparison with elliptic lips, together with the small effect of changing ellipse ratio *a/b* from the results of Blackaby and Watson (1954), are shown in Fig. 4.22(a). For capture ratios less than unity the duct loss variation shown in Fig. 4.22(b) illustrates the lower throat Mach number at which losses start to increase more rapidly for a circular arc lip shape in comparison to an elliptic lip.

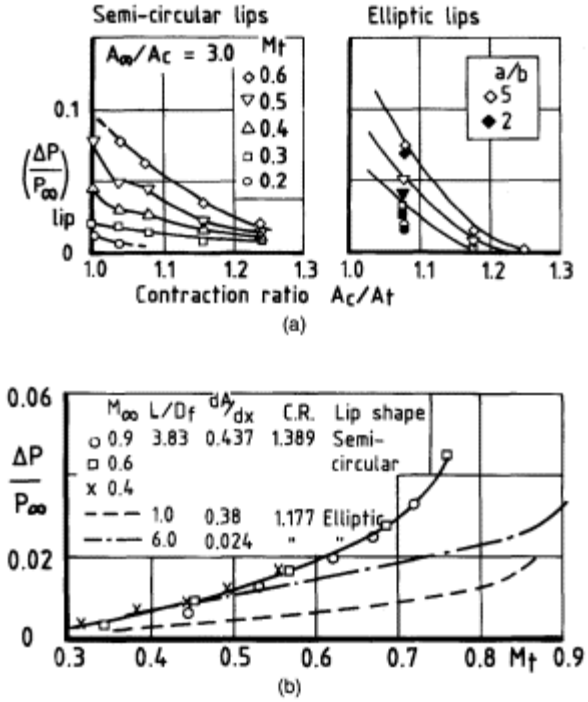

Figure 4.22
Influence of lip shape.

The rationale for presenting measurements in the form of a lip loss variation with inverse capture ratio and throat Mach number is so that this important source of loss can be applied to a variety of diffuser shapes. If the changes in rate of diffusion are obtained by, for instance, shortening of the diffuser from $L/D_f = 3.0$ to 1.5, then, as seen in Fig. 4.23, there is an effect on lip loss. If, however, the diffuser was lengthened and the diffusion rate was decreased, then little or no effect should result.

4.6
Total Pressure Loss with Separated Flow at Entry.

In terms of detailed cowl shape, the calculation of total-pressure loss when the flow is separated at the lip is not generally possible. A useful approach

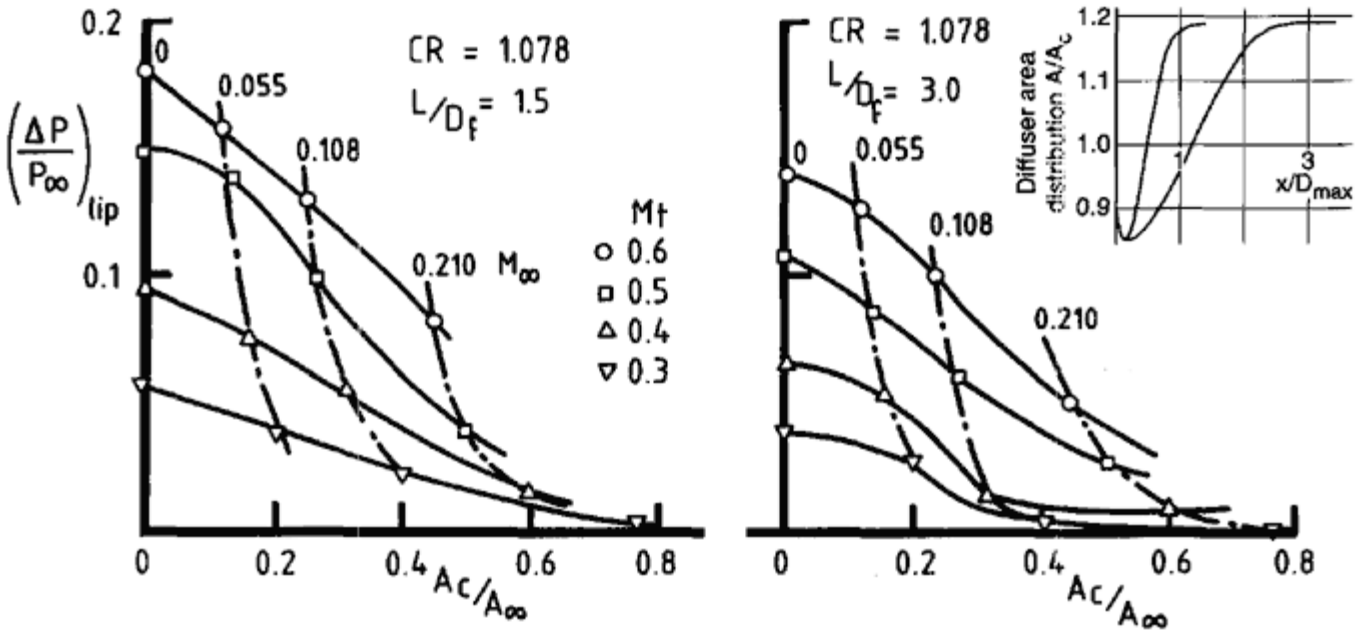

Figure 4.23
Influence of diffuser length on lip loss.

can be made, however, by considering the entry to be in the form of a cylindrical sharp-lipped cowl. When the free stream tube area is greater than the entry area, a momentum continuity analysis can be applied.

We begin by applying the momentum theorem in the *external flow*, as illustrated in Fig. 4.24. The cowl is considered to be a semi-infinite thin-walled cylinder. The control surface ABCDEA consists of the pre-entry stream tube AB, the cowl Surface BC taken to a point where the velocity has been restored to free stream level, entry and exit planes AE and DC and an outer cylinder ED of large diameter, where the velocity is again at free stream level. The cross-stream area at AE is *A*0 and that at DC, consequently, is *A*0 + *A*¥ *Ac*, *A*¥ and *Ac* having the usual connotations in relation to the internal flow.

Continuity demands that in order to balance the excess outflow across DC over the inflow across AE, an additional inflow, of amount (*A*¥ *Ac*) r¥ *V*¥, occurs on the boundary ED. The momentum theorem takes form

$$A_0\rho_\infty V_\infty^2 + (A_\infty - A_c)\rho_\infty V_\infty^2 + \int_{ABC} (p - p_\infty)\mathrm{d}A = (A_0 + A_\infty - A_c)\rho_\infty V_\infty^2 \qquad (4.3)$$

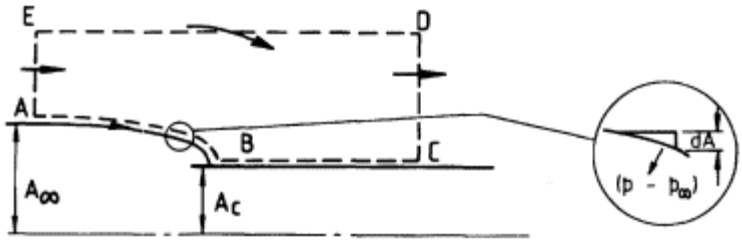

Figure 4.24
Application of momentum theorem to external flow.

whence it is seen that

$$\int_{ABC} (p - p_\infty) dA = 0$$

and since this integral is zero along BC, the surface being parallel to the mainstream, it follows that

$$\int_{AB} (p - p_\infty) dA = 0 \qquad (4.4)$$

This result, that the pressure integral along the dividing streamtube is zero, can now be transferred to the internal flow. Following Fradenburgh and Wyatt (1954), the momentum equation is applied within a control surface ABCDEA in Fig. 4.25. Points C and D, defining Station 1, are sufficiently downstream in the duct for uniform flow conditions to have been established following a disturbance at entry. The section of boundary BC consists of a portion of cowl external surface, from the stagnation point B forward to the lip, and the internal surface from the lip to Station 1. The equation is

$$\begin{matrix}\text{Momentum flux} \\ \text{at Station 1}\end{matrix} = \begin{matrix}\text{Momentum} \\ \text{flux at } \infty\end{matrix} + \begin{matrix}\text{Lip suction} \\ \text{force, } F \text{ say}\end{matrix} + \int_{AB} (p - p_\infty) dA$$

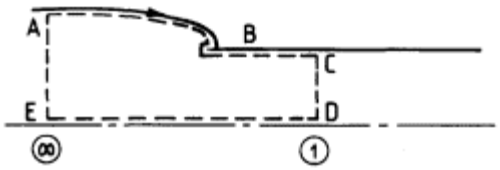

Figure 4.25
Application of momentum theorem to isentropic internal flow from station ¥ to station 1.

The pressure integral disappears, as does also the force F, which is zero because the lip is infinitely thin. So we have

$$2q_1 A_1 + (p_1 - p_\infty) A_1 = 2q_\infty A_\infty \qquad (4.5)$$

This may be written

$$\frac{2q_1}{P_1} + \frac{p_1}{P_1} - \frac{p_\infty}{P_\infty} \cdot \frac{P_\infty}{P_1} = \frac{2q_\infty}{P_\infty} \cdot \frac{P_\infty}{P_1} \cdot \frac{A_\infty}{A_1}$$

and thus

$$\frac{P_1}{P_\infty} = \frac{\frac{2q_\infty}{P_\infty} \cdot \frac{A_\infty}{A_1} + \frac{p_\infty}{P_\infty}}{\frac{2q_1}{P_1} + \frac{p_1}{P_1}} \qquad (4.6)$$

Then from continuity between Station ¥ and Station 1,

$$P_\infty A_\infty{}^* = P_1 A_1{}^*$$

so that

$$\frac{A_\infty}{A_1} = \frac{P_1}{P_\infty} \cdot \frac{A_1{}^*}{A_1} \cdot \frac{A_\infty}{A_\infty{}^*} \qquad (4.7)$$

Substituting in Equation (4.6) leads to the equation for pressure recovery

$$\frac{P_1}{P_\infty} = \frac{p_\infty / P_\infty}{\frac{2q_1}{P_1} + \frac{p_1}{P_1} - \frac{2q_\infty}{P_\infty} \cdot \frac{A_1{}^*}{A_1} \cdot \frac{A_\infty}{A_\infty{}^*}} \qquad (4.8A)$$

This can be evaluated at any free-stream Mach number *M*¥ for a series of values of *M*1. In Mach number terms instead of pressure terms, and writing 't' for the expression (1 + (g 1) *M*2/2), the equation is

$$\frac{P_1}{P_\infty} = \frac{(t_1/t_\infty)^{(\gamma+1)/2(\gamma-1)}}{(1+\gamma M_1{}^2)(t_\infty/t_1)^{\frac{1}{2}} - \gamma M_1 M_\infty} \qquad (4.8B)$$

The derivation gives no indication of how the loss in total pressure from *P*¥ to *P*1 is sustained, nor what is a relevant range of Mach number *M*1. In order to clarify these factors, we consider the approach used by Soffker and Renner (1965). This is in two parts, the first of which is to calculate the contraction of a jet of separated flow from the lip, assuming that at this stage the flow is isentropic. The second part evaluates the loss of total pressure as the jet expands in area back to the walls of the duct. The approach allows the flexibility of considering the expansion phase in different ways, according to the shape of the duct. Three such ways are illustrated in Fig. 4.26. We proceed with consideration of the simplest of these, that of Fig. 4.26(a), which corresponds effectively to the case considered by Fradenburgh and Wyatt.

The momentum equation for stage 1, as applied, that is, between Station ¥ and Station s (uniformly contracted jet) is

$$2q_s A_s + (p_s - p_\infty)A_s + (p_s{}' - p_\infty)(A_c - A_s) = 2q_\infty A_\infty \qquad (4.9)$$

Here *p*s' is the pressure in the separated region and *p*s that in the free jet. The two pressures are more or less equal unless the flow is complicated by the presence of shock waves. Rearranging and introducing total pressures to provide Mach number functions, the jet cross-sectional area can be expressed as

$$\frac{A_s}{A_c} = \frac{\frac{p_\infty}{P_\infty} \cdot \frac{p_\infty}{p_s} \cdot \frac{P_s}{p_s} - \frac{p_s'}{p_s}}{\frac{2q_s}{p_s} - \frac{2q_\infty}{P_\infty} \cdot \frac{P_\infty}{P_s} \cdot \frac{P_s}{p_s} \cdot \frac{A_\infty}{A_s} + 1 - \frac{p_s'}{p_s}} \qquad (4.10)$$

The continuity relation is

$$\frac{A_\infty}{A_s} = \frac{A_\infty}{A_\infty^*} \cdot \frac{P_s}{P_\infty} \cdot \frac{A_s^*}{A_s} \qquad (4.11)$$

Putting $P_s = P_¥$ (isentropic flow) and combining Equations (4.10) and (4.11), we obtain for the jet area ratio:

$$\frac{A_s}{A_c} = \frac{\frac{p_\infty}{P_s} \cdot \frac{P_s}{p_s} - \frac{p_s'}{p_s}}{\frac{2q_s}{p_s} - \frac{2q_\infty}{P_\infty} \cdot \frac{P_s}{p_s} \cdot \frac{A_\infty}{A_\infty^*} \cdot \frac{A_s^*}{A_s} + 1 - \frac{p_s'}{p_s}} \qquad (4.12)$$

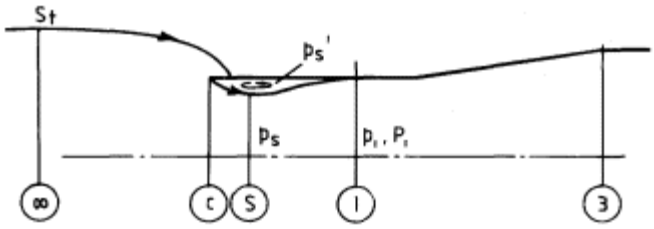

(a)

Figure 4.26
(a) Single enlargement with reattachment before subsonic diffusion

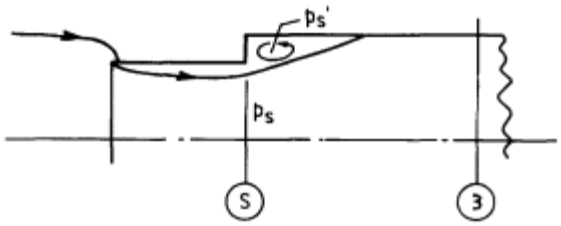

(b)

Figure 4.26
(b) single enlargement with no reattachment upstream of subsonic diffuser

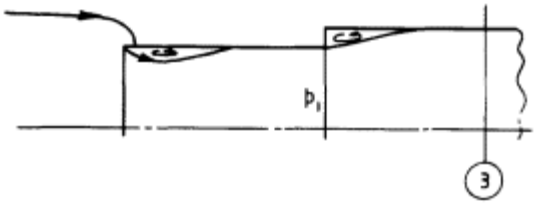

(c)

Figure 4.26
(c) double enlargement.

This can be evaluated for a range of values of *M*s from zero to 1.0, assuming *p*s' is equal to *p*s, and for a range of values of *p*s'/*p*s, with *M*s equal to 1.0.

To calculate the total-pressure loss, the momentum and continuity equations are applied to the flow between Station s and 1, the latter being at a downstream position where the flow fills the duct and is once more uniform. In this phase the flow is not isentropic. The momentum equation is:

$$2q_1A_1 + (p_1 - p_\infty)A_1 = 2q_sA_s + (p_s - p_\infty)A_s$$

$$+(p_s' - p_\infty)(A_1 - A_s) \qquad (4.13)$$

Continuity gives

$$\frac{P_1}{P_s} = \frac{A_1}{A_1^*} \cdot \frac{A_s^*}{A_s} \cdot \frac{A_s}{A_1} \qquad (4.14)$$

These two equations can be manipulated to provide

$$\left[\frac{p_s}{P_s} + \frac{p_s'}{P_s}\left(\frac{A_1}{A_s} - 1\right) + \frac{2q_s}{P_s}\right]\frac{A_s}{A_s^*} = \left[\frac{2q_1}{P_1} + \frac{p_1}{P_1}\right]\frac{A_1}{A_1^*} \qquad (4.15)$$

*A*1 in our case is the same as *A*c. Since the left-hand side of Equation (4.15) is a function of *M*s and *A*s/*A*c and the right-hand side is a function of *M*1 only, the equation can be evaluated in a manner similar to Equation (4.12), in this case to derive values of *M*1. The total pressure ratio then follows from Equation (4.14).

In Fig. 4.27 some calculated and measured values of total-pressure loss and flow ratio are shown plotted as functions of *M*1.

4.6.1
Special Conditions with Separated Flow

The theory can be illustrated usefully by considering certain special conditions. A first such condition is when *M*s *is equal to 1.0*, with *p*s' equal to *p*s. By Equation (4.12) the throat area is now a specific function of free-stream Mach number and at a given *M*¥ the flow through the intake is at a maximum. The total-pressure loss is similarly at a maximum for shock-free flow: it can be exceeded only if shocks are produced downstream of the throat as the flow becomes 'supercritical'. With *M*s = 1 and g = 1.4, Equation (4.12) takes the form

$$\frac{A_s}{A_c}\left[1 - 2.704\ \frac{q_\infty}{P_\infty}\left(\frac{A}{A^*}\right)_\infty\right] = 1.352\left(\frac{p_\infty}{P_\infty} - 0.528\right) \qquad (4.16)$$

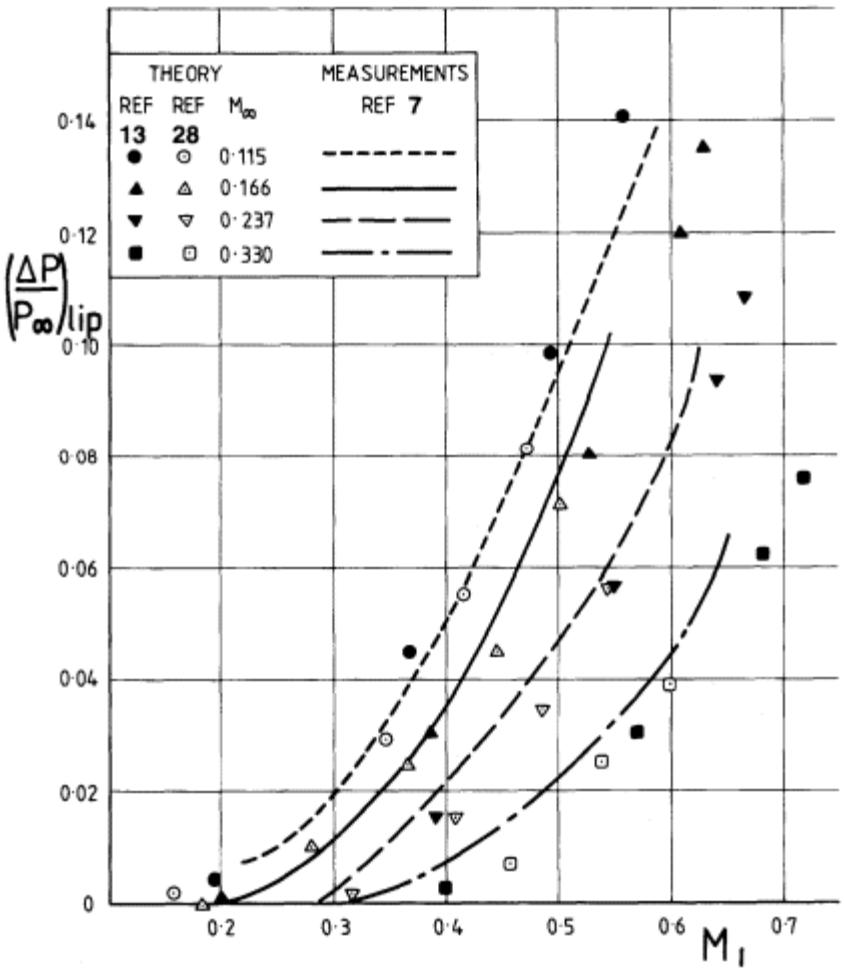

Figure 4.27
Comparison of calculated and measured lip loss for sharp lip.

This gives the variation of *A*s/*A*c with free-stream Mach number shown in Fig. 4.28. The value of *A*s/*A*c in the static condition (*M*¥ = 0) is 0.638. *A*¥/*A*c follows from the continuity relation and is also plotted in the diagram. Equation (4.15) now yields *M*1 in terms of *M*¥ and Equation (4.14) gives the pressure recovery. These two quantities are plotted in Fig. 4.29. It is seen that the maximum shock-free total-pressure loss is approximately 11% and occurs, as would be expected, in the static condition.

We may consider the *static condition* further. With *M*¥ put equal to zero, and *p*s' again equal to *p*s, Equation (4.12) reduces to

$$\frac{A_s}{A_c} = \frac{P_s/p_s - 1}{2q_s/p_s} = \frac{P_s}{2q_s} - \frac{1}{\gamma M_s^2} \qquad (4.17)$$

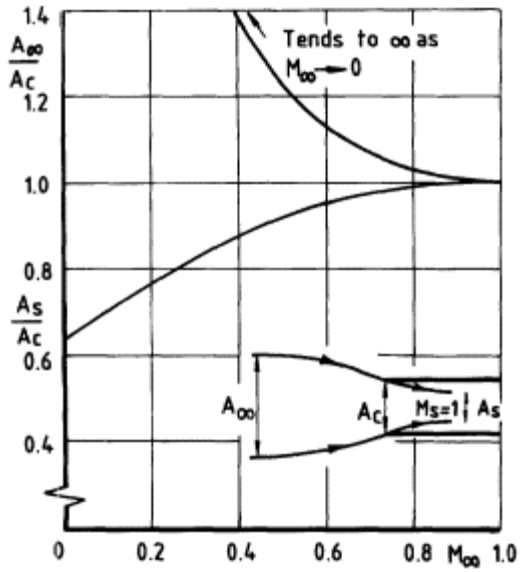

Figure 4.28
Free jet size for *M*s = 1 as function of *M*¥.

The throat size is now an explicit function of *M*s; this is shown in Fig. 4.30.

Of interest also is the condition of *incompressible flow*. The momentum relationship at Equation (4.19), with *p*s' equal to *p*s, may be written

$$\frac{A_s}{A_c} = \frac{p_\infty - p_s}{2q_s} + \frac{A_\infty}{A_c} \cdot \frac{q_\infty}{q_s} \qquad (4.18)$$

Using Bernoulli's equation, by which

$$p_\infty - p_s = q_s - q_\infty$$

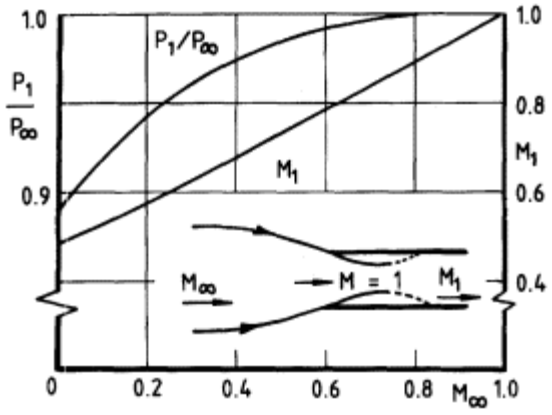

Figure 4.29
*M*1 and *P*1/*P*¥ for *M*s = 1 as functions of *M*¥.

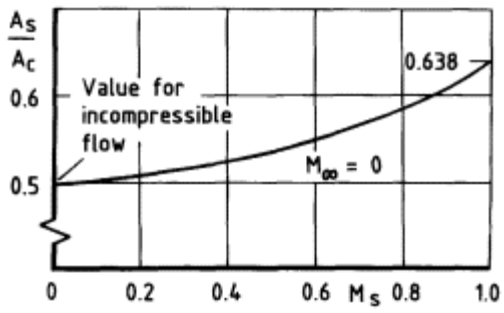

Figure 4.30
(*A*s/*A*c) as function of *M*s for static condition.

and the continuity equation

$$A_\infty V_\infty = A_s V_s$$

Equation (4.18) converts to a quadratic in *A*s for a given free-stream Mach number, viz:

$$\left(\frac{A_s}{A_\infty}\right)^2 \left(\frac{A_\infty}{A_c} - \frac{1}{2}\right) - \frac{A_s}{A_\infty} \cdot \frac{A_\infty}{A_c} + \frac{1}{2} = 0 \qquad (4.19)$$

The real solution is

$$\frac{A_s}{A_\infty} = \frac{A_c}{2A_\infty - A_c}$$

or

$$\frac{A_s}{A_c} = \frac{1}{2 - A_c/A_\infty} \qquad (4.20)$$

For the static conditions this gives

$$\frac{A_s}{A_c} = \frac{1}{2} \qquad (4.21)$$

which is the solution of the Borda mouthpiece flow of classical hydrodynamics (see for example Ramsey, 1935). The result appears at the left-hand end of Fig. 4.30. In the same way as for compressible flow, the throat area ratio increases to 1.0 as flow ratio *A*¥/*A*c decreases to 1.0. The variations with flow ratio for incompressible flow and for *M*s = 1 are compared in Fig. 4.31; the two curves embrace the full range of variability due to compressibility.

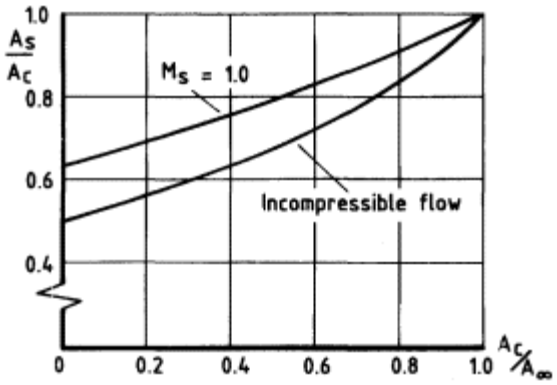

Figure 4.31
(*A*s/*A*c) as function of (*A*c/*A*¥) for
incompressible flow and *M*s = 1.0.

From Equation (4.20) and the expression for loss at a sudden area enlargement, derived in Chapter 2 Equation (2.23) the total pressure loss in incompressible flow is seen readily to be

$$\frac{\Delta P}{q_s} = \left(\frac{1 - A_c/A_\infty}{2 - A_c/A_\infty}\right)^2 \qquad (4.22)$$

and since

$$q_s = q_c \left(\frac{A_c}{A_s}\right)^2 = q_c(2 - A_c/A_\infty)^2$$

the loss may be written as

$$\frac{\Delta P}{q_c} = \left(1 - \frac{A_c}{A_\infty}\right)^2 \qquad (4.23)$$

For the static condition Equation (4.22) gives

$$\frac{\Delta P}{q_s} = 0.25 \qquad (4.24)$$

and this may be compared with the corresponding figure for compressible flow and *M*s = 1. The total pressure ratio at static condition in the latter case is 0.888 (Fig. 4.29) and since

$$\frac{q_s}{P_\infty} = \left(\frac{q_s}{P_s}\right)_{M=1} = 0.370$$

the loss in terms of qs is

$$\frac{\Delta P}{q_s} = \frac{0.112}{0.370} = 0.30 \qquad (4.25)$$

For compressible flow with Ms< 1, the loss expressed in this form lies between the two values given by Equations (4.24) and (4.25) and for throat Mach numbers up to 0.6, say, is closer to the incompressible flow value.

4.7
Static Loss in Practical Intakes

The approach of Section 4.6 gives useful indications both of the nature of the flow and of the order of magnitude of pressure loss associated with lip separation for an intake operating at low forward speeds, including the extreme condition of static operation (M¥ = 0). The assumption of a thin-lipped parallel-cylindrical intake is itself extreme as regards the actual separation occurrence, though not necessarily so as regards the subsequent flow development. In practice the lip radius, throat shape and diffuser geometry all play important parts in determining the degree of separated flow and the consequent total pressure loss. This is demonstrated in experimental data collected by Seddon (1952) and presented in Fig. 4.32.

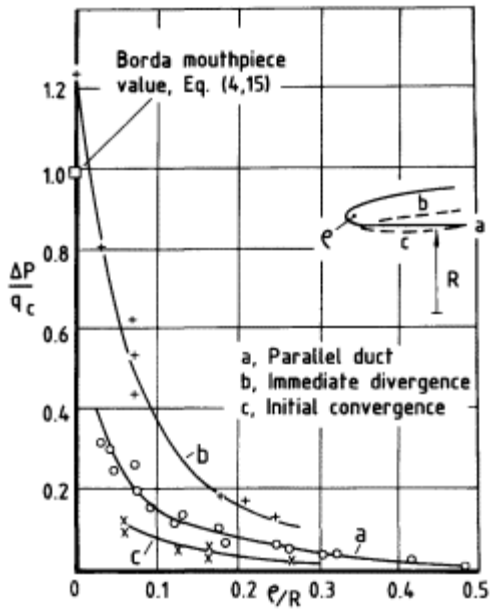

Figure 4.32
Correlation of total pressure
with lip radius of curvature.

Lip losses in static operation are shown as functions of lip radius for three categories of duct shape immediately following the lip.

The data are from British and German sources, obtained mostly in model tests but some from full-scale aircraft. The effects of differences in scale are insignificant compared with those of the parametric variations shown. At small lip radius the losses increase rapidly as radius decreases; it is noteworthy that the high value represented by Equation (4.23) lies within the range of possibilities. A divergence of the duct immediately following the lip radius is a bad feature and conversely a degree of convergence before the diffuser is advantageous: these trends are predictable, in kind though not in degree, from some of the inviscid pressure distributions discussed earlier in the chapter.

The practical significance of lip separation in static operation or during the take-off run varies with the type of aircraft and has changed in the course of aircraft evolution. A principal factor is the air-swallowing capacity of the engine in relation to its frontal area or, more specifically, to the frontal area allowed for the intake installation. The practicability of providing a large inner lip radius or convergent throat is more real for a podded installation of the type illustrated in Fig. 2.1 than for an integrated installation such as that of Fig. 2.2; and more real also for the fan-jet engine of Fig. 2.1 than for its predecessors in the transport field, which had smaller intakes in relation to the engine. The lip separation problem is considerably more severe on all types of supersonic aircraft, where there is a paramount need to retain sharp lips. On many aircraft, therefore, whilst not on all, special measures are required for static and low speed operation, to minimise the loss of total pressure from lip separation and with it a non-uniformity of flow at the engine which may be severe (see Chapter 11).

The usual measure is to provide an auxiliary inlet which functions only under static and low speed conditions. This may take the form, for example, of a spring-loaded door (or a group of doors) which opens automatically when the interior of the intake is under suction, as at the static condition, and closes as internal pressure builds up from the forward speed effect. A more refined version is the slotted intake pictured in Fig. 4.33. The slot ejects backwards into the duct and should be of sufficient length to control the air direction. The ideal form is a narrow slot using as much as possible of the intake perimeter. A device is required for sealing the outer end of the slot in flight. The use of a slotted intake enables the designer to use a smaller main entry and thinner lips, in other words to match the intake more closely to the conditions of high speed flight.

A problem of some consequence arises when the entry plane of the intake is not normal to the axis of the duct: this occurs for example with an intake in the leading edge of a swept wing. Under static conditions the average direction of flow at entry is approximately normal to the entry

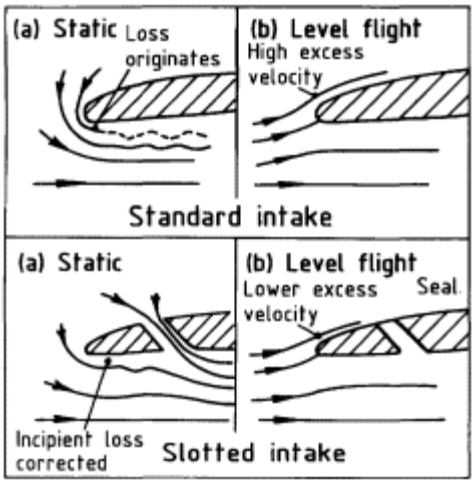

Figure 4.33
Flow patterns for static and level flight conditions;
comparison between slotted and unslotted lips.

plane, so that the air is then required to turn through an angle which may be quite considerable, particularly at the rearward end of the entry. The flow takes the form illustrated in Fig. 4.34, the separation accumulating inside the rearward end. Velocity distribution at the engine face may be particularly bad. Guide vanes breaking up the separated flow region or auxiliary inlets strategically placed may be used to improve the flow. The problem is liable to be encountered when intakes, either subsonic or supersonic, are given a forward overhang to improve the performance at high aircraft incidence (see Chapter 13).

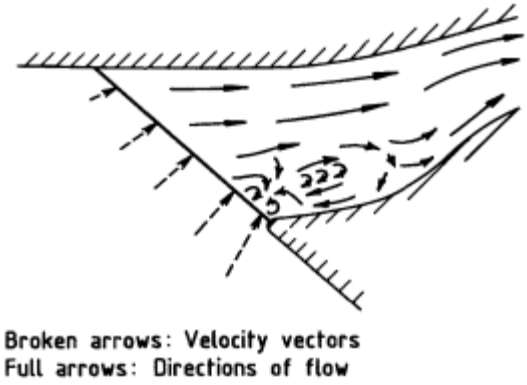

Figure 4.34
Flow pattern in swept intake at high flow ratio.

References

1 Albers, J.A. and Miller, B.A. (1973) 'Effect of subsonic inlet lip geometry on predicted surface and flow Mach number distributions'. *NASA TN D7446.*

2 Anderson, B.H. and Towne, C.E. (1981) 'Numerical simulation of flows in curved diffusers with cross-sectional transitioning using a three-dimensional viscous analysis'. *AIAA Paper 81 0003.*

3 Anderson, B.H., Huang, P.S., Paschal, W.A. and Cavatorta, E. (1992) 'A study on vortex flow control of inlet distortion in the re-engined 727-100 center inlet duct using computational fluid dynamics'. *AIAA 92 0152.*

4 Arlinger, B.G. (1975) 'Calculation of transonic flow around axisymmetric inlets'. *AIAA Journal*, 13, no. 12.

5 Baker, T.J. (1975) 'A numerical method to compute inviscid transonic flows around axisymmetric ducted bodies'. ARA Report 46, *Proceedings of Symposium Tanssonicum III Göttingen.* Berlin: Springer Verlag.

6 Baldwin, S. and Lomax, H. (1978) 'Thin layer approximations and algebraic model for separated turbulent flows'. *AIAA 78 257.*

7 Blackaby, J.R. and Watson, E.C. (1954) 'An experimental investigation at low speeds of the effects of lip shape on the drag and pressure recovery of a nose inlet in a body of revolution'. *NACA TN 3170.*

8 Chen, L. and Caughey, D. (1979) 'Calculation of transonic inlet flowfields using generalised coordinates'. *AIAA 79 0012.*

9 Cocanower, A.B., Kline, S.J. and Johnston, J.P. (1965) 'A unified method for predicting the performance of subsonic diffusers of several geometries'. Rept PD-10, Mechanical Engineering Dept, Stanford University, Stanford, California.

10 Doe, R.H., Brown, T.W. and Pagano, A. (1986) 'The development of practical Euler methods for aerodynamic design'. *ICAS 86 14.2.*

11 Fluid Dynamics Panel Working Group 13 (1991) *Air Intakes for High Speed Vehicles* (*Prises d'Air pour Véhicules à Grande Vitesse*). AGARD Advisory Report 270.

12 Fox, R.W. and Kline, S.J. (1962) 'Flow regimes in curved subsonic diffusers'. *J. Basic Eng. Trans ASME.*

13 Fradenburgh, E.A. and Wyatt, De Marquis, D. (1954) 'Theoretical performance characteristics of sharp lip inlets at subsonic speeds'. *NACA Report 1193.*

14 Goldsmith, E.L. (1990) 'The internal performance at incidence of pitot intakes with circular cross section and elliptic lip shapes'. *ARA Report 76.*

15 Goldsmith, E.L. and Seddon, J. (eds.) (1993) *Practical Intake Aerodynamic Design.* Oxford: Blackwell Science.

16 Green, J.E., Weeks, D.J. and Brooman, J.W.F. (1972) 'Prediction of turbulent boundary layers and wakes in compressible flow by a lag-entrainment method'. *RAE Report TR 72231.*

17 Green, J.E., Weeks, D.J. and Brooman, J.W.F. (1973) 'Prediction of turbulent boundary layers and wakes in compressible flow by a lag entrainment method'. *ARC R & M 3791.*

18 Horton, H.P. (1969) 'A semi-empirical theory for the growth and bursting of laminar separation bubbles'. *ARC CP 1073.*

19 Jameson, A., Schmidt, W. and Turkel, E. (1981) 'Numerical solutions of the Euler equations by finite volume methods using Runge-Kutta time stepping scheme'. *AIAA 81 1259.*

20 Johnston, L.J. (1984) 'Calculation of viscous transonic flow around axisymmetric cowls. *ARA Report 63.*

21 Kline, S.J., Abbott, D.E. and Fox, R.W. (1959) 'Optimum design of straight-walled diffusers'. *Trans. ASME,* Series D, 81, p. 321.

22 Lee, C.C. and Boedicker, C. (1985) 'Subsonic diffuser design and performance for advanced fighter aircraft'. *A/AA 85 3073.*

23 Peace, A.J. (1984a) 'The calculation of transonic potential flow around axisymmetric inlet configurations'. *ARA Report 60.*

24 Peace, A.J. (1984b) 'The calculation of transonic potential flow around inlet configurations'. *ARA Report 61.*

25 Ramsey, A.S. (1935) *A Treatise on Hydromechanics: Part II Hydrodynamics,* p. 56. London. G. Bell.

26 Reyhner, T.A. (1977) 'Transonic potential flow around axisymmetric inlets and bodies at angle of attack'. *AIAA Journal*, 15, no. 9.

27 Seddon, J. (1952) 'Air intakes for aircraft gas turbines'. *RAeS Journal*, October 1952.

28 Soffker, E. and Renner, A. (1965) 'Suction losses of sharp lip air intakes'. ('Ansaugverluste bei Scharflippen Lufteinlasser') *DLRFB 65 26.*

29 Sovran, G. and Klomp, E.D. (1967) 'Experimentally determined optimum geometries for rectilinear diffusers with rectangular, conical or annular cross-section'. *Fluid Mechanics of Internal Flow,* Elsevier: Amsterdam London New York, p. 270.

30 Thwaites, B. (1948) 'The development of the laminar boundary layer under conditions of continuous suction'. *ARC 11830.*

31 Tindell, R.M. (1987) 'Highly compact inlet diffuser technology'. *AIAA 87 1747.*

Chapter 5
External Supersonic Compression

5.1
Pitot Intake.

Intake characteristics for supersonic aircraft are dominated by the shock-wave systems that go into their design. In this and the following chapter we put aside temporarily the problems of boundary layer and flow separation and consider *ab initio* the nature and properties of the shock systems.

Suppose an aerodynamic duct (Fig. 1.2) to be placed in a uniform supersonic stream at Mach number *M*¥: the duct has the usual increase in area between station c (entry) and station f (maximum section) and some form of area control, for example a translating tapered plug, at station e (exit). Friction at the walls is neglected. We examine four stages as the area *A*c is increased from zero these are illustrated in Fig. 5.1.

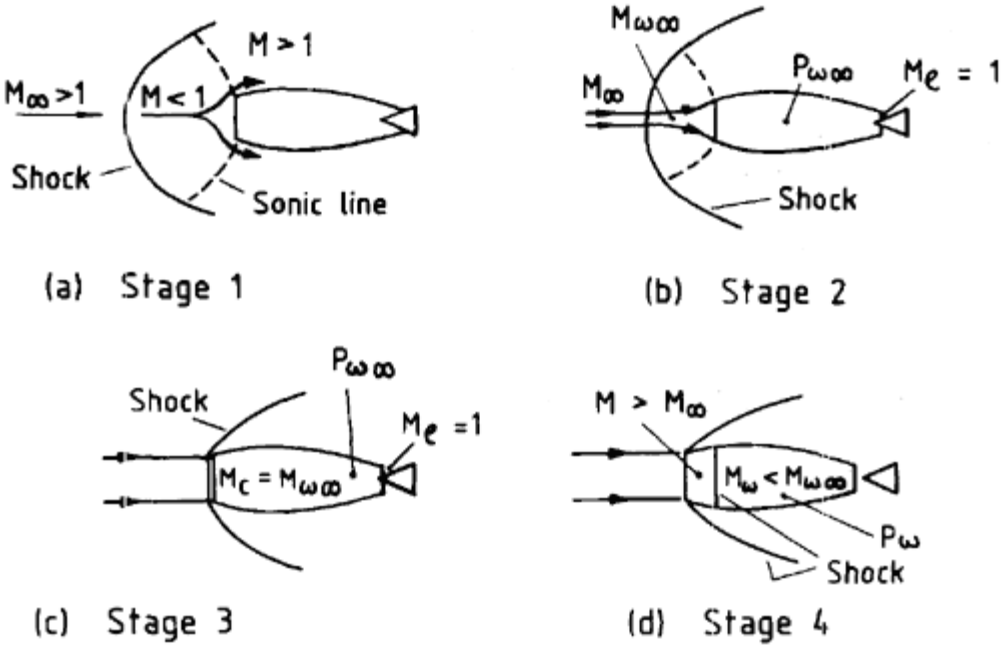

Figure 5.1
Flow through an aerodynamic duct in a supersonic stream.

At zero flow the duct acts as a solid body. A shock wave stands out ahead and a region of subsonic flow exists between the shock and the nose of the body, bounded by sonic lines as shown. On the centre line the shock is normal, with subsonic Mach number *M*w *Stage 1*. ¥, say, immediately behind it.

Stage 2.

With small *A*e, a narrow streamtube of air flows through the duct, effectively thinning the body and thereby allowing the shock to stand closer. Downstream of the shock the total pressure in the streamtube (no friction) is everywhere equal to *P*w ¥, the value behind the normal shock, as given by Equation (3.5). Flow in the streamtube is subsonic from *M*w ¥ onwards, decelerating further in the intake portion of the duct and re-accelerating in the exit portion. It can readily be shown that, whatever the supersonic Mach number *M*¥, the ratio Pw ¥/*p*¥ is greater than the value of *P*¥/*p*¥ for Mach 1.0 and it follows from this that the re-acceleration reaches Mach 1.0 at exit. In other words the exit is choked and the throughflow quantity is that corresponding to a sonic orifice with area *A*e and total pressure *P*w ¥.

Stage 3.

As *A*e is increased the shock continuously approaches the duct entry; then at some value of *A*e (less than *A*c) the shock lies across the entry plane. This, it can be seen, happens when the ratio *A*c/*A*e has the value of the sonic area ratio *A*/*A** corresponding to Mach number *M*c, which latter is itself now equal to *M*w ¥, the subsonic Mach number behind the normal shock. Qualitatively, conditions within the duct are unchanged from Stage 2, that is the flow is subsonic throughout but choked at exit. The flow ratio *A*¥/*A*c is now 1.0 and the duct is said to be running 'full'.

Stage 4.

If *A*e is increased beyond Stage 3, more flow tries to leave the duct, creating a depression which sucks the shock inside. Flow ratio remains unaltered, governed by the entry streamtube. As the shock travels along the diffuser its Mach number increases, as does therefore the loss of total pressure resulting from it. Equilibrium is reached when the total pressure downstream of the shock has fallen sufficiently to compensate for the increase in area and leave the mass flow unchanged, that is when

$$P_{\omega} \times A_{e_4} = P_{\omega_{\infty}} \times A_{e_3} \qquad (5.1)$$

It is to be noted that no solution exists for flow ratio greater than 1.0. This can be argued generally in the following way. Since subsonic flow is to be the ultimate product, the supersonic stream must of necessity pass through a shock. If the shock were to be out in front of the duct, with *A*¥ greater than *A*c, the pressure in the subsonic stream behind the shock would fall towards the entry (flow accelerating in a contracting streamtube). Such a shock position would not be stable, any small disturbance driving it towards the entry. Once the shock is inside the duct, an increase of suction downstream cannot be transmitted forward through the shock. An increase of pressure upstream can raise the level of pressures

throughout the system, thereby increasing the mass flow quantity but not affecting the flow ratio.

In the process described above, the flow and pressure recovery in the aerodynamic duct are as shown in Fig. 5.2. Ignoring friction, these are the characteristics of a *pitot* intake at supersonic speeds. The condition of maximum pressure recovery at maximum flow (Stage 3) is known as the critical point. Operation at lower flow ratio (e.g. Stage 2) is termed subcritical operation, while operation at maximum flow but lower pressure recovery (e.g. Stage 4) is termed supercritical operation.

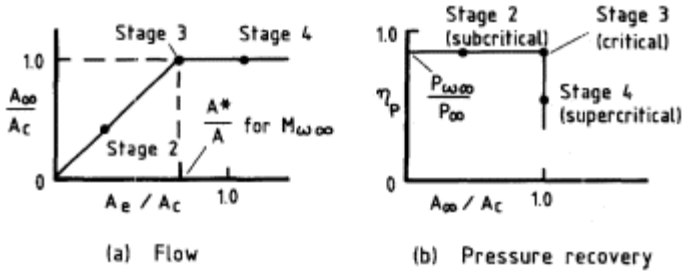

Figure 5.2
Flow and shock pressure recovery
of pitot intake at supersonic speed.

A pitot intake can have a number of attractive features, notably low drag and a stable flow characteristic with good flow distribution. Its disadvantage lies in the level of pressure recovery achieved, this being limited to the total pressure ratio behind a normal shock, *P*w ¥/*P*¥ in Fig. 5.2(b), with in practice a further two or three per cent reduction to allow for friction. A few values of normal shock recovery are given in Table 5.1.

Table 5.1 Total pressure behind a normal shock

M¥	1.0	1.3	1.6	2.0	2.5	3.0
*P*w ¥/*P*¥	1.0	0.98	0.90	0.72	0.50	0.33

Recalling that one per cent loss of intake total pressure results in between one and one-and-a-half per cent loss of engine gross thrust, the figures indicate that a pitot intake is probably acceptable at Mach 1.3, questionably so at Mach 1.6, depending on circumstances, but unacceptable at Mach 2.0 and above. Ways must be provided, therefore, of breaking down the shock system so that the eventual normal shock is at a suitably reduced Mach number, preferably around 1.3. Most of supersonic intake theory and practice is dictated by this requirement.

Some commonly used properties of normal shock flow are presented graphically in Fig. 5.3. Here for simplicity and generality we use suffixes 1 and 2 for upstream and downstream quantities.

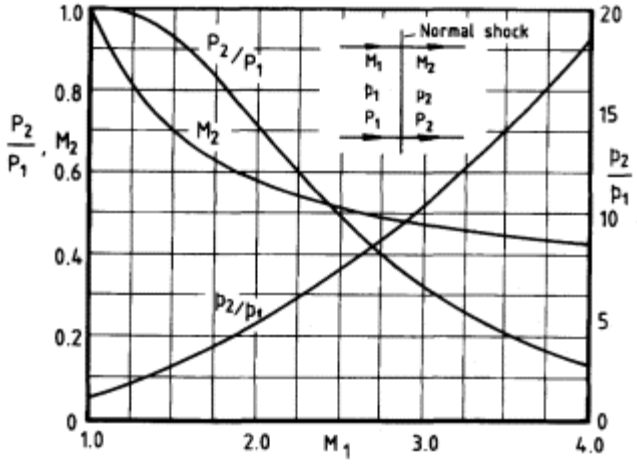

Figure 5.3
Properties of normal-shock flow.

5.2
Two-Shock Intakes

The principle of staging a supersonic compression so as to reduce the loss of total pressure can be appreciated from a closer look at normal-shock pressure recovery. Total pressure loss through a normal shock at upstream Mach $M1$ is shown plotted in Fig. 5.4. Two features of this variation are noted:

(i) up to Mach number 1.4 the loss is less than 4%;

(ii) above Mach number 1.4 the curve is reasonably well approximated by a straight line giving a loss rate of 4% per 0.1 Mach number.

Now, for a two-dimensional oblique shock of angle b (see inset) the loss is that corresponding to the component Mach number normal to the shock, $M1$ sin b. For small turning angles, d up to 10° say, the shock angle b (e.g. from tables) lies in a band between 25° and 50°, being smaller the higher the Mach number. It follows that the product $M1$ sin b varies only slightly with $M1$ and up to Mach 3 does not in fact exceed the value 1.4, so that the oblique shock loss is not greater than 4%. The reduction in Mach number to $M2$ is however very significant: a 10° turn lowers the Mach number by about 0.6, which is sufficient to reduce normal shock loss by approximately 24%. This profitable rate of exchange makes it possible to devise systems of supersonic compression by stages, yielding high pressure recovery overall. The number and types of stages used depends upon free-stream Mach number and other factors, as will be seen. Compression may be external to the duct (i.e. ahead of it) or internal; in the present chapter we are concerned with external compression systems.

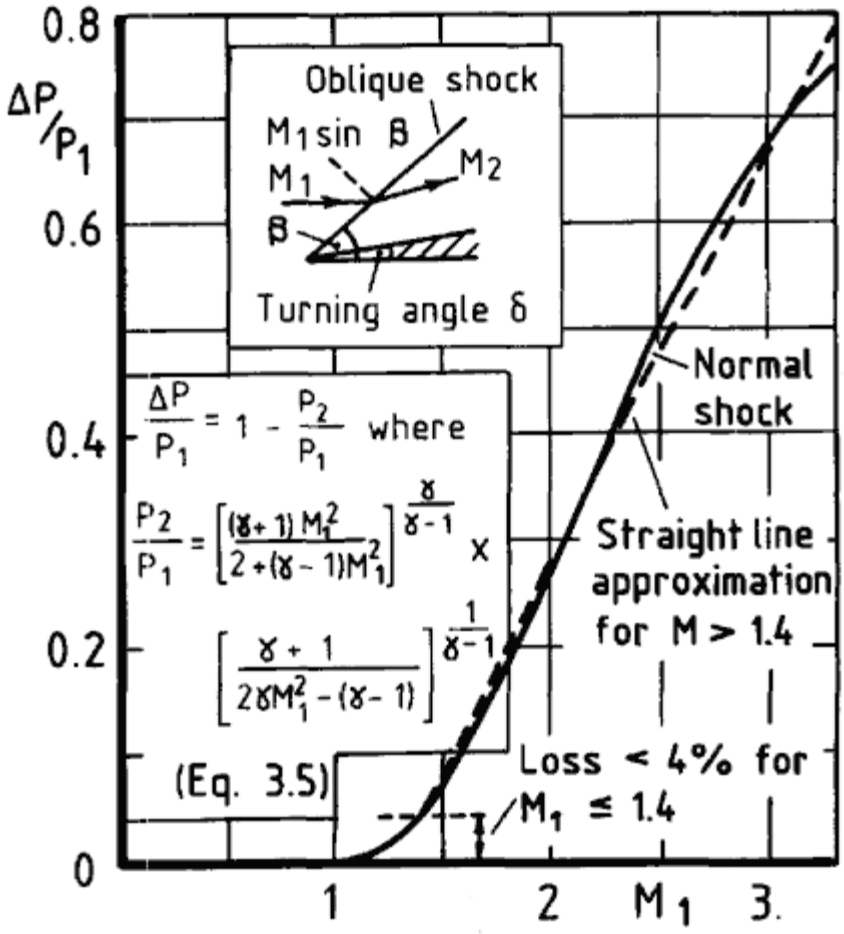

Figure 5.4
Character of normal-shock loss.

The simplest form of staged compression is the two-shock intake, in which a single-angled wedge or cone projects forward of the duct: this produces an oblique shock to reduce Mach number from the free stream value, followed by a normal shock at or near the entry through which the flow becomes subsonic. We consider the wedge and cone forms in parallel, noting as in Fig. 5.5 that the flow behind the oblique shock is different in the two cases. With a wedge this flow is at constant Mach number and parallel to the wedge surface. With a cone the flow behind the conical shock is itself conical, Mach number is constant along rays from the apex but varies along a streamline. For the same apex angle the conical shock is weaker than the wedge shock but the former is followed by isentropic compression in the conical flow see sketch (c) in the figure. The conical system is thus inherently the more efficient of the two: in practice however the choice is governed more by factors of engineering convenience.

In the sketch a single-sided wedge and a half cone are shown to illustrate the principle. Clearly the system is aerodynamically essentially the same with a double-sided wedge or a full cone; this then sits centrally with respect to the duct entry, which accounts for the term 'centrebody intake' being sometimes used. We shall use for preference the term 'forebody intake' as being synonymous with 'external compression intake of wedge or cone form'.

We discuss the characteristics of mass flow and pressure recovery. The entry area *Ac* (streamtube 'capture' area at entry) is defined as the area

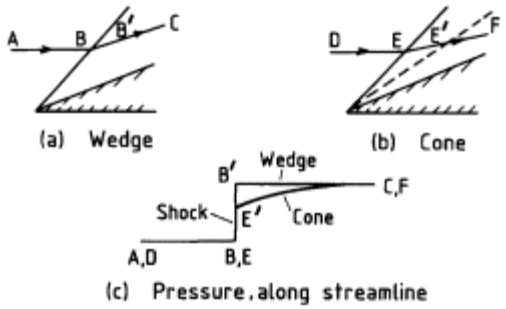

Figure 5.5
Difference between wedge and cone flow.

enclosed by the leading edge, or 'highlight', of the intake cowl, including the cross-sectional area of the forebody in that plane. As with a pitot intake, the maximum flow ratio achievable at supersonic speed occurs if and when *the boundary of the free streamtube A¥ arrives undisturbed at the lip.* This means that:

$$\frac{A_\infty}{A_c} = 1.0 \qquad (5.2)$$

The condition will be termed *full flow*. With a given arrangement at a given Mach number, the maximum flow achievable may or may not reach the full flow value. What will be termed *maximum flow* occurs when *the flow remains supersonic up to the entry*. This means that the normal shock is at the lip or inside; the flow value depends on the particular relationship between Mach number, the angle of the forebody and the position of the lip. Basically there are two cases, illustrated in Fig. 5.6. In case (a), the shock angle b is less than or equal to the angle bD subtended by the lip at the apex of the forebody. With this arrangement the capture streamtube can be increased until the flow arrives at the lip with the free stream Mach number. The situation is analogous to that for a pitot intake and we have

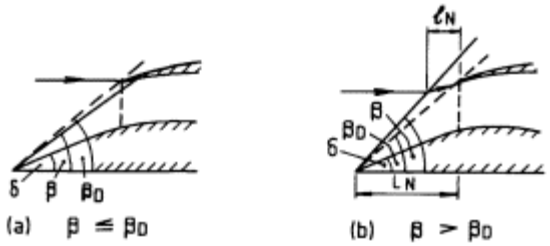

Figure 5.6
Maximum flow conditions for a single-wedge intake.

$$\left(\frac{A_\infty}{A_c}\right)_{max} = 1.0 = \left(\frac{A_\infty}{A_c}\right)_{full} \qquad (5.3)$$

In case (b), b is greater than bD and the maximum flow achievable is restricted by the necessary deflection of the bounding streamline in passing through the oblique shock. Hence

$$\left(\frac{A_\infty}{A_c}\right)_{max} < 1.0 \qquad (5.4)$$

that is to say the maximum flow achievable is less than full flow. Maximum flow as defined is a function of Mach number so that generally, at some Mach number higher than that portrayed in sketch (b), the oblique shock would fall on the lip and allow full flow to be reached.

The calculation of maximum flow in case (b) is simple for a wedge forebody. If in the figure the distance from apex to entry plane is *L*N and that from the intersection point of bounding streamline and oblique shock to entry plane is ℓ_n, then

$$\frac{A_\infty}{A_c} = \frac{(L_N - \ell_n)\tan\beta}{L_N \tan\beta_D} \qquad (5.5)$$

and since the flow behind the shock is parallel to the wedge surface, we have also

$$1 - \frac{A_\infty}{A_c} = \frac{\ell_n \tan\delta}{L_N \tan\beta_D} \qquad (5.6)$$

Eliminating L and ℓ from these two equations leads to the result:

$$\left(\frac{A_\infty}{A_c}\right)_{max} = \frac{\cot\delta - \cot\beta_D}{\cot\delta - \cot\beta} \qquad (5.7)$$

For a cone intake, the value of maximum flow can be determined numerically using conical flow tables (e.g. Kopal, 1947). Fraenkel (1951) has presented curves suitable for use in this connection. An analytical solution can be obtained by assuming that the streamlines behind the conical shock are portions of hyperbolae; the formula then arrived at by a process analogous to that for the wedge intake is:

$$\left(\frac{A_\infty}{A_c}\right)_{max} = \frac{\cot^2\delta - \cot^2\beta_D}{\cot^2\delta - \cot^2\beta} \qquad (5.8)$$

An alternative analytical form has been derived by Mascitti (1969): this uses the constant density (i.e. incompressible) solution for conical flow and

appears to give good results in comparison with numerical integration from the conical flow tables.

The pressure recovery of the shock system at critical point (maximum pressure recovery at maximum flow) is the product of the separate total-pressure ratios across oblique and normal shocks. This is explicitly definable for a wedge forebody: for a cone the normal shock Mach number varies to a small extent from cone surface to cowl lip but a mean of the end values is normally adequate for the calculation of pressure recovery. Shock pressure recoveries of wedge and cone two-shock intakes are presented in Fig. 5.7 as functions of centrebody angle d for free stream Mach numbers up to 3.0. The following points are noted:

(i) at optimum angles the conical form is about 1 1/2% better than the wedge;

(ii) for a given Mach number, large improvements can be obtained over the pitot intake (d = 0), for example from 72% to around 90% at Mach 2.0;

(iii) bearing in mind that boundary layer losses have yet to be taken into account, a two-shock intake is only moderately good at Mach 2.0 and unlikely to be adequate at higher Mach numbers though much depends, of course, on the type of aircraft mission to be performed.

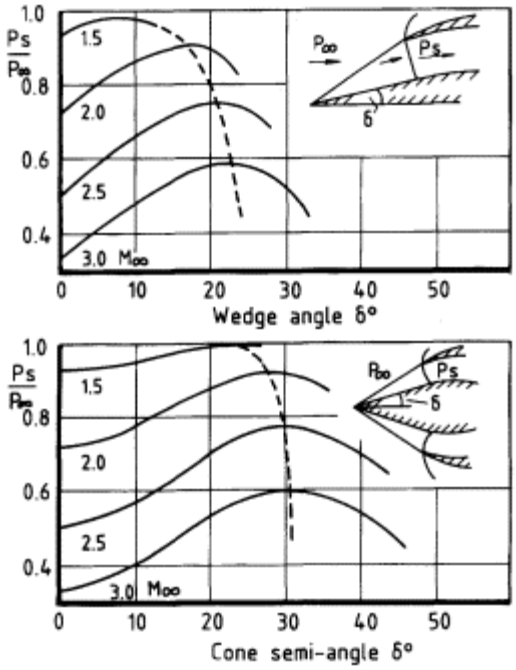

Figure 5.7
Shock pressure recovery of wedge
and cone two-shock intakes.

The nature of pressure recovery in subcritical operation can be examined in general terms at this stage. As flow ratio is reduced from the critical point, the normal shock moves forward from the entry, allowing subsonic flow spillage behind it. There are three cases: we write b for the oblique shock angle and bD for the angle subtended by the cowl lip at the apex of the forebody and we refer to the sketches in Fig. 5.8.

(a) b >> bD. At all reduced flows the capture streamline passes wholly through the two-shock system (sketch A). Shock pressure recovery remains constant (as in curve (a), sketch C), therefore, similar to the variation of a pitot intake (Fig. 5.2) but at the higher value corresponding to two-shock compression.

(b) b > bD *but difference small.* As flow is reduced from the critical value, the pattern of sketch A is maintained for a time, after which the shock intersection point moves inside the capture streamtube (sketch B). Part of the intake flow now passes through a single strong outer shock, yielding a lower pressure recovery. Thus the characteristic (curve (b), sketch C) follows that of case (a) near critical flow but at lower flows falls away towards the pitot intake value.

(c) b £ bD. In this case the shock intersection point lies inside the capture streamtube at all subcritical flows (sketch B), so as flow ratio is reduced (curve (c), sketch C) pressure recovery falls steadily from the critical value towards the pitot intake level.

Specific calculation of the shock pressure recovery in cases (b) and (c) requires a knowledge of the normal shock position as a function of flow ratio. When this is known, the proportions of flow passing through the single outer shock and two inner shocks can be calculated, whether for cone or wedge type systems, and thus a suitably weighted mean pressure recovery is derivable. A method for determining the position of the normal shock is given later in the chapter (Section 5.7) and this is followed (Section 5.8) by an outline of the calculation method.

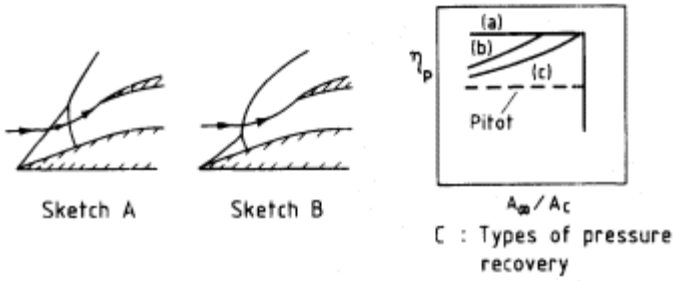

Figure 5.8
Nature of pressure recovery in subcritical operation.

5.3
Multi-Shock Intakes

The principle of breaking down an external shock system can be extended to any desired number of stages. A three-shock intake (two oblique and one normal) represents the next stage beyond that of the previous section; here the double-wedge and double-cone are the archetypal forms. The theoretical shock pressure recoveries of these two types constitute useful standards: they are presented in Figs 5.9 and 5.10 as functions of the second

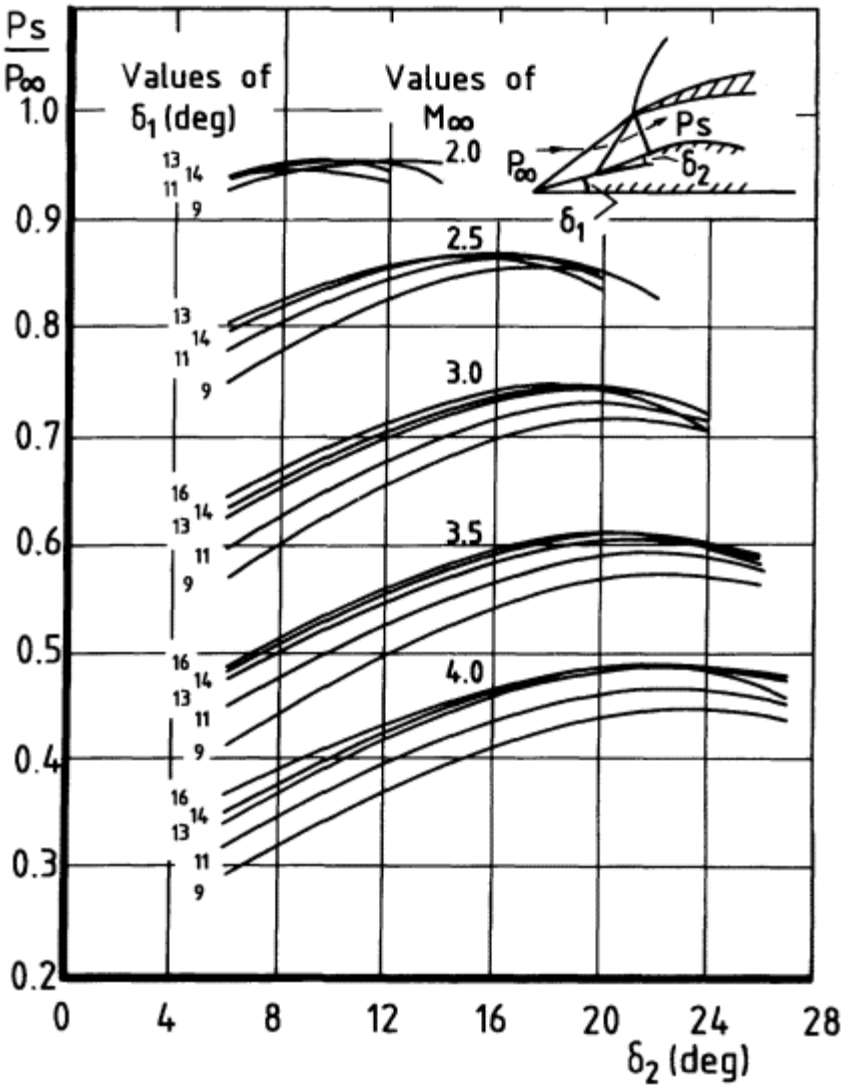

Figure 5.9
Shock pressure recovery of double-wedge intakes.

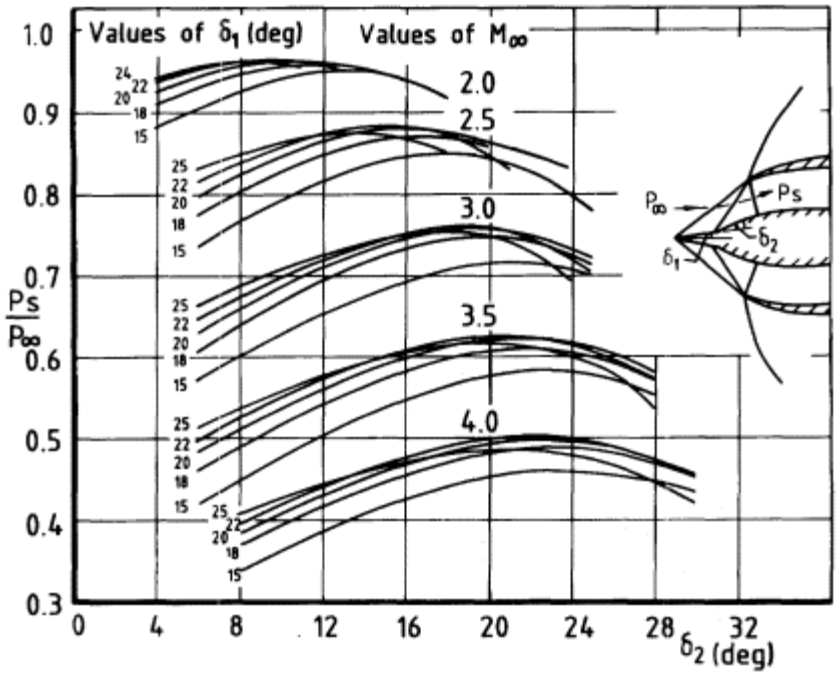

Figure 5.10
Shock pressure recovery of double-cone intakes.

deflection angle for a series of values of the first deflection angle at each of a series of Mach numbers. It is seen that the double-cone compression, for example, yields up to 96% shock recovery at Mach 2.0 and up to 88% at Mach 2.5.

The calculation of maximum flow ratio for a three-shock intake with arbitrary position of the junction between first and second compression surfaces is generally complex, since the shock configurations (Fig. 5.11) are not readily determined. If, however, in the double-wedge case a free stream Mach number exists, *M*D say, at which the two wedge shocks fall simultaneously on the cowl lip, then the expression for maximum flow ratio at any Mach number below *M*D is:

$$\left(\frac{A_\infty}{A_c}\right)_{\text{max.}} = \frac{\cot\delta_1 - \cot\beta_{1D}}{\cot\delta_1 - \cot\beta_1} \cdot \frac{\cot\delta_2 - \cot\beta_{2D}}{\cot\delta_2 - \cot\beta_2} \qquad (5.9)$$

where the angles d1, d2 determines the angles b1D and b2D (Fig. 5.11) and the geometry is such that

$$\frac{L_W}{L_N} = \frac{L_W}{h_c} \tan\beta_{1D} = \frac{\tan(\beta_{2D}+\delta_1) - \tan\beta_{1D}}{\tan(\beta_{2D}+\delta_1) - \tan\delta_1} \qquad (5.10)$$

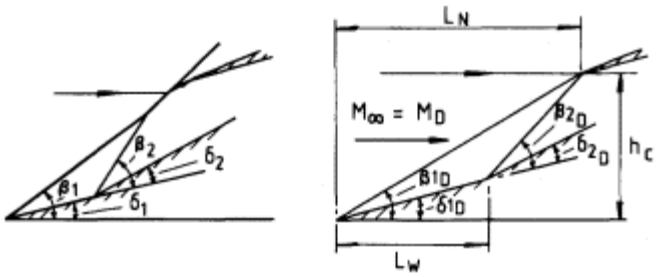

Figure 5.11
Doubl-wedge intake.

The value of maximum flow ratio in Equation (5.9) assumes the flow to be two-dimensional. This is a valid assumption close to the design Mach number if the oblique shocks are enclosed by endwalls, swept from the tip of the compression surface to the cowl lip. For Mach numbers well below *M*D, or if the endwalls are cut away, supersonic spillage occurs across the endwalls, reducing the maximum flow ratio attainable. McGregor (1971) proposed a correlation parameter G for the amount of this sideways spillage:

$$G = \frac{A_1}{A_c}\left(\frac{p_1}{p_\infty} - 1\right) + \frac{A_2}{A_c}\left(\frac{p_2}{p_\infty} - 1\right) \qquad (5.11)$$

in which *A*1, *A*2 are the areas available for spillage behind the first and second oblique shocks respectively and *p*1, *p*2 are the pressures in those areas corresponding to two-dimensional flow. An empirical correlation of the parameter *G* with measured deficiencies in maximum flow ratio is given in Fig. 5.12.

Continuing the process of breaking down the external shock system, three or more oblique shocks may be used ahead of the normal shock. For a system with *n* 1 oblique shocks (Fig. 5.13) the shock pressure recovery *P*s is given by the product of the individual total-pressure ratios

$$\frac{P_s}{P_\infty} = \frac{P_s}{P_1} = \frac{P_2}{P_1} \cdot \frac{P_3}{P_2} \cdots \frac{P_n}{P_{n-1}} \cdot \frac{P_s}{P_n} \qquad (5.12)$$

Oswatitsch (1944) showed that for such a system in two dimensions, maximum shock recovery is obtained when the oblique shocks are of equal strength. This means that Mach numbers perpendicular to the shocks are equal,

$$M_1 \sin \beta_1 = M_2 \sin \beta_2 = \ldots = M_{n-1} \sin \beta_{n-1} \qquad (5.13)$$

as are the individual total-pressure ratios in Equation 5.12 apart from the final one. The method of optimisation is complex but Hermann (1956) has

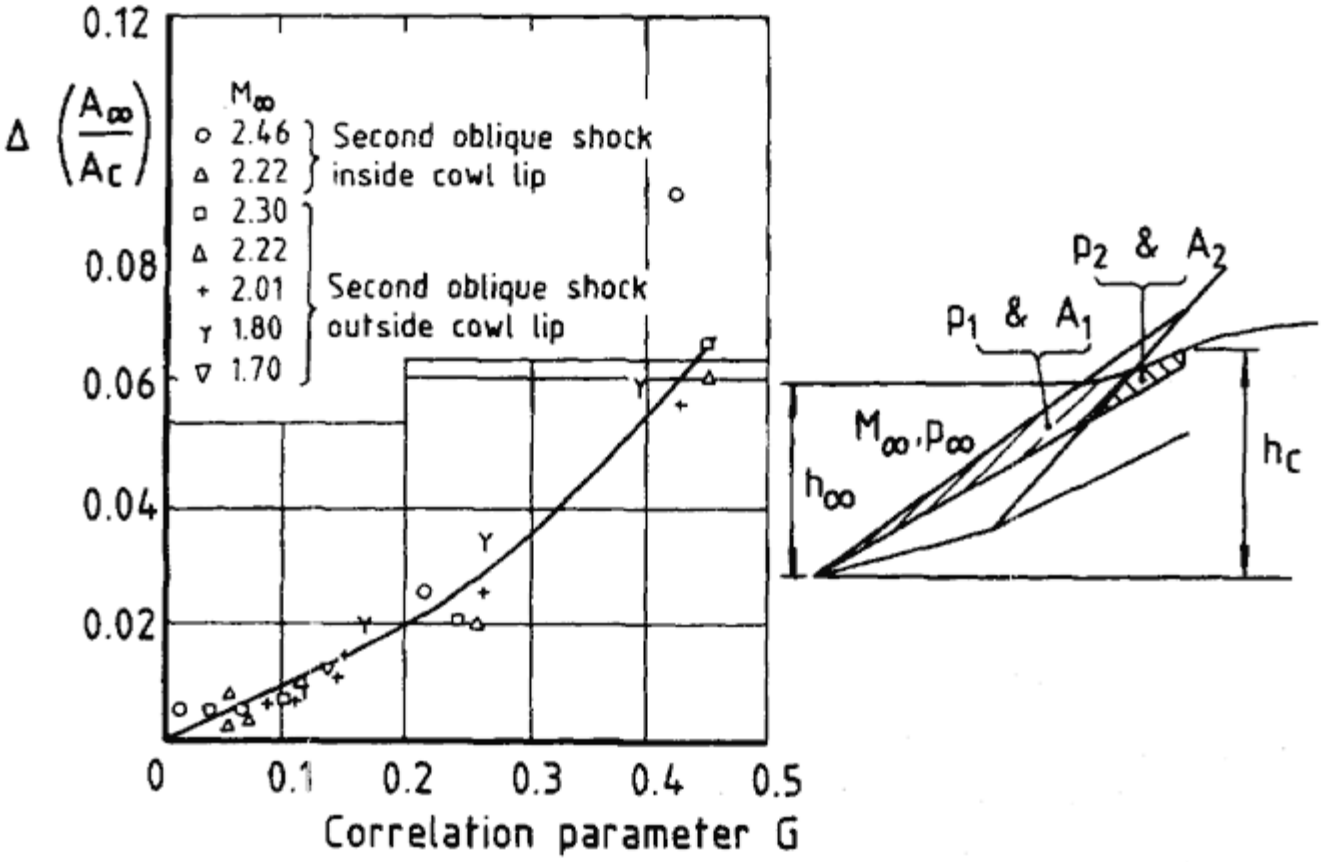

Figure 5.12
Sidespill correlation.

set it out at length: he further points out that *M*n, the Mach number before the normal shock, cannot be included in the equality at Equation (5.10). Numerical evaluation provides the approximate result that:

$$M_n \simeq 0.94\ M_1 \sin \beta_1$$

in a range of *M*1 from 1.5 to 5.0 for *n* = 2, 3 or 4. The method for evaluating an optimum arrangement is indirect. It is necessary to assume a value for *M*n, from which a value of *M*1 (i.e. *M*¥) can be determined using functional relationships developed in the proof. A value of b1 follows, hence the first wedge angle d1 and then the rest of the geometry, Mach numbers and pressure ratios. Iteration may then be needed in order to arrive at the required value of *M*¥.

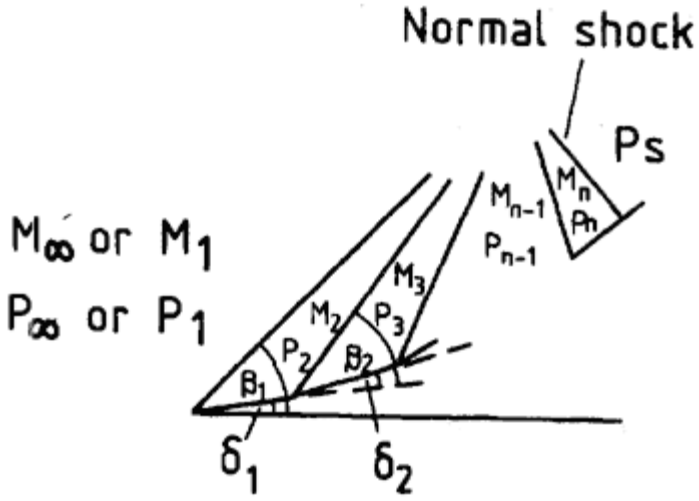

Figure 5.13
Scheme of (n 1) oblique shocks
for Oswatisch optimisation.

Optimum shock pressure recovery is presented in Fig. 5.14 as a function of free stream Mach number for two-dimensional systems with up to five shocks. Evaluation of the corresponding deflection angles shows that, in general, up to about Mach 2 equal deflections give the best results, while for higher Mach numbers the first deflection needs to be the smallest and the last the largest.

For axisymmetric intakes, optimum shock systems may be determined by graphical methods. Design criteria obtained in this way have been presented by Connors (1956).

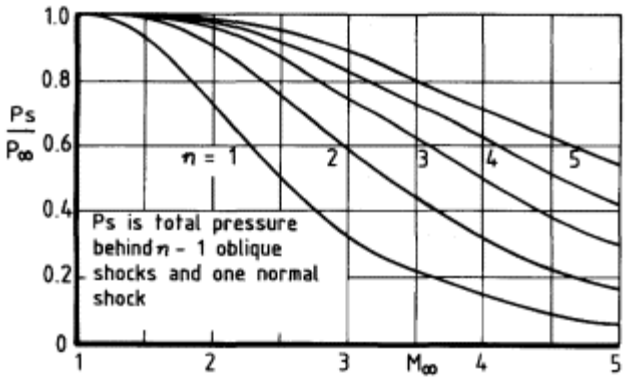

Figure 5.14
Shock pressure recovery for optimum arrangements of two-dimensional shocks.

5.4
Isentropic Compression

Extending the principle of multi-shock compression to its limit leads to the concept of isentropic compression, in which a smoothly contoured forebody produces an infinitely large number of infinitely weak oblique shocks (Fig. 5.15). These compress the supersonic stream with no loss of total pressure. In two-dimensional flow, for a focused system of zero-strength shocks, or characteristic lines, the process is the reverse of a Prandtl Meyer expansion flow around a sharp corner and the profile required can be calculated as a streamline of the Prandtl Meyer flow. Using coordinates r, f, the profile is obtained from the relations

$$\left.\begin{aligned} \frac{x}{r_0} &= \frac{r}{r_0}\cos(\mu - \nu) \\ \text{and} \qquad \frac{y}{r_0} &= \frac{r}{r_0}\sin(\mu - \nu) \end{aligned}\right\} \qquad (5.14)$$

Figure 5.15
Isentropic compression
(reversed Prandtl Meyer expansion).

in which μ = sin 11/M, v is the flow angle and we have

$$v = \phi + \mu - \frac{\pi}{2} \qquad (5.15)$$

and

$$\phi = \frac{1}{K} \tan^{-1} K\sqrt{(M^2 - 1)} \qquad (5.16)$$

where $K = \sqrt{[(\gamma - 1)/(\gamma + 1)]}$. Profiles calculated on this basis have been tabulated by Connors (*loc. cit.*) for Mach numbers up to 4.0. Since in practice the leading edge of a forebody inevitably has a non-zero constructional thickness or angle, a shock of measurable strength is generated there: Connors' calculations assume a one per cent loss of total pressure from this initial shock.

Calculations for axisymmetric flow are considerably more involved, as one now does not have straight characteristic lines with constant flow conditions. The method used by Connors is that an initial characteristics line is determined from the known flow field produced by a conical nose (again giving a one per cent loss) and at the focal point of the characteristics two-dimensional reverse Prandtl Meyer relations are assumed. From these two conditions the isentropic flow field is calculated using the method of characteristics for potential flow with axial symmetry. Streamlines of the flow are traced by applying continuity considerations and hence the surface contour is determined.

In theory one might expect that isentropic compression could be used to decelerate the flow all the way down to sonic speed. In fact, such fully isentropic compression cannot be achieved owing to compatibility conditions which are imposed by other parts of the flow; these conditions are examined in the next section. In practice the supersonic compression is always terminated with a strong shock at low supersonic Mach number. This means that the use of isentropic compression is restricted to intermediate stages, as for example for the second wedge of a multi-shock system. In such a context isentropic compression can be both practical and useful and it has been adopted in practice for a number of aircraft requiring

high intake performance. The intake of the Concorde aircraft shown in Fig. 12.7 is a good example.

5.5
Limits of External Compression

A feature of external supersonic compression is that the flow, in passing through the compression system produced by the forebody (whether isentropic or in discrete shocks), is turned outwards from the intake axis. At the entry plane therefore the flow is at an inclination corresponding to the total turning angle and in the normal way requires to be turned back to the axial direction within the subsonic diffuser. With efficient compression the turning angles can be quite large. Fig. 5.16 shows the total angles for optimum multi-shock systems and for complete isentropic compression. For the latter, the full angle of turn ν is given explicitly, from the Prandtl Meyer expansion relations, as

$$\nu = \sqrt{\left(\frac{(\gamma+1)}{(\gamma-1)}\right)} \arctan \sqrt{\left[\frac{\gamma-1}{\gamma+1}\,(M^2-1)\right]} - \arctan \sqrt{(M^2-1)} \quad (5.17)$$

and this is seen to be in the nature of an asymptotic curve to the series for optimum multi-shock arrangements. Unlike the multi-shock systems,

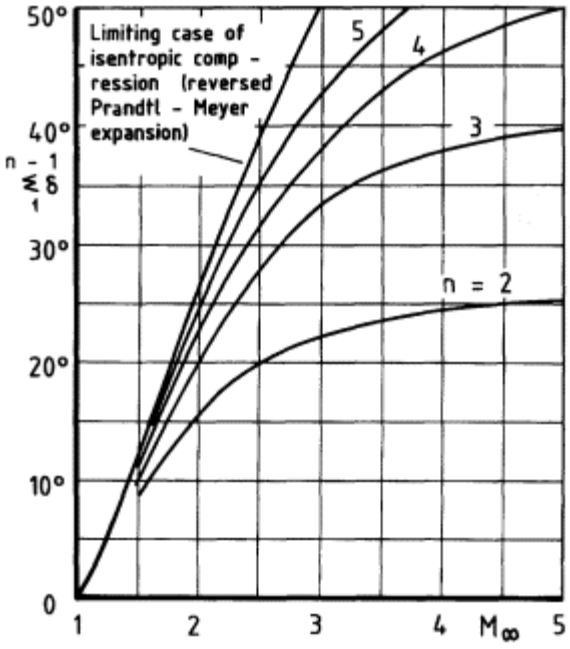

Figure 5.16
Total flow turning angle for
optimum two-dimensional shocks.

optimum isentropic compression involves no terminal strong shock, so since in practice one is always used, the flow turning angle corresponds to a sector of the Prandtl Meyer curve lying between initial and final Mach numbers of the isentropic portion of the compression.

Whether a large turning angle, and hence efficient compression, can be realised in a given situation depends on factors involving either the *external stream* around the cowl or conditions of the *internal flow* immediately within the duct entry.

5.5.1
External Shock Attachment with No Duct Angling.

A straightforwardly efficient arrangement with external compression of the internal flow is for the compression to be focused at the cowl lip and for the internal surface of the cowl to lie initially in line with the flow turning achieved. If the duct inner surface (continuation of the forebody) is aligned so as to maintain a constant cross-sectional area (with a wedge intake this means that the two surfaces are parallel), the normal shock sits across the entry and the flow in the duct is wholly subsonic. To be compatible with this arrangement the shock wave produced by the cowl in the external flow (i.e. outside the capture streamtube) must be attached to the lip; for if that shock is detached it will both modify the details of the focused compression system and increase the cowl external drag.

The external angle of the cowl must therefore not exceed the maximum for shock attachment at the particular value of free-stream Mach number. Allowing for a minimum manufacturing angle between external and internal surfaces of the lip, a limit is set to the cowl internal angle, which thereby limits the degree of flow turning. The shock attachment criterion can in all cases be taken to be that for two-dimensional flow, as given in standard flow tables, since the flow locally at the lip is effectively two-dimensional even for three-dimensional arrangements. The limit angle (external flow) is plotted in Fig. 5.17.

The shock attachment criterion is relevant to all forms of forebody compression: for isentropic compression in particular, the limiting pressure recovery is readily calculated. Using the notation of the sketch in Fig. 5.17, the flow turning angle di is given by the difference in values of ν (Equation 5.17) corresponding to initial and final Mach numbers, M¥ and Mi, of the supersonic compression. If these values are ν¥ and νi, respectively, the condition for external shock attachment is that

$$\delta_i = \nu_\infty - \nu_i \leq \eta_e - \eta_v$$

or

$$\nu_i \geq \nu_\infty - \eta_e + \eta_v \qquad (5.18)$$

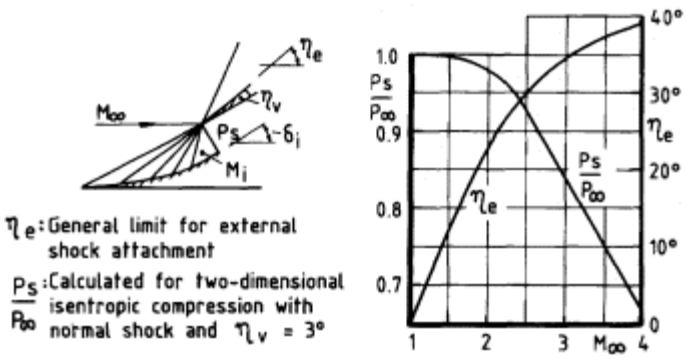

Figure 5.17
Limiting cowl external angle for shock attachment
and corresponding maximum pressure recovery
with isentropic-compression forebody.

and the equality in this relationship determines the minimum value of *v*i, hence the minimum value of *M*i. Maximum pressure recovery is then that of a normal shock at Mach number *M*i. This is shown plotted in Fig. 5.17 for an assumed 3° cowl vertex angle.

5.5.2
Internal Shock Attachment

If the initial part of the duct is angled in the reverse sense to that of the flow-turning on the forebody, *without introducing internal contraction*, an attached normal shock will still be obtained at the critical flow, provided that in the supercritical condition an attached internal oblique shock can form at the cowl lip. This can be seen by considering an approach to critical flow from supercritical; the progression of shock patterns illustrated in Fig. 5.18 (which for clarity ignores an expansion fan from the forebody at the entry plane) leads in the limit to an attached normal shock across the entry. Angling the duct in this way allows the cowl external angle he to be reduced, or alternatively it allows the turning angle of the forebody di to be increased to a value at which the internal oblique shock at the cowl lip is on the point of detachment. The increase in isentropic turning can be seen by comparing di and (di)max in Fig. 5.19: the resulting increase in normal-shock recovery is also shown.

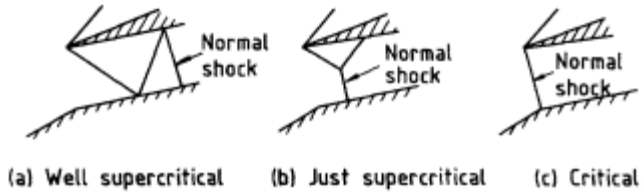

Figure 5.18
Shock configurations at entry of angled duct.

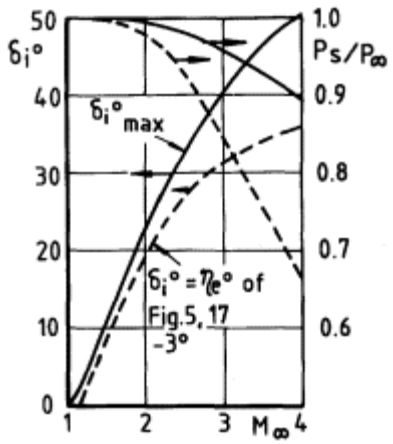

Figure 5.19
Maximum angle of isentropic forebody
and corresponding pressure recovery
for angled duct and he of Fig. 5.17.

The cowl internal angle can be set to any value* below the maximum for external shock attachment (he 3° in Fig. 5.17). The relation between cowl internal angle and (di)max, for isentropic external compression, results in the values of normal-shock recovery presented in Fig. 5.20, for values of hi from 0° to 25°. It is seen that as the cowl internal angle decreases, the achievable pressure recovery falls rapidly. A lower value of cowl external angle, however, means a lower value of cowl drag (Chapter 9) and a

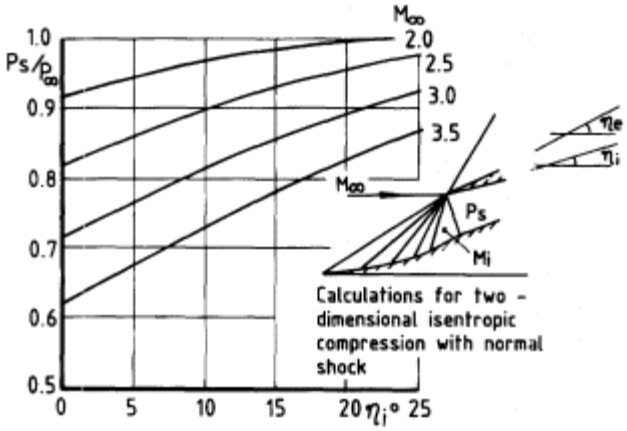

Figure 5.20
Relation between maximum shock pressure
recovery and cowl internal angle.

* True in principle only: in practice a large 'shoulder' angle on the forebody, which goes with the cowl angle, produces complications.

balance can be struck between reduction in pressure recovery and reduction in drag.

It has been found in experimental work that in the flow at critical point with a reverse-angled duct, the fully normal terminal shock may be replaced by a near normal shock corresponding to the 'strong oblique shock' solution for the wedge flow at the lip. A strong oblique shock can confer a small increase in pressure recovery: for example with a terminal supersonic Mach number 1.5 and internal cowl angle 12° (2° above the shock detachment angle), the shock recovery is increased by 0.013. The difference decreases, however, to an insignificant 0.002 if the terminal Mach number is reduced to 1.3. The occurrence of strong oblique shocks in this context was experienced during intake research for the Concorde aircraft. Neale and Lamb (1963), testing an external compression design for Mach 2.0, with 19° flow turning on the forebody and terminal Mach number 1.38, investigated the use of reverse angling of the duct as a way of reducing the cowl wave drag. With an internal angle 14° (i.e. 5° reverse angling) the theoretical oblique shock solutions are 54° (weak) and 82° (strong). A sequence of schlieren photographs taken during increase of back pressure from a supercritical condition (Fig. 5.21) showed firstly a combination of the weak oblique shock and a downstream normal shock, as illustrated earlier (Fig. 5.18), secondly, at the critical point, a single strong oblique shock and thirdly a normal shock when slightly detached from the lip. Oblique shock angles measured from the photographs were 60° (weak) and 73° (strong); these angles correspond to a lower terminal Mach number than 1.38, that is to say a larger forebody turn than 19°, which in the real flow could be attributed to a displacement effect of the boundary layer on the forebody.

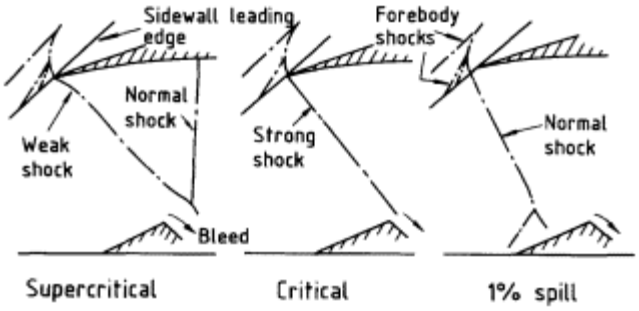

Figure 5.21
Sketches from schlieren photograph sequence
on intake for Mach 2.0 with boundary layer bleed.

5.5.3
Shock Structure

The limits described in the two previous sections are derived on an assumption that the forebody compression is focused on the cowl lip, in other words that the solid cowl surface extends forward to the focal point and thereby allows separate consideration of the external and internal downstream shock systems. In a practical design it may be preferred to focus the compression a short distance in front of the lip; this gives a greater freedom of operation in slightly varying conditions of flight (temperature, angle of incidence, etc.). It has then to be questioned whether the degree of forebody compression intended is possible within an overall structure of the shock system (both internal and external flow), unaffected by the presence of the cowl lip.

In absence of the cowl, the system to be examined was first analysed by Connors (*loc. sit.*) and is as portrayed in Fig. 5.22(a), assuming isentropic compression on the forebody. A vortex sheet springs from the focal point, generated by the difference in total pressure between the lower flow passing through isentropic compression and the upper flow passing through a strong shock. This replicates a similar feature discussed earlier (Chapter 3) in the context of shock and boundary layer interaction. Also, a wave of either compression or expansion may be reflected down from the focal point, adjusting the direction of the lower flow. Conditions across the boundaries of the indicated zones are:

Zones a, b : *p*a = *p*b, da = db (flow inclination),

Zones b, c : *p*b ¹ *p*c, db ¹ dc
(dc is the di of our more general notation).

*P*a ¹ *P*b,
*M*a ¹ *M*b

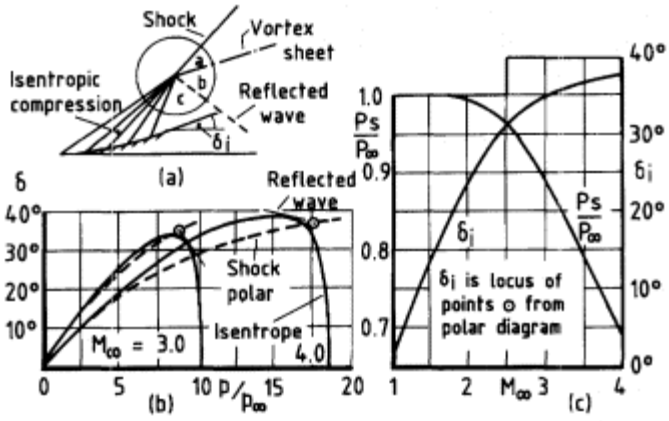

Figure 5.22
Shock structure limitation (a) system to be analysed (b) polar diagrams (c) maximum deflection and pressure recovery.

The determining condition is that of equal static pressure on the two sides of the vortex sheet separating upper and lower flows. The possibility of this being established for a given free stream Mach number is examined by overlaying (Fig. 5.22(b)) polar diagrams (static pressure versus flow deflection) for, on the one hand, all possible oblique shocks at the given Mach number and, on the other hand, the isentropic compression. A reflected wave polar, starting from the isentrope, may be added to extend the possible range of di, the isentropic turning. Intersection of the reflected wave polar with the shock polar gives the required conditions, so a maximum di is obtained when the reflected wave polar is tangential to the shock polar as shown. Of interest is the fact that in the worked examples the reflected wave appears as an expansion at Mach 4 but as a weak compression at Mach 3.

The variations of turning angle and final Mach number corresponding to the shock structure limit are shown in Fig. 5.22(c). Calculated shock pressure recovery has been added, on the assumption that compression is completed by a normal shock at the conditions of zone c. It is noted that the shock structure limit is fairly restrictive, less severe than that for external shock attachment without duct angling but considerably more severe than that for an optimally angled duct.

Practical flow situations are never ideal. Two 'non-idealisms' in the present instance are that shock waves have a non-zero thickness and sharp-lipped cowls a non-zero lip angle. Because of these realities, it is possible that the shock structure limit still applies, at least in some degree, when the compression shocks are nominally focused at the point of the lip, and that the limitation cases to be relevant only when the focal point is some way inside the cowl. Evidence on this is not conclusive but therefore it may be that with shocks focused at the lip, the shock structure limit prevents the use of compression to the value (d1)max of Fig. 5.19 but permits compression to limits represented by the lower values of hi in Fig. 5.20, thereby allowing a useful compromise to be reached between pressure recovery and drag.

5.6
Intakes A and B

It is of interest to construct a specimen supersonic intake on the basis of criteria so far discussed. This will illustrate a number of points already made and will also provide a standard of comparison in relation to aspects still to be considered, notably those of internal compression (Chapter 6) and external drag (Chapter 9).

The intake is to be, let us say, for Mach 2.2 (free-stream speed) and of wedge type, with shocks focused at the lip. Reference to Fig. 5.14 suggests that at least three shocks are needed and preferably four we choose the

latter. The optimum flow turning angle, according to Fig. 5.16, is 27° but Fig. 5.17 shows the external shock attachment limit to be 26°. This could be observed assuming, say, 4° lip vertex angle and using 22° cowl internal angle. With optimum flow turning the reverse angle of the duct would be 5° and a trial calculation for three 9° wedge turns leads to a value 1.20 for the Mach number *M*i of the terminal shock; at this Mach number a 5° turn with attached shock is not possible. We therefore ease the flow turning requirement to, say, 24° and elect to use three 8° wedges (there is of course no *a priori* reason for the wedge angles to be equal). The duct reverse angle is now 2°. The calculation proceeds as follows:

M_1 (or M_∞) = 2.2;
$\delta_1 = 8° \therefore \beta_1 = 33.8°$, $M_2 = 1.90$;
$\delta_2 = 8° \therefore \beta_2 = 39.3°$, $M_3 = 1.62$;
$\delta_2 = 8° \therefore \beta_3 = 47.3°$, M_4 (or M_i) = 1.34;

The values of *M* sin b are successively 1.22, 1.20 and 1.19 which, while not equal, are not greatly disparate. The terminal shock Mach number 1.34 is significantly higher, however, which suggests that a more nearly optimum arrangement would have resulted from using a larger third wedge angle, say 9°. The sequence of total pressure ratios corresponding to the values of *M* sin b and the terminal shock is 0.990, 0.993, 0.994, 0.972, the product of which gives the shock pressure recovery as

$$\frac{P_s}{P_\infty} = 0.950 \qquad (5.19)$$

An intake so constructed is shown in Fig. 5.23 (intake A). The free stream tube height *h*¥ sets a scale for the diagram. Intersection of the front shock with the bounding streamline locates the intake lip. By striking appropriate angles back from the lip the leading edges of the second and third wedges are located. Inside the duct, following a 2° reverse angling, the shape is such as to give the best subsonic diffuser terminating at the engine face *A*f, the

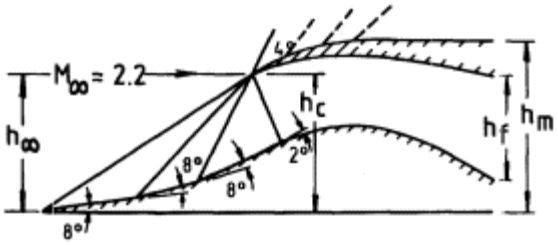

Figure 5.23
Intake A with shocks focused on cowl lip.

position and area of which are assumed to have been independently prescribed. The external cowl line, following an initial 4° vertex angle is an arbitrary shape terminating at the maximum frontal area, *A*m, also assumed prescribed: wave drag of this cowl shape is discussed in Chapter 9.

From the point of view of shock pressure recovery, it is not essential that the shock system should be focused. A design to the same specification as intake A but with unfocused compression is shown in Fig. 5.24 (intake B). The shock pressure recovery is the same as for intake A but intake B has a number of disadvantages, viz:

(1) the forebody length and height (hence weight) are increased;

(2) maximum ratio, *h*¥/*h*i is less than 1.0: this implies a spillage drag at critical point (Chapter 9);

(3) the longer forebody means a more extensive boundary layer development, which is detrimental (Chapters 7, 8);

(4) if, as is commonly the case, the duct has to be brought back towards the forebody axis, or even beyond, the extra outward displacement at entry plane complicates the duct design.

Whether the external cowl line is more or less favourable depends entirely upon installational details: this point is not pursued.

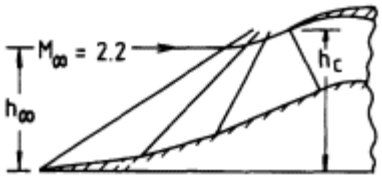

Figure 5.24
Intake B with shocks unfocused.

5.7
Position of Normal Shock in Subcritical Operation

In subcritical operation the normal shock is detached from the lip of the cowl and stands forward of the entry plane. The position of this shock affects the pressure recovery (except in the case of a simple pitot intake); it also affects the nature of spillage around the lip, and thereby the drag, and it varies the degree of impingement of the intake bow wave on adjacent wing or body surfaces. Furthermore it has a determining effect on the onset of flow instability, or 'buzz', to be described in Chapter 10. It is important therefore to be able to estimate the position of the detached normal shock as a function of flow ratio. The problem was first analysed by Moeckel (1949) for the pitot intake and his method has subsequently been extended

to the two-shock intake by Goldsmith and Griggs (1953). The two analyses are given below. A further extension to the case of double wedge intakes has been made by McGregor (1971).

5.7.1
Pitot Intake.

The notation adopted is illustrated in Fig. 5.25. It is assumed that the detached bow wave *in the external flow* is hyperbolic in form, approaching asymptotically a free stream Mach line (Mach angle μ) and with vertex at the point where it intersects the dividing streamline separating internal and external flow. It is further assumed that the sonic point on the cowl in the external flow is at the sharp lip (point B) and the sonic line BS is straight, making an angle x with the vertical. The point S is identifiable from the shock wave inclination. The distance L of the detached wave in front of the entry is thus:

$$L = x_c - x_0 = x_s + (r_s - r_c) \tan \zeta - x_0. \qquad (5.20)$$

rc is known and an approximate value can be assigned to z as shown below. xs and x0 can be obtained in terms of rs from the equation of the hyperbola.

$$r - r_\infty = (x^2 - x_0^2)^{\frac{1}{2}} \tan \mu \qquad (5.21)$$

The slope of the hyperbola at the sonic point S, bs say, is given by

$$\left(\frac{dr}{dx}\right)_{r=r_s} = \tan \beta_s = \frac{[(r_s - r_\infty)^2 \cot^2 \mu + x_0^2]^{\frac{1}{2}} \tan^2 \mu}{r_s - r_\infty} \qquad (5.22)$$

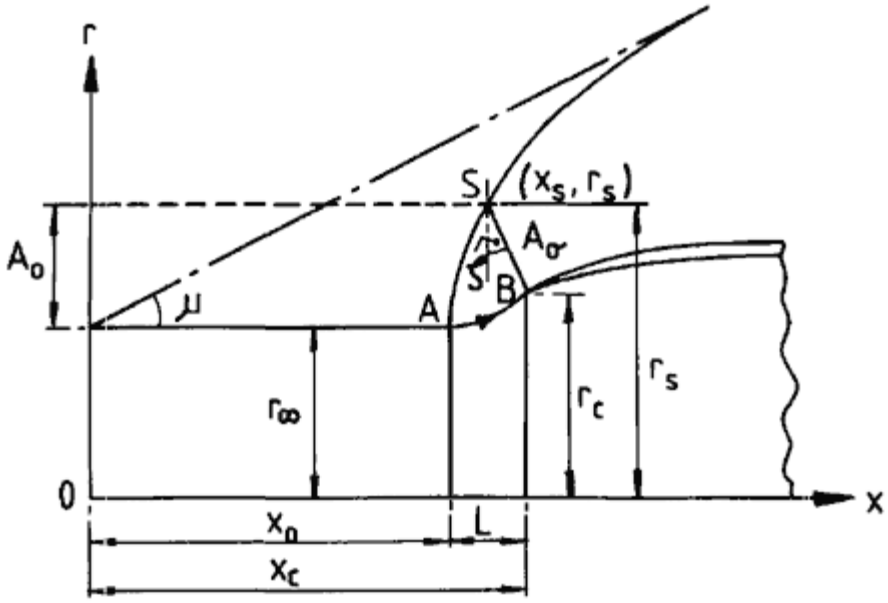

Figure 5.25
Notation for location of detached
shock in front of spilling pitot intake.

and from Equation (5.21), we have

$$x_s = [(r_s - r_\infty)^2 \cot^2 \mu + x_0{}^2]^{\frac{1}{2}} \qquad (5.23)$$

so that

$$x_s = \frac{(r_s - r_\infty) \tan \beta_s}{\tan^2 \mu} \qquad (5.24)$$

To determine *r*s, a continuity condition of the streamtube defined by areas *A*0 and *A*s (Fig. 5.25) is applied. We have

$$P_\sigma A_\sigma = P_\infty A_0{}^*$$

or

$$\frac{P_\sigma}{P_\infty}\left(\frac{A}{A^*}\right)_\infty = \frac{A_0}{A_\sigma} \qquad (5.25)$$

For an axisymmetric intake

$$\frac{A_\sigma}{\pi} = \frac{r_s{}^2 - r_c{}^2}{\cos \zeta} = \frac{P_\infty}{P_\sigma}\left(\frac{A^*}{A}\right)_\infty (r_s{}^2 - r_\infty{}^2)$$

so that

$$\frac{r_s}{r_c} = \left[\frac{1 - \mathrm{B} \cos \zeta \left(\frac{r_\infty}{r_c}\right)^2}{1 - \mathrm{B} \cos \zeta}\right]^{\frac{1}{2}} \qquad (5.26)$$

where

$$\mathrm{B} = \frac{P_\infty}{P_\sigma}\left(\frac{A^*}{A}\right)_\infty \qquad (5.27)$$

The corresponding relation for a two-dimensional intake is

$$\frac{r_s}{r_c} = \frac{1 - \mathrm{B} \cos \zeta \frac{r_\infty}{r_c}}{1 - \mathrm{B} \cos \zeta} \qquad (5.28)$$

Total pressure ratio *P*s/*P*¥ varies along the sonic line but a mean value can be taken appropriate to the centroidal

streamline. The shock inclination bc on this streamline is obtained from Equations (5.22) to (5.24) and hence the

value of *P*s/*P*¥ is determined. Values of bc and *P*s/*P*¥ for axisymmetric and two-dimensional intakes are shown in Fig. 5.26.

At *S* the inclination of the streamline, ls say, is known and at B the inclination is assumed to be the angle for shock detachment at the free stream Mach number, say lda or ldt for axisymmetric or two-dimensional flow respectively. A mean value is taken for the angle z, thus

$$\zeta = \frac{\lambda + \lambda_{da}}{2} \text{ (axisymmetric flow)} \qquad (5.29)$$

and for two-dimensional flow, since ls differs only slightly from ldt,

$$\zeta = \frac{\lambda_s + \lambda_{dt}}{2} \simeq \lambda_s \text{ (two-dimensional flow)} \qquad (5.30)$$

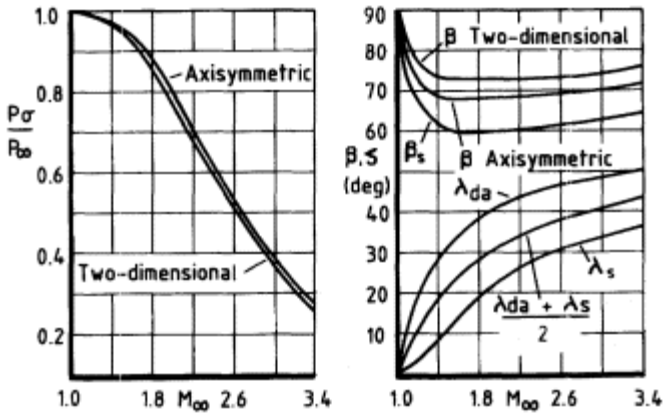

Figure 5.26
Variation of total-pressure ratio and shock-wave angle on centroid streamline and of inclination of sonic line with free stream Mach number.

These angles are presented as functions of free-stream Mach number in Fig. 5.26.

The necessary substitutions in Equation (5.20) now lead to expressions for the stand-off distance *L*. The general result is:

$$\frac{L}{r_c} = \frac{(r_s - r_\infty)\tan\beta_s}{r_c \tan^2\mu} = \left(\frac{r_s}{r_c} - 1\right)\tan\zeta - \frac{(r_s - r_\infty)(\tan^2\beta_s - \tan^2\mu)^{\frac{1}{2}}}{r_c \tan^2\mu} \qquad (5.31)$$

which may be written as:

$$\frac{L}{r_c} = \left[\frac{1 - \left(\frac{r_\infty}{r_c}\right)^2 B\cos\zeta}{1 - B\cos\zeta}\right]^{\frac{1}{2}} (C + \tan\zeta) - C\frac{r_\infty}{r_c} - \tan\zeta \qquad (5.32)$$

for axisymmetric flow, or as:

$$\frac{L}{r_c} = \left(1 - \frac{r_\infty}{r_c}\right)\left(\frac{C + \mathrm{B}\sin\zeta}{1 - B\cos\zeta}\right) \qquad (5.33)$$

for two-dimensional flow, where

$$C = \cot\mu\,[\cot\mu\tan\beta_s - (\cot^2\mu\tan^2\beta_s - 1)^{\frac{1}{2}}] \qquad (5.34)$$

B and *C* are essentially Mach number functions. In two-dimensional flow (Equation 5.33) *L*/rc varies linearly with the spillage ratio (1 *r*¥/rc), so that *L*/(1 *r*¥/rc) is a function of Mach number only. For Mach numbers between 1.15 and 2.5 the shock position can be approximated by the empirical expression

$$\frac{L}{r_c - r_\infty} = 0.6 + \frac{1.427}{M-1} + \frac{0.118}{(M-1)^2} \qquad (5.35)$$

Fig. 5.27 shows the calculated variation of *L*/rc with spillage ratio for both axisymmetric and two-dimensional flow at Mach 1.8. There is a wide difference between the two, the stand-off distances being in a ratio of about 2 1/2 to 1. Also shown is a series of measurements of shock position, from

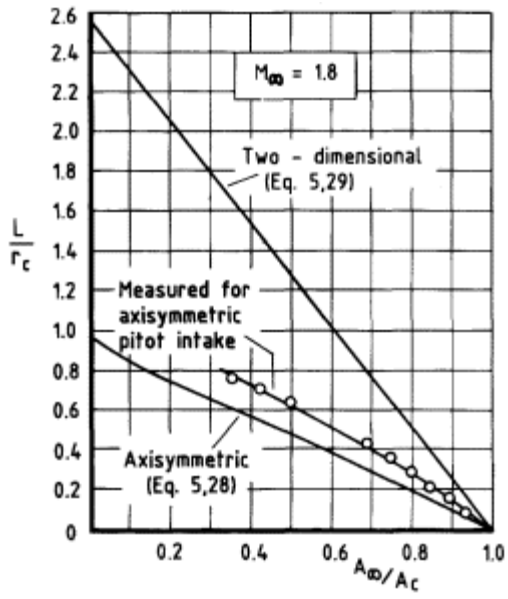

Figure 5.27
Comparison of measured and predicted shock position in front of pitot intake at *M*¥ 1.8.

schlieren photographs, for an axisymmetric pitot intake. The indication is that because the flow right at the lip is two-dimensional, at small spillage the variation of shock position shows a mixture of the axisymmetric and two-dimensional effects, then as spillage increases the axisymmetric effect dominates. As concerns the large difference between the two theoretical cases, it should be said that real intakes are never more than pseudo-two-dimensional and the stand-off distance of rectangular intakes varies considerably with the span-to-height ratio: a square intake would be expected to give results not greatly different from the axisymmetric case.

5.7.2
Two-Shock Intakes

The situation to be analysed is illustrated in Fig. 5.28. So long as the common intersection point of the two intake shocks with the third, or outer, shock lies on or inside the capture streamtube (*r*i £ *r*¥), a procedure similar to that given for the pitot intake can be followed. The length L to be calculated is the distance from the entry plane to the point where the outer shock crosses the stagnation streamline. A slope condition replaces the previous assumption that the hyperbola has its vertex on the stagnation streamline. It is now assumed that the outer shock is straight between the intersection point and the stagnation streamline and is inclined at angle f¥ (the suffix ¥ being used to correspond to the stagnation streamline $r = r¥$), which is to be determined from three-shock intersection calculations.

The vertex of the hyperbola is at $x = x0$, $r = r0$.

Equation (5.22) in general form is

$$\frac{dr}{dx} = \tan\beta = \frac{[(r - r_0)^2 \cot^2\mu + x_0^2]^{\frac{1}{2}} \tan^2\mu}{r - r_0} \qquad (5.36)$$

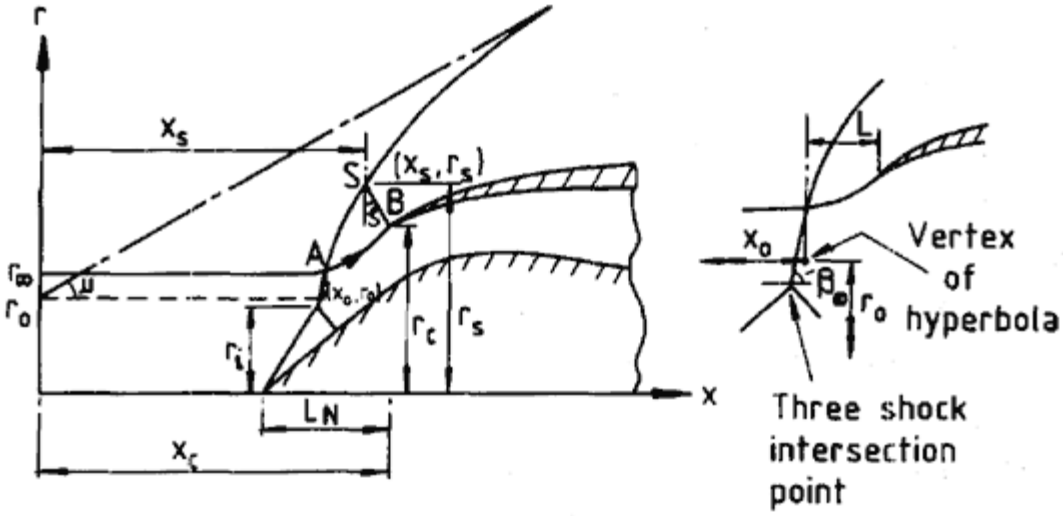

Figure 5.28
Notation for location of detached shock in front of spilling forebody intake.

and we now have the two conditions, b = bs when $r = r$s, as before and b = b¥ when $r = r$¥. Substituting and rearranging leads to

$$x_0 = \frac{r_s - r_\infty}{\tan^2\mu\,[(\tan^2\beta_s - \tan^2\mu)^{-\frac{1}{2}} - (\tan^2\beta_\infty - \tan^2\mu)^{-\frac{1}{2}}]} \qquad (5.37)$$

and

$$r_0 = r_\infty - x_0\,\tan^2\mu\,(\tan^2\beta_s - \tan^2\mu)^{-\frac{1}{2}}] \qquad (5.38)$$

and following the same procedure as before gives

$$\frac{L}{r_c} = \frac{r_s - r_\infty}{r_c\,\tan^2\mu\,[(\tan^2\beta_s - \tan^2\mu)^{-\frac{1}{2}} - (\tan^2\beta_\infty - \tan^2\mu)^{-\frac{1}{2}}]} \qquad (5.39)$$

$$\times\left[\frac{\tan\beta_s}{(\tan^2\beta_s - \tan^2\mu)^{\frac{1}{2}}} - \frac{\tan\beta_\infty}{\tan^2\beta_\infty - \tan^2\mu)^{\frac{1}{2}}}\right] + \left(\frac{r_s}{r_c} - 1\right)\tan\zeta$$

Equations (5.26) and (5.28) again apply.

The angle b¥ is determined by compatibility requirements between inner and outer flows at the shock intersection point. A shock 'polar' (curve of flow deflection versus static pressure ratio) is drawn for all oblique shocks (including both 'weak' and 'strong' solutions) occurring at free stream Mach number M¥. From a point on this curve corresponding to a selected cone or wedge angle, a second curve is drawn defining the polar relationship for shocks occurring in the supersonic flow downstream of the chosen cone or wedge. Intersection of the two polars defines the condition for coexistence of two inner shocks and one outer shock. Curves of b¥ determined for ranges of cone and wedge angles are given in Fig. 5.29. It is noted that at small forebody angles the values of b¥ are in excess of 90°, implying that the outer shock leaves the intersection point with a forward inclination.

5.8
Calculation of Subcritical Pressure Recovery

For calculating the shock pressure recovery of a two-shock intake in subcritical operation, a knowledge of the radius ri of the shock intersection point is required. This can be derived from the stand-off distance L. From the geometry of the system of Fig. 5.28 the distance Li of the intersection point ahead of the entry can be expressed either as

$$L_i = L + (r_\infty - r_i)\,\cot\beta_\infty \qquad (5.40)$$

or as

$$L_i - L_N - r_i \cot \beta_1 \qquad (5.41)$$

Equating the right-hand side leads to the required relation for *r*i:

$$\frac{r_i}{r_\infty}(1 - \cot \beta_1 \tan \beta_\infty) = 1 - \frac{L_N - L}{r_\infty} \tan \beta_\infty \qquad (5.42)$$

Goldsmith and Griggs (*loc. cit.*) have shown a number of comparisons of shock intersection position as calculated from Equation (5.42) and as measured from schlieren photographs of the flow: one such comparison is given in Fig. 5.30.

From Equation (5.42) can be determined, for any flow ratio, given by *r*¥/*r*c, the proportions of flow passing through the single outer shock and the two-shock system respectively. If the total pressures given separately by these two parts of the flow are denoted by *P*s1 and *P*s2, the mean shock recovery is determined, on an area weighted basis, as

$$\frac{P_s}{P_\infty} = \frac{P_{s1}}{P_\infty}\left(1 - \frac{{r_i}^2}{{r_\infty}^2}\right) + \frac{P_{s2}}{P_\infty} \cdot \frac{{r_i}^2}{{r_\infty}^2} \qquad (5.43)$$

for axisymmetric intakes and

$$\frac{P_s}{P_\infty} = \frac{P_{s1}}{P_\infty}\left(1 - \frac{r_i}{r_\infty}\right) + \frac{P_{s2}}{P_\infty} \cdot \frac{r_i}{r_\infty} \qquad (5.44)$$

for 'two-dimensional' (i.e. rectangular) intakes.

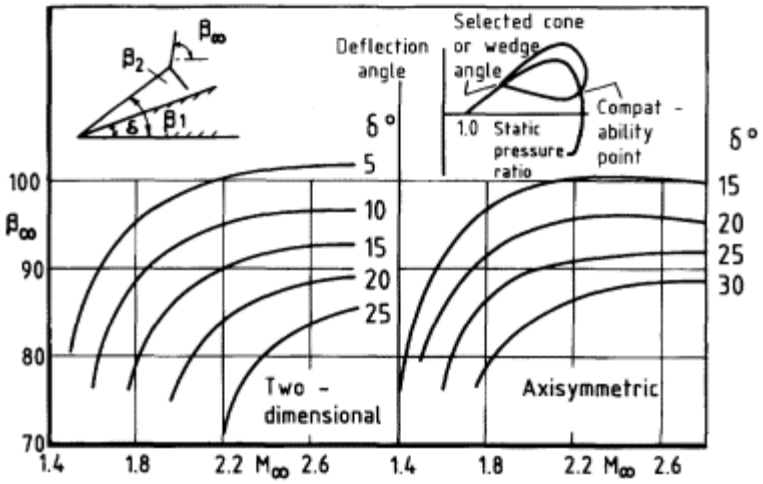

Figure 5.29
Outer shock angle for axisymmetric and
two-dimensional three-shock intersections.

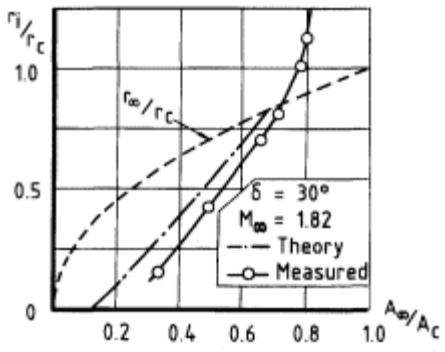

Figure 5.30
Comparison of measured and predicted position of
three-shock intersection point for axisymmetric forebody.

If the shock intersection point lies outside the capture streamtube (i.e. *r*i > *r*¥), the whole capture flow passes through the two-shock system and the shock pressure recovery is approximately the same as at critical flow. Owing to varying expansion effects around the shoulder of the forebody, there may be a small decrease in shock pressure recovery as flow ratio increases from subcritical to critical. Goldsmith and Griggs (*loc. cit.*) give a method of calculating this change, which however is not normally of significant magnitude.

A comparison is shown in Fig. 5.31 between calculated shock recovery and measured overall recovery for a conical centrebody intake, with 22.5° cone semi-angle, tested at Mach 1.61. This particular case is one in category (b) of Section 5.2, in which as flow ratio is reduced from critical, there exists a range of subcritical flow for which *r*i > *r*¥, followed by a range for which *r*i < *r*¥. Schlieren photographs of the flow are shown for a point near *r*i = *r*¥ (*P*1) and a point near critical (*P*2). The differences in characteristic for the

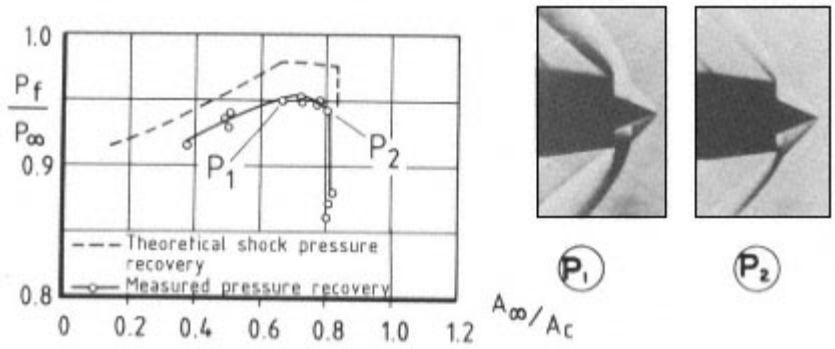

Figure 5.31
Comparison of measured and predicted pressure
recovery characteristic (d = 22.5, *M*¥ = 1.61).

different flow regimes are well brought out in both the calculated and measured results. The measured levels of pressure recovery lie well below the calculated values, however: this difference is explained by extra-to-shock losses, which are a subject of discussion in Chapter 7.

References

Connors, J.F. and Meyer, R.C. (1956) 'Design criteria for axisymmetric and two-dimensional supersonic inlets and exits'. *NACA TN. Note 3589.*

Fraenkel, L.E. (1951) 'Some curves for calculation of the performance of conical centrebody intakes at supersonic speeds'. *RAE Technical Note No. Aero 2135.*

Goldsmith, E.L. and Griggs, C.F. (1953) 'The estimation of shock pressure recovery and external drag of conical centrebody intakes at supersonic speeds'. *ARC Reports & Memoranda No. 3035.*

Hermann, R. (1956) *Supersonic Inlet Diffusers and Introduction to Internal Aerodynamics.* Minneapolis Honeywell Regulator Company.

Kopal, Z. (1947) 'Tables of supersonic flow around cones'. *MIT Centre of analysis TR.1.*

Mascitti, V.R. (1969) 'An approximate solution of additive drag coefficient and mass flow ratio for inlets utilizing right circular cones at zero angle of attack'. *NASA, TN D5537.*

McGregor, I. (1971) 'Some theoretical parameters relevant to the performance of rectangular air intakes with double-ramp compression surfaces at supersonic speeds'. *RAE Technical Report 71237.*

Moeckel, W.E. (1949) 'Approximate method for predicting form and location of detached shock waves ahead of plane or axially symmetric bodies'. *NACA Technical Note 1921.*

Neale, M.C. and Lamb, P.S. (1963) 'Tests with a two-dimensional intake having all external compression and a design Mach number of 2.0'. *NGTE, Memorandum M368.*

Oswatitsch, K.L. (1944) 'Der Druckruckgewinn bei Geschossen mit Ruckstossantrieb bei hohen Uberschallgeschwindigkeiten (der Wirkungsgrad von Stossdiffusoren). *Forschungen und Entwicklungen des Heereswaffenamtes, Bericht. Nr. 1005.*

Chapter 6
Internal Supersonic Compression

6.1
The Flow Starting Problem.

The outward turning of flow that goes with external compression leads to the use of outward angles on the intake cowl which, even with attached shocks, result in significant wave drag (Chapter 9). The question arises, to what extent can the supersonic compression be achieved by means of inward flow turning within an enclosed duct: this is the theme of internal supersonic compression.

We examine a succession of flow stages at constant free stream Mach number in a manner analogous to that used at the start of the previous chapter. In the present case our aerodynamic duct is a degree more complex than before in that, since supersonic compression involves a *decrease* in flow area, the duct must first contract to a throat, *A*t say, before expanding to the maximum area *A*f. Schematically this is shown in the illustrations of Fig. 6.1.

As flow through the duct is increased from zero (by deployment of an exit control), the first two stages, namely zero and small through-flow, are as before. With zero flow a normal shock stands out ahead of the duct; with small flow the shock is closer and the flow throughout the duct is subsonic, reaching in this case a first maximum velocity at the throat section, and ultimately, as before, attaining sonic speed at the exit. As exit area is further increased the throat Mach number *M*t increases and the normal shock moves closer to the entry. There are now two cases, according as the shock reaches the entry plane before the throat Mach number becomes unity or conversely. The next stages are illustrated in Figs. 6.1(a) to (d).

(a) *Shock attached with M*t < 1. When the shock becomes attached the intake is running full, i.e. *A*¥/*A*c = 1.0. If the exit area is increased further, Fig. 6.1(b), the shock moves inside the duct, passing through the throat and stabilising at a position in which the product of exit area and total pressure behind the shock is equal to the corresponding product with shock just attached (see Equation 5.1 for analogous case). The flow is wholly supersonic upstream of the shock and consists of a supersonic compression up to the throat and a supersonic

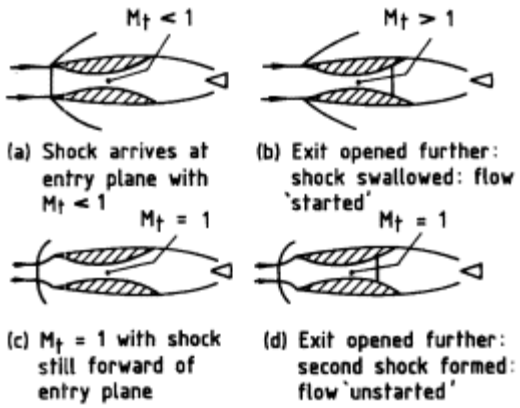

Figure 6.1
Flow through duct with internal throat.

expansion from the throat to the shock. An intake in this condition is said to be 'started' in a supersonic sense, in that controlled supersonic compression is taking place. Note that the shock cannot be stabilised in the contracting portion of the duct. Note also that for the purpose of this basic argument, one-dimensional flow is being assumed, implying that compression before the normal shock is isentropic.

(b) *Mt = 1 with shock detached.* If the duct chokes at the throat (*M*t = 1) whilst the shock is still ahead of the entry, further increase of exit area has no effect upstream of the throat. As *A*e is increased a second shock develops downstream of the throat, Fig. 6.1 (d), again stabilising at a position which maintains constant throughflow. The duct now has subsonic flow extending from the forward detached shock to the throat; an intake in this condition is said to be 'unstarted'.

6.2
Limiting Contraction Ratio

From the definitions (a) and (b) above, the critical condition for obtaining a starting intake is when the free stream shock reaches the duct entry simultaneously with the occurrence of choking at the throat. This defines a limit to the contraction ratio *A*t/*A*c, in the sense that any smaller value (implying a greater degree of compression) would result in condition (b) applying and the intake being unstartable.

The subsonic Mach number immediately downstream of the free stream shock is, let us say, *M*w ¥. When the shock is at the entry plane and the throat is choked the sonic area relationship can be applied, thus:

$$\frac{A_t}{A_c} = \left(\frac{A^*}{A}\right)_{M\omega\infty} = M_{\omega\infty}\left[\frac{\gamma+1}{(\gamma-1)M_{\omega\infty}{}^2+2}\right]^{(\gamma+1)/2(\gamma-1)} \qquad (6.1)$$

as in Equation (1.12). Now from the normal shock relations, *M*w ¥ can be expressed in terms of *M*¥ thus:

$$M_{\omega\infty} = \left[\frac{(\gamma-1)M_\infty{}^2 + 2}{2\gamma M_\infty{}^2 - (\gamma-1)}\right]^{\frac{1}{2}} \qquad (6.2)$$

From these two relations, the limiting contraction ratio is defined in terms of free stream Mach number:

$$\chi = \left(\frac{A_t}{A_c}\right)_{\lim} = \left[\frac{\gamma-1}{\gamma+1} + \frac{2}{(\gamma+1)M_\infty{}^2}\right]^{\frac{1}{2}}$$

$$\times \left[\frac{2\gamma}{\gamma+1} - \frac{\gamma-1}{(\gamma+1)M_\infty{}^2}\right]^{1/(\gamma-1)} \qquad (6.3)$$

In Fig. 6.2 the function c is shown plotted, along with the sonic area relationship *A*/*A** which represents idealised full internal contraction from free stream speed at Mach 1.0. It is seen that the starting criterion imposes a severe limitation on the allowable degree of contraction. The ultimate value of c as *M*¥ tends to infinity is given by

$$\chi_{M=\infty} = \left(\frac{\gamma-1}{\gamma+1}\right)^{\frac{1}{2}} \left(\frac{2\gamma}{\gamma+1}\right)^{1/(\gamma-1)} \qquad (6.4)$$

which, with g = 1.40, has the value 0.6.

When the normal shock has been swallowed, as in Fig. 6.1(a), that is to say the intake is started, a reduction in exit area will increase the back pressure, causing the shock to move forward towards the throat, thereby decreasing its Mach number. This movement is stable and produces an increase in pressure recovery, up to the point when the shock sits at the throat and the pressure recovery is a maximum. In Fig. 6.3 are shown the

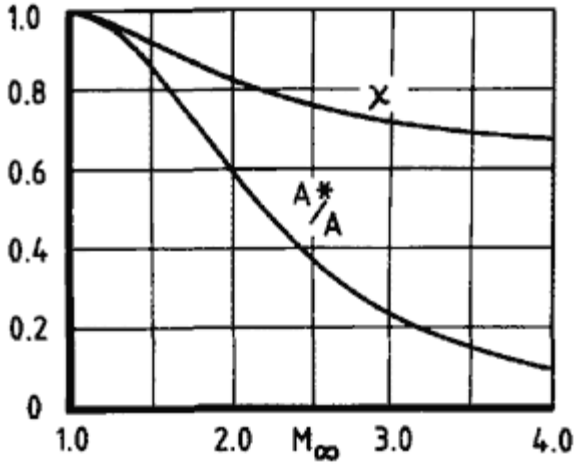

Figure 6.2
Limiting contraction c compared to sonic area ratio.

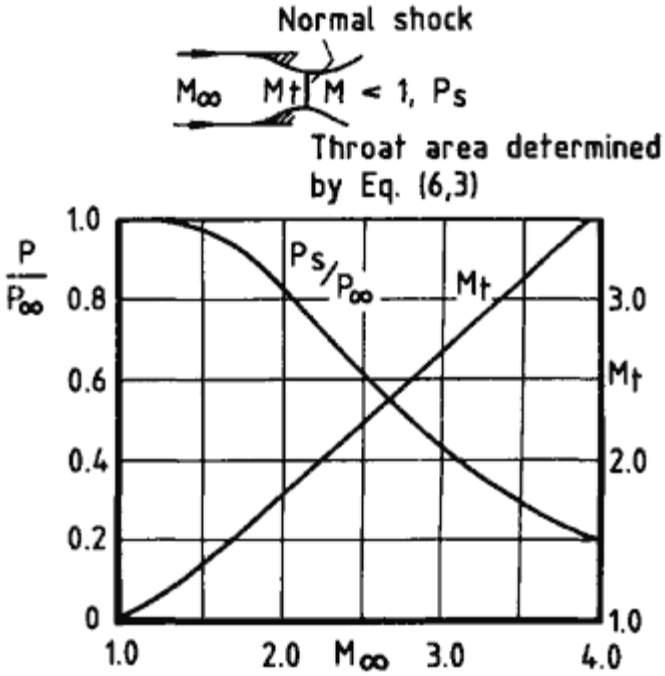

Figure 6.3
Shock pressure recovery and throat Mach number for self-starting contraction.

variations, with free stream Mach number, of throat Mach number (determined by the limiting contraction ratio) and the corresponding maximum pressure recovery. We see again that the limitation is severe: the pressure recovery obtainable from internal compression thus restricted is only a few per cent higher than for a plain pitot intake (Fig. 5.3). For internal compression to be competitive with external compression, a way of reducing the normal shock Mach number to lower values must be provided.

6.3
Perforated Intake

A type of fixed geometry intake that overcomes the restrictive starting condition and allows a high degree of internal compression is the 'perforated intake' devised by Evvard and Blakey (1956). The contracting portion of the duct is perforated in such a way that for any position of a normal shock in the contraction (Fig. 6.4) the total effective area of perforations downstream of the shock is sufficient to make up the deficiency between throat area and the area required for shock swallowing, according to Equation (6.3) as applied to the supersonic Mach number, *M*s, of the shock in that position. This allows the shock to proceed further down the contraction and ultimately through the throat.

It is necessary to factor the geometric areas of the perforations by suitable discharge coefficients to allow for angling of the flow and for boundary layer effects. The pressure drop available to perforations downstream of the shock is large enough to ensure a high flow rate, normally choked at exit. After the shock has passed there is a residual pressure drop because of the supersonically compressed flow in the contraction, so there is

Figure 6.4
Principle of perforated intake.

a continued, though reduced, outflow through the perforations. This is a disadvantage since it creates drag: it can however be largely avoided by the design of so-called 'educated holes', that is to say perforations which accept subsonic spillage behind the shock but reject supersonic spillage when the shock has passed. The principle is illustrated in Fig. 6.5.

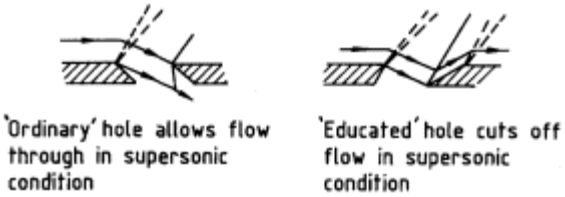

Figure 6.5
Principle of 'educated' hole for perforated intake.

Given an adequate margin of discharge area at all stages, the Evvard perforated intake provides a good stable system since the shock, in proceeding through the contraction, is effectively always at a throat position and is therefore stabilised. One result is that the final shock can be positioned at or very close to the real throat. If to this is added the further benefit that, using normal perforations, these act as boundary layer bleeds when the shock has passed, it is seen that a very efficient internal system can result, with no obvious limited short of compression to Mach 1.0 and 100% recovery. There is, however, in addition to the drag problem, the further disadvantage that as free stream Mach number is reduced from the design value, increasing amounts of perforation are required to compensate for the rising limit of contraction ratio, so in practice the intake soon becomes non-starting.

6.4
Variable Geometry for Flow Starting

A more flexible method of overcoming the starting problem is by the use of variable geometry. Basically the requirement is to provide a throat area which is large enough for the establishment of supersonic flow and which can subsequently be reduced to provide efficient supersonic compression in the running condition.

With a two-dimensional (in practice, rectangular) arrangement, using wedge compressions analogous to those for external compression, the most natural solution is to vary the angle of the final wedge. This involves a matching movement of the duct wall which forms a continuation downstream of the throat. In an axisymmetric arrangement the provision of suitable variable geometry is more complicated and can involve fore-and-aft translation of either the compression body or the cowl, or even both.

Further discussion of the use of variable geometry is postponed to the treatment of intake and engine matching (Chapter 12), where additional requirements emerge.

6.5 Types of Intake and Limiting Pressure Recovery

In the following considerations, it is assumed that the starting problem has been solved by introduction of appropriate variable geometry.

The method of obtaining efficient supersonic compression is basically the same for internal as for external compression: that is to say, a staged compression system is created by the use of discrete wedges or conical surfaces, or using isentropic contours, to reduce the Mach number of flow to a suitably low value for the terminal, normal shock. A principal difference is that with internal compression, since the system is enclosed, oblique shocks are reflected from an opposite wall and these reflections have to be taken into account.

The simplest form is a three-shock system, pictured in Fig. 6.6. Considered in two dimensions, the generator surface is a single wedge which turns the flow towards the opposite wall: the oblique shock is reflected from the opposite wall and the flow in passing through the reflected shock is restored to an axial direction. Where the reflected shock meets the generator surface, the latter is turned from the wedge slope to the axial direction, thereby cancelling out further reflections. A normal shock terminates the supersonic compression in the usual way. We note that here the reverse turning of the flow is achieved in the supersonic phase, in contrast to the situation with external compression where, apart from possibly a limited degree of duct angling, the reverse turn is left to the subsonic phase.

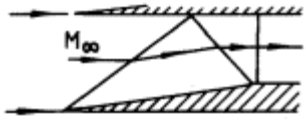

Figure 6.6
Single-sided three-shock
internal-compression intake.

A symmetrical version of the simple form is illustrated in Fig. 6.7. Here the 'reflected' shocks are part of a symmetrical four-shock intersection system.

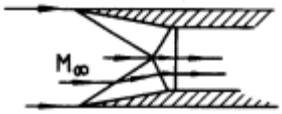

Figure 6.7
Symmetrical three-shock
internal-compression intake.

Multi-shock compressions can of course be used, as also isentropic compressions within their practical limitations. In order to restrict the length of intake to a minimum, and also to avoid over-complexity in the reflected shock system, the oblique shocks or isentropic compressions will tend to be focused on the opposite wall (assuming a single-sided arrangement). A single reflected shock then restores the axial flow direction, as in the simple case of Fig. 6.6. For the case of isentropic forward compression, the pressure recovery given by the reverse oblique shock and the normal shock can be calculated as a function of initial Mach number and turning angle d. The results are shown in Fig. 6.8. We see that for a given Mach number the pressure recovery reaches a maximum at a value of d just below the 'detachment' angle, that at which turning through a single reverse shock is not possible. Quantitatively this limit of pressure recovery is not greatly different from that set by shock structure in the case of external compression (Fig. 5.22), the present limit being somewhat lower at Mach numbers below about 3.5 and conversely above.

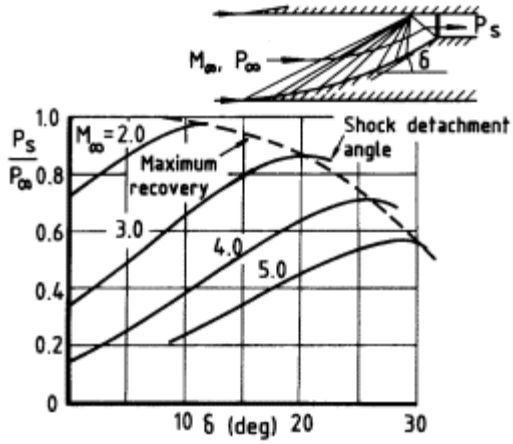

Figure 6.8
Shock pressure recovery of internal-compression
intake with isentropic compression and reverse
turn through single oblique shock.

In terms, therefore, of idealised design situations appropriate starting mechanisms, efficient oblique shock systems, normal shock at throat and no boundary layer complications internal compression offers pressure recoveries similar to those achievable from external compression; with additionally the promise of low cowl wave drag because the flow turning is contained within a more or less parallel-sided duct. Internal compression has, however, two serious disadvantages. The first is the problem of supersonic flow breakdown ('unstarting'), which occurs in two ways. At a given free-stream Mach number, with normal shock at the throat, any increase of back pressure drives the shock forward into the contraction, where however it cannot stabilise because shock Mach number is increased above the throat value, hence pressure recovery is decreased, whereas an increased pressure recovery would be required to maintain a constant flow ($A¥/Ac = 1.0$ as dictated by the entering streamtube) against the increase in back pressure. The shock therefore travels immediately through the contraction and out into the mainstream, settling at a position for reduced flow ratio appropriate to the back pressure increase. The flow is now in an unstarted condition and can be restarted only by going through whatever starting process is built into the design. Thus an internal compression intake has no subcritical operating range except as an inefficient pitot intake: this is illustrated in Fig. 6.9. Unstarting also occurs when the intake operates below design Mach number unless variable geometry is incorporated of sufficient scope to cater for the more severe restriction on contraction (Fig. 6.2).

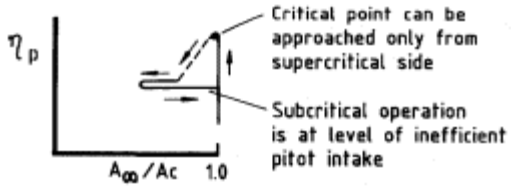

Figure 6.9
Pressure-recovery characteristic
of internal-compression intake.

The second significant disadvantage relates to boundary layer effects. These have not so far been discussed in details for supersonic intakes but it can be stated at this stage that the build-up of boundary layer is a serious deterrent to the use of internal compression. Not only is the surface area for boundary layer much increased by comparison with external compression but also, since all the shocks are enclosed, multiple interactions occur with the boundary layer on sidewalls (two-dimensional) and likewise strong interactions at focal loci (two-dimensional or axisymmetric). Bleed systems to counteract all these interactions are difficult if not impossible to design.

6.6
Mixed Compression, Intakes C and D.

Mixed compression implies the use of both external and internal compression, in appropriate degrees, in order to relieve the external drag problem of the former whilst avoiding excessive boundary layer or other disadvantage from the latter. Intakes C (Fig. 6.10) and D (Fig. 6.11) are examples of mixed compression intakes, designed to otherwise the same specification as intake A (Fig. 5.20). For intake C the first two wedge compressions are external and give 16° total turn. The shocks are focused at the lip where a reverse 8° turn is made by means of the internal cowl angle. The second wedge surface is continued until it meets the reversed shock: this gives the required contraction in duct area and distinguishes the system from one of reverse duct angling at constant area (Section 5.5.2). An 8° change of direction of the surface at this intersection cancels shock reflection and allows the normal shock to be positioned. The four-shock system of intake C may thus be termed 50/50 external/internal. With intake D the first shock only is external. A reverse shock is positioned at the cowl lip and a second on the cowl internal surface at a position which focuses the two reversed shocks on the extended wedge surface of the external shock. At this focal position a 16° change in surface angle cancels shock reflection and defines the throat for location of the normal shock. The shock system of intake D may be termed 25/75 external/internal.

Comparing the four specimen intakes A, B (Fig. 5.21), C and D at this stage, the following observations may be made:

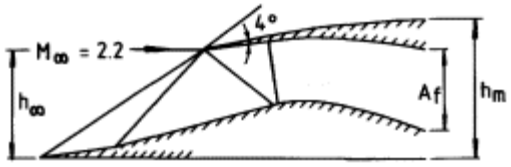

Figure 6.10
Intake C: 50/50 mixed compression,
with external shocks focused on cowl lip.

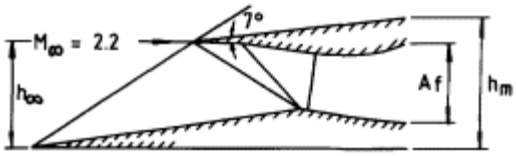

Figure 6.11
Intake D: 25/75 mixed compression
with internal shocks focused at shoulder.

(1) the sequence of compression Mach numbers is the same in all four cases; so is the throat size and so is the shock pressure recovery;

(2) whilst with A, C and D the shortest possible supersonic section (defined by the distance from forebody apex to normal shock) has been used in each case, consistent with the particular design philosophy, this section is nevertheless longer in C than in A and longer in D than in C (this affects weight considerations *inter alia*);

(3) both by reason of (2) and because of increased enclosure of shock waves, boundary layer effects can be expected to be more adverse in C than in A and more adverse in D than in C: this affects conclusions on the ultimate pressure recovery;

(4) design of the subsonic diffuser poses different problems in the four cases but since this is greatly dependent on the engine installational situation, no generalisation is attempted, beyond the observation that increasing the degree of reverse turning, as in C and more so in D, will usually ease the problem;

(5) a potentially major difference in performance between designs A, C and D is in the levels of cowl wave drag: this aspect is taken up in Chapter 9.

6.7
Some Design, Performance and Operating Aspects

With external compression, the shock configurations calculated for inviscid, two-dimensional or axisymmetric flow are closely approximated by those actually observed. Calculated shock pressure recovery is therefore largely achieved some geometries which cause departures are noted in Chapter 7. If a bleed is used (Chapter 8) it is normally positioned on the compression surface, downstream of the final (normal) shock and its action is to reduce viscous losses so that the ideal shock recovery is closely approached.

Intakes with internal compression, however, that must have variable geometry to establish internal shocks which will achieve the design-point pressure recovery, can fail to form these internal shocks at the desired optimum geometry. In Fig. 6.12 is shown a two-dimensional mixed-compression intake with variable cowl lip angle, giving a constant throat area and variable capture area as the lip angle is changed. In its most efficient condition it is designed to have an oblique internal shock, emanating from the lip, that is of approximately equal strength to the initial 14° wedge shock. Starting is accomplished by deflecting the cowl lip downward, thus reducing the capture flow until it is sufficiently low to pass through the fixed throat area, i.e. the internal contraction is reduced to the starting value (Fig. 6.2) for the wedge flow Mach number. When this has been achieved, the duct exit area can be increased until the intake is operating supercritically

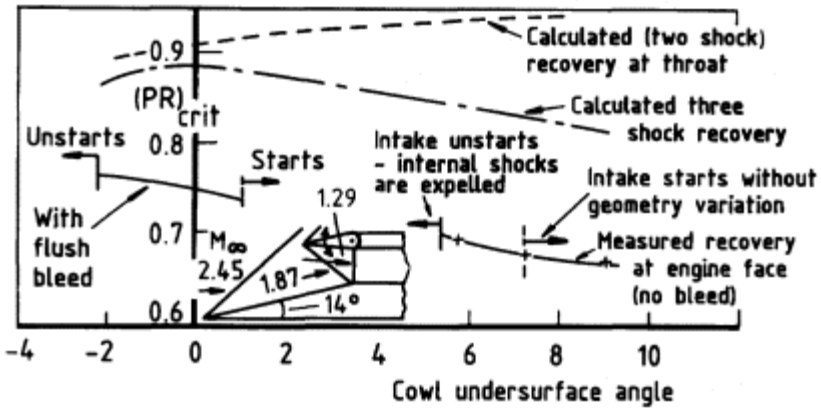

Figure 6.12
Mixed-compression intake with hinged cowl lip.

and the normal shock is positioned well downstream of the throat. If now the cowl lip is raised progressively so that capture flow and internal contraction are increased, then as indicated in Fig. 6.12, the cowl lip angle can only be decreased from 7.2° (for the starting condition) to 5.4° before the internal shocks are expelled. The continuity condition, expressed as

$$\frac{\text{Throat flow}, m_t}{\text{Capture flow}, m_\infty} = 1 = \frac{A_t P_t \left(\frac{A^*}{A}\right)_t}{A_\infty P_\infty \left(\frac{A^*}{A}\right)_\infty} \qquad (6.5)$$

when the flow is started (*m* signifying the mass flow quantity) cannot now be satisfied because the product of throat total pressure *P*t and sonic area ratio (*A**/*A*)t is not large enough. In inviscid flow, throat total pressure decreases with decreased cowl lip angle, as indicated in Fig. 6.12. Actual pressure recovery at the throat, however, decreases much faster, as the increasing strength of the cowl lip shock causes boundary layer thickening and then separation in the region of the compression surface corner. In these circumstances a compression surface bleed is essential, even for obtaining the desired shock configuration. In the first place a bleed removes an additional 1 2% of throat flow but more importantly it increases throat pressure recovery by inhibiting the separation tendency. This allows cowl angle to be reduced from the value of 5.4° (without bleed) to 2.2° as shown in Fig. 6.13 and hence enables the design internal shock system to be established.

It may readily be appreciated that certain types of bleed will not achieve the desired increase of contraction ratio before unstarting. Any bleed positioned downstream of the throat, for example, cannot increase the supersonic throat recovery *P*t and hence will not have the desired effect. A

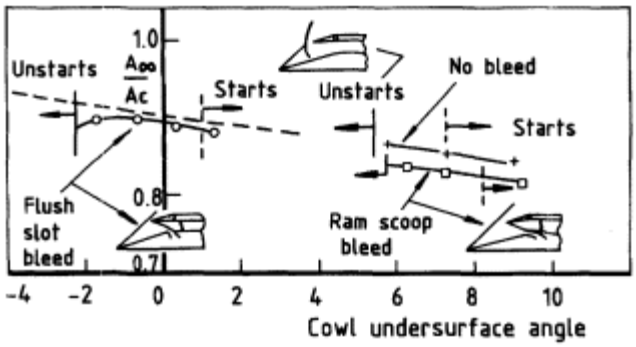

Figure 6.13
Capture-flow variation with cowl lip angle.

forward-facing or 'ram scoop' bleed at the compression surface corner see illustration in Fig. 6.13 will allow an increase of the unstarting contraction ratio only if the increase of total pressure at the throat more than compensates for the decrease in net throat area which results from the ram scoop. Fig. 6.13 indicates that the benefit obtained is small compared to the case without bleed.

A flush bleed slot, as illustrated, allows a strong lip shock to be established as required. Even then, however, the recovery achieved can still be appreciably lower than that calculated for the ideal shock pattern (Fig. 6.12). As the condition of normal shock at throat is approached from the supercritical side, the intake may unstart prematurely because, with normal shock still downstream of the throat, the throat recovery is affected sufficiently adversely by the boundary layers on both cowl and wedge. If to counter this the bleed is positioned just upstream of the throat, it may then not sufficiently influence conditions just ahead of the normal shock and a second bleed may be needed closely downstream of the first.

Figure 6.14 shows some results for the influence of bleed shape on pressure recovery, as a function of bleed flow, for a given internal contraction ratio. Some of the difference in performance results from differences in position of the normal shock with respect to the throat before the intake unstarts.

Because of the critical nature of positioning the cowl lip shock with respect to the bleed and compression surface corner, a complex variation of intake geometry may be needed as Mach number decreases from the design value. In Fig. 6.15 (from Anderson, 1969) is shown a two-dimensional intake designed to maintain the lip shock on the corner over the range $M¥ = 2.7$ to 1.8. To do this precisely the cowl has to be translated forward a short distance at the same time as the second ramp is lowered. Another way of dealing with this problem is to design the cowl compression as an unfocused compression fan, intersecting the external compression surface

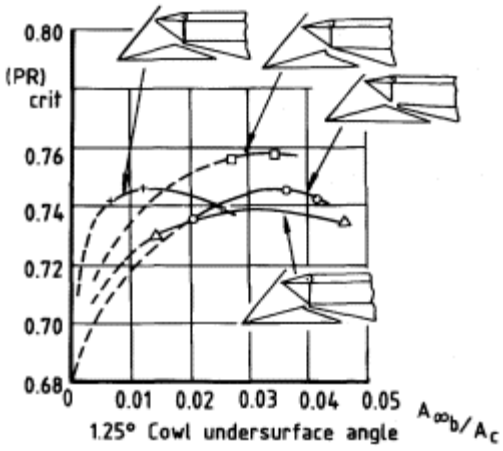

Figure 6.14
Influence of bleed shape and position
on critical-flow pressure recovery.

in the region of the corner and bleed (Fig. 6.16), as was demonstrated by Obery and Stitt (1957).

Longitudinal translation of the external compression body can be used to achieve flow starting and is particularly useful for axisymmetric intake designs. Two intakes designed in this way and achieving high contraction ratios by the use of flush bleeds just upstream of the lip-shock intersection position are illustrated in Fig. 6.17. In these cases, recovery falls off rapidly as the compression body is translated forward of the design position. As will be argued in Chapter 7, pressure recovery is related directly to the actual compression ratio achieved (*A*¥/*A*t) independently of detailed differences in shock configuration. Figure 6.18 (from Stitt and Salmi, 1960) illustrate this.

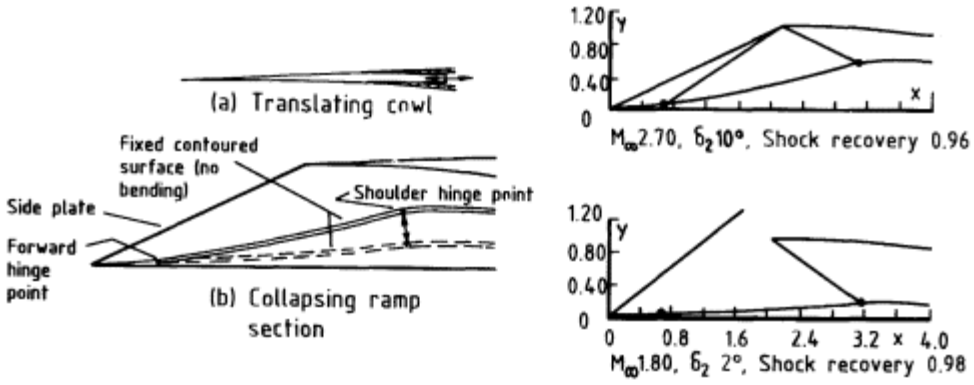

Figure 6.15
Mixed-compression intake with collapsing wedge
and translating cowl at Mach numbers 2.7 and 1.8.

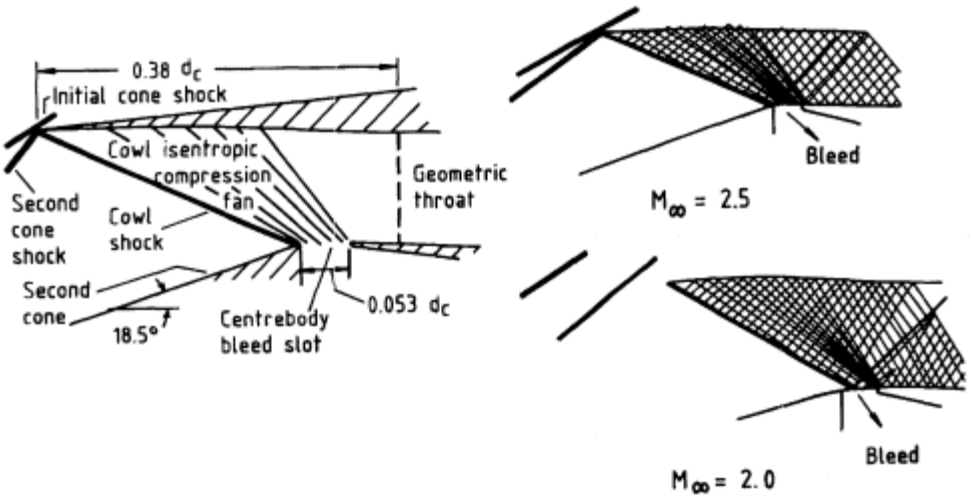

Figure 6.16
Mixed-compression intake with unfocused cowl compression fan at Mach numbers 2.5 and 2.0.

Even when a mixed-compression intake of the kinds under discussion achieves an optimum shock configuration for instance this last example (Fig. 6.18), having a high pressure recovery on design (0.83 at *M*¥ = 2.98) and with it a low level of cowl drag there are still operational problems of note in its use. The intake is always prone to unstarting, either from a sudden decrease in engine flow demand as could happen on encountering an abrupt increase in atmospheric temperature or from an increase in

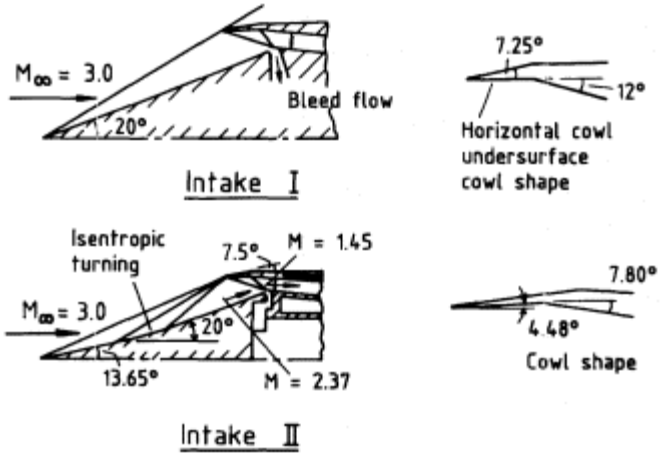

Figure 6.17
Two axisymmetric mixed-compression intakes designed for Mach number 3.0 (Stitt and Salmi).

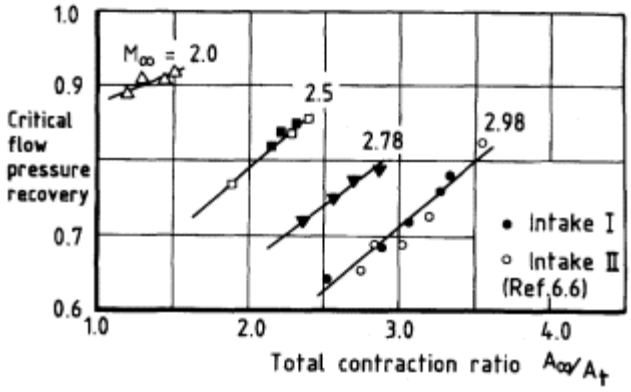

Figure 6.18
Performance of intakes of Fig. 6.17 as contraction ratio is varied by centrebody translation with intakes 'started'.

angle of incidence or yaw produced by a gust. Table 6.1 shows that the angle of incidence for unstarting is a function of bleed flow quantity and the intake operating point.

If unstarting occurs the shock pattern can change nearly instantaneously from that illustrated at (a) in Fig. 6.19 to that shown at (b). The maximum flow of the unstarted intake can be 20% or 30% less than that for the started condition and its equivalent operating point is a supercritical condition. This may well be associated with a level of flow distortion exceeding that which is acceptable for surge free operation of the engine (Chapter 11). With these considerations in mind it is obvious that intake unstarting must not be allowed to occur; hence as the normal shock begins to move forward from the throat it must be arrested by the rapid opening of valves to allow flow to spill and prevent the shock's further progress.

A scheme giving fast enough operation to achieve the desired result is illustrated in Fig. 6.20; here the exit to a throat bleed on the cowl is opened very quickly by the operation of pressure activated poppet valves and this effectively prevents the intake normal shock from moving forward, even for

Table 6.1 Effect of incidence on intake unstarting (Wasserbauer *et al.*, 1975)

Relative bleed flow	Operating point	Incidence for unstart (deg.)	Pressure recovery	Distortion coefficient (see Ch. 11)
0.02	supercritical	2.5	0.87	0.165
0.02	critical	1.75	0.885	0.125
0.041	supercritical	6.9	0.78	0.31
0.042	critical	4.2	0.86	0.20

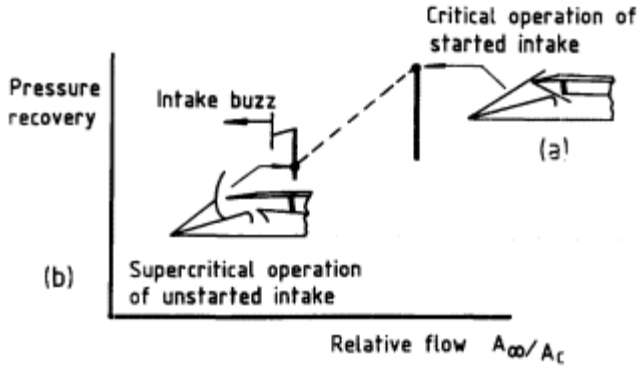

Figure 6.19
Characteristic of mixed-compression intake at 'started' and 'unstarted' conditions.

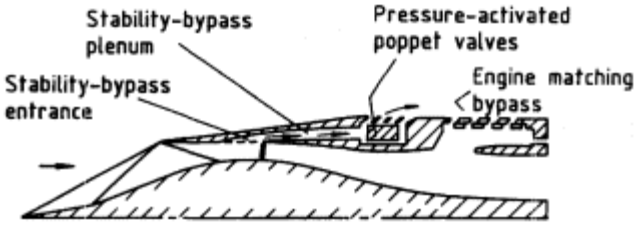

Figure 6.20
Pressure-activated poppet valves to prevent intake unstart (Mitchell and Sanders).

as much as 28% reduction in the main intake flow. The system is achieved at the expense of some increase in cowl drag, resulting from additional cowl frontal area needed to house the valves. Valve operation has to be checked dynamically as well as statically and it has been found (Mitchell *et al.*, 1974) that the valves need to react to a pressure rise in faster time than that of the original transient impulse.

References

Anderson, B.H. (1969) 'Characteristic design study of mixed-compression two-dimensional inlets with low-angle cowls for the Mach number range 2.7 to 1.8'. *NASA TN D5330.*

Evvard, J.C. and Blakey, J.W. (1956) 'The use of perforated inlets for efficient supersonic diffusers'. *NACA TN 3767.*

Kantrowitz, A. and Donaldson, C. du P. (1945) 'Preliminary investigation of supersonic diffusers'. *NACA WR L-713.*

Mitchell, G.A. and Sanders, B.W. (1974) 'Pressure activated stability by-pass control valves to increase the stable airflow range of a Mach *2.5* inlet with 40% internal contraction'. *NASA TM X2972.*

Obery, L.J. and Stitt, L.E. (1957) 'Performance of external internal compression inlets with abrupt internal turning at Mach numbers 3.0 to 2.0'. *NACA RM E57 H07a.*

Stitt, L.E. and Salmi, R.J. (1960) 'Performance of a Mach 3.0 external internal compression axisymmetric inlet at Mach numbers from 2.0 to 3.5'. *NACA TM X-145.*

Wasserbauer, J.F., Shaw, R.J. and Neumann, H.E. (1975) 'Design of a very-low-bleed Mach 2.5 mixed-compression inlet with 45% internal contraction'. *NASA TM X-3135.*

Chapter 7
Additional Loss in Supersonic Intakes

7.1
Introduction

The two previous chapters have concentrated on a primary problem in the design of supersonic intakes that of determining the shock wave system which is best suited to the task in hand. In all cases, however, it is necessary also to consider the question of additional losses of total pressure that may occur. Broadly these are in two categories which may or may not be linked, namely (1) boundary layer effects and (2) distortions of the idealised shock pattern. Boundary layers are always present in some degree, the minimum extent being the boundary layers of the subsonic diffuser, to which the discussion of Chapter 2 may be expected to apply. Towards the other extreme, boundary layer effects are often potentially severe enough to warrant the provision of diverters or bleeds: these are considered in detail in Chapter 8. The task of the present chapter is to bring additional losses of both categories (1) and (2) into a perspective which enables them to be estimated, at least empirically, in a given situation and thereby allows decisions on whether to accept the mechanical complications and aerodynamic penalties of bleed systems to be taken rationally.

7.2
Pitot Intake.

Owing to the complex geometries of most supersonic intakes, the terminal shock is rarely exactly plane and normal to the flow. A simple pitot intake is perhaps the only case for which the calculated normal shock loss corresponds accurately to the actual loss in total pressure through the intake shock. Additional loss in such a case is confined to the effects of boundary layer within the diffuser. Allowing for the possible presence of compressibility effects, the determining parameter for a given intake is the Mach number Mt at the throat behind the intake lip. If the additional loss is compared with the loss measured at subsonic speed for the same Mt,

experimental evidence (Fig. 7.1) shows the two to be for practical purposes identical.

7.3
Side Intake

The case of a side intake, that is to say an intake of normal shock type but adjacent to an aircraft surface such as a fuselage or wing, has been considered for modest supersonic Mach numbers in Chapter 3. There it is shown that an overall assessment of pressure recovery is obtained by adding to the theoretical normal shock loss and the frictional terms, Equation (3.4), an interaction loss of the form given by Equation (3.30), for the calculation of which empirical curves are provided.

For Mach numbers greater than about 1.3, the boundary layer from the adjacent surface separates under the influence of the shock and this results in a bifurcated shock being formed, as is discussed fully in Section 3.6. The shock loss is itself altered (normally decreased) by this change in formation. The change in shock loss is not calculated explicitly but is included in the overall assessment of Equation (3.30) along with the boundary layer effect, the latter being the main component.

If, however, a bleed or diverter separates the intake from the adjacent surface, the boundary layer will not pass into the intake but the shock bifurcation may still be present, affecting a proportion of the intake flow. A separate estimate may therefore be desired of the modification to normal shock recovery resulting from the bifurcation.

The proportion of entry streamtube affected is a function of the ratio of undisturbed boundary layer thickness to entry height; it will vary also with shock strength (i.e. with Mach number) and with the magnitude of pre-entry pressure rise, if any, behind the shock (i.e. with flow ratio). No

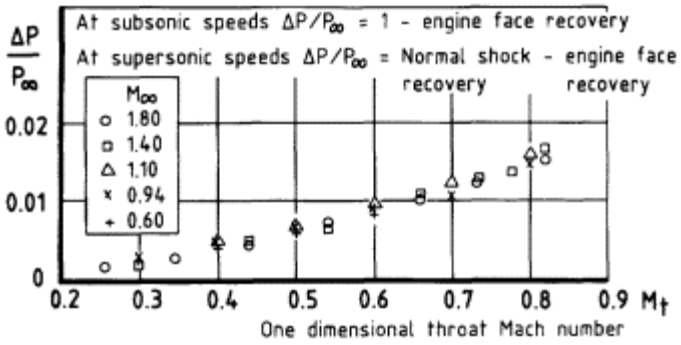

Figure 7.1
Subsonic diffuser loss for isolated axisymmetric intake.

systematic experimental evidence exists to quantify the effects of these parameters. It could be obtained by measurement of total pressure at the throat for a sufficient number of cases but it has not been usual in the past to measure throat pressure recovery. An indication of magnitude of the change from normal shock recovery can, however, be obtained by an indirect, iterative approach, using the assumption, on the basis of Fig. 7.1, that the internal duct loss is the same function of throat Mach number as for subsonic free stream conditions. An initial value of throat Mach number is derived from the flow continuity relationship (suffix 't' relates to throat):

$$\left(\frac{A}{A^*}\right)_t = \frac{P_t}{P_\infty} \cdot \left(\frac{A}{A^*_\infty}\right) \cdot \frac{A_t}{A_c} \cdot \frac{A_c}{A_\infty} \qquad (7.1)$$

corresponding to normal shock pressure at the throat. Knowing $(A/A^*)t$, Mt is determined. The duct loss corresponding to this value of Mt, determined from experiment or calculation *at subsonic free stream speed*, is now added back to a measured pressure recovery at engine face position to obtain a revised value for throat pressure recovery. This is substituted in Equation (7.1) to give a new value of Mt and the procedure is repeated until successive iterations yield the same value of Mt. An example is shown in Fig. 7.2, where the change to normal shock recovery is plotted as a function of Mt for each of two values of boundary layer thickness ratio, at free stream Mach numbers 1.40 and 1.81. It is seen that changes of from 2% to 6% are involved.

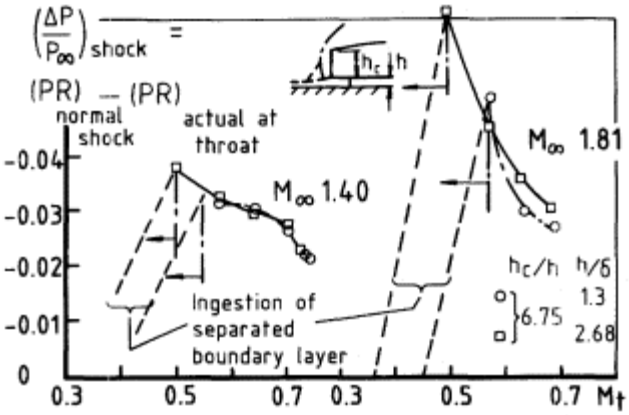

Figure 7.2
Change in shock recovery relative to
normal-shock value due to shock bifucation.

7.4
External Compression Intakes:
Adaptation of Interaction Formula

For external compression intakes generally, one approach to the calculation of additional loss is to adapt the interaction loss formula of Equation (3.30). A boundary layer is of necessity produced on the compression forebody and this takes the place of, or in some cases may be additional to, an aircraft surface boundary layer as postulated in Chapter 3. Free-stream conditions (Mach number and boundary layer) in the formula are replaced by those at the end of the oblique shock or isentropic compression and the interaction loss calculated is that emanating from the terminal normal shock: since this is always at low supersonic Mach number and conditions for application of the formula are effectively reproduced. Estimation of the 'initial' boundary layer condition in these circumstances is necessarily only approximate. In default of direct evidence it is usual to estimate the parameter *A*q (Equation (3.30)) on the basis of a fully turbulent layer over the wetted surface of the forebody and to neglect the effect of interactions at the oblique shocks (or in the isentropic compressive field) on the grounds that each of these is countered by a 'bridging' effect of the expanding forebody. It is recalled that the *A*q term is responsible for only about half the total interaction loss.

The substitutions involved in adapting the formula at Equation (3.30) are illustrated in Fig. 7.3 and are as follows:

Mach number *M*n in place of *M*¥;

Entry area *A*i in place of *A*c;

Streamtube area *A*n in place of *A*¥ (if the intake is at maximum flow, then *A*n = *A*i);

Representative duct area (at half length) is *A*h (not *A*H).

In Fig. 7.4 are shown three examples of comparisons between measured overall pressure recovery and estimated shock recovery, calculated by the methods of Chapter 5. Another and similar example is at Fig. 5.28. We see that the additional loss in such cases amounts to between 3% and 10% of total pressure, increasing generally as free stream Mach number increases.

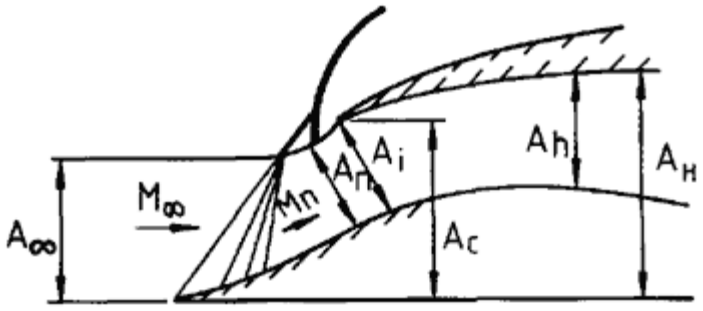

Figure 7.3
Definitions used in interaction-loss formula when
applied to external-compression supersonic intake.

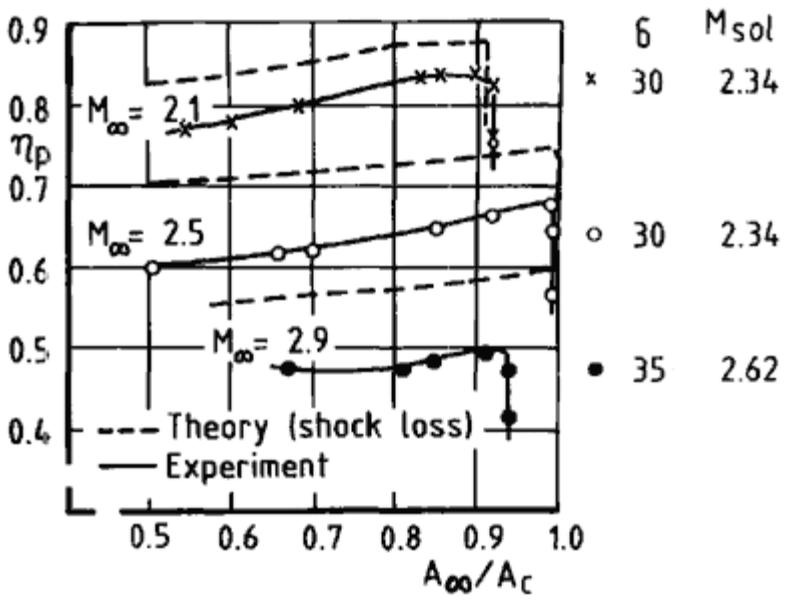

Figure 7.4
Additional loss of three conical-forebody intakes.

Applying the interaction loss formula, adapted as described, to the case for *M*¥ = 2.5 in Fig. 7.4 yields estimates 4% at flow ratio 1.0 and 6% at flow ratio 0.7. The friction terms in the total loss formula at Equation (3.29) account for a further 1%, leaving 1 1/2% to 2% loss unexplained in this particular case.

The chief deficiency of the interaction loss formula, adapted in this way to the environment of external compression intakes, is that it does not take into account 'cornering losses', i.e. any detailed changes occurring in the vicinity of the entry associated with restoring the flow to an axial direction. Mostly these come into the second category of Section 7.1, i.e. loss by distortion of the idealised shock pattern. Examination of effects in this category is important, both as an adjunct to the foregoing considerations and also in its own right, since in certain cases these can be more significant than the boundary layer losses. To such effects, therefore, we now turn.

7.5
Empirical Analysis of 'Cornering Losses' for Axisymmetric Intakes

It is usual, as we have seen in Chapter 5 for example, to calculate shock recovery in terms of angles of the compression surfaces. However, it can equally well be expressed as a function of the supersonic contraction ratio, i.e. the ratio of free streamtube area *A*¥ to the net flow area, *A*i, at entry, where it is assumed the normal shock is located. For a conical forebody intake and with the notation of Fig. 7.5 we have

$$\frac{A_\infty}{A_i} = \frac{\frac{r_\infty^2}{r_c^2}}{\left(1 - \frac{r_b^2}{r_c^2}\right) \sec\left(\frac{\eta_i + \delta}{2}\right)} \qquad (7.2)$$

where

$$\frac{r_b}{r_c} = \frac{\tan\delta \tan\frac{(\eta_i+\delta)}{2} + \frac{\tan\delta}{\tan\theta}}{1 + \tan\delta \tan\frac{(\eta_i+\delta)}{2}} \qquad (7.3)$$

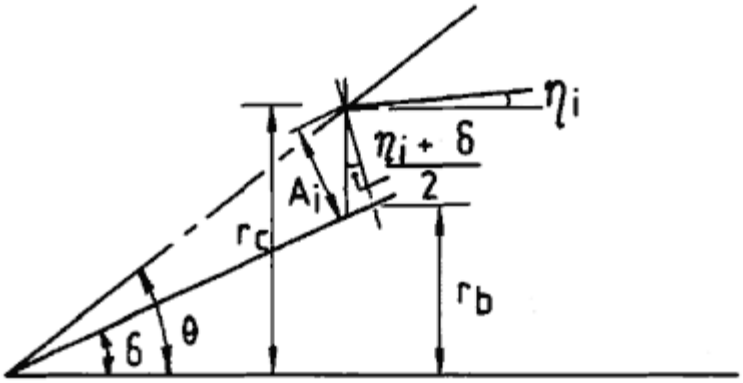

Figure 7.5
Notation for calculation of Ai.

Figure 7.6 shows that for a single cone forebody the variation of shock recovery with *A*¥/*A*i is practically linear except close to the maximum value. The characteristics may be compared with those of Fig. 5.7 which uses d as the independent variable. Any reduction of *A*¥/*A*i occurring in practice results in a reduction of shock recovery. If, for example, there is pre-entry curvature of the forebody, increasing the value of *A*i, *A*¥/*A*i is reduced and because the flow accelerates on the curved portion, Mach number of the terminal shock is increased locally, leading to a reduction in shock recovery.

It is a matter of experimental observation that two other geometrical features which affect pressure recovery are the cowl undersurface angle hi

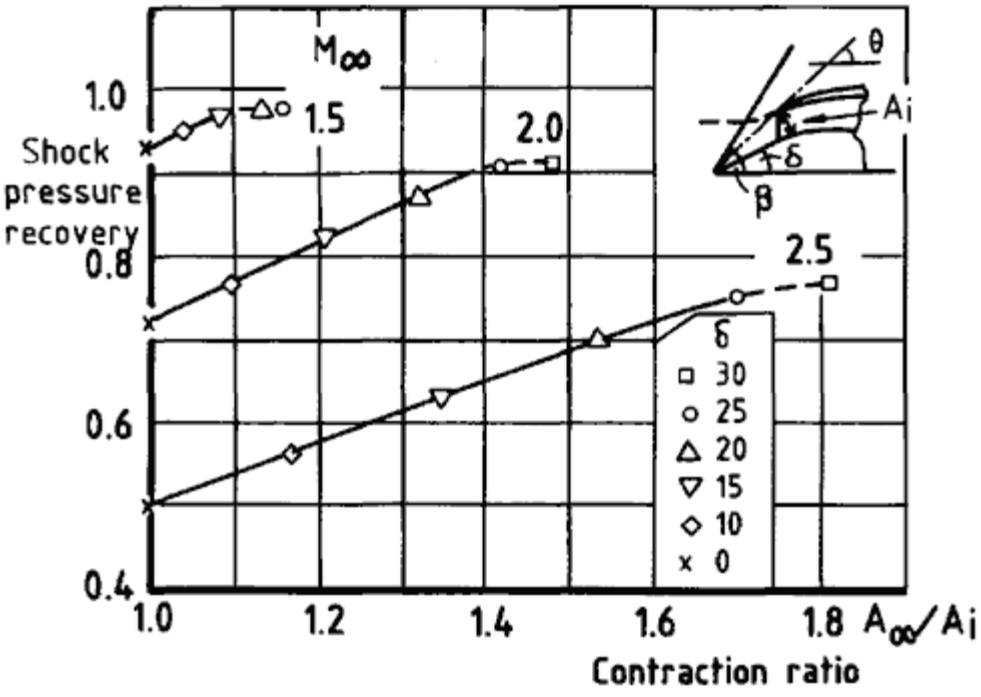

Figure 7.6
Dependence of shock pressure recovery on
contraction ratio (calculated for b = q).

(Fig. 7.5) and any internal contraction immediately following the entry, say to a minimum or throat area *A*t, smaller than *A*i. Internal contraction is beneficial provided it does not exceed the limiting value for retaining an attached shock at entry, which occurs when the subsonic flow behind the shock just achieves Mach 1 at the throat. The benefit comes from the favourable pressure gradient imposed on the boundary layer by the accelerating flow, and also, if the contraction is achieved by extending the conical forebody slope into the duct, from the fact that the forebody shoulder is then further removed from the foot of the shock. As regards cowl undersurface angle, if this is decreased for a given amount of internal contraction, the flow has to turn more rapidly at the shoulder and this is detrimental to pressure recovery.

The internal contraction effect, taken together with the basic dependence of pressure recovery on supersonic contraction ratio, suggests that an *overall contraction ratio*, *A*¥/*A*t, could provide a basis for empirical correlation. This indeed proves to be the case, as tests by Goldsmith (1962), summarised in Fig. 7.7, have shown. The elements of Fig. 7.7 are:

(a) data are presented for free-stream Mach numbers ranging from 1.5 to 2.9;

(b) for each Mach number, a horizontal line indicates the level of shock recovery for the idealised shock system (i.e. no additional loss);

(c) vertical lines indicate ranges of pre-entry expansion (from change in slope of the compression surface) and internal contraction (taken from zero to its limit as defined above);

(d) data are collected for two values of the cone angle d and a range of values of initial cowl undersurface angle hi;

(e) dotted lines represent results for the extreme case of a cylindrical cowl (i.e. hi = 0) calculated by an inviscid analysis described in the next section.

In the presentation of data the effect of variation in hi is expressed by modifying the pressure recovery by a factor cos hi, except for cases where the cone surface Mach number is lower than 1.3, when it is found that the scatter of results is reduced if this 'correction' is not applied. Also one parameter not covered in detail is the form of the subsonic diffuser. An indication is given by one set of results (for *M*¥ = 2.5) that if the initial rate of diffusion is significantly reduced, pressure recovery can be increased by about 2%. This is consistent with the findings of the earlier analysis on interaction loss (Chapter 3) and indeed the generalised results presented in Fig. 7.7 could if required be corrected to particular rates of subsonic diffusion by use of Equation (3.30).

With these provisos the correlations given in Fig. 7.7 effectively collapse

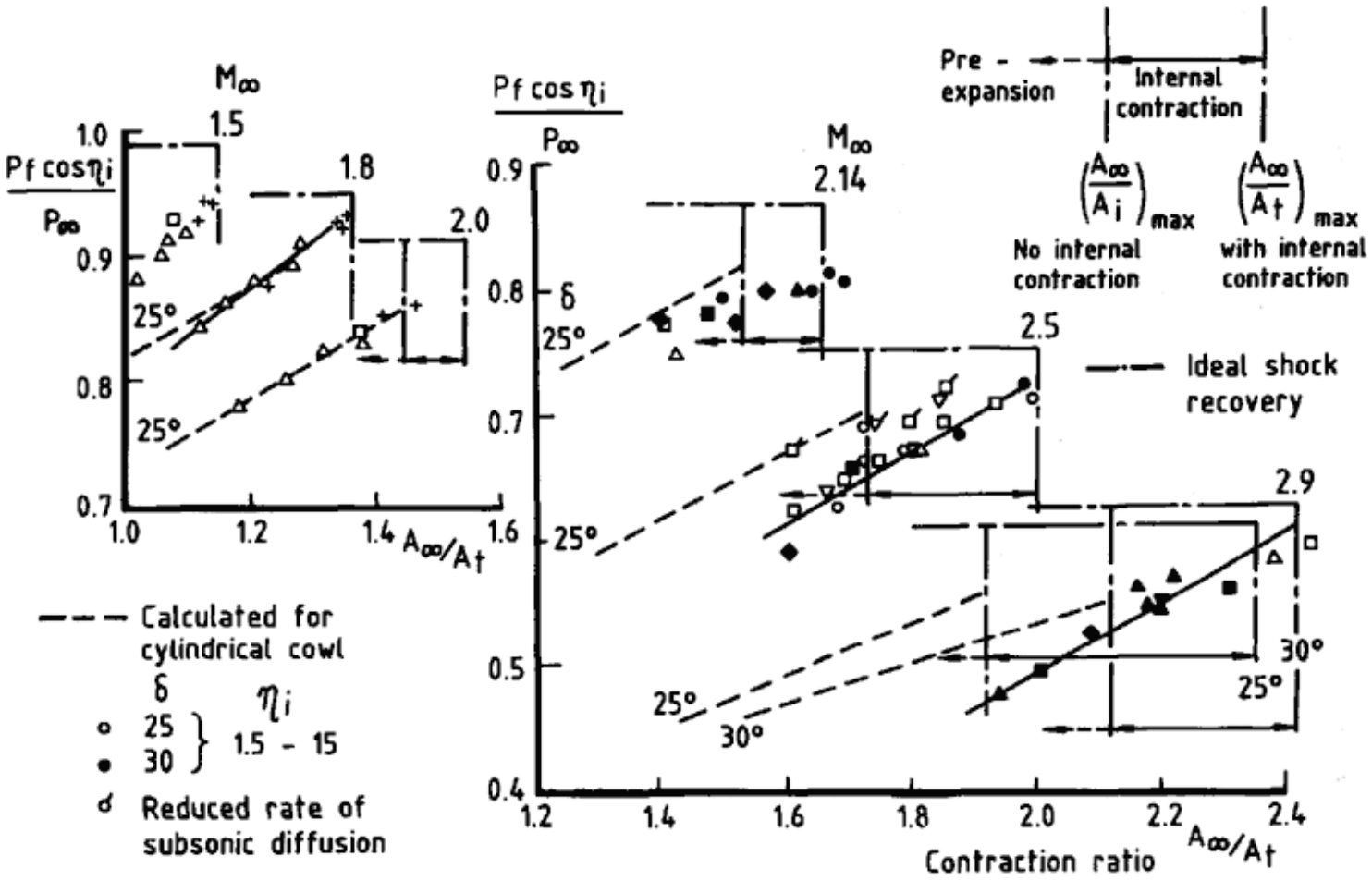

Figure 7.7
Correlation of pressure recovery with overall contraction ratio for conical-forebody intakes.

results for all cone angles, internal cowl angles and internal contraction ratios and thus provide a reasonably satisfactory method for prediction of the pressure recovery of axisymmetric intakes generally. Because of the importance of flow cornering effects for this category of supersonic intake, the method is probably more suitable for practical use than that of Section 7.4.

7.6
Inviscid Theory for Special Case of Cylindrical Cowl

For the case of a cylindrical cowl, a continuity momentum analysis due to Meyer (1957) can be used to make an inviscid calculation of the effect of flow turning into the axial direction at the cowl lip. The effect of pre-entry expansion of the flow, arising from curving of the centrebody, can be included. Applying the momentum equation to the control surface ABCDEFA shown in Fig. 7.8 gives

$$\rho_2 V_2^2 A_2 + p_2 A_2 - \rho_\infty V_\infty^2 A_\infty - p_\infty A_\infty + p_{\text{cone}} A_{\text{cone}} = 0 \qquad (7.4)$$

where *p*cone and *A*cone are the surface pressure and surface area of the conical forebody. This may be written in the form

$$2\,\frac{q_2}{P_2}\cdot\frac{P_2}{P_\infty}\cdot\frac{P_\infty}{q_\infty}\,A_2+\frac{p_2}{P_2}\cdot\frac{P_2}{P_\infty}\cdot\frac{P_\infty}{q_\infty}\,A_2-2A_\infty$$

$$-\frac{p_\infty}{q_\infty}\,A_\infty+\frac{p_{\text{cone}}}{q_\infty}\cdot A_{\text{cone}}=0$$

from which

$$\frac{P_2}{P_\infty}=\frac{A_\infty\left(2+\frac{p_\infty}{q_\infty}\right)-\frac{p_{\text{cone}}}{q_\infty}\,A_{\text{cone}}}{A_2\,\frac{P_\infty}{q_\infty}\left(\frac{2q_2}{P_2}+\frac{p_2}{P_2}\right)}\qquad(7.5)$$

The equation of continuity may be written

$$\frac{P_2}{P_\infty}=\frac{A_\infty{}^*}{A_\infty}\cdot\frac{A_2}{A_2{}^*}\cdot\frac{A_\infty}{A_2}\qquad(7.6)$$

and equating (7.5) and (7.6) gives

$$\frac{A_2}{A_2{}^*}\left(\frac{2q_2}{P_2}+\frac{p_2}{P_2}\right)=\frac{q_\infty}{P_\infty}\cdot\frac{A_\infty}{A_\infty{}^*}\left(2+\frac{p_\infty}{q_\infty}-\frac{p_{\text{cone}}}{q_\infty}\cdot\frac{A_{\text{cone}}}{A_\infty}\right)\qquad(7.7)$$

The left-hand side of Equation (7.7) can be evaluated for a range of values of *M*2 and the right-hand side is a function of intake geometry and free-stream Mach number. Thus the pressure recovery *P*2/*P*¥ of a uniform stream at the end of a constant area throat *A*2, having the same mass flow and momentum as the actual non-uniform intake flow, can be evaluated. It

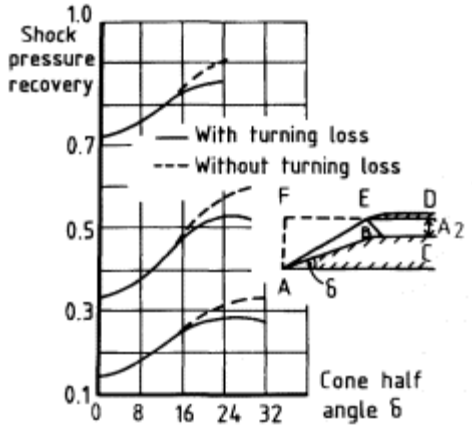

Figure 7.8
Calculated shock pressure recovery with and without turning loss for conical-forebody intakes with cylindrical cowl.

should be noted that the form of the intake shock system is not specifically defined. The only stipulation of Equation (7.7) is that the cone surface is acted on everywhere by the theoretical cone surface pressure and this is invalidated if the shock wave from the cowl lip impinges on the cone surface.

Values of pressure recovery for the cylindrical cowl (hi = 0) have been calculated from Equations (7.6) and (7.7) for the value of *A*¥/*A*i corresponding to no internal contraction and also for a range of values of *A*i as the forebody diameter is reduced and flow expansion takes place upstream of the normal shock. Curves of these values as functions of *A*¥/*A*t are included in the correlations of Fig. 7.7. Agreement with the empirical curves is good up to Mach 2.14 but for higher Mach numbers it is apparent that viscous effects are increasingly important and the inviscid method underestimates the losses. Additional loss allowance on some such basis as that of Section 7.4 should therefore be made.

The variation of recovery with cone angle and Mach number for a cylindrical cowl with no pre-entry expansion is shown in Fig. 7.8.

7.7
Situation with Two-Dimensional Intakes.

The same approach of relating shock recovery to contraction ratio *A*¥/*A*i can be used for rectangular intakes. Fig. 7.9 shows a plot on this basis for single and double wedge compression surfaces for which, assuming that hi is equal to d1 or (d1 + d 2) as the case may be, the contraction ratio is straightforwardly expressible in terms of the geometrical parameters. As with conical intakes, the variation of recovery with *A*¥/*A*i is almost linear up to near maximum recovery. A similar linear variation of shock recovery is obtained if the wedge shock position is varied within the cowl lip or if there are varying amounts of pre-entry expansion (Fig. 7.10).

Rectangular intakes differ from axisymmetric intakes in that with the former, unless the shock system is fully contained by sidewalls at the ends of the compression surface, there is a loss of compression owing to sideways spillage of the flow. The effect of loss of this flow to the intake can be evaluated approximately by use of the continuity relation. For a given geometric arrangement the amount of flow spilled sideways is calculated using the *G* parameter given in Chapter 5, which correlates sidewall spillage with effective spillage area and pressure difference. The continuity relation between free stream flow and flow in the entry plane can be written as

$$\frac{A_1}{A_1{}^*} = \frac{\frac{P_1}{P_\infty} \cdot \frac{A_\infty}{A_\infty{}^*}}{\frac{A_\infty}{A_c} \cdot \frac{A_c}{A_1}} \qquad (7.8)$$

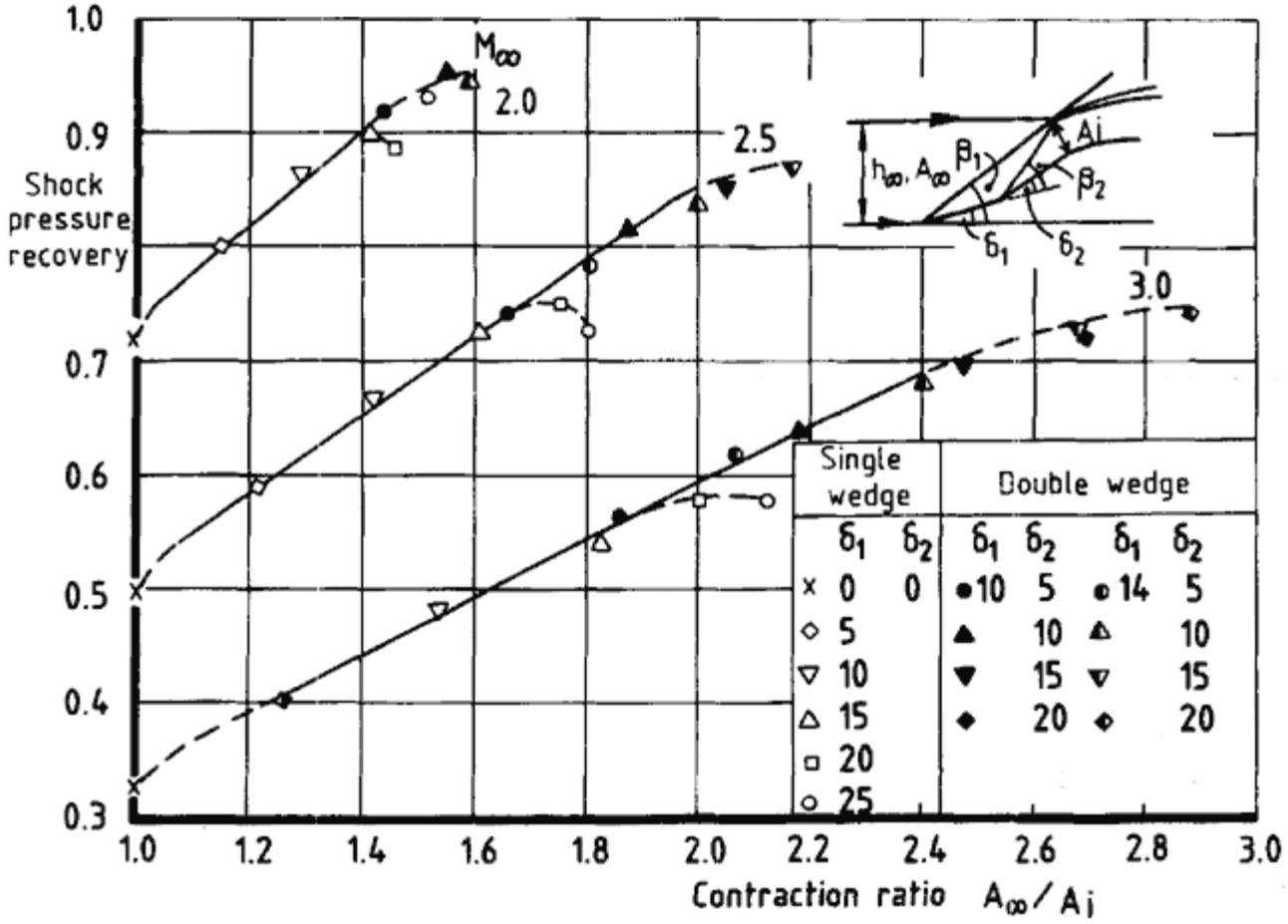

Figure 7.9
Variation of shock recovery for single and double wedge intakes.

where *A*¥/*A*c is actual flow ratio (as measured inside the intake) and *P*1/*P*¥ is the theoretical shock recovery associated with the oblique shocks only. From the value *A*1/*A*1* thus calculated an entry Mach number *M*1 is derived which will be higher than the theoretical value behind the oblique shocks in two-dimensional flow; this leads to a greater pressure loss through the normal shock and thereby provides a correction to the theoretical shock recovery for the effect of sideways spillage.

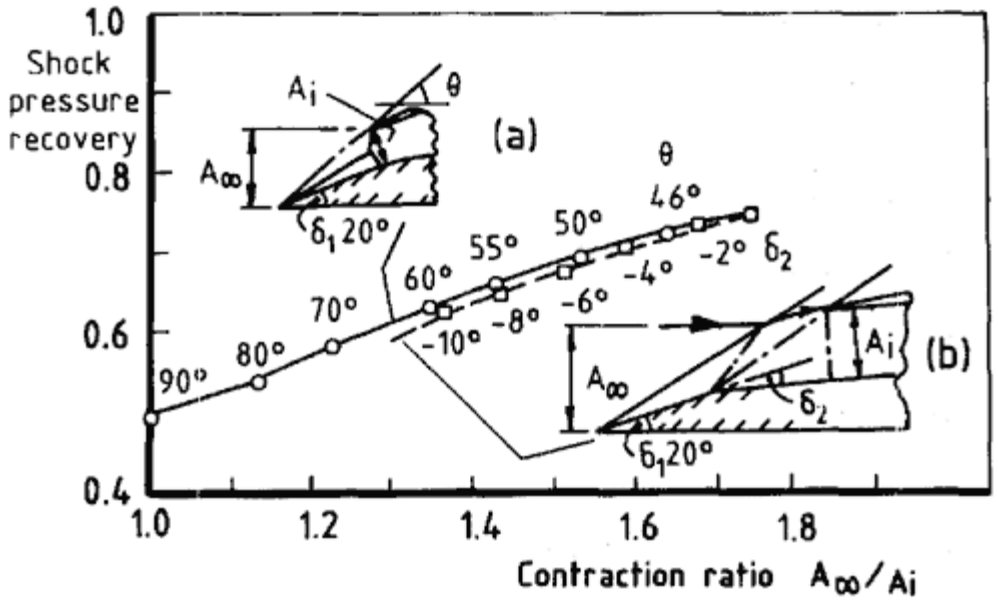

Figure 7.10
Dependence of shock pressure recovery on contraction ratio for single-wedge intakes with (a) changing lip position angle and (b) changing pre-entry flow expansion angle.

Calculated shock recovery and measured overall recovery are compared in Fig. 7.11 for a series of double wedge intakes in which both the second wedge angle and the height of sidewalls have been varied. Only the comparative trends are of interest: it is seen that these are similar except at the highest Mach number (M¥ = 2.46). Here it seems likely that the reduction in surface area with the smaller sidewall has more than compensated for the increase in shock loss from sideways spillage.

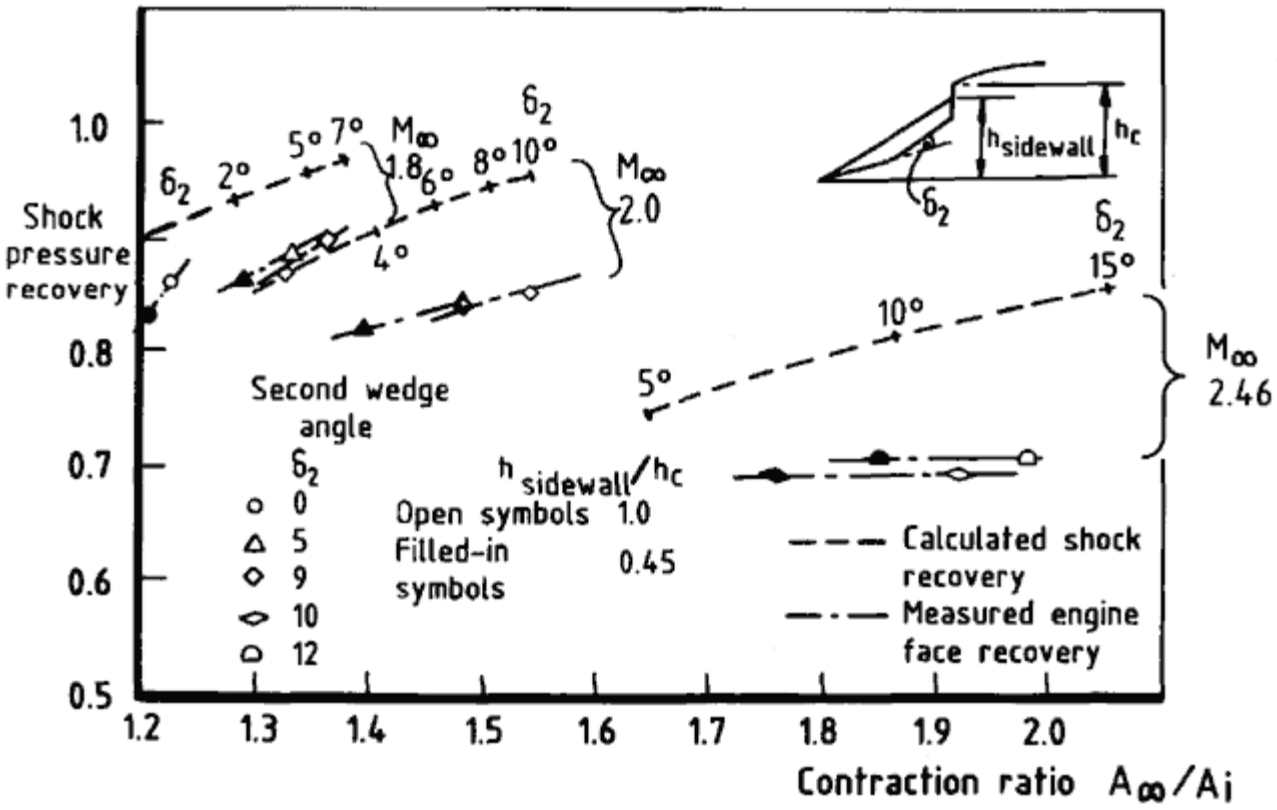

Figure 7.11
Comparison of calculated shock recovery and measured engine-face recovery for double-wedge intakes.

Meyer's continuity and momentum analysis can be applied to the two-dimensional corner flow which results with a zero-angle cowl. Referring to Fig. 7.12, the flow approaching the entry station EB is now uniform and a suitable control surface for application of the momentum theorem is BCDEB. The lip overhang angle f is a measure of the contraction ratio $A1/A2$:

$$\frac{A_1}{A_2} = \frac{\cos(\delta - \phi)}{\cos \phi} \qquad (7.9)$$

The momentum equation is

$$\rho_1 V_1 A_1 V_1 \cos \delta + p_1(\mathrm{EB}) \cos \phi - p_2 A_2 - \rho_2 V_2^2 A_2 = 0 \qquad (7.10)$$

whence

$$p_2 + \rho_2 V_2^2 = p_1 + \rho V_1^2 - \rho_1 V_1^2 \left(1 - \frac{\cos \delta \cos (\delta - \phi)}{\cos \phi}\right)$$

from which is obtained

$$\frac{P_2}{P_1} = \frac{\frac{p_1}{P_1} + \frac{2q_1}{P_1}\,\frac{\cos\delta\cos(\delta-\phi)}{\cos\phi}}{\frac{p_2}{P_2} + \frac{2q_2}{P_2}} \qquad (7.11)$$

Then by continuity,

$$\frac{P_2}{P_1} = \frac{A_1^*}{A_1}\cdot\frac{A_2}{A_2^*}\,\frac{\cos\phi}{\cos(\delta-\phi)} \qquad (7.12)$$

and equating (7.11) and (7.12) gives

$$\left(\frac{p_2}{P_2} + \frac{2q_2}{P_2}\right)\frac{A_2}{A_2^*} = \frac{A_1^*}{A_1}\,\frac{\cos\phi}{\cos(\delta-\phi)} \times \left(\frac{p_1}{P_1} + \frac{2q_1}{P_1}\,\frac{\cos\delta\cos(\delta-\phi)}{\cos\phi}\right) \qquad (7.13)$$

from which $M2$ can be evaluated and hence $P2/P1$. For f = d/2 there is no internal contraction. In Fig. 7.12, $P2/P1$ has been calculated for two-dimensional turning from the compression surface angle d to the horizontal: the diagram at (a) gives the results for no internal contraction and that at (b) those for maximum internal contraction (i.e. $M2 = 1$).

Generally speaking, rectangular intakes have not received the same systematic study of internal contraction and cowl shape as have axisymmetric intakes. An inviscid analysis is less appropriate to the rectangular intake because viscous losses are likely to be a greater proportion of the total loss. Fig. 7.13 shows differences in pre-entry wetted area, As, as a proportion of net inlet area Ai, between some rectangular, axisymmetric and half-axisymmetric external compression intakes, having the same shock recovery and the same Mach number for shock on lip. The higher values of the rectangular intakes accord with experimental measurements showing lower engine-face pressure recovery than for the axisymmetric forms.

Pursuing this aspect further and more explicitly, an analysis of losses for a double-wedge intake is given in Fig. 7.14: this intake had negligible side-ways spillage and no pre-entry expansion, so that actual shock losses were a close approximation to the theoretical. To the latter has been added the viscous losses, (a) frictional terms calculated by Equation (3.4) and (b) an interaction loss estimated as described earlier in the present chapter (Section 7.4). We see that this brings the total estimate close to the experimental result but there is a residual loss amounting to 2% 4% of total pressure. The latter can be attributed to the effect of flow turning in the region of the entry plane. A rough correlation of the turning loss (for the particular

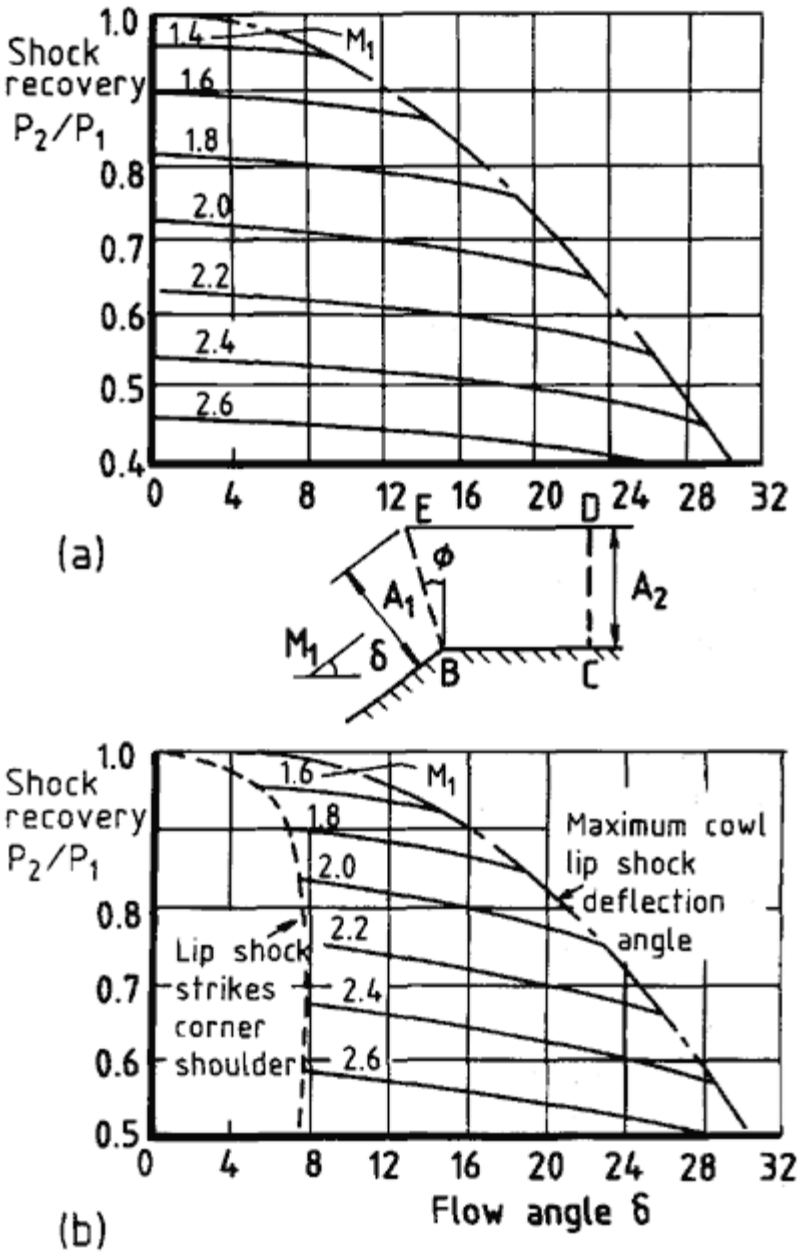

Figure 7.12
Calculated pressure recovery for two-dimensional corners
(a) without internal contraction (b) with internal contraction.

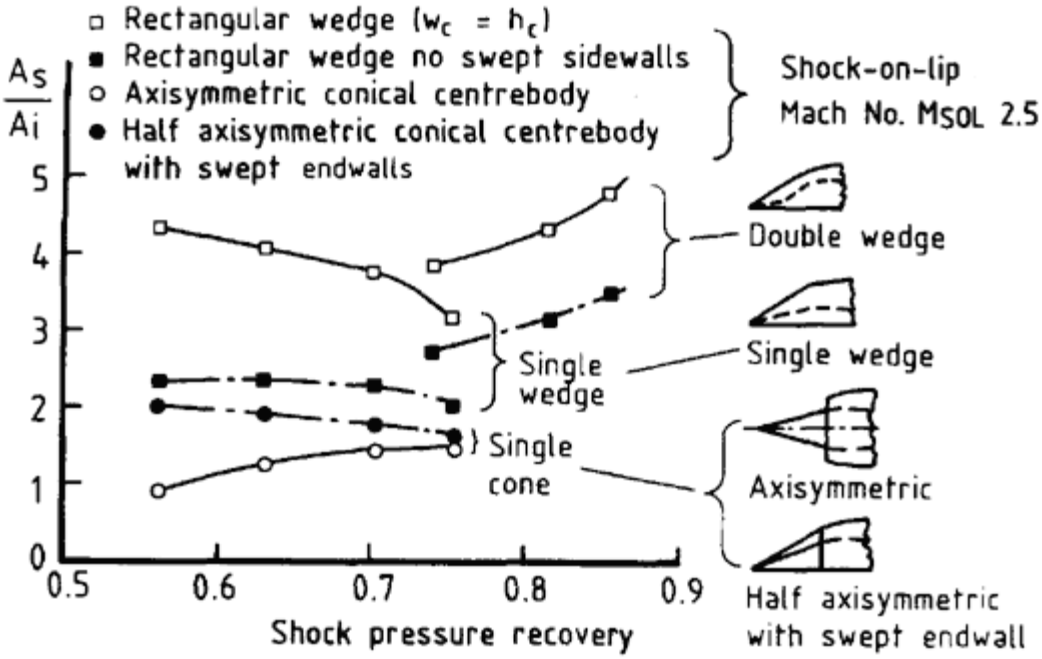

Figure 7.13
Differences in ratio of approach surface area
to intake entry area for various intake designs.

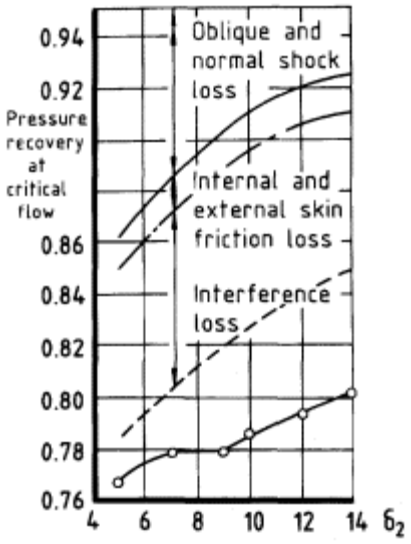

Figure 7.14
Analysis of losses for a
double-wedge intake.

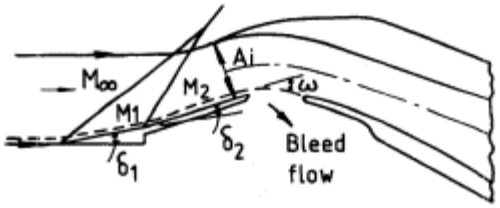

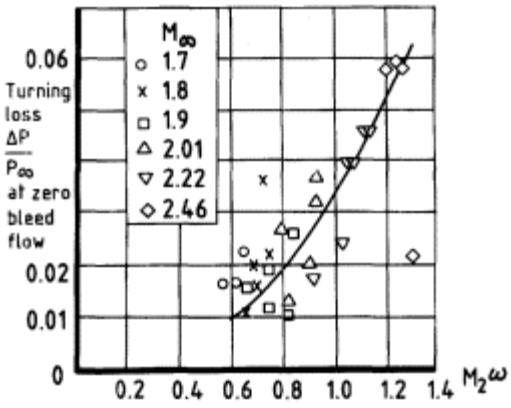

Figure 7.15
Correlation of turning loss
for double-wedge intakes.

geometry) is shown in Fig. 7.15 in terms of turning angle w (see sketch) and Mach number *M*2 before the normal shock.

For most practical supersonic intakes of rectangular form, the high potential level of viscous losses makes the addition of a boundary layer bleed system (Chapter 8) necessary. Generally this is not the case with fully axisymmetric intakes and indeed bleeds are not often adopted, partly because of the mechanical difficulty of ducting the bleed air away from the central compession body.

References

Goldsmith, E.L. (1962) 'The effect of internal contraction, initial rate of subsonic diffusion and cowl and centrebody shape on the pressure recovery of a conical centrebody intake at supersonic speeds. *ARC, R & M 3204.*

Goldsmith, E.L. and Grigg, C.F. (1953) 'The estimation of shock pressure recovery and external drag of conical centrebody intakes at supersonic speeds'. *ARC Reports & Memoranda No. 3035.*

Meyer, R.C. (1957) 'Flow turning losses associated with zero drag external compression supersonic inlets'. *NACA, TN 4096.*

Chapter 8
Boundary Layer Bleeds and Diverters

8.1
Brief Description

The adverse effects of external boundary layer on intake pressure recovery have been described in Chapters 2 (subsonic intakes), 3 (transonic effects) and 7 (supersonic intakes). The nub of the problem, as we have seen, is the interaction of boundary layer with the pre-entry pressure rise which is incurred in the process of producing a relative retardation of airspeed from the flight velocity towards that required at inlet to the engine. Broadly speaking the severity of the problem is greater the higher the flight speed and the presence of shock waves at supersonic speeds adds a special dimension to it. If the boundary layer separates or comes close to separation, the effects are particularly adverse and generally not restricted to a lowering of mean pressure recovery: other adverse features include total-pressure distortion (Chapter 11) and flow instability (Chapters 2 and 10).

Removing boundary layer at some stage from the intake provides an escape from, or easement of, the difficulties. This is done by means of bleeds or diverters. The term 'bleed' denotes a separate duct which leads away the boundary layer. The term 'diverter' implies that the intake stands off from a particular surface, allowing the boundary layer on that surface to escape down the intermediate channel. In either case the boundary layer removed from the intake usually becomes a part of the aircraft system, that is to say it represents an additional item in the aircraft drag, which needs to be assessed and set against the improvement in engine net thrust. An alternative procedure which can be adopted with a bleed is to return the boundary layer to the engine system in the form of secondary flow in the propulsive nozzle. In this case a special accounting of engine thrust is required.

No clear dividing line can be set between those intakes which require a bleed or diverter and those which do not. In broad terms, subsonic intakes usually do not while supersonic intakes usually do but the opposites can well apply. An intake in the root leading edge of a swept-wing, subsonic aircraft might benefit from having a step diverter on the fuselage side (see illustration in Fig. 8.1). With an external-compression supersonic intake for

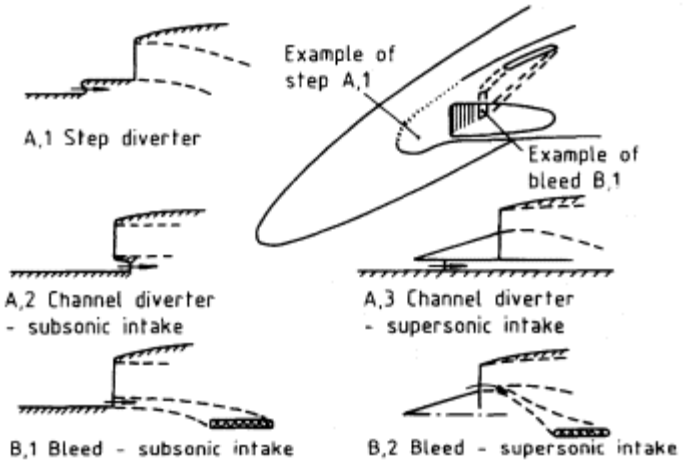

Figure 8.1
Common forms of bleed and diverter.

a Mach number below 2, a compression-surface bleed may not be essential and may be undesirable if disposal of the bleed air presents an awkward problem, as for example in an axisymmetric configuration.

Common forms of bleed and diverter are illustrated in Fig. 8.1. Diverters may be of the step type (A.1) or channel type (A.2, A.3). A step diverter is a useful form in the wing root of a subsonic aircraft, because the forward extension allows a good wing-root profile to be preserved. Step diverters are not recommended for supersonic aircraft, however, because fresh boundary layer initiated on the surface of the diverter may itself produce most of the interaction loss of the original longer boundary layer. Channel diverters are suitable for both subsonic and supersonic application, provided that a reasonably aerodynamic 'prow' shape can be obtained between the intake and the boundary-layer surface. The recommended width for step diverters is about one and a half times the thickness of the boundary layer, when this is undisturbed by the presence of the intake, and for channel diverters about one such boundary layer thickness.

Bleeds may be forward-facing (usually called 'ram' or 'ram scoop' bleeds), as illustrated in sketch B.1, or flush with the approach surface. A flush bleed must be located downstream of a substantial pressure rise in the flow (relative to free stream pressure) so that a pressure differential is available to operate the bleed. The recommended width of a ram bleed is one undisturbed boundary-layer thickness, though evidence shown later indicates that a smaller bleed will suffice if conditions are sufficiently well defined. A flush bleed should be at least as wide as a ram bleed; designed purely as a device to improve intake pressure recovery, this may be termed a 'narrow' flush bleed. By contrast, a 'wide' flush bleed may have additional advantages in off-design conditions this was shown to be the case with the

intake system for the Anglo-French Concorde aircraft. The type of flow obtained with a wide bleed is illustrated later in the present chapter and its particular advantage for matching of intake and engine flows is described further in Chapter 12.

With a ram bleed or a narrow flush bleed at subsonic speeds, the bleed duct should expand in area (say 30% or so) to make up for duct loss; in this way the whole, or effective whole, boundary layer is taken into the bleed. Bleed drag is calculated from the rate of change of momentum of the bleed flow taken to known exit conditions (Section 8.5). Diverter drag cannot be isolated in the same way since the flow associated with a diverter is not a controlled quantity. Also the definition of a datum configuration without the boundary layer control is more arbitrary with a diverter than with a bleed. At supersonic speeds, the wave drag of the prow of a diverter is a reasonably meaningful drag quantity (Section 8.6).

Two examples of bleed action illustrate the general situation. In Fig. 8.2 is shown the effect on shock formation and duct pressure behind a flat-plate boundary layer at Mach number 1.35. Without bleed, the boundary-layer separation and attendant lambda shock formation are clearly to be seen in the schlieren photograph. The static pressure rise is temporarily halted at

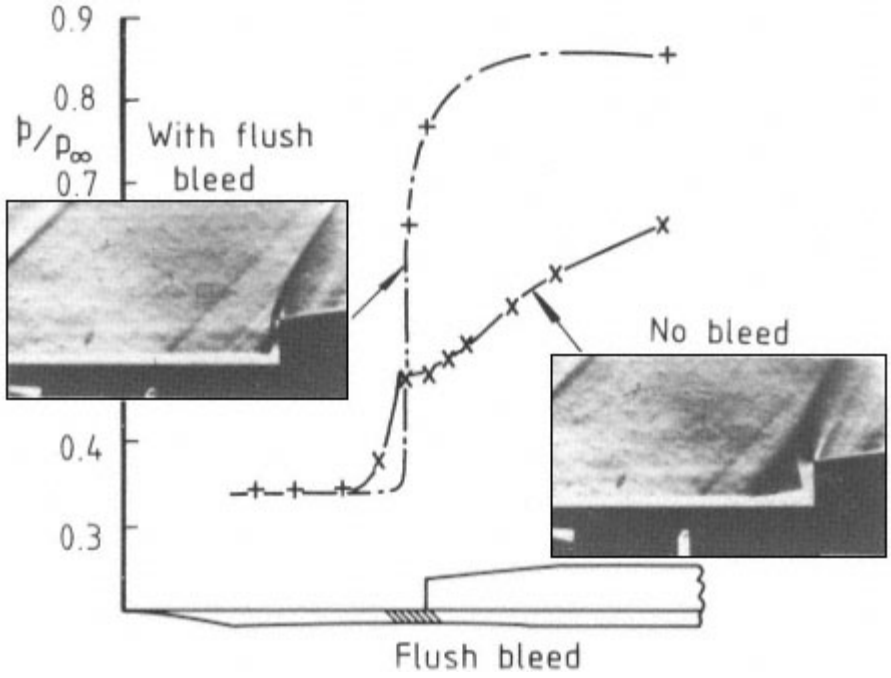

Figure 8.2
Pressure distribution with and without flush bleed for a normal-shock intake at *M*¥ 1.35.

the separation point and subsequently proceeds at a reduced rate a practical case of the classical shock and boundary-layer interaction pictured in Fig. 3.11. On total pressure, this flow leads to a large interaction loss, as has been described in Chapter 3. With bleed, however, flow separation is avoided and the intake shock is restored to normal, as the schlieren shows. Static pressure rise is that of a normal shock followed by duct diffusion, virtually identical to that which would occur with a duct free from external boundary layer.

In Fig. 8.3 is shown a comparison of efficiencies for ram and flush bleeds. With intake total-pressure loss expressed as the sum of four components (Equation 3.29), a measure of bleed efficiency is the extent to which the two components D*P*a (approach loss) and D*P*i (interaction loss) are removed by the bleed. Writing therefore *P*c(calc.) for the total-pressure recovery without bleed, calculated according to the methods of Chapter 3, and *P*c(meas.) for a measured result, the bleed efficiency is evaluated as

$$\eta_{\text{bleed}} = \frac{P_c(\text{meas.}) - P_c(\text{calc.})}{\Delta P_a + \Delta P_i} \qquad (8.1)$$

the component losses D*P*a and D*P*i as calculated in the determination of *P*c(calc.). In the diagram, bleed efficiency is plotted as a function of free-stream Mach number for each of the two bleed arrangements pictured. Flow ratio in the main intake is somewhat below 1.0. It is seen that the bleeds are equally efficient up to Mach 1.2 but at higher Mach numbers the efficiency of the flush bleed decreases markedly. This is because the normal

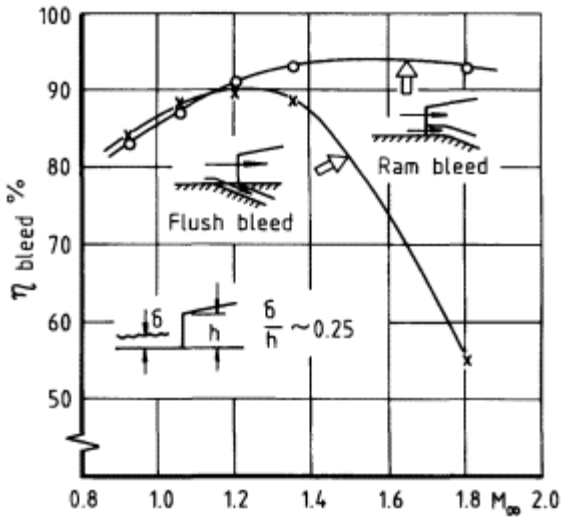

Figure 8.3
Comparative efficiencies of
particular ram and flush bleeds.

shock approaches very close to the entry as Mach number increases and therefore passes over the face of the bleed with the latter positioned as shown. A similar flush bleed positioned just inside the entry could remain efficient at all Mach numbers. Extra care would be needed, however, to ensure that the rise in pressure of the main duct flow (subsonic), which would accompany the removal of bleed flow, had no serious effect on the duct boundary layer. A similar caution should be applied to the ram-bleed situation as pictured.

The various considerations brought out in the foregoing examples apply in kind also to the important category of supersonic intakes with external compression. Bleed designs require to be developed carefully, having regard to particular requirements. Experience has shown, however, that with two-dimensional configurations, a flush slot at the shoulder of the compression surface, behind the position of the normal shock under design conditions, will generally provide a satisfactory form of bleed arrangement.

For intakes which include internal supersonic compression the problem of bleed provision is much more complex. Multiple shock and boundary-layer interactions occur, in varying forms; generally all internal surfaces of the duct need to be considered; and not least of the difficulties is that of collecting the bleed flow and leading it away from the intake. The development of very efficient mixed-compression intakes, of axisymmetric type with translating centre-bodies, was pursued in the USA during the nineteen sixties and early nineteen seventies. Design Mach numbers were generally in the range 3.0 to 3.5, at which level devising an efficient bleed system is probably the most important part of the design process for a low-drag, high-pressure-recovery intake. The bleed drag is often found to be the most significant component of the intake drag at cruise. Thus for the prototype Boeing supersonic-transport aircraft, the loss of range attributable to bleed drag was estimated to be 210 nautical miles. This figure has been given by Syberg and Koncsek (1973) in an account of bleed design technology. An example of the design process is described briefly in Section 8.4.2.

To follow this brief general account, some bleed and diverter situations are now described in more detail. The chapter ends with an account of the problems of determining bleed and diverter drag.

8.2
Parameters Relevant to Intake Performance

The quantitative effect on pressure recovery of removing boundary layer from an intake by means of a diverter or bleed depends on the mass flow of boundary layer in relation to free stream air being ingested, on the thickness of boundary layer in relation to entry height (a different quantity except for two-dimensional intakes) and on the state of the boundary layer,

in particular its proximity to separation. Nearly all published experimental measurements use a ratio of diverter or bleed height, *h*, to boundary layer thickness, d, for expressing the effect of boundary layer removal. This is satisfactory for a particular configuration but it has to be borne in mind that, as illustrated in Fig. 8.4, no simple parameter such as *h*/d, or *A*BL/*A*c which might also be considered, is adequate for comparing results for intakes differing either in cross-sectional shape or in height relative to the boundary-layer thickness.

Additional problems are involved in the representation of full-scale situations by scaled model experiments. A commonly adopted method is to test at model scale with the full scale value of *h*/d: since at the lower Reynolds number of the model test, d is proportionately greater than at full scale, the height of bleed or diverter has to be physically greater than the scaled value. With supersonic intakes, however, the size of a region of shock and boundary layer interaction (Chapter 3) is also proportional to boundary layer thickness, hence to maintain this in proportion requires the intake itself to be increased above the scaled value. An alternative to these two adjustments is for an initial non-representative bleed to be provided some distance ahead of the intake, to remove part of the boundary layer so that the residual layer has the correct scale thickness. Control of both thickness and profile by this method is obviously tricky.

No panacea can be offered to these difficulties; recognition of them, however, is important and can help to guard against the making of invalid comparisons or generalisations.

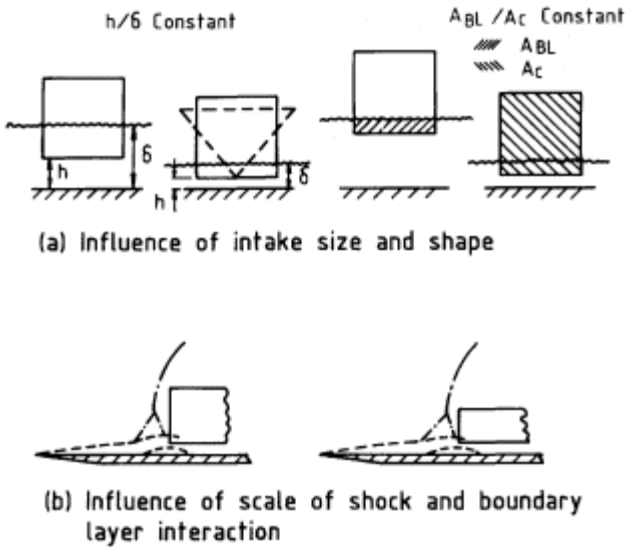

Figure 8.4
Problems of representation of bleed parameters.

8.3
Removal of Aircraft Boundary Layer.

8.3.1
Normal-Shock Intakes

The example at Fig. 8.3 shows that a ram scoop bleed in the entry plane of a normal-shock intake, adjacent to an aircraft surface, provides an efficient means of boundary-layer removal. Enhancement of the intake performance by this means is illustrated by some results of Frazer and Anderson (1953), shown in Fig. 8.5. Total-pressure loss additional to that of the normal shock is plotted as a function of *h*/d for each of three test Mach numbers. An additional loss amounting to 8% of total pressure without bleed is reduced by the bleed to less than 1%. At all three Mach numbers the optimum result is achieved when *h*/d is appreciably less than 1.0. These results are given for 0.9 flow ratio; generally it may be said that such improved performance will apply at full flow and over a limited range of flow ratio, this range decreasing with increasing Mach number, so that typical minimum values are 0.75 at Mach 1.3 and 0.9 at Mach 1.8. Below this minimum flow ratio, an oscillation of the flow (intake 'buzz', Chapter 10) is likely to occur.

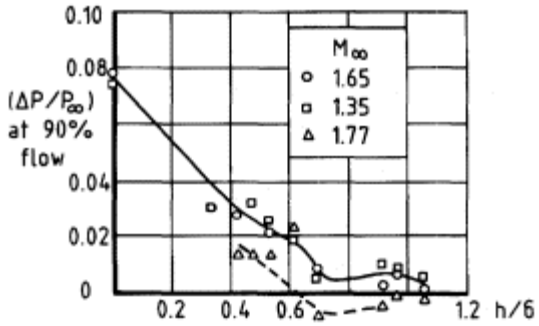

Figure 8.5
Extra-to-shock loss for semi-circular
normal-shock intake with ram scoop bleed.

A narrow flush bleed ahead of the entry, as in Fig. 8.3, will give similar results at moderate spillage, say 0.8 to 0.9 flow ratio, and probably a somewhat larger oscillation-free range but its performance at full flow or very low spillage, when the shock is at or close to the entry plane, is inferior to that of the ram bleed.

A diverter of adequate width gives the same order of improvement in intake performance as a ram bleed if the intake is at or near full flow. The actions of bleed and diverter differ, however, in relation to a situation involving boundary layer separation. Whereas a bleed restores the normal shock (Fig. 8.2), thereby removing the turbulent-mixing loss but at the same time sacrificing a beneficial effect of reduced shock loss from the bifurcated

system, with a diverter the bifurcated pattern is retained as the separated flow region passes outside the intake. A diverter can therefore give an intake efficiency higher than normal-shock level, at moderate spillage ratios. The effect was discussed in Chapters 3 and 7. A diverter is likely to be less effective than either type of bleed in postponing the onset of oscillation as flow ratio is reduced.

8.3.2
External-Compression Intakes

For external-compression supersonic intakes, the effect of being partly immersed in the boundary layer on an aircraft surface is largely influenced by the strengths and orientations of the shocks that impinge on the boundary layer before the flow enters the intake. Thus the effect is different for different configurations such as are pictured in Fig. 8.6. The presence or absence of a 'splitter plate', shown in (b) and (c), is influential. The 'scoop' intake (d) is a particular type of intake discussed in Chapter 14.

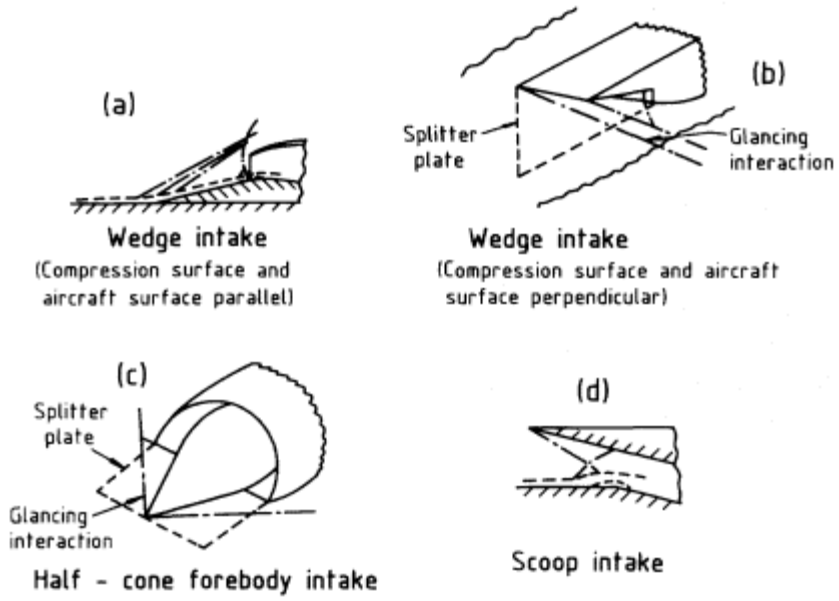

Figure 8.6
Shock and boundary layer interactions
for intakes with compression surfaces.

The fundamental aspects of interactions between a turbulent boundary layer and wedge or cone shocks have been studied extensively. Interactions relevant to intake situations such as those depicted have been examined particularly by Vas (1955), Kuehn (1961) and Roshko *et al.* (1963). Another such study, not involving an intake but aimed at understanding compres-

sion-surface behaviour in the presence of boundary layer, is that by Tanner and Gai (1967); in this a wedge with leading edge parallel to an adjacent surface (a situation relevant in orientation to the intakes of the Phantom or Concorde aircraft) was tested for various separation distances. Wedge and surface pressure distributions for different bleed flow rates and values of *h*/d are shown in Fig. 8.7. With the wedge on the surface, the upstream influence is quite marked, indicating a spreading of the shock and a decrease in pressure rise compared with inviscid-flow theory. At zero bleed flow, the effect of raising the wedge off the surface is to push the interaction region farther upstream but when bleed flow is applied, the upstream influence is much reduced and the wedge-surface pressure approximates to the value for inviscid flow.

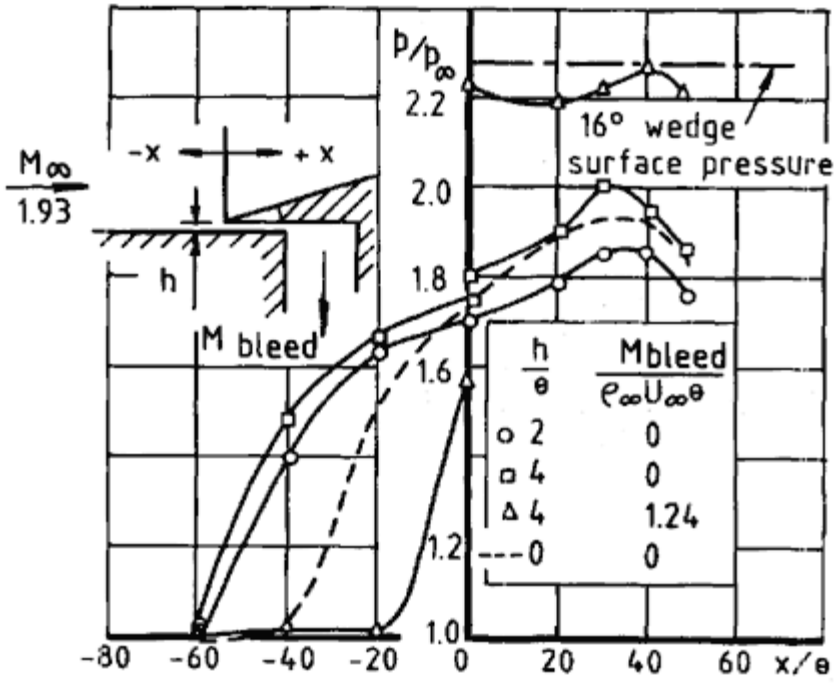

Figure 8.7
Pressure distribution on 16° wedge with ram scoop bleed.

For a half-cone intake (Fig. 8.8) in which only the cowl lip is distanced from the body surface, both conical and normal shock impinge on the body boundary layer and at flow ratios below unity large areas of separated flow are injected into the intake, as the results of Cook (1964) show. In these experiments it was found that results for intake pressure recovery and maximum flow did not correlate well with *h*/d when both *h* and d were varied. The relative quantity of boundary-layer air entering the intake is better represented in such a case by a factor (d *h*)/*h*c, where *h*c is a representative height for the main entry. In Cook's results this factor gave good correlations for maximum flow and pressure recovery through ranges of *h*, d and angle of yaw; with incidence variation a separate correlation was required for each incidence.

Results for different systems of boundary layer removal ahead of a half-cone side intake, assembled by Piercy and Johnson (1953), show the

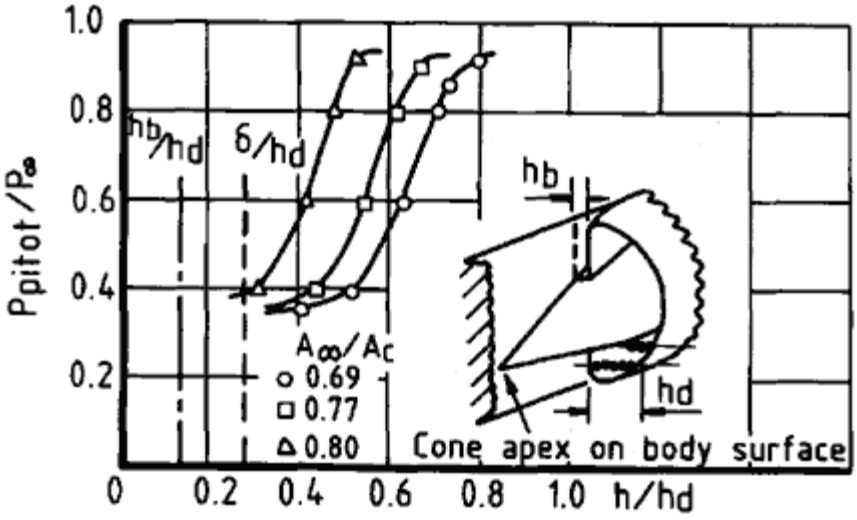

Figure 8.8
Pitot-pressure profile in entry plane of 25° half-cone intake mounted on a fuselage at a 5°, *M*¥ 1.95.

comparisons presented in Fig. 8.9. The use of a splitter plate, swept or unswept, is beneficial up to *h*/d = 0.9 to 1.1, which is where the optimum results lie. The cowl lip scoop, which is not unlike that of Fig. 8.8. seems to produce a large reduction of intake pressure loss at much higher values of *h*/d (1.3 and upwards), where however its cost in drag would be unnecessarily high.

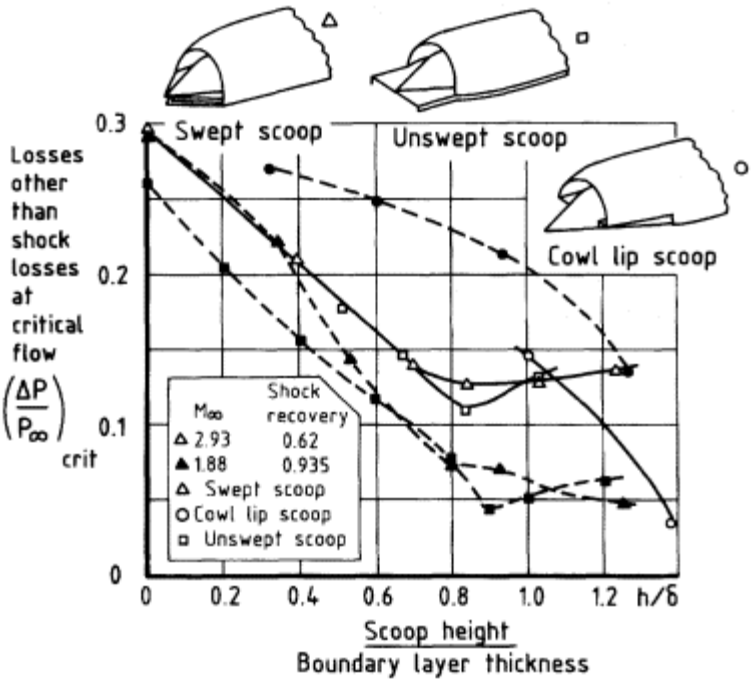

Figure 8.9
Influence of bleed form on extra-to-shock loss for half-conical-forebody intakes.

Typical results for channel-type diverters have been given by Johnson and Piercy (1954) for half-cone intakes and by Campbell (1957) for a wedge intake. The reduction of total-pressure loss as a function of *h*/d is shown for the latter case in Fig. 8.10. It is advantageous for the 'prow' of the diverter to be located some distance downstream of the compression-surface apex, as can be seen in the case shown.

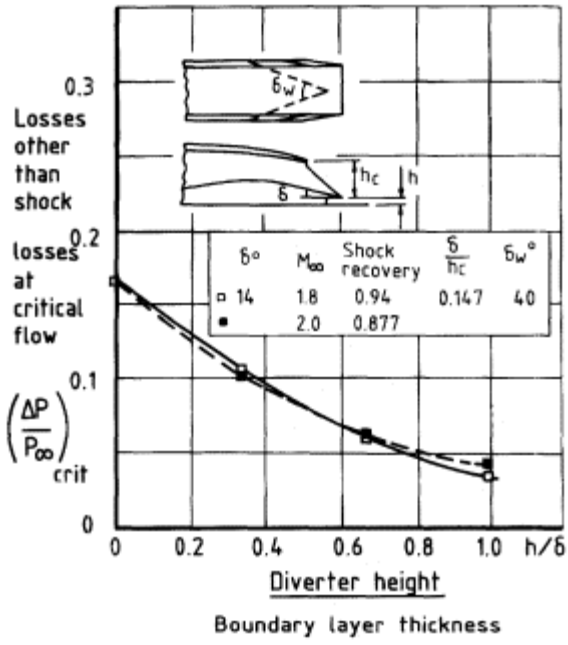

Figure 8.10
Influence of diverter height on extra-to-shock loss for intake with wedge forebody.

8.4
Compression-Surface Bleeds

8.4.1
External Compression

With an external-compression supersonic intake, the problem of whether a bleed is required exists independently of the presence or otherwise of an adjacent aircraft surface. The boundary layer formed on the compression forebody may pass through a number of oblique-shock interactions and in any case must interact with the terminal, normal shock in the vicinity of the entry. Since the normal shock is conventionally at a Mach number around 1.3 or 1.4, flow separation in some degree is a likely occurrence, as the study of transonic effects (Chapter 3) has shown. Whether such separation is of an extent to severely reduce the intake pressure recovery depends upon a

combination of aerodynamic and geometrical factors, of which a first assessment can be made using the transonic generalisations adapted as described in Chapter 7. In some cases, relatively small geometrical adjustments in the early part of the duct may obviate the need for a bleed. In many others, a bleed will be found desirable.

In general terms, the optimum position for a bleed is at the shoulder of the compression forebody, just downstream of the foot of the normal shock when the intake is at critical flow. Clearance of the external boundary layer in these circumstances means that the intake can operate in effect as a simple subsonic duct. A bleed in this position will control the boundary layer also over a range of flow ratio below critical, in a similar way to that described for a normal-shock intake in Section 8.3.1. In supercritical operation, when the normal shock moves inside the intake, hence down-stream of the bleed, pressure recovery is not usually important but flow distortion (Chapter 11) may be a particular concern, requiring additional measures. This last point is taken further in Chapter 12, in discussing the matching problem of the Anglo-French Concorde aircraft.

Obviously diverters are not applicable to this problem but a shoulder bleed may in principle be of either ram-scoop or flush types. In either case it has to be remembered that taking away the boundary layer, which may be ten per cent of the intake capture flow, will introduce additional pressure gradients in the first part of the duct and much may depend on the way this is done. In some of the early research, using ram-scoop bleeds with wedge compression surfaces, the bleed duct was progressively expanded in area, to discharge at a large exit area. This ensured that the bleed always ran 'full', the bleed duct operating in a supercritical condition. The effect of changing bleed flow quantity was studied by varying the size of bleed entry. As the bleed entry area increased, the throat area of the main intake decreased correspondingly. Results by Obery and Cubbison (1954) with this type of arrangement showed a significant decrease in intake loss at the maximum-recovery condition, which occurred at a flow ratio between 0.8 and 0.9, but at the critical point (Fig. 8.11) the loss decreased only for the first 3% of bleed flow ratio and thereafter increased again. In another case (Campbell, 1954) an effective decrease in loss was achieved only at undesirably large bleed flows. A similar trend to that of Obery and Cubbison was obtained with a narrow flush bleed, tested by Gawienowski (1955).

A particularly successful bleed arrangement was developed for the Concorde, the leading research being done by Leynaert (1965). This involved the use of a wide bleed slot, pictured in Fig. 8.12, which shows different types of flow field obtaining in supercritical, critical and subcritical conditions. A further description of the intake system is reserved for Chapter 12, where the problems of matching and control are discussed. For now we note the nature of the bleed flow, which is seen, in Fig. 8.13, to be

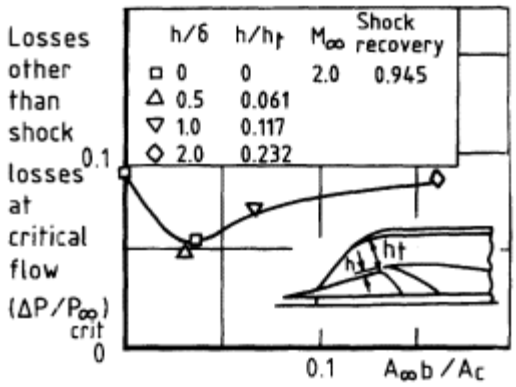

Figure 8.11
Effect of a ram scoop bleed at intake throat on
extra-to-shock loss for a wedge-forebody intake.

concentrated into a narrow supersonic free jet entering the bleed chamber (or 'void') and rapidly losing total pressure from the effects of shock waves and viscosity. It might be questioned, in view of the narrowness of the jet, whether a wide bleed slot was really required. The answer lies in the ability of the free shear surface across the slot to take up different positions for the different flow states, introducing an important degree of flexibility into the matching problem. A particular feature is the strong curvature of this

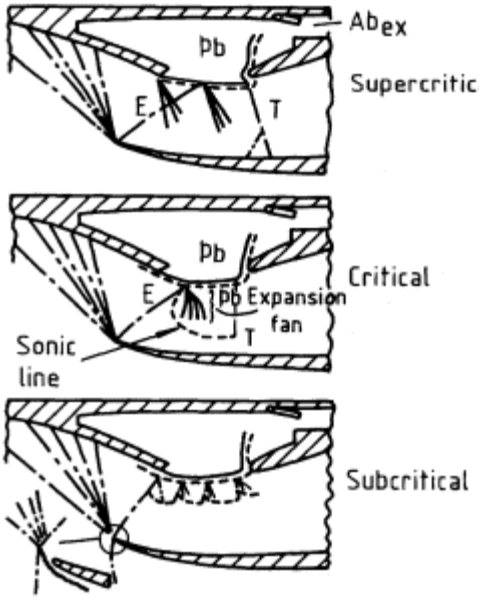

Figure 8.12
Shock and flow patterns for wedge-forebody
intake with a wide flush throat bleed.

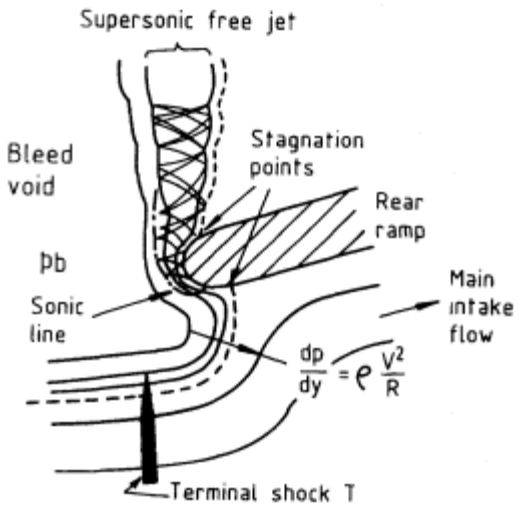

Figure 8.13
Flow pattern in vicinity of
rear lip of a wide flush bleed.

surface, and of the whole bleed flow, approaching the leading edge of the rear ramp. The curvature sharpens as the terminal shock ahead of it moves downstream, and the centrifugal pressure gradient associated with it compensates for the difference in static pressure between the bleed void and the main flow.

8.4.2
Internal or Mixed Compression.

Syberg and Hickox (1973) described a procedure for designing a distributed bleed system for an axisymmetric mixed-compression intake with translating conical centrebody. The steps involved were as follows.

(1) Variation of the longitudinal position of the forebody with free stream Mach number was determined so as to maintain the throat Mach number close to 1.25.

(2) Using this translation schedule, inviscid flow fields were computed at intervals of 0.1 Mach number to cover the required range.

(3) Boundary layer development on both cowl and centrebody, for the intake without bleed, was calculated for each Mach number of the inviscid solutions. Particular difficulties in this step were the specification of transition locations and the method of treatment of the oblique-shock and boundary-layer interactions. The resulting maps of shock position, with contours of either boundary-layer shape factor (incompressible) *H*i or profile power-law index *n*i, were used to identify bleed positions required to prevent flow separation. An additional requirement was that profiles at the throat should be

close to the standard one-seventh power law (ni = 7) of the turbulent layer.

(4) Areas were identified where rows of bleed holes or slots, feeding into plenum chambers, could be positioned.

(5) Assuming bleed flow rates, the boundary-layer development was recomputed with prescribed velocity normal to the surface as a function of axial position. Bleed flow rates were adjusted until satisfactorily low values of Hi were obtained.

(6) Arrangements of holes or slots were devised to provide the required bleed flows. This involved a knowledge of individual bleed-hole (or slot) characteristics. The holes were designed to operate with choked flow, in order to avoid recirculation between different rows in the same plenum chamber, and at the maximum plenum-chamber pressure which allowed choked flow, since this would minimise the bleed internal drag. Hole (or slot) characteristics involved were length to diameter ratio, angle to the surface, and diameter in relation to the calculated boundary-layer displacement thickness. For holes in the throat region, an additional property required was that of a high rate of change of flow quantity with local Mach number. This was to give some stability to the terminal, normal shock: it resulted, after experiment, in a choice of 90° (to the intake axis) for these particular holes.

(7) The total bleed system having been evolved primarily for the intake design Mach number, it was checked for off-design conditions and modified so as to continually avoid flow separation.

(8) Allowance was made for the shock impact locations on centrebody and cowl falling ahead of the computed positions, owing to the effect of cowl lip bluntness and to cumulative viscous effects.

This outline of procedure only begins to convey the complexity of the design process. Figs. 8.14 (a) and (b) show a resulting arrangement of bleed holes and plenum chambers for a Mach 3.5 design.

When such a design has been evolved, it may be possible by experimental measurements to refine it so as to obtain a large reduction in bleed flow for only a small degradation in intake pressure recovery. In one such case, an axisymmetric intake for Mach 2.5, having 60% internal contraction, gave originally (Cubbison *et al.*, 1969) 92% total-pressure recovery with 10% bleed flow. By a detailed investigation of bleed hole positioning, which showed in particular that holes spanning interaction regions were undesirable, the bleed flow was reduced subsequently (Fukuda *et al.*, 1977) to 3.1% for a reduction of pressure recovery to 89.2%.

Figure 8.15 shows results by Neale and Lamb (1962) for a less sophisticated wedge-intake system, in which only one oblique shock was internal

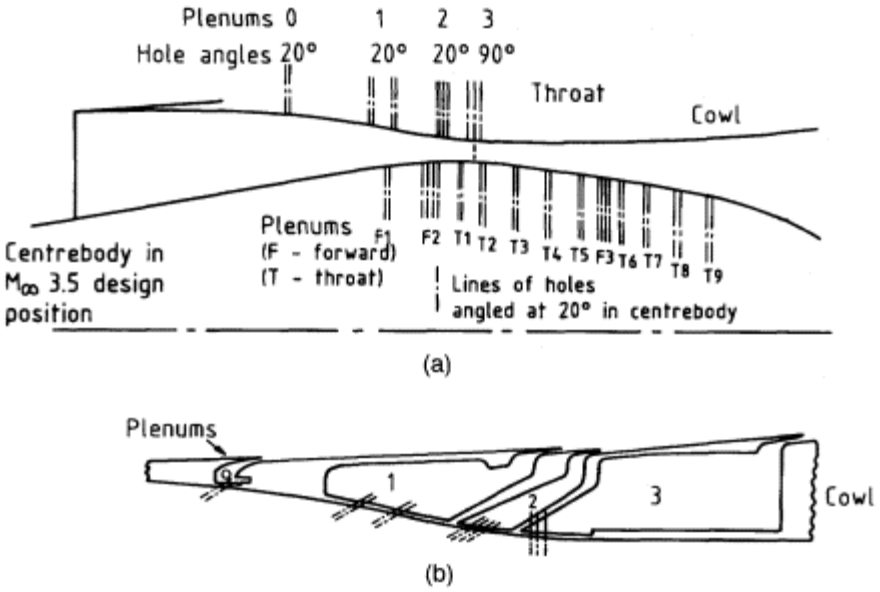

Figure 8.14
Flush bleed systems for mixed-compression intake: (a) cowl and centrebody bleed holes and plenums; (b) cowl bleed holes, plenums and exits.

and boundary-layer control was confined to a single bleed slot in the standard shoulder position on the compression forebody. With ram scoop bleeds the results were unsatisfactory but a 'step' or 'trap' bleed proved reasonably successful. The glancing interaction of an internal oblique shock on a sidewall boundary layer produces a downward component in the boundary-layer flow and the advantage of the step bleed probably lay in its ability to capture a proportion of that flow.

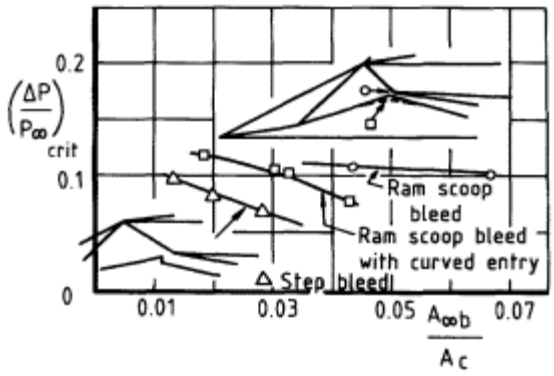

Figure 8.15
Influence of bleed entry shape on extra-to-shock loss for a mixed-compression intake at *M*¥ 2.2.

8.5 Bleed Drag

The subject of bleed drag has been treated for supersonic intakes by Goldsmith (1968). In general, boundary-layer bleed air may be jettisoned overboard from an aircraft in the most direct way possible or it may be used further in a variety of ways, for example as cooling air for equipment or as source of secondary air for the propelling nozzle. In these latter cases it may be difficult to evaluate a precise drag penalty to be associated with the intake bleed function. The essential thing is to be able to specify bleed exit conditions, real or effective; momentum calculations can then be made of the bleed internal drag, either to establish differences as between various ways of dealing with the flow, or to set the drag penalty directly against the thrust gain arising from improvement of the intake pressure recovery.

8.5.1 Types of Flow

Four flow conditions in a bleed duct can be distinguished: these are governed by the exit area of the duct, the internal shape near to the exit and conditions imposed at exit by the external flow. In the first place, the bleed may be essentially a version of the aerodynamic duct introduced in Chapter 1 as typifying the air intake itself. A correct choice of exit area enables the bleed to run 'full' at entry, that is effectively at unit flow ratio, accepting the full flow defined by its entry plane area. At subsonic speeds, the exit static pressure is determined by external flow conditions: at supersonic speeds, except near $M = 1$, unless the pressure recovery in the duct is very low, the exit is choked.

A second condition is obtained by adding an expanding passage downstream of the choked minimum duct area. The bleed flow is thus expanded down to free stream pressure, or possibly a base static pressure, and discharged at supersonic velocity.

A third condition is that usually known as *base bleed*, in which the air is controlled to emerge a low subsonic velocity into a base region. In doing so it occupies a relatively large exit area and has a low total pressure. Experiments have shown that under these conditions the level of pressure on any residual base area can be raised, so that taking this effect together with a reduction of boat-tail drag from the larger total base, the higher bleed internal drag associated with low total pressure may be more than offset.

The fourth condition is one in which the bleed flow is supersonic throughout the duct. If a constant area duct is used then the only net force acting is internal skin friction and the drag can be calculated approximately using an appropriate friction coefficient. The main problem is that of assessing whether or not a supersonic throughflow can be obtained, espe-

cially in model scale conditions: criteria applicable to small-scale model tests have been studied by Seddon (1957).

For bleed systems with subsonic intakes, only the first of these four conditions applies.

8.5.2
Application of Momentum Equation

The basic expression for calculating bleed internal drag is of course the same for all the above conditions. It expresses drag as the rate of change of momentum of the internal flow between suitable initial and final stations. The choice of stations must be consistent with the system adopted for defining the engine thrust and aircraft external drag. This is discussed in Chapter 9 and, anticipating the situation, the basic equation for bleed internal drag is

$$D_{\text{int}} = 2q_\infty A_\infty - [(p_{\text{ex}} - p_\infty) + 2q_{\text{ex}}]A_{\text{ex}} \qquad (8.2)$$

Here all terms relate to the bleed duct. *A*ex is the exit area and *A*¥ is the area at 'infinity upstream' of the flow which passes into the bleed. Expressed in this way, the drag takes account not only of pressure losses occurring within the duct but also of momentum change in the streamtube approaching the bleed, principally the friction drag of the surface 'wetted' by the bleed flow. It is often more convenient, however, to define bleed drag from the local conditions at bleed entry. The definition of aircraft drag must then be adjusted to include all the pre-entry drag to this station. The expression for bleed drag now becomes

$$D_{\text{int}} = \left[(p_\ell - p_\infty) + 2q_\ell \frac{\phi}{\phi_\ell}\right] A_{\text{en}} - [(p_{\text{ex}} - p_\infty) + 2q_{\text{ex}}]\, A_{\text{ex}} \qquad (8.3)$$

in which suffix ℓ denotes local conditions at the bleed entry, *A*en is the bleed entry area normal to the flow, and

$$\phi = \delta \int_0^{h/\delta} \rho V^2 \, \mathrm{d}(y/\delta), \quad \phi_\ell = h\rho_\ell V_\ell{}^2 \qquad (8.4)$$

Values of ϕ/ϕ_ℓ for different proportions of a standard 1/7 power boundary-layer profile are given in Fig. 8.16. The ratio has been calculated more extensively by Simon and Kowalski (1955), who give it for profile power indices 5, 7, 9 and 11 and for Mach numbers from 0.2 to 5.0. If *h*/d is greater than 1.0, so that some stream outside the boundary layer is being ingested by the bleed, the ratio is given by

$$\frac{\phi}{\delta_\ell} = \frac{\delta}{h}\left[\left(\frac{\phi}{\phi_\ell}\right)_{h-\delta} - 1\right] + 1 \qquad (8.5)$$

Equation (8.2) can be rewritten as a drag coefficient in the form

$$C_D = \frac{D_{int}}{q_\infty A_c} = \frac{2A_\infty}{A_c} - \left[\left(\frac{p_{ex}}{p_\infty} - 1\right)\frac{p_\infty}{q_\infty} + \frac{2q_{ex}}{P_{ex}} \cdot \frac{P_{ex}}{P_\infty} \cdot \frac{P_\infty}{q_\infty}\right]\frac{A_{ex}}{A_c} \qquad (8.6)$$

where Ac is the main-intake capture area and the other terms relate to the bleed duct. For the condition of a sonic exit this becomes

$$C_D = \frac{2A_\infty}{A_c} - \left[\left(0.528\,\frac{P_{ex}}{P_\infty} \cdot \frac{P_\infty}{p_\infty} - 1\right)\frac{p_\infty}{q_\infty} + 0.740\,\frac{P_{ex}}{P_\infty} \cdot \frac{P_\infty}{q_\infty}\right]\frac{A^*_{ex}}{A_c} \qquad (8.7)$$

where A*ex is the sonic exit area, so that

$$\frac{A^*_{ex}}{A_c} = \frac{A_\infty}{A_c} \Big/ \frac{P_{ex}}{P_\infty} \cdot \left(\frac{A}{A^*}\right)_\infty \qquad (8.8)$$

For either the subsonic case or the supersonic fully-expanded duct, if the static pressure at exit is free-stream pressure, Equation 8.6 becomes

$$C_D = 2\left[\frac{A_\infty}{A_c} - \frac{q_{ex}}{P_{ex}} \cdot \frac{P_{ex}}{P_\infty} \cdot \frac{P_\infty}{q_\infty} \cdot \frac{A_{ex}}{A_c}\right] \qquad (8.9)$$

where the exit Mach number Mex, and hence $q$ex/$p$ex and (A/A*)ex, follow from evaluating

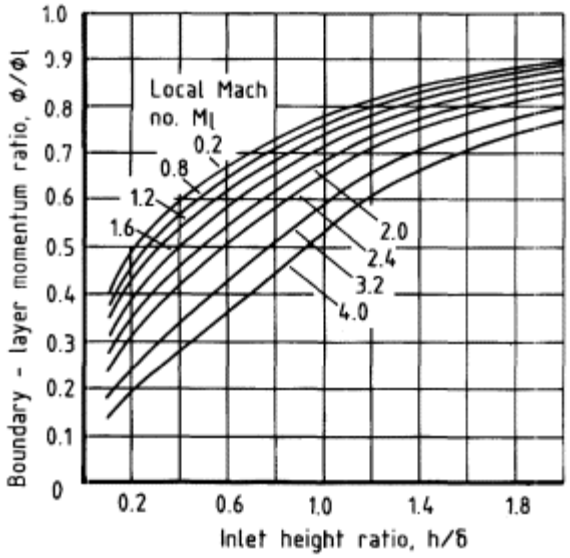

Figure 8.16
Variation of boundary-layer momentum ratio with
local Mach number (velocity profile parameter n = 7).

$$\frac{p_{ex}}{P_{ex}} = \frac{p_\infty}{P_\infty} \Big/ \frac{P_{ex}}{P_\infty} \qquad (8.10)$$

and

$$\frac{A_{ex}}{A_c} = \left(\frac{A}{A^*}\right)_{ex} \cdot \frac{A^*_{ex}}{A_c} \qquad (8.11)$$

For ejection at low subsonic velocity with *p*ex = *p*b (a base pressure), *M*ex and the dependent ratios follow from

$$\frac{p_{ex}}{P_{ex}} = \frac{p_b}{p_\infty} \Big/ \frac{P_{ex}}{P_\infty} \cdot \frac{P_\infty}{p_\infty} \qquad (8.12)$$

where now *p*ex/*p*¥ has to be specified or evaluated from experiment with a suitable base-bleed arrangement.

For sonic exit flow the relationship corresponding to the alternative drag definition at Equation 8.3 is

$$C_D = \left[\left(\frac{p_\ell}{p_\infty} - 1\right)\frac{p_\infty}{q_\infty} + \frac{2\phi}{\phi_\ell} \cdot \frac{q_\ell}{q_\infty}\right]\frac{A_{en}}{A_c}$$

$$-\left[\left(0.528\,\frac{P_{ex}}{P_\infty} \cdot \frac{P_\infty}{p_\infty} - 1\right)\frac{p_\infty}{q_\infty} + 0.740\,\frac{P_{ex}}{P_\infty} \cdot \frac{P_\infty}{q_\infty}\right]\frac{A^*_{ex}}{A_c} \qquad (8.13)$$

where

$$\frac{A^*_{ex}}{A_c} = \frac{A^*_{ex}}{A_{en}} \cdot \frac{A_{en}}{A_c} = \frac{m}{m_\ell} \cdot \frac{A_{en}}{A_c} \Big/ \frac{P_{ex}}{P_\ell} \cdot \left(\frac{A}{A^*}\right)_\ell \qquad (8.14)$$

in which m/m_ℓ is the boundary layer mass flow ratio, that is the mass flow in a given fraction of the boundary layer as a proportion of that in an equal area of the local stream. Thus

$$\frac{m}{m_\ell} = \delta \int^{h/\delta} \rho V \mathrm{d}\left(\frac{y}{\delta}\right) \Big/ h\rho_\ell V_\ell \qquad (8.15)$$

This ratio has been charted by Simon and Kowalski in a manner similar to that for the momentum ratio ϕ/ϕ_ℓ and is shown in Fig. 8.17.

Values of bleed drag coefficient from Equation (8.7) and (8.9) are shown in Fig. 8.18 as functions of free stream Mach number, bleed duct pressure recovery *P*ex and bleed flow *A*¥. Pressure recovery for a bleed with normal shock at entry, assuming *h*/d = 1 and profile power index *n* = 7, is shown in Fig. 8.19. For this purpose the loss after the shock has been calculated as

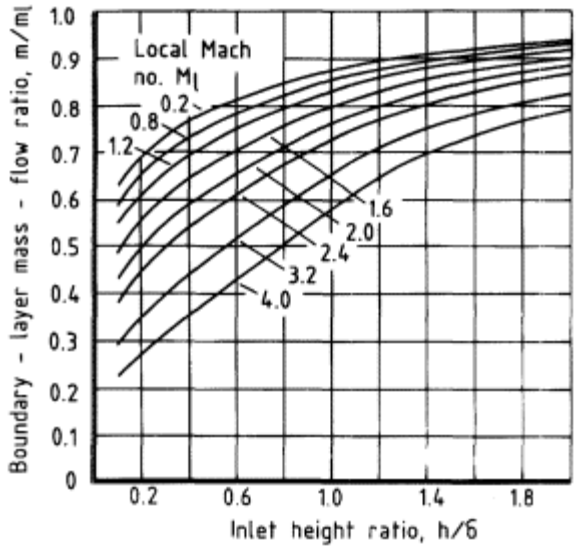

Figure 8.17
Variation of boundary-layer mass-flow ratio with local Mach number (velocity profile parameter n = 7).

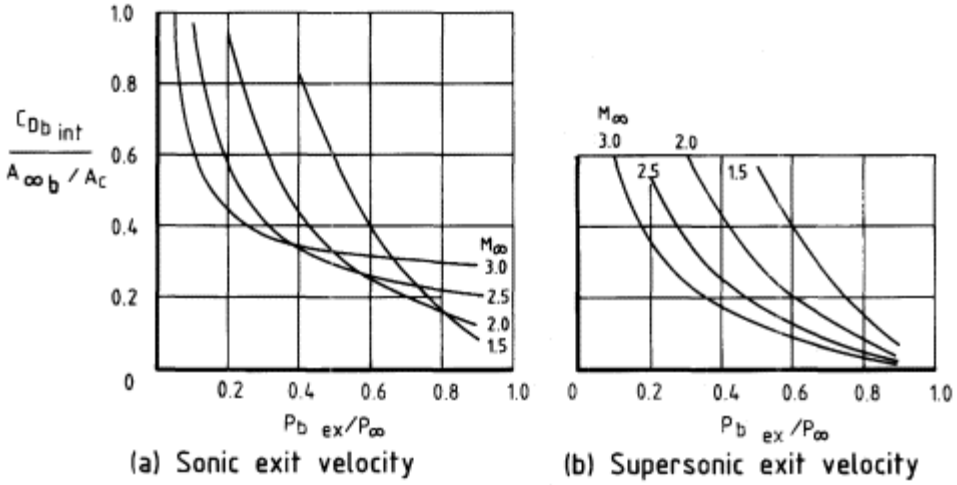

Figure 8.18
Variation of bleed drag with bleed total-pressure ratio (a) with sonic exit velocity (b) with supersonic exit velocity and exit static pressure equal to p¥.

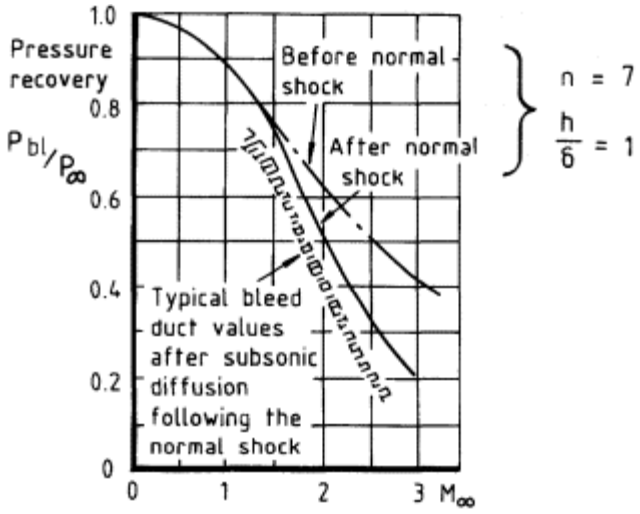

Figure 8.19
Pressure recovery of normal-shock ram scoop bleed.

that associated with flow mixing to a uniform profile in a constant-area duct.

8.6
Diverter Drag

The wave drag of channel diverters with wedge-shaped prows at supersonic speeds has been correlated in one form by the North American Rockwell Corporation (undated). In another form it has been presented by Jell and Ballinger (1981). Figure 8.20 shows this presentation in terms of a drag coefficient based on diverter frontal area with *h*/d equal to unity. As a general indication, this drag is about 40% of that calculated for a two-dimensional wedge in the free stream. Jell and Ballinger also indicate that a good estimate of diverter friction drag can be obtained by applying flat plate skin friction for compressible flow to the 'total wetted area' inside a diverter passage. A study by Davenport (1968) has indicated that at subsonic speeds the drag coefficient of a diverter, based on frontal area, may be taken as 0.25 for Mach numbers up to 0.8, rising to 0.28 for Mach 0.95 and that these values are virtually independent of diverter planform shape and height.

The value of such estimates depends upon the way in which they are intended to be used. For a breakdown of total drag into components, one of which is diverter drag, the above guidelines are useful. Estimating the cost in drag of a diverter *as an additional feature* on an aircraft which would otherwise be without one (and hence would have a different intake pressure

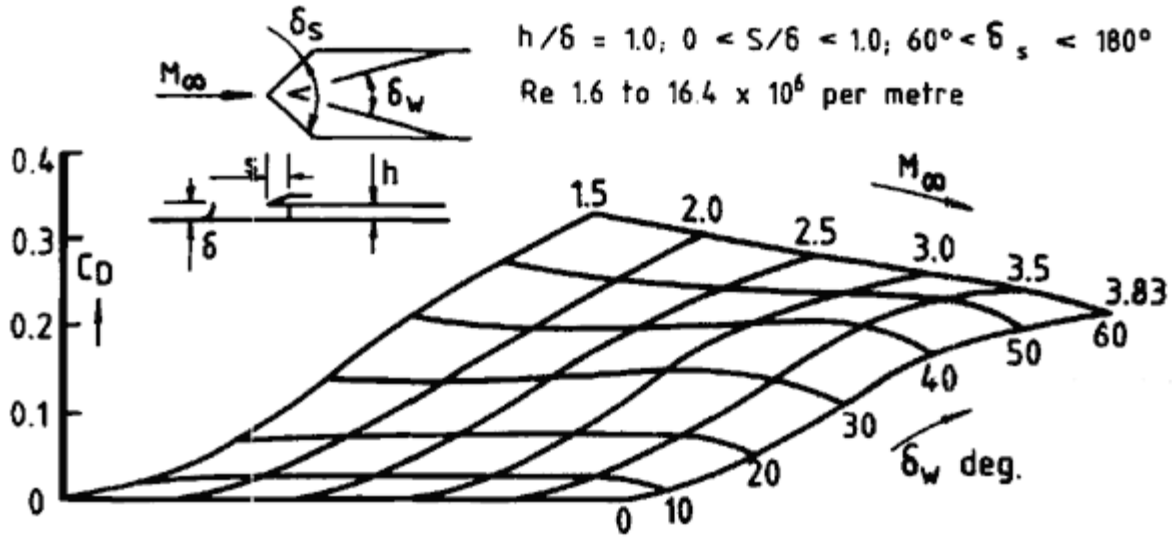

Figure 8.20
Wedge-diverter wave drag.

recovery and therefore a different engine thrust) involves the difficulty of defining a 'without diverter' configuration, a process which is often arbitrary, especially on subsonic aircraft.

References.

Campbell, R.C. (1954) 'Performance of a supersonic ramp inlet with internal boundary layer scoop'. NASA RM E54 101.

Campbell, R.C. (1957) 'Performance of supersonic ramp type side inlet with combinations of fuselage and inlet throat boundary layer removal'. NASA RM E56A17.

Cook, T.A. (1964) 'Supersonic wind tunnel tests on a half-conical centrebody side intake'. RAE Report, Aero 2689.

Cubbison, R.W., Meleason, E.T. and Johnson, D.F. (1969) 'Performance characteristics from Mach number 2.58 to 1.98 of an axisymmetric mixed compression inlet system with 60% internal contraction'. NASA TMX 1739.

Davenport, C. (1968) 'A further investigation of the drag at subsonic speeds of side intake boundary layer diverters'. BAC AX 316.

Frazer, A.C. and Anderson, W.E. (1953) 'Performance of a normal shock scoop inlet with boundary layer control'. NASA RM A53 D29.

Fukuda, M.K., Hingst, W.R. and Reshotko, E. (1977) 'Bleed effects on shock/ boundary layer interactions in supersonic mixed compression inlets. *Journal of Aircraft* 14, no. 2.

Gawienowski, J.J. (1961) 'The effects of boundary layer removal through slots on the internal performance of a side inlet at Mach numbers of 2.0 and 2.3'. NASA TMX-502.

Goldsmith, E.L. (1968) 'Boundary layer bleed drag at supersonic speeds. *ARC, R & M* 3529.

Jell, C.S. and Ballinger, T.J. (1981) 'An assessment and analysis of available literature on side intakes for air breathing missiles'. BAe DG, BT 11096.

Johnson, H.W. and Piercy, T.G. (1954) 'Effect of wedge type boundary layer

diverters on performance of half-conical side inlets at Mach 2.96'. NASA RM E54E20.

Kuehn (1961) 'Turbulent boundary layer separation induced by flares on cylinders at zero angle of attack'. *NASA TR*, R-117.

Leynaert, J. (1965) 'Fonctionnement du piège à couche limite interne d'une prise d'air à compression supersonique externe'. ONERA TP No. 288.

Neale, M.C. and Lamb, P.S. (1962) 'Tests with a variable ramp intake having combined external/internal compression and a design Mach number of 2.2'. NGTE, M358.

North American Rockwell Corporation, NR-68-H-434, vols I to III.

Obery, L.J. and Cubbison, R.W. (1954) 'Effectiveness of boundary layer removal near throat of ramp-type side inlet at free stream Mach number of 2.0'. NASA RM E54114.

Piercy, T.G. and Johnson, H.W. (1953) 'A comparison of several systems of boundary layer removal ahead of a typical conical external-compression side inlet at Mach numbers 1.88 and 2.93'. NASA RME 53 F16.

Reyhner, T.A. and Hickox, T.E. (1972) 'Combined viscous-inviscid analysis of supersonic inlet flow fields'. *Journal of Aircraft* 9, no.8.

Roshko, A. and Thomke, G.J. (1963) 'Supersonic turbulent boundary layer interaction with a compression corner at very high Reynolds number'. McDonnell-Douglas Astro Co. Paper 10163.

Seddon, J. (1957) 'The flow through short straight pipes in a compressible viscous stream;. *ARC Technical Report CP 355.*

Seddon, J. (1966) 'Boundary layer interaction effects in intakes with particular reference to those designed for dual subsonic and supersonic performance'. *ARC R & M*, no. 3565.

Simon, P.C. and Kowalski, K.L. (1955) 'Charts of boundary layer mass flow and momentum for inlet performance analysis in Mach number range 0.2 to 5.0'. NACA, TN 3583.

Syberg, J. and Hickox, T.E. (1973) 'Design of a bleed system for a Mach 3.5 inlet'. NASA CR 2187.

Syberg, J. and Koncsek, J.L. (1973) 'Bleed system design technology for supersonic inlets'. *Journal of Aircraft* 10, no. 7.

Tanner, L.H. and Gai, S.L. (1967) 'Effect of suction on the interaction between a shock wave and a boundary layer at a compression corner'. ARC 28770.

Vas, I.E. (1955) 'A detailed study of the interaction of a 14° shock wave with a turbulent boundary layer at M = 2.9'. Princeton University Department of Aero Engineering Report 296.

Chapter 9
Intake External Drag

9.1
Introduction

Discussion of alternative forms of supersonic intake (Chapters 5, 6) has inevitably raised questions of intake drag, since coupled always with the problems of providing efficient supersonic compression is that of ensuring that the drag is not over compromised in the process. Also the treatment of boundary layer bleeds (Chapter 8) has included a discussion of bleed drag and diverter drag. Before proceeding, therefore, with special aspects of the internal-flow problem, we now address the general subject of intake external drag.

9.2
Definitions of Thrust and Drag

It is necessary to ensure that the reckoning of drag in the external flow is consistent with the definition of thrust in the internal flow; and since a degree of arbitrariness exists in the latter, the joint situation is examined. Consider as in Fig. 9.1 the aerodynamic duct, with engine enclosed, in an airstream extending from 'upstream infinity', where the usual free stream conditions apply, to 'downstream infinity', where the ambient pressure is restored to p¥ and suffix j relates to conditions within the propulsive jet. The thrust, expressed as the overall rate of change of momentum between the two stations, is

$$X_0 = \rho_j V_j^2 A_j - \rho_\infty V_\infty^2 A_\infty \qquad (9.1)$$

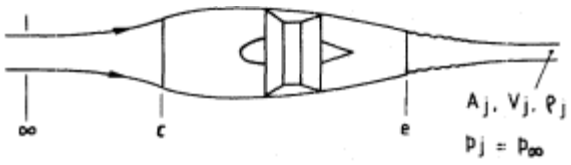

Figure 9.1
Stations in flow for definitions of thrust.

X0, defined in this way, is termed the *overall thrust.* The definition, however, is unsatisfactory for practical use, because downstream of the exit the jet mixes with the external flow in an imprecise way so that the postulated conditions at downstream infinity are not in fact definable, apart from a special case when the pressure at exit is p¥ and the exit itself serves as the downstream station.

Thrust might alternatively and reasonably be defined as the resultant streamwise component of all internal pressures or surfaces contained within the duct. The appropriate momentum flux is that between entry and exit: this yields an expression for the *intrinsic thrust:*

$$X_I = [(p_e - p_\infty) + \rho_e V_e^2] A_e - [(p_c - p_\infty) + \rho_c V_c^2] A_c \qquad (9.2)$$

Again, however, the definition is unsatisfactory in practice, because whilst the exit terms are determined by the engine nozzle and can therefore be related to test bed conditions, the entry terms concern the intake and will vary from one type of aircraft to another or with a change of entry area on a particular installation.

The thrust definition which satisfies the needs of both engine and aircraft designer is a compromise determined by expressing the momentum flux between upstream infinity and the exit station, which gives

$$X_N = [(p_e - p_\infty) + \rho_e V_e^2] A_e - \rho_\infty V_\infty^2 A_\infty \qquad (9.3)$$

This is known as *net standard thrust* and is generally accepted as the practical thrust definition. The first term on the right-hand side is referred to as *gross thrust* and the second as *momentum drag.* The difference between *X*N and *X*I corresponds to the resolved component of internal pressures at the surface of the capture stream tube (Fig. 9.1): this is expressible precisely from Equations (9.2) and (9.3) and constitutes a *pre-entry thrust force* which is included in the definition of *X*N.

The situation as it concerns intake drag is pictured in Fig. 9.2. Drag terms on the cowl itself are friction drag, *D*f, and pressure drag, *D*p. For allocation of drag to the intake *per se*, the terms are normally reckoned from the cowl lip to the maximum section: this assumes in effect that the external shape continues beyond the maximum section as a semi-infinite parallel cylinder. In addition to the cowl drag terms, it is necessary to cancel out the pre-entry thrust force by including an equal and opposite force in the drag direction. This determines a *pre-entry drag force, D*pre in the diagram, defined from Equations (9.2) and (9.3) as

$$D_{pre} = [(p_c - p_\infty) + \rho_c V_c^2] A_c - \rho_\infty V_\infty^2 A_\infty \qquad (9.4)$$

and positive in the drag sense so long as the flow ratio *A*¥/*A*c is less than 1.0.

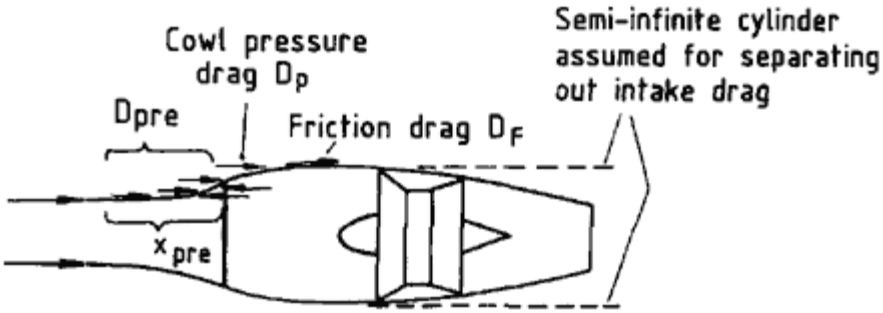

Figure 9.2
Forces that comprise external drag.

At subsonic speeds the pre-entry flow is not associated with either wave or skin friction drag or the effects of shock and boundary layer interaction, and is therefore not a drag in terms of the definition used in AGARDo-graph No. 237 (a guide to in-flight thrust measurements of turbojet and fan engines). This defines 'drag' as a force which is a positive term only when there is a loss of fluid momentum downstream at infinity. At supersonic speeds, however, it is correct to call this conceptual force a drag as it is now linked to the presence of shock waves whose pressures can be said to act on the pre-entry streamline. Thus the term 'additive drag' was introduced by Ferri in the USA in these circumstances to accord with the definition of thrust as discussed. In the UK the term 'pre-entry' rather than 'additive' has come into universal use as being more usefully descriptive. However, with this explanation as to its origin we shall use as appropriate either pressure force in the drag direction at subsonic speeds or, for brevity, pre-entry drag.

In coefficient form:

$$C_{\mathrm{Dpre}} = \frac{\mathrm{D_{pre}}}{q_\infty A_\mathrm{c}} = \frac{(p_\mathrm{c} - p_\infty)}{q_\infty} + \frac{2q_\mathrm{c}}{q_\infty} - \frac{2A_\infty}{A_\mathrm{c}} \qquad (9.5)$$

and in terms of tabulated flow functions:

$$C_{\mathrm{Dpre}} = \left[\frac{p_\mathrm{c}}{P_\mathrm{c}} \cdot \frac{P_\mathrm{c}}{P_\infty} \cdot \frac{P_\infty}{q_\infty} - \frac{p_\infty}{q_\infty} + \frac{2q_\mathrm{c}}{P_\mathrm{c}} \cdot \frac{P_\mathrm{c}}{P_\infty} \cdot \frac{P_\infty}{q_\infty}\right] - \frac{2A_\infty}{A_\mathrm{c}} \qquad (9.6)$$

where at subsonic speeds

$$\frac{P_\mathrm{c}}{P_\infty} = 1$$

and at supersonic speeds for a pitot intake

$$\frac{P_\mathrm{c}}{P_\infty} = \left(\frac{P}{P_\infty}\right)_{\mathrm{NS}}$$

the stagnation pressure ratio across a normal shock wave. It is shown plotted in Fig. 9.3 as a function of flow ratio over a range of Mach numbers

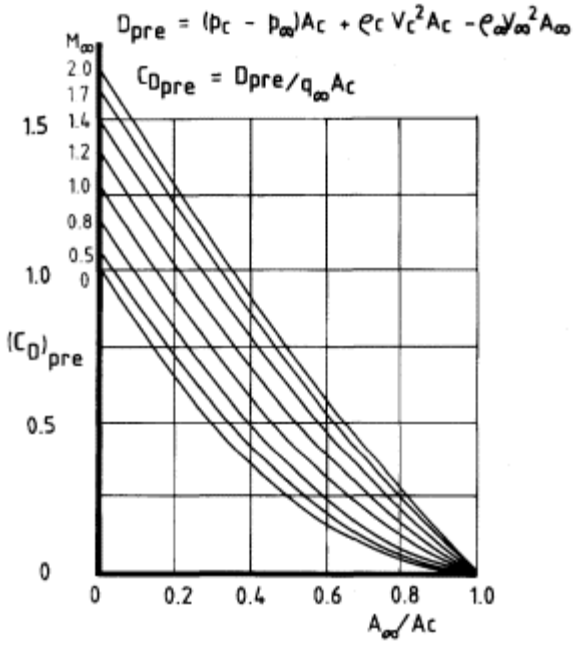

Figure 9.3
Variations of pre-entry drag with flow ratio and free stream Mach number.

from zero to 2.0. In such a calculation the assumption is made that the flow is one-dimensional and that the stagnation point is at the cowl highlight or capture area position. For a sharp-lipped cowl, errors due to both these assumptions are probably reasonably small until *A*¥ << *A*c. For a thick-lipped cowl the situation must be examined more carefully as is discussed in Section 9.6.

Generally then, we consider the intake drag, *D* say, to be comprised of the three terms

$$D = D_f + D_p + D_{pre} \qquad (9.7)$$

Boundary layer bleed drag or diverter drag (Chapter 8) may need to be added for a full assessment.

It is convenient to divide the cowl drag into its value at full flow (*A*¥/*A*c = 1.0) and the change in drag from that condition: thus Equation (9.7) may alternatively be written as

$$D = (D_f + D_p)_0 + \Delta D_0 + D_{pre} \qquad (9.8)$$

When the flow ratio is less than 1.0, D*D*0 is usually negative, since the additional acceleration of flow around the cowl lip involves higher negative

pressures, which have a forward (i.e. cowl thrust) component. Since pre-entry drag is zero at full flow, the last two terms taken together express the change in drag caused by variation from full flow to any other value: this net effect is known as spillage drag

$$D_{\text{spill}} = D_{\text{pre}} + \Delta D_0 \qquad (9.9)$$

9.3
Subsonic Intake Drag below Critical Mach Number

The presentations in this and the following section are made in terms of the podded engine nacelle for subsonic transport aircraft, since most attention in research and development has gone into that area of application.

For a typical subsonic cowl, having a rounded nose and well-faired shape to the maximum section, the profile drag at full flow the first two terms on the right of Equation (9.8) will, so long as the flow is wholly subsonic, approximate to flat plate skin friction at the appropriate Reynolds number plus a few per cent for form drag the *D*p term. Stanhope (1968) has examined this situation and suggests that an appropriate correlating factor is (*C*D/*C*f)0.6 where *C*D is the intake drag coefficient and *C*f is the corresponding flat plate skin friction coefficient. The factor is based on classical derivations of momentum thickness for a boundary layer assumed to be turbulent from the cowl leading edge. From an examination of extensive test data, both American (NACA) and British (Rolls-Royce/ARA), for cowls of the NACA 1-Series, which are widely used for podded nacelle design (see fuller reference in Section 9.4), Stanhope concludes that a suitable empirical relationship for cowls at full flow is

$$\left(\frac{C_D}{C_f}\right)^{0.6} = 1 + 0.33\,\frac{(d_m - d_c)}{\ell} \qquad (9.10)$$

Here *d*c and *d*m are the cowl diameters at entry and maximum section respectively and ℓ is the length between them: the expression $(d_m - d_c)/\ell$ is thus a thickness to chord ratio of the cowl profile.

Since the normal cruise flight condition for a subsonic intake is at a flow ratio below 1.0, any spillage drag for this condition must by Equation (9.8) be added to the above. We first examine the idealised case of an inviscid, wholly subsonic flow without separation. Applying the momentum theorem within the control volume ABCDEA pictured in Fig. 9.4 gives

$$\rho_\infty V_\infty{}^2 A_\infty = \int_{AC} (p - p_\infty)\mathrm{d}A + \int_{BC} (p - p_\infty)\mathrm{d}A + \rho_\infty V_\infty{}^2 A_1$$
$$+(\rho_\infty V_\infty A_0 - \rho_\infty V_\infty A_1)V_\infty \qquad (9.11)$$

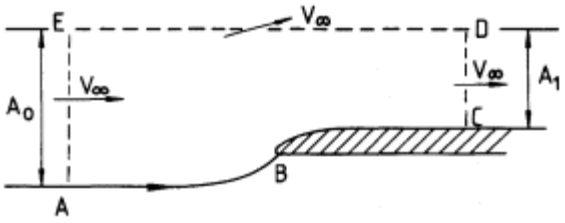

Figure 9.4
Application of momentum theorem for
spillage drag of well-faired subsonic cowl.

which reduces to

$$0 = \int_{AB} (p - p_\infty) dA + \int_{BC} (p - p_\infty) dA$$

or

$$\int_{BC} (p - p_\infty) dA = - \int_{AB} (p - p_\infty) dA$$

That is to say, the axial pressure force on the cowl is equal and opposite to the axial pressure force on the pre-entry streamline, or in our nomenclature:

$$D_p = D_{pre}$$

Here *D*p relates to the total cowl pressure drag in the spillage condition illustrated. Performing the same exercise for full flow when *D*pre is zero, yields the result

$$(D_p)_0 = 0 \qquad (9.12)$$

(which expresses the fact that at full flow the pressures on the cowl adjacent to the stagnation point are in balance, in a drag sense, with suctions farther back on the profile). It follows that

$$\Delta D_0 = D_p - (D_p)_0 = -D_{pre} \qquad (9.13)$$

which is to say that

$$D_{spill} = 0 \qquad (9.14)$$

Thus in inviscid, shock-free flow the increase of suction on the cowl lip when flow ratio is reduced from unity exactly balances the pre-entry

pressure force in the drag direction. In practice, because the boundary layer on the cowl displaces the potential flow, the suction force becomes progressively deficient as the flow ratio decreases, though in the absence of separation the effect is not large. Stanhope's result for the general case with spillage is

$$\left(\frac{C_D}{C_f}\right)^{0.6} = 1 + 0.33\,\frac{(d_m - d_c)}{\ell}\left[1 + 1.75\,\frac{(A_c - A_\infty)}{(A_m - A_c)}\right] \qquad (9.15)$$

A general treatment of spillage drag is given later in the chapter. It is of interest that whereas the NACA results are all for low Mach number ($M¥ = 0.4$), the Rolls-Royce data are for higher Mach numbers, going up to 0.85. Thus while the Stanhope analysis is basically one for incompressible flow, the measure of agreement suggests that the effect of compressibility, before the critical drag rise and in the absence of flow separation, is not significant.

If spillage is increased indefinitely, then with most cowl profiles a critical flow ratio is reached at which the flow separates from the external surface, owing to the large effective incidence of the profile to the stagnation streamline. The situation is similar to that of internal separation at high flow ratio discussed in Chapter 4. Below the critical flow ratio, spillage drag increases much more rapidly than is given by Equation (9.15). The critical flow ratio may be expected to correlate with cowl lip radius, r say, which for NACA 1-Series cowls is given, according to Stanhope by

$$\frac{\rho}{d_m} = 0.1365\,\frac{(1 - d_c/d_m)^2}{\ell/d_m} \qquad (9.16)$$

Stanhope's analysis leads to the correlation reproduced at Fig. 9.5. Of interest is the wide range of critical flow ratios obtainable in practice. Thus on the one hand, if *d*c/*d*m is close to 1.0, or alternatively the cowl is very long, the critical flow ratio is itself close to 1.0, that is to say separation occurs at very small spillage. On the other hand, with relatively bluff cowls, for which *d*c/*d*m is smaller or the cowl relatively short, separation can be avoided effectively down to zero flow ratio.

9.4 Cowl Design.

9.4.1 Subcritical

Whether in a spillage condition or at full flow, an intake cowl creates local velocities on the external surface that are in excess of free stream velocity. As free stream Mach number increases subsonically a point is reached at

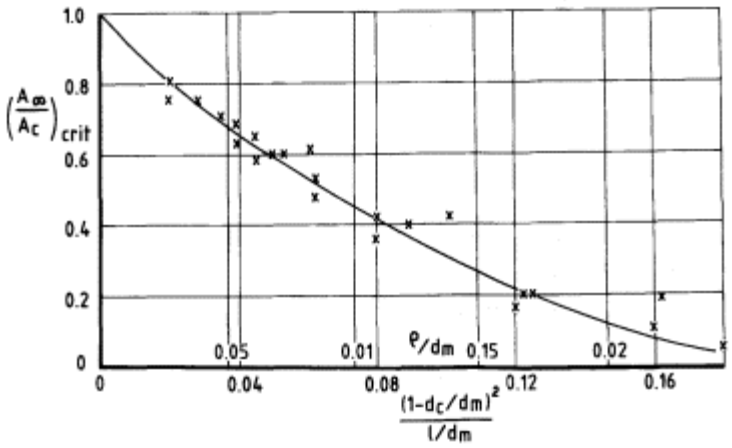

Figure 9.5
Correlation of critical flow ratio for cowls
below drag-rise Mach number (Stanhope).

which sonic velocity is attained on the cowl. With further increase thereafter, a region of supersonic flow develops, terminating normally in a shock wave. This situation, with or without flow separation which may be a part of it, is at some stage responsible for a rapid rise in drag. The primary object of high Mach number design is not so much to minimise the actual drag level, either before or during the rise, but rather to ensure that the drag-rise Mach number (suitably defined) is sufficiently high as to be compatible with the performance target of the aircraft as a whole.

The most obviously satisfactory situation is if sonic velocity is not exceeded on the cowl at the required flight Mach number. By analogy with wing theory, this is referred to as subcritical design. The condition for it can be examined by use of the momentum theorem, applied as in Fig. 9.6. The internal shape is taken to be a parallel duct of area A_c. Applying the momentum theorem within the control boundary shown gives

$$\rho_\infty V_\infty{}^2 A_0 = \rho_c V_c{}^2 A_c + (\rho_\infty V_\infty A_0 - \rho_c V_c A_c) V_\infty + (p_c - p_\infty) A_c + \int_{BC} (p - p_\infty) dA \qquad (9.17)$$

which reduces to

$$\int_{BC} (p - p_\infty) dA = \rho_c V_c A_c (V_\infty - V_c) - (p_c - p_\infty) A_c \qquad (9.18)$$

For incompressible flow the result is particularly simple. Bernoulli's equation substituted on the right-hand side leads to

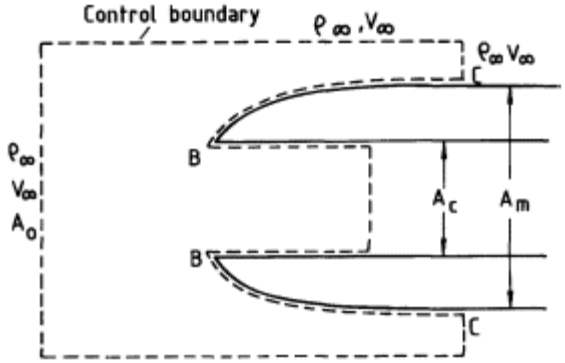

Figure 9.6
Application of momentum theorem
to subcritical cowl design.

$$\int_{BC} (p - p_\infty) dA = -\tfrac{1}{2}\, \rho V_\infty{}^2 A_c\, (1 - V_c/V_\infty)^2 \qquad (9.19)$$

so that, if F is written for the cowl thrust force, we have

$$\frac{F}{q_\infty A_c} = \frac{1}{A_c} \int_{BC} (-C_p) dA = \left(1 - \frac{V_c}{V_\infty}\right)^2 = \left(1 - \frac{A_\infty}{A_c}\right)^2 \qquad (9.20)$$

The pressure coefficient Cp is related to local velocity on the cowl surface, V say, by

$$C_p = 1 - \left(\frac{V}{V_\infty}\right)^2 \qquad (9.21)$$

It is therefore seen from Equation (9.20) that (a) the cowl thrust force is purely a function of flow ratio and (b) for a given flow ratio, the force will be achieved with a minimum excess velocity V over free stream V¥ if V (and hence Cp) is constant along the profile. In this case we have

$$\left(1 - \frac{A_\infty}{A_c}\right)^2 = -C_p \left(\frac{A_m}{A_c} - 1\right) \qquad (9.22)$$

Hence if Cps is the value of pressure coefficient corresponding to sonic speed at a particular free stream Mach number, the amount of forward facing area required to carry the suction force at a constant pressure Cps is given by

$$\frac{A_m}{A_c} = 1 + \frac{\left(1 - \frac{A_\infty}{A_c}\right)^2}{-C_{ps}} \qquad (9.23)$$

If the pressure distribution on the cowl profile is other than uniform, a greater area is required to avoid sonic speed being exceeded at the points of minimum pressure.

The foregoing derivation was first given by Küchemann and Weber (1940). It is valid, under the assumption of incompressible flow, for intakes of any cross-section. Values of minimum area ratio given by Equation (9.23) are plotted in Fig. 9.7 for different values of *C*p; this illustrates the general nature of the variations involved. Küchemann and Weber (1953) also derived subsequently the mathematically more complex compressible flow version of Equation (9.23). The result is

$$\frac{A_m}{A_c} = 1 + \frac{\frac{\gamma M_\infty^2}{2} \cdot \frac{F}{q_\infty A_c}}{1 - \left[1 + \frac{\gamma-1}{2} M_\infty^2 \left\{1 - \left(\frac{V_{max}}{V_\infty}\right)^2\right\}\right]^{\gamma/(\gamma-1)}} \qquad (9.24)$$

where now the following relationship for the thrust force *F* replaces Equation (9.20)

$$\frac{F}{q_\infty A_c} = 2\frac{V_c}{V_\infty}\left(\frac{V_c}{V_\infty} - 1\right)\left[1 + \frac{\gamma-1}{2} M_\infty^2 \left\{1 - \left(\frac{V_c}{V_\infty}\right)^2\right\}\right]^{1/(\gamma-1)}$$

$$+ \frac{2}{\gamma M_\infty^2}\left(\left[1 + \frac{\gamma-1}{2} M_\infty^2 \left\{1 - \left(\frac{V_c}{V_\infty}\right)^2\right\}\right]^{\gamma/(\gamma-1)} - 1\right) \qquad (9.25)$$

The compressible flow result for *C*p = 0.2 is shown in Fig. 9.7: this value of *C*p corresponds to sonic speed at a free stream Mach number M¥ = 0.89.

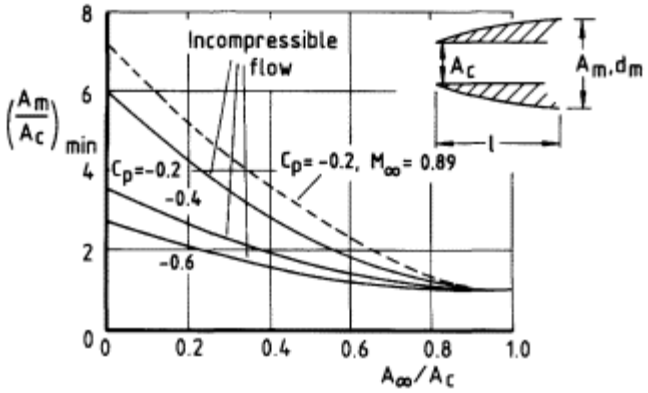

Figure 9.7
Minimum cowl projected
area for subcritical flow.

We see that in general the effect of compressibility is to increase the frontal area required.

A profile giving a uniform pressure distribution, usually referred to as the constant velocity profile, was first calculated by Ruden (1940). Baals, Smith and Wright (1949) developed the NACA 1-Series cowls, which have gained wide acceptance for practical use. Members of the series vary in length and diameter ratio but have the same basic profile which is defined in Table 9.1.

Table 9.1 NACA 1-Series ordinates

x/ℓ	y/Y	x/ℓ	y/Y
0	0	0.260	0.6035
0.004	0.0663	0.300	0.6489
0.008	0.0933	0.340	0.6908
0.015	0.1272	0.380	0.7294
0.025	0.1657	0.420	0.7648
0.035	0.1994	0.460	0.7974
0.050	0.2436	0.500	0.8269
0.080	0.3181	0.580	0.8795
0.110	0.3815	0.660	0.9220
0.140	0.4366	0.740	0.9548
0.170	0.4840	0.820	0.9787
0.200	0.5270	0.900	0.9940
0.230	0.5666	1.000	1.0000

In Fig. 9.8 the 1-Series profile is compared with Ruden's constant velocity profile and the two are seen to be closely similar. For prescribed conditions of diameter ratio, intake flow ratio and free stream Mach number, a particular length of profile is appropriate. In broad terms, if the profile length is shorter than optimum the general level of velocities on the cowl is raised, if longer the pressure distribution takes on a different form, having a high suction peak near the nose. This last is important as

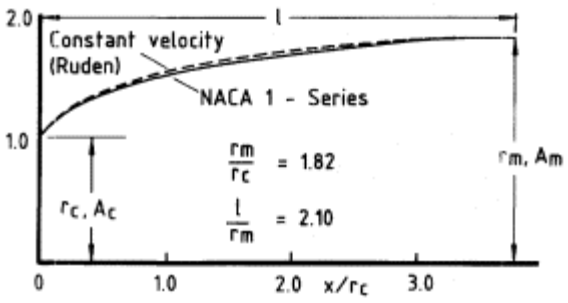

Figure 9.8
Comparison of NACA-1 series and

Ruden's constant-velocity profiles.

will be discussed in Section 9.6 where further reference is made to the NACA 1-Series profiles.

9.4.2
Supercritical

To take a particular example from Fig. 9.7, for a flow ratio 0.7 a typical cruise condition the minimum area ratio required to avoid supersonic flow on the cowl at flight speed $M\infty = 0.89$ (using the curve for compressible flow) is 1.85. For a circular cowl this means that the entry diameter must be no more than 0.73 times the maximum cowl diameter. With engines of the pure jet type, nacelle diameter ratios, dictated essentially by engine diameter and airflow consumption, are generally in the range of 0.5 to 0.7, so that subcritical cowl design is more often than not a practical possibility. The advent of turbofan engines, with high bypass ratio and low specific thrust, has significantly altered the relationship of engine airflow to engine diameter, so that a more typical range of diameter ratio in these cases is 0.8 to 0.9. Many practical considerations weight, ground clearance, basic profile drag, etc. prevent the maximum nacelle diameter being increased to produce a lowering of this ratio. Consequently it has been necessary to consider the design of thinner cowls, for which, since it is not possible to satisfy the area relationship of Equation (9.24), the flow inevitably becomes 'supercritical', that is, locally supersonic on the cowl.

Following the lead given by aerofoil research, the direction of work has been towards the development of so-called 'peaky' sections, first propounded by Pearcey (1960). An initial strong curvature of the profile creates a high suction peak near the nose; careful control of the curvature thereafter leads to a high degree of virtually isentropic compression, so that the shock wave, if and when it appears, is both weak and also positioned near the crest of the profile, where positive pressures behind the shock can have but little detrimental effect on the overall cowl suction force resolved axially.

In point of fact it is found that cowls of the NACA 1-Series can be employed successfully as supercritical designs. The crucial factor is use of an appropriate length ratio for the profile in a given set of conditions. For example, the 1-Series cowl at 0.85 diameter ratio and 0.45 length ratio shows drag rise Mach numbers above 0.85 for all flow ratios above 0.5. Stanhope presents a correlation of 1-Series data at zero incidence, which for drag rise Mach numbers (MD) above 0.8 amounts to the empirical relationship

$$M_{\mathrm{D}} = 1 - \frac{1}{8}\,\frac{\sqrt{\left[1 - \left(\frac{d_{\mathrm{c}}}{d_{\mathrm{m}}}\right)^2\right]}}{\ell/d_{\mathrm{m}}} \qquad (9.26)$$

Variation of *M*D with flow ratio is stated to be negligibly small within the range of flow ratio typical of high speed cruise. An increase of incidence of the cowl is accompanied by a reduction in *M*D at the rate of about 0.003 per degree of incidence up to 6°.

9.5 Spillage Drag

We can now return to the subject of spillage drag as we defined it in Section 9.2:

$$D_{spill} = -D_{pre} + \Delta D_0$$

and look briefly at simplified ways of predicting it, using in general the one-dimensional evaluation of *D*pre exemplified in Fig. 9.3.

At subsonic speeds, when the flow over an intake cowl is smooth, spillage drag is nominally zero, as was demonstrated in Section 9.3, and in fact small, as in the empirical formula given for NACA 1-Series cowls at Equation (9.15). When the flow is disturbed, by local shock waves and more particularly by separation, cowl suction is lost and spillage drag becomes larger. Such flow disturbances arise at Mach numbers close to 1.0, or when the flow ratio is reduced beyond a certain level, or of course in a combination of the two situations. At supersonic speeds the same principles apply but in addition, because the pressure level of the flow field around the cowl is raised by the detached shock above that of the mainstream flow, cowl suction is in effect further reduced and spillage drag correspondingly increased.

It is instructive to consider the hypothetical case of a cowl in the form of a parallel cylinder with infinitely thin wall, shown for subsonic speeds in Fig. 9.9(a). Here the suction force is necessarily zero, since the cowl has no forward-facing surface. Spillage drag is thus equal to the full pre-entry drag *D*pre. In fluid motion terms the loss of suction is associated with disturbed flow, in this case separation at the leading edge, which occurs at all flow ratios below 1.0, so we refer to a *disturbed-flow drag*, which in this extreme form will be labelled *D*DF and is given by Equation (9.4). The situation, though hypothetical, can be closely approached in practice with thin sharp-edged cowls, as will be seen.

In the corresponding situation at supersonic speeds, a normal shock stands off the entry and is follows by subsonic flow, represented by the base conditions *M*w, *p*w immediately behind the shock Fig. 9.9(b). The entry is thus again in subsonic flow and by the preceding argument a disturbed-flow drag can be defined in terms of the 'free stream' pressure *p*w, namely

$$D_{DF} = [(p - p_w) + \rho_c V_c^2] A_c - \rho_w V_w^2 A_\infty \qquad (9.27)$$

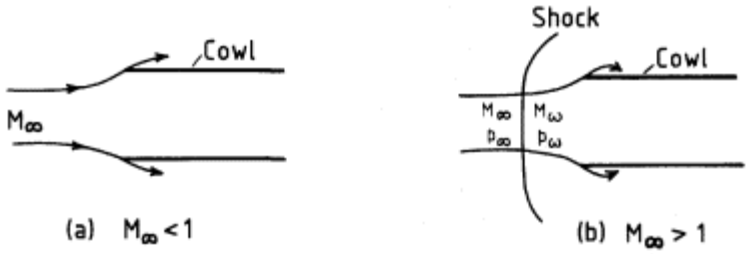

Figure 9.9
Spillage drag of thin-walled parallel-cylindrical cowl.

Maximum disturbed-flow drag, *D*DF, defined by Equation (9.4) for subsonic speeds and Equation (9.27) for supersonic speeds, is shown plotted in Fig. 9.10, in coefficient form, as a function of flow ratio for several values of Mach number. Continuing the examination of Fig. 9.9(b), in the supersonic situation, as in the subsonic, there can be no thrust on the thin-walled parallel cowl and hence the overall spillage drag is again equal to pre-entry drag. There is therefore, for the supersonic case, an additional term in spillage drag, given by the difference between Equations (9.4) and (9.27): this difference is

$$D_{\text{pre}} - D_{\text{DF}} = (p_{\text{w}} - p_{\infty})A_{\text{c}} - (\rho_{\infty}V_{\infty} - \rho_{\text{w}}V_{\text{w}}{}^{2})A_{\infty} \qquad (9.28)$$

This additional quantity, related directly to the pressure rise through the shock wave, may be termed the *normal-shock drag* component of spillage drag and labelled *D*NS. When the condition of constant momentum through the shock, namely

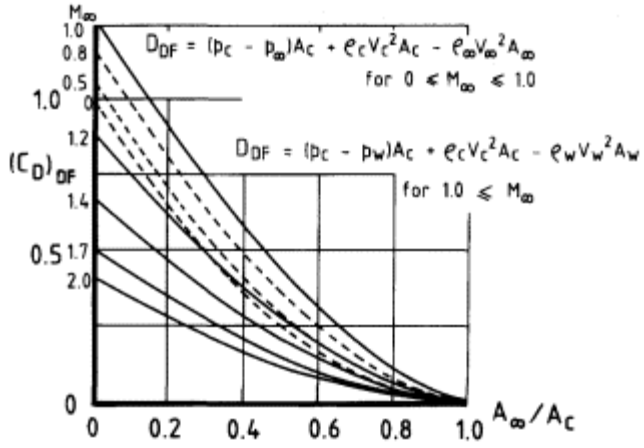

Figure 9.10
Variation of disturbed-flow drag coefficient
with flow ratio and free stream Mach number.

$$p_\infty + \rho_\infty V_\infty{}^2 = p_w + \rho_w V_w{}^2 \qquad (9.29)$$

is substituted in Equation (9.28), we see that the normal-shock drag becomes simply

$$D_{NS} = (p_w - p_\infty)(A_c - A_\infty) \qquad (9.30)$$

This is the equation first derived by Fraenkel (1950) for spillage drag at supersonic speeds. It is known to give a good approximation for Mach numbers above about 1.8, particularly if the cowl lip is sharp and the cowl projected area is small. Thus:

$$D_{NS} \simeq D_{spill}$$

and in coefficient form this can be written very simply as

$$C_{D_{NS}} = C_{D_{spill}} = \frac{10}{6}\left(1 - \frac{A_\infty}{A_c}\right)\left(1 - \frac{1}{M_\infty{}^2}\right) \qquad (9.31)$$

However, in the transonic range spillage drag is more generally constituted of the two components, disturbed-flow drag and normal-shock drag, extreme values of which are given by Equations (9.4) and (9.27) for the former and Equation (9.30) for the latter. Maximum normal-shock drag is plotted in Fig. 9.11. Fig. 9.12 shows how the two components, in extreme form, vary with Mach number at a constant flow ratio 0.7. Disturbed-flow drag *D*DF reaches a maximum at Mach 1.0, while *D*ns, zero at subsonic speeds, increases progressively from Mach 1.0 upwards, the total of the two at all Mach numbers being equal to the pre-entry drag.

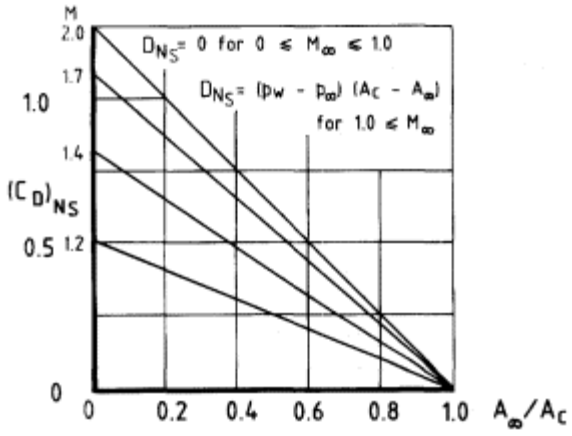

Figure 9.11
Variation of normal-shock drag coefficient
with flow ratio and free stream Mach number.

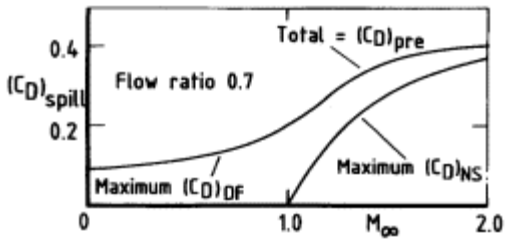

Figure 9.12

Variation of maximum disturbed-flow drag and
maximum normal-shock drag at constant flow ratio.

These general considerations indicate that spillage drag can take any value from zero (subsonic speeds only) to the full pre-entry drag. Its values in a particular case depend upon the shape of the cowl and its environmental location and the greatest complexity occurs at transonic speeds, where shock systems and flow separations exercise a dominant influence.

Mount (1965) has expressed spillage drag as additive (i.e. pre-entry) drag multiplied by an empirical factor *K*add but from his collected results *K*add is not invariant with flow ratio and depends also on both cowl geometry and Mach number in unspecified ways. Seddon (1954), going further along similar lines, proposed a generalisation in the form

$$D_{\text{spill}} = \alpha D_{\text{DF}} + \beta D_{\text{NS}} \qquad (9.32)$$

Based on an analysis of some free-flight model tests made by Sears *et al.* (1953), values of a and b have been suggested: a depends primarily on the slope of the cowl profile averaged over the initial 10% of the length of the cowl. The variation of both a and b is shown in Fig. 9.13, where b is the value of b at Mach number 1.0 and the general formula for b is

$$\beta = \beta_1 + \frac{(M_\infty - 1)}{0.8} \cdot (1 - \beta_1) \qquad (9.33)$$

The overall system suggested for spillage drag estimation can now be summarised.

(1) For Mach numbers below *M*D, the critical flow ratio for rapid increase of spillage drag is estimated from Fig. 9.5. Below the critical, the increase in drag is calculated as a*D*DF where a is determined from Fig. 9.13 and *D*DF is evaluated using the critical flow ratio as origin, that is to say *D*DF corresponds to a flow ratio

$$\frac{A_\infty}{A_c} + 1 - \left(\frac{A_\infty}{A_c}\right)_{\text{crit.}}$$

(2) For Mach numbers from *M*D to 1.8 the critical flow ratio for spillage is assumed to be 1.0 and spillage drag is calculated according to the formula at Equation (9.33).

(3) For Mach numbers above 1.8 the Fraenkel formula at Equation (9.30) is used.

The discontinuities in this system at Mach numbers *M*D and 1.8 are unlikely to introduce serious errors.

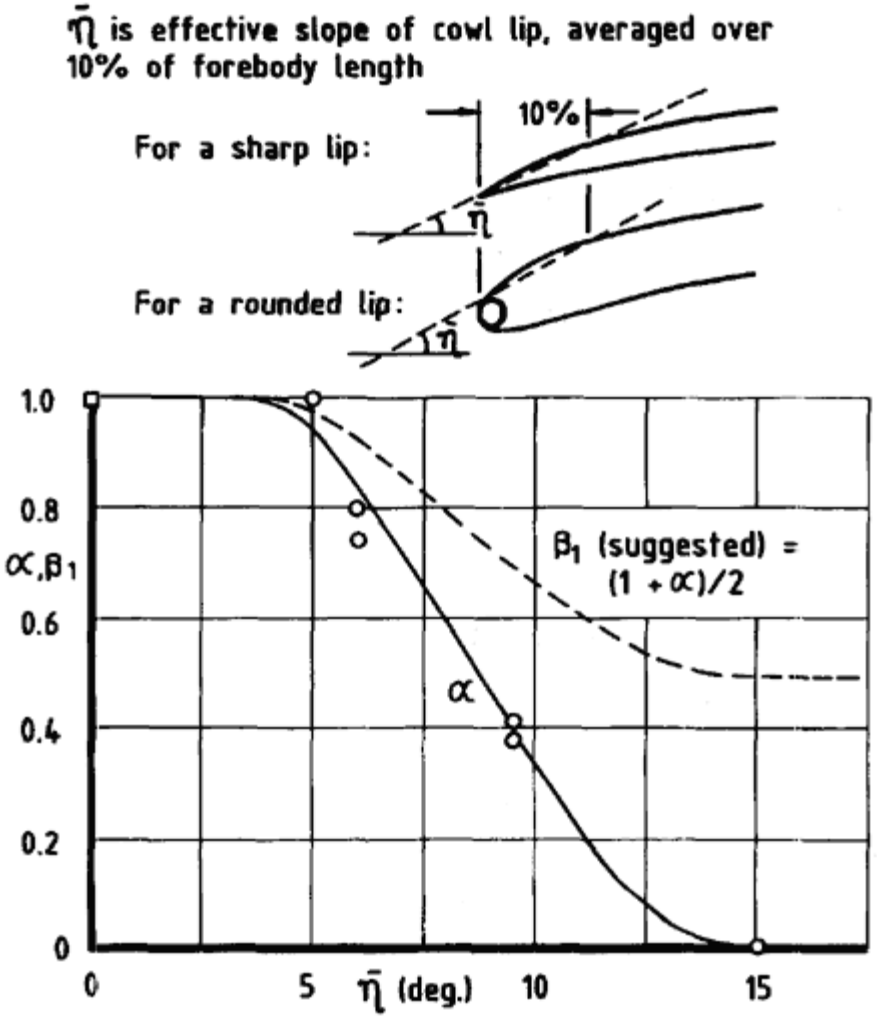

Figure 9.13
Empirical factors a and b1 for
calculation of transonic spillage drag.

9.6
Intake Drag for Subsonic Cowl Shapes

As we have see, as free-stream Mach number rises above the drag-rise Mach number, a region of supersonic flow develops that usually terminates in a shock wave; cowl suction forces are then reduced below their incompressible potential flow values and the exact balance between pre-entry and cowl forces no longer occurs. It is now time to look for more accurate values of both pre-entry and cowl pressure forces than have been presented either separately or combined in Sections 9.2 and 9.5.

These have been measured extensively in both the UK (Ref. 10) and the USA (Ref 18). They can also in general be calculated under all flow and free-stream Mach number conditions until separation starts to occur at the

cowl lip. When this happens, the separation bubble usually grows very rapidly and soon envelops the whole of the forward-facing cowl surface. Under these conditions the compressible potential flow methods of Peace (up to 1.6 or 1.7) or by the Euler methods discussed in Chapter 4 are no long applicable.

9.6.1
Evaluation of Pre-Entry Pressure Force.

In theory this can be obtained from a calculation method by integrating pressures along the pre-entry streamline. However, in experimental measurements this cannot be done and it is convenient for both measurements and calculations to use a similar approach to the one-dimensional change of momentum calculation of Equation (9.4), but using a station far down-stream in the duct rather than the capture plane. Here, unlike at the capture plane, the flow in a calculation method will be uniform and axial and approximately so in measurements.

The first step is to locate the stagnation point and this is found by examining the sign of the calculated velocity along the cowl surface. As the velocity is positive in the clockwise direction, the stagnation point lies between two points where the velocity changes sign. The value of the stagnation line radius *r*stag is found by using a linear fit of *r* versus velocity and evaluating the value of *r* where the velocity is zero.

A similar procedure can be used for evaluating the stagnation line radius from measurements of *C*p around the cowl lip. The cowl length *S* either side of the maximum measured *C*p is divided into ten equal intervals, and using a cubic curve fit for *C*p versus *S*, the maximum value of *C*p from this curve defines *S*stag and hence *r* after some smoothing of the variation of *S*stag values with flow ratio. A typical comparison of *A*stag/*A*c at *M*¥ = 0.94, calculated and measured for three different cowl shapes, is shown in Fig. 9.14.

Using engine face data (from measurements or calculation) where the flow is now axial and reasonably uniform, the internal thrust *X* from upstream infinity station ¥ to station *f* is

$$X = \rho_\infty V_\infty A_\infty V_f + (p_f - p_\infty)A_f - \rho_\infty V_\infty{}^2 A_\infty \qquad (9.34)$$

and

$$C_X = \frac{X}{q_\infty A_c} = \frac{2A_\infty}{A_c}\left[\frac{V_f}{V_\infty} - 1\right] + (p_f - p_\infty)\cdot\frac{A_f}{q_\infty A_c}$$

where

$$\frac{V}{\sqrt{\gamma RT}} M\left[1 + \frac{\gamma - 1}{2} M^2\right]^{-\frac{1}{2}}$$

and *M*f is derived from

$$\frac{A_f^*}{A_f} = \frac{\frac{A_\infty}{A_c} \times \frac{A_\infty^*}{A_\infty} \times \frac{A_c}{A_f}}{P_f/P_\infty}$$

Now

$$C_X = C_{X\,int} + C_{X\,pre}$$

and as

$$C_{X\,pre} = C_{D\,pre}$$

$$C_{D\,pre} = C_X - C_{X\,int}$$

where *C*X int is the duct internal pressure force coefficient integrated from the stagnation point to station f.

As has been seen, the stagnation point can be found by locating the point at which the surface velocity changes sign; *A*¥/*A*c = 1 and *C*Dpre = 0 are limiting conditions at supersonic speeds. At subsonic speeds this can be

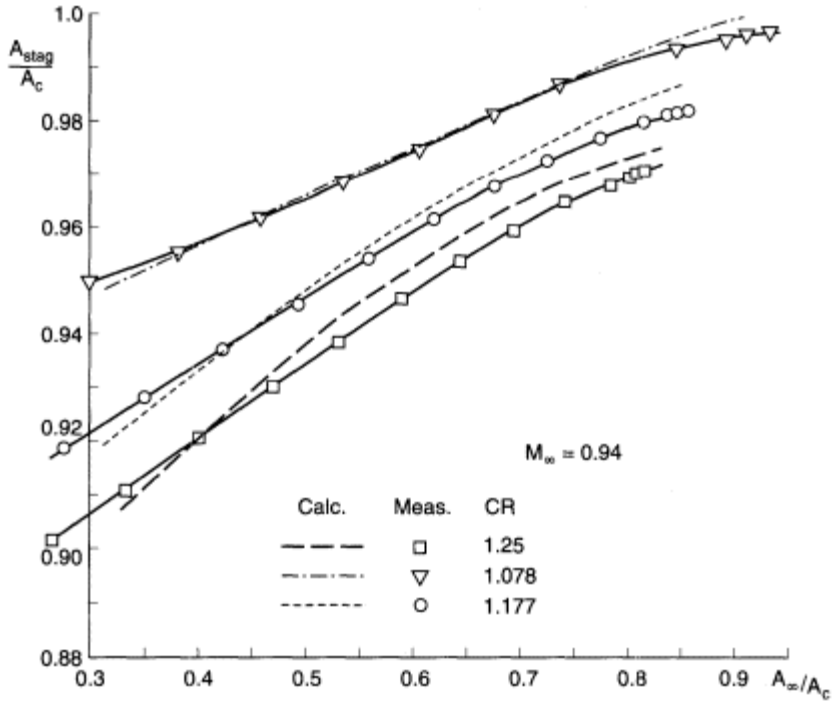

Figure 9.14
Variation of stagnation line area ratio *A*stag/*A*c with capture flow ratio *A*¥/*A*c for cowls with contraction ratios *CR* of 1.25, 1.777 and 1.078.

regarded as a convenient datum condition, but it is not a limiting condition. This is obtained when the intake flow is choked either at its capture plane or at the throat plane 't' downstream of the capture plane. Thus at low subsonic speeds if the lip is not thin (so that separation from the undersurface of the lip does not occur), the flow can increase beyond $A¥/Ac = 1$ to the choking flow $(A¥/Ac)max$ derived from $A¥/Ac = A¥/A¥^*$. At high subsonic and low supersonic speeds internal contraction to At will create a choking condition (Mt = 1) at a flow ratio $A¥/A¥ < 1.0$ which then precludes the datum condition ever being reached, as illustrated in Fig. 9.15.

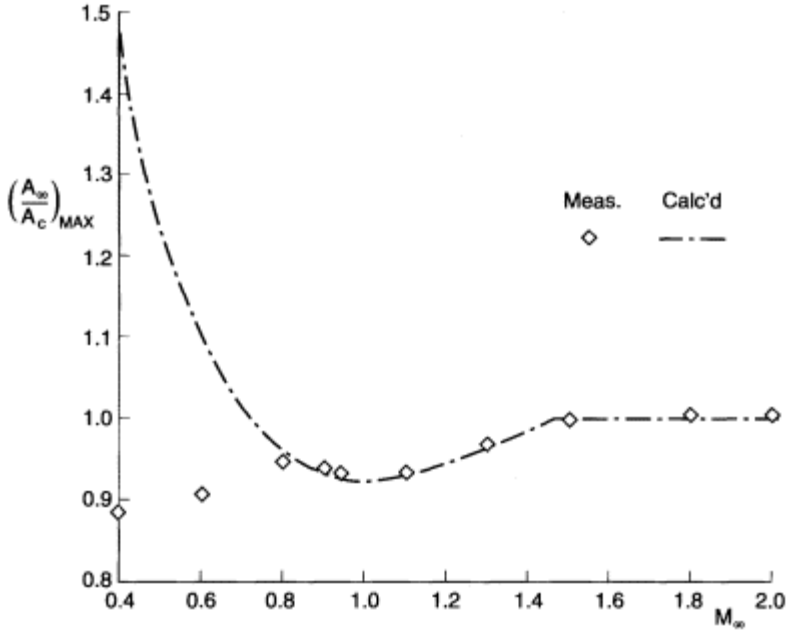

Figure 9.15
Variation of maximum flow ratio with free-stream Mach number for a cowl with a contraction ratio of 1.078.

Now that we can obtain the stagnation point (or rather the line position around the cowl periphery) either from measurement or from potential flow calculation, it is possible to calculate pre-entry drag one-dimensionally based on this stagnation line area $C_{D_{pre_s}}$ rather than the capture area. This has been done and compared to what should be a more accurate evaluation from the procedure just described where the downstream engine face position is used as the rear position for evaluation of the momentum equation and which we designate as $C_{D_{pre_{ie}}}$. This procedure can be derived both from measurements at the engine face and from potential flow calculations. The latter approach does not include skin friction forces on the internal cowl profile and the former may do so in

part, depending on how detailed the engine face flow survey is towards the duct walls.

A comparison of these four evaluations is shown typically in Fig. 9.16. $C_{D_{pre_C}}$ is of course independent of the geometry of the cowl downstream of the highlight position. The potential flow results appear to be inaccurate towards full flow, probably because of neglect of skin friction, and the measured results for $C_{D_{pre_R}}$ distinguish only marginally between the different lip shapes but are nevertheless smaller than the $C_{D_{pre_C}}$ values. Values of $C_{D_{pre_S}}$ also vary with lip shape and agree well with measured results of $C_{D_{pre_R}}$.

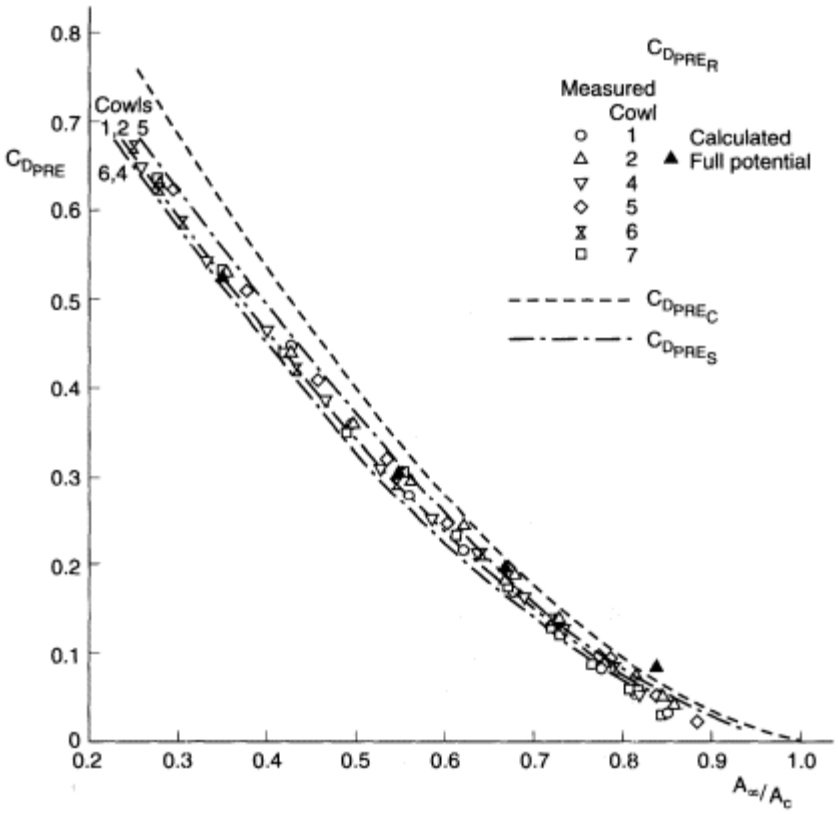

Figure 9.16
Variation of pre-entry drag coefficient (based on capture area) with flow ratio at $M_\infty = 0.9$.

9.6.2
Change of Cowl Drag (or Thrust)

Cowl pressure force is obtained by integration of external surface distributions from the stagnation point to the maximum (and thereafter constant) diameter of the nacelle. Fig. 9.17 shows a typical variation of cowl

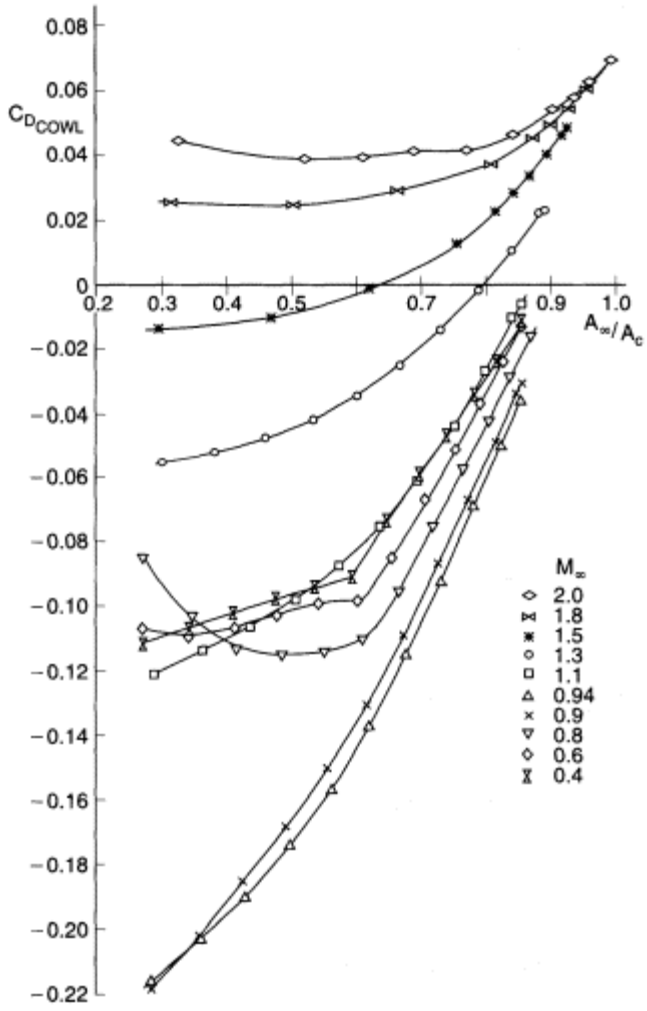

Figure 9.17
Measured variation of cowl drag coefficient
with flow ratio for NACA-1-85-100 cowl.

pressure force with flow ratio over a range of free-stream Mach numbers for a cowl with a NACA 1-Series shape (see Section 9.4 for a definition of the shape and proportions of the shapes embodied in the 85-100 nomenclature). At subsonic speeds cowl pressure force at all flows is negative and generally increasingly so as flow is reduced. At supersonic speeds it is positive near to full flow and reduces as flow is reduced, but only becomes negative at low flows at low supersonic speeds. The onset and growth of external lip separation is indicated by a decrease in the positive slope of the curve followed by a region of zero or near-zero slope and finally *A*¥/*A*c vs. *C*Dcowl negative slope as cowl thrust decreases substantially.

At $M\infty$ = 0.9 over a large range of flow ratio, supersonic attached flow predominates over the cowl profile and reduced cowl suction force now comes from the formation of shock waves in conjunction with a thickened or locally separated boundary layer. There is now no obvious cowl lip separation (at least down to a flow ratio of 0.27) and this is typical of all subsequent increases of free-stream Mach number to 2.0.

Cowl thrust can be predicted by the potential flow calculations of the Peace method at subsonic and low supersonic speeds and by Euler methods at supersonic speeds until the flow ratio is reached at which the flow separates at the lip. The departure of measured and calculated curves clearly indicates the onset of lip separation (Fig. 9.18).

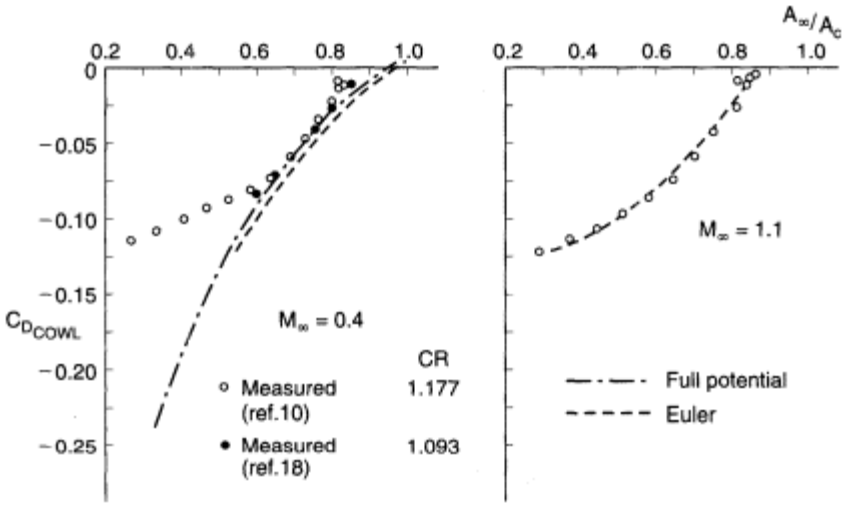

Figure 9.18
Comparison of measured and calculated variation
of cowl drag coefficient for NACA-1-85-100 cowl.

Cowl pressure distributions also graphically illustrate the same point, as can be seen from the collapse of the cowl suction peak just downstream of the highlight as flow ratio changes from 0.586 to 0.516 and 0.444 at $M\infty$ = 0.8 (Fig. 9.19). When there is no separation, very good agreement is obtained with potential flow predictions at subsonic speed (Fig. 9.20) and Euler calculations at supersonic speeds (Fig. 9.21).

This section concludes with a brief account of the Engineering Sciences Data Unit (ESDU) Euler method calculations as given in ESDU Data Item 94013. These evaluated the characteristics of a range of NACA 1-Series profiles from *D*c/*D*max of 0.5 to 0.9 and *L*f/*D*max from 0.2 to 1.4 at all free-stream Mach numbers below 1.5 which resulted in supercritical flow over the cowl surfaces. To do this satisfactorily, it was found necessary to:

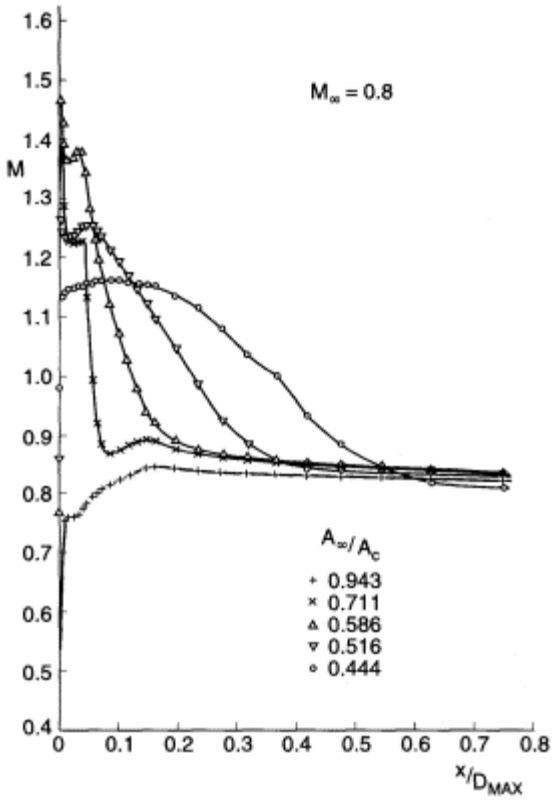

Figure 9.19
Variation of surface Mach number distribution with flow ratio for NACA-1-825-100 cowl at *M*¥ = 0.8.

(a) Redefine the NACA 1-Series profile using a more realistic internal geometry than was used in the original definition. This entails altering the original normalising dimensions. The changes are illustrated in Fig. 9.22, where the quarter-circle radius $r = 0.025Y$ is not the radius of curvature r of the external profile at the highlight. The X normalising dimension for both (a) and (b) remains the forecowl length Lf, but the Y dimension changes from

$$\text{(a)}\quad Y = \frac{D_{\max} - d}{2} - r \quad \text{to} \quad \text{(b)}\quad Y = \frac{D_{\max} - D_c}{2}$$

To convert between the systems of nomenclature:

$$\frac{d}{D_{\max}} = 1 - \frac{2.05}{2}\left(1 - \frac{D_c}{D_{\max}}\right)$$

and

$$\frac{D_c}{D_{max}} = 1 - \frac{2}{2.05}\left(\frac{1-d}{D_{max}}\right)$$

It should be noted that the calculations and definitions used in Ref. 10 and the examples given in Figs. 9.20 and 9.21 are all strictly as defined in the original NACA 1-Series profile (as defined in Fig. 9.22(a)).

(b) Use a smooth series of ordinates of the NACA-1 profile. Although the first divided differences of the profile in Table 9.1 are smooth, the second

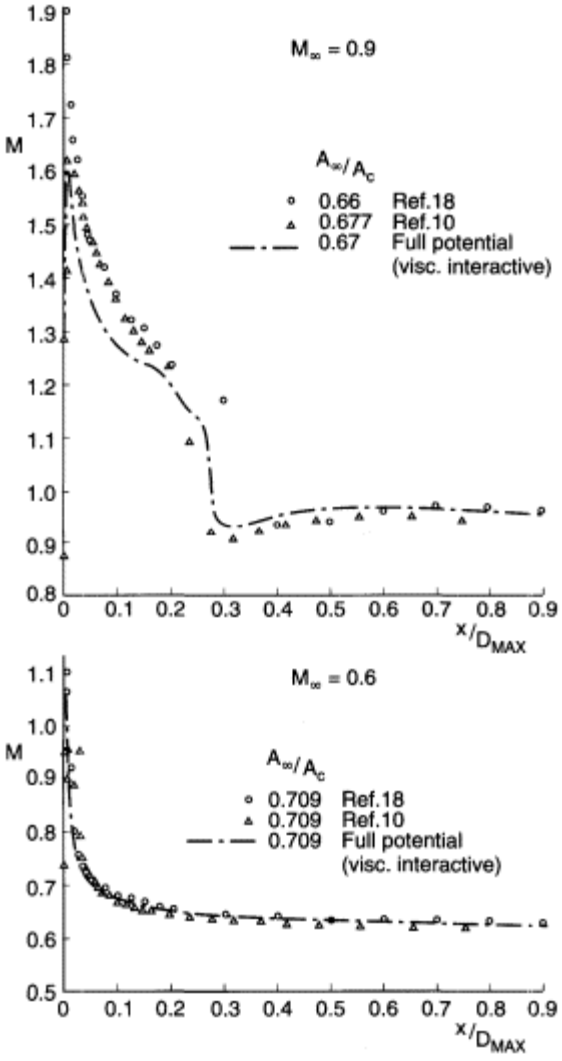

Figure 9.20
Comparison of measured and calculated cowl surface Mach number distributions at $M¥ = 0.6$ and 0.9 for NACA-1-85-100 cowl.

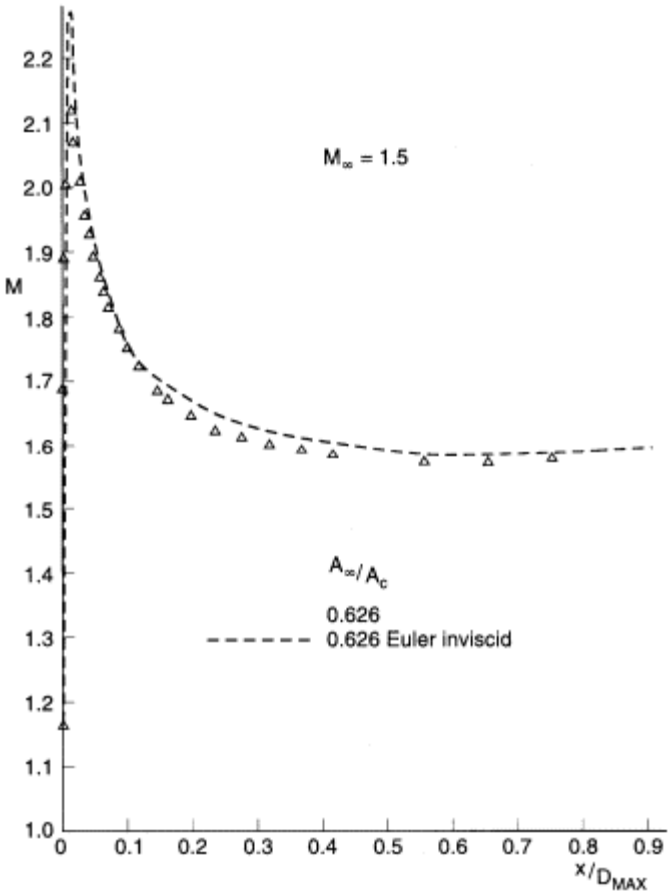

Figure 9.21
Comparison of measured and calculated cowl surface Mach number distribution at *M*¥ = 1.5 for NACA-1-85-100 cowl.

divided differences are not. To overcome this difficulty and to ease computational procedures, an analytical representation of the NACA-1 profile series was used that was a very close approximation to the original coordinates. Fig. 9.23 shows the lack of smoothness of the NACA-1 profile compared to the ESDU analytical expression, and Fig. 9.24 the effect of smoothing on the computed cowl surface *C*p distribution as compared to the original NACA-1 profile.

Two examples at either end of the Mach number range suffice to show the excellent agreement between the measurements of Ref. 18 and the ESDU Euler calculations (Fig. 9.25) from ESDU Data Item 94015.

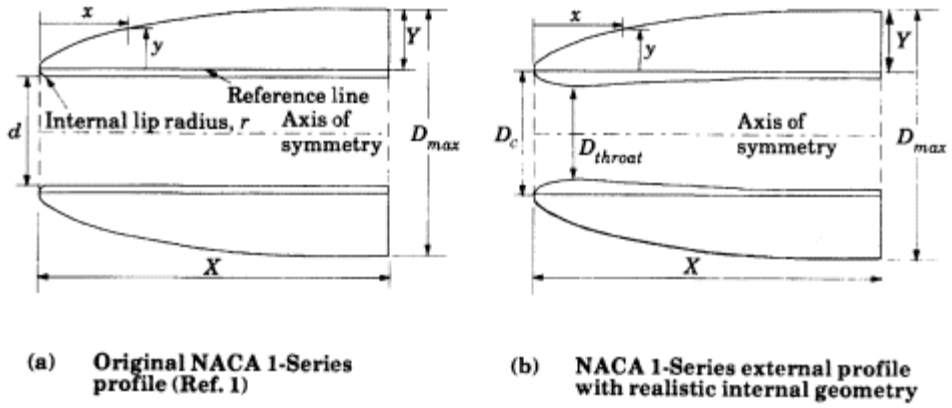

Figure 9.22
Definitions of NACA 1-Series profiles.

9.6.3
Variation of Total External Drag with Flow

To conclude this section on the drag of pitot intakes with subsonic-type cowl shapes at subsonic, transonic and supersonic speeds, it is necessary to make the obvious point that the combination of pre-entry and cowl forces must be consistent. Thus, as shown in Fig. 9.26, an integrated pressure force around the external surface of the cowl from the stagnation point to the

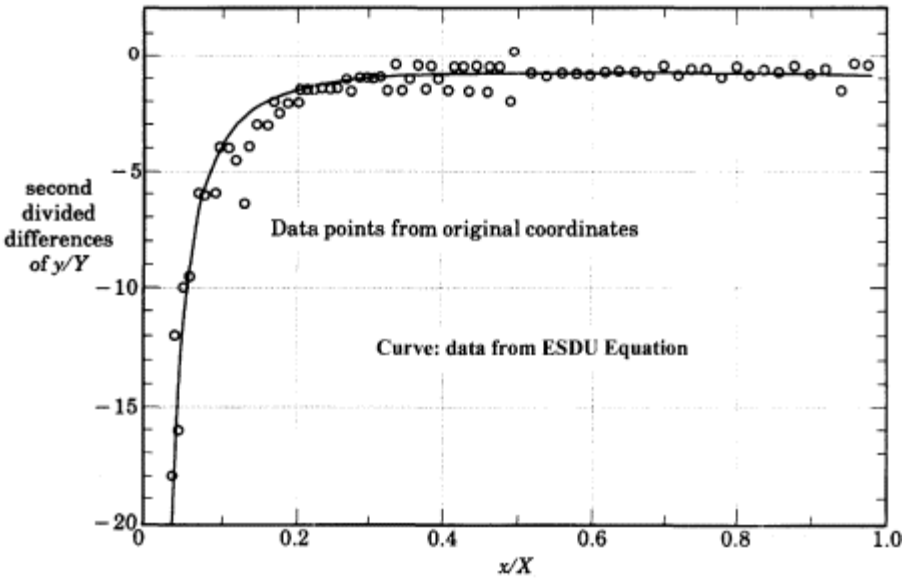

Figure 9.23
Lack of smoothness of NACA 1-Series ordinates,
as shown by second divided differences.

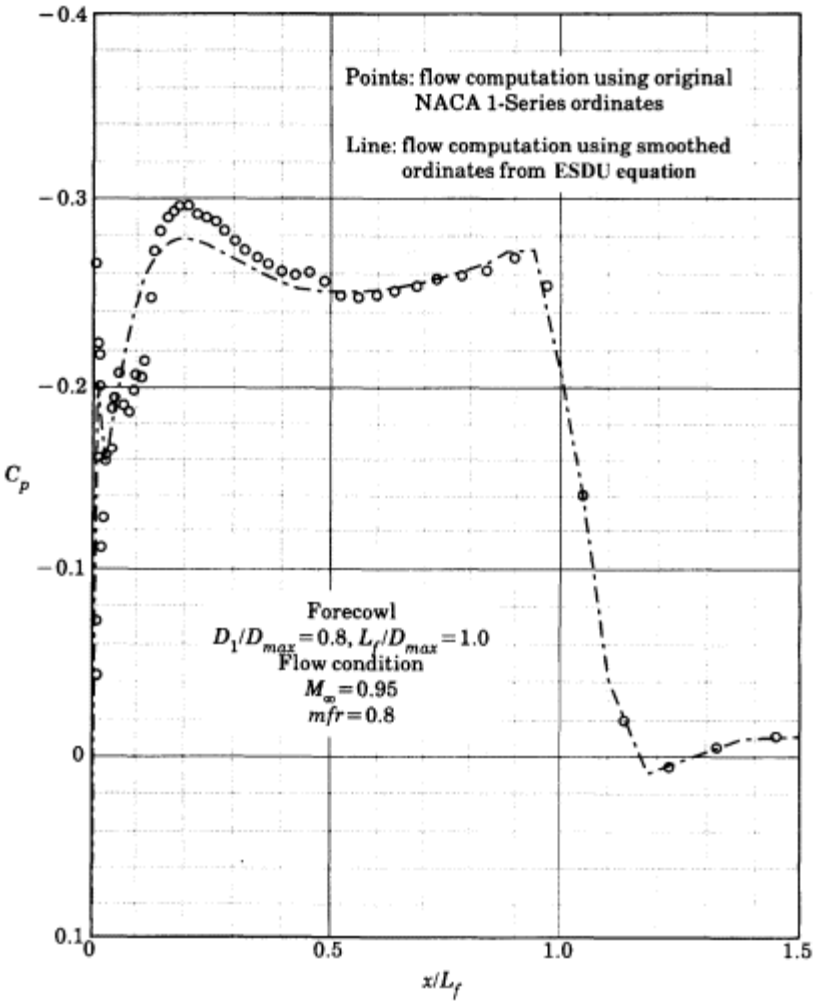

Figure 9.24
Effect of smoothing NACA 1-Series forecowl profile on computed surface pressure coefficient distribution.

maximum area section must not be added to a pre-entry force integrated from the free-stream station to the capture plane (or indeed the simple one-dimensional calculated pre-entry force) to obtain total external drag variation with flow ratio.

9.7
Drag at Supersonic Speeds

Before considering the drag of typical supersonic intakes with sharp-lipped cowls and compression surfaces protruding forward of the capture plane,

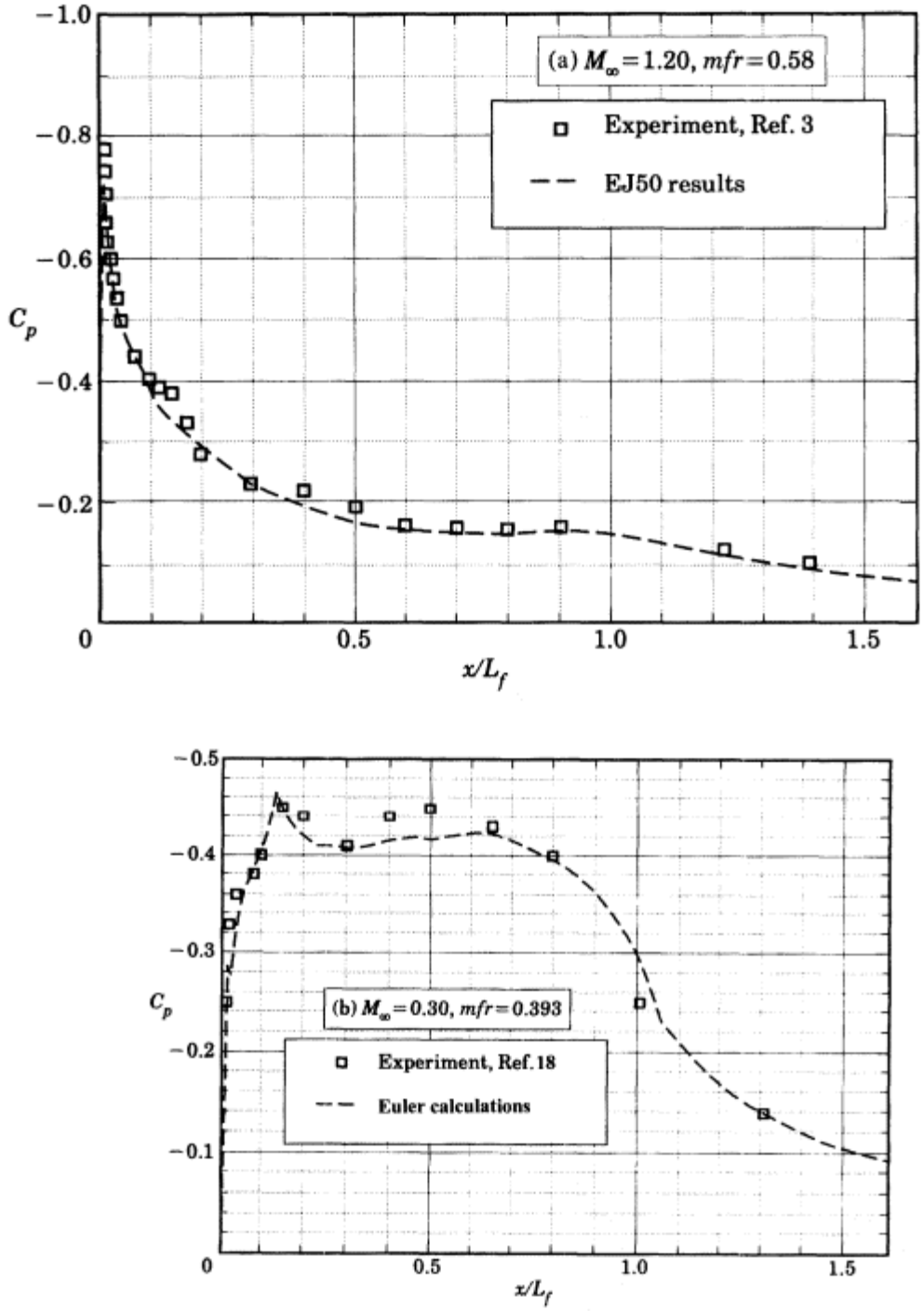

Figure 9.25
Comparison of calculated and observed pressure distribution for NACA 1-Series forecowl with $D1/D\text{max} = 0.71$, $Lf/D\text{max} = 0.50$.

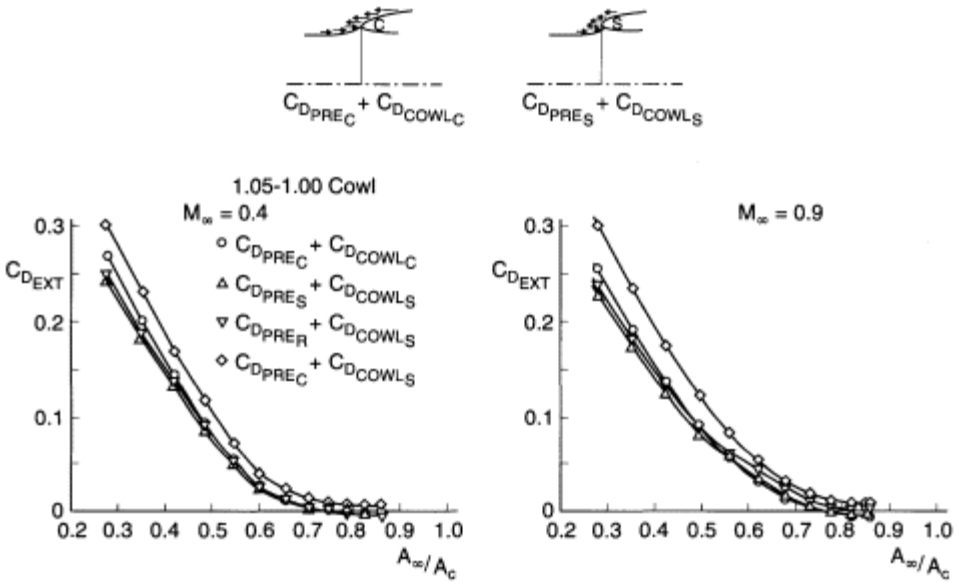

Figure 9.26
Variation of *C*D ext with flow ratio from
differing combinations of *C*D pre + *C*D cowl.

we will, at the risk of some repetition of Sections 9.5 and 9.6, start with the simple pitot intake.

9.7.1
Pitot Intake at Supersonic Speeds

At supersonic speeds, since the normal-shock component is always present in some degree, spillage drag exists for all flow ratios less than 1.0. A disturbed-flow component may also exist, corresponding usually to a lip separation, of the short bubble type, in the flow behind the detached shock (Fig. 9.27): on reattachment, the flow being then supersonic again, a further shock is formed which contributes wave drag to the disturbed-flow component. Typical pressure distribution for a sharp-lipped cowl with a straight two-slope profile are shown in Fig. 9.28. The short separated-flow bubble can be seen to exist at the lowest flow ratio. In Fig. 9.29 the variation of cowl suction with flow ratio for the same cowl is compared with pre-entry drag at two supersonic Mach numbers.

The cowl suction force is now relatively small and consequently spillage drag, particularly at the higher Mach number, is almost equal to pre-entry drag.

9.7.2
External-Compression Intakes.

The distribution of cowl and pre-entry forces and their variation with flow ratio are more complex when the intake has an external-compression

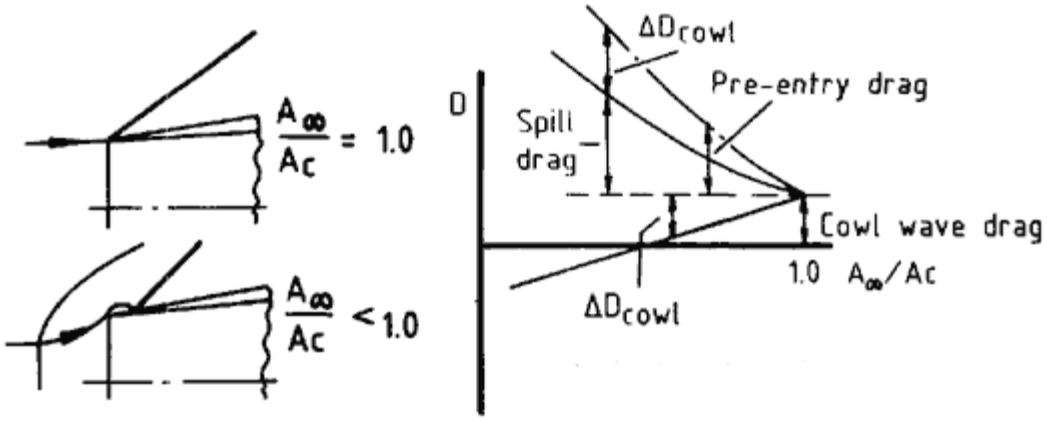

Figure 9.27
Components of drag for pitot intake at supersonic speeds.

forebody. If the oblique shock from the forebody tip lies ahead of the cowl lip, flow ratio for that free-stream Mach number is restricted to a maximum value less than unity, because of the flow deflection through the shock. Maximum flow ratio is therefore associated with a pre-entry drag, (*D*pre)0 say, corresponding to the *supersonic* spillage. For a single-wedge compression surface, this drag is given by:

$$(D_{\text{pre}})_0 = (p_1 - p_\infty)[A_c - (A_\infty)_{\max}] \qquad (9.35)$$

or in coefficient terms, based on *A*c and *q*¥,

$$(C_{D\,\text{pre}})_0 = \frac{p_\infty}{q_\infty}\left(\frac{p_1}{p_\infty} - 1\right)\left[1 - \left(\frac{A_\infty}{A_c}\right)_{\max}\right] \qquad (9.36)$$

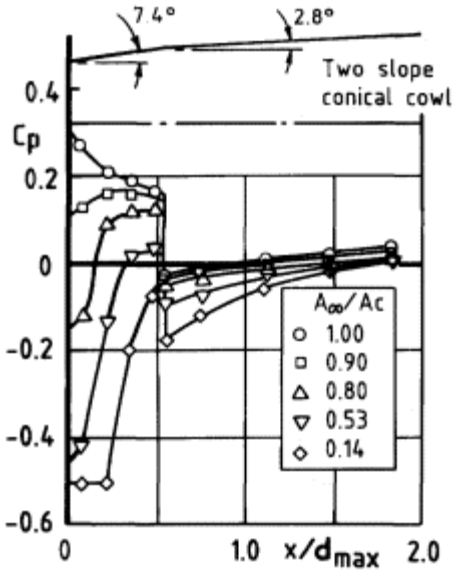

Figure 9.28
Pressure distribution over sharp-lipped two-slope conical cowl.

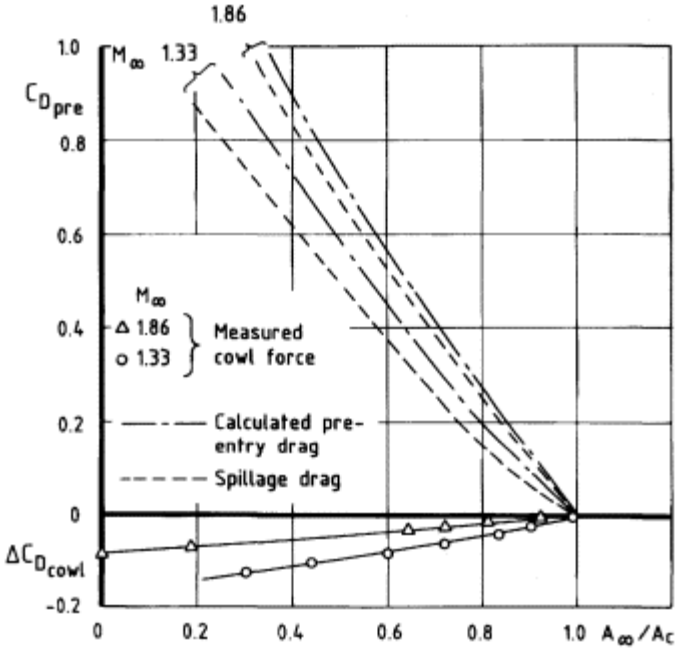

Figure 9.29
Variation of spillage drag, pre-entry drag and change in cowl force with flow ratio at *M*¥ 1.86 and 1.33 for cowl of Fig. 9.28.

where *p*1 is the static pressure behind the oblique shock. (*A*¥/*A*c)max was derived in Chapter 5, at Equation 5.7. For a single-cone compression surface, pressure is not constant between the conical shock and the cowl lip (Section 5.2) but writing $\bar{p}$ as a mean value, we have the approximate relationship

$$(C_{D\,pre})_0 = \frac{p_\infty}{q_\infty}\left(\frac{\bar{p}}{p_\infty} - 1\right)\left[1 - \left(\frac{A_\infty}{A_c}\right)_{max}\right] \qquad (9.37)$$

where (*A*¥/*A*c)max is now given by Equation (5.8). Exact values for the cone case, as given by Fraenkel (1951), are shown in Fig. 9.30(a): for these the pressures have been integrated numerically along the conical streamlines. For 30° cone angle the evaluation from Equation (9.37) is given for comparison. The underestimation is caused mainly by an overestimation of maximum flow ratio, which comes from using the hyperbolic streamline approximation in Equation (5.8). Values of (*C*Dpre)0 for single-wedge intakes are shown in Fig. 9.30(b).

For a double-wedge intake the pre-entry drag at maximum flow is:

$$(D_{pre})_0 = (p_1 - p_\infty)[A_1 - (A_\infty)_{max}] + (p_2 - p_\infty)(A_c - A_1) \qquad (9.38)$$

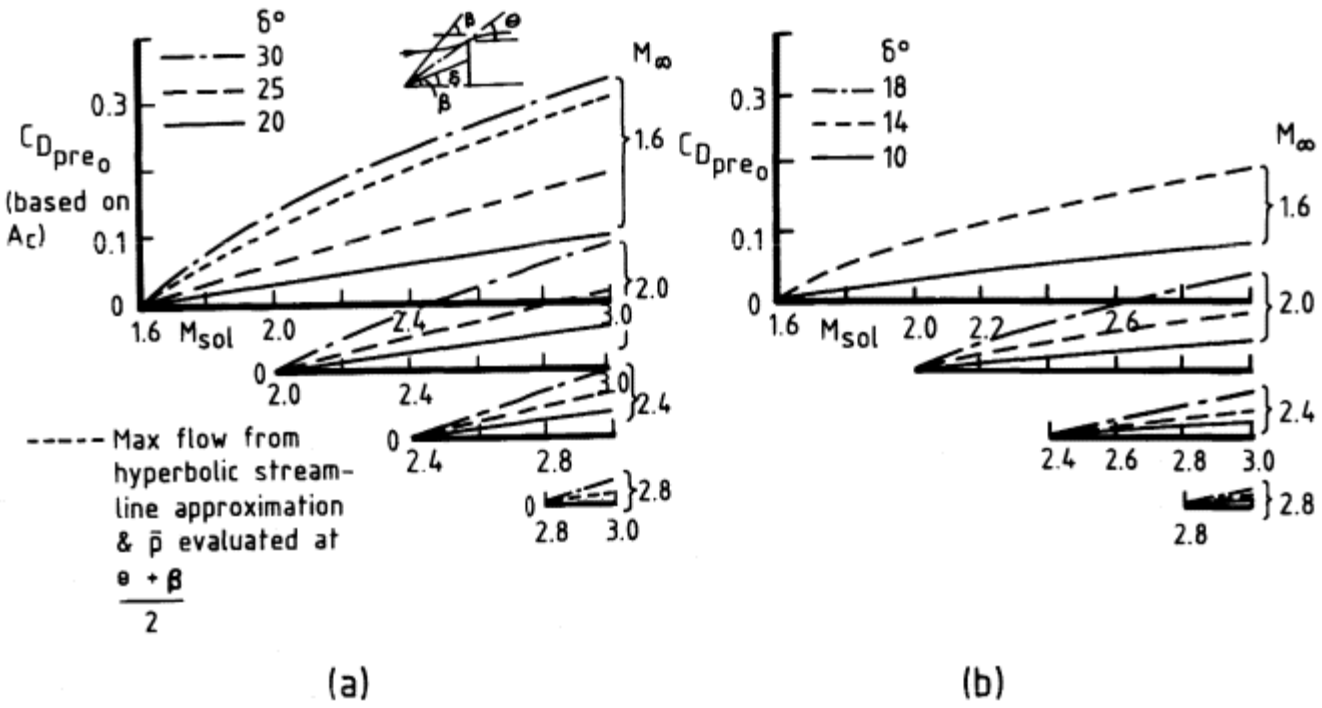

Figure 9.30
Variation of pre-entry drag at maximum intake flow with free stream and shock-on-lip Mach numbers for (a) single-cone and (b) single-wedge intakes.

where $A1$ is the area enclosed by the maximum-flow streamtube at its intersection with the second oblique shock. In coefficient form, this is:

$$(C_{D\,pre})_0 = \frac{p_\infty}{q_\infty}\left(\frac{p_1}{p_\infty} - 1\right)\left[\frac{A_1}{A_c} - \left(\frac{A_\infty}{A_c}\right)_{max}\right]$$

$$+\frac{p_\infty}{q_\infty}\left(\frac{p_2}{p_\infty} - 1\right)\left(1 - \frac{A_1}{A_c}\right) \qquad (9.39)$$

which can be expressed in the form:

$$(C_{D\,pre})_{0\ (2\text{-wedge})} = (C_{D\,pre})_{0\ 1\text{-wedge})} + (C_{D\,pre})_{0\ (\delta 2)} \qquad (9.40)$$

where

$$(C_{D\,pre})_{0\,(\delta 2)} = K\left[\left(\frac{A_\infty}{A_c}\right)_{max\,(1\text{-wedge})} - \left(\frac{A_\infty}{A_c}\right)_{max\,(2\text{-wedge})}\right] \qquad (9.41)$$

d2 is the angle of the second wedge. The parameter K is a function of $M¥$, $M2$ and the first-wedge angle d1: its variation, as given by ESDU (1975) is shown in Fig. 9.31. Maximum flow ratio for a double-wedge intake is determined by Equation (5.9).

Drag from subsonic spillage occurs directly the flow ratio is reduced from the maximum value. The process is illustrated in Fig. 9.32. At and below the flow ratio Ap/Ac say at which the shock intersection point coincides with the dividing streamline (conditions C and D, see also Chapter 5, Section 5.2) the spillage situation is similar to that of a pitot intake, since the compression surface shock is contained within the internal flow, so the

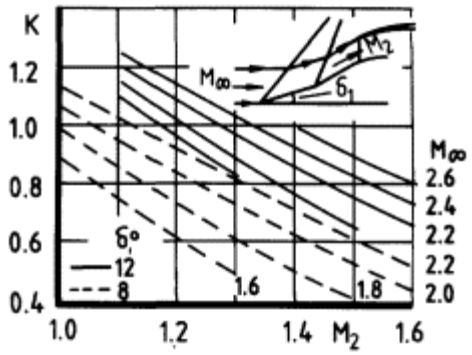

Figure 9.31
Double-wedge pre-entry drag factor K
for first-wedge angles 8° and 12° (ESDU).

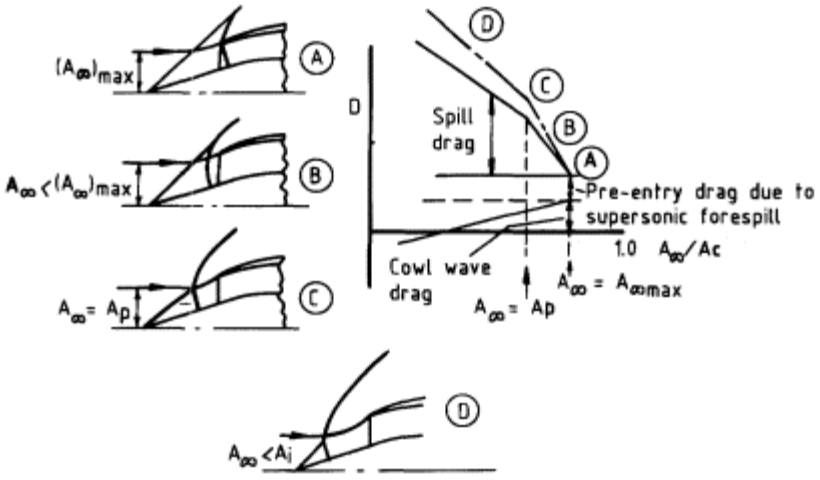

Figure 9.32
Components of drag for forebody intakes at supersonic speeds.

variation of pre-entry drag with flow ratio is as for the pitot. Between (*A*¥/*A*c)max and *A*p/*A*c however, the rate of increase of pre-entry drag is greater (condition B). Cowl drag at maximum flow, (*D*c)0, is usually calculated for the free-stream Mach number and flow direction, the influence of the compression surface being demonstrably small. Change in cowl drag D*D*c with flow ratio can then be assumed the same as for a pitot intake.

A simple method of estimating spillage drag can be constructed by analogy with the Fraenkel method for pitot intakes. In Fig. 9.33 cases A, B and C illustrate conditions for the different positional relationships between compression surface and cowl. With conditions as in B or C, the drag at any flow ratio is given by

$$D = \int_{ab} (p - p_\infty)\mathrm{d}A + \int_{bc} (p_{w2} - p_\infty)\mathrm{d}A + D_c \qquad (9.42)$$

*p*w2 being the pressure behind the second (i.e. normal) shock. It is assumed that the last two terms can be replaced by the Fraenkel approximation, since for pitot intakes this is closely valid at Mach numbers above 1.8, thus

$$D = \int_{ab} (p - p_\infty)\mathrm{d}A + (p_{w2} - p_\infty)(A_c - A_b) + (D_c)_0 \qquad (9.43)$$

We may note that the substitution implies that an underestimate in the second term of Equation (9.42) which is made by writing it as the Fraenkel product in Equation (9.43) is compensated by neglecting in the latter the D*D*c term. Spillage drag being the difference between *D* and its value *D*0 at maximum flow, and *D*0 being the sum of (*D*pre)0 and (*D*c)0, we have

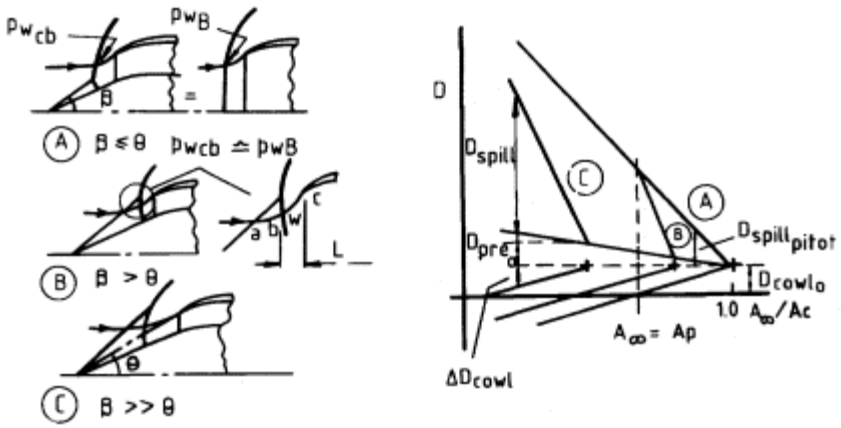

Figure 9.33
Influence of forebody position on drag components.

$$D_{\text{spill}} = \int_{\text{av}} (p - p_\infty)\mathrm{d}A + (p_{\text{w2}} - p_\infty)(A_{\text{c}} - A_{\text{b}}) - (D_{\text{pre}})_0 \qquad (9.44)$$

The area *A*b at point b is derived by assuming a linear movement of the normal shock with spillage ratio, from *L* = 0 see sketch at B when *A*¥ = (*A*¥)max to *L* = *L*max when *A*¥ = 0, where *L*max is the calculable stand-off distance of a bow shock for a bluff solid body with the same external geometry as the intake.

If the shock intersection point coincides at some stage with the dividing streamline (case B) then at this point and for all lower flow ratios

$$D_{\text{spill}} = (p_{\text{w3}} - p_\infty)(A_{\text{c}} - A_\infty) - (D_{\text{pre}})_0 \qquad (9.45)$$

where *p*w3 is the pressure behind the third (i.e. outer) shock as calculated from the compatibility considerations described in Chapter 5, Section 5.5.3.

When the position of the compression surface is such that b is less than or equal to q case A (*D*pre)0 is zero and thus

$$D_{\text{spill}} = (p_{\text{w3}} - p_\infty)(A_{\text{c}} - A_\infty) \qquad (9.46)$$

In many cases, *p*w3 approximates closely to the pressure behind a normal shock at free stream Mach number, so that *D*spill is very close to the pitot intake value.

9.8
Cowl Pressure Drag

In this section we are concerned essentially with cowl pressure drag at supersonic speeds and *full flow*. Expressed in Equation (9.8) as (*D*p)0, this is

one of the two main components of supersonic intake drag, the other being spillage drag. To reduce notational complexity the symbol (Dp)0 is reduced to D (or CD as a coefficient) throughout the section.

9.8.1
Axisymmetric Sharp-Lipped Cowls

Historically the first predictions of supersonic cowl pressure drag (or *wave drag*) were obtained for axisymmetric sharp-lipped cowls, at full flow and zero angle of incidence, using linear, i.e. first-order, theory. The full gas dynamic equation in cylindrical coordinates x (axially) and r (radially) is:

$$\left(1-\frac{u^2}{a^2}\right)\frac{\partial u}{\partial x}+\left(1-\frac{v^2}{a^2}\right)\frac{\partial v}{\partial r}-\frac{uv}{a^2}\left(\frac{\partial u}{\partial r}+\frac{\partial v}{\partial x}\right)+\frac{v}{r}=0 \qquad (9.47)$$

where u and v are axial and radial velocities respectively and a is the velocity of sound. The equation is linearised by introducing perturbation potentials.

$$u_{\mathrm{p}}=\frac{\partial \phi}{\partial x},\ v_{\mathrm{p}}=\frac{\partial \phi}{\partial r}$$

and assuming

$$u=U+u_{\mathrm{p}},\ v=v_{\mathrm{p}} \qquad (9.48)$$

where up and vp are small compared with U and a. Substituting the relations (9.48) in Equation (9.47) and neglecting squares and products of the perturbation potentials leads to the linearised form

$$\frac{\partial^2 \phi}{\partial r^2}-\beta^2\frac{\partial^2 \phi}{\partial x^2}+\frac{1}{r}\frac{\partial \phi}{\partial r}=0 \qquad (9.49)$$

where b2 = M2 1. Using this equation, Lighthill (1945, 1948) derived expressions for pressure coefficients on slender bodies with both continuous and discontinuous variations of body surface angle. Fraenkel (1951) extended this work to open-nosed bodies of revolution. Willis and Randall (1955) applied slender body theory to a more general family of curved profiles, defined by the relation for radius

$$r=r_{\mathrm{m}}-(r_{\mathrm{m}}-r_{\mathrm{c}})\left(1-\frac{x}{\ell}\right)^n \qquad (9.50)$$

The symbols are illustrated in Fig. 9.34: the definition includes both conical (n = 1) and parabolic (n = 2) profiles. Willis and Randall obtained the

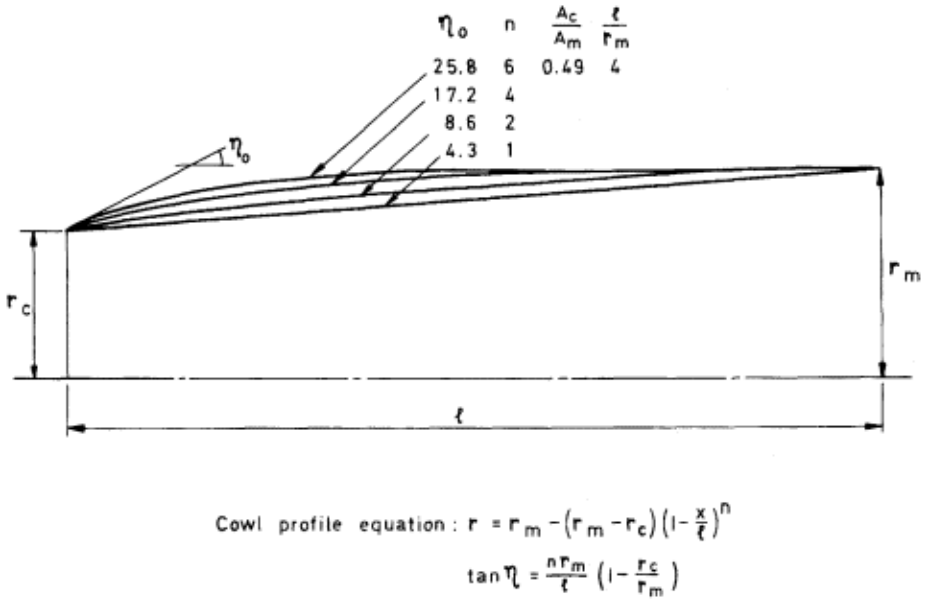

Figure 9.34
Family of cowl profile shapes (Willis and Randall).

following general expression for the drag coefficient *C*D, based on maximum cross-sectional area:

$$C_D\left(\frac{\ell}{r_m}\right)^2 = 2n^2\left(1-\frac{r_c}{r_m}\right)^2\left(a + b\frac{r_c}{r_m} + c\frac{A_c}{A_m} + \frac{A_c}{A_m}\log\frac{2\ell}{\beta r_c}\right) \qquad (9.51)$$

in which *a*, *b* and *c* are functions of *n*, plotted in Fig. 9.35. The conical profile (*n* = 1) has discontinuities in slope at the beginning and end and the expression for drag is

$$C_D\left(\frac{\ell}{r_m}\right)^2 = 2\left(1-\frac{r_c}{r_m}\right)^2\left\{\frac{r_c}{r_m} - \left(1+\frac{A_c}{A_m}\right)\left(\frac{1}{2} - \log\frac{2\ell}{\beta r_m}\right) - \frac{A_c}{A_m}\log\frac{r_c}{r_m}\right\} \qquad (9.52)$$

Using quasi-cylinder approximations rather than those of slender bodies, Ward (1949) deduced a simple expression for the drag of a closed conical body, namely

$$C_D = \frac{D}{\pi \bar{r}^2} = 4\eta^2 U_1\left(\frac{\ell}{\beta \bar{r}}\right) \qquad (9.53)$$

in which $\bar{r}$ is the mean radius, h the cone semi-angle and $U1(x)$ is the function shown plotted in Fig. 9.36. Warren and Gunn (1948) showed that for an open-nosed body a weighted mean radius

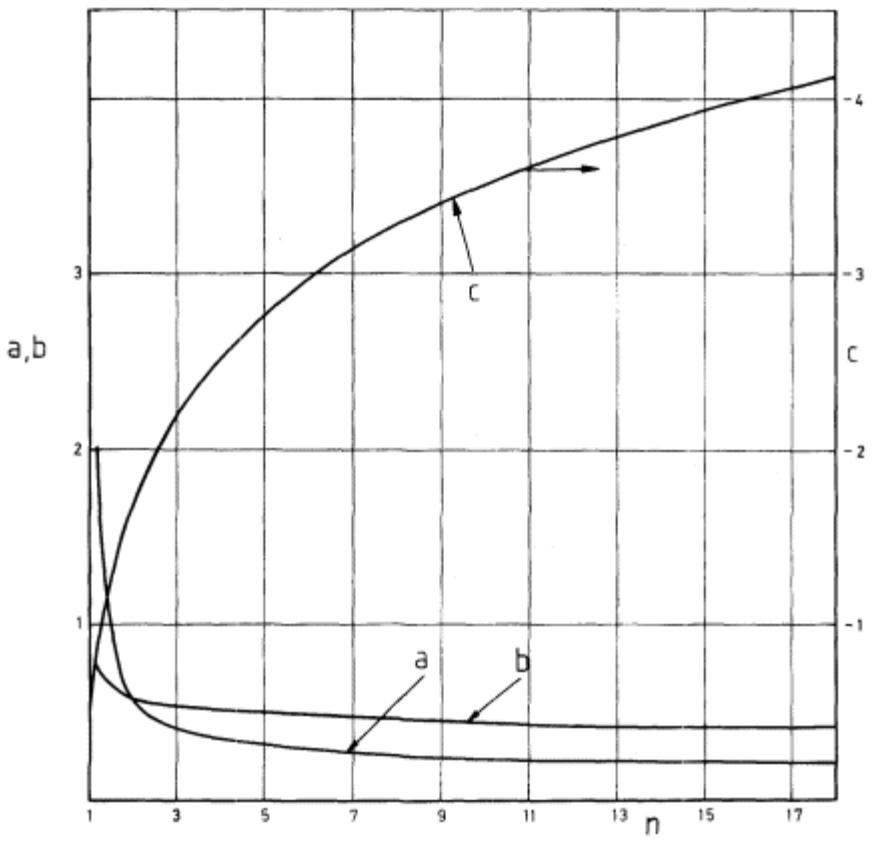

Figure 9.35
Variation of Willis and Randall functions *a*, *b*, *c*.

$$\bar{r} = (r_c^2 + r_m^2)/2$$

gives a better result than a simple arithmetic mean and substituting for $\bar{r}$ and ℓ, Equation (9.53) becomes

$$C_D = \frac{D}{\pi r_m^2} = 2\eta^2\left(1 + \frac{r_m^2}{r_c^2}\right) U_1 \left\{ \frac{\sqrt{2}}{\eta\beta} \cdot \frac{1 - \frac{r_m}{r_c}}{\left(1 + \frac{r_m^2}{r_c^2}\right)^{\frac{1}{2}}} \right\} \qquad (9.54)$$

Fraenkel (1951), applying the quasi-cylinder approximations to open-nosed bodies, gave the drag of conical profiles in the form

$$C_D \left(\frac{\ell}{r_m}\right)^2 = 4\left(\frac{\bar{r}}{r_m}\right)^2 \left(\frac{\ell}{L}\right)^2 U_1\left(\frac{\ell}{\beta\bar{r}}\right) \qquad (9.55)$$

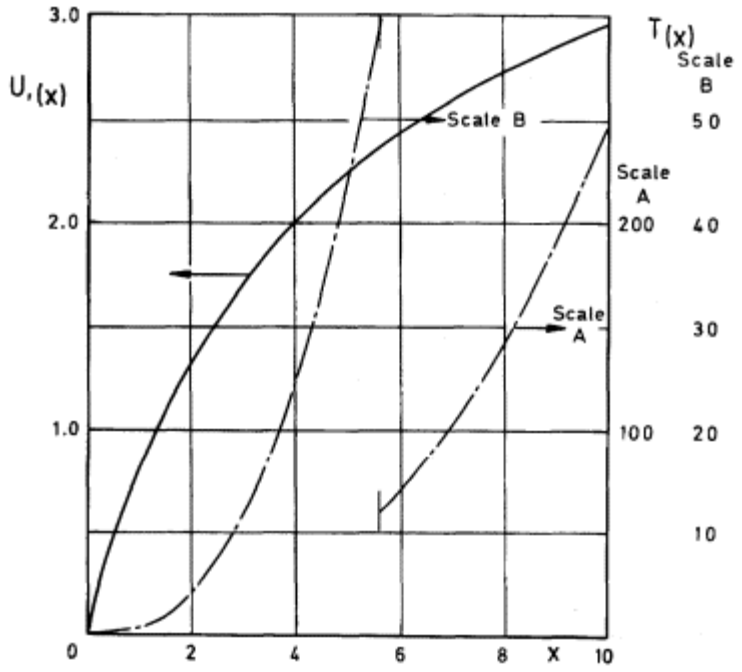

Figure 9.36
Functions $U(x)$ and $T(x)$.

which for the cowl with a two-straight-line profile shown in Fig. 9.28 leads to:

$$C_D = 4\left(\frac{\bar{r}}{r_m}\right)^2 \left[\eta_1^2\, U_1\left(\frac{\ell_1}{\beta\bar{r}}\right) + \eta_2^2\, U_1\left(\frac{\ell_2}{\beta\bar{r}} - \frac{\ell_1}{\beta\bar{r}}\right) + \eta_1\eta_2 \left\{U_1\left(\frac{\ell_2}{\beta\bar{r}}\right) - U_1\left(\frac{\ell_1}{\beta\bar{r}}\right) - U_1\left(\frac{\ell_2}{\beta\bar{r}} - \frac{\ell_1}{\beta\bar{r}}\right)\right\}\right] \qquad (9.56)$$

For parabolic profiles Fraenkel's result is:

$$C_D\left(\frac{\ell}{r_m}\right)^2 = 8\left(\frac{r_m}{\ell}\right)^2\left(\frac{\bar{r}}{r_m}\right)^4\left(\frac{\ell}{L}\right)^4 \cdot T\left(\frac{\ell}{\beta\bar{r}}\right) \qquad (9.57)$$

where T(x) is a function also plotted in Fig. 9.36. L is the length of the full pointed body, of which the open-nosed portion is of length ℓ. Subsequently (1952) Fraenkel produced a synthesis of the slender body and quasi-cylinder methods, which used each in its best range of application and included a gradation between the two. Charts are given of $C_D(\ell/r_m)^2$ as functions of Ac/Am for different values of $\beta r_m/\ell$. In Fig. 9.37 Fraenkel's results for conical profiles are compared with those of Willis and Randall and with the results of characteristics calculations by Valentine (1961).

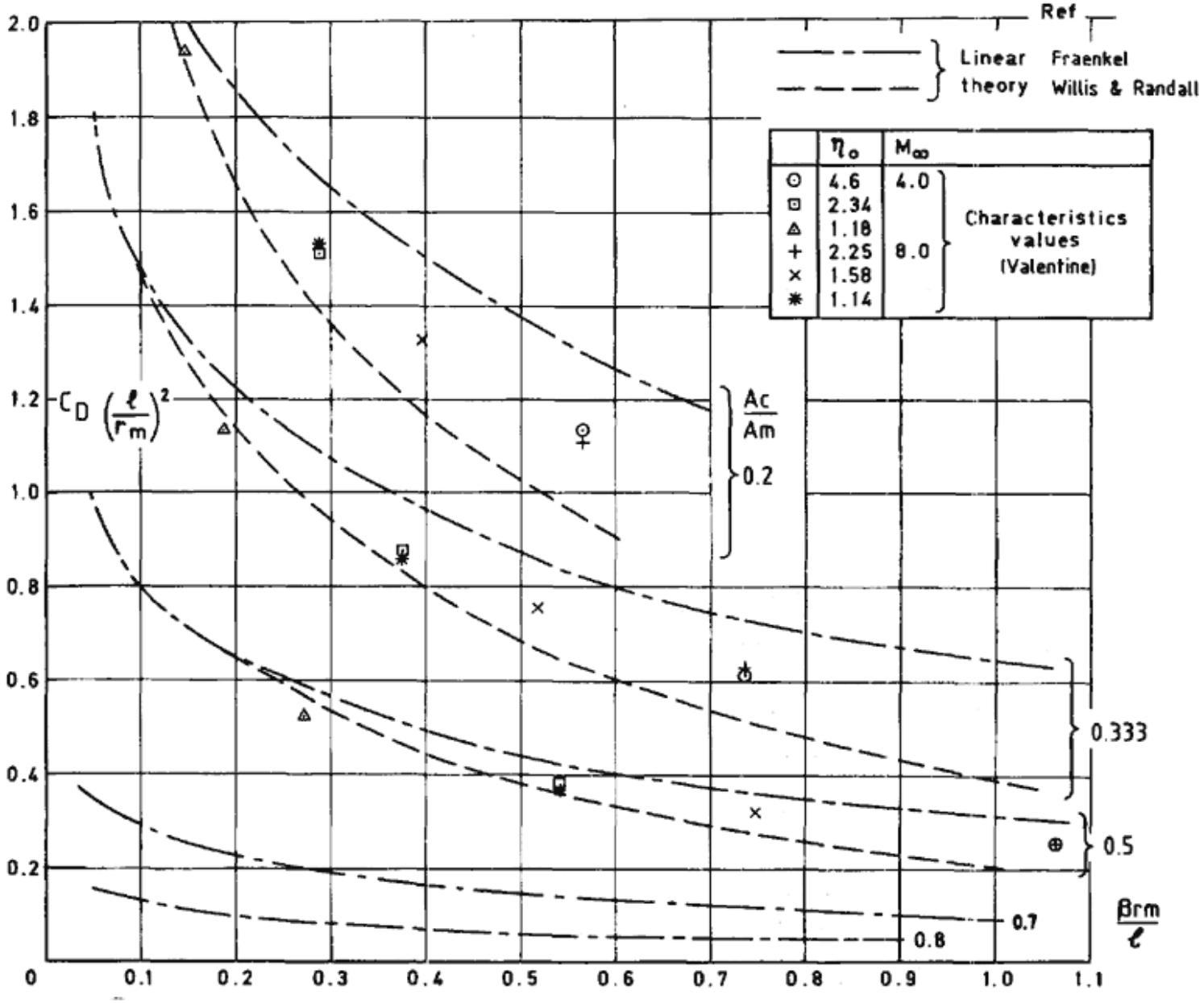

Figure 9.37
Comparison of slender-body values and characteristics values for axisymmetric cowl drag.

Second-order flow theory has been studied by Van Dyke (1952). However, both first and second order theory become increasingly inaccurate as the initial angle of the cowl approaches free stream Mach angle and this situation is relevant especially to intakes with external compression, where the cowl external surface tends to be aligned fairly close to the local flow direction produced by the compression surface. Other methods may then need to be used for the evaluation of wave drag. Most accurate is the method of characteristics: others, in order of decreasing complexity but also decreasing accuracy, are the methods of second order shock-expansion, generalised shock-expansion, tangent-wedge and impact theory. Fig. 9.38 is used to illustrate the essentials of these methods: for each it is convenient to divide the cowl profile into a number of straight line segments and to evaluate the pressure coefficient on each segment before summing to obtain the drag. The method of characteristics cannot be fully illustrated in the diagram. Presley and Mossman (1958) have given all the information

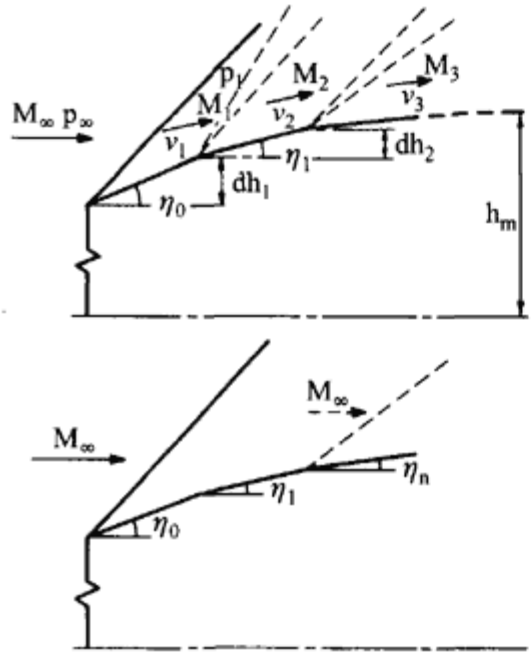

Generalised shock-expansion
1st segment: p_1 is static pressure behind oblique shock for $M = M_\infty$ and deflection η_1
2nd segment: M_1 defines Prandtl – Meyer angle ν_1
$\nu_2 = \nu_1 - (\eta_0 - \eta_1)$ defines M_2 and p_2

2nd order shock expansion
After Prandtl – Meyer expansion, pressure on segment falls exponentially towards cone surface pressure (cone angle η_n, $M = M_\infty$) – Ref 17

Tangent wedge: p_n is static pressure behind oblique shock for $M = M_\infty$ and deflection = η_n

Impact theory: $C_{p_n} = 2\sin^2 \eta_n$

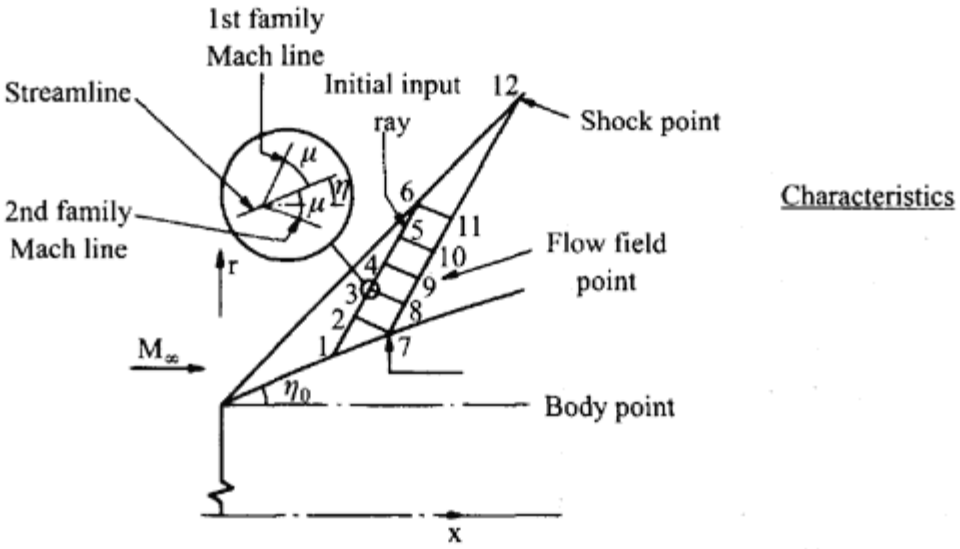

Figure 9.38
Methods of evaluating cowl pressure distributions.

necessary for calculating the geometry of points on the input ray 1 to 6, at the field points 8 to 11 (these are at the intersection of first and second family Mach lines) and at the body and shock-wave points 7 to 12. Presley and Mossman present results from applying all the above-mentioned methods to the same family of cowl profiles as was studied by Willis and Randall.

Samanich (1959) has given experimental drag values, obtained from surface pressure measurements, for a series of elliptic-profile cowls (which can be approximated by the Willis and Randall family). In Fig. 9.39 these results are displayed first in linear-theory form, that is plotting $C_D(\ell/r_m)^2$ against $\beta r_m/\ell$, and also using hypersonic similarity parameters, g*M*¥2*C*d/2 and *M*¥h0. On the latter presentation, the collapse of experimental points in groups according to area ratio, independently of fineness ratio, is interesting, as is the collapse of characteristics values for different Mach numbers. Comparison with two-dimensional shock-expansion theory is indicated in the linear-

theory presentation.

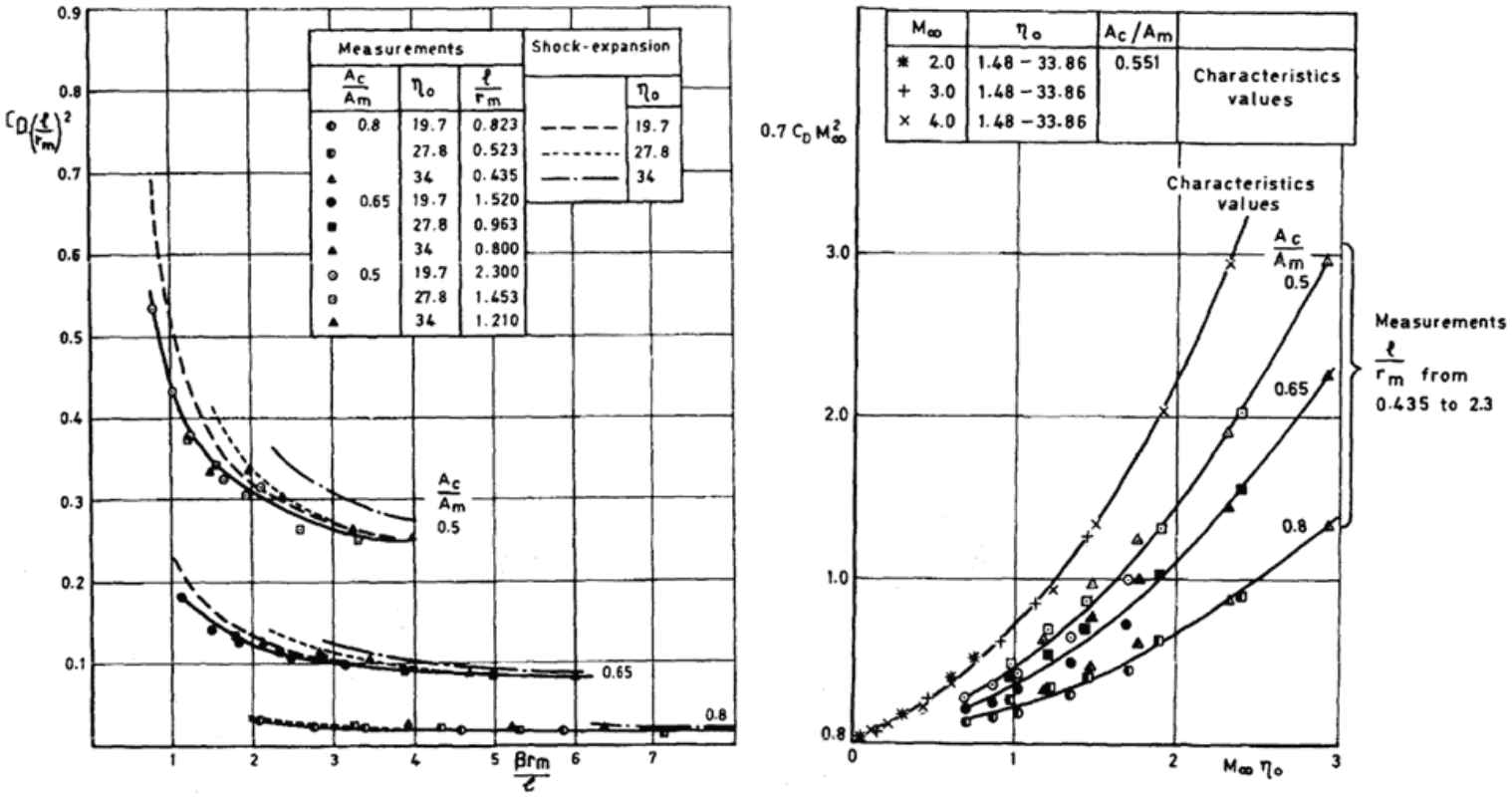

Figure 9.39
Correlation of cowl drag values from measurement and shock-expansion calculations.

Differences between characteristics values and those of the other methods are shown in Fig. 9.40 for a cowl of medium area ratio (*Ac*/*Am* = 0.551) and high fineness ratio ($\ell/r_m = 10$) at Mach numbers from 2.0 to 4.0. For this cowl, with nose angle h0 varying from 1° to 36°, second-order shock expansion theory is seen to give very good results. With the lower fineness ratios and generally higher area ratios of the experimental cases of Fig. 9.39, the simpler shock-expansion method is sufficiently accurate for most purposes, until conditions for detachment of the nose shock are approached. In Fig. 9.41, selected measurements are compared with shock-expansion calculations and also with slender body theory.

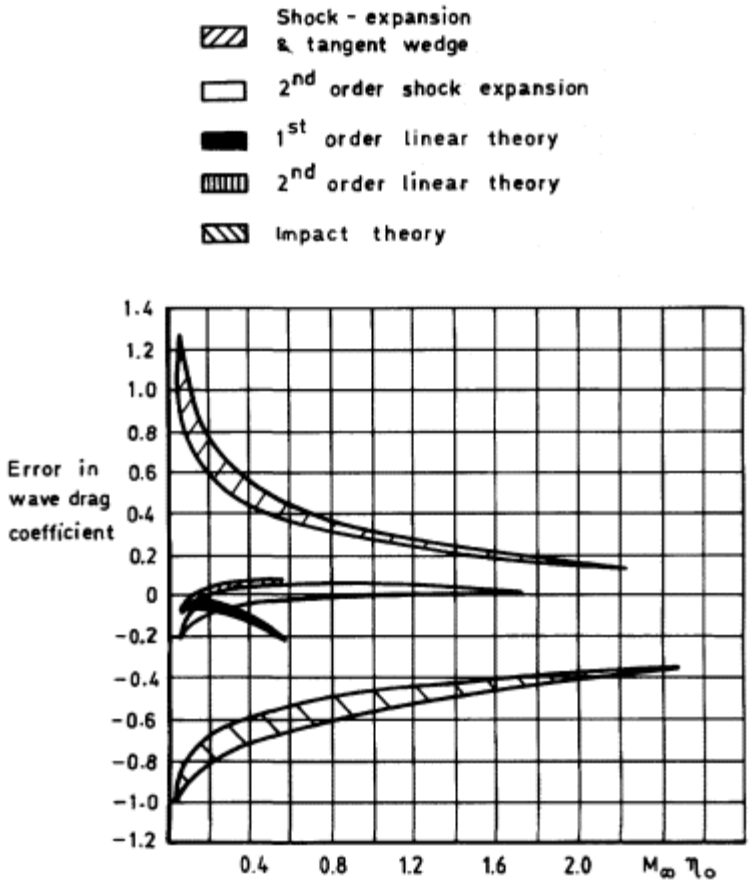

Figure 9.40
Error in wave drag compared to
characteristics method (Presley and Mossman).

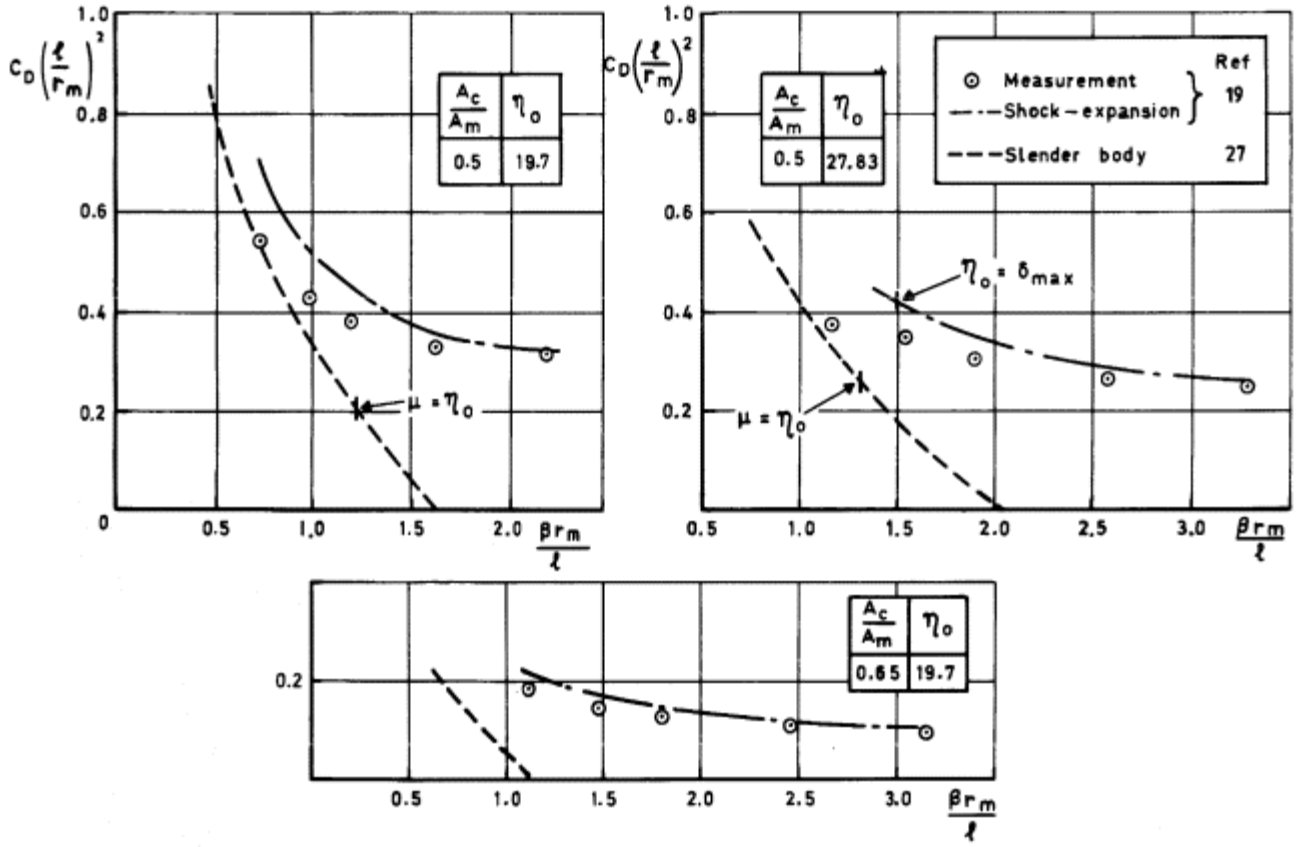

Figure 9.41
Comparison of measurements, shock expansion and slender body theory.

9.8.2
Two-Dimensional Sharp-Lipped Cowls

In two dimensions, cowl drag at full flow may be calculated step by step using the shock-expansion method. Considering the illustration in Fig. 9.38, we have for a first element $^{d\ell}$, of the cowl surface, at angle h0 to the mainstream,

$$D_1 = (p_1 - p_\infty)\mathrm{d}\ell_1 \sin \eta_0 = (p_1 - p_\infty)\mathrm{d}h_1 \qquad (9.58)$$

so that, in terms of a drag coefficient based on *A*m,

$$C_{D1} = \frac{p_\infty}{p_\infty}\left(\frac{p_1}{p_\infty} - 1\right)\frac{\mathrm{d}h_1}{h_m} \qquad (9.59)$$

For a second element, by a similar process,

$$C_{D2} = \frac{p_\infty}{q_\infty}\left(\frac{p_2}{p_1}\cdot\frac{p_1}{p_\infty} - 1\right)\frac{\mathrm{d}h_2}{h_m} \qquad (9.60)$$

A curved profile is represented by a suitable number of straight segments, enabling the progressive calculation to be made.

We now examine the relative cowl drags of the specimen external-compression design, intake A, used for illustration in Chapter 5, and the comparable mixed-compression designs, intakes C and D, introduced in Chapter 6. For intake A (Fig. 5.20), the cowl initial angle is 26°, as determined by the internal-flow requirements. Taking the cowl profile to be composed of four straight-line segments at angles 26°, 20°, 10° and 0°, the calculated drag coefficient is

$$C_D = 0.1432$$

This represents a high drag: in terms of cowl projected area the figure is five times that shown and so is approaching a flat-plate drag coefficient. The first segment is of course the primary contributor, because of its large angle to the flow. With intake C (Fig. 6.10) the cowl initial angle is reduced to 12° by the effect of having one stage of internal oblique-shock compression. For a cowl profile with segments successively at 12°, 8°, 4° and 0°, the drag coefficient comes out to be

$$C_D = 0.0419$$

showing a big reduction compared with intake A. Finally, for intake D (Fig. 6.11), in which the cowl internal line behind the lip is parallel to the free stream, a straight-line external profile at a single 7° angle is suggested: this

reaches the maximum area at an appropriate length. The calculated drag coefficient is then

$$C_D = 0.0295$$

Lower wave drag would have been obtained by using the minimum 4° external angle but this would have resulted in an over-long cowl for the given maximum area. The complete exercise demonstrates the sensitivity of cowl wave drag to lip angle and hence to the degree of flow turning in external compression of the internal flow.

9.8.3
Blunt-Lipped Cowls

Blunt-lipped cowls at supersonic speeds are important in two contexts. The first is when it is required to combine low spillage drag and good high-incidence performance, both at subsonic speeds, with low supersonic wave drag. The second is if a degree of cowl blunting is required to alleviate local rates of aerodynamic heating at high supersonic speeds, yet excessive wave drag needs to be avoided through the supersonic range. The two situations call for somewhat different treatments.

In the first case the supersonic speed range of interest is Mach number from 1.0 to 1.6 or 1.8. The cowl profile may be assumed to be from the NACA 1-series or a similar shape. The rounded lip implies between 5% and 20% contraction in duct area from the highlight to the throat. Maximum flow ratio is consequently lower than the full-flow value 1.0, which would be obtained with a sharp-lipped cowl; the maximum is determined by choking of the throat behind the intake normal shock and is given by

$$\left(\frac{A_\infty}{A_c}\right)_{max} = \frac{P_t}{P_\infty} \cdot \left(\frac{A}{A^*}\right)_\infty \left(\frac{A^*}{A}\right)_t \cdot \frac{A_t}{A_c} \qquad (9.61)$$

If drag is measured on a force balance, it includes a pre-entry drag as well as the cowl drag. Cowl drag can be isolated by surface pressure plotting but a value for the full flow condition has to be obtained by extrapolating the results at lower flow ratios. Some collected results for NACA 1-series profiles of varying length and diameter ratios are shown in Figs. 9.42 and 9.43. Whilst the applicability of linear theory is nominally precluded by the lip rounding, comparisons with linear theory values, calculated for parabolic cowls, is interesting. Fig. 9.42 indicates that the variation of drag with fineness ratio, at constant area ratio, is quite well predicted by linear theory, although the variation with $M¥$ is not. In Fig. 9.43 it is seen that the variation with area ratio at constant fineness is also well predicted.

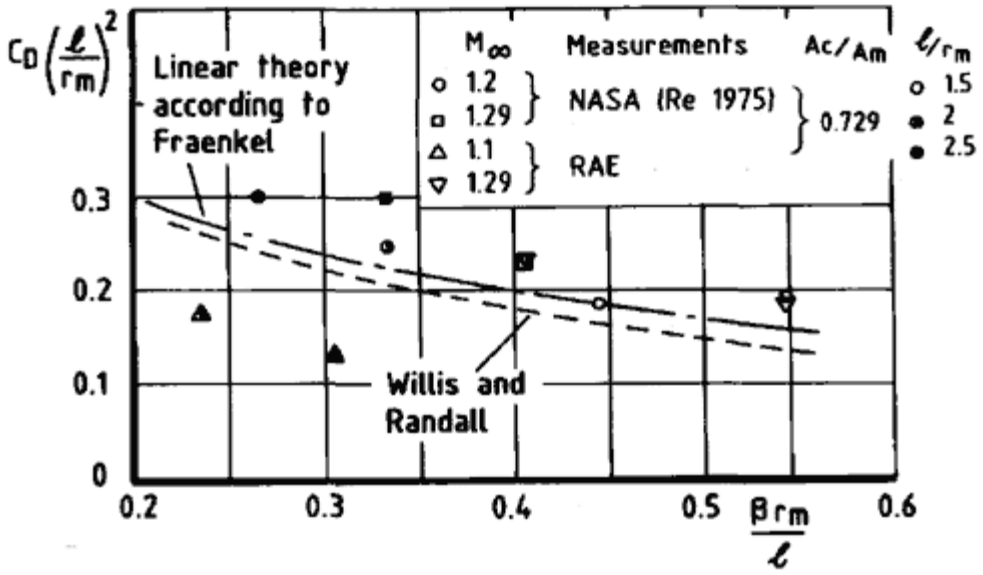

Figure 9.42
Cowl drag of NACA 1-series profiles at
supersonic speeds: variation with fineness ratio.

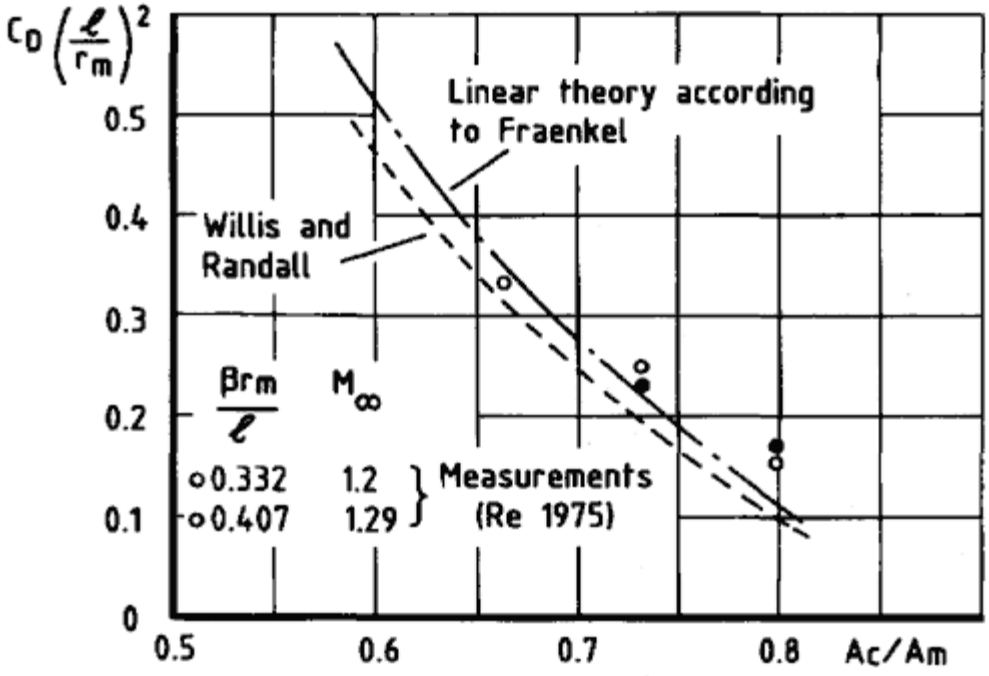

Figure 9.43
Cowl drag of NACA 1-series profiles at
supersonic speeds: variation with area ratio.

Another collection of data for NACA 1-Series cowls for the cowl drag at full flow at supersonic speeds from both UK and NASA measurements is shown in Fig. 9.44. The agreement between the two sources of data and with Euler calculation values for $L/D\text{max} = 1.00$ is good.

The second case concerns the addition of a circular-arc lip to a cowl profile of low angle and zero or small curvature. Fraenkel (1951) suggested following Maccoll's form for the drag of a bluff body, which is

$$C_D = \frac{KP_w - p_\infty}{q_\infty} \tag{9.62}$$

< previous page page_240 next page >

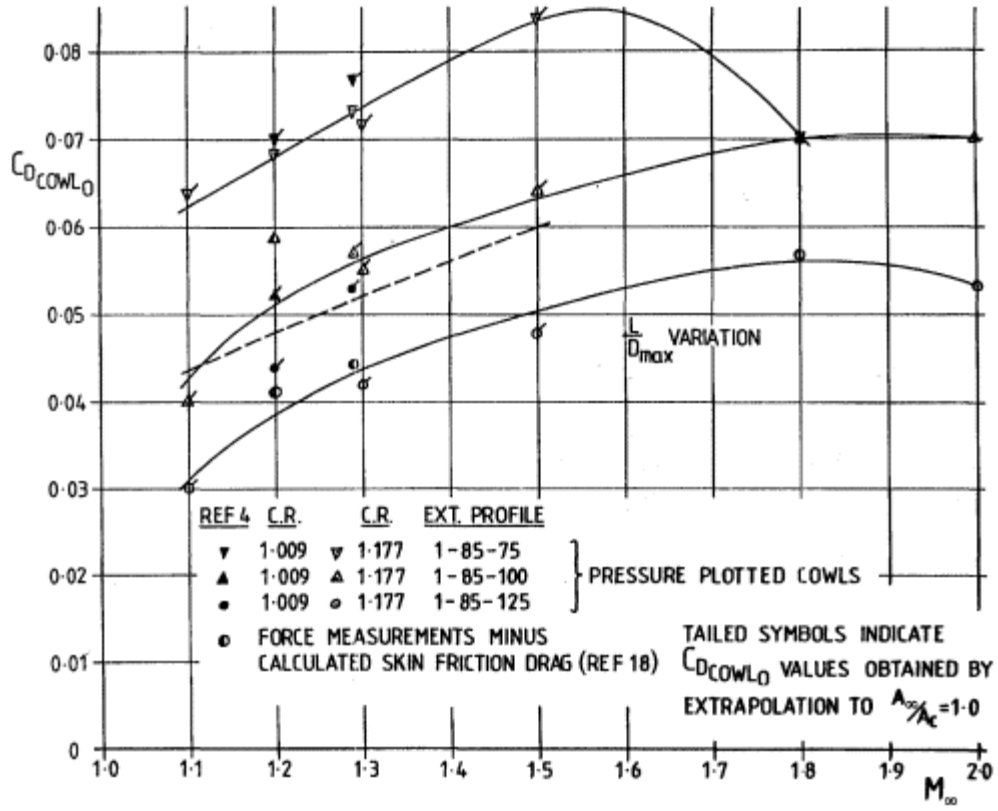

Figure 9.44
Variation of cowl drag at full flow $C_{D\,cowl_0}$ with M¥ for cowls with constant d/Dmax.

where Pw is the total pressure behind a normal shock. For a blunt-lipped intake, the lip drag on this basis becomes

$$(C_D)_{lip} = \frac{(KP_w - p_\infty)}{q_\infty} \cdot 4\frac{r_\ell}{r_c}\left(\frac{r_\ell}{r_c} + 1\right)\frac{A_c}{A_{max}} \qquad (9.63)$$

in which r_ℓ and rc are the lip radius and cowl entry radius respectively. The factor K, as determined from a series of tests on straight profiles with circular-arc lips, is given by:

$$K = 0.24\frac{A_c}{A_m} + 0.57 \qquad (9.64)$$

Pressure plotting measurements on the cowl of a blunt-lipped isentropic-forebody intake (Cubbison and Samanich, 1958) confirm this value at a

higher Mach number, M_∞ = 3.0. Lip drag thus defined is plotted in Fig. 9.45 for values of A_c/A_m from zero to 1.0. This is added to the drag of the profile behind the lip (DC in diagram) treated as a sharp-lipped cowl.

A more detailed method of estimation has been given by Hurd (1965). Valentine (1963) has treated the problem for high supersonic speeds: his analysis leads to results illustrated in Fig. 9.46.

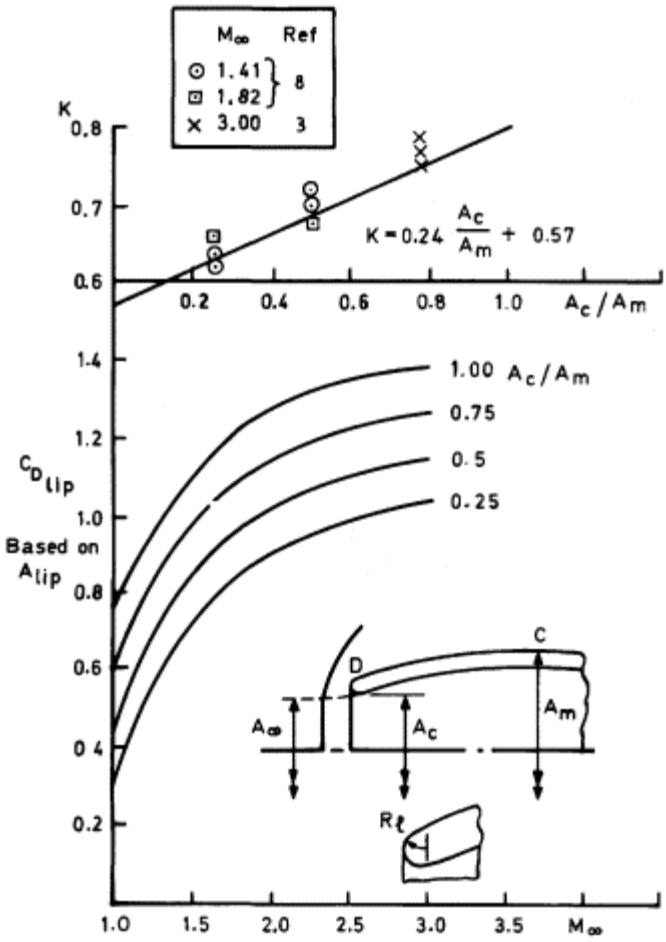

Figure 9.45
Lip-bluntness drag correlation.

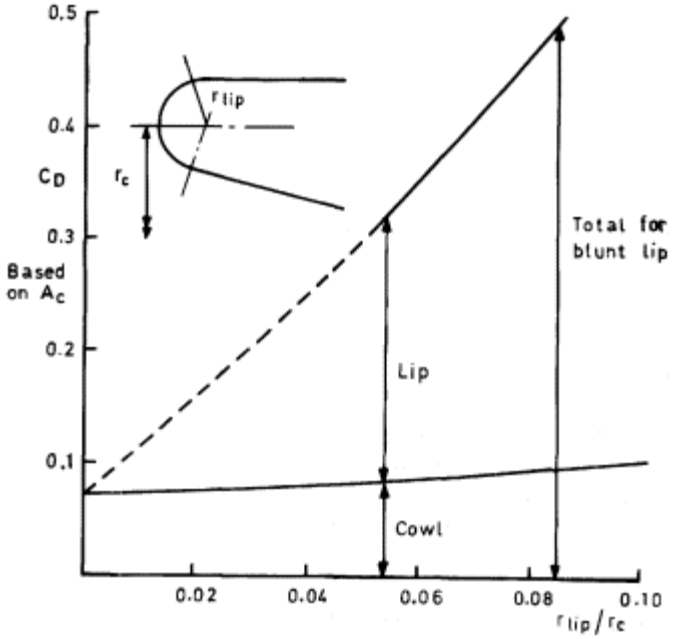

Figure 9.46
Cowl and lip drag at a Mach number of 4 (Valentine).

References.

1 Baals, D.D., Smith, N.F. and Wright, J.B. (1949) 'The development and application of high-critical-speed nose inlets'. NACA, TR 920.

2 Baker, T.J. (1975) 'A numerical method to compute inviscid transonic flows around axisymmetric ducted bodies'. ARA Memo 173: ARC 36314: *Proc. Symposium Transsonicum II.* Gottingen, Berlin: Springer Verlag.

3 Cubbison, R.W. and Samanich, N.E. (1958) 'The effect of spike tip and cowl lip blunting on inlet performance of a Mach 3 external-compression inlet'. NASA, RM E58G02a.

4 ESDU (1975) 'Performance data for the critical operation of nominally two-dimensional double-ramp supersonic intakes'. *Engineering Sciences Data.* Item 75005.

5 Fraenkel, L.E. (1950) 'The external drag of some pitot-type intakes at supersonic speeds. RAE'. I Aero 2380. ARC 13537.

6 Fraenkel, L.E. (1951). 'The theoretical wave drag of some bodies of revolution'. ARC, R & M 2842.

7 Fraenkel L.E. (1951) 'Some curves for the calculation of performance of conical centrebody intakes at supersonic speeds and maximum mass flow'. RAE. TN Aero 2135.

8 Fraenkel, L.E. (1951) 'The external drag of some pitot intakes at supersonic speeds'. Pt. II. RAE Report Aero 2422.

9 Fraenkel, L.E. (1952) 'Curves for estimating the wave drag of some bodies of revolution based on exact and approximate theories'. RAE. TN Aero 2184.

10 Goldsmith, E.L. (1990) 'Forces and pressure distributions at subsonic and supersonic speeds on circular section pitot intakes'. ARA. Report No. 75.

11 Hurd, R. (1965) 'Method for calculating the drag of a supersonic intake having a blunt cowl lip. Rolls-Royce BSE/AP5306 report.

12 Küchemann, D. and Weber, J. (1953) *Aerodynamics of Propulsion.* New York: McGraw-Hill.

13 Lighthill, M.J. (1945) 'Supersonic flow past bodies of revolution'. ARC. R & M 2003.

14 Lighthill, M.J. (1948) 'Supersonic flow past bodies of revolution the slope of whose meridian section is discontinuous. *Quarterly Journal of Mechanics and Applied Mathematics* 1, pt 1.

15 Mount, J.S. (1965) 'Effect of inlet additive drag on aircraft performance. *Journal of Aircraft* 2, no. 5.

16 Pearcey, H.H. (1960) 'The aerodynamic design of section shapes for swept wings'. *Second International Congress, ICAS*, Zurich.

17 Presley, L.L. and Mossman, E.A. (1958) 'A study of several theoretical methods for computing the zero-lift wave drag of a family of open nosed bodies of revolution in the Mach number range 2.0 to 4.0'. NACA, TN 4368.

18 Re. R.J. (1975) 'An investigation of several NACA 1-series inlets at Mach numbers from 0.4 to 1.29 for mass flow ratios near 1.0'. NASA. TM X 3324.

19 Samanich, N.E. (1959) 'Pressure drag of axisymmetric cowls having large initial lip angles at Mach numbers from 1.90 to 4.90'. NASA Memo 1-10-59E.

20 Sears, R.I., Merlet, C.J. and Putland, L.W. (1953) 'Flight determination of drag of normal-shock nose inlets with various cowling profiles at Mach numbers from 0.9 to 1.5'. NACA RM L53 125a.

21 Stanhope, F.W. (1968) 'The performance of NACA 1-series intakes'. Rolls-Royce Power Plant Research Report IAR 85002.

22 Valentine, E.F. (1961) 'External drag estimation for slender conical ducted bodies at high Mach numbers and zero angle of attack'. NASA. TN D648.

23 Valentine, E.F. (1963) 'Some pressure drag effects of rounding the leading edges of hypersonic inlets'. *AIAA Journal* 1, no. 8.

24 Van Dyke, M.D. (1952) 'A study of second order supersonic flow theory'. NACA Report 1081.

25 Ward, G.N. (1948) 'The approximate external and internal flow past a quasi-cylindrical tube moving at supersonic speeds. *Quarterly Journal of Mechanics and Applied Mathematics* 1, pt 2.

26 Warren, C.H.E. and Gunn, R.E.W. (1948) 'Estimation of external drag of an axially symmetric conical nose entry for jet engine at supersonic speeds'. RAE TN Aero 1934.

27 Willis, J.H. and Randall, D.G. (1955) 'The theoretical wave drag of open nose axisymmetrical forebodies with varying fineness ratio, area ratio and nose angle'. RAE TN Aero 2360.

Chapter 10
Shock Oscillation of Supersonic Intakes

10.1
Introduction

In preceding chapters the emphasis has been placed on the flow in and around intakes as it affects internal mean total pressure and external drag. These performance-related quantities are of outstanding importance, but consideration must also be given to the quality of flow delivered by the intake to the engine. The general term for this area of the subject is *compatibility* of the intake and engine: for an engine to perform smoothly, effectively and without malfunction, compatibility with the intake must exist at all operating conditions. Particular aspects of the quality of flow are its stability, its uniformity and its angle of impingement at the engine face. Questions of uniformity and angle are discussed in Chapter 11: in the present chapter we examine an important problem of flow stability, namely the phenomenon of shock oscillation of supersonic intakes.

All supersonic intakes with external compression, having a good level of performance at the critical point, exhibit a marked instability of flow in subcritical operation below some value of the flow ratio, in the form of an oscillation of the shock system, colloquially known as 'buzz'. The phenomenon was first observed and described by Oswatitsch (1944) in experiments on axisymmetric intakes. It received a great deal of attention on similar configurations throughout the 1950s, both in America and in Britain. With the advent of rectangular intake configurations, for both transport and combat aircraft, having variable geometry in the form of adjustable ramps and afterspill vents, the importance of the phenomenon to practical designs receded somewhat because in those cases it could the more readily be avoided. The use of variable geometry is discussed more fully in Chapter 12. There are many instances, however, in both aircraft and missile technology, in which variable geometry is precluded by considerations of weight and cost, and in any event an intake designer needs to be able to predict the extent of stable subcritical flow for a particular intake geometry. The problem of buzz therefore retains, in addition to its

considerable intrinsic interest, a basic practical importance related to its onset and the nature of its development as intake flow ratio is reduced.

10.2
General Description

The details of buzz onset and development as the flow throttle setting is reduced from critical can vary, but typically with a conical forebody there are three phases. Firstly, at small spillage, a high-frequency, low-amplitude oscillation of the normal shock (together with its extension in the outer flow) sets in (Fig. 10.1a) and persists for a time. This is succeeded, as the throttle is closed further, by a range in which the flow is stable. Further closing of the throttle then leads to another phase of buzz, in which the amplitude is much larger than before and the oscillation cycle involves the whole shock system. Shock configurations at the 'forward' end of the oscillation are of two kinds. If the cone projection is long and the cone-surface Mach number exceeds about 1.3, the limit is that of a large-angle conical shock associated with extensive flow separation from the cone surface (Fig. 10.1b). With a smaller cone projection, having a larger cone angle and lower cone-surface Mach number, the limit is a detached bow shock ahead of the cone tip (Fig. 10.1c). In both cases the limit at the 'rearward' end of the oscillation is a supercritical configuration. The forward and rearward limits thus straddle the configuration that would be formed were a stable condition possible at the given throttle setting. When the shocks are at the forward limit, the mass outflow through the exit throttle is greater than the incoming flow: this causes a collapse of the forward limit and a switch to the rearward limit, where the reverse is the case. Such alternative emptying and filling of the duct volume constitutes the main oscillation cycle. Additionally there may occur a burst of small-

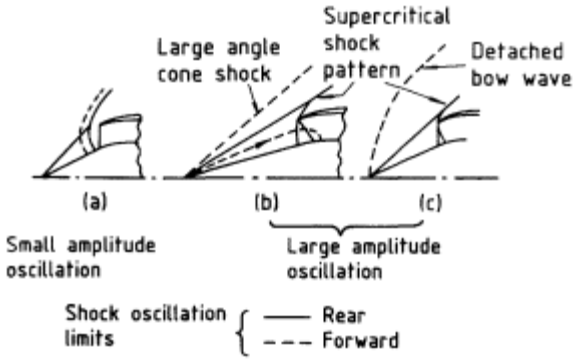

Figure 10.1
Forward and rear limits of shock oscillation.

amplitude, high-frequency oscillation of the bow wave in its forward position, while the duct volume is in the emptying process. This is caused by a boundary of separated flow impinging on the cowl lip and inducing an edge-tone resonance in the duct.

In some cases, as throttle opening is reduced, the initial low-amplitude buzz merges directly into the larger-amplitude form without an intermediate, stable-flow range.

These and other details of the overall buzz process have been deduced from studies of the records of instantaneous pressures measured at various positions in the duct, as for example by Brown and Dailey (1956), Griggs and Goldsmith (1952) and Stewart (1962). A typical series of amplitudes, frequencies and shock patterns linked to an intake total-pressure characteristic is given in Fig. 10.2 from Goldsmith's tests. The forward and rearward limits of shock movement can be discerned in the schlieren photographs. A sequence of short-duration schlieren photographs Figure 10.2(b) shows typical shock positions during one cycle.

10.3
Buzz Initiation

10.3.1
Vortex-Sheet (Ferri) Criterion.

Ferri and Nucci (1951) observed experimentally, in a large number of instances with axisymmetric intakes, that shock oscillation commenced when the vortex sheet from the intersection point of normal and oblique shocks, in subcritical flow, moved across the cowl lip, from outside to inside. This occurrence has become generally known as the Ferri criterion. It was seen in Chapter 5 that the condition of equal static pressure behind the shock intersection point implies a difference in velocity between the flow passing through the oblique-shock system and that passing through the single outer shock. Ferri and Nucci showed that if these two streams are assumed to diffuse one-dimensionally, without mixing, the outer, slower stream, which is adjacent to the cowl inner surface when the vortex sheet has crossed the lip, suffers conditions likely to lead to flow separation from that surface. In general terms the slower stream, so long as it constitutes only a small proportion of the total flow, is required to match the pressure rise occurring in the quicker major stream and this, for the slower stream, involves a rapid further reduction in velocity. Using the same assumptions as Ferri, Fisher (1970) has calculated the Mach number variations shown in Fig. 10.3 for the two streams, assuming representative initial Mach numbers for an intake operating at about Mach 2. The tendency to separation of the slower stream increases with increasing strength of the total-pressure discontinuity across the vortex sheet and decreases as the sheet moves away from the cowl lip.

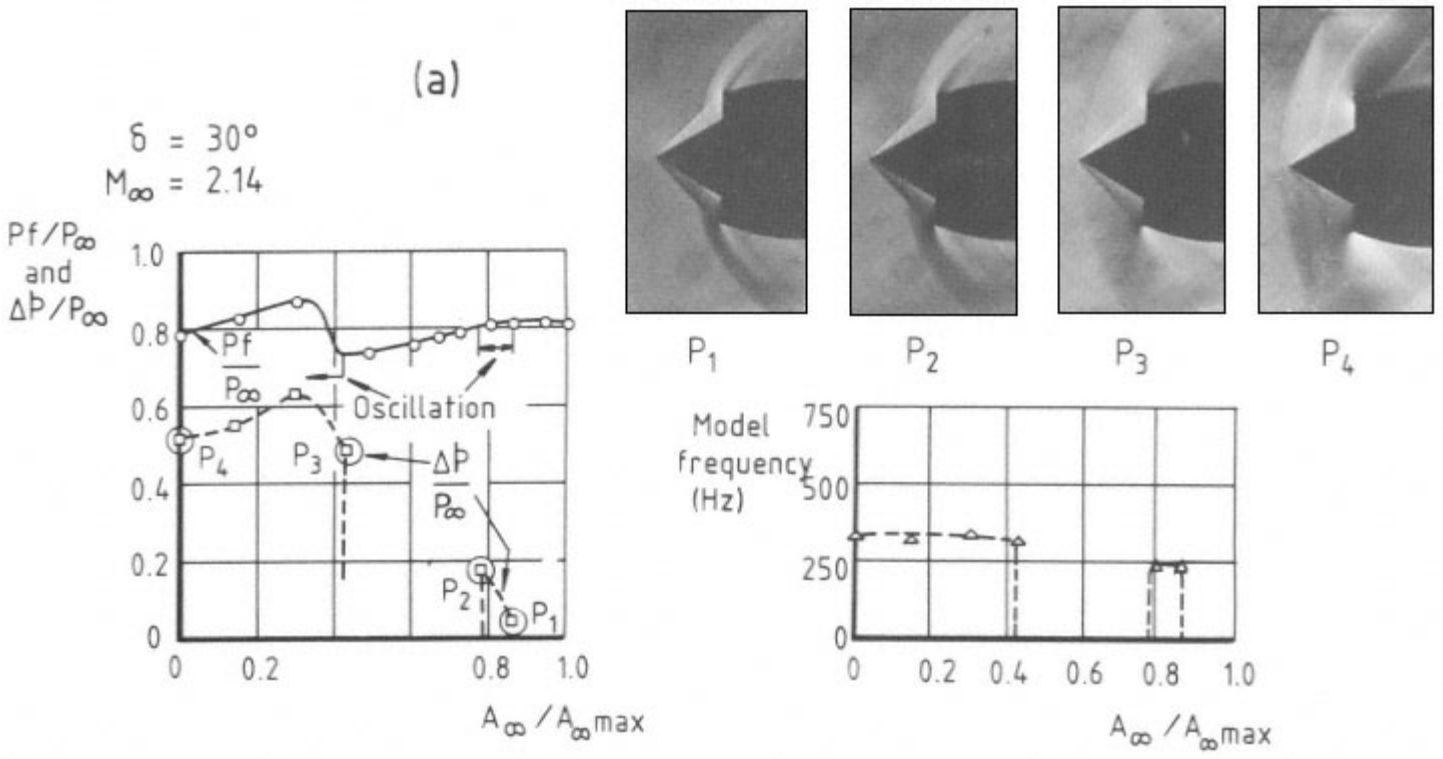

Figure 10.2
(a) Amplitude and frequency of shock oscillations related to an intake characteristic

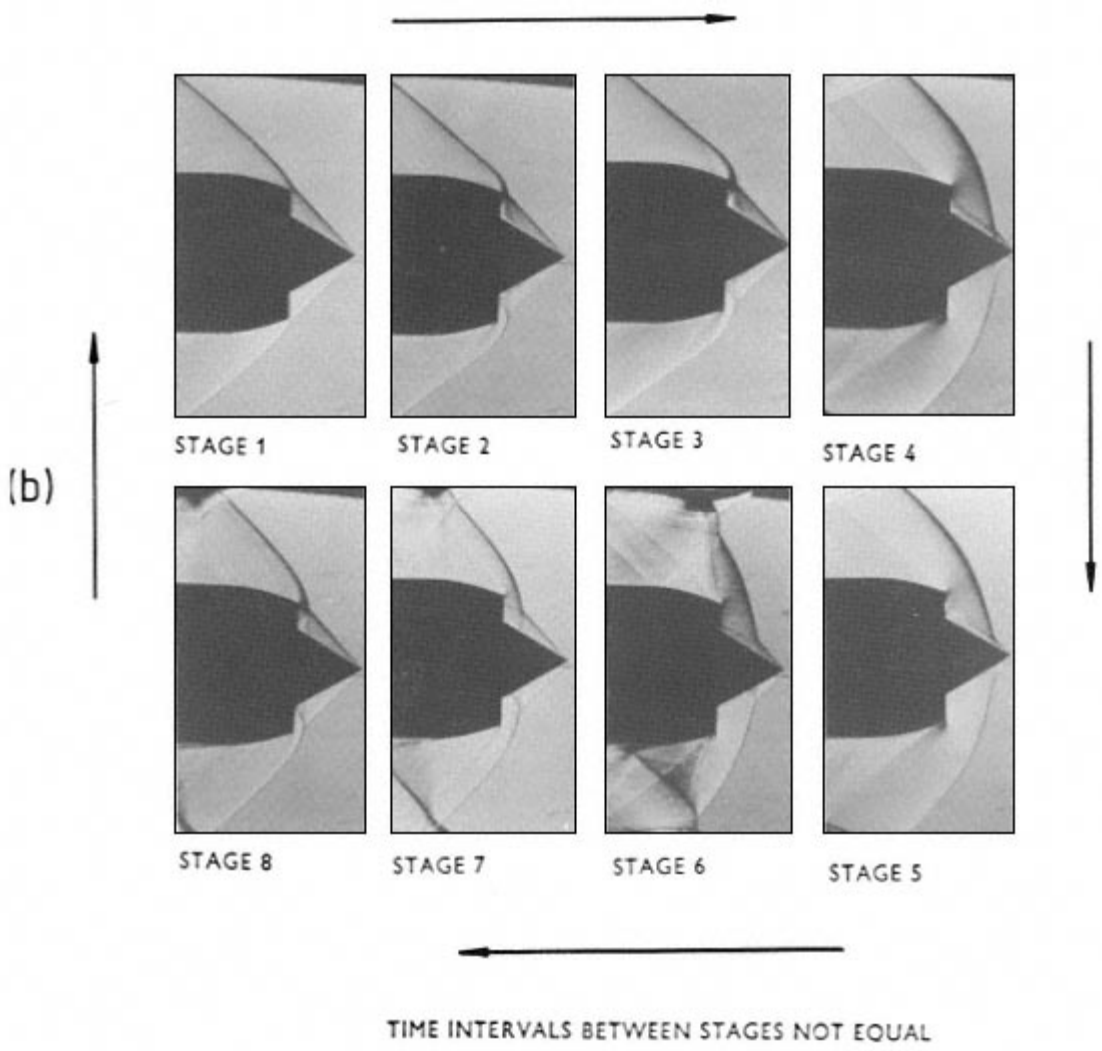

Figure 10.2
(b) Typical shock positions during one cycle.

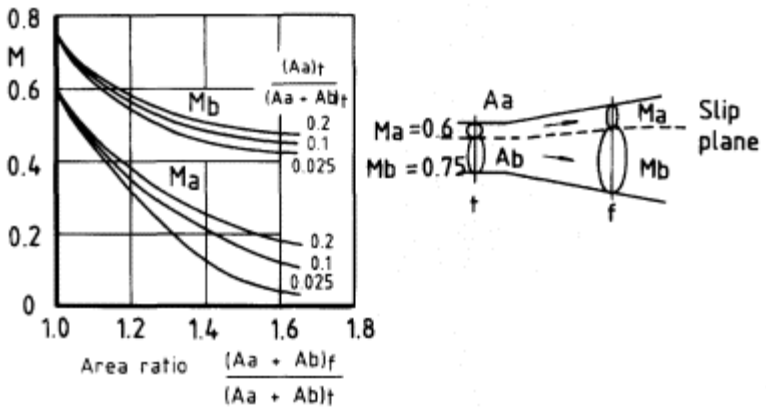

Figure 10.3
Theoretical behaviour of diffuser with velocity discontinuity at entry.

The instability cycle proposed by Ferri and Nucci involved choking in the subsonic diffuser as a result of the flow separation. Fisher, however, describes a cycle in which this choking is not necessary. The process is illustrated in Fig. 10.4: it involves matching choked *exit* conditions with two intake characteristics, one for no flow separation, the other for flow separation as an assumed stable condition. Oscillation occurs in the range shown because of the impossibility of operating stably at either of the two intersection points A and B. When the vortex sheet has moved sufficiently far from the cowl inner surface, stable flow is again possible.

Experiments on the relationships between strength of the vortex sheet, the presence of flow separation and the occurrence of buzz not unexpectedly show differences in detail between axisymmetric and two-dimensional situations. Fisher, Neale and Brooks (1970), working with variable-ramp rectangular intakes at Mach 2, found that buzz was induced by entry into the cowl of a vortex sheet of strength 6% 7%, strength being defined as the

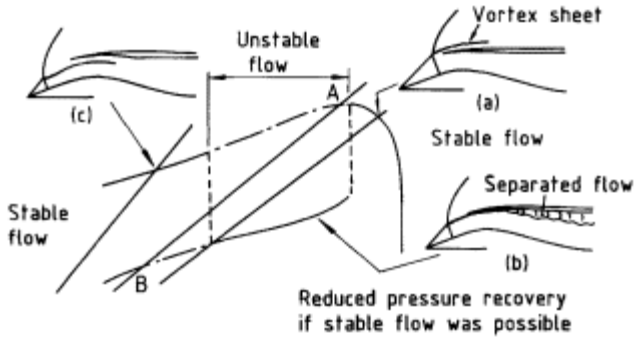

Figure 10.4
Instability cycle based on steady state characteristics.

total-pressure difference across the sheet at its source divided by the upstream total pressure. In contrast, Zhang, Yu and Peng (1983), testing an axisymmetric intake with variable cone angle and axial position, found no buzz for sheet strengths up to 11%. Above 10% strength, a degree of flow separation inside the cowl was detectable.

Whatever may be the precise details of the oscillation cycle, there is no doubt that entry of the vortex sheet within the cowl boundary can trigger an instability. The flow ratio at which a three-shock intersection point coincides with the stagnation streamline separating internal and external flow can be calculated by methods given in Chapter 5 and is a function of lip-position angle q for a given angle of the compression surface. A calculation for a conical intake with cone semi-angle 25° at Mach number 1.8 is compared in Fig. 10.5 with the results of measurement of flow ratio for buzz initiation, taken from a number of sources. Proceeding from the shock-on-lip condition (q = b), where stable-flow range is theoretically zero, and experimentally is seen to be very small, as q decreases the agreement is good until the calculated curve begins to drop away rapidly towards a minimum q value. At this stage the measured results depart from the curve and it is evident that thereafter, as the cone projection increases, buzz is being initiated by some other mechanism. For greater completeness, indications are given in the diagram of where, as flow ratio is reduced, a stable-flow range is re-established. It is seen that this happens only in cases where the first initiation of buzz is in agreement with the Ferri criterion.

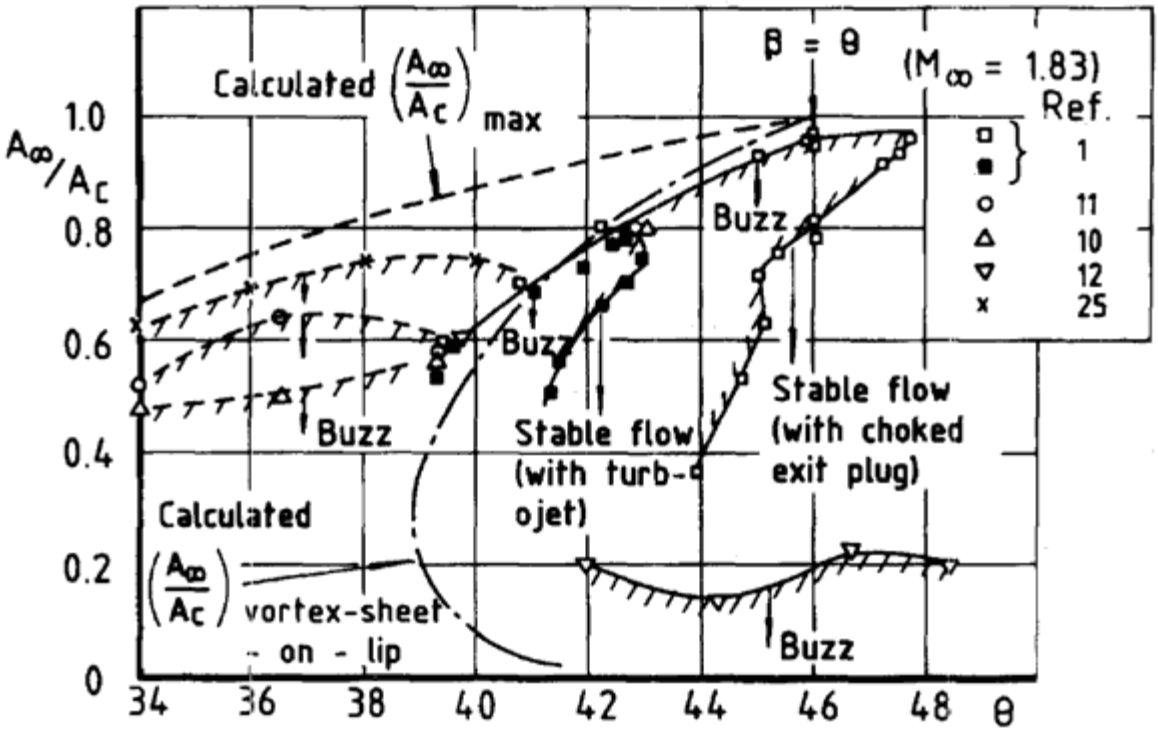

Figure 10.5
Influence of lip position angle on buzz boundaries for
a conical-forebody intake at *M*¥ 1.80 (d 258, *M*c 1.27).

10.3.2
Flow Separation from Compression Surface

Results similar to those of Fig. 10.5 are obtained at higher Mach numbers: generally with increase of Mach number, departures from the Ferri criterion occur closer to the q = b condition and where a stable-flow range has been re-established with decrease of flow ratio, second-phase buzz occurs sooner and more prominently thereafter. Griggs and Goldsmith, analysing results for a large number of axisymmetric single-cone configurations tested by them, deduced that, for lip-position angles away from q = b, departures from the Ferri criterion were prominent if the cone-surface Mach number exceeded about 1.3. Recalling general conclusions drawn in Chapter 3 about the nature of shock and boundary-layer interaction, this points to a determining influence of flow separation from the compression surface. Both Dailey and Stewart separately studied this aspect and concluded that an area of separated flow had to grow to a critical size for buzz to be initiated. Ferri and Nucci maintained that in these circumstances a vortex sheet criterion still applied, buzz being initiated when a vortex sheet emanating from the edge of the separated flow region had progressed across the entry to approach the cowl lip from the compression-surface side.

Although again the exact mechanism is not known with certainty, it is not in doubt that the margin of stable flow is decreased by an increase in the amount of boundary layer being ingested and particularly by an increase in compression-surface Mach number, hence in strength of the normal shock. Fig. 10.6 illustrates the influence of these parameters: changes in angle attack, a, are here correlated by the use of cone-surface Mach number on the lee side.

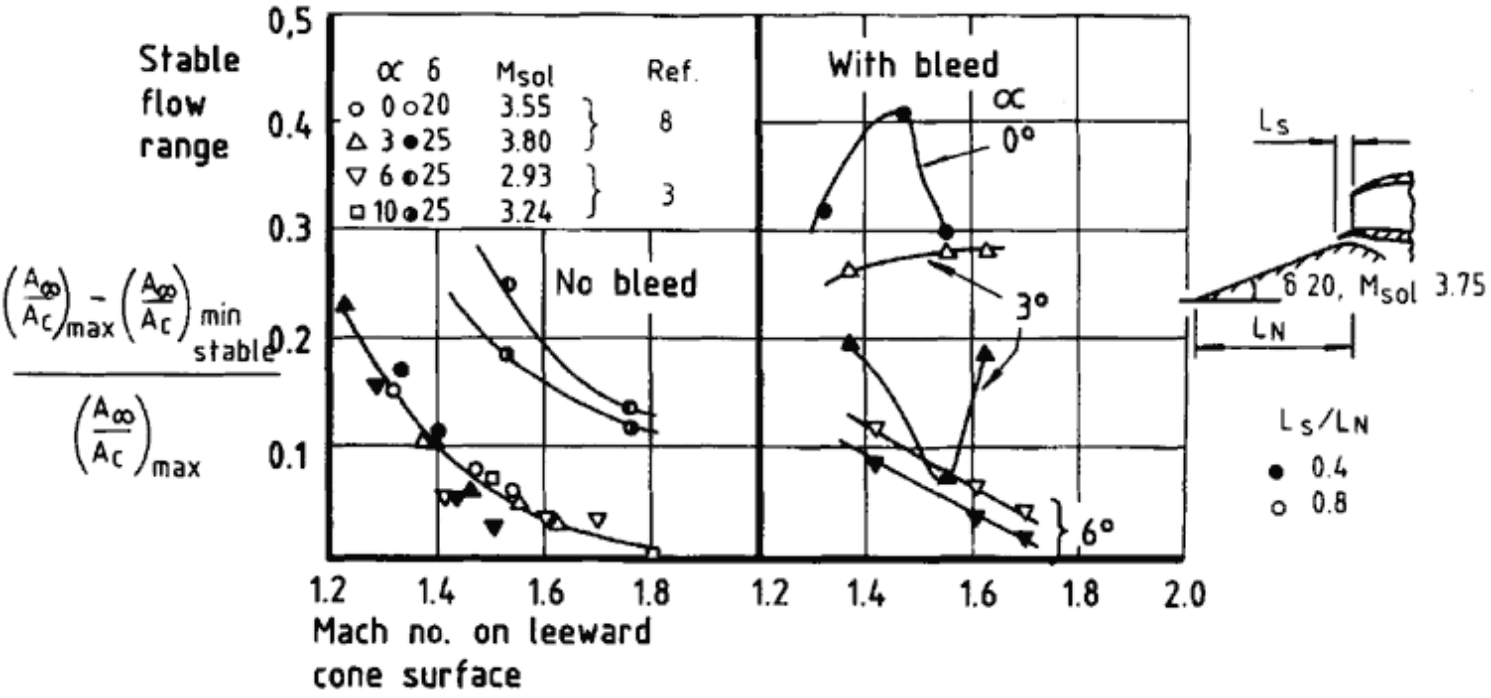

Figure 10.6
Correlation of stable flow range with Mach number on leeward cone surface (with and without forebody bleed).

10.3.3
Pressure-Slope Criterion

Several workers have proposed criteria related to the slope of the intake total-pressure or static-pressure variation with flow ratio. Orlin and Dunsworth (1951) postulated conditions for flow breakdown which are analogous to those described in Chapter 2 for the initiation of flow asymmetry in twin intakes. The conclusion reached is that breakdown of stable flow occurs when the slope of the static-pressure characteristic at entry passes from negative to positive as flow ratio is reduced. Using suffix i to denote the pressures and *net* flow-area at entry, the condition that

$$\frac{\mathrm{d}p_\mathrm{i}}{\mathrm{d}\left(\frac{A_\infty}{A_\mathrm{i}}\right)} = 0$$

can be interpreted as follows. The equation of continuity is

$$A_\mathrm{i}P_\mathrm{i}\left(\frac{A^*}{A}\right)_\mathrm{i} = A_\infty P_\infty \left(\frac{A^*}{A}\right)_\infty$$

After expressing A^*/A in terms of Mach number, by Equation 1.12, and using also the fact that

$$M^2 = \left[\left(\frac{P}{p}\right)^{\frac{\gamma-1}{\gamma}} - 1\right] \Big/ \frac{\gamma-1}{2}$$

by Equation 1.10, the continuity equation can be differentiated to give

$$\frac{\mathrm{d}\left(\frac{p_\mathrm{i}}{P_\infty}\right)}{\mathrm{d}\left(\frac{A_\infty}{A_\mathrm{i}}\right)} = \frac{\frac{A_\mathrm{i}}{A_\infty}\cdot\frac{P_\mathrm{i}}{P_\infty} f_1\left(\frac{P_\mathrm{i}}{p_\mathrm{i}}\right) - \mathrm{d}\left(\frac{P_\mathrm{i}}{P_\infty}\right) \Big/ \mathrm{d}\left(\frac{A_\infty}{A_\mathrm{i}}\right)}{f\left(\frac{P_\mathrm{i}}{p_\mathrm{i}}\right)} \qquad (10.1)$$

where

$$f_1\left(\frac{P_\mathrm{i}}{p_\mathrm{i}}\right) = \frac{2\gamma}{\gamma-1}\left[\left(\frac{P_\mathrm{i}}{p_\mathrm{i}}\right)^{\frac{\gamma-1}{\gamma}} - 1\right]\left[2\left(\frac{P_\mathrm{i}}{p_\mathrm{i}}\right)^{\frac{\gamma-1}{\gamma}} - 1\right]^{-1} \qquad (10.2)$$

and

$$f_2\left(\frac{P_i}{p_i}\right) = \left\{\left[\left(\frac{P_i}{p_i}\right)^{\frac{\gamma-1}{\gamma}} - 1\right] \frac{P_i}{p_i}\frac{(\gamma+1)}{(\gamma-1)} - \left(\frac{P_i}{p_i}\right)^{\frac{2(\gamma-1)}{\gamma}}\right\} \times \left[2\left(\frac{P_i}{p_i}\right)^{\frac{\gamma-1}{\gamma}} - 1\right]^{-1} \tag{10.3}$$

When the right-hand side of Equation 10.1 is equated to zero an expression for the slope of the *total-pressure* characteristic at entry is obtained, namely

$$\frac{d\left(\frac{P_i}{P_\infty}\right)}{d\left(\frac{A_\infty}{A_i}\right)} = \frac{A_i}{A_\infty} \cdot \frac{P_i}{P_\infty} \cdot f_1\left(\frac{P_i}{p_i}\right) \qquad (10.4)$$

This slope can be evaluated as a function of flow ratio for given values of *P*i/*P*¥ and *p*i/*P*¥ and examples for Mach 2.0 and 3.0 are shown in Fig. 10.7. The curves define the maximum positive slope allowable for stable flow. The values decrease rapidly with reduction in *A*¥/*A*i and also with increase in Mach number. We note that for a pitot intake the slope of entry-plane total-pressure recovery versus flow is small and negative throughout the subcritical range. With an external-compression intake the same applies so long as spillage is small and the shock intersections are outside the entry streamtube. Positive slope in the sense of Equation 10.4 takes over when, with increasing spillage,

(a) shock intersections move inside the entry streamtube, bringing air of lower total pressure into the intake; and

(b) boundary layer interaction effects on the compression surface increase in severity because of the additional pressure gradient behind the normal shock.

The criterion at Equation (10.4) is in general accordance with experimentally-observed decreases in stable-flow range as Mach number increases.

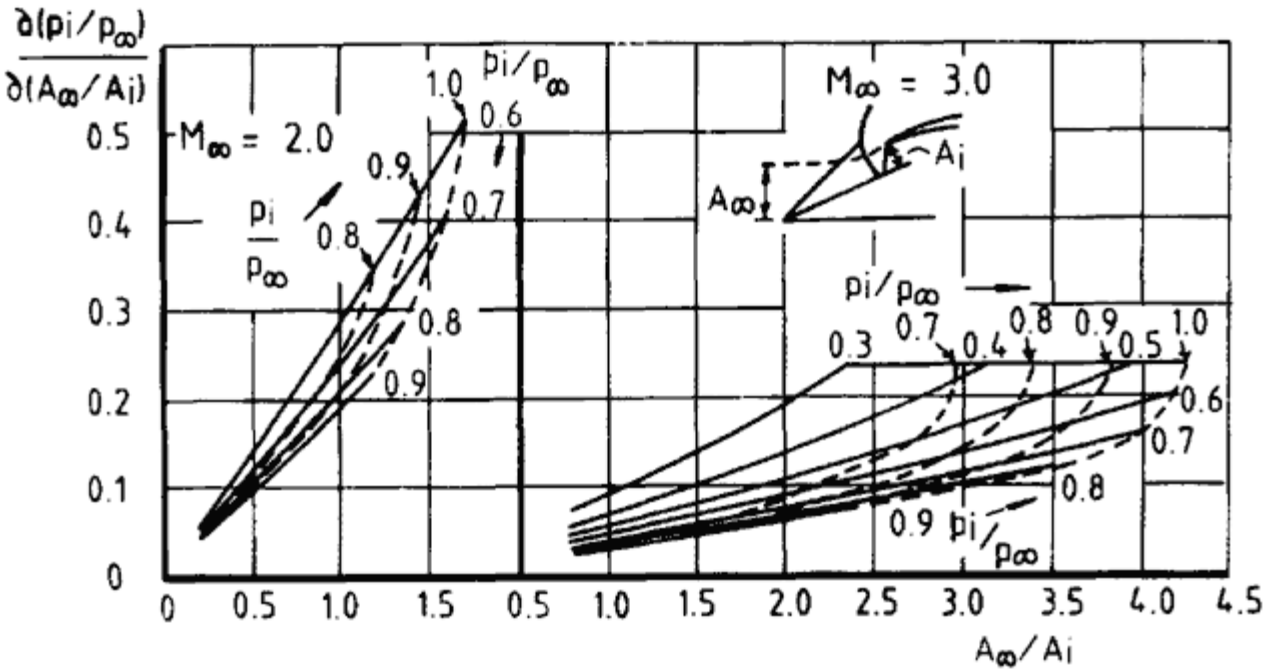

Figure 10.7
Slope of total pressure versus flow ratio calculated for condition of zero slope of static pressure versus flow ratio at *M*¥ 2.0 and 3.0.

10.3.4
Dynamic Stability Theories

Various theories which have been produced to examine the problem of flow stability as a dynamic process are usually mathematical in content and concerned with one-dimensional motion of a weak pressure wave moving in either direction, with sonic velocity relative to the steady flow in the duct. The wave is reflected successively at the entry and exit planes and if successive reflections increase its amplitude, the system is dynamically unstable and shock oscillation results. For this linear system, the method of small perturbations can be used to analyse the wave motion. If, however, a weak incident wave leads to large-scale changes at the entry, such as flow separation or a large shock movement, the system is non-linear and the weak incident wave probably acts as a trigger in initiating a buzz cycle. The phenomenon might then be expected to depend primarily on the aerodynamics of the intake without particular regard to the remainder of the configuration. Generally though, a dynamical study must involve the total system, including the engine. In this respect a ramjet is more amenable to treatment than a turbojet; for a ramjet engine consists of a combustion chamber and an exhaust nozzle and in such a case the influence of combustion chamber length and volume and the effect of heat addition can readily be studied.

Dynamic-flow analyses, using various sets of assumptions, have been made by Mirels (1955), Sterbentz *et al.* (1955) and Trimpi (1952). For details the reader is referred to the authors' original papers. The approach by Sterbentz, using a Helmholz resonator analogy, is of particular interest in that the condition for instability which emerges is that the slope of variation of total pressure with mass flow shall be positive and above a certain value, a condition similar to that described in Section 10.3.3.

10.4
Buzz Avoidance

An aircraft or missile designer aims to avoid buzz at all times, no matter what excursions into the subcritical regime have to be made within the flight envelope. Any method of increasing the range of stable subcritical flow therefore merits attention.

A natural way of avoiding buzz according to the Ferri criterion would seem to be to arrange the compression-surface geometry so that as spillage increases the shock intersection point always remains outside the entry streamtube. Strictly this means choosing the value of cowl-lip angle, q, to be smaller than the minimum value which allows the oblique shocks to fall on the lip. As an example, from Fig. 10.5 with 25° cone semi-angle, this would set the following *upper* limits for q:

Table 10.1 Minimum q for shock on lip with 25° semi-angle cone

	Shock-on-lip values		
M¥	qmin	*M*min	b
1.80	38.9	2.31	46.0
1.91	39.6	2.24	44.0
2.0	39.4	2.25	42.5

In these circumstances, however, buzz would generally be initiated by a mechanism related to shock and boundary layer interaction on the compression surface. For values of q lying between qmin and the shock angle *3*, the Ferri criterion might in principle be circumvented by distorting the shape of the vortex sheet spanwise, or circumferentially, so that it does not impinge uniformly on the cowl lip. Some experimental evidence on this has been provided by Trimpi and Cohen (1955), using longitudinal grooves on a conical forebody, and by Leissler and Hearth (1952), using a wedge-compression surface within a circular cowl. Little favourable effect was shown in either case.

Alternatively, the compression surface might be designed to spread the shock intersections, so as to produce a series of small velocity changes across several vortex sheets, instead of a single large discontinuity. The strengths of individual vortex sheets might in this way be reduced to below the minimum levels which have been shown to apply (Section 10.3.1). Fisher *et al.* (*loc. cit*), following this line as illustrated in Fig. 10.8, obtained significant reductions of the flow range over which Ferri-type buzz occurred.

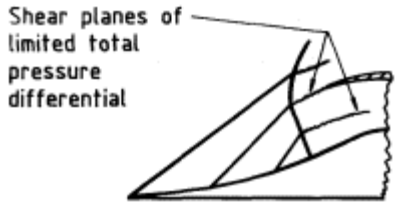

Figure 10.8
Arrangement of oblique shocks from forebody
to reduce strength of slip-plane vortex sheets.

Since the Ferri criterion depends upon the low-energy stream being subjected to an immediate pressure rise within the duct, the inclusion of a constant-area throat may be expected to change the buzz initiation characteristic. Nettles (1956) has shown this to be the case, in tests of an axisymmetric intake with the cone shock on or close to the lip (q = 43°) at *M*¥ = 2.0 and 1.8, for which the Ferri criterion predicts negligible or small

stable-flow range respectively. Adding a constant-area throat gave a progressive and ultimately large increase in stable-flow range with increase of throat length (Fig. 10.9) apart from an initial small reverse effect at the higher Mach number. With a geometry for which forebody flow separation was the initiating mechanism rather than the Ferri criterion, the maximum throat effect measured by Stewart (1962) was fairly small.

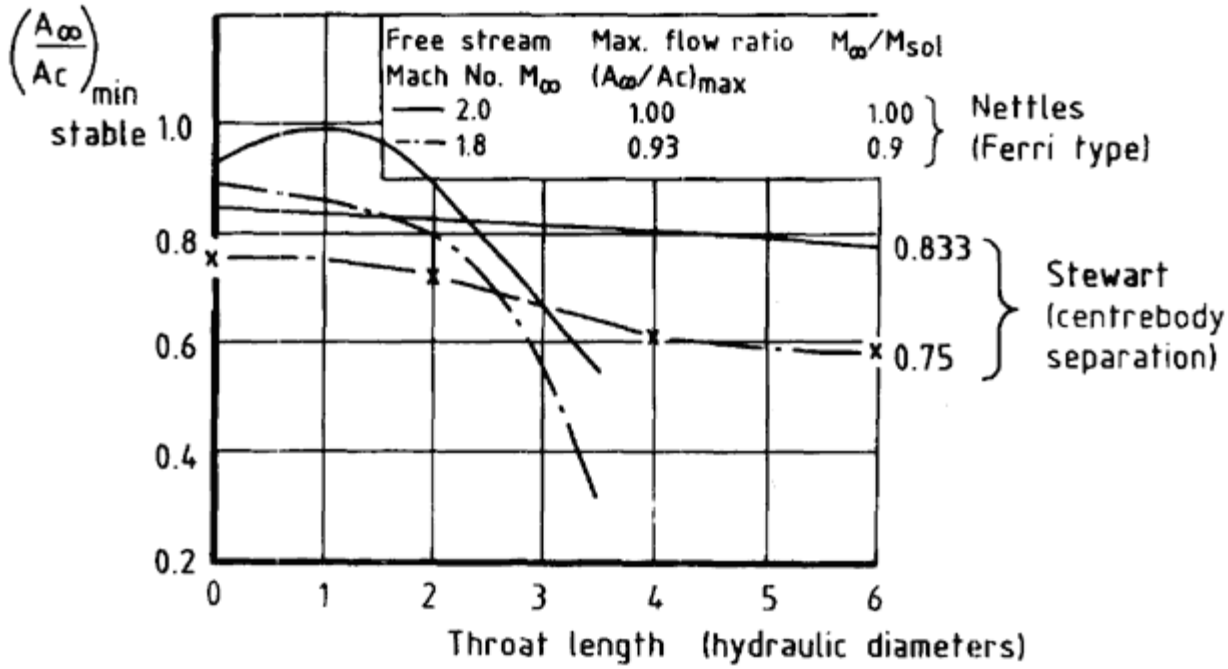

Figure 10.9
Influence of throat length on onset of flow oscillation at *M*¥ 1.8 and 2.0.

In other work, Stewart (1964) has shown significant increases in stable flow range by the use of flush bleed holes on a conical compression surface, with bleeds flows from one half to one per cent of intake flow. Fig. 10.10 illustrates. Considerable gains were also measured by Griggs (1958) using ram-scoop bleeds, where in general, positioning the bleed ahead of the entry plane gave progressively greater increases in stable flow range (Fig. 10.11). In both these instances, some benefit was observed from the presence of the bleeds even at zero bleed flow. This led to experiments being made with a forward-facing solid step, results for which are shown in Fig. 10.12. Increases in stable flow range were again observed, the gain being greater the further forward the step was placed. The effect appeared to be one of boundary-layer separation being anchored at the step position, independently of spillage. In the example shown the oblique shock induced by separation covered the whole of the entry streamtube. Total-pressure losses were comparatively independent of step position but in all cases were higher than without the step.

Boundary layer bleed was investigated by Bryce (1971) for possible use in the twin-intake arrangement of the Concorde aircraft, with particular reference to flow stability at small angles of yaw. Fig. 10.13 shows that an increase in stable-flow range was achieved by use of bleed perforations

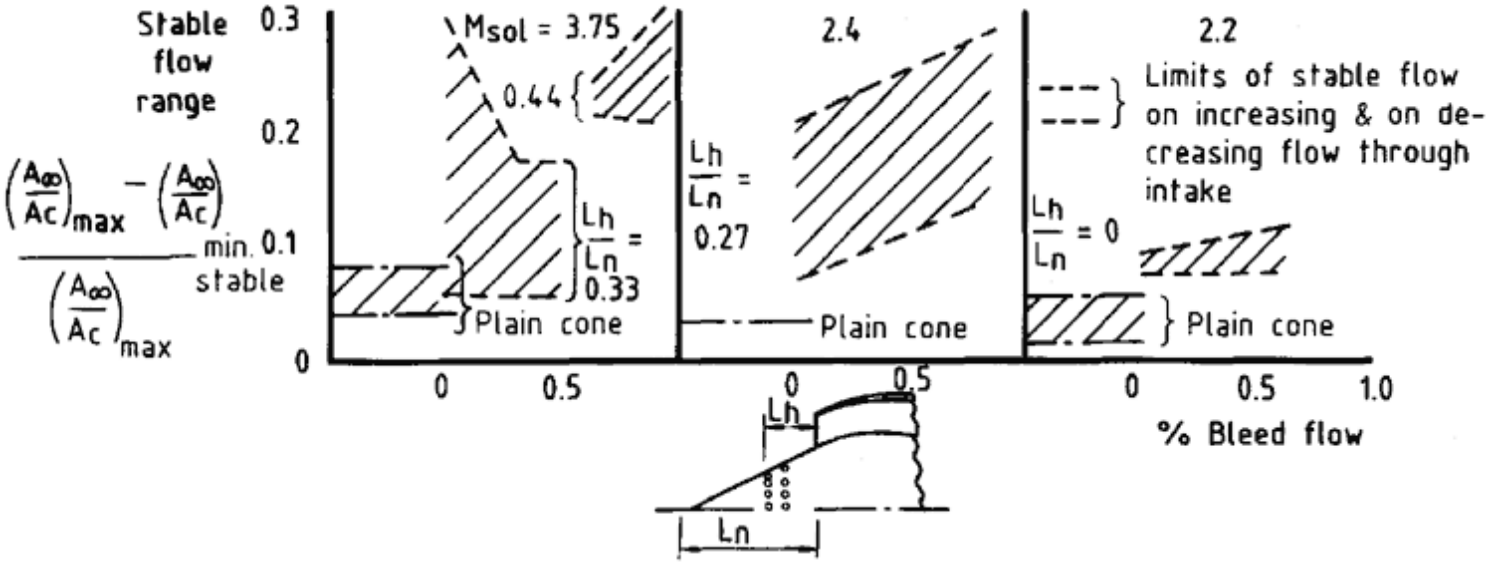

Figure 10.10
Effect on stable flow range of suection through cone-surface holes at *M*¥ 2.14 (Stewart).

located near to the intersection of the cowl lip with the splitter plate separating the two intakes.

Boundary layer injection ('blowing') can be a possible alternative to boundary layer bleed ('suction'). Dailey (1950) tried the use of injection at a position on the forebody just downstream of the entry plane, but the effect on stable-flow range was negligible. This suggests that boundary-layer control, whether by blowing or by suction, needs to be applied at a more forward position, as Griggs (*loc. cit.*) also found. Further confirmation comes from experiments by Kowalski and Piercy (1957), who investigated both forms of control using a slot located well forward on the cone surface. The effect of blowing was favourable, especially for small slot heights (Fig. 10.14); this applied particularly at zero angle of attack. A rather better

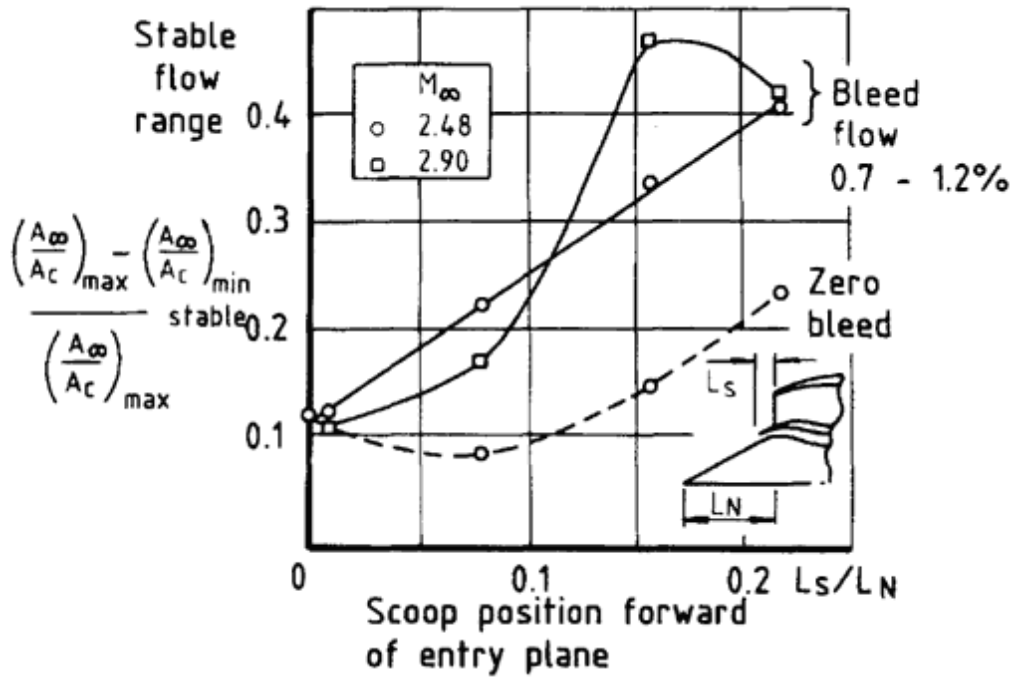

Figure 10.11
Effect on stable flow range of position of boundary layer ram scoop in front of entry plane at M_∞ 2.48 and 2.90.

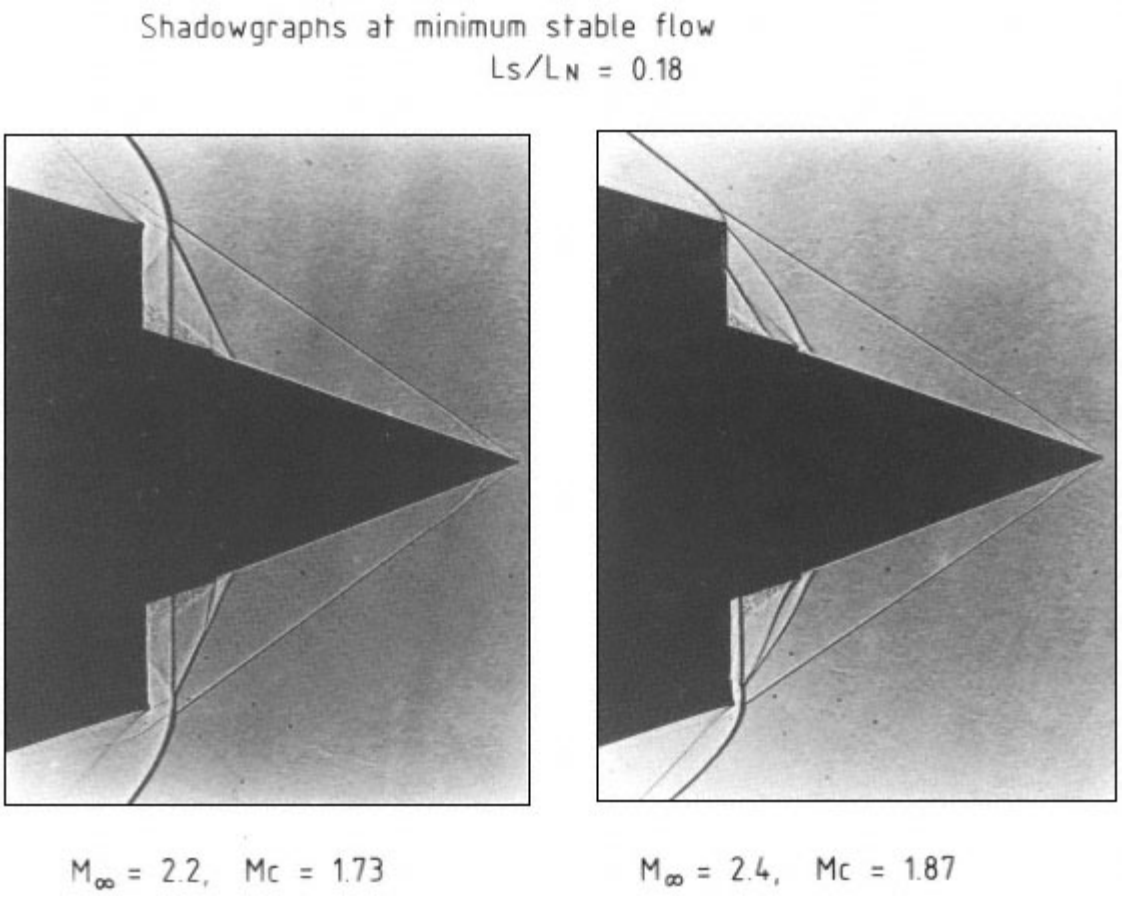

Figure 10.12
Influence of step position on stable flow range and extra-to-shock loss at cone surface Mach numbers from 1.4 to 1.9.

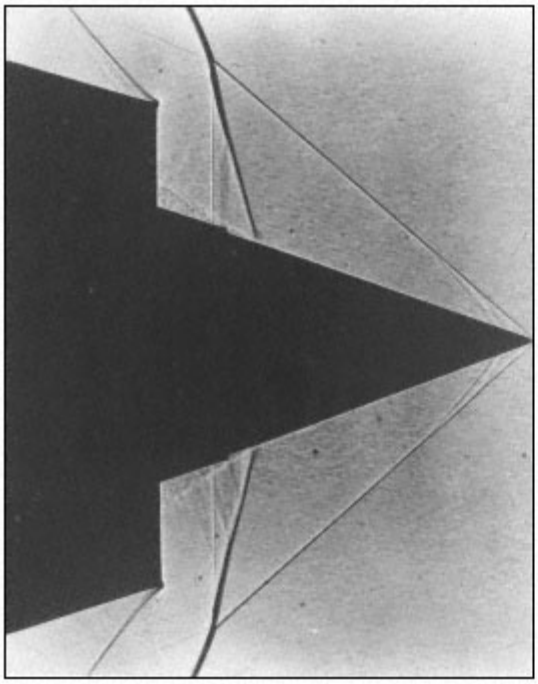

$M_\infty = 1.8, \quad Mc = 1.42$

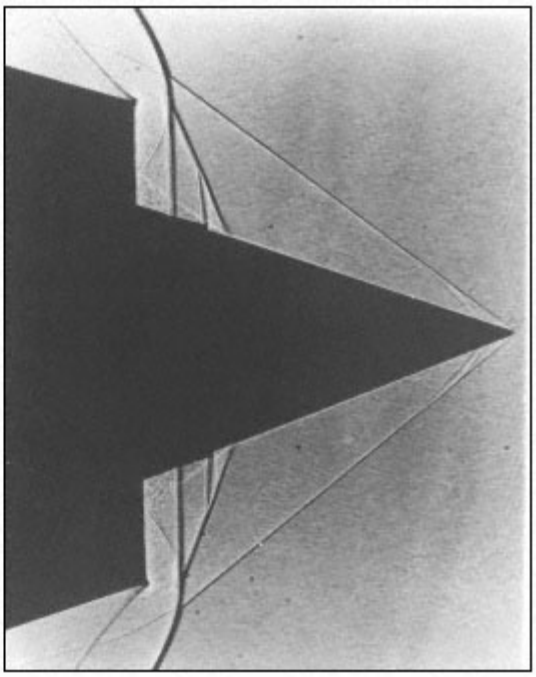

$M_\infty = 2.0, \quad Mc = 1.57$

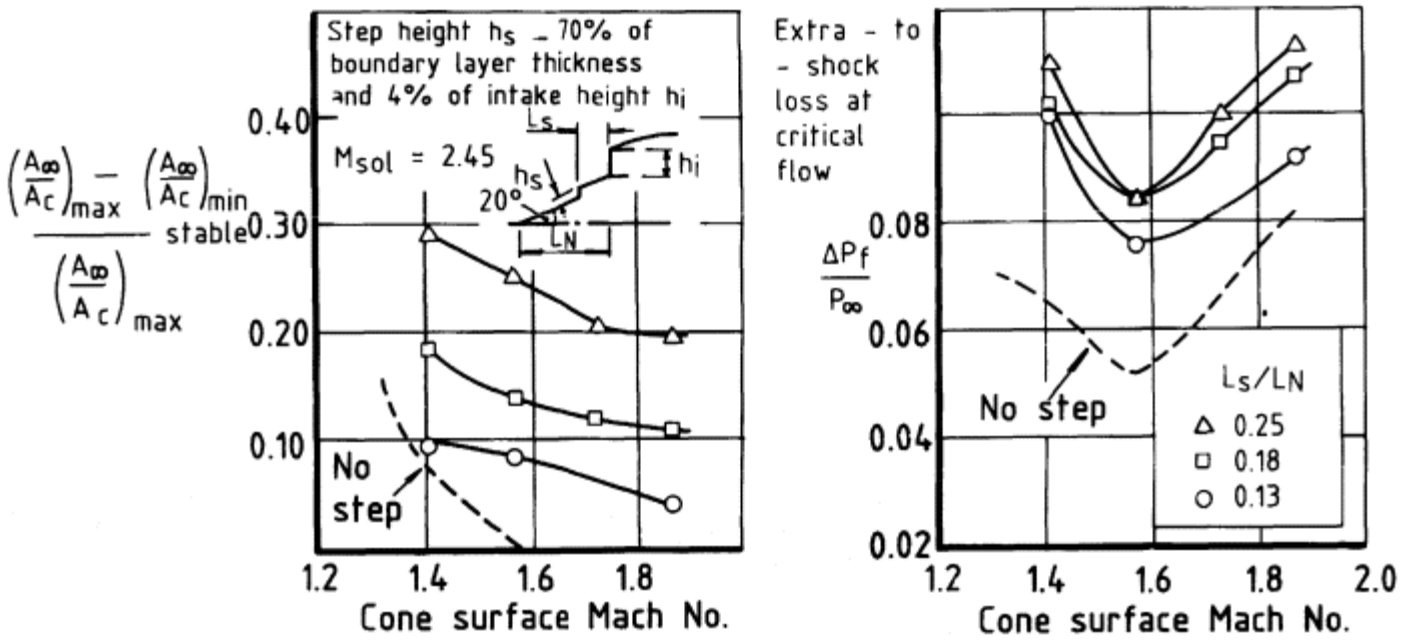

Figure 10.12
(continued)
Influence of step position on stable flow range and extra-to-shock loss at cone surface Mach numbers from 1.4 to 1.9.

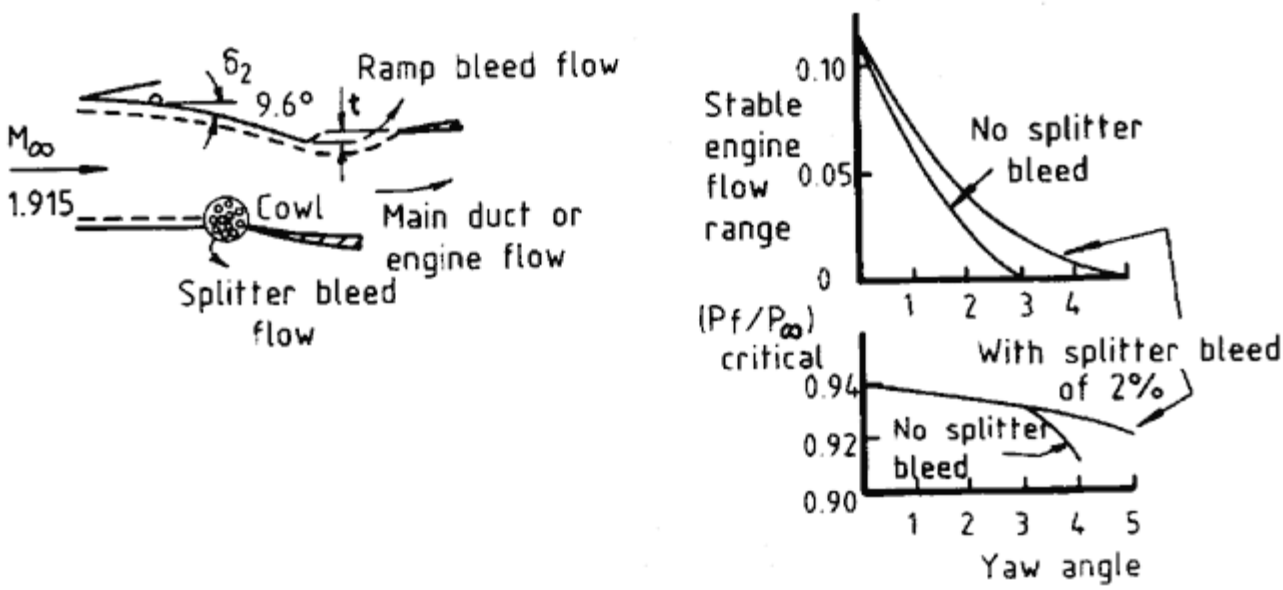

Figure 10.13
Effect of splitter-plate bleed on stable flow and pressure recovery variation with angle of yaw for Concorde nacelle.

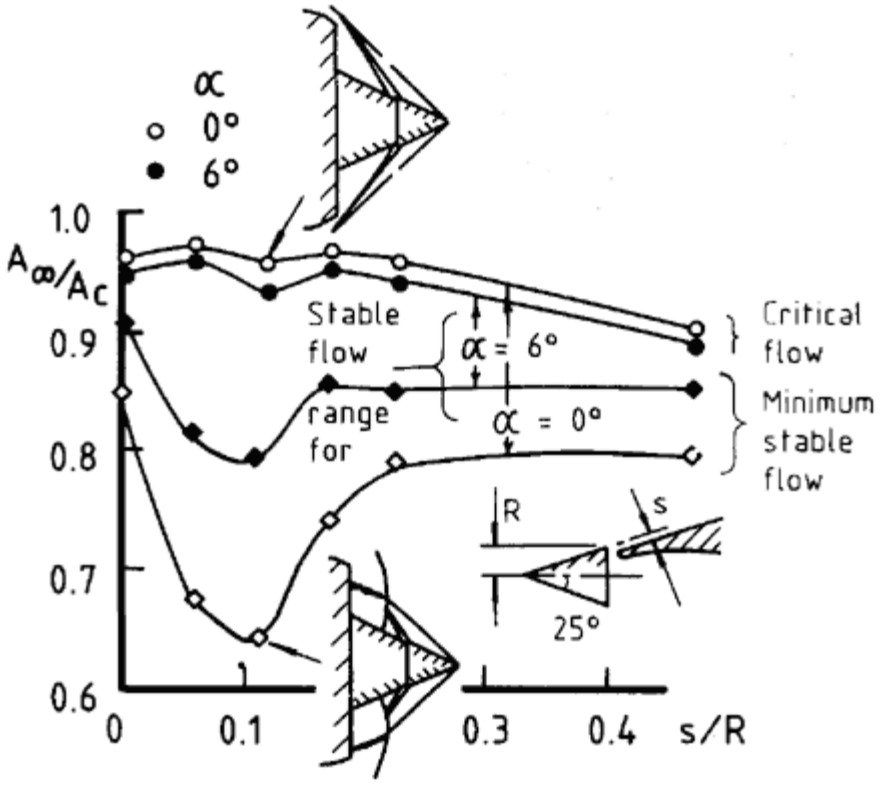

Figure 10.14
Variation of critical flow and minimum stable flow with injection slot height at *M*¥ 1.91 and a 0° and 6°.

result was obtained from suction, as is shown in Fig. 10.15. The diagram shows also the effect of alternative suction on the cowl lip, using perforations close behind the leading edge. Although this arrangement allowed the

vortex sheet to be ingested without initiating buzz, the increase in stable-flow range produced was not as great as that obtained from boundary-layer control on the compression surface.

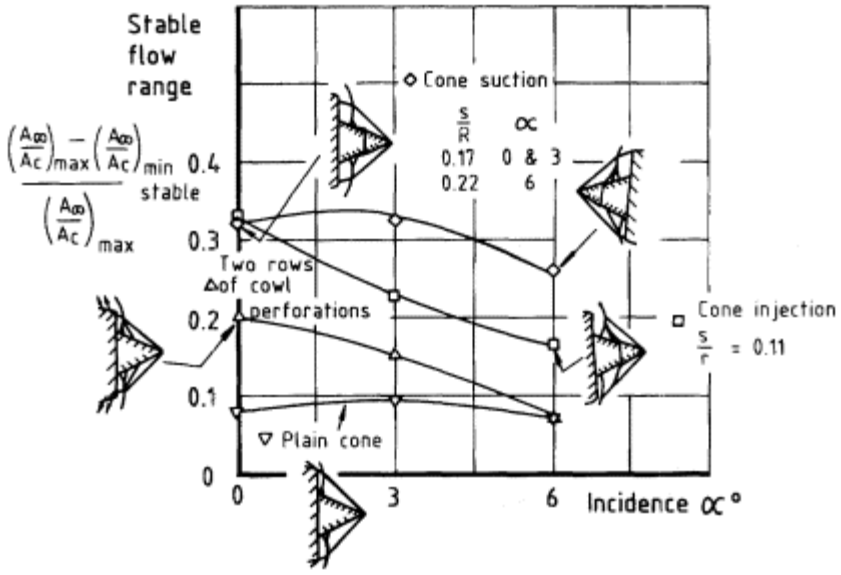

Figure 10.15
Comparison of effect of cone slot injection
and cone and cowl suction on variation of stable
flow range with incidence (*M*¥ 1.91, *M*SOL 2.15).

10.5
Other Forms of Shock Oscillation.

Shock oscillation has been observed to occur with pitot intakes. When the intake is adjacent to an aircraft surface, the phenomenon is basically the same as has been described throughout this chapter in relation to the effects of shock and of boundary-layer interaction. Where oscillation has been reportedly observed with pitot intakes in isolation, the reasons for it are not clear, but may be associated with particular test conditions, for example with the effects of shocks reflected from test-chamber walls, where the interactions with wall boundary layers would themselves be unsteady.

More importantly, shock unsteadiness occurs inside intake ducts under conditions of *supercritical* operation and contributes to the level of dynamic distortion (Chapter 11) in the flow. The general problem is one of unsteady transonic flow in a Laval nozzle, as described, for example, by Meier (1974). More recently, Peng, Yu and Ma (1984) have been studying the situation in a two-dimensional diffuser, with divergence angles and shock Mach numbers appropriate to situations existing in intakes for aircraft Mach numbers around 2. The amplitude of shock oscillation is greater the larger the divergence angle of the duct. Also if the shock is strong enough to cause flow separation, a phenomenon of shock 'flipping' can occur: the separation bubbles on top and bottom walls are unequal in size and as the shock moves

along the duct during an oscillation, the flow flips from one configuration to the opposite one, causing an abrupt change in both flow direction and total-pressure distribution downstream. A return flip occurs as the shock moves back. Further investigation seems to be justified; in practice, the degree of supercritical operation of an intake that can be permitted is generally limited by the distortion effects that occur.

References

1 Beheim, M.A. and and Englert, G.W. (1956) 'Effects of a J34 turbojet engine on supersonic diffuser performance'. NACA RM E55 121.

2 Brown, A.C. and Dailey, C.L. (1956) 'Investigation of supersonic diffuser instability'. USCEC Report 41-101.

3 Bryce, J.D. (1971) 'Suppression of shock instability in the Concorde intake by application of boundary layer control'. NGTE Report R315.

4 Dailey, C.L. (1950) 'Diffuser instability in subcritical operation'. USCEC Report dated 26 September 1950.

5 Dailey, C.L. (1955) 'Supersonic diffuser instability'. CIT PhD Thesis (1954), Summary in *JAS* 22, no. 11.

6 Englert, G.W. and Obery, L.J. (1952) 'Evaluation of five conical centrebody supersonic diffusers at several angles of attack'. NACA RM E51 L04.

7 Ferri, A. and Nucci, L.M. (1951) 'The origin of aerodynamic instability of supersonic inlets at subcritical conditions'. NACA, RM L50 K30.

8 Fisher, S.A. (1970) 'On the mechanism of supersonic intake instability'. ARL ME 313.

9 Fisher, S.A., Neale, M.C. and Brooks, A.J. (1970) 'On the subcritical stability of variable ramp intakes at Mach numbers around 2'. NGTE Report R3111.

10 Gorton, G.C. (1953) 'Investigation of a translating spike supersonic inlet as means of mass-flow control at Mach numbers of 1.5, 1.8 and 2.0'. NACA RM E53 G10.

11 Gorton, G.C. (1954) 'Investigation at supersonic speeds of a translating spike inlet employing a steep lip cowl'. NACA RM E54 G29.

12 Gorton, G.C. and Dryer, M. (1955) 'Comparison at supersonic speeds of translating spike inlets having blunt and sharp lip cowls'. NACA RM E54 J07.

13 Griggs, C.F. and Goldsmith, E.L. (1952) 'Shock oscillation ahead of centrebody intakes at supersonic speeds'. RAE Report Aero 2477.

14 Griggs, C.F. (1958) 'An investigation of two methods of suppressing shock oscillations ahead of conical centrebody intakes'. RAE Tech Note Aero 2551.

15 Kowalski, K. and Piercy, T.G. (1957) 'Stability of supersonic inlets at Mach 1.91 with air injection and suction'. NACA RM E56 D12.

16 Leissler, L.A. and Hearth, D.P. (1952) 'Preliminary investigation of angle of attack on pressure recovery and stability characteristics for a vertical wedge nose inlet at Mach number of 1.90'. NACA RM E52 E14.

17 Meier, G.E.A. (1974) 'Shock induced flow oscillations'. AGARD CP 168. Paper 29.

18 Mirels, H. (1955) 'Acoustic analysis of ramjet buzz'. NACA TN 3574.

19 Nettles, J.C. (1956) 'The effect of initial rate of subsonic diffusion on the stable subcritical mass-flow range of a conical shock diffuser'. NACA RM E53 E26.

20 Orlin, W.J. and Dunsworth, L.C. (1951) 'A criterion for flow instability in supersonic diffuser inlets'. Marquardt Aircraft Co., Report No. 5144.

21 Oswatitsch, K. (1944) 'Der Druckrückgewinn bei Geschossen mit Rückstorsantrieb bei hohen Uberschallgeschwindigkeiten'. Göttingen paper. English translation NACA, TM 1140.

22 Peng, C.Y., Yu, S.Z. and Ma, J.J. (1984) 'Shock oscillation and unsteady flow in two-dimensional transonic diffusers'. NAI Report, Nanjing, China.

23 Sterbentz, W.H. and Davids, J. (1955) 'Amplitude of supersonic diffuser flow pulsations'. NACA TN 3572.

24 Sterbentz, W.H. and Evvard, J.C. (1955) 'Criterions for prediction and control of ramjet flow pulsations'. NACA TN 3506.

25 Stewart, D.G. (1962) 'Supersonic intake instability; the effect of design geometry on intakes of 25° cone semi-angle at *M* 1.83]. ARL Report ME 104.

26 Stewart, D.G. (1964) 'Supersonic intake instability, further investigation of intakes of 25° cone semi-angle at Mach numbers up to 2.14 with and without boundary layer bleed'. ARL Report ME 112.

27 Trimpi, R.L. (1952) 'An analysis of buzzing in supersonic ramjets by a modified one-dimensional non-stationary wave theory'. NACA RM L52 A18.

28 Trimpi, R.L. (1953) 'A theory for stability and buzz pulsation amplitude in ramjets and an experimental investigation including scale effects'. NACA RM L53 G28.

29 Trimpi, R.L. and Cohen, N.B. (1955) 'Effect of several modifications to centrebody and cowling on subcritical performance of a supersonic inlet at Mach number 2.02'. NACA RM L55 C16.

30 Zhang, K., Yu, S. and Peng, C. (1983) 'Effect of a shear layer on stability of an axisymmetric external compression air intake'. *Acta Aeronautica et Astonautica Sinica* 4 (NAI, Nanjing Report in Chinese with English abstract).

Chapter 11
Distortion and Swirl

11.1
Introduction and Historical Note

Intake and engine must remain aerodynamically compatible throughout an aircraft flight envelope. This is to say that situations which lead to compressor stall, engine surge or other malfunctioning of the propulsion system must be avoided or at least reduced to a tolerably low frequency of occurrence. Such situations are produced by departures of the airflow, as delivered by the intake to the engine, from the ideal of a flow uniform in pressure, temperature, gaseous and other content and uniformly axial in direction. No real flow ever achieves this ideal, but in the pursuit of high intake pressure recovery on design, flows are usually sufficiently close to it as to pose no compatibility problem. In the outer regions of the flight envelope, however, or in non-standard atmospheric conditions, serious deteriorations in flow quality can and do occur.

It is of interest to recall a number of examples from the many in which problems of incompatibility have been revealed in flight, during prototype development of new aircraft or with established aircraft operation in abnormal circumstances. Of the occurrences quoted, three the first three were purely aerodynamic in origin; the fact that these all relate to American aircraft is indicative of the leading part played by the USA in the early development of operational supersonic aircraft.

F. 100 (1954)

On the F.100 with J.57 engine, engine surge occurred in high g turns at 35 000 ft altitude and above. The aircraft had a pitot-type intake in the nose of the fuselage the best form possible from a level-flight performance aspect. The intake lip was fairly sharp, however, corresponding to the supersonic performance envisaged, and the presumed cause of surging was flow separation inside the windward lip at the angles of attack for high g turns.

F.101 (1954).

The F.101 had two J.57 engines, fed by fuselage side intakes with boundary layer diverters. The engines surged at around 40 000 ft altitude in steady flight at transonic speeds (Mach numbers 0.8 to 1.2) with high engine revs/min. It appeared that the fuselage boundary layer was not fully diverted in these conditions and the duct was consequently near to choking. A forward extension of the front of the intake, the intended purpose of which was to prevent buzz at higher supersonic speeds, was found to raise the transonic altitude limit by a significant amount, presumably by providing a more complete diversion of the boundary layer.

F.111 (1966)

The F.111 (TF 30 engine), an advanced tactical aircraft designed for speeds in excess of Mach 2, was required to operate at extremes of altitude and aircraft attitude outside previous experience. The intake was a variable-geometry, external-compression design of approximate quarter-cone form, located in the junction of fuselage side and wing undersurface. The position gave a useful measure of shielding, reducing the effects of aircraft incidence and yaw (see Chapter 13) but disposal of the boundary layers on fuselage, wing and cone was difficult and on the prototype aircraft, despite the use of an elaborate bleed system, a residual low energy area was identifiable on the inboard side of the duct, at the engine face. In the flight development testing, engine surges were experienced both in subsonic manoeuvres (high subsonic Mach number and medium altitude) and in supersonic steady flight (Mach numbers above 2 at high altitude). An extensive research and development programme led to a successful conclusion, in the course of which the importance of time-variant or 'dynamic' distortion, as distinct from steady-state distortion, was established: this is discussed later in the chapter.

Hunter (1955)

The Hunter, a subsonic fighter aircraft, had intakes in the wing root leading edge and gun ports under the fuselage nose. On the Hunter 1, with RA7 Avon engine, firing the guns at high altitude was found to cause engine surge and at times flame-out. At least three factors, acting singly or in combination, were identified as likely causes:

(a) the pressure wave from the expanding gases disturbing the intake flow;

(b) the heat of the weapon gases raising the air temperature in the intake;

(c) the combustible nature of the weapon gases causing a transient over-fuelling of the engine.

Arrangements of flow deflectors on the fuselage were of some value but the main solution came from engine modifications These involved increasing the separation between engine surge line and working line a permanent change and restrictive control of the fuelling during gun firing. Several other aircraft, American and British, experienced the same problem at about this time and the weapon firing situation has continued since to require the attention of intake designers.

Britannia (1956)

The Britannia civil airliner was powered by four Proteus propeller turbine engines carried in nacelles on the wings. The intake of each nacelle had an annular entry situated behind the propeller roots, after the manner typified in Chapter 2 (Fig. 2.15), but the engine configuration was unusual in being of reverse flow type, so that the intake duct made a 180° turn inside the nacelle in order to feed the axial compressor. The problem experienced was that during normal aircraft cruise at about 20 000 ft altitude in the tropics, passage through cloud could lead to engine surge and sometimes flame-out. Ambient temperature in these conditions was about 0°C. The cause of trouble was found to be ice accretion in the vicinity of the intake bend: when the accretion reached a certain stage the ice broke away into the compressor in quantities sufficiently large to cause the malfunction. The problem was eventually overcome by means of a series of modifications to the duct, coupled with carefully regulated use of the cowl leading-edge heating system.

The examples serve to illustrate a wide variety of circumstances that can upset the stable operation of a propulsion system. Immediate causes of engine malfunction could be classified as being in the categories: (a) aircraft operating conditions Mach number, Reynolds number, attitude in incidence and yaw, (b) intake design inadequacy sizing, shaping, boundary layer control, (c) engine sensitivity the relationship between surge line and operating line, (d) special external sources as in the last two examples. Ultimately all these aspects have to be brought together in a total operational system and it is clearly desirable that, insofar as can be, the totality should be considered, in the design sense, as an integrated whole. The air intake, being specific to a particular combination of airframe and engine, is the place where design requirements relating to compatibility should be met as far as possible, but concessions may often have to be made from either the aircraft side or the engine side.

The decade or so represented by the examples quoted above was a time

when development of the axial compressor progressed rapidly, largely by increases in tip speed and blade loading. Experience indicates that such trends bring naturally an increased sensitivity of the engine to flow irregularities. Progress has continued in subsequent years but greater efforts have also been made to investigate and develop systems in a more integrated fashion on ground rigs, for example by free-jet testing of intake and engine combinations, and thereby to reduce the probability of compatibility problems being met for the first time only when the flight development stage is reached.

11.2 Total-Pressure Distortion

Of the possible forms that departures of the intake flow from a uniform ideal can take, that to which most practical significance is normally attached is the variation of total pressure across the engine face. The term applied to this variation is 'distortion'. Total-pressure distortion may be steady or time-variant ('dynamic') and if the latter, may be of the spatially uniform ('buzz') type discussed in Chapter 10 or of a spatially non-uniform ('turbulence') type.

11.2.1 Criteria in Steady Flow.

Consistent with the concept of total-pressure recovery as a representative mean, across the engine face position, of time-averaged values of total pressure, is the concept of distortion as being a measure of the spatial non-uniformity of those time-averaged values. This will be referred to as 'steady-state' distortion, notwithstanding the fact that where large transverse gradients of pressure are present the flow timewise can at best be no more than quasi-steady.

Some degree of radial non-uniformity will always exist, since in the absence of flow separation, a boundary layer will be present at the duct walls. For an appreciation of the basic significance of distortion, however, radial non-uniformity can be neglected, the primary concern being with the changes in aerodynamic loading of the compressor which are associated with blade rotation. A simple form of circumferential non-uniformity is the square-wave distribution, in which two distinct levels of total pressure exist in different parts of the azimuthal range; and although this is an idealised concept, it serves well to illustrate the implication of distortion for the engine. The situation is illustrated in Fig. 11.1. Total pressure distribution at the compressor inlet shows a single region of uniformly low pressure ('spoiled' flow). Whether the inlet static pressure is uniform or has a corresponding depression is not basic to the argument. The controlling

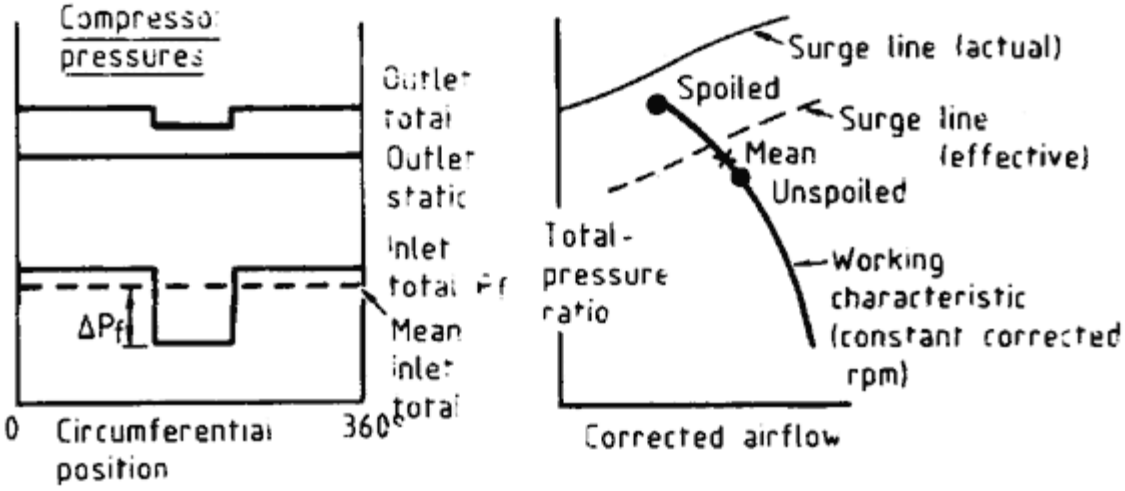

Figure 11.1
Parallel-compressor theory.

factor is uniform static pressure at the compressor outlet and this has the effect that more work is done on the spoiled flow than on the unspoiled flow. Thus if the two systems are regarded as identical compressors in parallel, each operating on an undistorted flow characteristic, the spoiled flow compressor operates higher on the characteristic, as indicated in the right-hand part of the illustration, that is to say, closer to the surge line. If this operating point reaches the surge line the spoiled component stalls and if the spoiled component is of sufficient circumferential extent this leads to surging of the whole compressor. In terms of the whole compressor therefore, the effect of distortion is to bring the surge line closer to the operating point, as indicated.

Some Rolls-Royce test results presented in Fig. 11.2 show the surge line movement in a particular case, in which the inlet flow to a five-stage research compressor was progressively distorted by means of gauze screens.

It is necessary to have a quantitative measure of distortion, by which both the quality of intake flow and the tolerance of an engine can be judged. Distortion coefficients may be defined in various ways: in the UK the usual form is

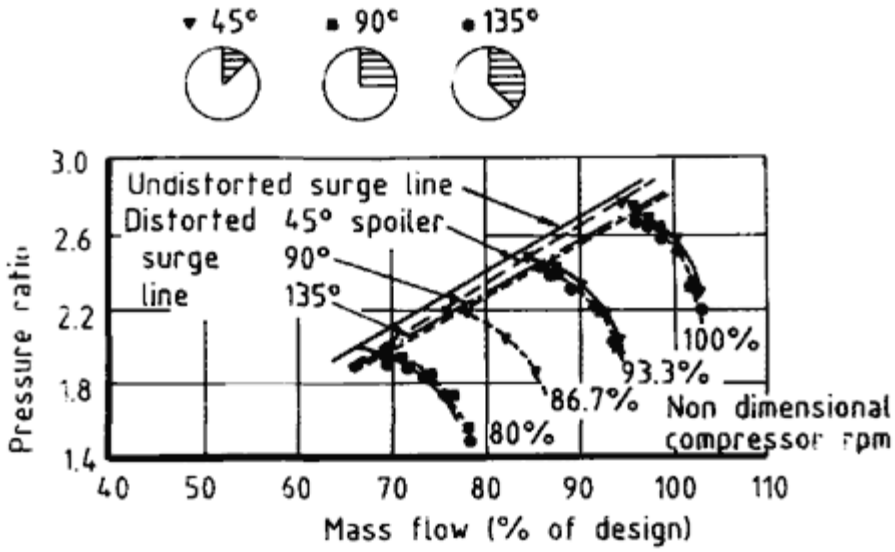

Figure 11.2
Effect of circumferential distortion

on surge line (Hercock & Williams).

$$DC(\theta) = \frac{P_f - P_\theta}{q_f} \qquad (11.1)$$

where *P*f is the mean total pressure at engine face, (the symbol as used throughout the book), *q*f is the corresponding mean dynamic head and *P*q is the mean total pressure in the 'worst' sector of the face, of angle q (Fig. 11.3 illustrates). The sector q must be of significant extent and 60° is usually regarded as a satisfactory minimum. Thus a commonly used coefficient is DC(60): others which are also used are DC(90) and DC(120).

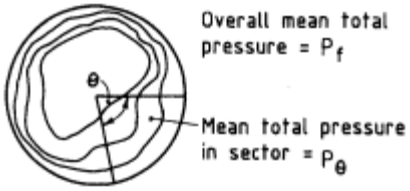

Figure 11.3
Illustration of total-pressure contours and q sector for definition of distortion coefficient.

In the USA more complex descriptors have been evolved to take proper account of the relation between radial and circumferential distortion and to correlate all aspects of distortion shape and intensity which affect surge pressure ratio. One such descriptor, known as *K*A2, combines circumferential and radial factors in a relationship

$$K_{A2} = K_\theta + b \,.\, K_{rad}$$

where *b* is a weighting factor that changes with engine type. The separate circumferential and radial factors are determined by pitot measurements around *n* concentric rings with *m* equispaced points on each ring, using the formulae:

$$K_\theta = \frac{2}{m\, q_f \sum_n \left(\frac{1}{D_n}\right)} \sum_n \left[\frac{1}{D_n} \left\{ \left(\sum_m P_f \cos\theta\right)^2 + \left(\sum_m P_f \sin\theta\right)^2 \right\}^{\frac{1}{2}}\right]$$

$$K_{rad} = \frac{1}{q_f \sum_n \left(\frac{1}{D_n{}^2}\right)} \cdot \sum_n \frac{[\bar{P}_f - (\bar{P}_f - (\bar{P}_f)_n]}{D_n{}^2}$$

in which q is the circumferential location and *D* is the ring diameter.

A simpler descriptor is a radially weighted circumferential index using five rings and defined by:

$$K_{DA} = 100 \sum_{n=1}^{5} \left[\left(\frac{\Delta P_n}{\bar{P}_n} \theta \right)_{max} \cdot \frac{r_f}{r_n} \right] \Big/ \sum_{n=1}^{5} (r_f / r_n)$$

where D*P*n = $(\bar{P} - P_{min})_n$ and $\bar{P}$, Pmin are respectively the mean and the lowest total pressures in a ring. As an alternative to this, D*P* is sometimes defined as half the difference between the highest and lowest total pressures in a ring: the descriptor is then written as *K*DM. These and other descriptors are to be found in treatments by Martin and Melick (1972), Farr (1973), Moore and Lueke (1973) and elsewhere. Comparisons between various descriptors have been made by Hercock and Williams (1974), who give moreover a full account of the distortion problem from an engine response aspect.

11.2.2
Dynamic Distortion

The first realisation that maximum allowable values of steady-state distortion could be inadequate for predicting the onset of compressor surge came with the analysis of flight test results on the F.111 aircraft with the TF 30 engine. It was revealed, as illustrated in Fig. 11.4, that many surges occurred for values of the steady-state factor *K*D well below the maximum allowable values that had been derived from static tests of the engine with simulated distortion. On the suspicion that unsteady flow was the cause of the discrepancy, it was next shown, by both flight and static tests, that the critical values of steady-state distortion were affected by turbulence levels, as characterised by root-mean-square values of total-pressure fluctuations. A typical correlation is shown in Fig. 11.5. A satisfactory quantitative link between unsteady-pressure measurements and the onset of surge was made when it was realised that surge would follow if the critical value of distortion

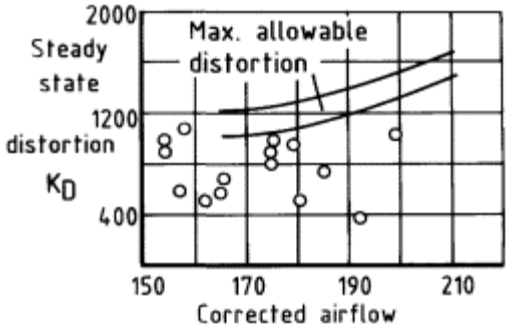

Figure 11.4
Measurements in flight of occurrence of
compressor stall (Van Deusen and Mardoc).

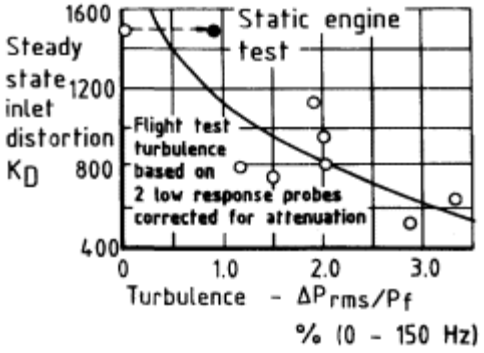

Figure 11.5
Influence of turbulence on occurrence of compressor stalls (from measurements in flight by Van Deusen and Mardoc).

coefficient were exceeded for a time period of the order of that for one engine revolution about 5 milliseconds.

Many examples of the relationship between values of instantaneous distortion coefficient and surge onset have been given by Burcham and Hughes (1970), in the form of variations of *K*DA or *K*DM with time. A similar record of DC(90) variation given by Hercock and Williams is shown in Fig. 11.6, taken from a full-scale ground test of intake and engine in simulated supersonic flight conditions. Over the 350 milliseconds of record shown, several peak transients occurred at levels around 0.5, exceeding the steady-state value 0.37. At about 330 milliseconds a peak at 0.6 was obtained and 20 milliseconds later the engine surged. The time lag is of the usual order and represents the time taken for the distorted flow to stall the

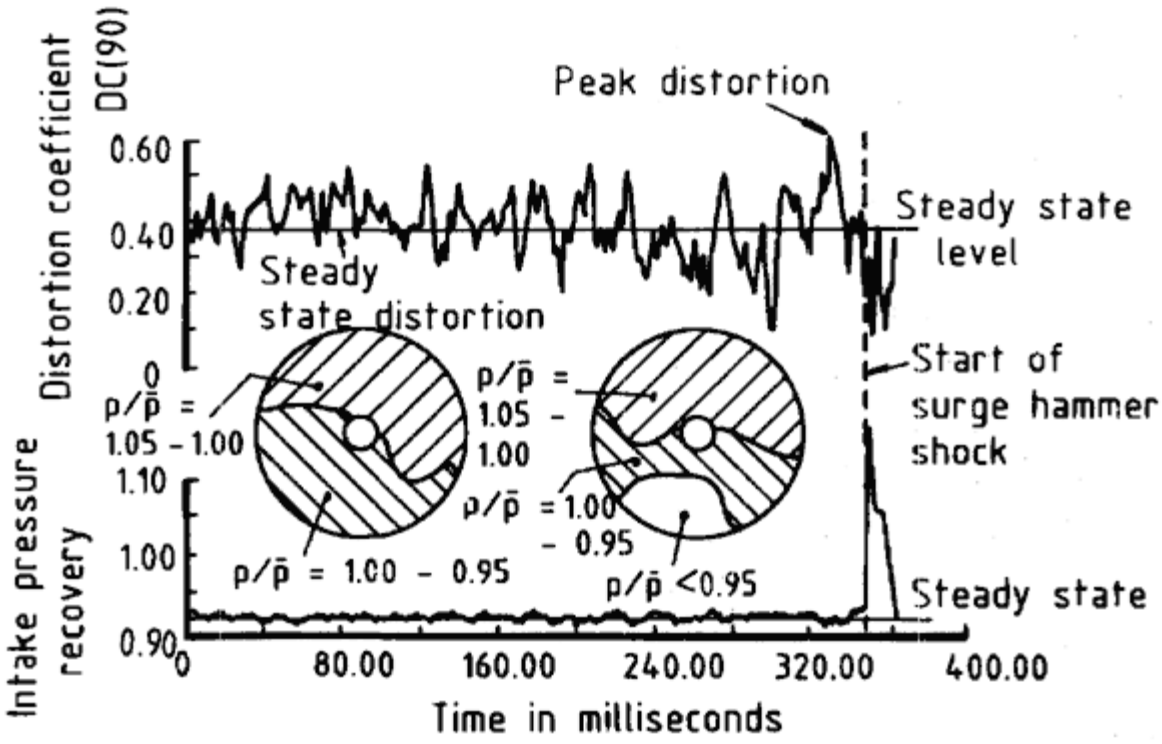

Figure 11.6
Engine surge caused by intake dynamic distortion (Hercock & Williams).

compressor and for the resulting shock wave usually termed 'hammer-shock' to travel forwards out of the engine. The effect of this in pressure terms is seen on the lower curve, which plots intake total-pressure recovery. Prior to the surge, fluctuations in this quantity (timewise oscillations about a steady-state value) were small. The essential difference in pressure distribution between steady-state and peak distortions is illustrated and is seen to have been a transient occurrence of low total pressure in a region near the bottom of the duct.

11.2.3
Intake Considerations

In terms of intake aerodynamics, it is evident that any loss of total pressure which occurs in a manner other than uniformly across the intake stream-tube results in a degree of distortion in the flow; and experience shows that distortion thus formed, though it may attenuate in the duct, is unlikely to have disappeared by the time the flow arrives at the engine face. Sources of distortion therefore are many: they include boundary layer profile distension on the inside walls of bends, wall separation from high diffusion rates, lip separation at high flow ratio (Chapter 4), shock and boundary layer interaction (Chapter 3), inadequate boundary layer bleeds (Chapter 8), parallel ingestion of different shock systems in an un-matched flow condition (Chapter 5), flow asymmetry with twin intakes (Chapter 2) and so on. The effect of aircraft incidence, whether in low speed level flight, high altitude level flight or high g manoeuvres, can be particularly significant; the more so if intakes are located on the fuselage side or in the wing root, where local flow angles are exaggerated by an upwash from the fuselage. Sensitive conditions can also occur when an aircraft is manoeuvring on the ground in a wind: there in addition to the possible adverse effects of high flow ratio and low Reynolds number, vortices may be ingested either from the ground boundary layer or as a result of cross-wind flow separation from intake side-plates or other protuberances.

Some effects of intake flow have been studied to the extent that experimental results can be quoted for particular configurations and qualitative generalisations can be made from them. The examples which follow are taken from reviews by Sterbentz (1956) and Piercy (1956) and from specific tests by Johnston (1951), Bendot, Heins and Piercy (1984) and Rolls-Royce (unreported results, *circa* 1976). In most of these cases, distortion is expressed in terms of the factor

$$\frac{P_{max} - P_{min}}{P_{mean}} \text{ or } \frac{\Delta P}{\bar{P}}$$

measured at a particular station in the duct. This does not distinguish between radial and circumferential variations but is a convenient factor,

often useful for comparative purposes. A particular convenience is that, in contrast to definitions based upon local *q*, the factor is not sensitive to changes in flow rate or duct area.

Marked variations in total pressure across the duct are introduced when, under spillage conditions, the shock intersection point of an external-compression system falls inside the capture streamtube. In an example at Fig. 11.7 the distortion factor at a position just inside the entry rises rapidly as flow ratio is reduced from 1.0 to 0.8 and remains high for further reduction. For an axisymmetric intake at zero incidence, as in this case, the distortion is fundamentally radial and remains so to the engine face. At incidence, however, circumferential symmetry is disturbed and when the same situation occurs with a wedge intake or a part-conica intake, distortion at the engine face is strongly circumferential. An interesting assembly of results by Rolls-Royce is shown in Fig. 11.8, where peak *dynamic* distortion, in DC(120) terms, is plotted against the difference in total pressure of the two streams, ratioed to mean dynamic pressure. A good correlation is obtained for a range of free-stream Mach numbers and a range of incidences.

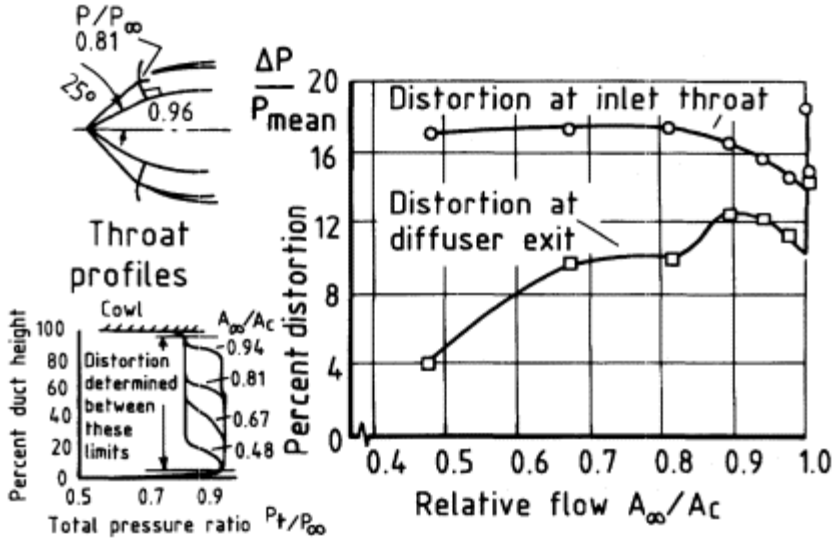

Figure 11.7
Radial distortion caused by changes in shock pattern.

When flow distortion is present at the entry, its magnitude is usually reduced by mixing which takes place during passage through the subsonic diffuser. The example at Fig. 11.7 is a case in point. An important proviso is that flow separation does not occur in the diffuser. For a given diffuser length, increasing the area ratio *A*c/*A*f reduces distortion (subject to no flow separation) by reducing the mean velocity. For a given area ratio, an

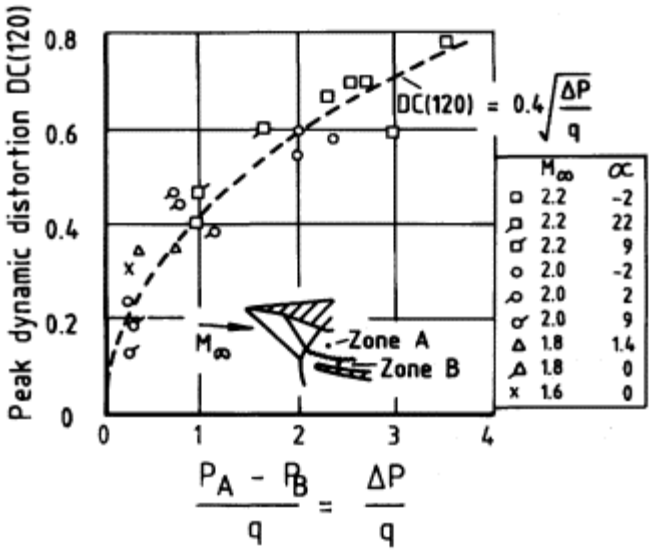

Figure 11.8
Correlation of peak dynamic distortion with difference
in total pressure of a two-stream flow at entry.

increase in diffuser length is normally beneficial. With a particular diffuser, distortion is substantially reduced by the addition of a section of constant-area duct at the end and even more so by a contracting section such as occurs naturally in the presence of a compressor hub. These last two trends are illustrated by results shown in Fig. 11.9.

Forced-mixing devices such as a screen, a grid or a freely-running blade row, located between the end of the diffuser and the engine face, will normally reduce the level of distortion by redistributing the energy of the flow, at some additional loss in mean total pressure. Two examples are

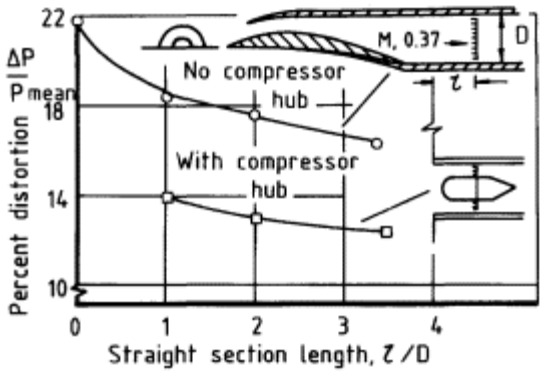

Figure 11.9
Effects of straight length of duct and of
contracting passage on steady-state distortion.

given. In the first a high-solidity grid was shown by Bendot *et al.* to be particularly useful for a ramjet intake operating at incidence in a super-critical condition, in which without the grid the distortion was so great as to preclude stable combustion. The individual passages of the grid were accurately shaped to be convergent-divergent nozzles. The action of the grid was to limit the downstream travel of the ramjet normal shock, thus reducing its Mach number and the consequent non-symmetrical loss from shock and boundary layer interaction at the diffuser wall. The overall loss was made up, even slightly exceeded, by similar losses occurring in the individual nozzles of the grid but these were now distributed more uniformly through the flow. Fig. 11.10 shows the nature of results and some types of grid that might be used in this way.

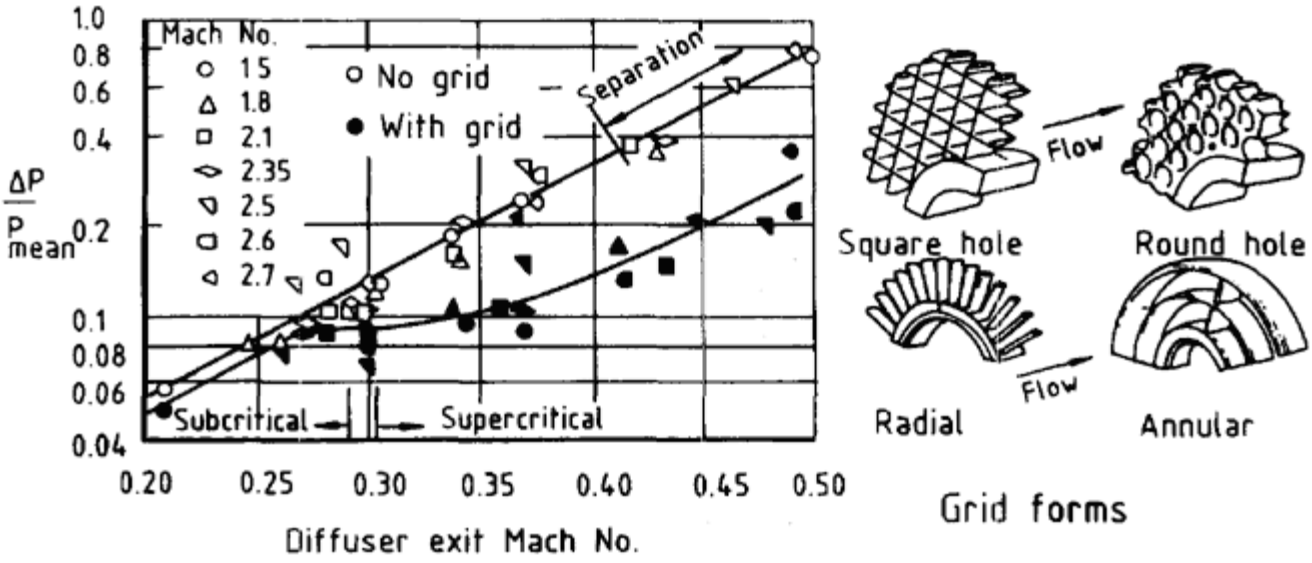

Figure 11.10
Aerodynamic grids and their effect on distortion.

A second example is that due to Johnston, illustrated in Fig. 11.11. A freely-rotating blade row, followed by a fixed row to take out flow angularity, was shown to produce reductions in both circumferential and radial distortion. The rotating blades act as a turbine where the flow velocity is higher than average and as a compressor in the lower velocity flow, thus transferring energy from high to low velocity regions without net work being produced, except that required to overcome bearing friction. It will be noted that without the free blade row an initial reduction in distortion level occurred between stations A and B, owing to the presence of the hub.

Forced-mixing devices are not popular with designers because of the danger of their breaking away into the compressor following damage by bird or debris ingestion and because of the difficulty of protecting them against blockage by ice accretion.

It is often the case that measures which improve intake mean pressure recovery will at the same time reduce the distortion, since they involve 'cleaning up' the flow in an aerodynamic sense. Nevertheless, it cannot safely be assumed that high pressure recovery is sufficient in itself to ensure

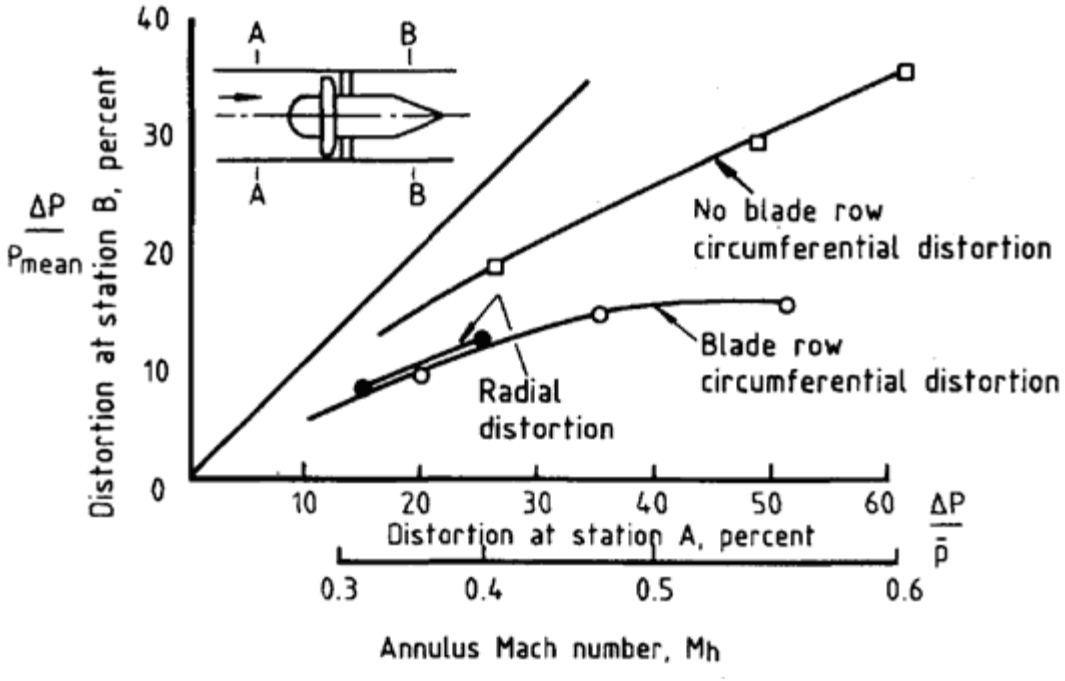

Figure 11.11
Effect of freely-rotating blade row on radial and circumferential distortion.

low distortion in the sense of avoiding the engine surge problem. As the definition at Equation (11.1) indicates if written in the form

$$DC(\theta) = \frac{\Delta P_\theta - \Delta P_f}{q_f} \qquad (11.2)$$

the distortion depends upon the difference between mean total-pressure loss in the q sector, D*P*q, and that for the engine face as a whole, D*P*f, and these are not uniquely related. Thus, for example, a localised flow separation in the duct could have a large effect on D*P*qwith only a relatively small effect on D*P*f. Pursuing the relationship of definitions further, we have

$$\begin{aligned} \mathrm{DC}(\theta) &= \frac{P_f}{q_f} \cdot \frac{P_\infty}{P_f} \frac{(\Delta P_\theta - \Delta P_f)}{P_\infty} \\ &= \frac{P_f}{q_f} \cdot \frac{1}{\eta_p} \left[\frac{\Delta P_\theta}{P_\infty} - (1 - \eta_p) \right] \end{aligned} \qquad (11.3)$$

The factor *P*f/*q*f is basically a function of engine inlet Mach number (specifically so for uniform flow) and for inlet Mach numbers from 0.4 to 0.5 has values approximately in the range 7 to 10. To see the effect of this at high levels of mean pressure recovery, let us assume as an example that total pressure in the (2p q) sector is everywhere equal to *P*¥. Then the mean pressure recovery is given by

$$\eta_p = 1 - \frac{\theta}{2\pi} \cdot \frac{\Delta P_\theta}{P_\infty} \qquad (11.4)$$

so that

$$\frac{\Delta P_\theta}{P_\infty} = \frac{2\pi}{\theta}(1 - \eta_p)$$

and Equation (11.3) for the distortion becomes

$$DC(\theta) = \frac{P_f}{q_f}\left(\frac{2\pi}{\theta} - 1\right)\frac{(1 - \eta_p)}{\eta_p} \qquad (11.5)$$

For a q = 90° sector, as used in the example quote in Fig. 11.6, the total factor multiplying the pressure recovery quotient is between 20 and 30. Thus a 2% drop in pressure recovery is reflected by a rise in distortion coefficient of magnitude between 0.4 and 0.6. As the example shows, such changes may be of the same order as the critical absolute value of distortion coefficient for a particular engine.

For incompressible flow, as for example in low-speed wind-tunnel tests, the definition of distortion coefficient, as an Equation (11.1), is unchanged but the relationship with mean pressure recovery needs to be expressed in terms of the recovery coefficient hsi, as defined in Equation (1.28). The relationship corresponding to Equation (11.5) is readily shown to be

$$DC(\theta) = \frac{q_\infty}{q_f} \cdot \left(\frac{2\pi}{\theta} - 1\right)(1 - \eta_{\sigma i}) \qquad (11.6)$$

Here the factor *q*¥/*q*f is a function of flight speed and engine flow demand and would typically have a value around 2 or 3 to represent a high subsonic cruise.

In Fig. 11.12 are shown two sets of total-pressure contours obtained by Guo (1983) during low speed wind tunnel tests of an S-shaped intake. The contours indicate constant levels of hsi and mean pressure recovery is given in hsi terms. The result for zero incidence shows a thickening of boundary layer on the inside wall relative to the initial bend; mean pressure recovery is reasonably high and distortion coefficient DC(60) in this instance is low. The result for high incidence is dominated by the effect of extensive flow separation at the entry lip: no boundary layer is separately definable, the flow being stratified across the duct. Mean pressure recovery is low and distortion coefficient is high.

It is noteworthy that in a further test, at the same high incidence, for which an internal fence was fitted to even out the flow, the mean pressure recovery remained at the same low value but distortion was reduced to one tenth of the level shown in Fig. 11.12(b). Thus, as high-pressure recovery is not a guarantee of low distortion, so conversely low-pressure recovery does not necessarily entail a high distortion level. Distortion therefore is a fea-

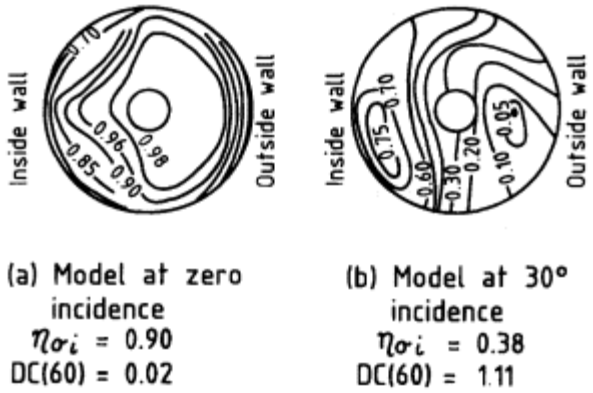

Figure 11.12
Examples of low and high circumferential distortion (wind tunnel model tests by Guo) (a) model at zero incidence (hs*i* = 0.90, DC (60) = 0.02) (b) model at 30°incidence (hsi = 0.38. DC (60) = 1.11).

ture of intake flow to be evaluated in parallel with but separately from, and additionally to, the mean pressure recovery. Owing to the evident complexity of flows involved, distortion is not generally amenable to theoretical assessment and its determination, and where necessary its reduction, are essentially matters of experiment. As such, they can be seen to represent a very considerable extension of the pressure recovery problem. Where only steady-state distortion is required, this is assessed from the same measurements as yield the mean pressure recovery, so that when pressure recovery is itself required, additional analysis is the only extra task.

For the determination of dynamic distortion, however, much additional instrumentation is required (see Chapter 15) and both experiment and analysis take on a different order of complexity. The significance of distortion, moreover, persists throughout the whole flight envelope of an aircraft, including conditions such, for example, as those of transient manoeuvring in which the level of pressure recovery may not be of major concern. Normally, therefore, the range of investigation of an intake design is considerably extended by the need to cover distortion aspects.

Where separated flow is concerned, it seems that little generalisation is possible by way of direct quantitative correlation between disturbances generated in an intake or externally to it and the degree of dynamic distortion at the engine face. In his experiments on S-ducts, Guo (1982) uncovered a number of points which may be useful to future thinking on the subject.

(1) Fluctuations of wall static pressure associated with a region of separated flow in the duct could be either narrow-band or broad-band in character, depending apparently on the degree of instability of the separated flow region.

(2) Fluctuations of total pressure in the nominal engine-face plane followed the wall static-pressure fluctuations in character.

(3) Power spectral densities indicated that the energy of fluctuation in wall static pressures was relatively weak for a point deep within a separated flow region but much stronger for a point at the periphery, that is in a region of reattachment, where the pressure gradient was large.

(4) Total-pressure fluctuations at engine face correlated well with the strong wall pressure fluctuation of (3). The time delay between signals was in reasonable agreement with the transport time of flow between respective points. This cross-correlation was not uniform, however, over the engine-face section and the position of strongest cross-correlation could not itself be correlated with the position of flow separation in the duct.

Zhang and Gao (1983) have presented work on the experimental and theoretical design of distortion simulators. Using a simple momentum method, an initial calculation is made to provide a preliminary design: a small amount of trimming by experiment then leads to an accurate simulation of the required distortion coefficient.

For a preliminary assessment of dynamic distortion in a given intake, a rough rule of thumb can be applied, based on turbulence of the flow expressed as values of root-mean-square of the fluctuations in static pressure. If (D*p*)rms/*P*f is not greater than one per cent, the problem of dynamic distortion can confidently be excluded: if the same factor is as high as four or five per cent, then detailed distortion measurements are advisable. Research is being done to forge closer links between turbulence and both static and dynamic distortion, so as to alleviate the problem of the high cost, in time and money, of assessing the last of these. A technique of synthesis of dynamic distortion values, from measurements of steady-state pressures and a relatively small number (from 4 to 12) of (D*p*)rms values at the engine-face position, has been described by Melick (1978) and by Borg (1981). The method combines these measurements with an artificial instantaneous pattern generated on a random number basis by a computer programme.

11.3
Swirl

The problem of angular swirl of flow at the engine face has come to the fore in recent years. Instances have occurred of engines surging in flight because the angle of swirl, in the absence of inlet guide vanes, has been sufficient to stall the compressor. The problem is associated specifically with installa-

tions in which the engine is carried in the aircraft fuselage and the intake is located in an offset position (on the side, top or bottom of the fuselage), necessitating thereby a double-bend or S-shaped duct. It depends furthermore upon the presence of flow separation from a source *independent of the bend itself*, occurring in fact in a longitudinal plane more or less at right angles to the plane of the bend. The most obvious example of this is the case of a side intake with separation occurring from the bottom lip of the entry when the aircraft is at a high angle of attack. Other situations include top or bottom intakes in yaw and supersonic intakes in which separation may occur from angled ramp surfaces. The phenomenon as known is essentially confined to the subsonic flow within the duct itself.

Stocks and Bissinger (1981) and Aulehla (1982) have described the swirl problem and methods of amelioration, largely in the context of the development programme for the European Tornado aircraft.

11.3.1
Intrinsic Nature of Flow

Swirl develops in the first bend of an S-duct, as the result of interaction between the centrifugal pressure gradient and a low energy region associated with flow separation. We follow the physical explanation given by Dunham (1979) and consider the flow round a single bend in the horizontal plane. The centrifugal pressure gradient is proportional to r*U*2/*R*, where *U* is the mainstream velocity and *R* is the radius of the bend. This results in the pressure at the outside wall of the bend being greater than that at the inside wall. If now there is a region of reduced velocity *U'* at the bottom of the duct and local centrifugal gradient, being proportional to r*U'*2*R*, is not sufficient to balance the pressure difference between the walls, so the flow in this region is directed towards the inside wall, in other words a swirl is set up in the duct. If there were a similar region of reduced velocity at the top of the duct, as for example with symmetrical boundary layers at zero incidence (Fig. 11.13), the net result would be a double swirl, the flow returning towards the outside wall across the middle of the duct. The important practical case, however, is the asymmetrical one in which either the top or bottom has a particularly low velocity region, resulting from flow separation, in which case the swirl is singly directed and of significant magnitude.

Considering now a complete S-duct, in the second bend the transverse pressure gradient is reversed in direction but the low energy flow, having largely collected on the inside (relative to the first bend) wall by the process just described, is not now in a position to be driven back circumferentially. The swirl tends therefore to persist to the engine face, in the same sense as originally generated.

The process is well illustrated by experimental results obtained by Guo (1983). In tests of an S-duct of typical air intake proportions, without

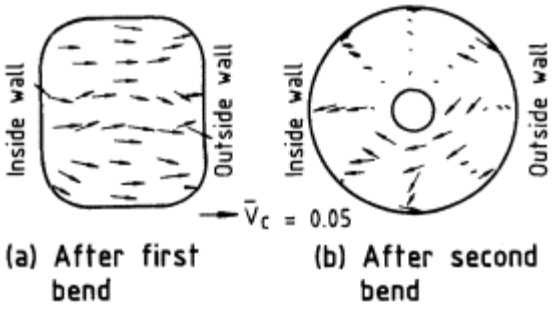

Figure 11.13
Cross-flow velocities in S-duct
at zero incidence (Guo).

fuselage representation, at an incidence high enough for flow separation from the bottom lip, the patterns of cross flow after the first bend and at the engine face position are as shown in Fig. 11.14. These may be compared with the results for zero incidence in Fig. 11.13 where the ultimate cross-flow velocities are small and multi-directional. Longitudinal pressure distributions for the two cases are shown in Figs 11.15 and 11.16, as measured along the centre-line of each wall. At zero incidence the top and bottom pressure distributions are identical, while the sidewall distributions show the opposing transverse pressure differentials on the two bends. At high incidence the lip separation is evidenced by a constant pressure region on the bottom wall, superseded by a more extensive one on the inside wall as the swirl is generated. An important feature is that in the second bend the bottom wall pressures are higher than those on the top wall: since at entry to the second bend the low energy flow is largely in the region of the inside wall, this pressure differential provides a second stimulus to the swirl generation.

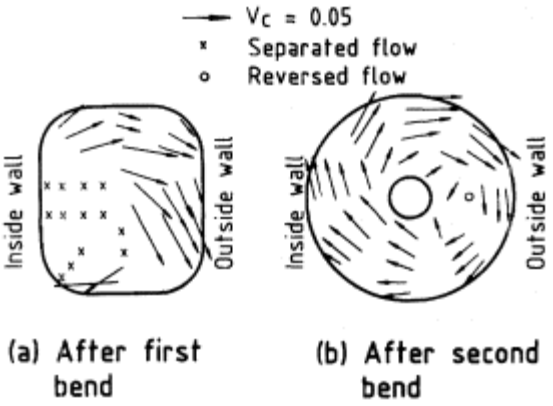

Figure 11.14
Cross-flow velocities (swirl) produced by flow
separation at entry of S-duct at 30° incidence (Guo).

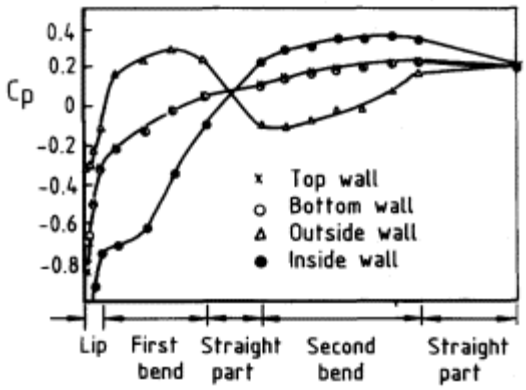

Figure 11.15
Longitudinal pressure distributions in
S-duct for conditions of Fig. 11.13.

For a quantitative measure of swirl, Guo proposed the use of a coefficient SC(q) defined in an analogous manner to distortion coefficient DC(q). SC(q) is thus the maximum average circumferential component of cross-flow velocity in a q ° sector of the measuring station, nondimensionalised by dividing by the mean duct velocity at the throat section. An arbitrary choice of sign considers the swirl to be positive for clockwise rotation facing downstream: swirl generated at high incidence in the manner described above is then positive for a port-side intake and negative for a starboard-side intake. Using a 60° sector, the growth of swirl coefficient with incidence for Guo's intake is as given in Fig. 11.17. The variation of distortion coefficient DC(60) is also shown: in broad terms the total-pressure distortion increases as swirl increases, which is not unexpected since both variations are related to the flow non-uniformity developing inside the intake lip.

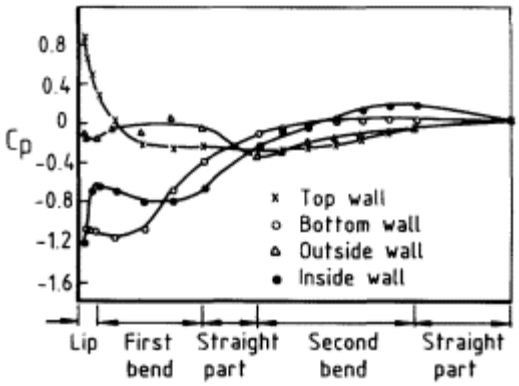

Figure 11.16
Longitudinal pressure distributions in
S-duct for conditions of Fig. 11.14.

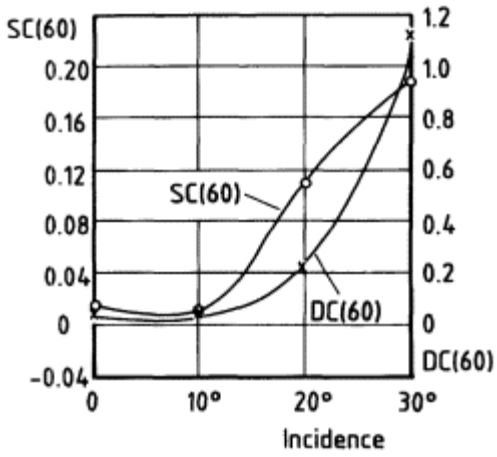

Figure 11.17
Growth of swirl and distortion
in S-duct with increase of incidence.

11.3.2
Sensitivities and Correlation Potential.

The degree of swirl arriving ultimately at the engine face is sensitive to changes which modify the flow pattern in the first bend. Modification of the flow pattern can take various forms. Continuing the consideration of a side intake at high incidence, if auxiliary inlet area is provided behind the bottom lip, this decreases the severity of the flow separation and the swirl is reduced in consequence. The action of the additional inflow is analogous to a reduction of incidence for the unmodified inlet and this applies not only to the overall result but also to the detailed longitudinal pressure distributions.

To take a different example, Guo found that swirl could be reduced by fitting a spoiler consisting of a vertical strip projecting a short way across the entry from the inside lip. With a spoiler projection 13% of the entry width, the swirl was reduced to zero and for any larger projection, the final swirl was in the opposite direction. The action of a spoiler is clearly different from that of an auxiliary inlet: the spoiler produces an outflow component which resists the onset of swirl-producing inflow in the first bend. A pressure distribution along the bottom wall with spoiler fitted reveals an *extended* constant-pressure region at approximately the same low pressure value as denotes the original separation without spoiler.

A modification which may be considered a reasonable practical solution to the swirl problem is the fitting of a fence to control the flow around the first bend. Some experimental results obtained by Bacon and Magowan (1983) and presented by Seddon (1984) are shown in Fig. 11.18. The fences were fitted along either the bottom wall or the sidewall generator of the duct (or both in the case of arrangement K), the fence leading edges were some distance inside the entry (20% to 40% of the bend length) and fence lengths were about 75% of the bend length. All the arrangements produced

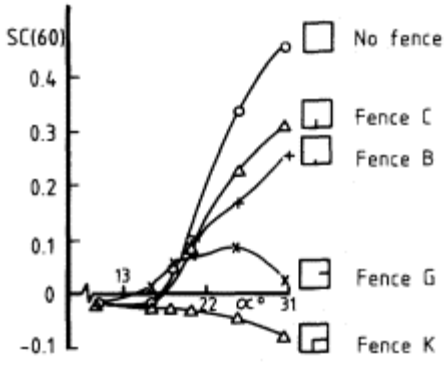

Figure 11.18
Use of fences in first bend of S-duct to
reduce distortion (Bacon and Magowan).

useful reductions in swirl coefficient, the best single fence being that on the sidewall, fence G, where the crossflow velocities evidenced in Fig. 11.14 are high. The action of a fence is directly to prevent these velocities developing as the flow negotiates the first bend. This is basically different from the two actions described above, but there is a significant analogy with the spoiler situation in that the bottom wall pressure distributions are similar in the two cases; in other words the flow separation is not reduced in extent but rather induced to proceed more directly down the centre of the duct. The effect of this change is considered below.

On more representative aircraft models, in which the intake is located on the side of a fuselage, it has been observed that, as incidence is increased from zero, the swirl initially develops progressively as for the isolated intake but at very high incidences say 30° and upwards the trend is reversed and the net swirl may be reduced to zero and even itself reversed. The cause of this change in trend is observed to be the development of a significant outward crossflow at entry, which arises from the flow around the forward fuselage when this is at high incidence. There is a clear analogy here with the type of flow induced by Guo's spoilers at lower incidences.

From observation of his own experimental data, Guo was led to suggestion that swirl might be found to correlate quantitatively with a *vertical* pressure differential near the end of the duct. He defined DCpbt2 as the difference between static-pressure coefficients on the bottom and top walls at the end station of the second bend and was able to show a good correlation between this difference and SC(60) for his tests with and without spoilers. Later the correlation was successfully extended to include the results from a second design of intake (Guo, 1982). Without commitment to the particular pressure differential used, which was regarded as a relatively simple criterion rather than necessarily the best, it is important to recognise the fluid dynamical principle lying behind its adoption.

As evidence accumulates, it becomes clearer that whilst largescale swirl owes its origination to the influence of transverse pressure gradient *in the plane of the first bend*, its development or repression in the second bend depends not so much on the reverse gradient as on the transverse gradient *at right angles to the bend plane*. Having accepted the evidence for this fact, it is not difficult to explain: swirl developing in the first bend transfers a good portion of the low energy air resulting from lip separation to the inside wall of that bend; in the second bend, therefore, the pressure gradient so placed as to continue or reverse the trend, *by the same process*, is not the second-bend gradient but that at right angles to it. Following this argument, the greater the extent to which the separation zone in the first bend can be 'steered' down the centre of the duct, the greater is the influence of the reverse gradient in the second bend and the smaller is the influence of the gradient at right angles. The beneficial effects of spoilers or of fuselage outflow in reducing the final swirl are explained in this way.

The factors which govern the gradient at right angles to the second-bend plane have not been investigated systematically but longitudinal pressure distributions measured with fence G can be seen to support the argument of the previous paragraph. Fig. 11.19 shows first-bend pressure distributions along the bottom wall and on either side of the sidewall fence. The latter illustrate the load taken by the fence in restraining swirl development. More to the present point, the bottom-wall distribution shows an extended constant-pressure region as compared with the distribution without fence. The effect of this on pressures in the second bend is illustrated schematically in Fig. 11.20. Clearly, the further the constant pressure extends round the first bend, the smaller becomes the excess of bottom-wall pressure over top-wall pressure in the second bend: the evidence is that swirl is thereby reduced. The significance of Guo's particular choice of pressure difference

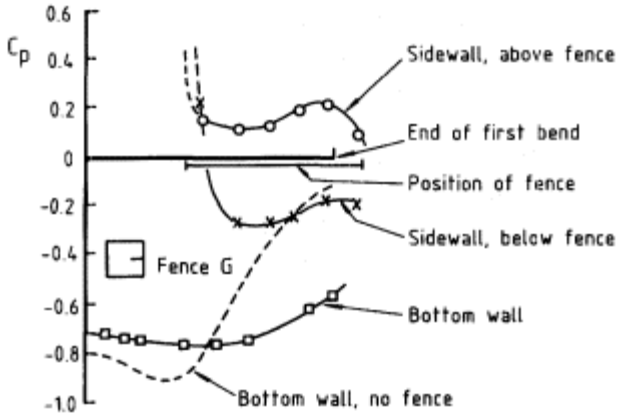

Figure 11.19
First-bend pressure distributions
in S-duct with sidewall fence.

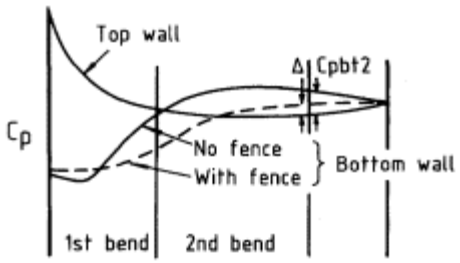

Figure 11.20
Significance of bottom-to-top pressure
difference in second bend of S-duct (schematic).

can be appreciated, although it may be supposed that a difference integrated round the second bend would be a more reliable indicator for the general case.

From a design aspect, fences appear to provide an acceptable method of negating S-duct swirl. Their effect on intake pressure recovery is small at low incidence a loss of perhaps one per cent and probably favourable at high incidence. Experimental development for particular cases is needed in order to quantify these effects, in particular to ensure that the loss of total pressure at low incidence is not excessive. It may be possible, however, to correct for swirl in the initial duct design, which would seem a preferable route to take. Thus, in a case where a double offset (horizontal and vertical) is involved, the possibility may exist of deploying the second offset specifically in the second bend, in such a way as to create a bend pressure gradient at right angles to the first and in the sense to counter the initial swirl.

References

Aulehla, F. (1982) 'Intake swirl, a major disturbance parameter in engine/intake compatibility. *13th Congress of ICAS/AIAA*, Seattle, August 1982.

Bacon, L.D. and Magowan, J.M. (1983) 'An investigation into anti-swirl devices for S-shaped air intakes. University of Bristol, Department of Aeronautical Engineering, Report No. 293.

Bendot, J.G., Heins, A.E. and Piercy, T.G. (1984) 'Ramjet air induction system design for tactical missile application'. AGARD, LS 136.

Borg, R. (1981) 'A synthesis method for estimating maximum instantaneous inlet distortion based on measured inlet steady rate and RMS pressures'. AGARD, CP 301.

Burcham, F.W. and Hughes, D.L. (1970) 'Analysis of in-flight pressure fluctuations leading to engine compressor surge in an F-111A airplane for Mach numbers to 2.17'. AIAA, 70 624.

Dunham, J. (1979) 'The generation of swirl in an S-duct with axial inflow'. NGTE unpublished memo.

Farr, A.P. (1973) 'Evaluation of F-15 inlet dynamic distortion'. AIAA, 73 784.

Guo, R.W. and Seddon, J. (1982) 'Some unsteady flow characteristics of two S-shaped intake models tested at high incidence'. University of Bristol, Department of Aeronautical Engineering, Report No. RWG/JS/3/82.

Guo, R.W. and Seddon, J. (1983) 'Swirl characteristics of an S-shaped air intake with both horizontal and vertical offsets'. *Aeronautical Quarterly*, May 1983.

Guo, R.W. and Seddon, J. (1983) 'The swirl in an S-duct of typical air intake proportions'. *Aeronautical Quarterly*, May, 1983.

Hercock, R.G. and Williams, D.D. (1974) 'Distortion-induced engine instability. Aerodynamic response'. AGARD, LS72-Paper No. 3.

Johnston, I.H. (1951) 'The use of freely rotating blade rows to improve velocity distributions in an annulus'. NGTE report.

Martin, R.J. and Melick, H.C. (1972) 'A feasibility study for definition of inlet flow quality and development criteria'. AIAA, 72 1098.

Melick, H.C., Ybarra, A.H. and Bencze, D.P. (1978) 'Estimating maximum instantaneous distortion from inlet total pressure RMS measurements'. AIAA, 78 970.

Moore, M.T. and Lueke, J.E. (1973) 'A similarity parameter for scaling dynamic inlet distortion'. ASME, 73-WA/Aero-3.

Piercy, T.G. (1956) 'Factors affecting flow distortions produced by supersonic inlets'. NACA, RM E55L19.

Seddon, J. (1984) 'Understanding and countering the swirl in S-ducts: tests on the sensitivity of swirl to fences'. *Aeronautical Journal*, R.Ae.Soc.

Sterbentz, W.H. (1956) 'Factors controlling air-inlet flow distortions'. NACA, RM E56A36.

Stocks, C.P. and Bissinger, N.C. (1981) 'The design and development of the Tornado engine air intake'. Paper No. 10, *AGARD FDP Symposium*, Toulouse, May 1981.

Van Deusen, E.A. and Mardoc, V.R. (1970) 'Distortion and turbulence interaction, a method for evaluating engine and inlet compatibility'. AIAA, 70 632.

Zhang, S.Y. and Gao, S.I. (1983): 'Experiments and mathematical simulation of plate distortion simulators'. *Sixth International Symposium on Airbreathing Engines.* Paris.

Chapter 12
Matching and Control

In the design of an air intake it is important to ensure that, not only at the design point but under all significant conditions of operation, the intake provides an adequate supply of air to the engine, with pressure recovery sufficient for the particular operational condition and without an undue penalty in drag. To ensure that these requirements are met over the operational span is the problem of matching: matching is thus a necessary follow-on from and complement to the basic study of on-design performance.

12.1
Subsonic Intake

With a subsonic intake, as distinct from a supersonic intake flying at subsonic speeds, matching is usually no great problem, though not completely automatic. The essential change from one flight condition to another is the variation in flow ratio, illustrated in broad terms in Fig. 12.1. The following comments apply.

(a) *High speed cruise.* The on-design condition, with flow ratio less than 1.0, usually in the range 0.5 to 0.8. Internal duct performance is at its best. If an external wetted surface is present, entry area is chosen to give a relatively high flow ratio, in order to avoid the flow separation problem described in Chapter 3.

(b) *Climb.* The lower flight speed and, probably, higher engine power lead to a higher flow ratio, probably greater than 1.0. Lip and throat design allow this condition to be accepted without flow separation (Chapter 4). Any external boundary layer development takes place in a negative pressure gradient, a more favourable condition than in case (a).

(c) *Ground running.* For the extreme static condition (flow ratio infinite) an auxiliary inlet system is probably required as described in Chapter 4. The extra inlet can be arranged to close automatically when the flow ratio falls below a certain value, usually during the take-off run. This is the one matching device normally needed for a subsonic intake.

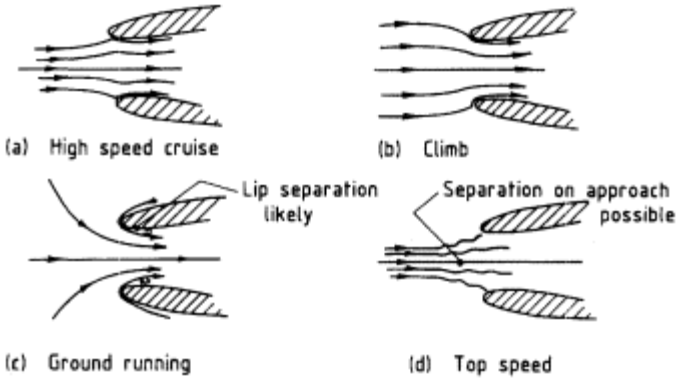

Figure 12.1
Range of flight conditions for subsonic intake.

(d) *Top speed.* At the limiting aircraft speed, reached say in a dive under power, the flow ratio falls below that for condition (a). If an external boundary layer is present (but only in this case) the additionally adverse pressure gradient may cause flow separation: this can then lead to rough engine operation, even in severe cases to surge, or to the flow asymmetry problems of twin intakes described in Chapter 2. A special boundary layer bleed may be required to avoid such occurrences, which however are relatively rare.

12.2 Supersonic Intake: Nature of the Problem

With a supersonic intake, the first point to note is that as flight conditions change, an intake will always adapt to the engine requirement: the difficulty is that untenable situations may be encountered in the process. We assume that at the design Mach number the intake is operating at or near its critical point; the flow ratio is at or near the value $(A¥/Ac)max$, which in turn is at or near the value $(A¥/Ac)full$, namely 1.0. Let us examine the conditions applying to an external-compression intake at a supersonic Mach number below the design value; these are illustrated in Fig. 12.2. For the new value of $M¥$ the intake has a pressure recovery characteristic in the usual form, as shown. At the critical point the maximum flow capture are is $A¥$, which is now less than Ac because the oblique shock system (a single shock suffices for the illustration) lies forward of the cowl lip. If this critical flow ratio is too large for the engine and nozzle condition, the intake runs subcritically as indicated but the penalties are high spillage drag and the probable occurrence of buzz. If the critical flow ratio is too small, this cannot be increased but compensation is provided by the intake running super-

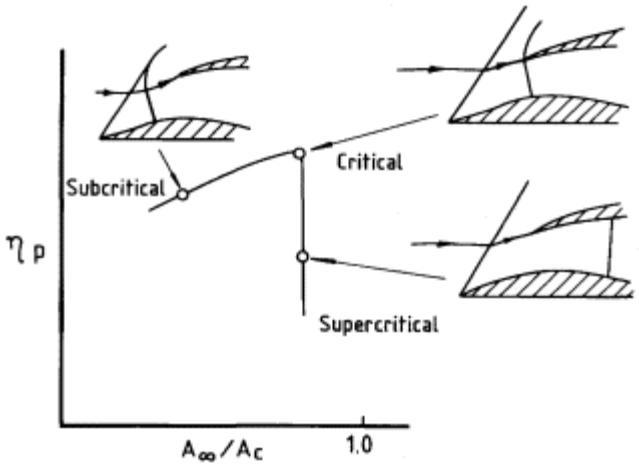

Figure 12.2
Range of flow conditions for supersonic intake at Mach number below design.

critically at lower total pressure; here the penalties are high thrust loss and flow maldistribution, possibly leading to engine surge.

One part of the matching problem, therefore, is to ensure that at supersonic Mach numbers off design, the intake operates sufficiently close to the critical points to minimise these effects. However, even with critical point operation, the shock system is no longer matched to the entry, so that pre-entry drag may be high and pressure recovery low. Hence another requirement of matching is that critical point operation shall be with flow ratios reasonably close to 1.0. Whilst the illustration of Fig. 12.2 applies specifically to supersonic Mach numbers below design, consideration must also be given to subsonic speeds, particularly close to Mach 1, where the main sizing problem of the intake occurs. Finally, in the static and take-off conditions the problem of matching is basically the same as for a subsonic intake, though likely to be intensified by reason of the intake lip being sharp.

For an intake with internal supersonic compression, subcritical operation leads to a discharge of internal shocks, which adds a significant drop in pressure recovery to the other effects of a mismatch. The flow starting problem has to be reconsidered in the off-design context.

12.3
Supply and Demand.

The mass flow m in a streamtube of cross-sectional area A is:

$$m = \rho V A \qquad (12.1)$$

which may be written

$$m = \frac{\rho}{\rho_0}\frac{V}{a}\frac{a}{a_0} \cdot \rho_0 a_0 A \qquad (12.2)$$

where suffix '0' denotes stagnation values. Using the relations

$$\frac{p}{\rho} = RT, \; a = \sqrt{(\gamma \, \mathrm{RT})}$$

we have

$$\rho_0 a_0 = \frac{P}{RT_0}\sqrt{(\gamma \, RT_0)} = P\sqrt{\frac{\gamma}{RT_0}} \qquad (12.3)$$

so that Equation (12.2) becomes

$$m = \sqrt{\frac{\gamma}{RT_0}} \cdot PMA\frac{\rho}{\rho_0} \cdot \frac{a}{a_0}$$

$$= \sqrt{\frac{\gamma}{RT_0}} \cdot PMA\left(1 + \frac{\gamma - 1}{2}M^2\right)^{-(\gamma+1)/2(\gamma-1)} \qquad (12.4)$$

From the formula for sonic area ratio, Equation (1.12), this may be further written

$$m = \sqrt{\frac{\gamma}{RT_0}} \cdot \left(\frac{2}{\gamma + 1}\right)^{(\gamma+1)/2(\gamma-1)} \cdot \left(\frac{A^*}{A}\right) PA$$

or

$$\frac{m\sqrt{T_0}}{AP} = \text{Constant} \times \left(\frac{A^*}{A}\right) \qquad (12.5)$$

This general expression can be used to formulate the engine flow demand as follows. For the purpose of illustration we assume the working relationship of an engine to be such that 'corrected' airflow is proportional to 'corrected' rotational speed, that is:

$$\frac{m\sqrt{T_0}}{P_f} = \text{Constant} \times \frac{N}{\sqrt{T_0}} \qquad (12.6)$$

Using Equation (12.5) to express conditions at infinity in the engine-flow streamtube and equating the mass flows at infinity and at the engine face, we obtain a relation for the demand flow ratio in the form

$$\frac{A_\infty}{A_c} = \text{Constant} \times \frac{\eta_p}{A_c} \cdot \frac{N}{\sqrt{T_0}} \left(\frac{A}{A^*}\right)_\infty \qquad (12.7)$$

in which h*p* is the intake total-pressure ratio *P*f/*P*¥. Thus an engine demand curve as a function of flight speed, for constant engine rev/min and at constant static temperature, for example as in the tropopause, is characteristically as shown in Fig. 12.3. Minimum flow ratio occurs close to Mach 1.0. As subsonic speed decreases, flow ratio increases, roughly according to the sonic area ratio, and tends towards infinity as *M*¥ tends to zero (static condition). As supersonic speed increases, the sonic area again increases but this is countered by an increasing total temperature and a decreasing pressure recovery, so the trend is not strong upwards or downwards. These trends are representative but we recall that the diagram is illustrative only: in practice Equation (12.6) would be replaced by the actual engine working relationships.

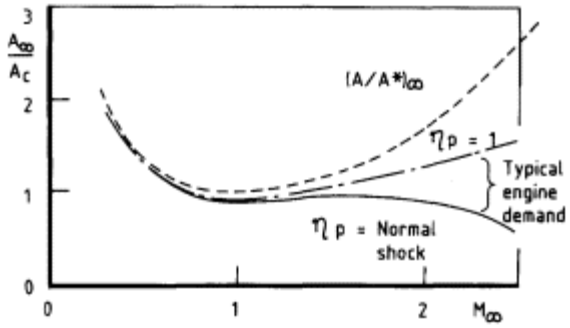

Figure 12.3
Examples of normalised engine demand and intake supply.

To assess the intake supply situation in general terms, it is necessary merely to recognise that a supersonic intake has a near-sonic throat both at the design supersonic Mach number and also at Mach 1.0. By throat we refer to the minimum net area, *A*t say, through which the air passes at entry. Thus on design, this area is roughly equal to (actually somewhat larger than) the ratio

$$A_c \Big/ \left(\frac{A}{A^*}\right)_\infty$$

which for Mach 2.0, for example, has an approximate value 0.6. Hence if the intake geometry is fixed, the value of maximum flow ratio at supersonic speeds varies from about 0.6 at Mach 1.0 to 1.0 at the design Mach number. This is a much wider range of variation than that of engine demand as illustrated in Fig. 12.3. One of two consequences follows. On the one hand if

intake supply is matched to engine demand at design Mach number, the intake will be considerably undersized at Mach 1.0 and forced therefore to run strongly supercritically, with dire consequences for pressure recovery and distortion. If, on the other hand, this is avoided by sizing the intake for Mach 1.0, then at design Mach number the maximum supply is much greater than the demand and the intake will run subcritically with considerable spillage drag and perhaps flow instability. The way out of this difficulty is by the use of variable geometry.

In practice, when the second of the above procedures is followed, the intake is sized for a high-subsonic Mach number condition, say Mach 0.9 in the tropopause, using a throat Mach number not greater than about 0.8.

12.4
Variable Geometry and Practical Examples

Variable intake geometry conventionally has two forms. A valuable way of reducing normal spillage now to be called *forespillage*, indicating that it occurs ahead of the entry is by use of spill vents in the cowl (Fig. 12.4). When the engine flow requirement is less than *A*max, extra air making up the deficit is taken into the intake and ejected through the vents as *afterspillage.* Some drag is of course incurred but this can be considerably lower than that associated with forespillage and since the intake can now operate at maximum flow, the problem of buzz does not arise. It is undesirable, however, to have to deploy spill vents on design, other than in a fine-trimming capacity. Moreover, spill vents cannot be used to match an external shock system to the cowl, nor can they contribute to relief of the flow starting problem when internal compression is being used. Spill vents are therefore used essentially as an adjunct to varying the actual compression-system geometry, including possibly the cowl.

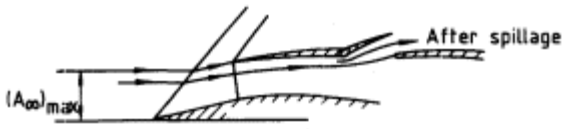

Figure 12.4
Function of spill vent.

Practical forms of variable geometry depend upon the type of intake. For a two-dimensional external-compression configuration, a hinged wedge in the compression system is usually the most appropriate form. With an axisymmetric intake a translating cone may need to be used. In the case of fully internal compression, a variable throat area is required to overcome the starting problem. The intake necessarily flows full, so for matching,

either the capture area *A*c must also be varied or afterspillage must be provided. For axisymmetric internal compression, a design suggested by Mossman (NACA) is perhaps the only practicable solution (Fig. 12.5). This combines a reduced capture area at speeds below design with increased throat area for starting: the loss of total pressure from the low-angle conical spike when protruding is small. For mixed compression in two dimensions, as for example with intake C, Fig. 6.10, a good result may be obtained from the following combination of procedures:

(i) move the second wedge to lower angle as free stream Mach number is reduced, to improve both pressure recovery and drag;

(ii) use afterspillage to adjust to the engine flow demand. For an axisymmetric mixed-compression design a translating spike moving inwards for the lower Mach numbers may be feasible.

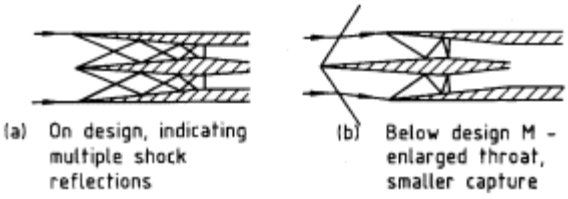

Figure 12.5
Axisymmetric internal-compression intake (after Mossman).

Some illustrations of the results of interactions between engine demand and intake supply, calculated for both fixed and variable external-compression intakes, are given in Fig. 12.6. In case (a) the half cone forebody is fixed, case (b) is two-dimensional with variable second-wedge angle and case (c) has a half cone that translates along a circular path. Steps in the calculation procedure were:

(i) Engine flow data were obtained in the form of variation of $m\sqrt{T_0}/P_t$ with *T*0.

(ii) (*A*¥/*A*c)max was calculated for all positions of the compression surface, at Mach numbers for which the shocks remained attached.

(iii) The intake was sized to accommodate the required engine flow at Mach 0.9 in tropopause conditions, with a throat Mach number *M*t = 0.75.

(iv) A variation of intake pressure recovery with Mach number was assumed and the engine flow-ratio demand, *A*¥/*A*c, was calculated from the variation of $m\sqrt{T_0}/P_t$.

(v) The results of (ii) and (iv) were plotted together, as in Fig. 12.6.

(vi) At the intersections of demand and supply curves, intake pressure recoveries were checked for agreement with known intake char-

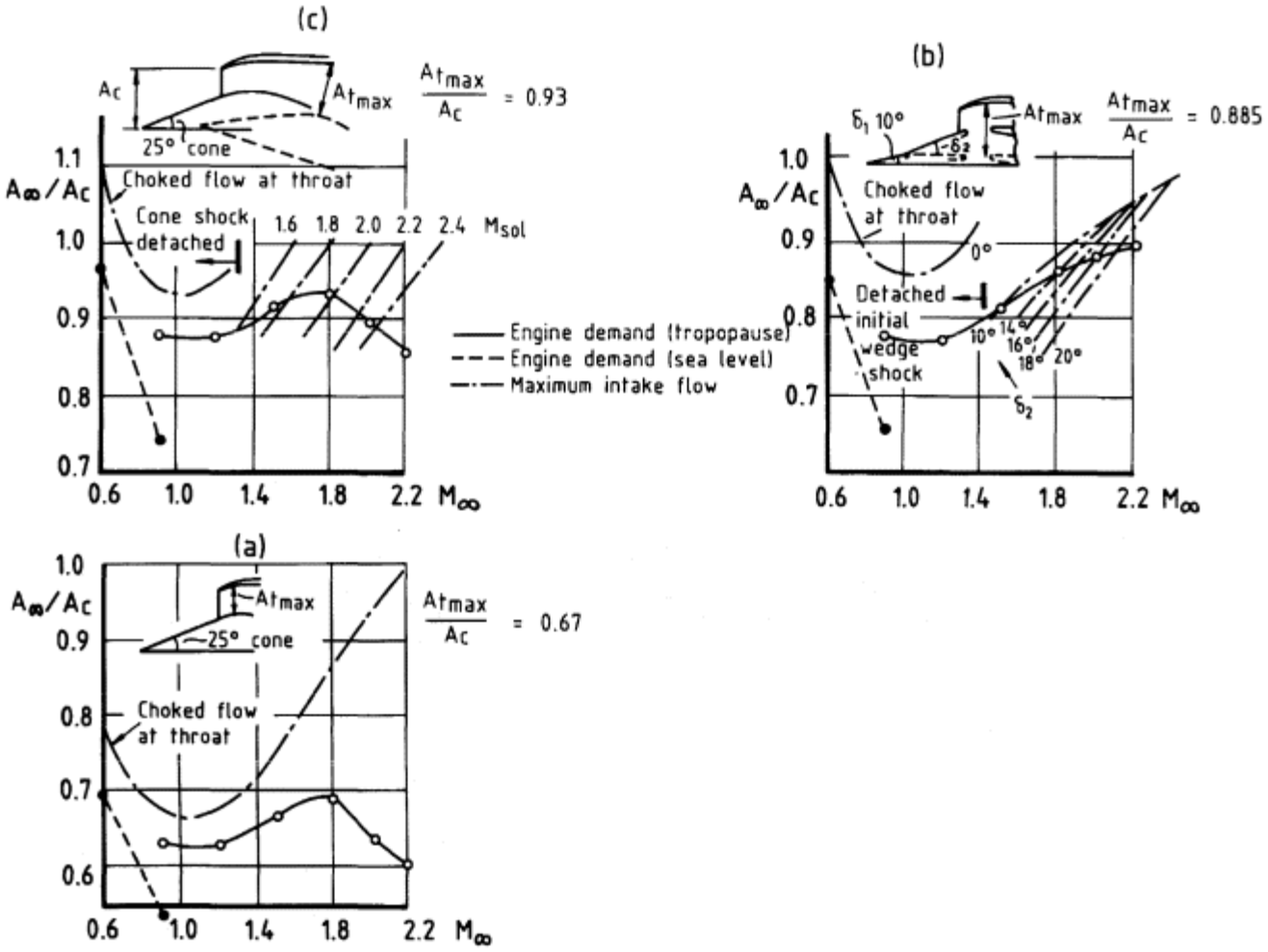

Figure 12.6
Matching of engine demand and intake supply for intakes having (a) fixing conical forebody (b) variable-wedge forebody (c) translating and rotating half-conical forebody. All intakes sized for *M*t 0.75 at *M*¥ 0.9 (tropopause).

acteristics. Where necessary, adjustments were made and the procedure was iterated. Rapid convergence was obtained.

(vii) Spillage drag could then be calculated and comparative performance assessments could be made.

In the results, the high degree of spillage required of the fixed half cone forebody intake can be seen. For both variable-geometry designs, intake and engine can be matched throughout the supersonic range by suitably scheduling the variable geometry against flight Mach number. The translating-rotating cone, Fig. 12.6(c), has the advantage of producing the largest throat area-ratio *A*t/*A*c, at Mach 1.0, hence requiring the smallest intake area, *A*c.

The following broad principles are normally followed for the control of variable geometry.

(a) The position of a variable wedge, cone or cowl is controlled on a schedule related to aircraft Mach number. Position adjustment can be relatively slow without serious consequence.

(b) With afterspill vents maintaining critical-point operation, a fast control may be needed to prevent the intake going into buzz. A pressure signal detecting small movements of the normal shock is conventionally used.

(c) With a non-self-starting intake, an override control is necessary to cycle the variable geometry if for any reason the intake accidentally unstarts.

There are various ways of interpreting these principles and an actual system is a matter of particular design.

12.5 Additional Complexities: A Case in Point

In the evolution of a practical supersonic aircraft for civil or military use, other aspects of the matching problem have also to be considered. Thus firstly, many supersonic intake systems, particularly those intended for efficient long-range flight, include the provision of an internal boundary layer bleed. In such cases the total intake flow capture area, *A*¥, is shared between engine flow and bleed flow, say

$$\frac{A_\infty}{A_c} = m_E + m_B$$

and interaction between these two components may be important. Secondly, a long-range aircraft needs to be able to perform efficiently

within a significant spread of ambient air temperatures, determined by route and climate; hence the matching of engine and intake in a range of 'on-design' conditions is an important consideration. Thirdly, the intake control system must be capable of protecting the engine from buzz or surge which can occur from the effects of atmospheric transients temperature fronts, pressure changes and wind gradients during a flight.

12.5.1
The Concorde Intake

The nature and effect of these complexities can be conveyed to an extent by reference to a particular case that of the Anglo-French supersonic transport aircraft, Concorde. Details of the design and mode of operation of the intake for this aircraft have been variously described by Neale (1965), Leynaert (1965), Rettie and Lewis (1968), Talbot and Brown (1976) and Leyman (1980) and these sources are used in the following description. Principal aerodynamic features of the intake are illustrated in Fig. 12.7.

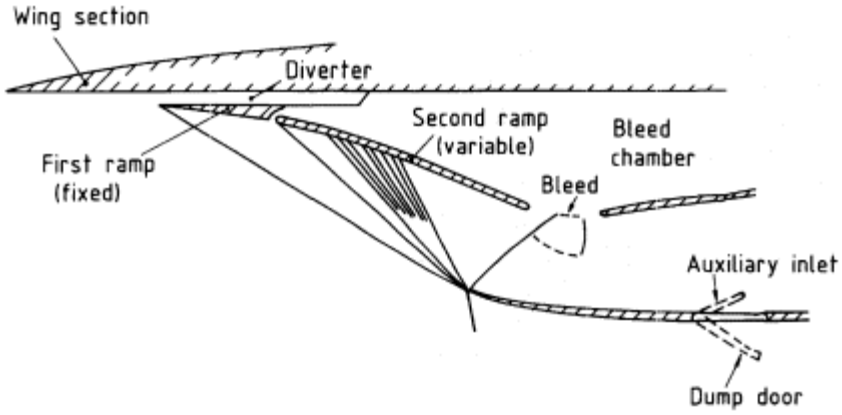

Figure 12.7
Aerodynamic features of Concorde intake.

A basically three-shock external-compression system gives the potential for 95% pressure recovery at Mach 2 (Fig. 5.14). That potential is improved by the second-stage compression being partly isentropic, as shown, and is further enhanced by a complex arrangement of shocks at entry, replacing the standard normal shock. This arrangement was contrived by careful choice of the cowl internal angle and surface curvature, involving ultimately a small degree of internal compression, together with the use of a wide bleed slot on the opposite wall of the duct. The resulting shock system consists of a curved oblique shock across the entry, strong near the lip with subsonic flow downstream and weaker near the bleed with supersonic flow downstream, this latter terminating in a normal shock towards the rear lip

of the bleed, reaching only part way across the duct. The primary function of the bleed is to minimise the additional total pressure loss (Chapter 7) but it also contributes significantly to solution of the matching problem by providing an automatic adjustment potential, as will be seen. The boundary layer removal function is aided by a diverter above the first ramp, taking away the wing undersurface boundary layer.

Typical pressure recovery characteristics at various levels of bleed flow, as derived from wind tunnel tests, are shown in Fig. 12.8. Two features are significant in the present context. Firstly the curve of bleed chamber pressure recovery hB is to a sufficient approximation the same for a substantial range of bleed flows, so that the level of bleed recovery defines the intake operating condition relative to the critical point, independently of bleed flow quantity. This becomes important in the definition of a matching system. Secondly, the vertical characteristic in the supercritical regime indicates that as bleed flow decreases, the main duct flow increases to compensate and vice versa. Looked at another way, this implies that a change in engine demand can, up to a point, be accommodated by an opposite change in bleed flow, without disturbing the external shock formation and intake flow capture ratio *A*¥/*A*c. Thus the intake has a useful degree of automatic matching capability.

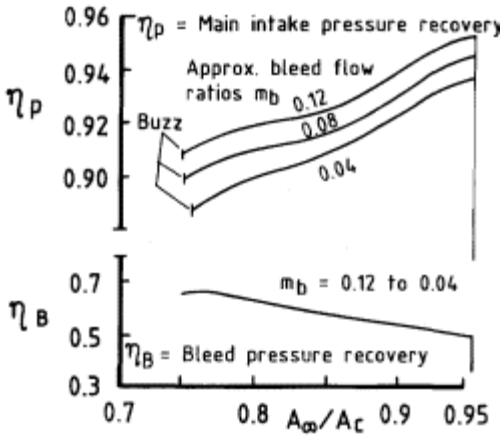

Figure 12.8
Measured pressure recovery at various bleed flows for Concorde intake.

Both these properties stem from the particular nature of the entry shock formation and its relationship to the wide bleed. Supercritical flow in the sense of the diagram begins when the lip shock becomes attached. If the engine demand increases from this condition there is no further increase in capture ratio but the entry shock formation changes in the sense that the shock from the lip becomes progressively more oblique and the partial

normal shock behind it becomes more prominent. The points of intersection of these shocks with the free boundary at the bleed opening move downstream: this movement results in a decrease of bleed flow (since the mean total pressure at bleed entry is progressively reduced) and a corresponding increase in main duct flow. The bleed-chamber pressure is closely related to the static pressure across the free boundary in the zone between oblique and normal shocks and this pressure, determined by a complex conjunction of oblique shock pressure rise and flow turning angle, stays approximately constant during the adjustment process. The process terminates when the normal shock reaches the rear lip of the bleed slot and fixes the main duct flow ratio, *m*E.

Matching of intake and engine through the Mach number range is provided by varying the ramp angle of the second stage of external compression, the internal ramp downstream of the bleed being always moved to suit. Spilling of excess air in cases of engine throttling or shut down is achieved by a combination of the variable ramp (moving to higher angles to produce forespillage) and an after-spillage vent, or 'dump door', located on the bottom of the cowl some distance behind the entry. Additional intake area for the static condition and take-off is provided by a freely-floating inwardly-opening door set inside the dump door frame, operating under the pressure differential between internal and external flow.

12.5.2
Matching in High-Speed Flight

At a given Mach number, a supersonic intake and an engine respond in differing degrees to a change in ambient temperature. Equation (12.4) indicates that the intake mass flow varies inversely as the square root of temperature, whereas by Equation (12.6) the variation for the engine (at constant rotational speed) is inversely as the temperature. It is therefore possible to match intake and engine for optimum performance at only one temperature. Adjustment of the combination for other temperatures in the cruising condition is an important aspect of the intake design. The Concorde solution is illustrated in Fig. 12.9. To examine the situation, pressure recovery characteristics of the intake for various ramp angles are overlaid with engine demand lines for various ambient temperatures: a constant engine demand can, as we have seen, be expressed as a line of constant *m*E/hP which by Equation (12.6) with *m*E substituted for *A*¥, at constant Mach number and engine speed, varies only with temperature. Note that the abscissa in this presentation is the engine flow ratio *m*E and not total intake flow ratio *A*¥/*A*c; *m*E is not constant in the supercritical regime owing to the exchange which takes place between engine flow and bleed flow.

The selected design point temperature is ISA + 5°C. A basic match is

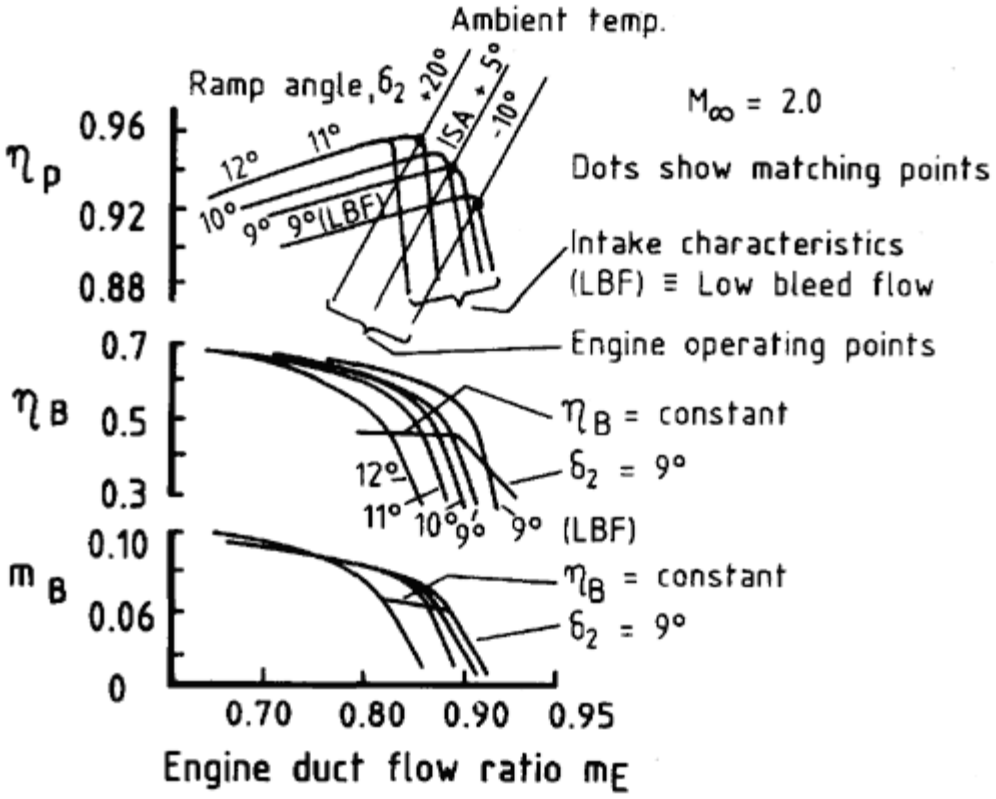

Figure 12.9
Matching of intake and engine airflows
for ambient temperature variation at Mach 2.0.

obtained between the demand curve and the intake pressure characteristic for a ramp angle close to, but not necessarily equal to, the 'minimum', that is the angle for which at the particular Mach number the ramp shock is on (or close to) the cowl lip. The intake operating point is close to critical and the bleed flow is around 6%, as desired. For higher ambient temperatures the ramp angle is increased to allow forespillage and it is seen that if the control is such as to maintain a constant bleed pressure ratio hB, the matching points give near-critical operation over a considerable temperature range. The bleed flow remains roughly constant. For temperatures below the design condition the ramp angle is first decreased to the 'minimum' value and thereafter the intake is allowed to operate supercritically, since it can be shown that this is more efficient than reducing the engine rotational speed to maintain intake pressure recovery. In this part of the adjustment range the bleed flow decreases as engine flow increases.

Temperature variation is not the only factor which may have to be taken into account: both engine and aircraft can introduce maladjustments in flow characteristics. A successful supersonic intake needs to have the kind of flexibility illustrated to be adaptable to these variations, the importance of which will of course vary with the application. A further factor in the present example is that the bleed flow is utilised for engine bay cooling and is then introduced as secondary airflow into the propelling nozzle. The additional matching problem was successfully solved on the aircraft and the details are not pursued here.

The intake control system for the Concorde is a hybrid digital-analogue system based on a special purpose digital processor. The arrangement is outlined in Fig. 12. 10. Aerodynamic inputs are the aircraft freestream total and static pressures and incidence and a 'ramp void static pressure' *p*V, closely related to the bleed static pressure *p*B. The digital processor, using dynamic control loops, computes the control laws and monitoring functions. Fundamentally the system is one of closed loop control of the ramp void pressure as a function of intake local Mach number. The schedules of ramp angle and dump door angle are linked, as already mentioned.

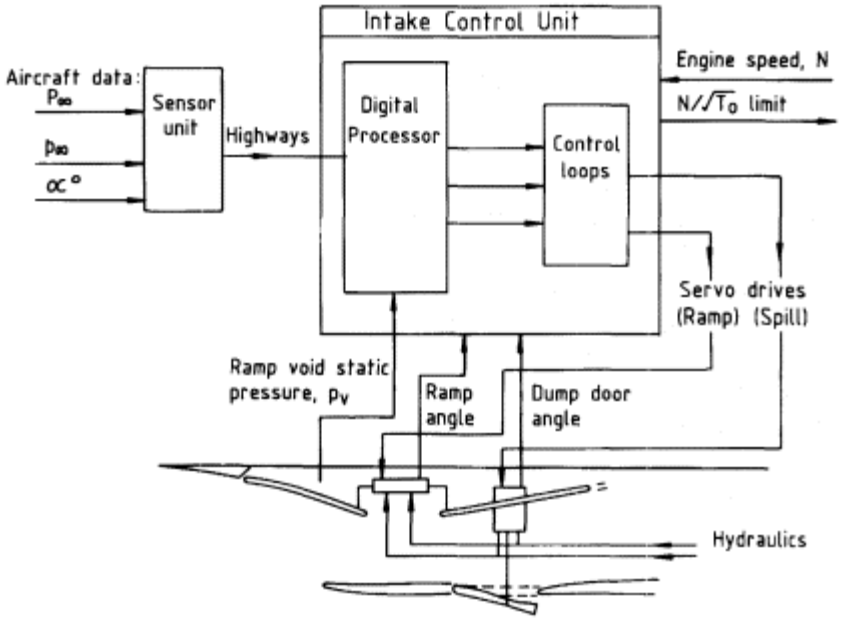

Figure 12.10
Outline of Concorde intake control system.

12.5.3
Transients.

To preserve engine safety and stability of operation, the task of the intake is to prevent the onset of buzz at the subcritical side and the occurrence of engine surge from excessive flow distortion on the supercritical side. For the latter purpose an engine speed limiter is incorporated into the intake control system: this is indicated in Fig. 12.10.

From an input of compressor speed, *N*, the control sets a limit to the value of $N/\sqrt{T_0}$ as a function of intake Mach number in the range of higher flight speeds, such that a margin is preserved to the predicted engine surge threshold. Transient atmospheric disturbances at high flight speed may occur at rates which are beyond the response capability of the engine, working to the limiter, to follow; the

objective of the margin is to ensure that actual surge occurrences are acceptably infrequent.

With engine operating to the limiter and without control inputs, different transients produce different paths on a diagram of corrected rotational speed versus Mach number. This is illustrated in Fig. 12.11. Thus a rapid fall in temperature increases both engine flow demand and flight Mach number: a sudden headwind increases the latter but reduces the former. Different control responses are necessary to preserve the required margin. In the Concorde system the limiter reduces engine speed as intake Mach number increases or temperature decreases. The intake ram and dump door move to spill air as required, maintaining low flow distortion at the engine face. The faster the transient, the closer the engine operating line moves to surge. An example of this is given in Fig. 12.12, where the controlled response to a series of temperature transients is shown.

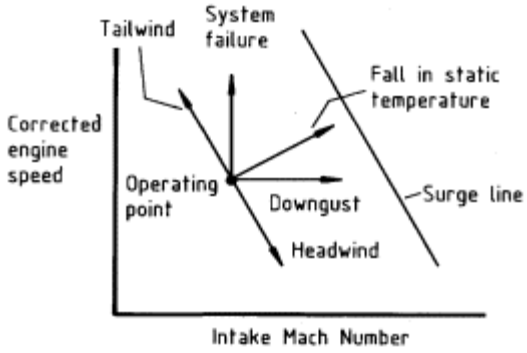

Figure 12.11
Illustration of uncontrolled propulsion-system response to transient effects (Concorde).

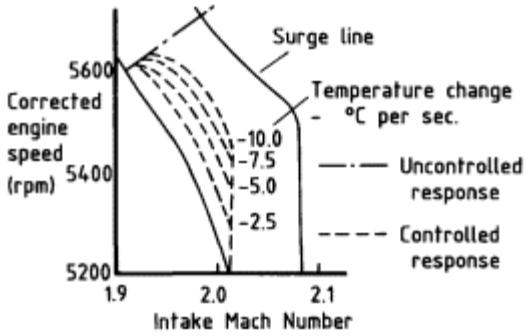

Figure 12.12
Controlled system response to temperature transients (Concorde).

12.6
Matching of a Ramjet Intake

Ramjet engines are practical only at supersonic speeds in excess of about Mach 1.5: below this speed the ram element in the compression process in other words the pressure recovery of the intake is not of itself sufficient to provide efficient propulsion. Owing to the high supersonic speed the exit nozzle of a ramjet is choked at its throat (whether convergent or convergent-divergent). Thus at the throat, since the sonic area ratio is unity, we have, in conformity with Equation (12.4), and using suffix 'n' to denote nozzle quantities.

$$m_n = \left(\frac{2}{\gamma_n + 1}\right)^{(\gamma_n+1)/2(\gamma_n-1)} \sqrt{\left(\frac{\gamma_n}{R_n}\right)} \frac{A_n P_n}{\sqrt{T_{0n}}} \qquad (12.8)$$

At entry to the combustion chamber the mass flow is given by Equation (12.4) itself, using suffix 'f' to denote the 'engine face area' in the usual way. If the weight of fuel added is ignored, as also the changes in g and the gas constant R from combustion, the two mass flows can be equated to give

$$\frac{A_n P_n}{\sqrt{T_{0n}}} = \frac{A_f P_f}{\sqrt{T_{0f}}} \left(\frac{A^*}{A}\right)_f \qquad (12.9)$$

This yields an equation for the ratio An/Af, which is a geometric constant. To a first approximation any change in total pressure from the heat addition and burner baffles can be ignored, so that Pn and Pf are equal and we have

$$\frac{A_n}{A_f} = \sqrt{\left(\frac{T_{0n}}{T_{0f}}\right)} \cdot \left(\frac{A^*}{A}\right)_f \qquad (12.10)$$

Indications of the way in which the intake operating point moves as input conditions are varied can be obtained directly from this equation. Table 12.1 summarises these.

From these trends it emerges that as a ramjet accelerates and climbs away from a ground launch, the intake operating point can be maintained in approximately the same position. Also for a given fuel addition there is a tendency for acceleration to be self-limiting because movement of the operating point into the supercritical means a significant decrease in pressure recovery, hence the thrust decreases as the ramjet travels faster. In general the ramjet engine is opposite to the turbojet in its reaction to ambient and engine conditions. Thus, for example, a reduction of turbojet rev/min is accompanied by a reduction in fuel flow and results in the intake operating point moving towards the subcritical.

Table 12.1 Movements of ramjet intake operating point

Input	$T0n$	$T0f$	$\left(\frac{A^*}{A_f}\right)$	Mf	Movement of intake operating point
More fuel added	Increased	Constant	Decreased	Decreased	Towards subcritical
Altitude increased from sea level towards tropopause	Constant	Decreased	Decreased	Decreased	Towards subcritical
Flight velocity increased at constant altitude	Constant	Increased	Increased	Increased	Towards supercritical
Less fuel added	Decreased	Constant	Increased	Increased	Towards supercritical

References

Leyman, C.S. and Rech, J. (1982) 'Concorde aerodynamics and associated systems development'. *AIAA Professional Study Series.*

Leynaert, J. (1965) 'Fonctionnement du piège à couche limite interne d'une prise d'air à compression supersonique externe'. AGARDograph 103.

Neale, M.C. (1965) 'Intake design and performance around a Mach number of 2.2'. AGARDograph 103.

Rettie, I.H and Lewis, W.G.E. (1968) 'Design and development of an air intake for a supersonic transport aircraft'. *Journal of Aircraft* 5, no. 6.

Talbot, J.E. and Brown, T.W. (1976) 'Effects of atmospheric conditions on the operating characteristics of supersonic cruise aircraft'. (Contribution, in association with Schweikhard, W.G. and Gilyard, G.B.) *IAF27th Congress*, Paper 76 112.

Chapter 13
Intakes at Incidence

13.1
Introduction

Highly manoeuvrable strike-fighter aircraft have to operate within limiting conditions imposed by the strength of the aircraft structure, by buffet boundaries and above all by the ability of a pilot to withstand the centrifugal forces caused by rapid horizontal or vertical turns. These conditions are usually expressed as a 'g' envelope for the aircraft, which can then be translated into a domain of incidence and yaw angles. Two such domains for a typical aircraft, one for subsonic-transonic speeds and one for supersonic speeds, as given by Hawkins (1974), are illustrated in Fig. 13.1. These represent a relatively modest set of manoeuvre requirements.

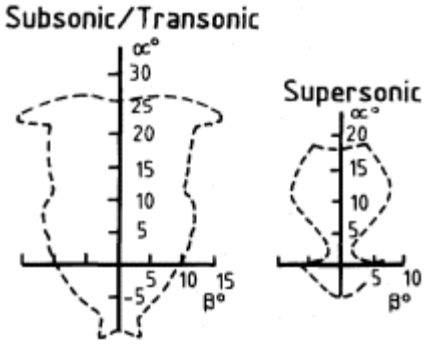

Figure 13.1
Manoeuvre envelope for aircraft
at subsonic and supersonic speeds.

Some aircraft have demonstrated a so-called 'stopping' manoeuvre at low speeds; this is accomplished by generating a very high drag through a rapid increase of incidence to eighty or ninety degrees. Under these circumstances it is very important that the engine continues to operate and does not surge or flame-out.

Aircraft which are required to take off and land either vertically or in a very short distance also need the engines, and hence the intakes, to operate efficiently at large angles of incidence. In these cases the large angles occur

either because of strong upwash associated with high wing lift coefficient (generated for example by the use of jet-induced flow over flaps) or because the engine nacelles are required to rotate from a horizontal to a vertical position. In both situations there is a need for intakes to operate efficiently at incidences from zero to eighty or ninety degrees at low aircraft forward speeds.

In the circumstances described, intake behaviour is dominated by the state of flow around the entry lip. The situation is analogous to that in static and low forward speed operation at zero incidence, discussed in Chapter 4, in that an important geometric parameter determining whether the flow remains attached to, or separates from, the lip is the area contraction ratio (CR) between entry highlight and throat. The flow at high incidence, however, has the obvious additional complexity of being no longer symmetrical about the longitudinal axis of the intake. The stagnation position (the dividing point between internal and external flow) varies around the entry circumference from being well outside the highlight on the windward lip (bottom lip for positive incidence) to being inside the highlight on the leeward lip. Longitudinal pressure or Mach number distributions around the lip are functions of flow ratio and mean throat Mach number and vary with circumferential position in a manner typified in Fig. 13.2.

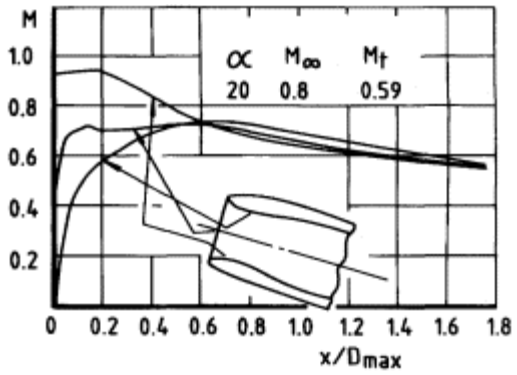

Figure 13.2
Distribution of surface Mach number on three internal generators of an axisymmetric intake at incidence.

As illustrated in Fig. 13.3, the flow inside the windward lip can be attached at a flow ratio of 0.56 even at 20° incidence. After separation has occurred at a flow ratio of 0.604 the separation bubble gradually increases in extent as flow increases further. Development of the internal boundary layer is the result of widely differing pressure distributions on different generators, so the viscous part of the flow can be expected to be highly three-dimensional, and when separation is present the whole flow in the

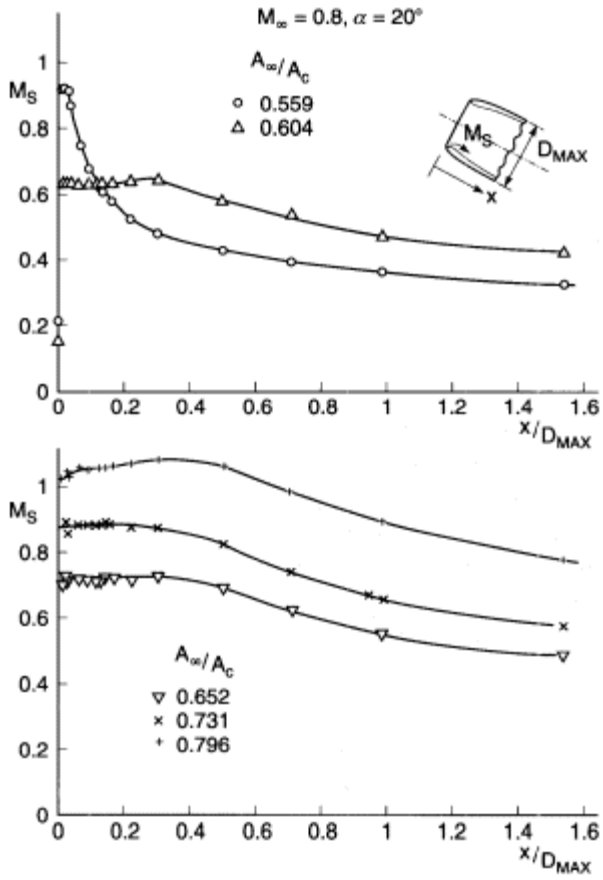

Figure 13.3
Internal lower lip Mach number distributions for
RAE model 742L cowl 2 at *M*¥ = 0.8, a = 20°.

diffuser is rotational because the total pressure is non-uniform at the throat.

Sections 13.2, 13.3 and 13.4 refer to intakes with rounded lips, approximately describable as subsonic intakes, and section 13.5 to intakes with sharp lips, i.e. supersonic intakes. In these sections the intake is considered to be in isolation, though at incidence which in practice may depend, as already described, not only upon the aircraft attitude but also upon other environmental factors. Use of the installational situation to shield the intake from the worst effects of incidence is the subject of section 13.6.

13.2
Separation and Reattachment Boundaries.

The separation process is normally complex. Jakubowski and Luidens (1975) have described the flow around the windward lip region in the

manner illustrated in Fig. 13.4. The strength of the shock and boundary layer interactions determines whether a laminar flow separation bubble exists, how and where the transition to turbulent flow takes place and when a final separation occurs and these are all functions of airflow turbulence, surface roughness and boundary layer Reynolds number. This is a pattern of the flow around a longitudinal generator; a face-on view in Fig. 13.5 shows a typical pattern as observed by Hurd (1976) in oil-flow experiments.

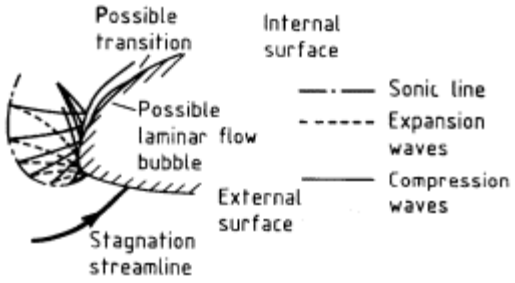

Figure 13.4
Flow in vicinity of highlight of windward lip.

The nature of the boundaries of conditions which cause flow separation is indicated in Fig. 13.6, where low-speed data from Luidens and Abbott (1976) and high-speed data from Hurd (*loc. cit.*) are combined. The abrupt change of slope shown on the low-speed boundaries occurs when the mean throat Mach number reaches a value around 0.5: the change is probably associated with the onset of shock and boundary-layer interaction, as illustrated in Fig. 13.4. Although depicted in Fig. 13.6 as lines, the boundaries in reality are regions with up to 5° spread in incidence; also considerable hysteresis is exhibited, whereby the angles for separation (incidence increasing) and for attachment (incidence decreasing) can differ by more than 10° (Fig. 13.7).

An incompressible method of calculation of duct flow at incidence together with compressibility corrections and a linked viscous flow calculation due to Albers and Stockman (1975) leads to estimates of the boundaries of flow separation as determined by the criterion of zero skin

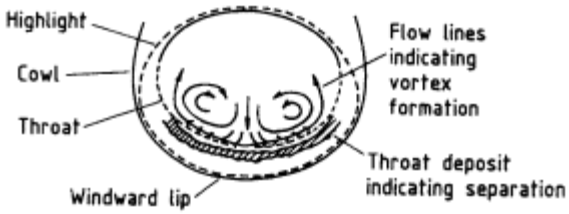

Figure 13.5
Oil flow pattern indicating flow separation inside
windward lip of axisymmetric intake at a 16°, *M*¥ 0.8.

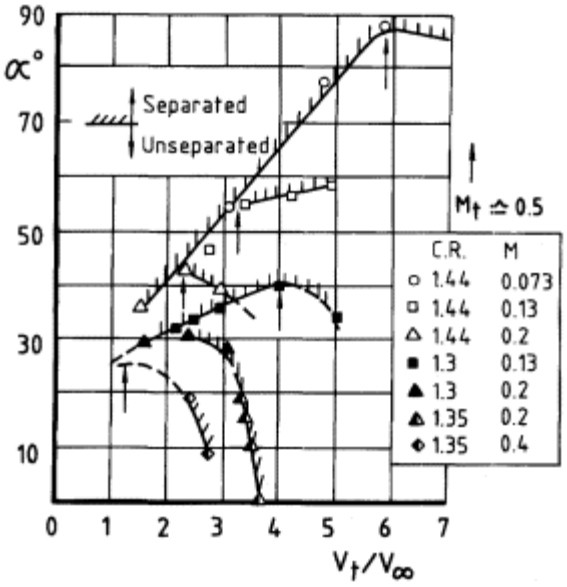

Figure 13.6
Boundaries of flow separation
at high and low subsonic speeds.

friction. Applying their approach, it is found that separation may occur either in the region of the lip or downstream in the subsonic diffuser. Fig. 13.8 illustrates the two situations.

A typical comparison between predicted and measured separation boundaries is shown in Fig. 13.9. Agreement is tolerably good at high values of throat Mach number, where lip separation is both predicted and observed. For throat Mach numbers below about 0.6, the measured separation boundary agrees with the predicted boundary for *diffuser*

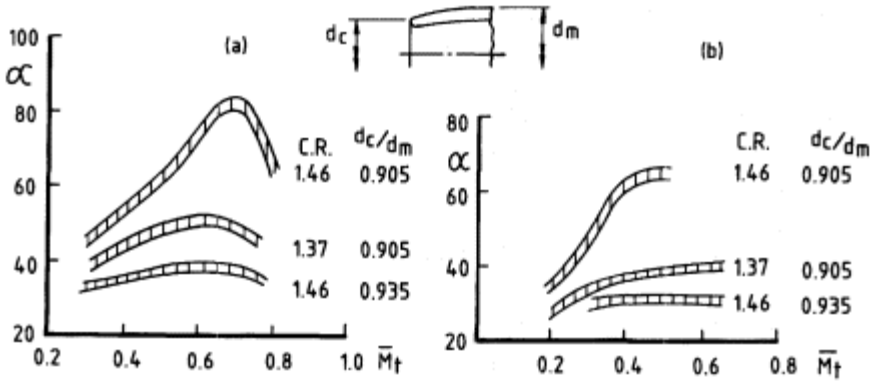

Figure 13.7
Variation of boundaries of flow separation (a) incidence
angle increasing (b) incidence angle decreasing.

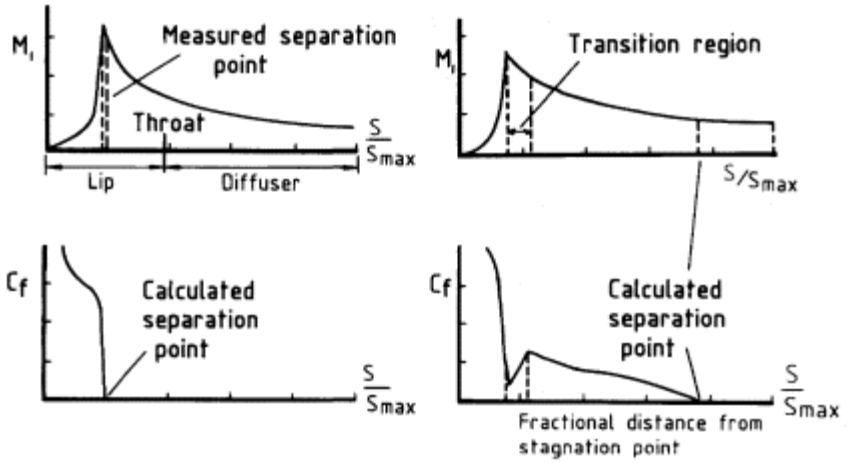

Figure 13.8
Separation point at lip and in duct.

separation but the observed separation is still *at the lip.* A stability argument has been advanced (Chou *et al.*, 1978) to explain this discrepancy and can be seen to be plausible. It depends upon the fact that when separation occurs the mass flow is reduced. Since the predicted curve for diffuser separation goes through a maximum near *M*t = 0.6, when *M*t is greater than this, a flow reduction consequent upon separation is stabilising, that is, it tends to move the operating point into the attached flow region. For values of *M*t below 0.6, the opposite is the case reducing the flow moves the operating point further into the separated flow region and this instability has the effect of moving the separation point forward into the lip region. It should however be recognized that shortcomings of the boundary layer calculation in the prediction method could also have a bearing on the discrepancy. Thus no

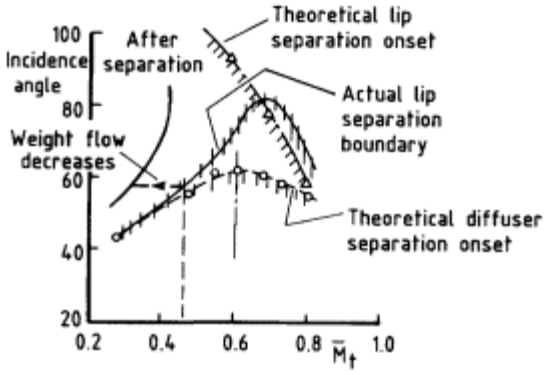

Figure 13.9
Comparison of measured and predicted
boundaries of flow separation.

specific account is taken of shock and boundary layer interaction, or of laminar separation bubbles, and axial symmetry is implied which is an assumption of dubious validity for large angles of incidence.

13.3
Internal Total Pressure Losses at Subsonic Speeds

Total pressure loss associated with lip internal separation, at zero incidence and with flow ratio, *A*¥/*A*c, greater than unity, is discussed in Chapter 4. The dependence of loss upon flow ratio, mean throat Mach number and relevant geometrical parameters principally the contraction ratio is illustrated in Figs. 4.13 and 4.14. A similar approach to the correlation of lip loss can be followed when the intake is set at non-zero incidence. For a particular geometry the loss is now a function of flow ratio, mean throat Mach number and angle of incidence and since the incidence can itself be responsible for causing separation, the range of interest of flow ratio is not restricted to values greater than unity.

Some examples of the variation in lip loss coefficient, defined as in Chapter 4, are given in Fig. 13.10, where the abscissa is inverse flow ratio, *A*c/*A*¥. In the static condition (*A*c/*A*¥ = 0), incidence has no physical significance in relation to the flow, so the losses are the same for all three incidences. Up to 20° incidence, the lip separation typical of the static condition (Chapter 4) disappears gradually as inverse flow ratio increases to 1.0, indicating little or no separation augmentation from the incidence. For the higher incidences, however, a strong incidence effect is manifested, in which lip loss now for the most part increases as inverse flow ratio increases. The trend is similar to that shown in Fig. 2.10 for external boundary layer separation and indeed at high incidence the forward

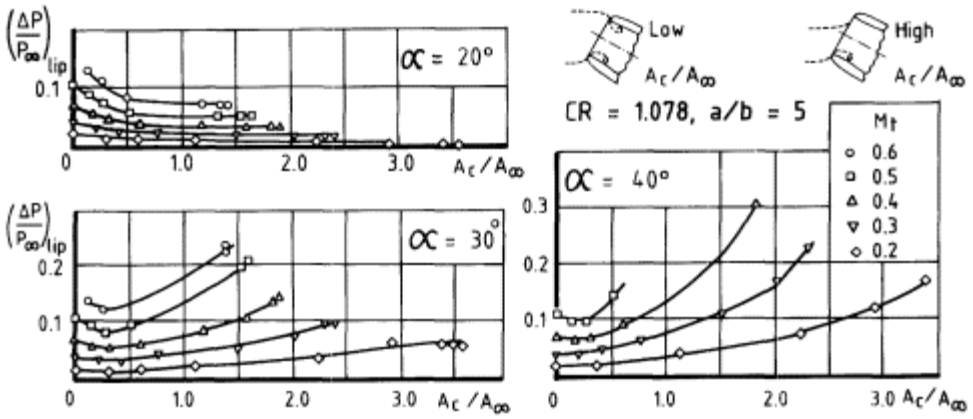

Figure 13.10
Lip loss at angles of incidence 20°, 30° and 40°.

surface of the windward lip may be thought of as external, rather than internal, to the duct, after the manner of a swept intake as illustrated in Fig. 2.7.

Taking this analogy further and regarding the throat section as providing a more realistic 'capture' area under these conditions than the highlight section, a useful empirical correlation is obtained by plotting the lip loss against the Mach number ratio $M¥/M$t. However, at supersonic speeds $M¥$ must become a parameter in its own right because at incidence it controls the effects of shock and boundary layer interaction on the inside of the windward lip as flow ratio approaches close to full flow. Fig. 13.11 shows such a correlation at subsonic and supersonic speeds of both lip loss and a distortion parameter *D*. At low free-stream Mach numbers (< 0.2), measurements at all incidences and flow conditions can be conveniently expressed as a carpet plot of the lip loss in terms of the mean dynamic pressure at the throat versus $M¥/M$t (Fig. 13.12).

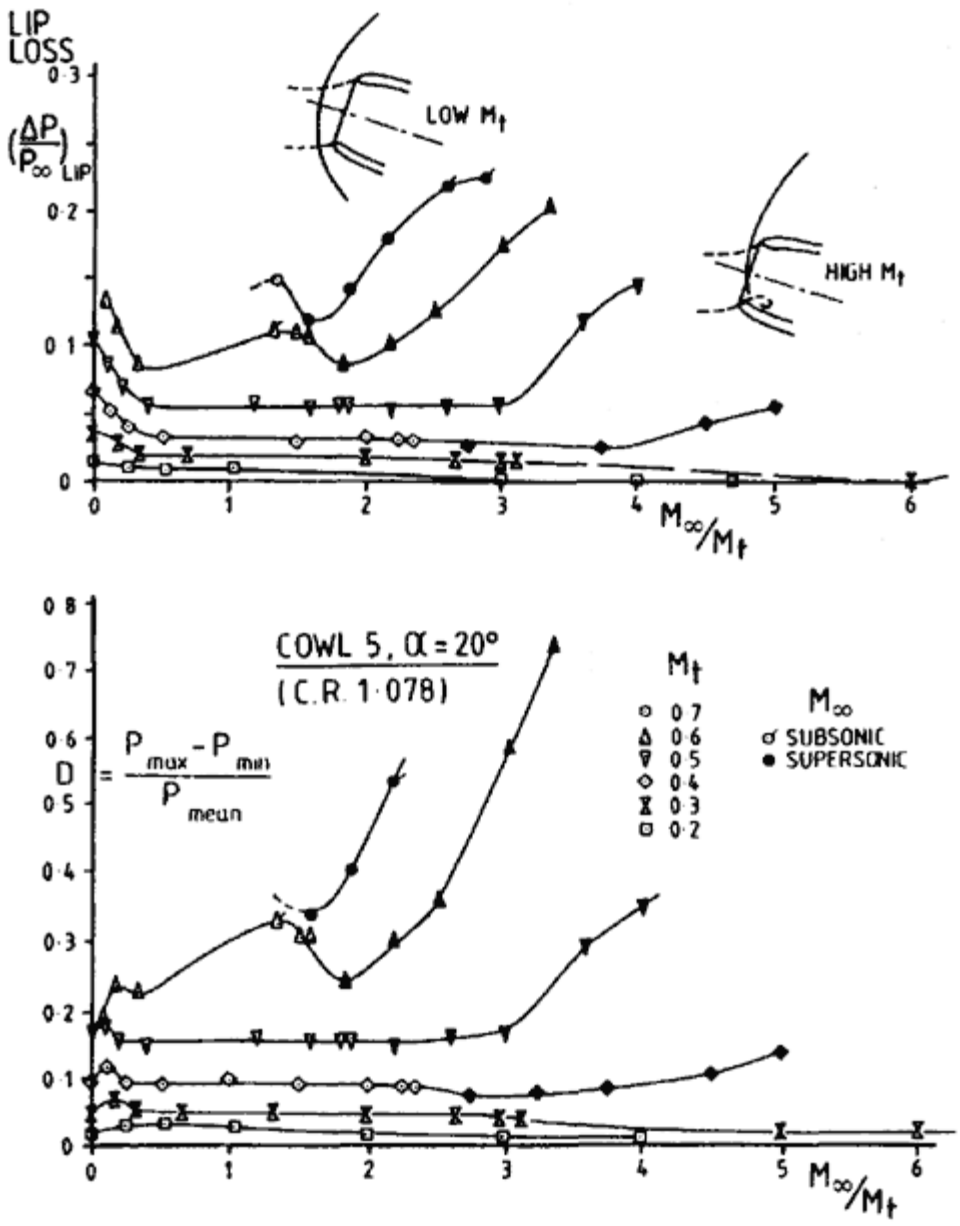

Figure 13.11
Correlation of measured values of lip loss and flow distortion over the Mach number range $M¥$ = 0 2.0.

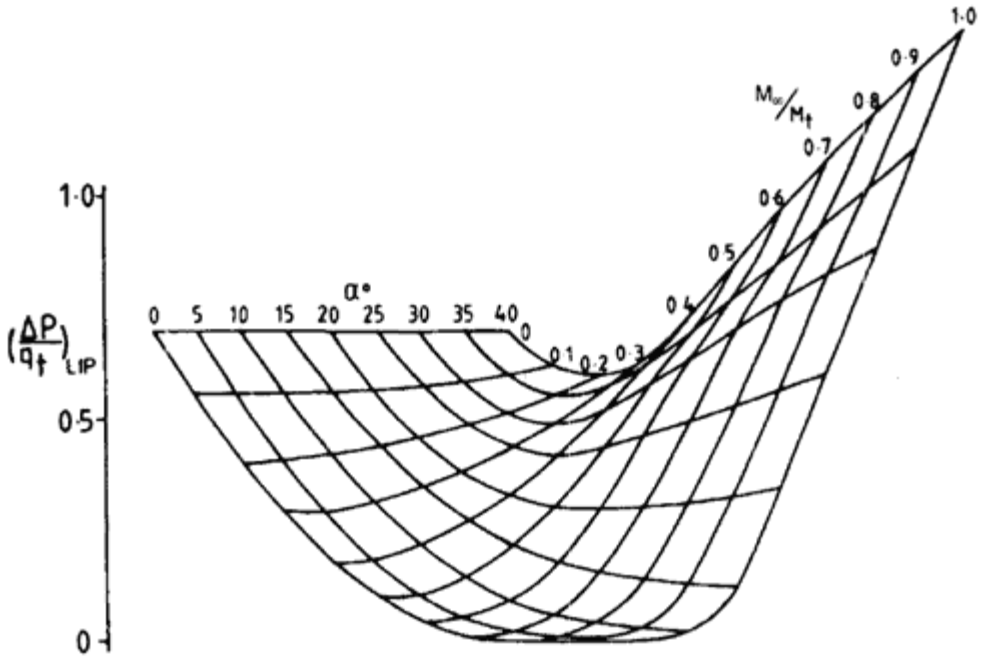

Figure 13.12
Correlation of measured values of lip loss at *M*¥ = 0 0.2.

13.4
Effects of Entry Shape

As may be expected, the total pressure loss of an intake at incidence can be affected substantially by entry shaping of a kind designed to ease the flow over the windward lip, in the sense of either delaying the onset of separation or reducing its severity. Some such measures are discussed below.

13.4.1
Contraction Ratio and Lip Shaping

As would be expected, if lip separation is present then contraction ratio (*CR* = *A*c/*A*t) has a major effect on total pressure loss at incidence. Fig. 13.13(a) illustrates the effect of changing *CR* from 1.078 to 1.25 at 20° incidence and low forward speed. In this case the differences in performance between the contraction ratios are principally the result of whether or not separation has occurred. In the second illustration (Fig. 13.13(b)) the streamtube size is smaller than the capture area and the incidence is such that separation will have occurred at all contraction ratios, but the separation region will be smaller the higher the value of the contraction ratio.

When, as is usually the case, the variation of incidence is predominantly to one side of the zero position, the contraction into the duct from the highlight can be increased on one lip (the lower lip for positive incidence variation) and decreased on the other without altering the overall contraction ratio. The effect of this for a rectangular intake is shown in Fig. 13.14. A further improvement is obtained as shown by cambering the windward lip in the direction of the incident flow.

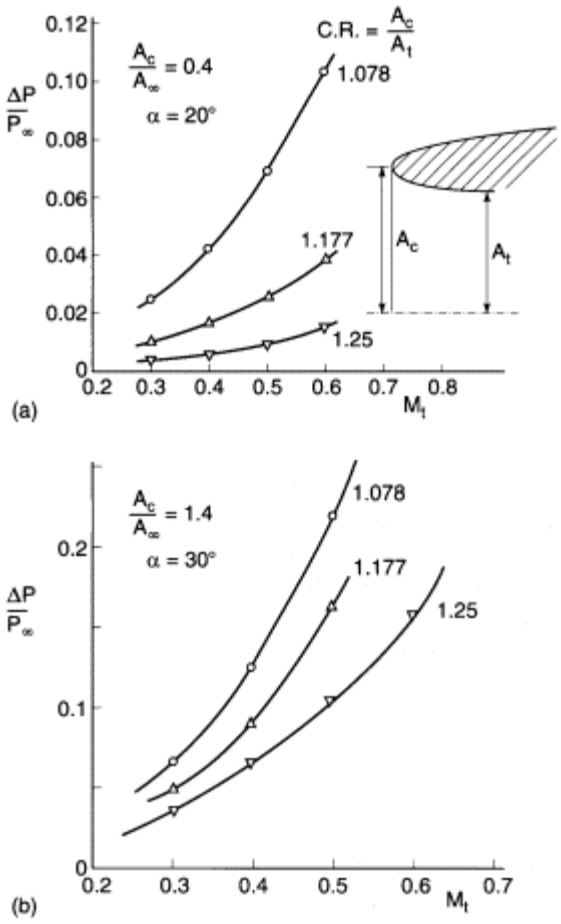

Figure 13.13
Effect of contraction ratio on lip loss variation with throat Mach number *M*t.

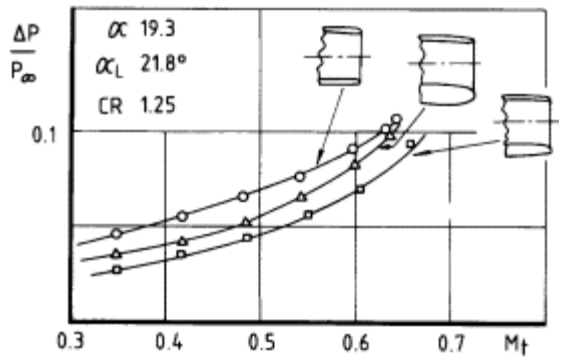

Figure 13.14
Effect of lip thickness distribution on total-pressure loss.

13.4.2
Variable Lip Geometry

More potent improvements can be obtained by the use of variable lip geometry. Hingeing the lip leading edge effectively increases the contraction ratio to any desired value. Fig. 13.15(a) shows the effect of lip angle variation between zero and 50° at incidence angles 30°, 40° and 56°, as given by Latham *et al.* (1977). It is seen that at 40° incidence a 50° lip deflection causes higher losses than a 30° one: this is because the larger deflection angle is excessive and leads to flow separation just downstream of the hinge position. Results for an alternative slotted flap arrangement are shown in Fig. 13.15(b): the gains are comparable generally with those for the hinged flap and somewhat larger at the higher incidence. Again, at 40° incidence the biggest gain is obtained with an intermediate flap deflection angle.

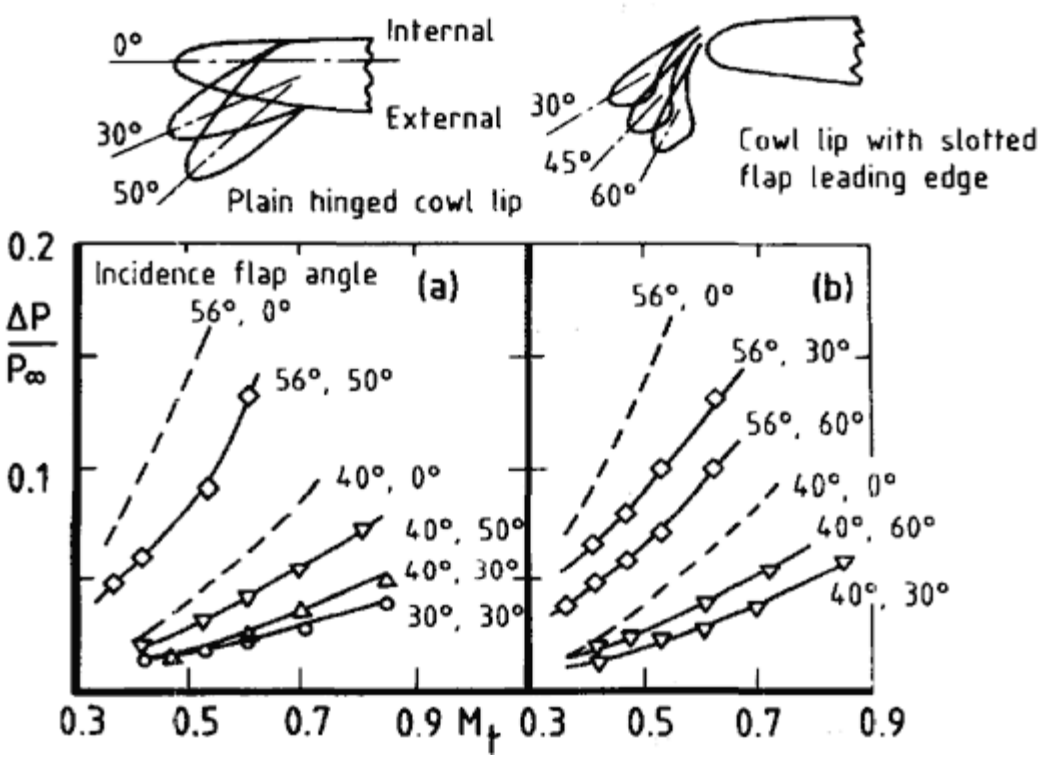

Figure 13.15
Reduction of loss at incidence by use of
variable-angle cowl leading edge, plain and slotted.

13.4.3
Cross-Sectional Shape.

A study of losses at incidence has been made in which results for a circular entry were compared with those for a semi-circular entry in different orientations. The other geometric properties diffuser length, area distribution and longitudinal lip profiles were maintained the same for all cases. Lowest losses (Fig. 13.16) were consistently obtained for the semi-circular entry, orientated with the plane surface vertical, i.e. in the incidence plane. The probable explanation is that this configuration gives the smallest region of separated flow.

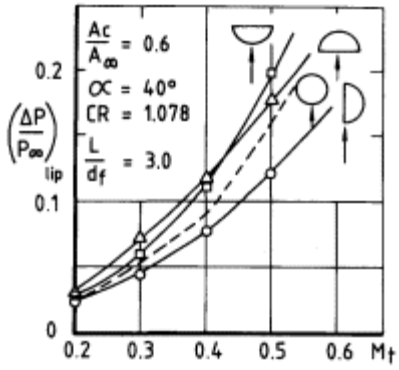

Figure 13.16
Dependence of lip loss on
cross section shape of entry plane.

13.4.4
Entry Plane Stagger

The term 'stagger' refers to a geometry in which the upper lip of the entry overhangs the lower lip. The angle of stagger is the angle between the plane of highlight points and the normal to the duct axis. Other terms used to define the same feature are 'rake and 'scarf'.

Ross, McGregor and Priest (1981), using an incompressible, two-dimensional, potential flow analysis originally developed for flapped aerofoils, deduced that positive stagger could have a considerably favourable effect on intake performance at incidence. Fig. 13.17 shows that increasing the stagger angle decreases the maximum velocity on the inside of the lower lip and hence reduces the tendency to flow separation. For flow ratios less than or equal to unity, a modest 20° of stagger produces a

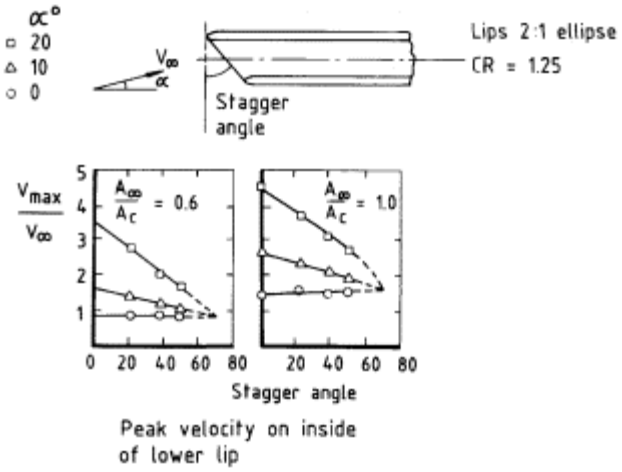

Figure 13.17
Potential-flow calculations of the effect of
stagger angle on peak supervelocities on lip.

worthwhile reduction in maximum velocity, while 70° of stagger practically eliminates the effect of incidence. The upper lip effectively turns the intake flow from the freestream incidence so that the lower lip is shielded and if the stagger angle is high enough, lower lip separation is delayed probably until incidences of 50 60° are reached. Fig. 13.18 shows the variation of loss with inverse capture ratio and throat Mach number for both 0° and 50° stagger at 30° incidence. Losses fall continuously with increase in *A*c/*A*¥ in contrast to the loss variation of the unstaggered intake.

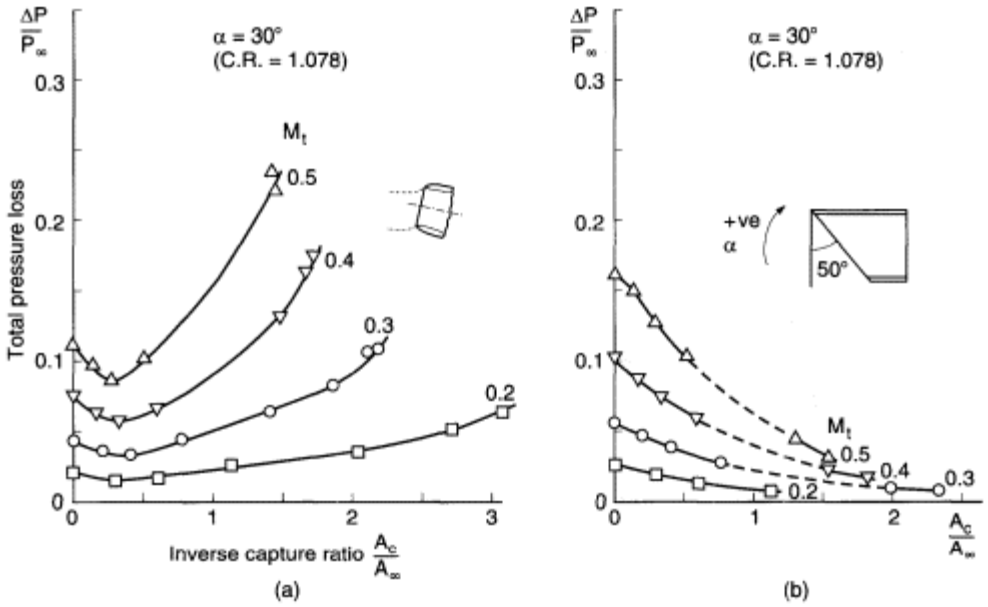

Figure 13.18
Effect of lip stagger on total pressure loss at subsonic speeds.

At low forward speeds with *A*c/*A*¥ << 1.0, a staggered intake has more flow sucked over the lower lip than the upper one, so the unstaggered intake with its symmetrical separation region suffers less as shown in the comparison of Fig. 13.19. However, as forward speed increases from about *M*¥ 0.1 to 0.2 0.3 (inverse capture ratios of 0.3 0.6 approximately depending on throat Mach number), a cross-over point occurs and at higher inverse capture ratios the favourable effect of lip stagger increases rapidly.

The effect of stagger on the internal performance of a typical fuselage-side, rectangular intake at incidence is shown in Fig. 13.20. Local incidence aL is used for the diagrams, this being the model aircraft incidence corrected for fuselage upwash, as illustrated in the sketch. Both pressure recovery and distortion are improved by the use of moderate stagger and this is as predicted. With 50° of stagger, there is no increase of distortion and

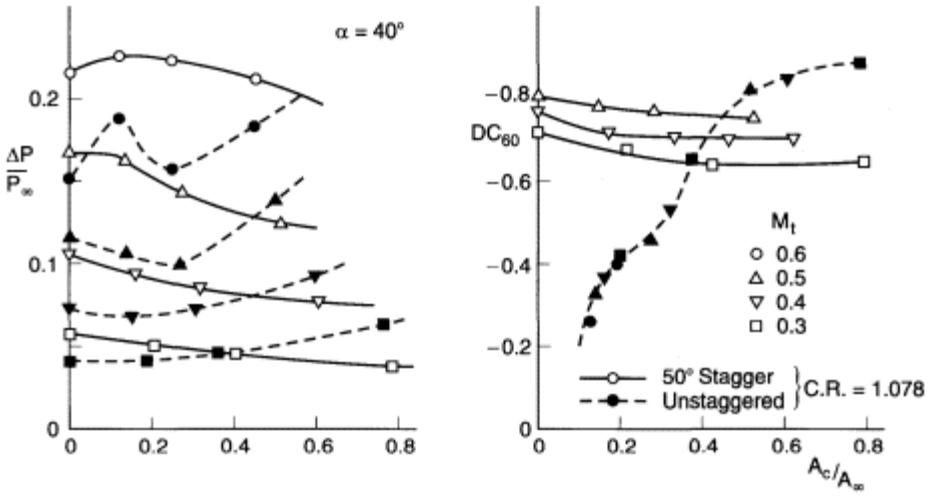

Figure 13.19
Effect of lip stagger at low forward speeds.

little loss of pressure recovery (as compared with results at zero incidence) for incidences up to 40°.

With rectangular intakes, matching of the endwall(s) to the plane of stagger is important. Without swept endwalls, the flow turning process of the overhung upper lip is less effective. An experimental comparison in Fig. 13.21 shows this.

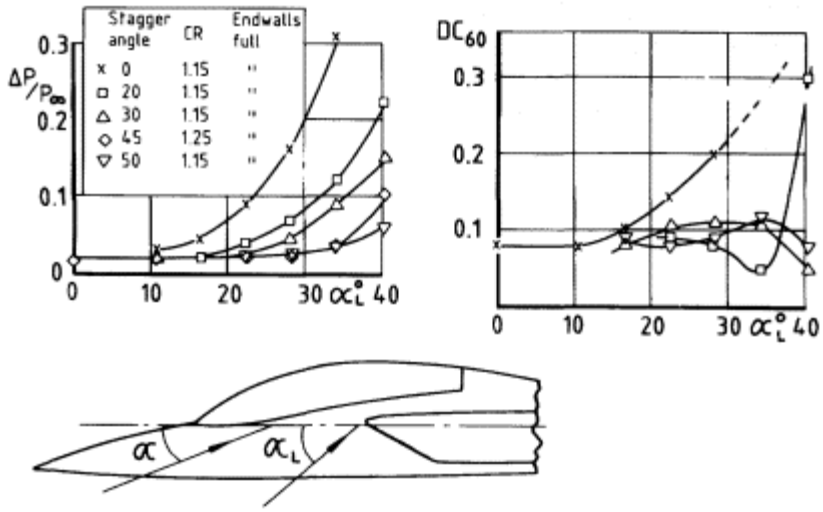

Figure 13.20
Effect of stagger angle on performance of
fuselage-side mounted intake at *M*¥ 0.9 and *M*t 0.5.

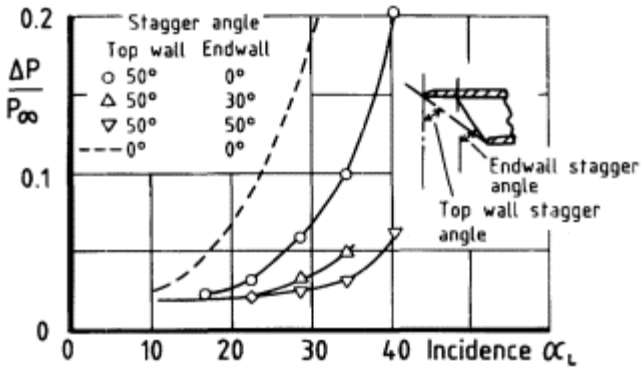

Figure 13.21
Influence of endwall shape on
performance of 50°-staggered intake.

It may be noted at this point that the effect of stagger can be disadvantageous at supersonic speeds. The gain in recovery vis-a-vis the normal shock recovery that occurs at zero incidence (Section 3.7) for an unstaggered intake progressively changes into a loss as the stagger angle increases from 20° to 50°. At 20° stagger angle the majority of the intake and shock boundary layer intersection is upstream of the upper lip and swept endwalls and is, therefore, still on the body boundary layer. At 50° stagger, this interaction is wholly on the surfaces of the intake and hence the lambda shock formation only results in wholly deleterious ingestion of separated flow into the intake, which completely overwhelms the small favourable effect of the lambda shock pattern. Fig. 13.22(a) and (b) shows the progressive change in *gain* with *M*t due to lambda shock formation at the stagger angles of 20° and 50° and Fig. 13.22(c) summarises the change with stagger angle on a basis of losses other than the theoretical normal or two-shock loss (which depends on angle of incidence and not on the formation of a lambda shock). The unfavourable effect can be reduced by (a) cutting back the endwalls, which as has been seen reduces the effectiveness of the stagger at subsonic speeds and (b) by converting the upper wall into a wedge compression surface to reduce the Mach number of the normal shock.

13.5
Incidence Effects at Supersonic Speed

In this section the basic forms of supersonic intake are considered in turn. The intakes are assumed to have sharp lips.

13.5.1
Pitot Intake

With a pitot intake, operating critically or subcritically in a supersonic stream, as incidence is increased from zero the entry plane inclines to the

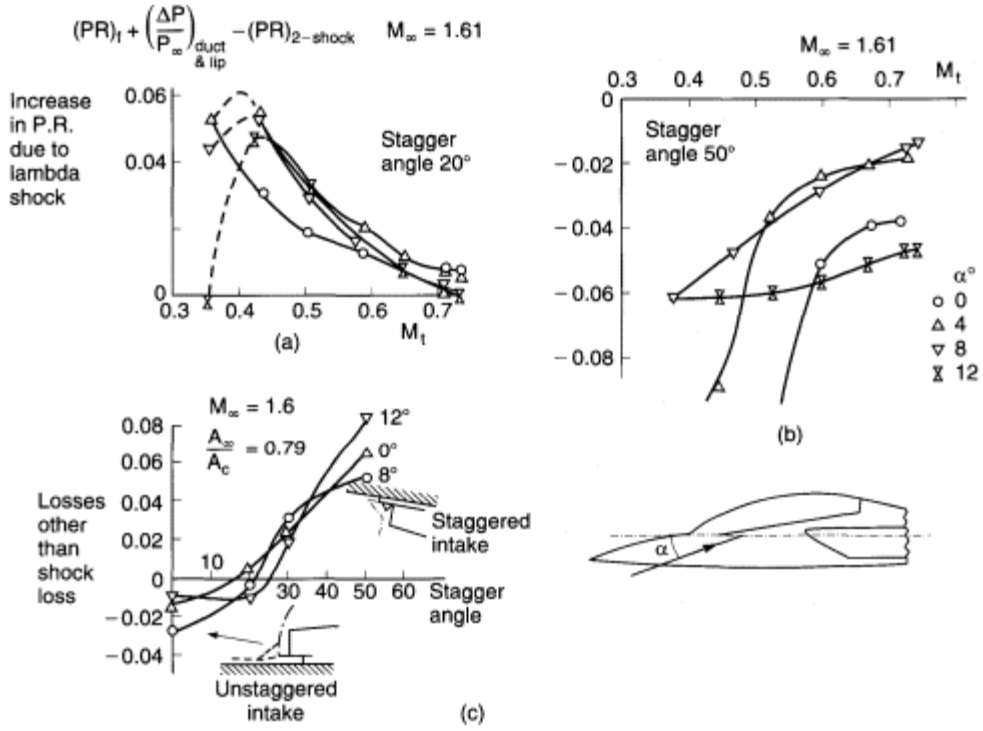

Figure 13.22
Changes in lambda shock effect at supersonic speeds due to intake stagger.

'vertical' but the intake shock remains approximately normal to the free stream direction. At a given incidence, as the flow ratio is reduced from unity the shock becomes detached from the leeward lip and moves upstream across the entry face. Flow at the windward lip remains attached and unaffected until, with increasing spillage, the shock reaches that position, after which the shock becomes completely detached from the entry plane.

The progression is illustrated by schlieren photographs in Fig. 13.23. The diagram shows variations of total pressure loss, other than the normal shock loss, with mean throat Mach number at three values of free stream Mach number. So long as the shock is clear of the entry plane (low values of *M*t) the variation of total pressure loss as defined is independent of free stream Mach number: this is a continuation of the situation described for zero incidence in Chapter 4. When, however, the normal shock is impinging on the 'internal' windward surface (higher values of *M*t) the loss increase with *M*t is at a higher rate than at subsonic stream speed, owing to the expansion flow round the windward lip and the subsequent shock and boundary layer interaction. The additional loss is a function of the strength of the normal shock.

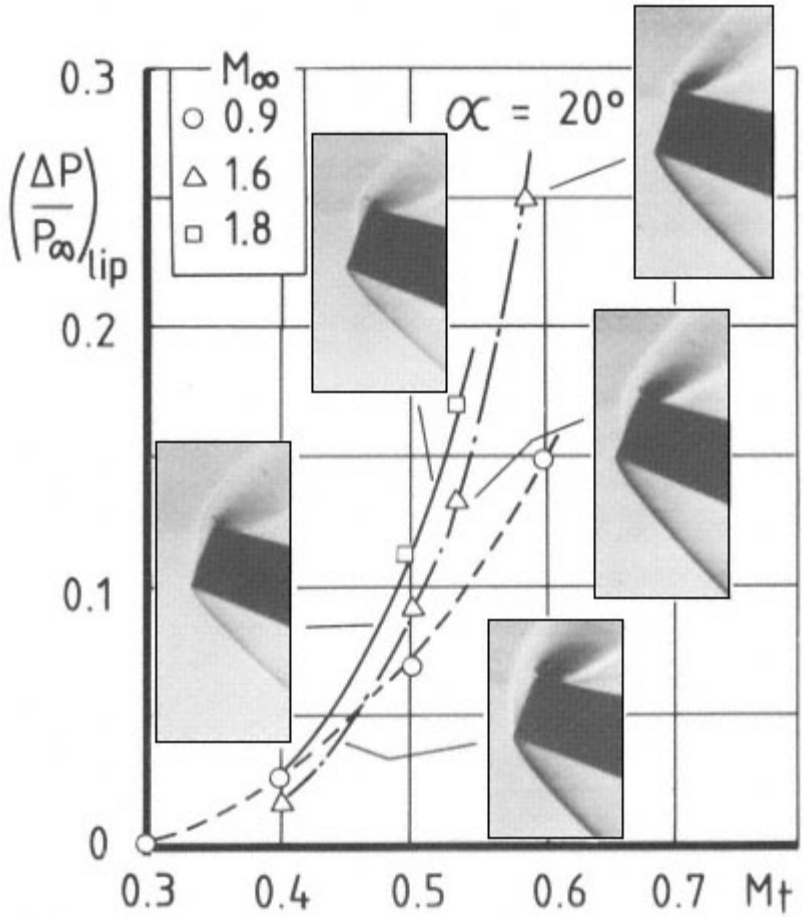

Figure 13.23
Comparison of lip loss at *M*¥ 0.9, 1.6 and 1.8 at 20° incidence.

13.5.2
Wedge-Compression Intake

For external-compression intakes of the two-dimensional or wedge type, having the wedge in the most usual, i.e. horizontal, attitude, the most important feature in relation to incidence performance is the variation of shock loss with change of attitude of the compression surfaces. Fig. 13.24 shows the measured pressure recovery of a representative double-wedge intake, over a range of incidence and at two Mach numbers. The variation of the relevant angles and corresponding shock systems is illustrated and the calculated shock recovery is shown by broken curves. Additional losses (Chapter 7), while not insignificant, have to some extent been controlled by use of a throat bleed on the compression surface. It is seen that the changes in actual pressure recovery with incidence parallel closely the calculated variations in shock recovery.

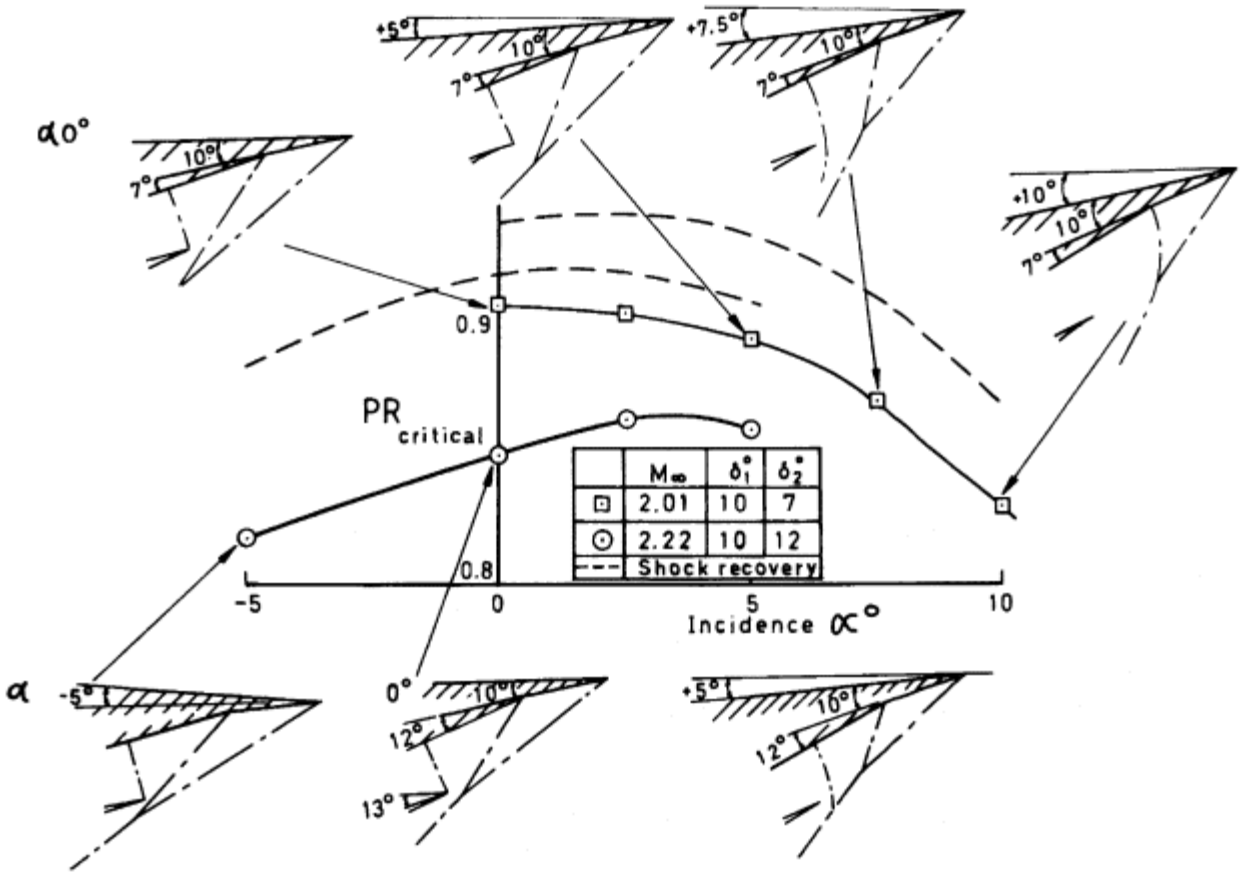

Figure 13.24
Effect of incidence on pressure recovery and shock wave patterns for a horizontal double-wedge intake.

If the wedge is in a vertical attitude, incidence has the effect of yawing the wedge to the airflow and the variation of shock loss for the yawed wedge is not readily predictable. The flow is influenced strongly by whether or not endwalls are fitted to the compression surface. In Fig. 13.25, pressure recovery is expressed as a proportion of the value at zero incidence. It is seen that when both upper and lower endwalls are present, the pressure recovery falls off rapidly as incidence increases. The reason lies in the details of flow around the lower endwalls, where (a) supersonic expansion on the upper surface leads to a stronger subsequent shock and (b) a vortex may be shed from the swept leading edge and ingested by the intake. The fall-off in pressure recovery with incidence is much less severe when the lower endwall is omitted.

Maximum flow ratio for a single or double wedge intake, in the attitude illustrated in Fig. 13.26, can be calculated using the formulae derived for zero incidence in Chapter 5 (Equations 5.7 and 5.9) but referring the

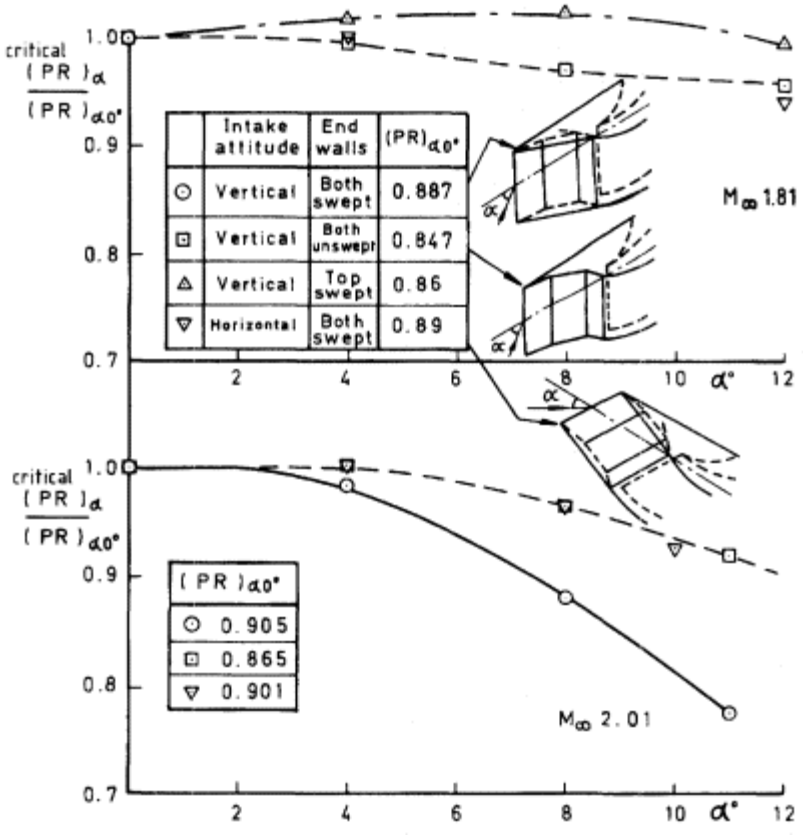

Figure 13.25
Effect of incidence on pressure recovery
of a vertical double-wedge intake.

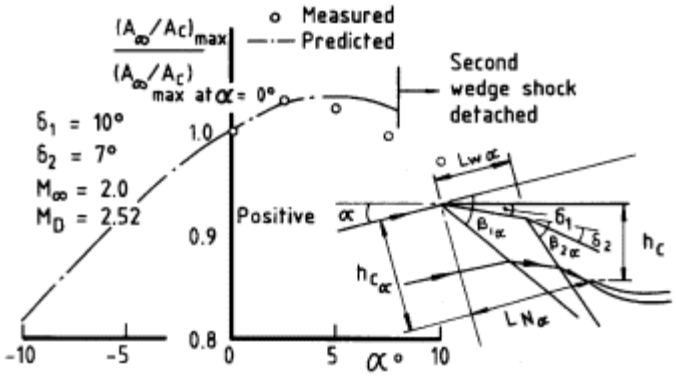

Figure 13.26
Effect of incidence on maximum flow of a double-wedge intake.

geometry to the actual free-stream direction. Thus for the double wedge we have

$$\left(\frac{h_\infty}{h_{c,\alpha}}\right)_{\max} = \frac{\cot\,\delta_{1,\alpha} - \cot\,\beta_{1D,\alpha}}{\cot\,\delta_{1,\alpha} - \cot\,\beta_{1,\alpha}} \cdot \frac{\cot\,\delta_2 - \cot\,\beta_{2D,\alpha}}{\cot\,\delta_2 - \cot\,\beta_{2D,\alpha}} \qquad (13.1)$$

where

$$\delta_{1,\alpha} = \delta_1 + \alpha \qquad (13.2)$$

$$h_{c,\alpha} = h_c \cos\alpha + L_N \sin\,\alpha \qquad (13.3)$$

$$\cot\,\beta_{1D,\alpha} = \frac{L_{N,\alpha}}{h_{c,\alpha}} = \cot\left(\tan^{-1}\frac{h_c}{L_N} + \alpha\right) \qquad (13.4)$$

Equation (13.4) defines the Mach number *M*D at which the shock from the first wedge falls on the cowl lip. The value of b2D,a follows from adapting and rearranging Equation (5.10), to give

$$\tan\,(\beta_{2D,\alpha} + \delta_{1,\alpha}) = \frac{1 - tan\;\delta_{1,\alpha}\dfrac{L_{w,\alpha}}{h_{c,\alpha}}}{\cot\,\beta_{1D,\alpha} - \dfrac{L_{w,\alpha}}{h_{c,\alpha}}} \qquad (13.5)$$

in which the length *L*w,a of the first wedge resolved in the free-stream direction is given by

$$\frac{L_{w,\alpha}}{h_{c,\alpha}} = \frac{L_w}{L_N} \cdot \frac{\sec\,\delta_1 \cos\,\delta_{1,\alpha}}{\left[1 + \left(\frac{h_c}{L_N}\right)^2\right]^{\frac{1}{2}} \sin\,\beta_{1D,\alpha}} \qquad (13.6)$$

After evaluating Equation (13.1), we have finally

$$\left(\frac{A_\infty}{A_c}\right)_{max} = \left(\frac{h_\infty}{h_c}\right)_{max} = \frac{h_{c,\alpha}}{h_c} \cdot \left(\frac{h_\infty}{h_{c,\alpha}}\right)_{max} \qquad (13.7)$$

13.5.3
Cone-Compression Intake.

With external compression in the axisymmetric form, the flow in detail at incidence is complex but the basic pattern of shock-angle variation is akin to that for a pitot intake. The conical forebody can be seen as pivoting about its apex, with the shock angles changing much less than the surface angles, relative to the free-stream direction. As incidence increases, the windward lip moves into the cone shock, the leeward lip moves away from it and the overall variation of loss is dependent upon the relation between the lip position angle, q say, relative to the cone apex and cone shock angle, b say, at zero incidence. If b £ q, the cone shock moves increasingly inside the windward lip as incidence increases, an increasing proportion of the flow, therefore, is compressed through a normal shock only and a sharp fall-off in pressure recovery results. If b > q by an appreciable margin, the fall-off in recovery as incidence increases is significantly slower. The comparison can be seen in results for some single and double cone intakes, taken from quoted references and collected in Fig. 13.27. In the keys to the diagrams the shock-on-lip (SOL) Mach number is quoted; comparison with the value of *M*¥ shows whether the conical shock is inside or outside the lip at zero incidence. The small differences between two sets of results for double-cone intakes in the diagram at (b) are not seen as being significant.

A second influence on pressure recovery comes from a tendency for the boundary layer to be swept up to the leeward side of the forebody. A comparison in Fig. 13.28 of results for double-cone intakes with varying lengths of forebody, at incidences 5° and 10°, shows the consequence at the higher incidence the long forebody associated with SOL Mach number 4 gives distinctly the poorest result, because of the effect of a thickened leeside boundary layer. It should be noted that the trend is in the opposite sense to that associated with lip position angle.

There is no simple theoretical approach to the determination of maximum flow ratio for axisymmetric intakes at incidence. Fig. 13.29 shows some experimental results for the variation of maximum flow ratio, referred to the zero incidence value, for single-cone, double-cone and isentropic intakes at Mach 1.9.

13.6
Intake Shielding

The concept of sustaining intake performance at high angles of incidence by positioning an intake beneath the aircraft fuselage or wing applies to both

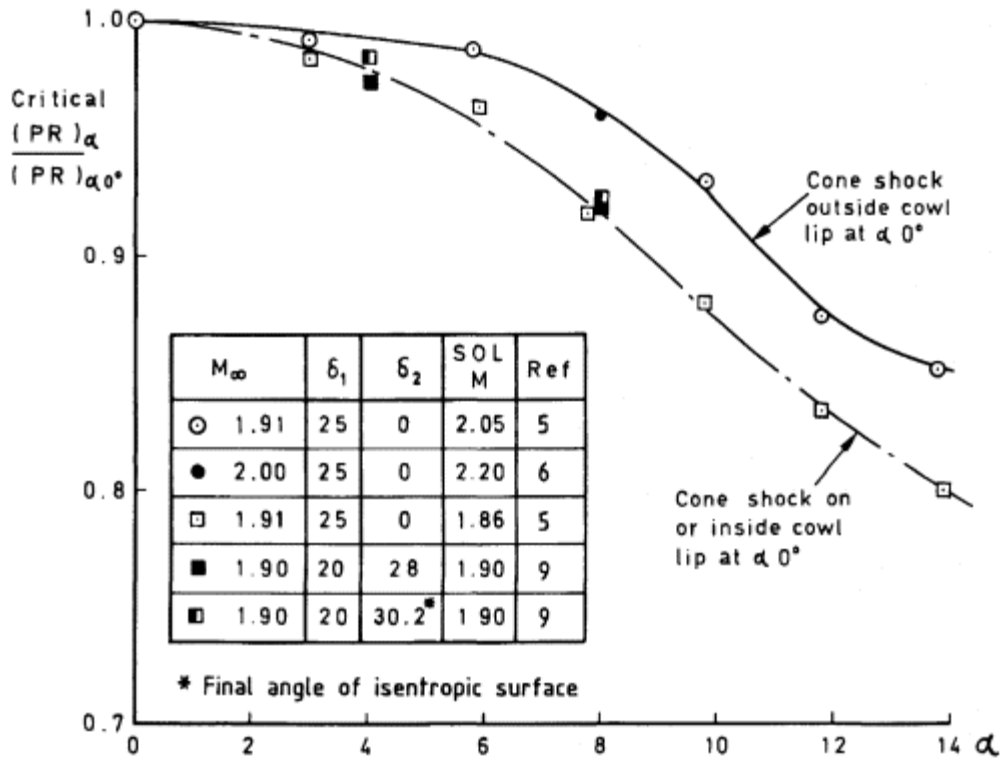

Figure 13.27
Effect of incidence on pressure recovery of axisymmetric forebody intakes.

subsonic and supersonic aircraft and has been used many times in design. The principle is simply that when incidence is varied, the airflow direction at the intake is controlled by the aircraft surface, so to that extent the intake is 'not aware' of a change in attitude. Additionally, at supersonic speeds advantage can usually be taken of a reduction in local Mach number, hence a reduction in shock loss, as incidence increases.

The underbody position is a relatively uncomplicated application aerodynamically. Typical results are shown in Fig. 13.30. The shielding at subsonic speeds is excellent up to 35° incidence. At supersonic speed (Mach 1.8) the results for positive incidence up to 15° are even better, a substantial increase of pressure recovery with incidence being shown. A problem which usually has to be considered is that of ingestion of debris sucked in or thrown up during ground operations.

An 'armpit' position is more difficult aerodynamically; here the intake is both underneath a wing or wing-root strake and alongside a fuselage and the boundary layer clearance problem is complex. The study by Ross *et al.* (*loc. cit.*) showed (Fig. 13.31) that a strake has the effect, at subsonic speeds, of reducing the local mean incidence to about half the free-stream value but

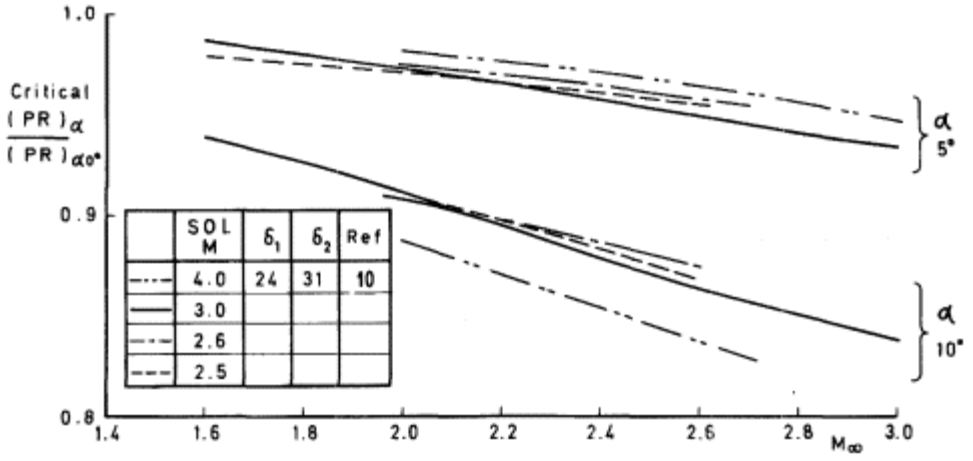

Figure 13.28
Influence of forebody length on pressure
recovery at incidence of double-cone intakes.

at the expense of increasing the local sidewash angle. The potential level of pressure recovery is considerably reduced as a result of fuselage boundary layer drifting towards the lee side at incidence but being trapped beneath the strake (Fig. 13.32). A longitudinal bleed slot in the strake-fuselage junction relieves the accumulation of low energy air but slightly reduces the effectiveness of incidence shielding (Fig. 13.31). A prediction of pressure recovery, based on the measured performance of the intake tested in isolation and calculated for the local conditions of incidence and sidewash, agrees well with the measured performance as installed and with bleed (Fig. 13.33).

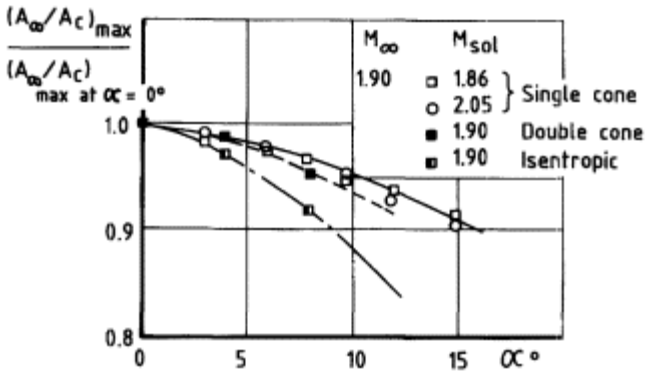

Figure 13.29
Effect of incidence on maximum flow
of axisymmetric forebody intakes.

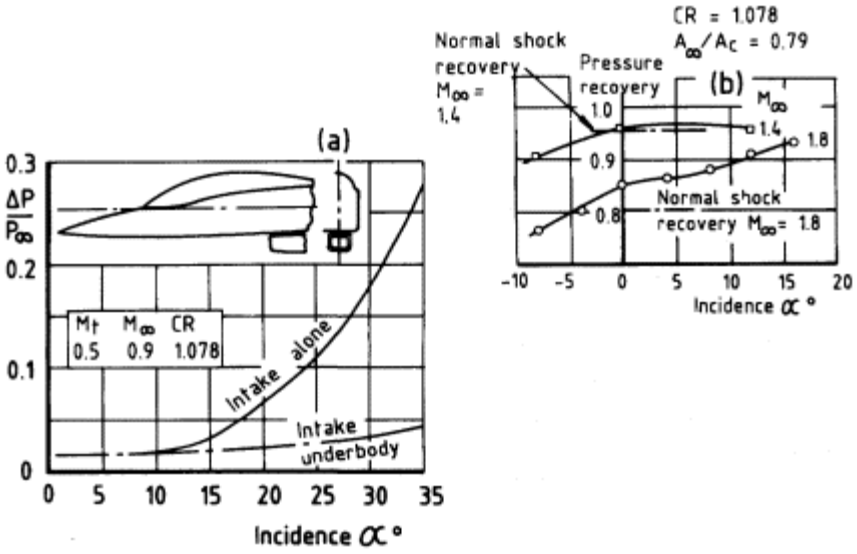

Figure 13.30
Variation of total-pressure loss with incidence for an underfuselage pitot intake.

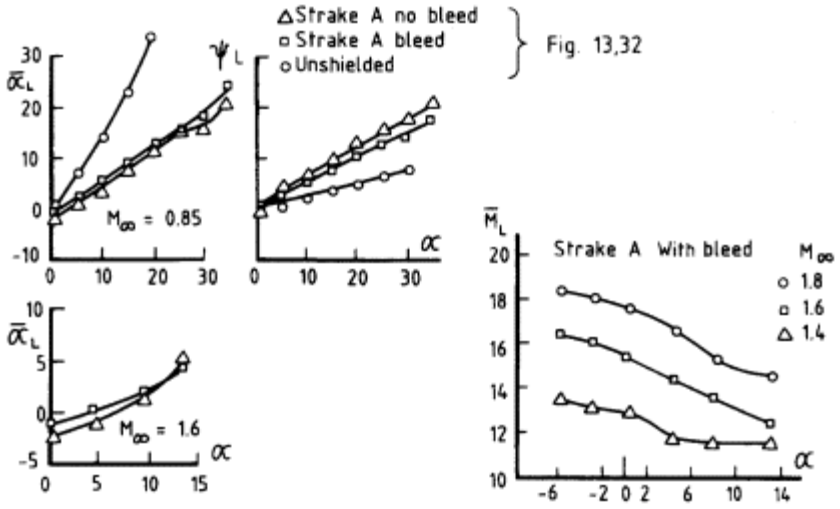

Fig 13.31
Flow angle and Mach number on a
fuselage side and under a wing-root strake.

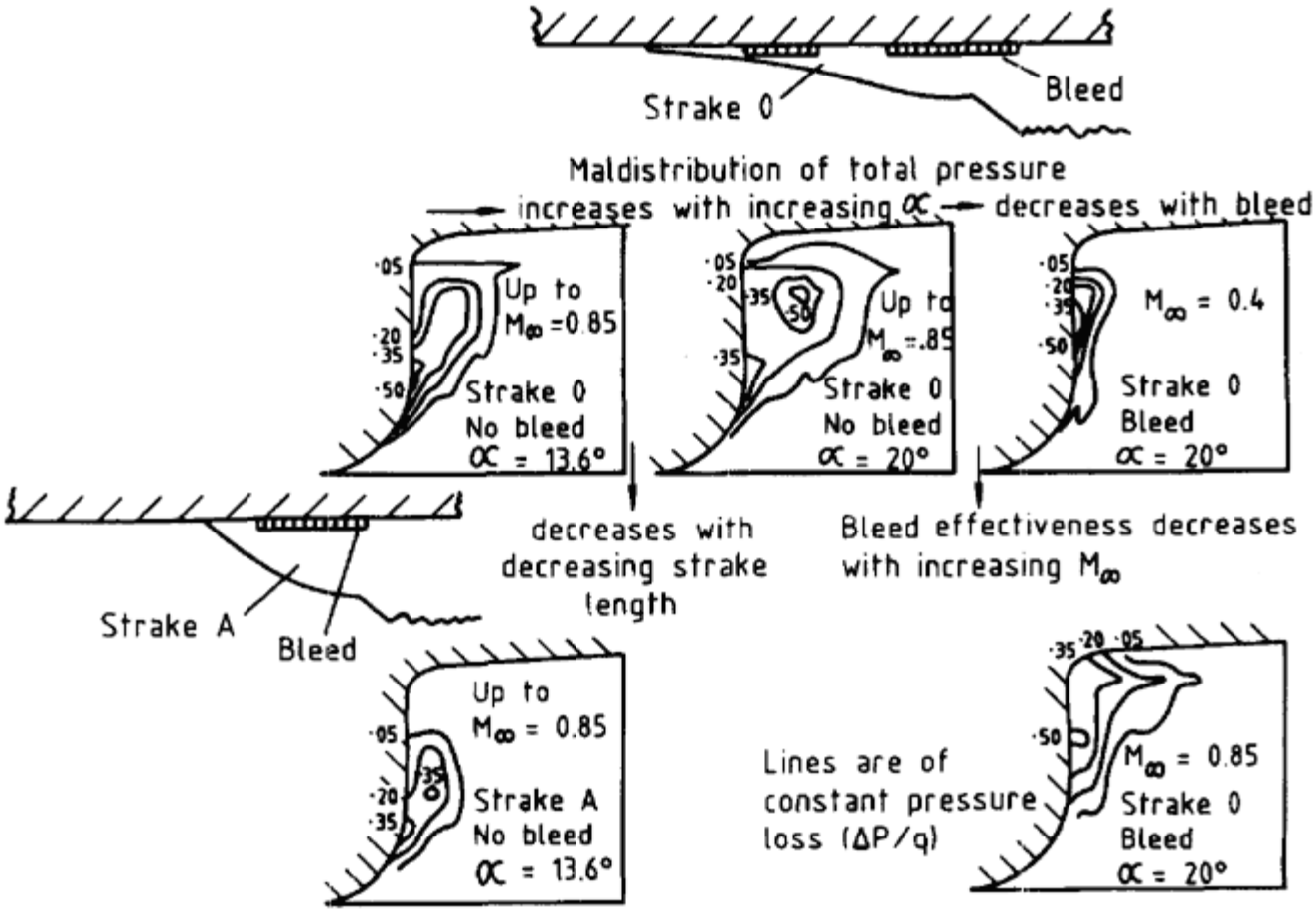

Figure 13.32
Loss contours (D*P*/*q*) on a fuselage side and beneath a wing-root strake.

At moderate supersonic speeds, the interactions of shock and boundary layer, both on the underside of the strake and on the side of the fuselage, result in considerable modification of the intake shock configuration. The situation at Mach 1.8 is pictured in Fig. 13.34. The complex system of bifurcated shocks illustrated at (a) can be deduced from distributions of total pressure in the intake throat, shown at (b). One result is a favourable effect on mean pressure recovery, given at (c); the curve for isolated intake at local conditions shows the benefit of decreasing local Mach number as incidence increases and on top of this, up to about 10°, is a further gain from the shock bifurcations.

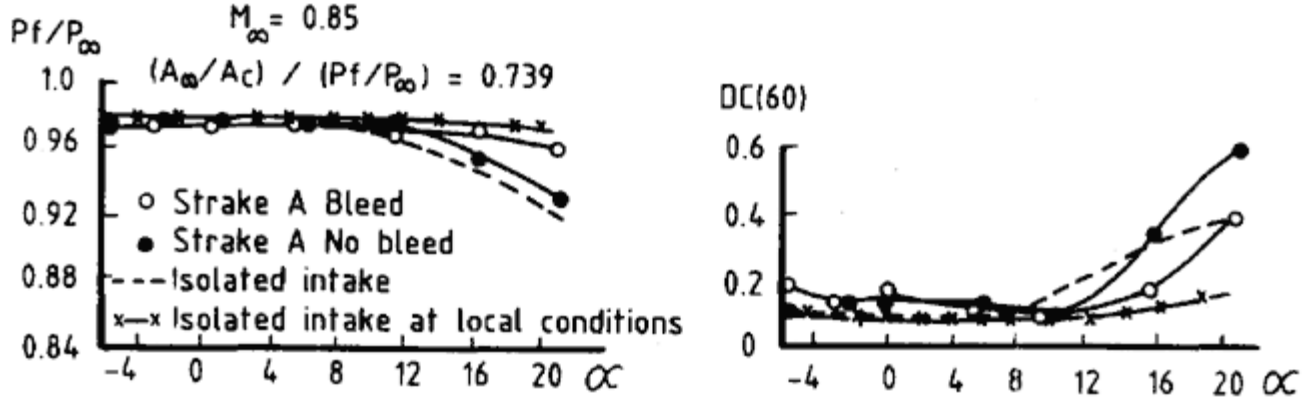

Figure 13.33

Pressure recovery and flow distortion at incidence
for an intake underneath a strake at M_∞ 0.85.

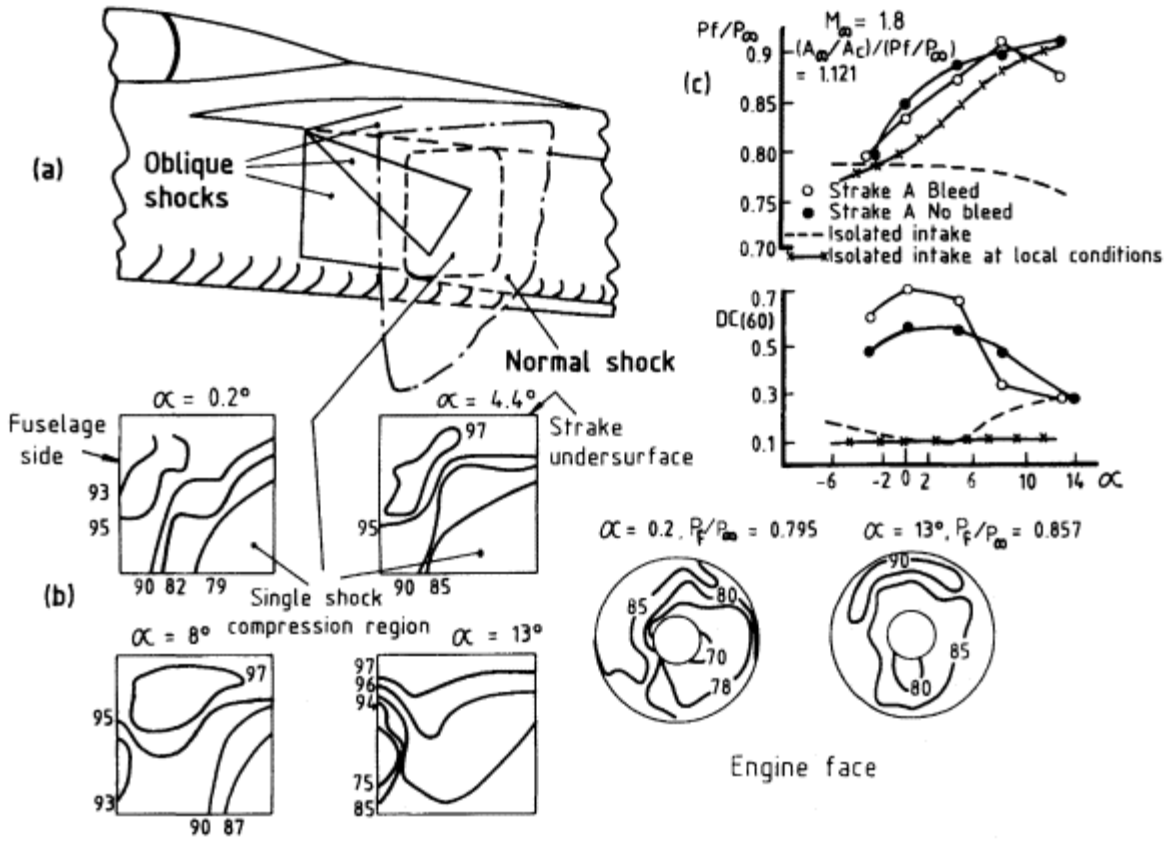

Figure 13.34
Pressure recovery and flow distortion at incidence
for an intake underneath a strake at *M*¥ 1.8.

Distortion levels, however, are high until, above 10° the locus of intersection of the oblique shocks with the normal-shock plane moves outside the intake capture area. Taking off the long fuselage boundary layer ahead of the entry by means of a forward-extending splitter plate may reduce the distortion. If the plate projects ahead of the normal-shock position, a question arises as to whether an additional bleed is required between the splitter plate and the intake. Furthermore a second splitter plate may be needed to control the strake or wing boundary layer. Thus the complication can mount in a practical case of an armpit intake location. This is illustrated by the history of the General Dynamics F.111 intake, which at one stage in its development comprised the details shown in Fig. 13.35.

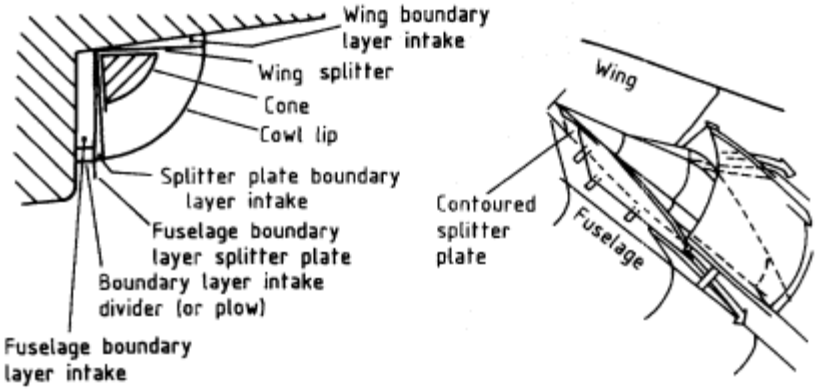

Figure 13.35
Intake on the F.111 aircraft.

The overbody position for an intake has not been generally popular with designers but has been used for three-engined transport aircraft such as the British Aerospace Trident, Lockheed Tristar and Dassault Falcon 900, where its use for one engine is almost inevitable. The position gives a measure of shielding from directional flow changes in the incidence plane but local Mach number effects tend to be disadvantageous, particularly at supersonic speeds. The position is also unfavourable in that fuselage boundary layer collects on the leeward upper surface at incidence and may be prone to separate, so that a high diverter or pylon-type mounting may be necessary, leading to high drag. Some results comparing the pressure recovery of an overbody installation at supersonic speed with those of other installational positions, from measurements by Williams, Nelms and Smelzer (1981), are given in Fig. 13.36. The overbody position does have two advantages over alternatives: (1) for VSTOL aircraft, susceptibility to hot gas ingestion is lower, and (2) for attack aircraft or missiles, the vehicle is less visible from ground-based radar.

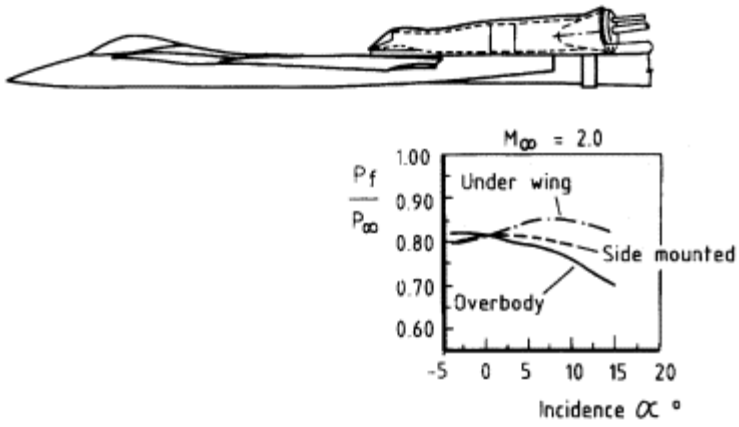

Figure 13.36
Performance of an overbody intake at *M*¥ 2.0.

References

1 Albers, J.A. (1973) 'Theoretical and experimental internal flow characteristics of a 13.97 cm diameter inlet at STOL take-off and approach conditions'. NASA, TN D7185.

2 Albers, J.A. (1973) 'Application of compressibility correction to calculation of flow in inlets'. *Journal of Aircraft* 10, no. 7.

3 Albers, J.A. (1973) 'Comparison of predicted & measured low speed performance of two 51 centimetre diameter inlets at incidence angle'. NASA TM X2937.

4 Albers, J.A. and Stockman, N.O. (1975) 'Calculation procedures for potential & viscous flow solutions for engine inlets'. Trans. *ASME Journal of Engineering Power* 97, Series A, no. 1.

5 Beheim, M.A. (1953) 'A preliminary investigation at Mach number 1.91 of a diffuser employing a pivoted cone to improve operation at angle of attack'. NACA, RM E53 130.

6 Beheim, M.A. and Piercy, T.G. (1957) 'Preliminary investigation of shield to improve angle of attack performance of nacelle type inlet'. NACA, RM E57 G25a.

7 Burley, R.R. (1979) 'Effect of lip & centrebody geometry on aerodynamic performance of inlets for tilting-nacelle VTOL aircraft'. AIAA, 79-038.

8 Chou, D.C., Luidens, R.W. and Stockman, N.O. (1978) 'Prediction of boundary layer flow separation in V/STOL engine inlets'. *Journal of Aircraft* 15, no. 8.

9 Connors, J.F. and Meyer, R.C. (1955) 'Performance characteristics of axisymmetric two-cone & isentropic nose inlets at Mach No. 1.9'. NACA RM E55 F29.

10 Hawkins, R. (1962) 'The effects of incidence upon the performance of 24° 31° double cone intakes'. Bristol-Siddeley Engines Report AP 5081.

11 Hawkins, J.E. (1974) 'YF16 inlet design and performance'. AIAA, 74-1062.

12 Hurd, R. (1976) 'Subsonic pitot intakes high-speed high-incidence performance'. Rolls-Royce (Bristol) Report PD 2029.

13 Jakubowski, A.K. and Luidens, R.W. (1975) 'Internal cowl separation at high incidence angles'. AIAA, 75-64.

14 Latham, E., Gawienowski, J. and Merriweather, F. (1977) 'Investigation of inlet concepts for manoeuvres improvement at transonic speeds'. NASA TMX 73, 215.

15 Lieblein, S. and Stockman, N.O. (1972) 'Compressibility correction for internal flow solutions'. *Journal of Aircraft* 9, no. 4.

16 Luidens, R.W. and Abbott, J.M. (1976) 'Incidence angle bounds for lip flow separation of three 13.97 cm diameter inlets'. NASA, TM X-3351.

17 Ross, J.A., McGregor, I. and Priest, A.J. (1981) 'Some RAE research on shielded & unshielded fuselage mounted air intakes at subsonic & supersonic speeds'. AGARD, CP 301.

18 Williams, T.L., Nelms, W.P. and Smelzer, D. (1981) 'Top mounted inlet system feasibility for transonic-supersonic fighter aircraft'. AGARD. CP 301.

Chapter 14
Novel Designs and Devices

14.1
Introduction

In this chapter some unusual forms of intake are described. These include novel forms of variable geometry and mechanical or fluid-mechanical devices and forms of fixed geometry that have useful properties such as low values of radar signature but also have unusual shapes that require ingenuity to confer on them acceptable aerodynamic performance. The features have all received study because of some potential merit. Some may offer improved pressure recovery under particular conditions, or reduction in drag relative to conventional shapes: alternatively they incorporate devices which aim to reduce weight, simplify the variation of intake geometry and so on. Results have been variable but since results generally carry qualifications relating to particular circumstances, the criterion used for inclusion here is one of fluid-dynamic interest rather than proven success. Applications to missiles as distinct from piloted aircraft are referred to where appropriate.

14.2
Intake Geometry.

Proposals for unusual intake designs have sometimes centred on using parts of simple known flow fields, for example those behind plane or conical shocks, to create compression-surface shapes that could have particular advantages. At other times, intake shapes and locations have been devised to avoid high cowl drag without getting deeply into the problems of internal compression.

14.2.1
Compression Surfaces Derived from Plane-Shock Flow

The use of the flow field behind a plane oblique shock to derive the lower-surface shape of an aircraft wing for high supersonic speeds was suggested originally by Nonweiler (1963). Many interesting shapes, for both lower and upper wing surfaces, derived from a variety of simple compressive and

expansive flow fields, have been suggested by Flower (1963) and others. The generic name for these shapes is *caret wings*. Both Flower and Townend (1967) have also suggested that the same compressive flow fields be used for intakes and this can be done at any supersonic Mach number. Fig. 14.1 shows a single-shock caret-flow intake. The caret shape provides in effect both compression surface and endwalls. The 'aspect ratio' can be increased by opening out the angle of the caret and the shock-on-lip Mach number depends on the lip position chosen: these points are illustrated. Multi-shock or isentropic ridge lines can be used to produce higher shock recovery and by combination of caret surfaces, intakes with two or more facets can be obtained (Fig. 14.2).

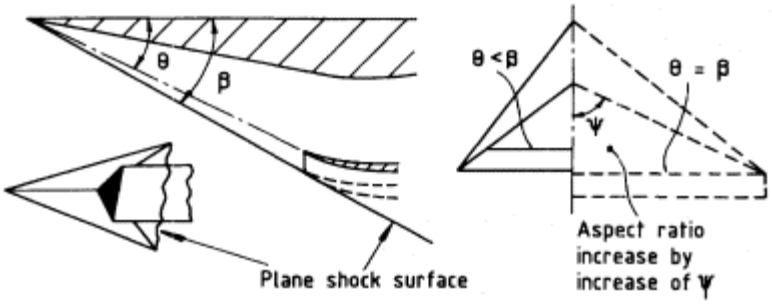

Figure 14.1
Single oblique-shock caret intake.

Intakes of this kind may be unattractive for some aircraft applications because of (a) awkwardness of transforming a triangular section at entry into a circular section at the engine face and (b) the difficulty of combining this with variable geometry. For a missile however, where variable geometry is probably not admissible and where a combustion chamber does not necessarily have to be circular in cross-section, a caret intake may be advantageous, as for instance if the pressure recovery is less sensitive to incidence or yaw then that of a more traditional design. An advantage at

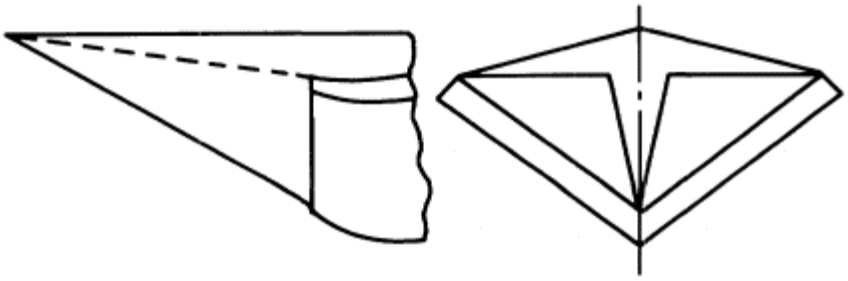

Figure 14.2
Single oblique-shock caret intake with two facets.

high supersonic speeds is the ability to use geometries in which all the surfaces have swept leading edges, and therefore relatively low kinetic heating rates.

14.2.2
Bump Intake

The use of streamlines in the flow field of a cone that is intercepted by an off-the-axis plane, to define a 'bump' compression surface, was suggested by Ferri and adopted in the Grumman Super-Tiger aircraft. The object is to provide an intake which is wider and flatter than a conventional half-circular intake but which still uses a known shock shape and flow field. Because the cone flow produces isentropic compression behind the shock (Chapter 5), the defined surface has spanwise pressure gradients which help to divert the boundary layer away from the intake entry.

Development of a bump surface shape is facilitated by using a hyperbolic approximation for the cone-flow streamlines, as was done in Chapter 5. This follows the analysis presented by Bower *et al.* (1959). The plane which intercepts the cone flow represents the side of an aircraft fuselage. Cylindrical shapes may be used but the treatment is then more complex. Referring to Fig. 14.3, the equation of the plane is

$$y = K = \text{constant} \qquad (14.1)$$

and if b is the cone-shock angle, we have

$$\tan \beta = \frac{y_w \sec \theta}{z} \qquad (14.2)$$

The equations for the intersection of plane and shock surface are

$$z = K \cot \beta \sec \theta, \; x = K \tan \theta$$

which yield

$$z^2 \tan^2 \beta - x^2 = K^2 \qquad (14.3)$$

The streamline equation is

$$r^2 = y^2 \sec^2 \theta = z^2 \tan^2 \delta + c \qquad (14.4)$$

and combining the above relations leads to an equation for the cross-section of the stream surface at station $z = zs$, namely

$$y_s{}^2 = A \cos^2 \theta + B \qquad (14.5)$$

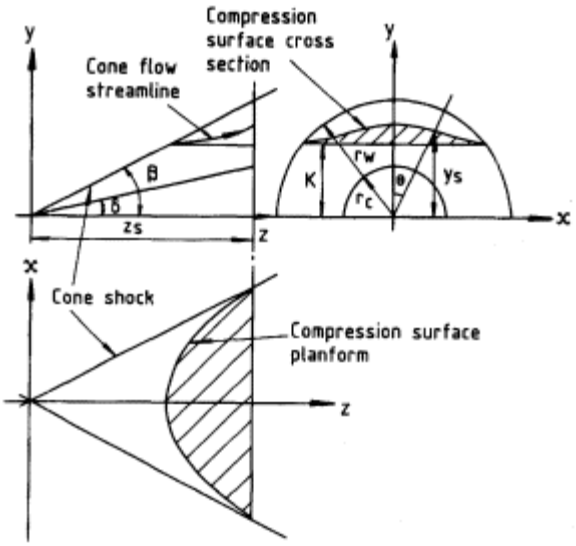

Figure 14.3
Bump intake compression surface derived from conical flow field intercepted by plane surface.

in which A and B are constants, defined by

$$A = z_s^2 \tan^2 \delta;\ B = K^2\left(1 - \frac{\tan^2\delta}{\tan^2\beta}\right) \qquad (14.6)$$

Fig 14.4 shows a typical bump surface derived for Mach number 3.06, with calculated and measured pressure distributions. The lateral pressure gradients are well demonstrated. In performance comparisons at lower Mach numbers, by Simon, Brown and Huff (1957), a bump intake with perforated bleed at entry was found to give some increase in pressure recovery and reduction in drag compared with a wedge intake with slot bleed and diverter (Fig. 14.5).

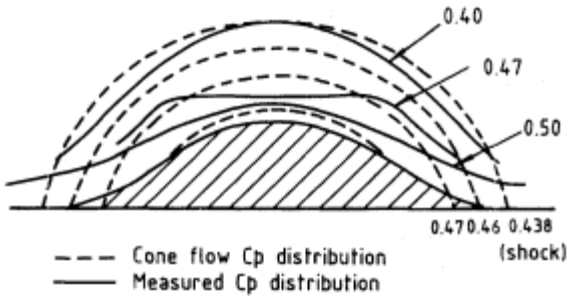

Figure 14.4
Bump surface flow field designed for M¥ 3.06.

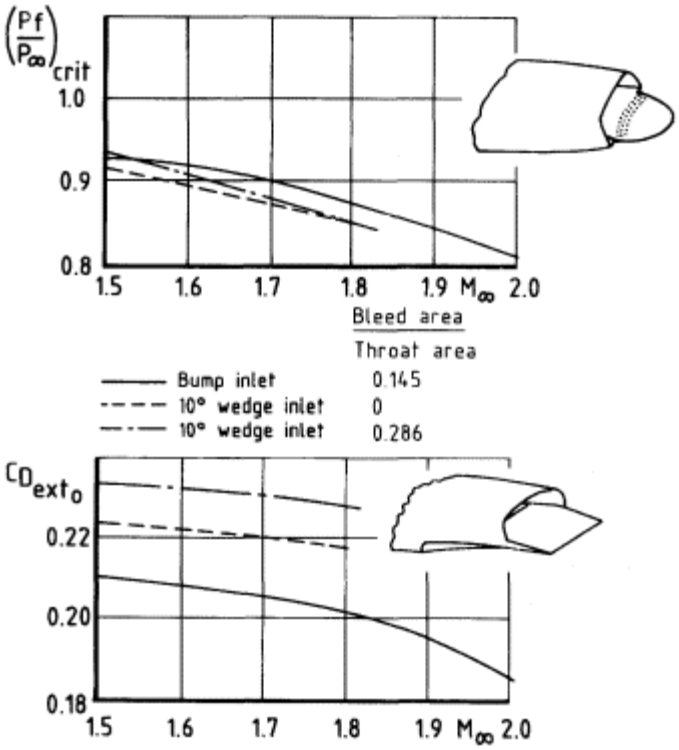

Figure 14.5
Comparison of single wedge
and bump intake performance.

14.2.3
Scoop Intake

As design Mach number increases above, say 2.5, the increasing degree of oblique-shock compression required leads on an external-compression intake, as we have seen, to high values of cowl wave drag. The alternative of using internal compression in large measure may be undesirable because of the difficulties of achieving good variable geometry and efficient boundary-layer control. One way which in principle eliminates the cowl wave drag without recourse to variable geometry is to use a so-called 'scoop' intake (Fig. 14.6). This can be done when the intake is adjacent to a body or wing surface; geometrically it amounts to an inversion of the normal external-compression intake. The compression surface is on the side opposite to the aircraft surface and the flow is thereby turned inwards towards the aircraft. The advantageous features are firstly, that the usual intake cowl is now in effect 'buried' within the aircraft, so that its drag is eliminated, and secondly, that the compressive turning directs the flow inwards towards the engine, thereby eliminating the cornering losses discussed in Chapter 7. This type of intake was used in a wing root position on the Republic F105

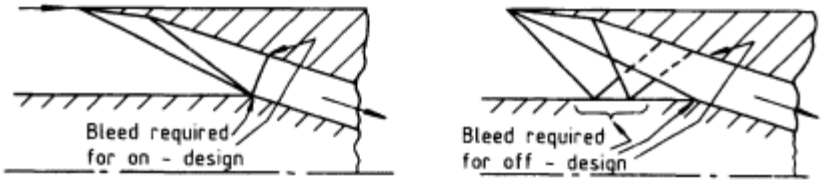

Figure 14.6
Scoop intake at and below design Mach number.

aircraft and as a four-intake installation on the American ramjet research vehicle LASRM.

There are two inherent difficulties in the design. Firstly, although in principle a scoop intake with open ends is self-starting, in practice this depends very much on the aspect ratio, that is intake width compared to intake height. The problem is illustrated in Fig. 14.7, which shows how the normal shock will be anchored in a non-started position if the choked-flow quantity at entry plane and the choked-flow quantity being spilled sideways through the triangular area illustrated are in total less than full intake flow. The larger the width in relation to height, the more likely is this to occur. The relation between shock pattern and the two flow quantities can be estimated by a method similar to that employed in Chapter 5 for estimating shock position in front of a conventional intake under spillage conditions. The attainable contraction ratio for self-starting can be calculated as a function of aspect ratio (Fig. 14.8), on the assumption of a theoretical pressure recovery for the branched shock structure shown in Fig. 14.7 for both throat flow and sideways-spilled flow.

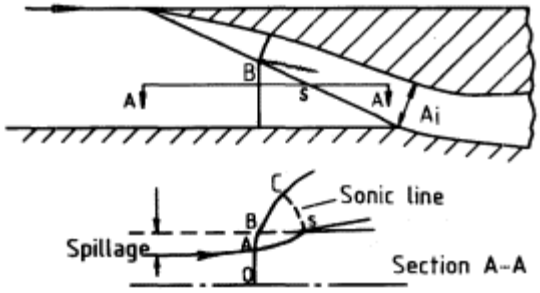

Figure 14.7
Scoop intake during 'starting' process.

The second difficulty of design stems from the fact that in practice the pressure recovery of the branched shock system, already low, is reduced further by shock and boundary-layer interaction during the starting process: this affects particularly the pressure recovery of the throat flow and hence the flow quantity that can pass through. There is therefore a problem of

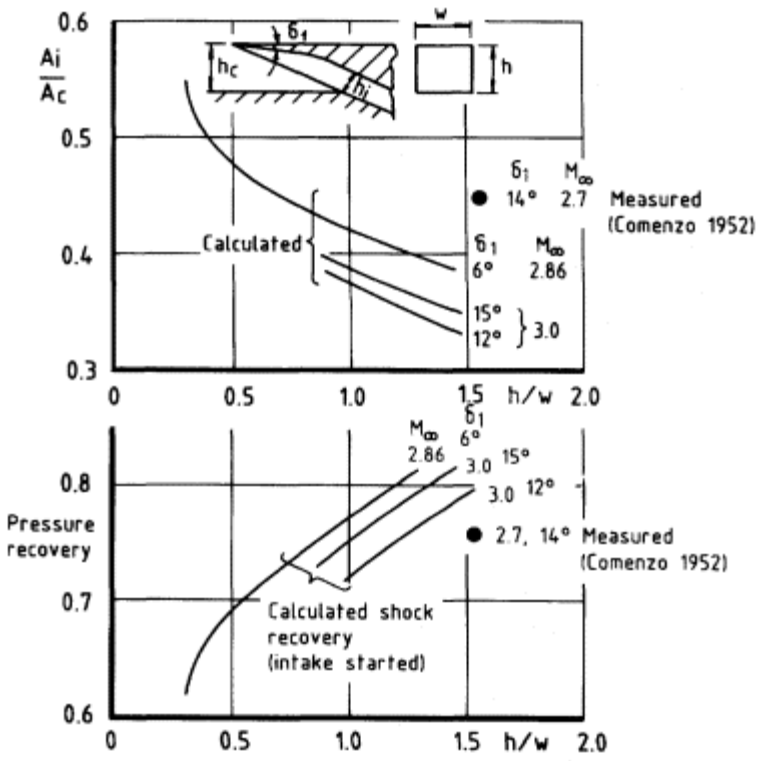

Figure 14.8
Dependence of attainable contraction ratio and pressure recovery on scoop-intake aspect ratio.

providing efficient boundary-layer control, not only for the started condition but also during the starting process, when the relevant interaction may be considerably upstream of the throat. A bleed system has to provide control for both the compression-surface boundary layer and also the more extensive boundary layer on the body surface. Furthermore this latter is subjected on design to the focussed effect of all shocks of the compression system.

The boundary layer problem can be eased by raising the scoop intake off the body surface on a boundary-layer diverter. If this is done, however, a cowl wave drag is in effect reintroduced into the system in conjunction with a diverter drag, so an initial incentive for the scoop design is at least partly sacrificed. Nevertheless, some potential advantage remains and Laruelle (1981) has explored the comparison between such a system and a conventional external-compression intake. It appears that the 'semi-scoop' design may be superior to a conventional geometry as an intake for missile application, in which angles of incidence and roll are varied in flight.

14.2.4
Intakes to Give Low Values of Radar Cross-Section (RCS)

A considerable amount of research and development in the USA has been devoted to producing designs for combat aircraft that incorporate many technological aspects that reduce the radar 'signature' of the aircraft. This is achieved by a combination of external shaping, structural design using unconventional materials, and the use of radar-absorbing materials on all internal and external surfaces. The effect of the first two is to reflect radar energy away from the line of sight of the transmitter and receive antenna and the third is to trap and absorb the radar energy.

Stonier (1991) has produced generalised and hence unclassified information on stealth aircraft technology which emphasises the crucial importance of aerodynamic shaping in achieving low values of radar cross-section. In particular, as regards the engine installation, he stresses the need to (a) bury the jet engines in a convoluted duct shape, so that no line of sight from the intake to the engine is possible, (b) shape the intake entry plane so that like all other external surfaces radar reflections are diverted away from the 'threat' direction, (c) avoid orthogonal intersections and cavities such as conventional boundary layer diverter passages, and (d) try to shield the intake when the aircraft is in its cruise attitude. The general effect on intake design appears to be to rake, sweep, curve and perhaps serrate all the leading edges of the capture plane. Many of these features can be seen in the illustrations of F117 (shielding, rake and sweep), F22 (rake and sweep) and B2 (shielding by the wing surface, low profile, serration and non-orthogonal intersections) in Figs. 14.9 14.11.

It should be noted that the data on the effects of sweepback in intake performance in Chapter 2 is relevant. Some of this data was acquired in research on the intake for the Avro Vulcan V bomber of the 1950s and, as Stonier notes, due to its nearly all-wing shape small vertical fin and buried engines, at some angles this aircraft was nearly invisible to radar. The other data of interest is contained in Chapter 13 where the effects of stagger or rake at both subsonic and supersonic speeds are featured. Thus it should not be too difficult to combine the effects of sweepback and stagger to make reasonable estimates of the performance of intakes such as are shown in Figs. 14.9 and 14.10. However, actual wind-tunnel measurements to make comparisons with estimates from these types of intake geometry are not currently available.

14.3
Arrangements Related to Specific Performance Features.

14.3.1
Increase of Pressure Recovery at Incidence

It is not difficult to devise ways of decreasing the rate of fall of pressure recovery as angle of incidence is increased in one direction. For highly

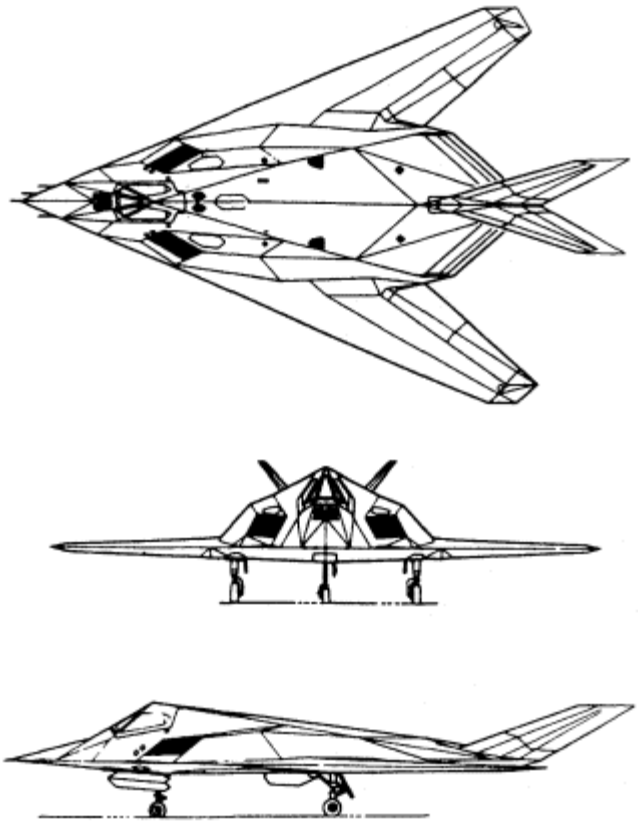

Figure 14.9
The F117 aircraft

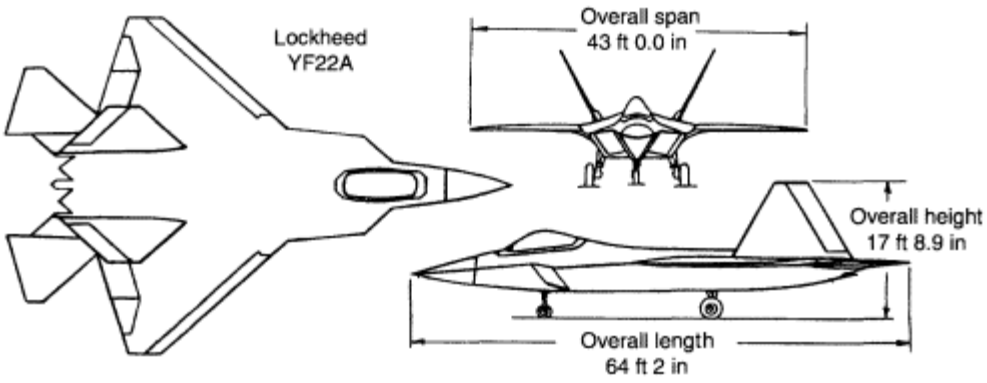

Figure 14.10
The F22 aircraft.

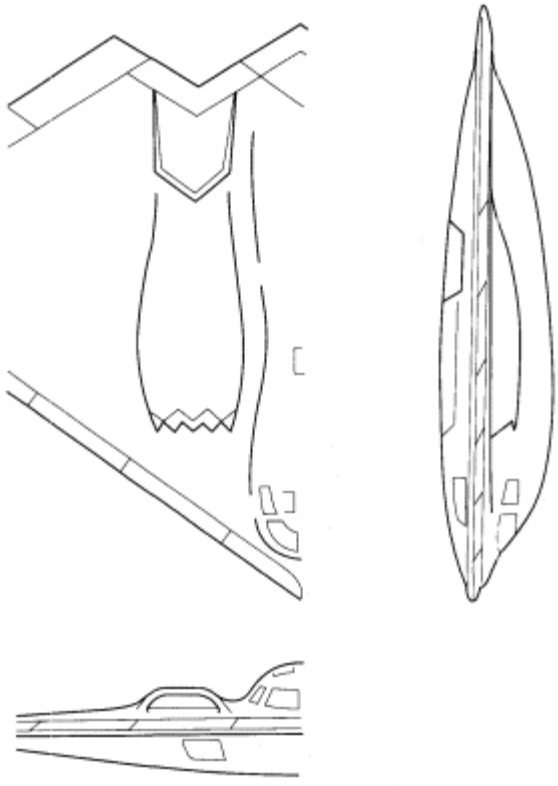

Figure 14.11
The intakes of the Northrop B2 aircraft.

manoeuvrable aircraft, an intake can be placed under the fuselage or wing, in a position where local flow angle is practically invariant with aircraft incidence. At supersonic speeds, increase in incidence also reduces the local Mach number, usually with little penalty in total pressure. For example, the pressure recovery of the underbody intake on the F16 aircraft at Mach 2, as given by Hawkins (1974) increases from 0.72 at zero incidence to 0.85 at 20° incidence, owing to the decrease in Mach number at entry. Something of the same effect can be achieved by the addition of a small flow-directing surface above and in front of a nose-mounted intake. At subsonic speeds the effect of such a surface is confined to reducing the change in flow angle almost to zero, as in the use of intake stagger discussed in Chapter 13.

For supersonic speeds, various devices have been suggested, by Beheim (1953 and 1957), Schueller *et al.* (1956) and others. One proposal employs a half-cone intake, flat side uppermost, with either swept or unswept top plate. Another uses a full axisymmetric layout with a cowl shield mounted forward of the entry plane. Fig. 14.12 indicates that above +7° incidence, the half-cone configuration is superior to the fully axisymmetric one, with or without shield. Another way to increase recovery at incidence with an

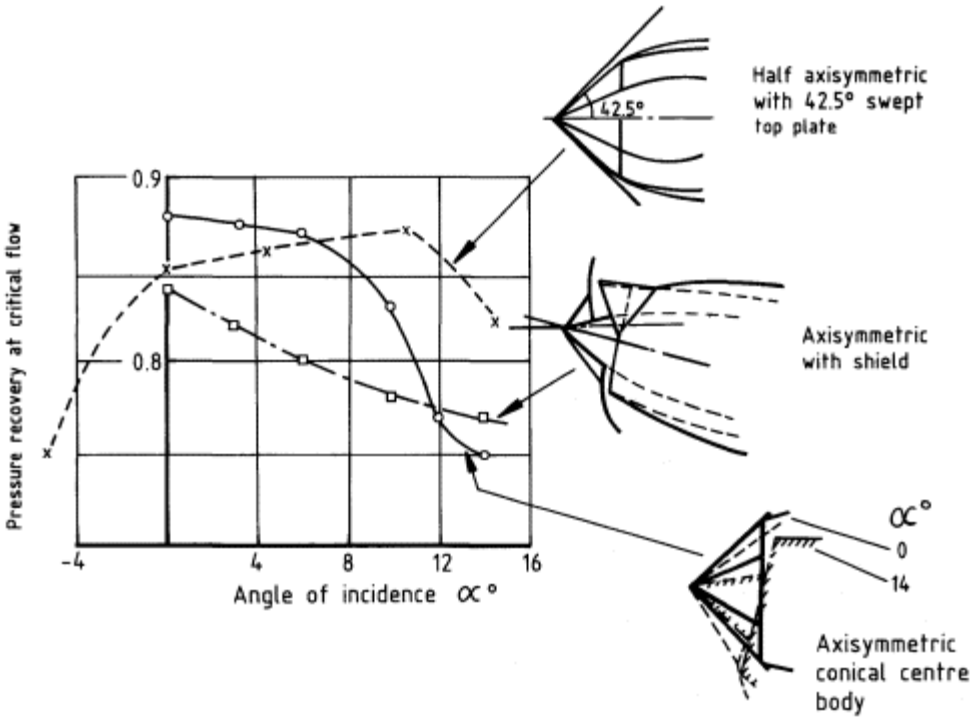

Figure 14.12
Effect of shields on performance of axisymmetric and half-axisymmetric intakes at incidence a M¥ 1.91.

axisymmetric intake is to pivot the conical forebody so as to keep it aligned with the incident flow. A further gain is obtained if the entry plane is staggered so that the lower lip stays clear of the conical shock (Fig. 14.13). For high efficiency at both positive and negative incidences, the additional complexity of pivoting both forebody and cowl is needed. Samanich *et al.* (1958) showed that this combination, together with boundary layer control on the forebody, could be very effective up to at least 14° incidence (Fig. 14.14).

Connors and Woollett (1954) tested an arrangement consisting of an asymmetric compression surface housed in a circular-cylindrical nacelle. The results (Fig. 14.15) showed inferior performance, at zero incidence, to the equivalent axisymmetric intake but better performance above 7°. The addition of boundary layer control at the throat, and possibly a more refined design method that ensured an attached shock at the cowl lip, would probably have improved the performance significantly. In principle an intake of this type in a missile application might roll on its axis so that the compression surface was always in the best position with respect to the incident flow, giving therefore the benefit of the asymmetric design at both positive and negative attitudes in both incidence and sideslip.

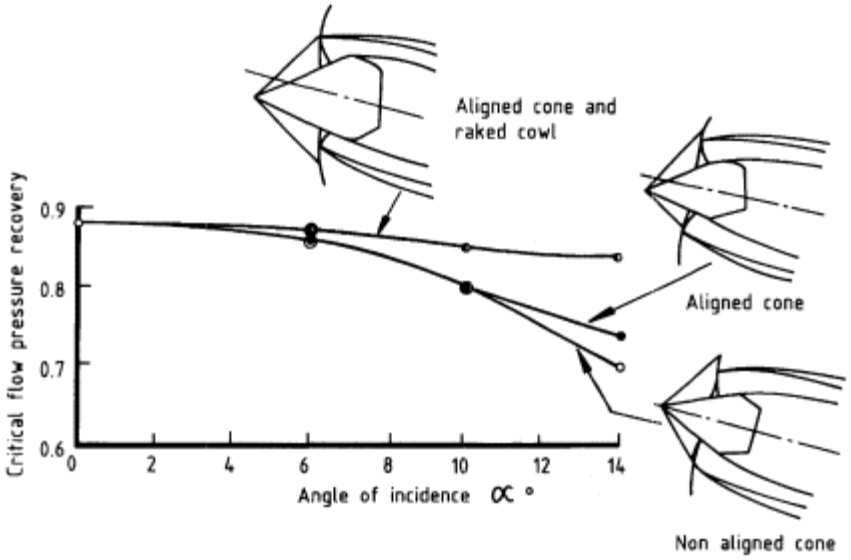

Figure 14.13
Effect of cone pivoting and cowl entry-plane stagger on performance at incidence a *M*¥ 1.91.

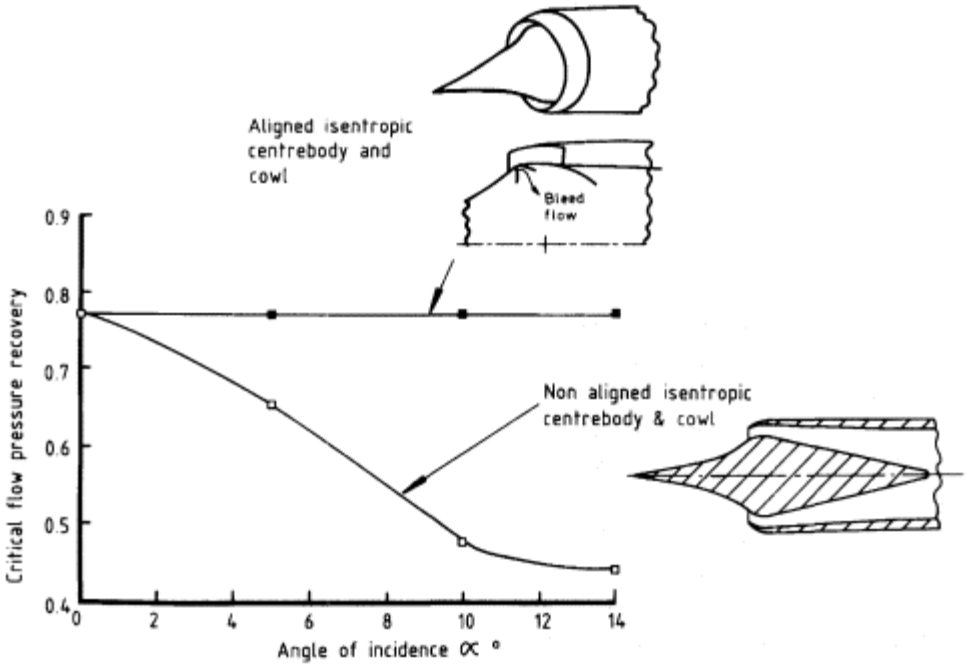

Figure 14.14
Effect of centrebody and cowl pivoting on performance at incidence a *M*¥ 3.0.

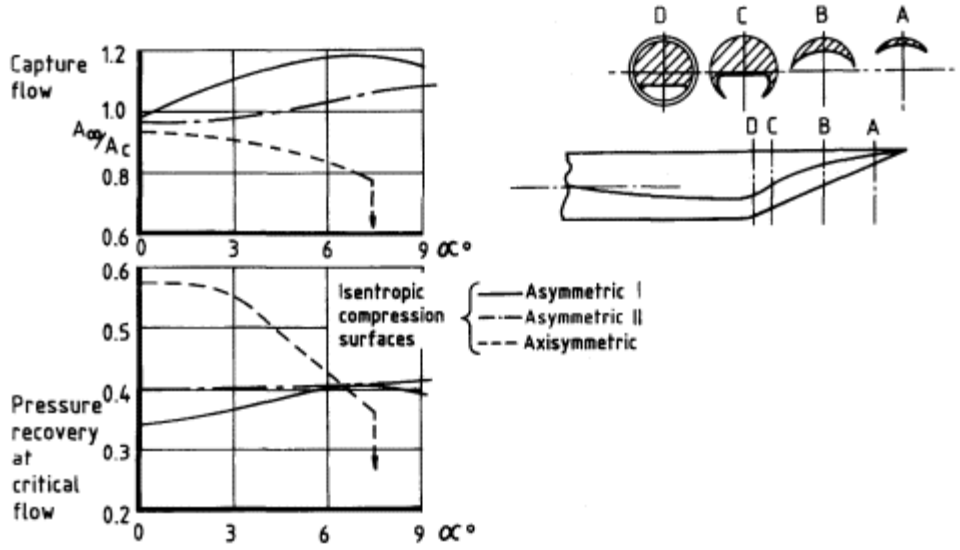

Figure 14.15
Performance of an asymmetric circular intake at M_∞ 3.85.

A simple but ingenious scheme for improving the performance of an unshielded axisymmetric intake at high angles of incidence and subsonic speeds has been proposed by Miller (1977). Boundary layer control is obtained on the inner surface of the windward lip by a suction slot at the throat connected to outlet holes in the lower-pressure region just inside the entry highlight. The suction slot, inclined at about 40° to the surface, occupies the base (i.e. most windward) sector of the entry; the outlet holes are located in sectors on either side, to avoid recirculation of the bleed flow. Static pressure distributions in Fig. 14.16 illustrate the suction pressure difference available and results for pressure recovery and flow distortion show both to be improved substantially at incidences above 40°.

14.3.2
Reduction of Cowl Wave Drag

The scoop intake (section 14.2.3) in principle provides one way of avoiding the high cowl drag that conventionally goes with a high degree of external supersonic compression. As an alternative, Rae (*ca* 1950) suggested that the use of a low-angle visor in front of the conventional high-angle cowl would break down the external shock system in a manner analogous to the multi-shock system for internal compression. With an axisymmetric cowl a comparatively large slot must be provided between visor and cowl to ensure self-starting (assuming there is no variability of throat area). Loss of flow through the slot when the intake is started causes a reacceleration ahead of the normal shock, which results in reduced pressure recovery. A decrease in

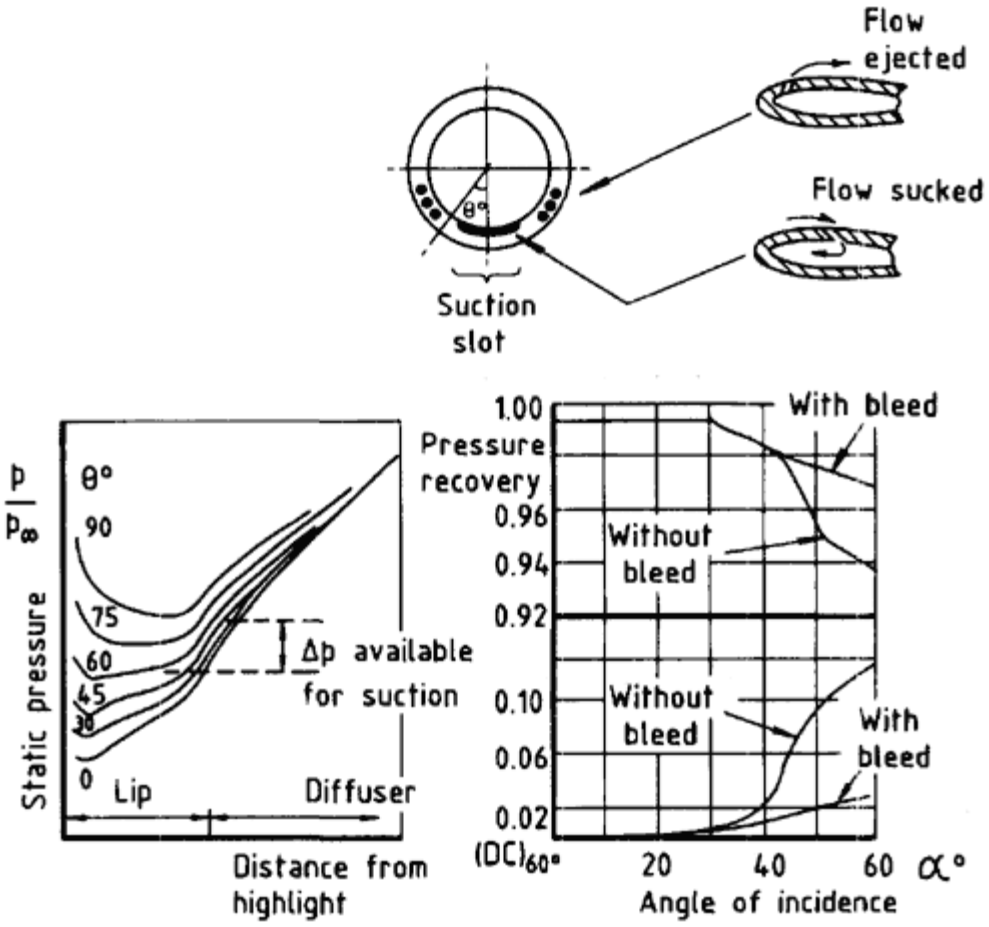

Figure 14.16
Improvement in subsonic intake performance at incidence by naturally-aspirated boundary-layer control.

cowl drag, however, was measured by Calogeras and Meleason (1967); Fig. 14.17 illustrates the results. With a rectangular intake, since the visor does not totally enclose the cowl, the starting slot can be smaller. Testing such an arrangement, Gertsma (1959) found no significant effect of the visor on pressure recovery, except for a small decrease at high incidence, but considerable reductions in drag, as Table 14.1 shows.

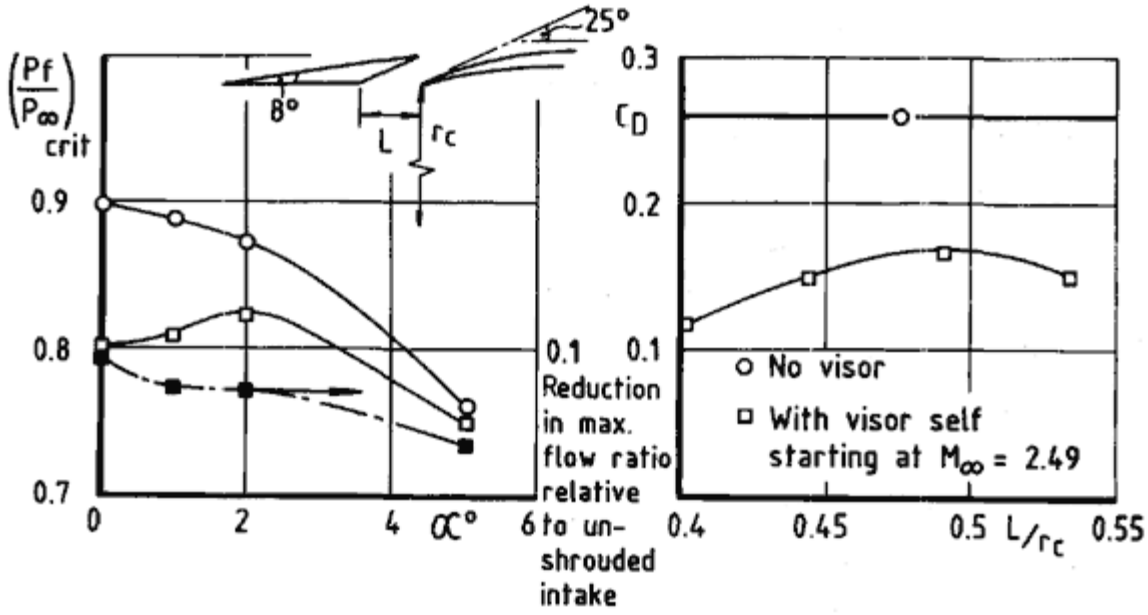

Figure 14.17
Performance of an axisymmetric isentropic centrebody intake with and without a cowl visor at *M*¥ 2.49.

Table 14.1 Effect of visor on wave drag of rectangular intake (Gertsma)

	*C*D (based on engine face area)	
Configuration	*M*¥ = 3.07	*M*¥ = 1.89
Basic cowl	0.180	0.205
Cowl and visor	0.044	0.072

14.4 Variable Geometry

Very often the quest for high aerodynamic efficiency of variable-geometry features in aircraft, such as high-lift wing flaps, air intake ramps or exit-nozzle controllers, leads to high mechanical complexity. This usually results in considerable increase in weight and cost, despite much ingenuity on the part of designers. As has been tellingly put, designers are under continual pressure 'to simplicate and add more lightness' Ed Heinemann, Douglas Aircraft Company.

In the search for simplication of intake variable geometry, several proposals have been made to utilise controlled separated-flow regions in place of physical surfaces for providing supersonic compression. All such schemes rely on the basic principle, described in Chapter 3, that flow separation at supersonic speeds, because it involves the flow turning outwards from a solid surface, produces an oblique shock system analogous to that produced by a wedge or a cone. Using separated flow regions in this way may reduce the number, weight or complexity of moving surfaces and their actuators. Control of the separated flow and minimisation of the loss of total pressure involved constitute the particular aerodynamic problems of such arrangements. Schemes that have received attention are described in the next two sections. A different approach to the problem of simplification is the subject of Section 14.4.3.

14.4.1 Step-Bleed Intake

A forward-facing step on an aircraft surface at supersonic speeds causes the boundary layer ahead of the step to separate, the angle of flow for a turbulent layer being approximately 10°. Thus a pitot intake in conjunction with a step near the entry plane has a two-shock external-compression system similar to that given by a 10° wedge. Increasing the height of the step increases the length of separated flow without changing the angle, so the step height can be adjusted until the shock system matches the intake. The step is retracted for subsonic operation. The separated boundary layer, or mixing region, must be removed by a bleed downstream of the step. This can be done efficiently if the lip of the bleed is at the height of the top of the

step or above, but the bleed duct is then likely to be an over-large restriction to the main duct when the step is retracted. A bleed lip more nearly in the flush position with step retracted is not restrictive but is less efficient when the step is in position. Design of the bleed is thus a particular development problem with this arrangement. The general scheme is illustrated in Fig. 14.18 where some results at Mach 2, from Goldsmith and Osborne (1975), are shown. Pressure recovery can be quite good but the bleed flow required, not unnaturally, is fairly high.

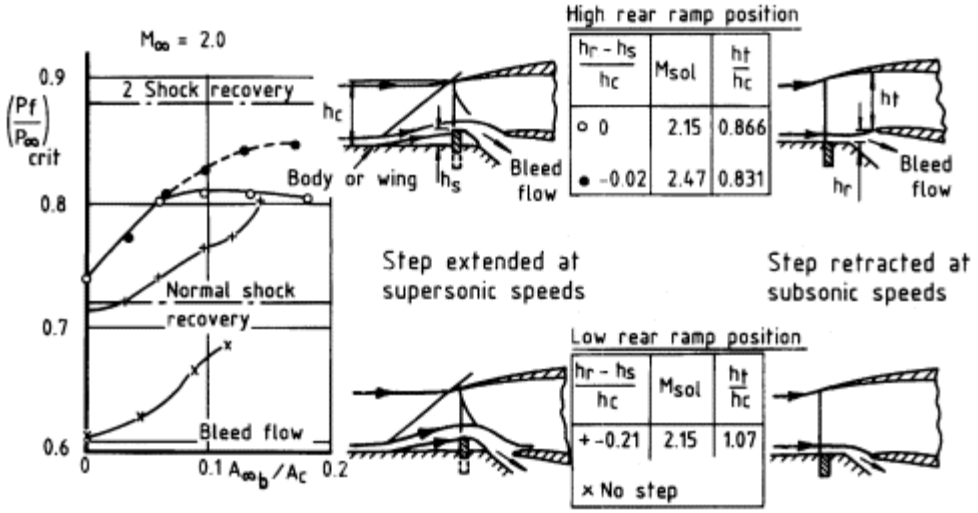

Figure 14.18
Performance of a step-bleed intake with no diverter.

A further development of the idea consists in mounting the intake on a channel-type diverter (Chapter 8) which removes the boundary layer in the normal way at subsonic speeds. Then for supersonic operation the step is raised in front of the diverter, creating the desired compressive flow field, and the bleed behind the step operates efficiently, the bleed lip being at the level of the top of the step. The arrangement, pictured in Fig. 14.19, works as expected at Mach 2 but has the disadvantage that the intake is oversized at subsonic speeds. In effect it may be regarded as an intake having constant throat area with variable capture area, in contrast to the original scheme which has variable throat area and constant capture area. Depending upon the nature of the matching problem, it may well be possible in a given situation to effect a satisfactory compromise between diverter height and bleed lip position.

A small improvement in performance results from shaping the step so that it has a 'mushroom' head. In Fig. 14.20 the pressure-recovery characteristic of a step-bleed intake is compared with those of a pitot intake and

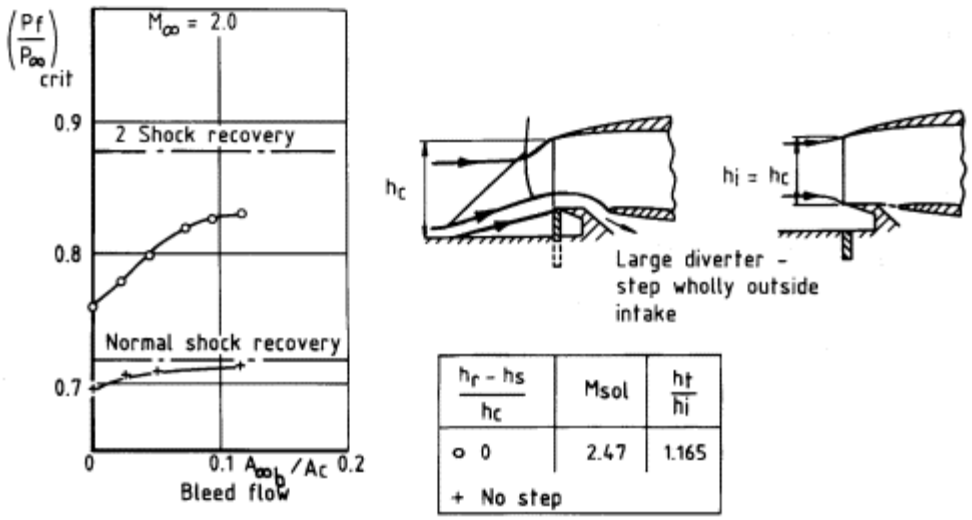

Figure 14.19
Performance of a step-bleed intake with a diverter.

a 10° wedge intake at a Mach number where nominally the shock-on-lip condition is obtained. It is seen that maximum flow ratio is lower for the step-bleed intake than for the other two. Sideways spillage is partly responsible but while the addition of swept endwalls increases the maximum flow ratio, it has been found also to reduce the pressure recovery somewhat. More study is needed of the detailed nature of flow diversion caused by the step-induced separation.

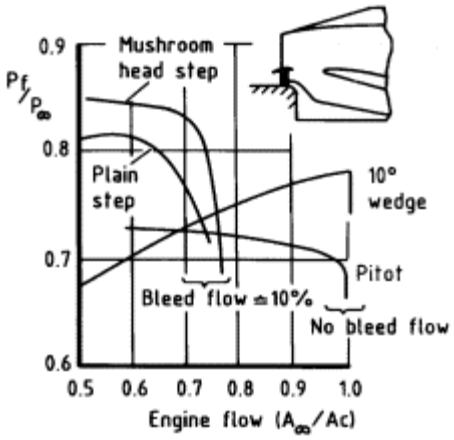

Figure 14.20
Pressure recovery characteristics of pitot,
10°-wedge and step-bleed intakes.

14.4.2
Devices for Conical Flow.

The use of flow separation to simplify variable geometry for an axisymmetric intake was suggested by Moeckel and Evans (1951). The effect of translating a conical forebody in the matching process is simulated by extending or retracting a thin spike in front of a fixed blunt centrebody. Conical flow separation is obtained from the spike. With the arrangement pictured in Fig. 14.21, maximum pressure recovery and maximum flow ratio on test were comparable with those given by a conical forebody of 25° semi-angle.

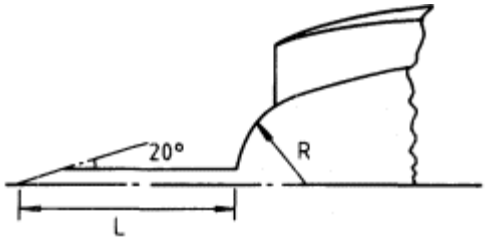

Figure 14.21
Conical-flow-separation spike.

A more complex version of this concept is the telescoping forebody, which when extended produces a series of small separated flow regions, approximating to an isentropic profile. Connors and Meyer (1955) tested this for geometries giving shock-on-lip at Mach numbers 1.90 and 3.05 (Fig. 14.22) and achieved pressure recoveries only slightly inferior to those obtained with smooth contours.

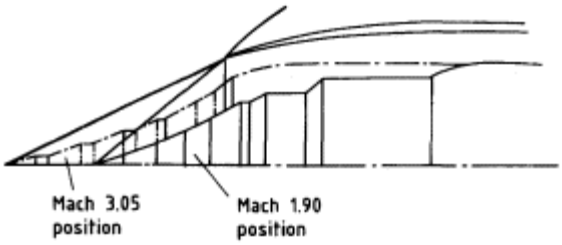

Figure 14.22
Telescoping axisymmetric forebody.

14.4.3
Multifunction Variable Geometry

One way of obtaining simplication of intake variable geometry is to incorporate surfaces that can be varied in a variety of ways, to meet different demands within the total flight envelope. A simple example is the afterspill door for supersonic matching which, by opening inwards as well as

outwards, becomes also an auxiliary inlet for take-off. A form of variable geometry which has not been taken to its limits in this respect is that of hinged leading edges in a two-dimensional layout. For a highly manoeuvrable aircraft, having vertical or short take-off and landing, coupled with supersonic capability up to Mach 2.5 say, it can be shown that in principle two hinged surfaces only could be adapted to provide all the following:

(a) high pressure recovery at take-off;

(b) high pressure recovery at low subsonic speed and high incidence;

(c) low spillage drag at high subsonic speed;

(d) high pressure recovery low supersonic speed;

(e) high pressure recovery at high supersonic speed;

(f) low cowl drag at high supersonic speed.

The different geometrical arrangements for these adaptations are illustrated in Fig. 14.23. The control system would be somewhat complex but readily handled by digital methods with on-board computers.

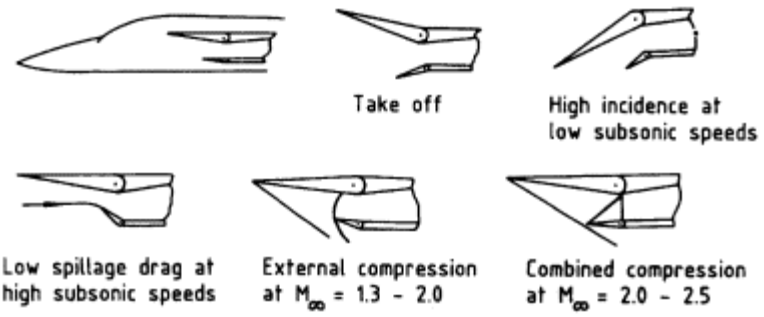

Figure 14.23
Intake multifunction variable geometry.

The most radical feature of the intake on the Eurofighter (Fig. 14.24) is the hinged cowl lip. As the top Mach number for this aircraft is below 2.0, the addition of a hinged compression surface is unnecessary. The function of the hinged cowl lip is to ensure good take-off performance and low spillage drag at high subsonic speeds (Fig. 14.23). The shielded position of the intake underneath the fuselage ensures good performance at high angles of incidence without the necessity for variation of the angle of the cowl lip outward away from the fuselage.

Figure 14.24
The twin intake on the Eurofighter 2000 with the cowl lip deployed in the take-off position on the starboard intake.

14.5
Fluid Injection

14.5.1
Boundary Layer Blowing

Boundary layer blowing has been mentioned in Chapter 10, as a possible method of extending the stable flow range of an intake. The principle involved in blowing is that of re-energising a boundary layer by injecting a jet of air at higher velocity along the surface in the direction of flow (Fig. 14.25) and thereby preventing flow separation. As an alternative to boundary layer bleed, blowing so far as is known has not been adopted in a practical design, probably because in an intake system on design, the airflow is mostly at pressures above ambient and a bleed is therefore a more natural way of controlling the intake boundary layer.

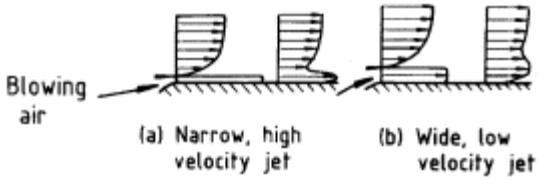

Figure 14.25
Blowing to re-energise the boundary layer.

There are situations, however, where this argument does not apply and experimentally at least, blowing has been shown to give good results. A particular role is where blowing can be applied in a region of low pressure, such as on a lip which is at a high angle to the local flow. Thus Gregory (1971) investigated the use of a blowing slot just inside an intake lip for preventing flow separation in the static condition (Chapter 4) and obtained about 3% increase in total-pressure recovery for 2% blowing quantity. Burley and Hwang (1982) have shown that blowing inside the windward lip of an intake at high incidence and low speed can greatly increase the separation-free range. If operation at angles of incidence approaching 90° is required, this offers a clear alternative to a suction scheme such as that of Miller (Section 14.3.1).

The use of boundary layer blowing for a fuselage-side intake on a subsonic aircraft, in a situation where the duct was short and highly curved, was studied by McGregor (1971). The arrangement is pictured in Fig. 14.26, which shows two alternative positions for the blowing slot. Results indicate a progressively favourable effect of pressure ratio of the blowing jet, *P*j/*P*¥, on intake pressure recovery for each arrangement tested; the rear slot position gives the better results of the two and of two slot sizes the larger, using a wider jet at lower velocity (Fig. 14.25), is probably the more economical. Improvements (i.e. reductions) in distortion follow a similar pattern.

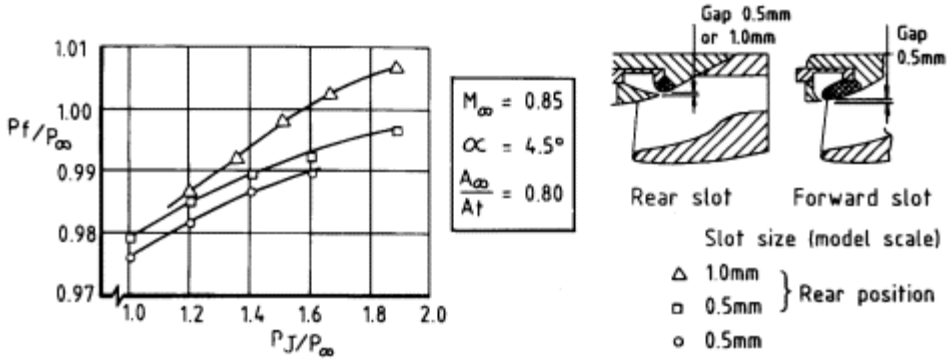

Figure 14.26
Effect of blowing on performance of a single-engined twin-duct intake.

An example of the use of blowing with a supersonic intake is illustrated in Fig. 14.27, due to Wong and Hall (1975). At free-stream Mach number 2.0, blowing was applied on a 7° wedge-compression surface upstream of the entry plane. The gain in pressure recovery is seen to have been substantial and in this case somewhat greater than that obtained with a distributed bleed. Distortion was reduced and buzz-free flow was retained down to flow ratios at which the normal shock had practically reached the position of the blowing slot.

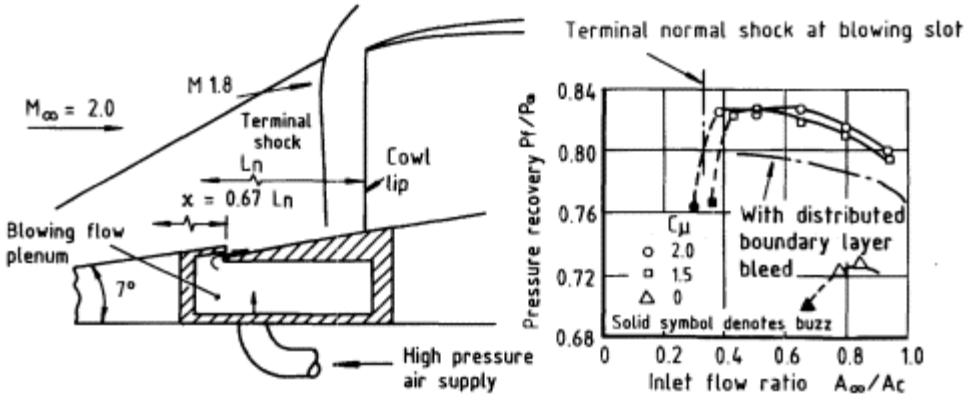

Figure 14.27
Effect of blowing on performance of a supersonic intake.

14.5.2
Isothermal Compression

Compression through shock waves at supersonic speeds is adiabatic (constant total temperature) and aims towards isentropic compression when the shock waves are of zero strength and the total-pressure ratio is unity. Using a simple theoretical approach, Perchonok (1956) pointed out that an ideal *isothermal* compression (constant static temperature) corresponds to an area contraction ratio greater than that associated with isentropic compression and a total-pressure ratio greater than unity. The general principle is used to boost pressure ratio temporarily in a compressor, by injecting water or a water alcohol mixture.

From the equations of state, continuity and energy for one-dimensional flow in a duct which changes in area from $A1$ to $A2$, Perchonok derived the following relations for static pressure, total pressure, total temperature and flow area:

$$\frac{p_2}{p_1} = \frac{A_1 M_1}{A_2 M_2} \tag{14.7}$$

$$\frac{P_2}{P_1} = \frac{A_1 M_1}{A_2 M_2}\left(\frac{T_{02}}{T_{01}}\right)^{\gamma/(\gamma-1)} \tag{14.8}$$

$$\frac{T_{02}}{T_{01}} = \frac{1+\frac{\gamma-1}{2}M_2^2}{1+\frac{\gamma-1}{2}M_1^2} \tag{14.9}$$

$$\frac{A_1}{A_2} = \frac{M_2}{M_1}\cdot \exp\frac{\gamma}{2}(M_1^2 - M_2^2) \tag{14.10}$$

These ratios, for isothermal compression from $M1$ to $M2$ with $M2$ equal to 1.0, are compared with isentropic values in Fig. 14.28.

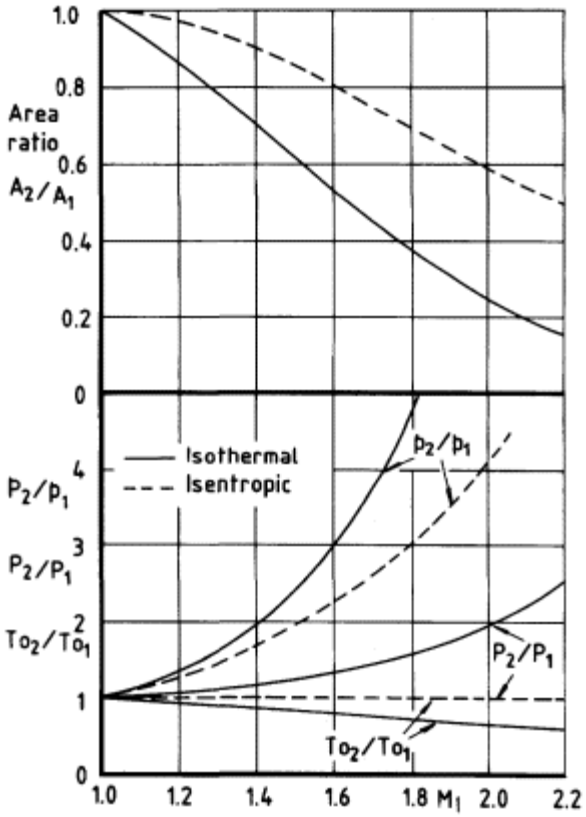

Figure 14.28
Comparison of isothermal
and isentropic compression.

It was recognised that the rapid cooling of a supersonic stream to achieve the large compression area ratios (small *A*2/*A*1) shown in Fig. 14.28 would not be a simple process and that the exchange of momentum between airstream and coolant would imply a loss in total pressure. If this loss is assumed to take place at constant area and constant total temperature, before the heat transfer between air and coolant occurs, then using the equations of state and continuity, including now the mass of liquid injected but assuming that its volume is small compared with that of the air, the total-pressure ratio can be derived as

$$\frac{P_b}{P_a} = \frac{M_a}{M_b}\left(\frac{1+\frac{\gamma-1}{2}M_b^2}{1+\frac{\gamma-1}{2}M_a^2}\right)^{-1/2(\gamma-1)} \qquad (14.11)$$

From conservation of momentum between station 'a', where the liquid is injected, and station 'b', where it is assumed to be uniformly distributed, a

relation for the liquid-to-air volume ratio $^{\ell/a}$, can be derived in terms of Ma, Mb and the Mach number $^{M_\ell}$ of the injected liquid. It is found that

$$\frac{\ell}{a} = \frac{\left(1 - \frac{M_a}{M_b}\sqrt{\frac{T_b}{T_a}}\right)\frac{1}{\gamma M_a} + M_a - M_b\sqrt{\frac{T_b}{T_a}}}{M_b\sqrt{\frac{T_b}{T_a}} - M_\ell} \qquad (14.12)$$

Using values zero and 0.4 for $^{M_\ell}$ the relation between PbPa and $^{\ell/a}$ is plotted in Fig. 14.29 for values Ma = 1.6 and 2.0.

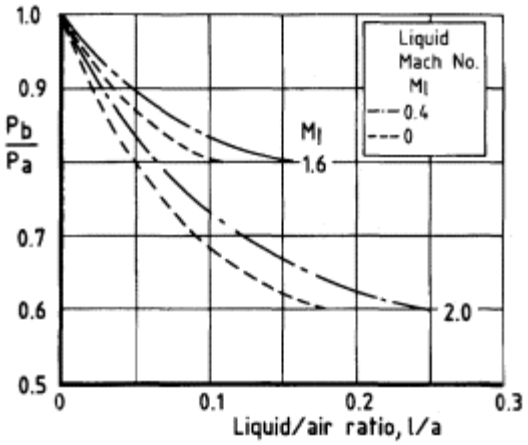

Figure 14.29
Total-pressure loss due to fluid injection.

Combining the gain in total pressure from cooling (Equation 14.8) with the loss by momentum exchange (Equation 14.11), an overall increase in total pressure can be anticipated. Experiments have failed to realise such an increase, however. In the experiment for which results are shown in Fig. 14.30, disturbance to the flow was minimised by injecting the fluid from behind a step on the compression surface. Ammonia, which has a high latent heat of vapourisation, was the fluid used. Although considerable cooling was achieved, the expected rise in total pressure did not occur. Indications were that the area change (Equation 14.10) was not taking place in the supersonic flow but was postponed to the subsonic diffuser. In an attempt to advance the compression process, coolant was sprayed into the flow upstream of the intake; this, however, introduced a further loss of total pressure from the wakes of the spray nozzles and feed pipes. To increase the rate of evaporation, the core of the wind-tunnel airstream was heated to flight stagnation temperatures; this measure resulted in failure to attain even the adiabatic pressure recovery. It would appear that the theoretical advantage of isothermal compression is not realisable in practice.

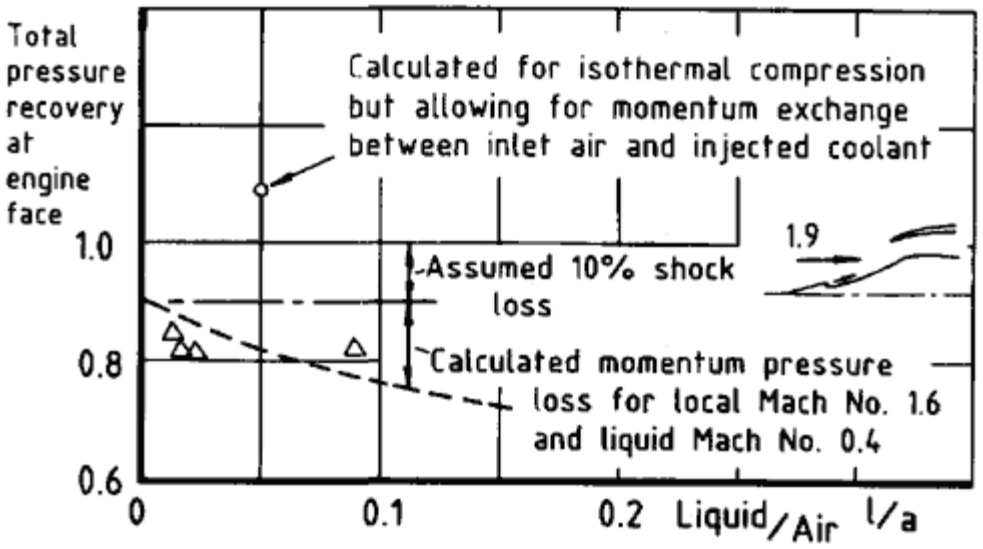

Figure 14.30
Measured and calculated performance of isentropic-forebody intake with injection of ammonia.

14.5.3
Water Injection to Aid Matching.

A different use of liquid injection was investigated by Beke (1956). In this case the object was to reduce the value of corrected airflow $m\dot{O}(T0)/AP$ by reducing the air temperature, in order to assist the matching of intake and engine. Using water injection, a 5% reduction in corrected airflow was achieved with negligible change in intake pressure recovery but despite this the margin of stable flow (before occurrence of buzz) was scarcely affected. Both the temperature drop and evaporation efficiency were some 40% less than theoretical values. Subsequent experience and progress in the techniques of matching (Chapter 12) make it unlikely that water injection will be considered for this purpose in the future.

References

Beheim, M.A. (1953) 'A preliminary investigation at Mach number 1.91 of an inlet configuration designed for insensitivity to positive angle of attack operation'. NACA, RM E53 E20.

Beheim, M.A. (1953) 'A preliminary investigation at Mach number 1.91 of a diffuser employing a pivoted cone to improve operation at angle of attack'. NACA, RM E53 I30.

Beheim, M.A. and Piercy, T.G. (1957) 'Preliminary investigation of shield to improve angle of attack performance of nacelle-type inlet'. NACA, RM E57. G25.

Beke, A. (1957) 'Experimental investigation of water injection in subsonic diffuser of a conical inlet operating at a free stream Mach number of 2.5'. NACA, RM E56 J15.

Bower, R.E., Davies, R.S. and Dowd, R.E. (Part I); Brook, J. and Kachler (Part II) (1959) 'Design and development of pre-compression bump surfaces for use with supersonic inlets'. Grumman Aircraft Engineering Corporation, Research Department Reports 122 and 129.

Burley, R.R. and Hwang, D.P. (1983) 'Application of tangential blowing applied to a subsonic V/STOL inlet'. *Journal of Aircraft* 20, no. 1, November, 1983.

Calogeras, J.E. and Meleason, E.T. (1967) 'Wind tunnel investigation of techniques for reducing cowl drag of an axisymmetric external compression inlet at *M*¥ 2.49'. NASA, TMX 1516.

Comenzo, R.J. and Mackley, E.A. (1952) 'Preliminary investigation of a rectangular supersonic scoop inlet with swept sides designed for low drag at a Mach number of 2.7'. NACA, RM L52 J02.

Connors, J.F. and Meyer, R.C. (1956) 'A variable geometry axisymmetric supersonic inlet with telescoping centrebody'. NACA, RM E55 F30.

Connors, J.F. and Woollett, R.R. (1954) 'Preliminary investigation of an asymmetric swept nose inlet of circular projection at Mach number 3.85'. NACA, RM E54 G26.

Flower, J.W. (1963) 'Configurations for high supersonic speeds derived from simple shock waves and expansions'. *RAeS Journal* 67, May 1963.

Gertsma, L.W. (1959) 'Effect on inlet performance of a cowl visor and an internal contraction cowl for drag reduction at Mach numbers of 3.07 and 1.89'. NACA, Memo 3-18-59E.

Goldsmith, E.L. and Osborne, W.K. (1975) 'The step bleed intake: a progress report on its performance and potential'. RAE, TM Aero 1626.

Gregory, N. (1971) 'On the static performance of two-dimensional intakes with momentum injection in the form of boundary-layer control by blowing'. ARC, R & M 3656.

Hawkins, J.E. (1974) 'YF 16 inlet design and performance'. AIAA, 74-1062.

Laruelle, G. (1951) 'Comparaison de differentes configurations d'entrée d'air de missiles supersoniques'. AGARD, CP 307.

McGregor, I. (1971) 'Some applications of boundary layer control by blowing to air inlets for VSTOL aircraft'. AGARD, CP 91.

Miller, B.A. (1977) 'A novel concept for subsonic inlet boundary layer control'. *Journal of Aircraft*, April 1977.

Moeckel, W.E. and Evans, P.J. (1951) 'Preliminary investigation of use of conical flow separation for efficient supersonic diffusion'. NACA, RM E51 J08.

Nonweiler, T.R.F. (1963) 'Delta wings of shapes amenable to exact shock wave theory'. *RAeS Journal* 67, January 1963.

Perchonok, E. and Wilcox, F. (1956) 'Preliminary attempts at isothermal compression of a supersonic airstream'. NACA, RM E55 129.

Rae, R.S. (*ca* 1950) 'Some recent results obtained with the streamline cowling diffuser'. Johns Hopkins University, Applied Physics Laboratory Report.

Samanich, N.E. and Cubbison, R.W. (1958) 'A pivoting cowl and spike technique for efficient angle of attack operation of supersonic inlets'. NACA, RM E58 G11a.

Schueller, C.F. and Stitt, L.E. (1956) 'An inlet design concept to reduce flow distortion at angle of attack'. NACA, RM E56 K28b.

Simon, P.C., Brown, D.W. and Huff, R.G. (1957) 'Performance of external compression bump inlet at Mach numbers 1.5 to 2.0'. NACA, RM E56 L19.

Stonier, R.A. (1991) 'Stealth aircraft and technology from World War II to the Gulf', Part I, *SAMPE Journal* 27, July/Aug. 1991; Part II, ibid. 27, Sept./Oct. 1991.

Townend, L.H. (1967) 'On hypersonic cruising aircraft which can have all leading edges swept'. Part I, 'Design of air intakes'. RAE Report TR 67046.

Wong, W.F. (1974) 'The application of boundary layer suction to suppress strong shock induced separation in supersonic inlets'. AIAA, 75 1063.

Wong, W.F. and Hall, G.R. (1975) 'Suppression of strong shock boundary layer interaction in supersonic inlets by boundary layer blowing'. AIAA, 75 1209.

Chapter 15
Techniques of Wind-Tunnel Testing and Analysis

15.1
Types of Model and Test

The ultimate objectives of a programme of wind tunnel tests tend to determine the detailed shape of a model, the method of support in the tunnel, the means of making measurements and the range of test conditions. Differing emphases and compromises among these features distinguish between tests of a basic research nature and tests that are aimed at estimating the performance of a specific design of aircraft. Basic research tests in intake work are usually performed on an isolated intake or on an intake carried on a body of simple shape. Often some distortion of the intake configuration is tolerated. For example, Fig. 15.1 shows a wedge intake with endwalls extended so that large windows can be inserted, enabling the shocks, both external and internal, to be studied by shadow-graph or schlieren optical apparatus. In practice the arrangement would entail penalties in internal performance owing to increased skin friction and to shock and boundary-layer interactions. Another acceptable distortion is to the external geometry at the rear of an intake nacelle, if only internal performance is being studied. Fig. 15.2 shows a twin nacelle on a Concorde wing where the arrangements for flow control and intake pressure measurement are housed in non-representative shapes at the rear.

For the measurement of internal characteristics, particularly on an isolated intake at supersonic speed, the free stream does not need to be much larger in cross section than the intake capture area, nor does it have to extend far downstream of the exit. The technique, described by Seddon and Haverty (1953) and by Ross and Britton (1973), of using a shock plate to create a uniform flow, the Mach number of which can be varied by changing the inclination of the plate, and to provide at the same time a two-dimensional flat-plate boundary layer ahead of the test model, is a particularly fortunate arrangement for conducting basic intake research. The shock plate in Fig. 15.3 was used to provide a range of Mach number from 1.5 to 2.0 in a wind tunnel whose minimum Mach number was 2.5.

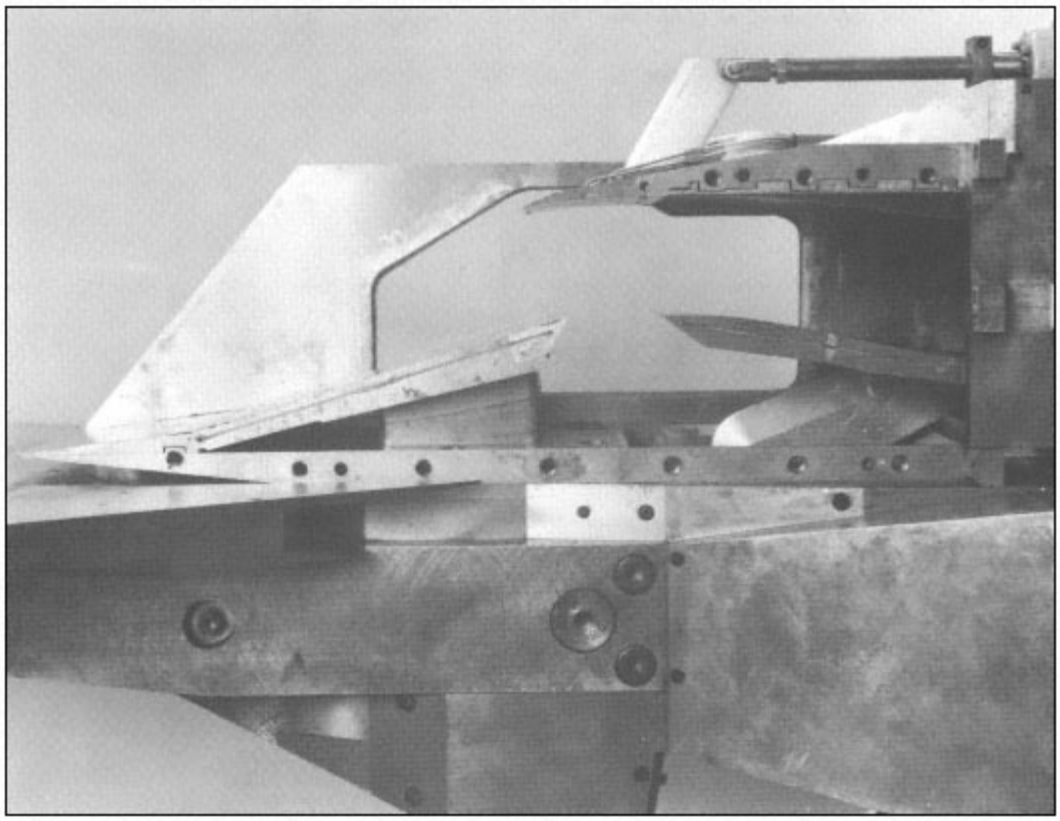

Figure 15.1
Three-wedge intake with extended sidewalls containing schlieren-quality glass windows.
(*Crown copyright*)

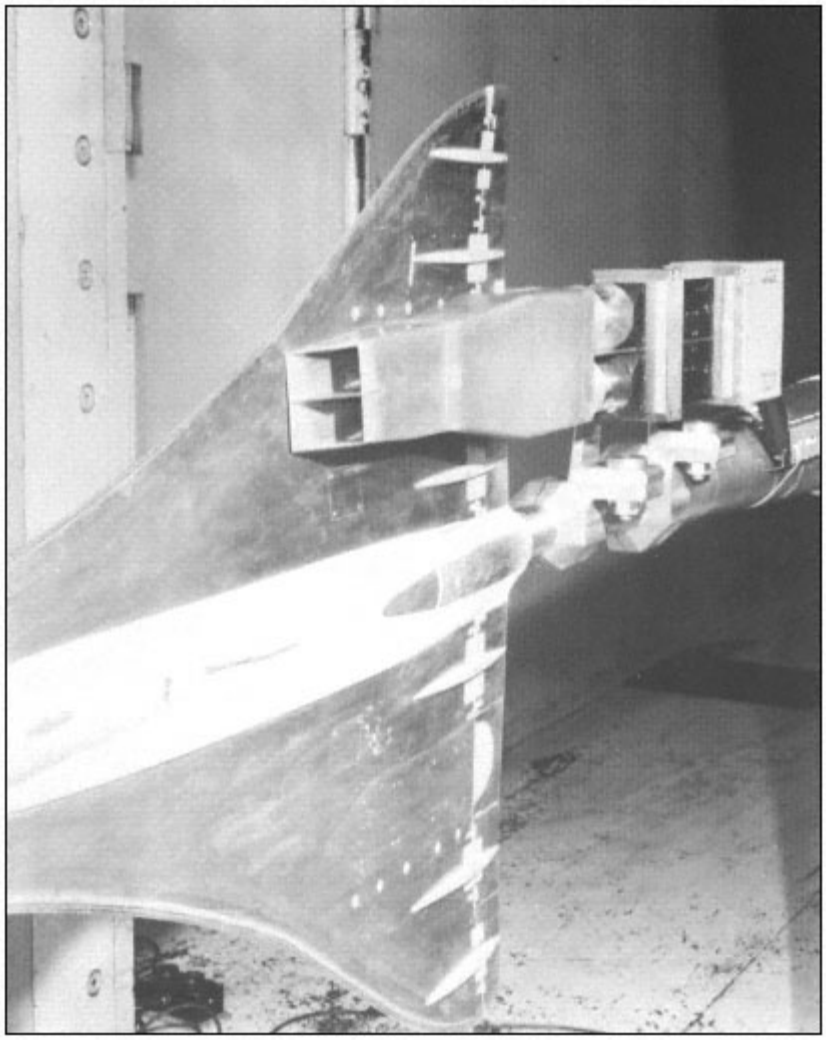

Figure 15.2
Twin intake on Concorde wing.
(*Crown copyright*)

For basic research, often only limited objectives are sought, such as for example the variation of zero-lift drag with intake flow ratio and free stream Mach number. Tests directly in support of an aircraft design, however, are likely to be concerned with multiple overall forces lift, drag, pitching moment, etc. for wide ranges of aircraft attitudes pitch and yaw and free-stream Mach number. Such tests usually form part of a larger series, illustrated in Fig. 15.4, which is needed for the prediction of aircraft performance.

The pattern of Fig. 15.4 is generally followed in most project testing, with some variation depending on the past experience of aircraft and engine

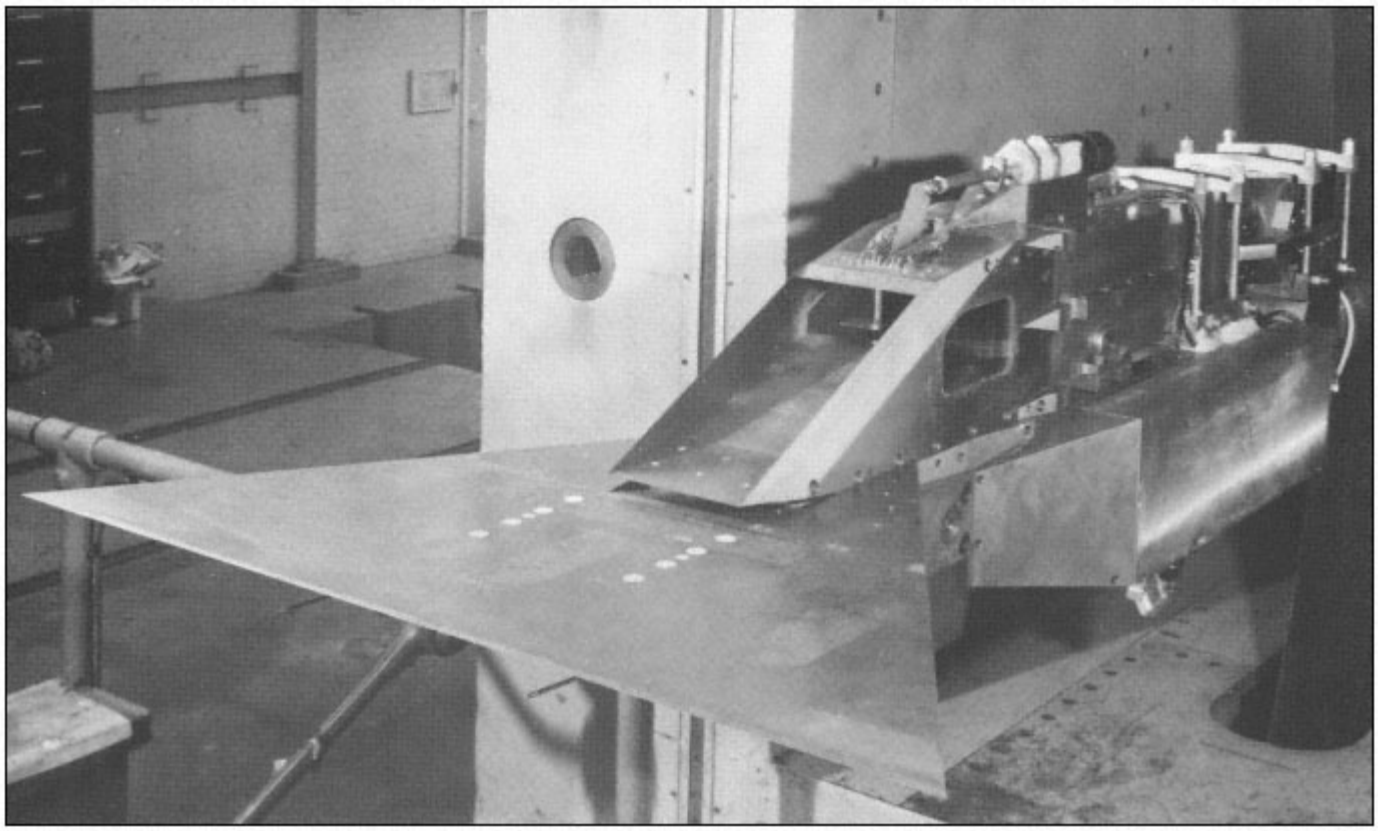

Figure 15.3
Three-wedge intake mounted on a shock plate.
(*Crown copyright*)

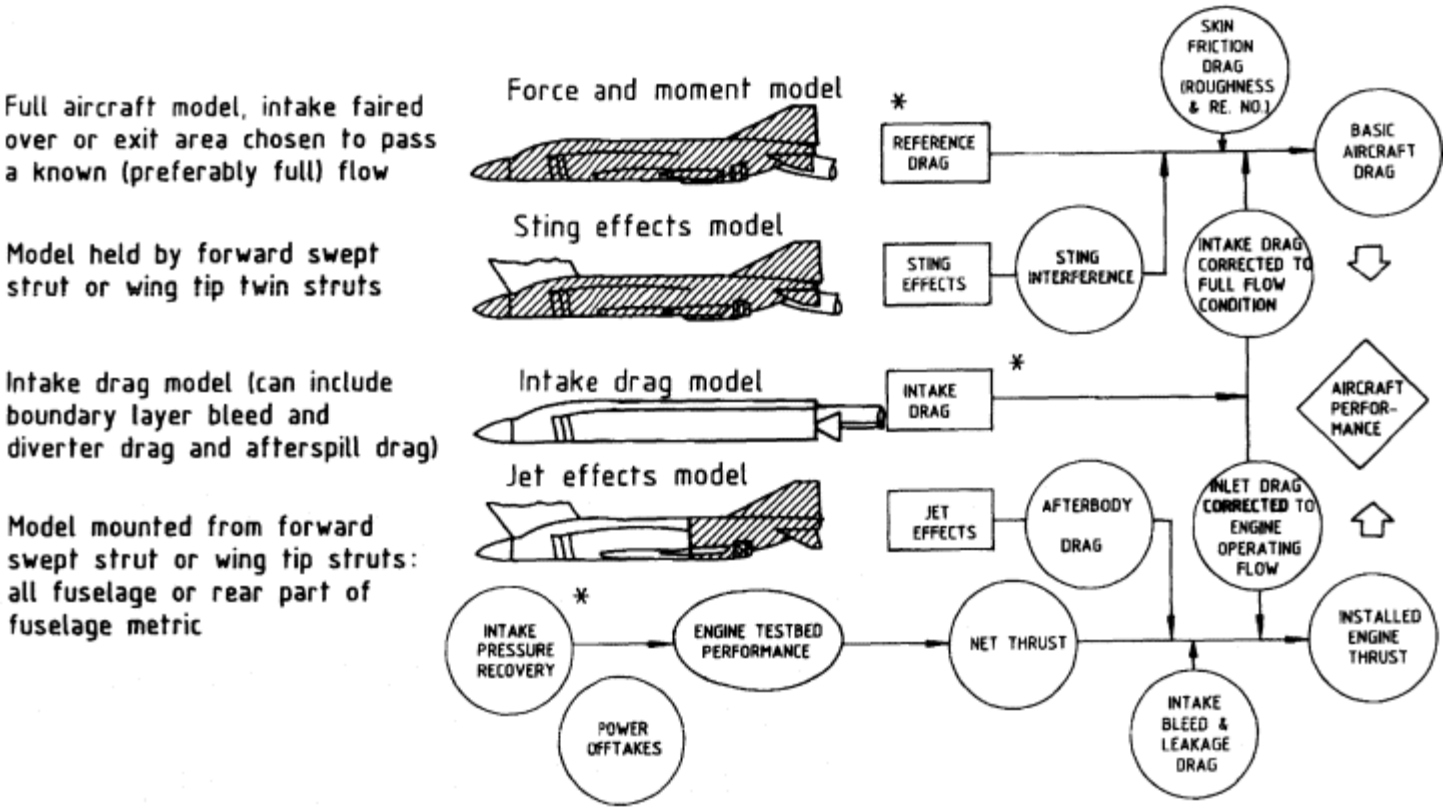

Figure 15.4
Schematic of wind tunnel and engine tests needed to predict aircraft performance.

manufacturers, their wind-tunnel and test-bed facilities and the funds that are available. In this chapter we are concerned with the items starred in the diagram, namely the intake characteristics of flow and pressure recovery and the contributions of the installation to aircraft forces and moments, with special emphasis on drag at the cruising incidence. In addition, however, to these performance-related characteristics, a further important concern is the question of intake and engine compatibility, for which information is required on the distribution of total pressure, static pressure, flow angle and in some cases temperature, the definition of buzz boundaries and of twin-duct instability if applicable and, where multi-engine nacelles are employed, the extent of interference of one intake characteristic upon another.

An important assumption implicit in the scheme of Fig. 15.4 is that the flow fields of intake and jet do not interfere significantly. The assumption is generally valid for combat aircraft, where the ducts are usually long, but may not be so with pylon-mounted engines or more particularly with specialist aircraft such as the Harrier (vertical take-off) where intake and jet are closely coupled. It may be necessary, for the model test programme, to install model turbojet engines so as to obtain realistic simulation of both intake and jet simultaneously. The techniques, problems and advantages of using such units form a large subject, which it is not intended to treat here. Descriptions have been given by Harris and Carter (1981), Pugh and Harris (1981), Wood (1971) and others.

Intake testing for external forces can be performed in subsonic, transonic and supersonic wind tunnels, using the same methods of supporting the model and varying its attitudes as are used for most other aerodynamic tests when forces or pressures are to be measured. At supersonic speeds the natural difference between static and stagnation pressure available in the tunnel stream is sufficient to provide all flow ratios up to the maximum that the entry will pass; control of the flow ratio is therefore a matter simply of setting the exit area of the duct to a particular value or series of values. At subsonic speeds a flow ratio appropriate to cruise can normally be obtained in the same way: if, however, it is desired to attain flow up to the maximum, that is when the entry throat chokes, then for $M¥$ below about 0.8, extra pressure difference has to be provided by connecting the exit to a suction pump or using a special ejector nozzle. This requirement may preclude the use of a standard rear-sting mounting but the model may then be conveniently mounted on transverse struts from the tunnel floor or roof (Fig. 15.5).

If only internal performance of the intake is required, then since the freestream jet does not need to be much larger than the intake capture-area, particularly at supersonic speeds, a full-scale intake, with or without engine, can be tested using a jet that is not prohibitively large in terms of airflow or

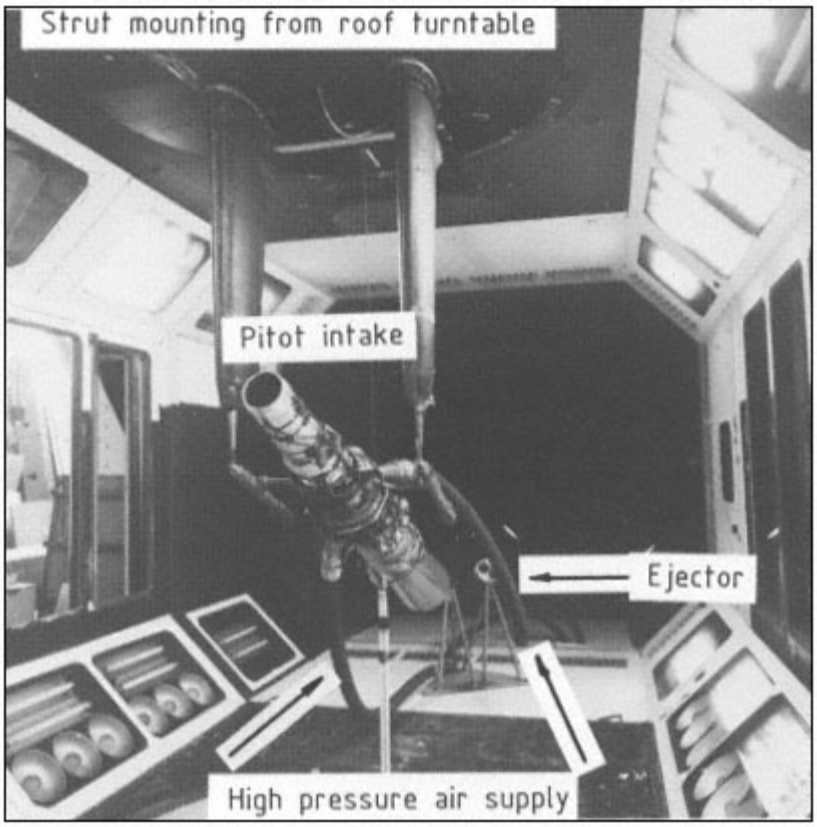

Figure 15.5
Pitot intake with ejector-powered suction unit
mounted from roof struts in low speed wind tunnel.
(*Courtesy of British Aerospace*).

power consumption (Fig. 15.6). If external forces are to be measured, however, the test jet must be large enough to avoid undue wall interference: thus for example at supersonic speeds the intake compression shocks must not reflect back on to a sensitive part of the model.

15.2
Internal Performance

15.2.1
Measurement of Flow Ratio and Pressure Recovery.

It is important that the mass flow through an intake duct should be measured to the highest accuracy which is reasonably possible. A desirable target error is ± 1/2% but the difficulties of accurate measurement are real; more often only ± 1% is achieved and errors as great as ± 10% are not uncommon if the flow is markedly non-uniform. Basically the information required is a sufficiently detailed knowledge of total and static pressures at

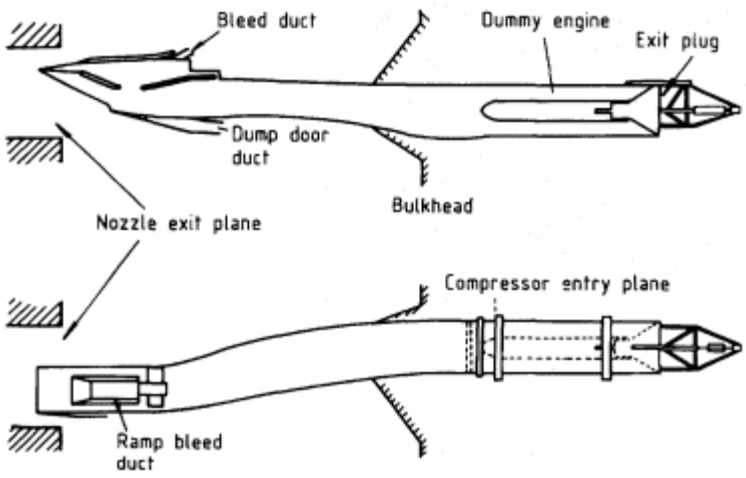

Figure 15.6
Full scale double-wedge intake and
dummy engine mounted in engine test cell.

a known area in the duct, or total pressure only at a choked orifice of known area, which is equivalent. Given an assumption about total temperature, which for the usual cold-flow tests would be that total temperature is constant throughout, the mass flow can be calculated. The least accurate method of determination, often used for rough work, is to measure total pressures from an array of pitot tubes across the duct and static pressures at points on the duct wall, using a section at the end of the subsonic diffuser: this is convenient, since the same total-pressure readings are used to record also the pressure recovery, but inaccurate because of lack of uniformity in the flow.

There is no doubt that accurate measurement can always be achieved by adopting an arrangement typified by the French 'debitmetre' in which the flow is discharged into a large settling chamber equipped with flow-smoothing screens and then returned to the tunnel stream through a calibrated choked nozzle or led to a suction pump through a calibrated venturi. ONERA has used this approach extensively in many tests of isolated intakes and of more complete integrated configurations as shown in Figs 15.7 and 15.8. These test arrangements have the advantage that the flow rate is measured and related to the actual engine-face flow distortions that are being encountered. This has obvious advantages over attempting to reproduce engine-face distortions by artificial means in a separate calibration process (as described in Section 15.2.4). This difference in the test philosophy becomes particularly important when measuring axial force and will be discussed in Section 15.4.2. It is usually not practicable, however, to incorporate this equipment into any arrangement for measuring, say, axial force on a model; in such circumstances the debitmetre can be used to

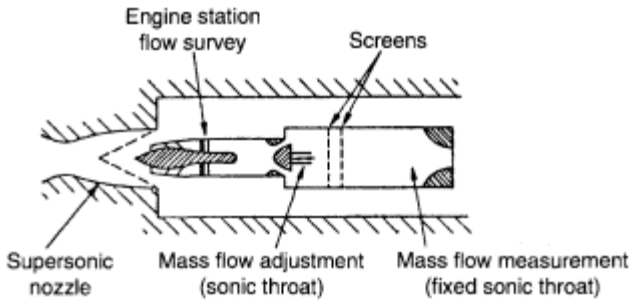

Figure 15.7
Isolated intake high Reynolds number test mounting.

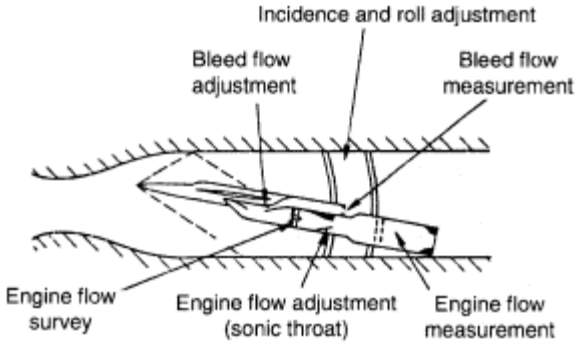

Figure 15.8
Integrated intake test set-up.

make a separate calibration of a more compact device which can be carried in a model for the purpose of recording all the measurements required at the nominal engine-face position.

15.2.2
Engine Face Instrumentation

A readily portable, self-contained unit for measuring both mass flow and pressure recovery has been described by McGregor (1971) and is shown in Fig. 15.9. Here the duct section and instrumentation for the nominal engine-face position are part of the measurement unit, so the size of the cell determines the scale of an intake and generally a number of cells of different sizes will be required. The unit was designed originally with a rotating rake of pitot tubes, to minimise duct blockage and permit any degree of detail of the flow to be studied. Experience has led in the main to abandonment of the rotating rake, in favour of fixed multi-arm rakes, typically with twelve arms though sometimes with twenty-four, carrying from five to eight pitot tubes on each arm. This speeds up the collection of data in a wind tunnel test and the interferences can be 'calibrated out' by a suitable procedure (section 15.2.4).

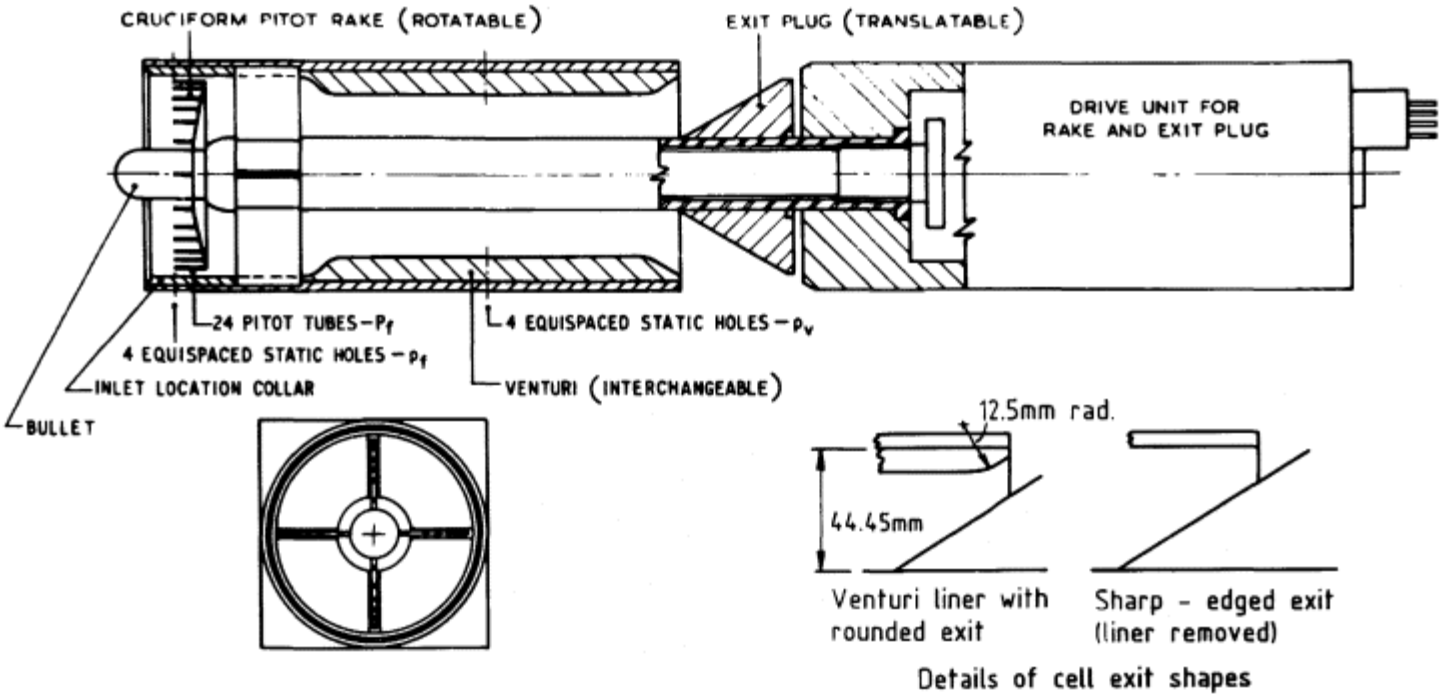

Figure 15.9
Flow cell for measurement of pressure recovery, flow distortion and flow rate.

In another version of this type of cell, the rotating rake and translating exit plug are carried cantilever fashion from the unit housing the mechanisms of actuation and position measurement. The cell in this form can be used with a range of duct sizes by changing the rake diameter and exit plug size. A twin-cell version is pictured in Fig. 15.10.

For tests of short subsonic nacelles, pressure recovery needs to be evaluated with a precision of 0.001 and as the total pressure loss is concentrated near to the duct wall, a typical pitot rake has six arms radiating from a central bullet containing ten pitot tubes per arm and a further six-arm rake emanating from the duct wall with eight pitot tubes per arm, most of these being positioned close to the duct wall. The addition of 24 wall and static pressure measurements makes a total of 136 engine-face pressure measurements. Under these circumstances, particularly if the model scale is small, interference effects on the static pressures and possibly choking around the rakes at high flow ratio become problems.

For longer duct models typical of military aircraft installations, and particularly for supersonic intakes, this precision towards the duct wall is not required. Indeed, McGregor (1971) showed that the error resulting from a finite number of pitot tubes is small. The maximum error over a wide range of practical flow distributions for a four-arm, six tubes per arm rake is 0.3%.

Nevertheless the trend has been towards greater detail of flow measurement, and if for instance the intake is supplying air to an engine without inlet guide vanes, then flow direction at the engine face must be measured. Thus there is a need for a multiplicity of engine-face instrumentation, either in combination (Fig. 15.11) in a single test or in separate series of tests with specialised instrumentation in each series (Fig. 15.12).

The peculiar difficulties in the measurement of dynamic distortion are dealt with in Section 15.3. It is sufficient to say here that there is a common practice for pairing tubes so that a high-response transducer measures the fluctuating pressure component and the low-response probe measures the steady-state pressure (Fig. 15.13). However, ONERA has used the contrary practice where both steady and unsteady components of pressure are measured on differential pressure transducers in a five-tube, eight-arm rake. This leads to economy of testing as the 40-tube rake can simultaneously measure pressure recovery and static and dynamic distortion. The sensors have to be satisfactorily compensated for thermal drifts so that the absolute values of the difference from the backing reference pressure can be measured precisely. In practice it has been found (in a continuous-flow wind tunnel) that if the backing pressure is provided by a few conventional pitot tubes at the engine face, then an accurate result is obtained by using the miniature transducer to provide not only the fluctuating pressures but also, when time-averaged, the 'steady-state' value.

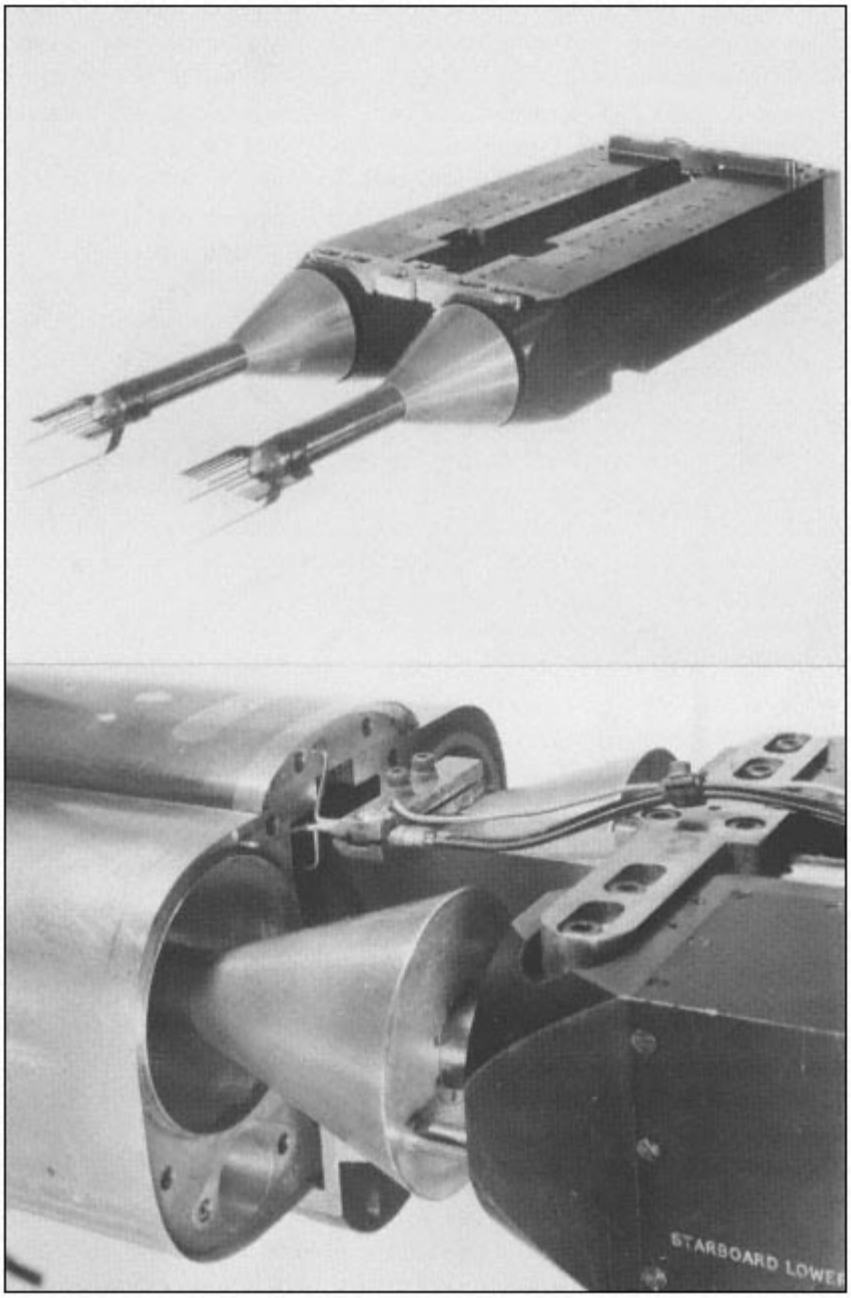

Figure 15.10
Twin flow measurement cell with rotatable pitot and static tubes.
(*Crown copyright*)

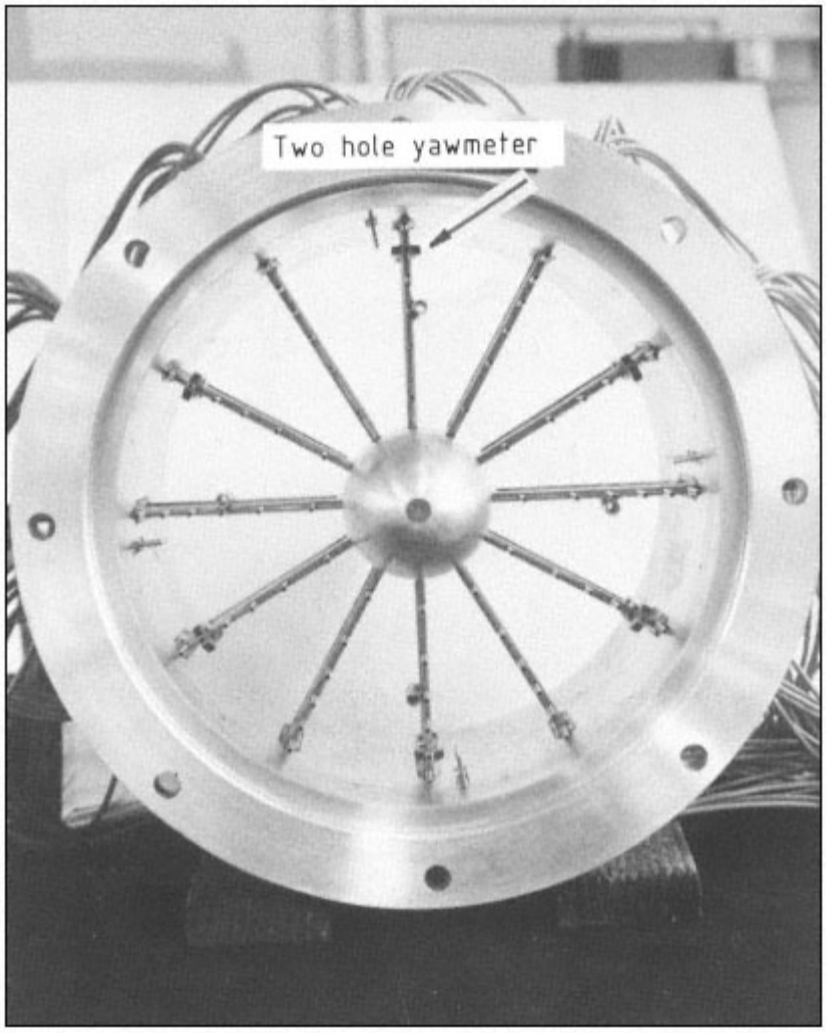

Figure 15.11
Engine-face rake containing pitot tubes, two-hole yawmeters and miniature pressure transducers for measurement of unsteady pressures.
(*Courtesy of British Aerospace*)

15.2.3
Evaluation of Pressure Recovery

The following ways can be defined of averaging pitot measurements in a non-uniform duct flow to produce a mean value of total pressure. In this discussion, a bar is used over symbols where it is necessary to distinguish the mean value over an area from the value at a point.

A. Area weighting, by which

$$\bar{P}_f = \frac{1}{A_f}\int P \mathrm{d}A \qquad (15.1)$$

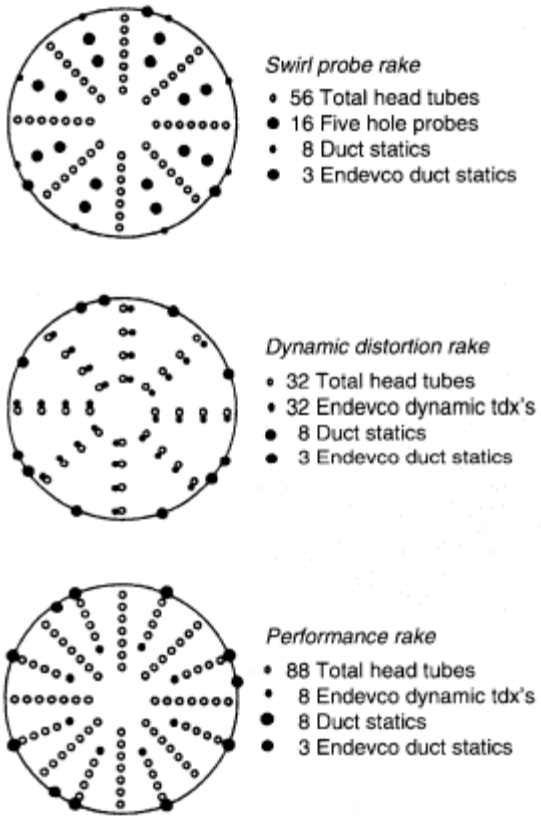

Figure 15.12
Dynamic and steady distorsion rakes
(*British Aerospace, Warton Division*).

B. Mass weighting, by which

$$\bar{P}_f = \frac{1}{m}\int P\,dm \qquad (15.2)$$

C. Mass derived, which involves a determination of mass flow coefficient, *m*Ö(*To*)/*Ap*,, from a measurement independent of the total pressure; the ratio $\bar{P}_f/p_f$ can then be derived and hence $\bar{P}_f$ is obtained if $\bar{p}_f$ is measured.

D. An assumption of mixing at constant momentum, in a constant-area duct without friction, leads to a uniform flow whose static pressure, $\bar{p}_d$ say, is different from that at the plane of measurement; the value is

$$\bar{p}_d = \frac{\int p_f(1+\gamma M^2)\,dA}{(1+\gamma \bar{M}^2)\,A} \qquad (15.3)$$

and from this a value of total pressure is obtained, which corresponds to uniform flow and includes a mixing loss.

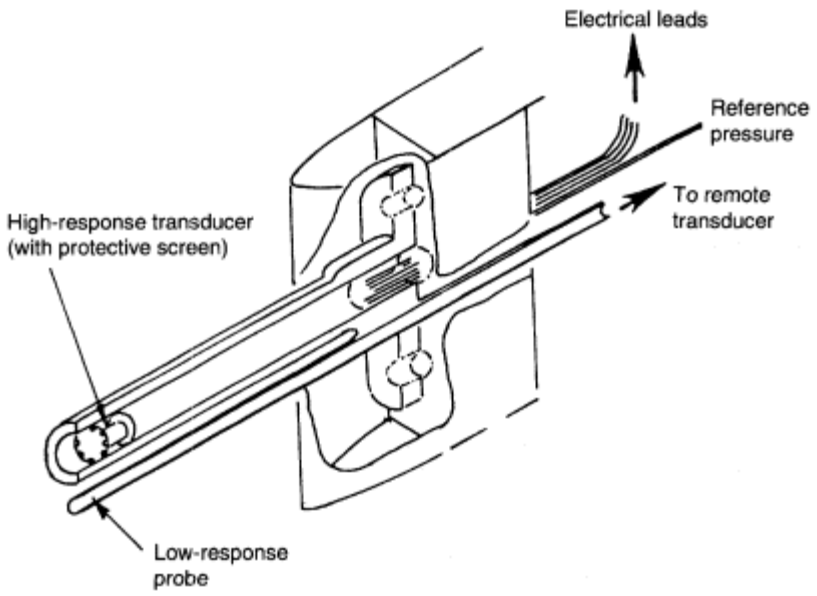

Figure 15.13
Total-pressure probe design example.

E. A mean value based on entropy flux, by which

$$m \log_e \bar{P}_f = \log_e P_f \, dm \qquad (15.4)$$

Mean total pressures obtained in these various ways have been compared by Livesey (1982) for both axisymmetric and two-dimensional flow, having a series of boundary-layer thicknesses with different power-law velocity profiles, for either subsonic or supersonic free-stream Mach number. For intake testing, the principal interest is confined to axisymmetric flow with duct Mach numbers in the range 0.3 to 0.6. In Table 15.1 are shown values of mean total pressure derived according to each of the methods A to D, divided by that according to method E. Results are given at duct Mach number 0.4, for three boundary-layer thicknesses, d, ratioed to duct radius *R*, and two very different velocity profiles, 1/7 power (n = 7) and linear (n = 1).

If constant total temperature is assumed for the entropy-flux mean, *E*, then total pressure is also constant. Values in excess of unity in the table imply a contravention of the Second Law of Thermodynamics thus the mass-weighted total pressure is not to be recommended. The excesses shown in the table could be regarded as being negligibly small: a further argument however against the mass-weighted mean is the relative inaccuracy of point velocity measurements in the engine-face plane. A mass-derived mean is not of great practical use because an accurate, independent

Table 15.1 Comparison of methods for evaluating pressure recovery

$\frac{\delta}{R}$	$n = 7$				$n = 1$			
	A/E	B/E	C/E	D/E	A/E	B/E	C/E	D/E
0.3	0.996	1.0002	0.996	0.997	0.977	1.0005	0.968	0.990
0.6	0.995	1.0002	0.995	0.996	0.973	1.0008	0.964	0.984
0.9	0.996	1.0002	0.995	0.998	0.982	1.0005	0.975	0.989

measurement of mass flow is often not available. The mean after constant-momentum mixing is largely irrelevant to the intake problem because an engine normally ingests the non-uniform flow. Thus the entropy-flux mean and the area-weighted mean are the most practical and the latter, being the simpler of the two, has been generally adopted for intake and engine performance work.

This being the case, it is common practice to position the pitot tubes in an array so that they are at the centres of equal areas of the measuring section. An arithmetic mean of readings is then used. McGregor (*loc. cit.*) has analysed the error resulting from the fact that the number of tubes is finite. The error is generally small; for example, with the arrangement of Fig. 15.9, which uses six tubes on each of four rake arms at right angles, the maximum error over a wide range of practical flow distributions is 0.3%.

15.2.4
Evaluation of Flow Ratio

Mass flow measurement, using the cell shown in Fig. 15.9, can achieve an accuracy of ± 1% when the cell has been independently calibrated. Evaluation consists in deriving a non-dimensional flow ratio, usually *A*¥/*A*c.

For a choked exit condition the flow ratio is given by

$$\frac{A_\infty}{A_c} = \frac{P_f}{P_\infty} \cdot \frac{A_e}{A_c} \left(\frac{A}{A^*} \right)_\infty \qquad (15.5)$$

*P*f is a suitable value of mean total pressure at station 'f' (section 15.2.2). For accurate evaluation the choked area *A*e must be an effective area, which is slightly different from the geometric area. The ratio of the two is a discharge coefficient

$$C_d = \frac{A_e \text{ (effective)}}{A_e \text{ (geometric)}} \qquad (15.6)$$

which is normally derived in the calibration process. *C*d varies with the exit shape and is an increasing function of the pressure ratio *P*f/*p*c until this ratio

reaches a 'hard' value, beyond which *C*d remains constant. Examples of these variations are given in Fig. 15.14. As can be seen, the exit having a sharp edge to the outer cowl shows a discharge coefficient independent of exit area, reaching a constant value at a pressure ratio around 2.8. The exit with rounded edge gives a series of discharge coefficients for different exit areas, reaching constant values at pressure ratios 2.2 to 2.4. Generally when the cells are in use, the exact value of pressure ratio is not known, hence the practical way of using the calibration information is to ensure that the pressure ratio is well in excess of the 'hard' choked value.

It is sometimes convenient to use, in place of *P*f, a derived total pressure *P*v relating to the reduced area of venturi section downstream of the measuring section but upstream of the choked exit (Fig. 15.9). *P*v is not measured directly but is calculated from the mean, *p*v, of wall static pressures measured in the venturi section and the area *A*v of that section. The area ratio *A*v/*A*c is the *A*/*A** corresponding to the subsonic Mach number *M*v in the venturi; thus *M*v is determined, the ratio *p*v/*P*v is then known and the derived total pressure *P*v follows from a knowledge of *p*v. The advantage of using *P*v in place of *P*f for mass flow evaluation is one of less sensitivity to distortion, because the venturi contraction increases flow uniformity.

When the exit section is not choked, the flow ratio is given by

$$\frac{A_\infty}{A_c} = \frac{P_f}{P_\infty}\left(\frac{A^*}{A}\right)_f \cdot \frac{A_f}{A_c}\left(\frac{A}{A^*}\right)_\infty \qquad (15.7)$$

Each measurement of total pressure at station 'f' is associated with an adjacent wall static pressure, so that local Mach number is determined and hence the local value of (*A*/*A**)f. The individual products of *P*f/*P*¥, (*A**/*A*)f and the element of area D*A*f associated with the pitot position are summed and to minimise errors, a calibration factor *K*f is introduced, *K*f being determined from calibration of the cell using a known flow. The formula as applied is thus:

$$\frac{A_\infty}{A_c} = \left[\sum_1^n \frac{P_f}{P_\infty}\left(\frac{A^*}{A}\right)_f \frac{\Delta A_f}{A_c}\right]\left(\frac{A}{A^*}\right)_\infty \cdot K_f \qquad (15.8)$$

where *n* is the number of total-pressure points.

Inaccuracy in the result stems primarily from any difference in flow distribution between the intake test flow and the calibration flow. As with the choked exit evaluation, a highly distorted flow is best dealt with by relating the evaluation to a venturi station 'v', where static pressure is measured and is generally close to being uniform. In these circumstances the formula is applied in terms of mean values, thus:

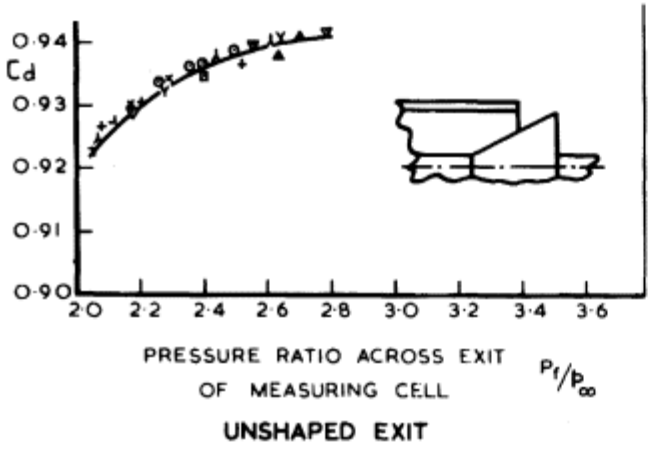

Variation of discharge coefficient for choked variable exit with pressure ratio and exit area

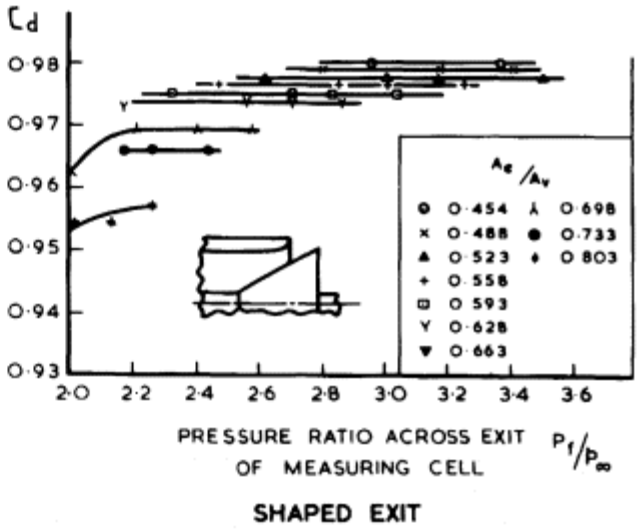

Variation of discharge coefficient for choked variable exit with exit area and pressure ratio

Figure 15.14
Dependence of choked-exit discharge coefficient on pressure ratio and exit area.

$$\frac{A_\infty}{A_c} = \frac{P_f}{P_\alpha}\left(\frac{A^*}{A}\right)_v \frac{A_v}{A_c}\left(\frac{A}{A^*}\right)_\infty K_v \qquad (15.9)$$

where (*A*/*A**)v is derived from *p*v/*P*f and *K*v is determined from this same equation applied to a calibration test in which the mass flow is known.

Clearly the unchoked exit situation applies to all tests at subsonic free stream speeds, unless for any reason the exit is subjected to pressures significantly below the free stream static pressure. Much testing is done in low speed wind tunnels, at speeds of order 20 to 50 metres per second. Representative intake tests are made by adjusting the exit to obtain the correct flow ratio; many such have been described in Chapter 2. In these circumstances it is normal to use the equations of incompressible flow. The relation for flow ratio corresponding to Equation (15.7) is then:

$$\frac{A_\infty}{A_c} = \frac{A_f}{A_c}\left(\frac{P_f - p_f}{q_\infty}\right)^{\frac{1}{2}} \qquad (15.10)$$

where *q*¥ is the free-stream dynamic pressure. Evaluation procedures analogous to those leading to Equations (15.8) and (15.9) can be followed. If high accuracy is not required, which may often be the case when tests are for comparative rather than absolute purposes, Equation (15.10) can be applied directly, using mean values of total and static pressure.

If the alternative approach favoured by ONERA is employed using an in-situ flowmeter, the flow rate is evaluated from a wall static pressure measurement in the settling chamber and a value for the sonic throat area. The assumption is made that the stagnation temperature is the same as the wind-tunnel stagnation temperature, which is valid for a continuous-flow tunnel. In a blow-down wind tunnel this may not be so, due to the settling chamber screens being at a different initial temperature. In this case the stagnation temperature in the flowmeter just upstream of the throat has to be measured using thermocouples.

The geometric sonic throat area has to be corrected for the curvature of the throat profile and the thickness of the throat boundary layer. Figs. 15.15 and 15.16 show the values of these two corrections in terms of the throat radius to throat height ratio *h*/*R*, where Reth is the Reynolds number (*ath*/*vt*) based on stagnation values at the throat.

15.2.5
Calibration of Flow Cells

To obtain an accuracy of half to one per cent in flow measurement, a cell requires to be calibrated in an independent experiment. This can be done in a variety of rigs, of which two examples are shown in Fig. 15.17. Accurate measurement of the flow is achieved by using either a standard orifice plate

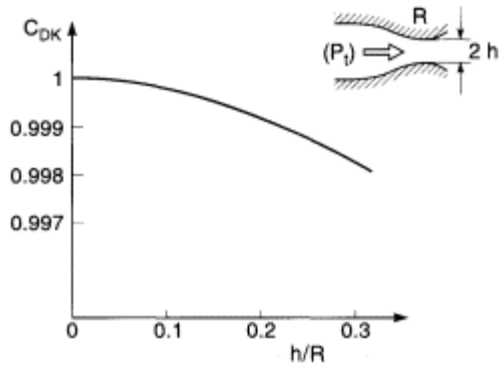

Figure 15.15
*C*DK; sonic throat restriction
coefficient due to the throat curvature.

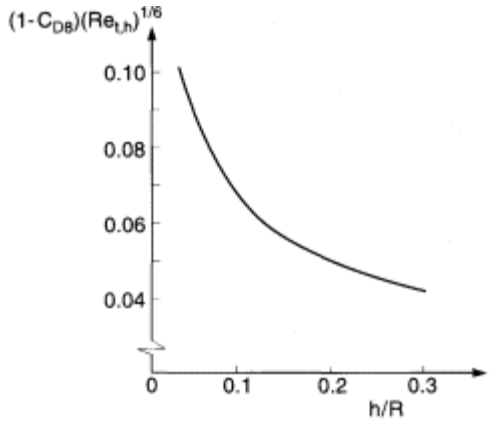

Figure 15.16
CDd, sonic throat restriction
coefficient due to the boundary layer.

(Fig. 15.17(a)) or choked nozzles in a range of sizes (Fig. 15.17(b)). In the latter case the pressure ratio available must be sufficient to choke both the throttle of the test duct and the calibrating nozzle in series. Standard nozzles have been described by Herbert and Pinker (1964); these have a constant discharge coefficient above pressure ratio 2.3 and an accuracy of ± 1/4%, obtained by a process involving direct thrust measurement.

Another way of calibrating a flow cell is to measure the flow through a number of differently sized sharp-lipped pitot intakes in a supersonic stream. At critical or supercritical conditions the full streamtube equivalent to the intake capture area is ingested and this is equated to the flow as measured by the cell. In an example in Fig. 15.18, values of the effective choked exit area of the cell so derived are compared with the geometric areas. The definitive curve is seen to be an envelope of curves derived for each size of pitot intake. As each intake goes increasingly supercritical, the

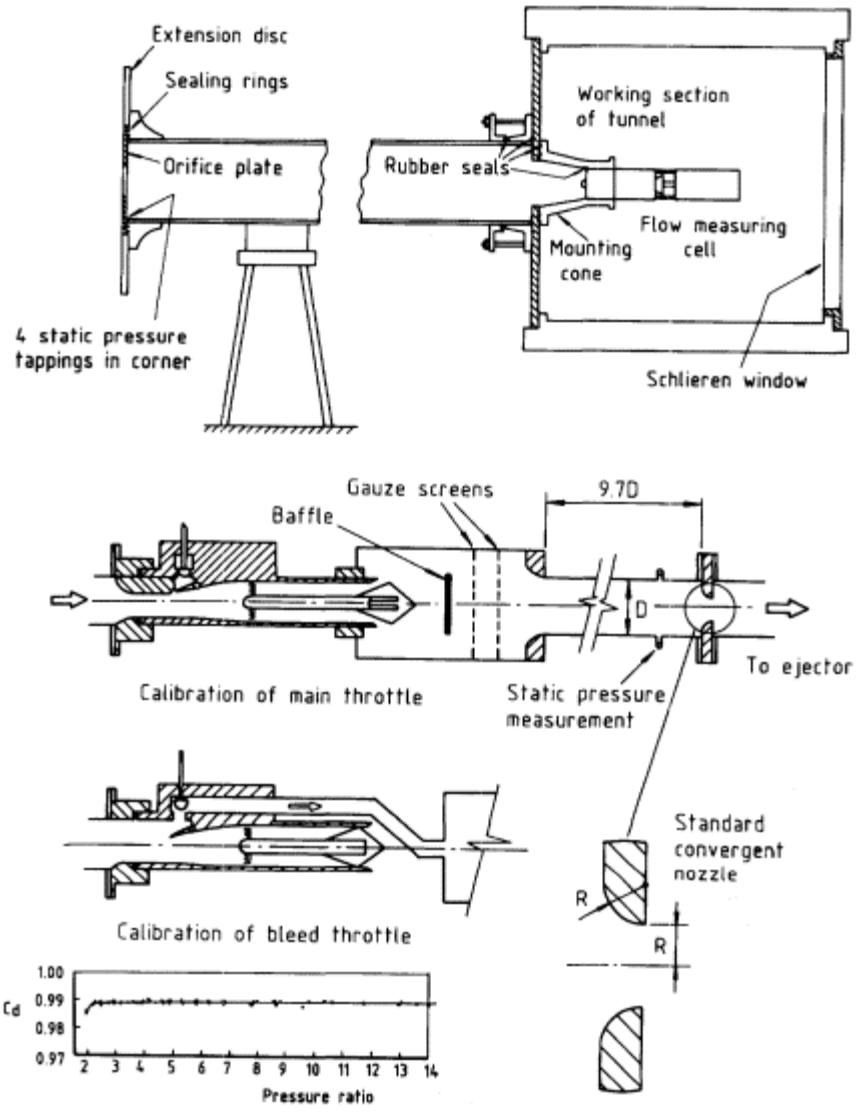

Figure 15.17
Rigs for calibration of flow cells (a) using orifice plates and (b) using choked nozzles for flow measurement.

derived effective area departs from the envelope; this is because the pressure recovery falls below that required to maintain a hard-choked exit.

15.3
Compatibility Features.

The maldistribution factors discussed in Chapter 11 are the static and dynamic distortions of total pressure and the flow angularity or swirl. The

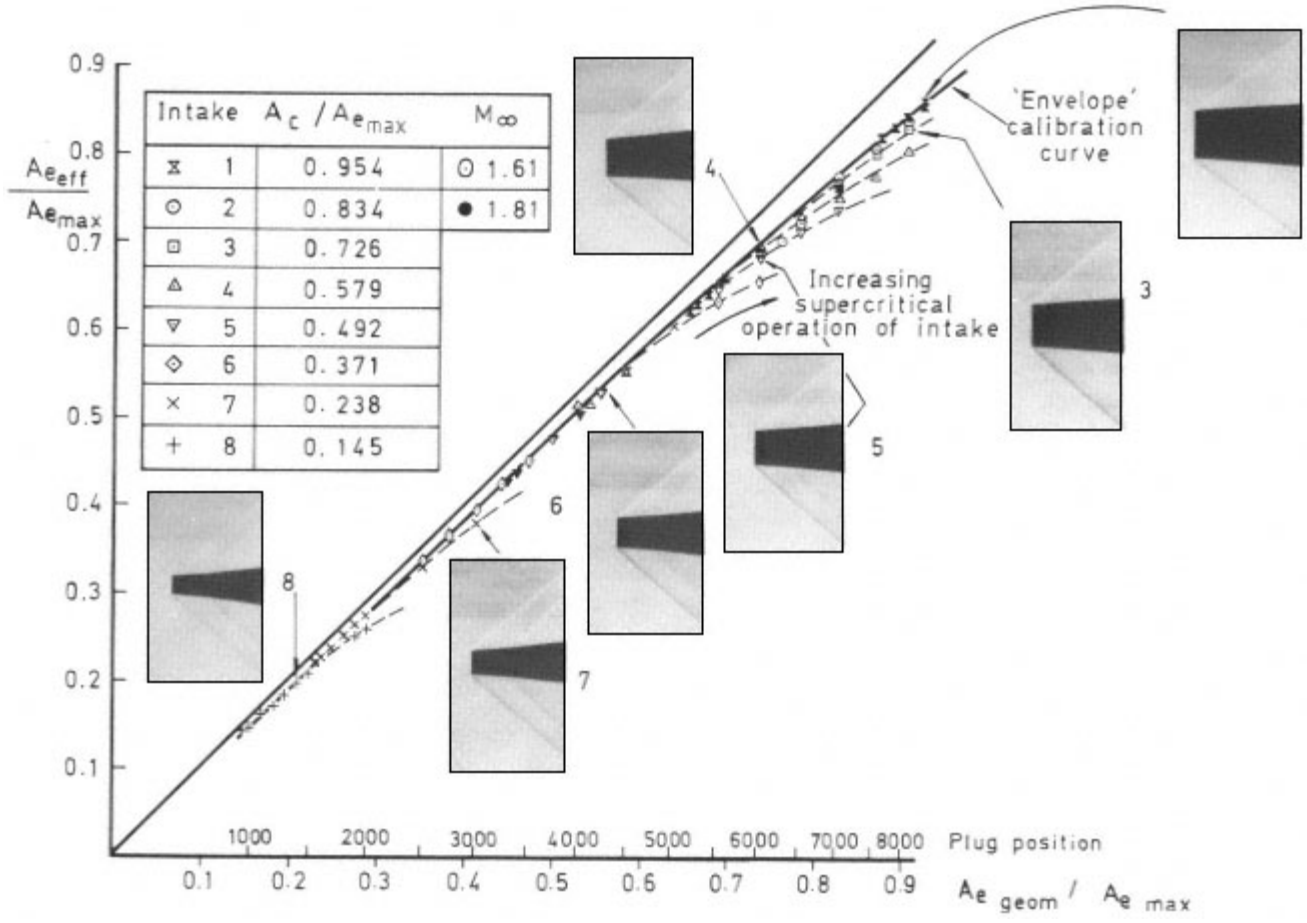

Figure 15.18
Comparison of effective and geometric choked exit areas.

engine-face instrumentation shown in Fig. 15.11 is capable of providing data for a preliminary assessment of all three factors and is typical of the instrumentation needed in tests of a basic research nature. For assessing particular intake designs, considerably more detailed instrumentation is required, particularly in the case of dynamic distortion measurement (Fig. 15.12).

Pitot-tube measurements provide the data for assessment of static distortion. There are various ways of evaluating the DC (q) parameter defined at Equation 11.1. One of the simplest is to average the total-pressure values along each arm of the rake and fit a polynomial curve to these averages plotted circumferentially. The q sector of lowest levels can be decided and the mean total pressures both in this sector and for the whole circumference can be derived. A more sophisticated method is to fit a Fourier series to the rake-arm mean values; this process has been described by Calvert and Merryweather (1977). Mean dynamic pressure qf can be evaluated as the incompressible value given by Pf pf, or from the relation:

$$q_f = \frac{\gamma}{2} p_f M_f^2$$

where Mf is derived either from the ratio of mean values pf/Pf or as the mean of individual Mach numbers obtained from pf/Pf for each pitot tube.

Swirl is assessed from yawmeter measurements. A yawmeter may have two, three, four or five tubes, provided only that at least two are aligned in the circumferential direction. An individual calibration is needed for each yawmeter. The design and use of such instrumental is discussed in standard texts on wind-tunnel instrumentation, as for example that of Pankhurst and Holder (1952).

The remainder of this section is concerned with dynamic distortion. The techniques and procedures for determining and interpreting dynamic distortion are much more complex, costly and time-consuming than those associated with static distortion or with swirl. To link instantaneous distortion factors with the onset of compressor surge requires an engine to be tested either in flight or in a static test behind a distortion simulator. A simulator may take the form of a choked venturi with an excessive diffusion rate downstream of the throat, causing unsteady shock-induced flow separation. An alternative to this is a flat plate containing an irregular array of holes, which generates both steady and unsteady distortion.

For an intake, unsteady pressures have to be measured at a large number of points at the engine-face position, for representative free-stream conditions in a wind tunnel. The number of points necessary in a development test has been variously recommended as between 36 and 60. These pressures are recorded on miniature high-response differential-pressure transducers. If the steady-state pressure levels given by the direct current

output of the transducers are liable to drift, owing to changes in tunnel temperature, the true steady-state values must be obtained from a duplicate set of pitots equipped with low-response transducers. Because the engine-face section thus needs to accommodate typically 80 or 90 pitot tubes in close pairs, the scale of an intake model cannot be less than about 1/5.

A typical engine rotational speed (fan or compressor) is 200 rev/s, so if critical persistence time is taken to be that of a half revolution, say, the minimum band width of frequencies to be considered is up to 400 Hz at full scale or 2000 Hz at 1/5 scale. To obtain a good digital representation of the signal from the high-response transducers, the values are digitised at five times the basic frequency. The digitised data are then time-averaged over the 2.5 milliseconds corresponding to a half revolution (full scale), before the pressures are combined to give whichever form of distortion factor is being considered.

In the UK, the equipment necessary for dynamic distortion measurement in project-type testing has been taken to be:

(a) a pitot rake carrying 40 high-response and 40 low-response transducers, disposed as five pairs on each of eight equi-spaced arms of the rake;

(b) a high-stability direct-current amplifier and a low-pass filter for each high-response transducer, the cut-off frequency depending on model scale;

(c) a 42-channel multi-track tape recorder, or alternatively a 14-channel recorder with frequency multiplexing to record up to 56 channels.

From 4 seconds of recording, typically 1 second only of the record is used to compute distortion factors.

Prediction can be made by statistical means of the probability of higher values of dynamic distortion occurring in much longer times than can be recorded and analysed. Jacocks (1972) has given a method which is summarised as follows:

(1) Peak DC60 values are calculated for each of the N blocks of data in the 3 4 seconds of recording time. N is normally in the range 15 25.

(2) Peak DC60 values are arranged in ascending order of value and assigned an index m where $m = 1, 2, \ldots, N$.

(3) The reduced variable $Y = \log_e \log_e [(N + 1)/m]$ is calculated.

(4) Peak DC60 values are plotted versus Y and a least-squares fit straight line through the points is calculated.

(5) Extrapolation of this straight line allows estimation for a longer time period such as 2 minutes at full scale but may be only 10 20 seconds at model scale. A typical Jacocks-type plot is shown in Fig. 15.19.

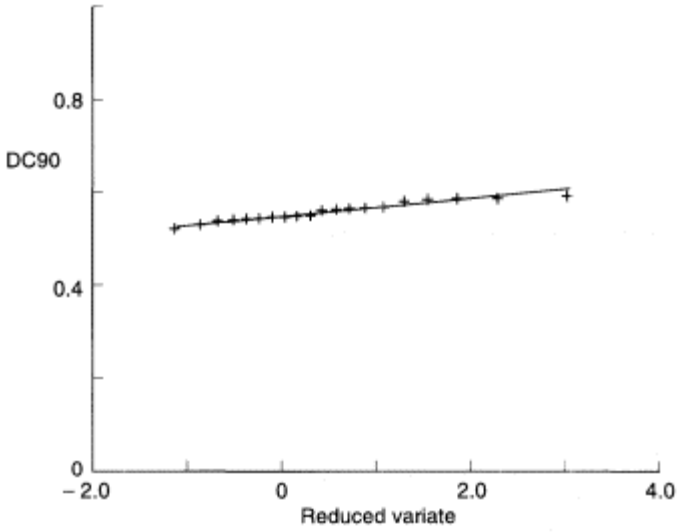

Figure 15.19
Jacocks-type plot to evaluate an instantaneous value of DC90 for a pitot intake at $M¥ = 0.79$ and a = 30°.

An interesting comparison exercise in measuring instantaneous values of DC60 is reported in Section 4.5 of AGARD Advisory Report 270 (1991). Three geometrically identical pitot intake models at slightly different scales were tested in UK German and French wind tunnels (Fig. 15.20(a) (c), each with their own engine-face and mass flow instrumentation. The conclusion from this comparative exercise was that there was a good measure of agreement at all the common test conditions of $M¥ = 0.75$ 0.9 and 1.8 and incidences from 0° to 25°. An investigation of repeat measurements led to the conclusion that in flows of moderate to high turbulence the naturally occurring random variations in peak instantaneous distortion are likely to be of much greater significance than differences due to detail differences in experimental techniques.

For assessment of instantaneous distortion for projected aircraft intakes, a number of complex systems have been assembled. Typically they employ an analogue computer to continuously monitor and update maximum values of one particular distortion criterion and then have the capability of further digital analysis of other distortion criteria off line. Two such systems are shown in Figs. 15.21 and 15.22 and further details are given in AGARD Advisory Report 270.

If only an indication of dynamic distortion values is required when, say, a particular intake is to be selected from a number of candidates, then a statistical procedure can be employed that uses only steady-state probe values plus a small number of root mean square values of total pressure. The procedure for this simple approach, which requires no analogue

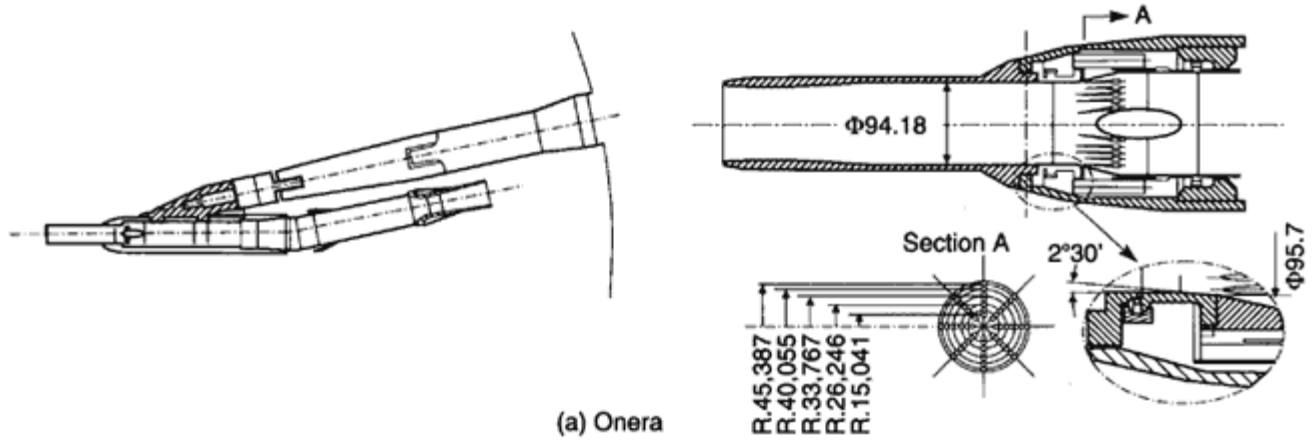

(a) Onera

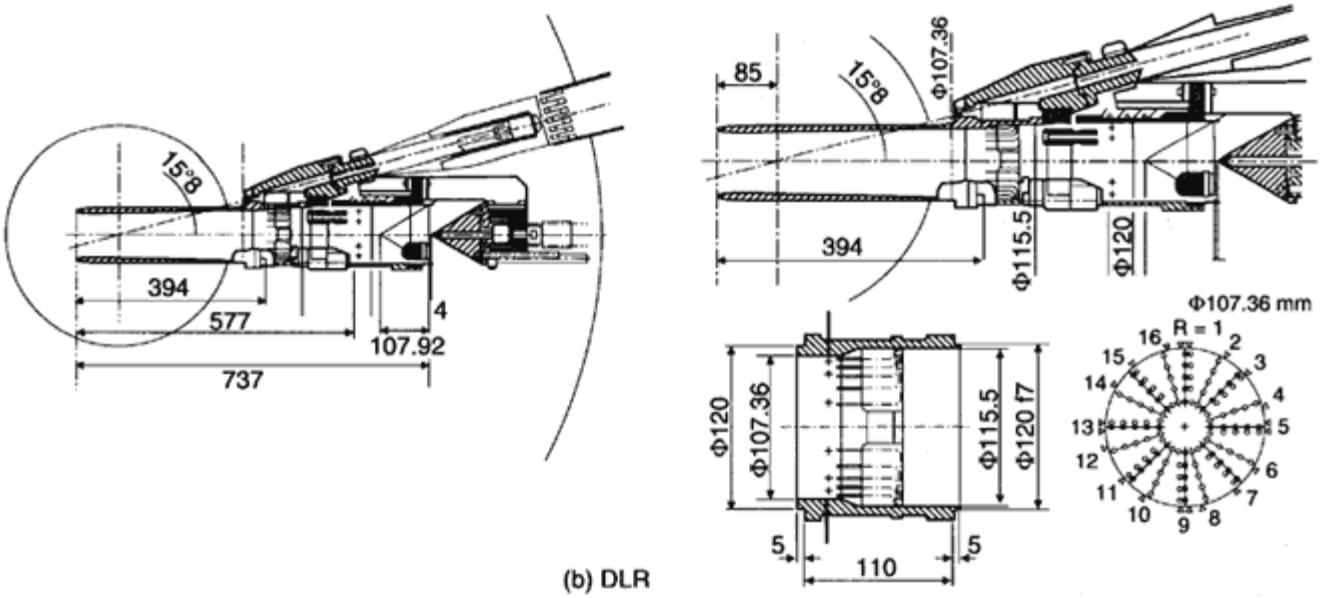

(b) DLR

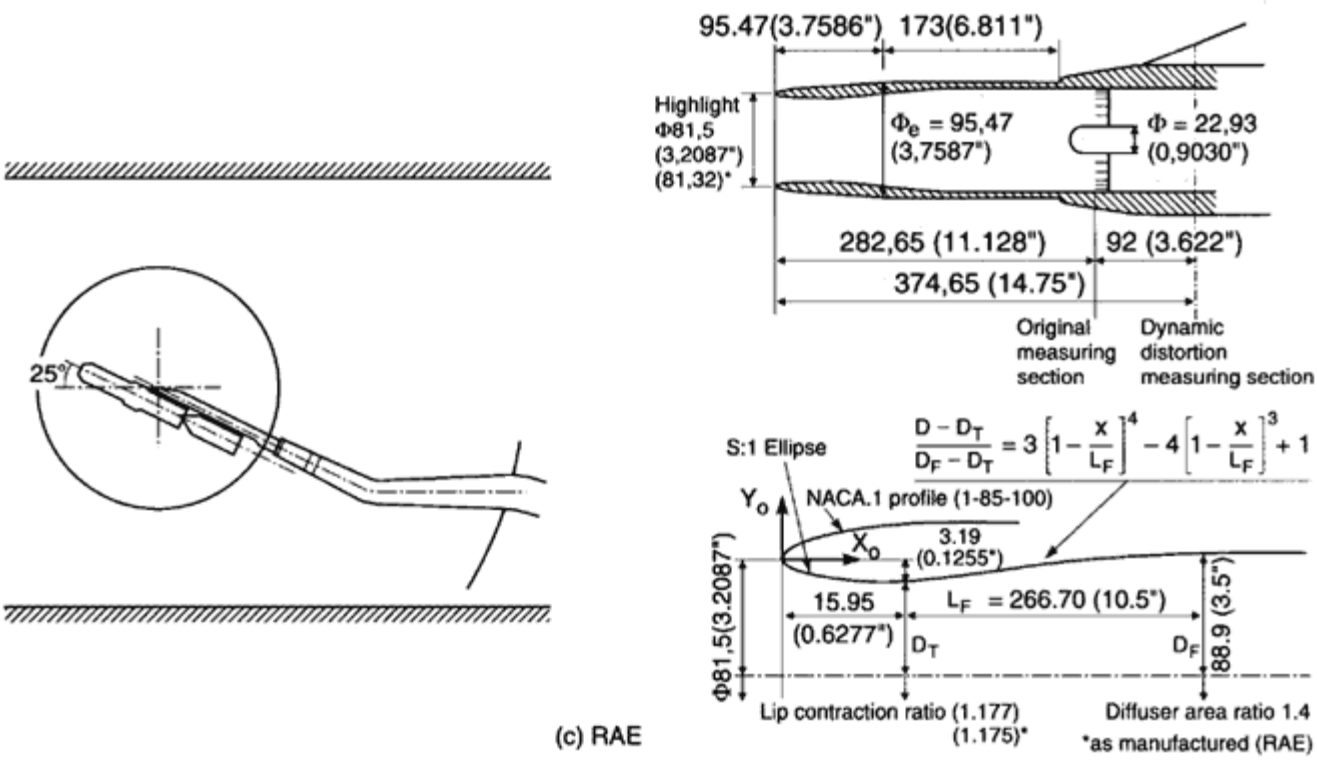

$$\frac{D - D_T}{D_F - D_T} = 3\left[1 - \frac{x}{L_F}\right]^4 - 4\left[1 - \frac{x}{L_F}\right]^3 + 1$$

(c) RAE

(d) Intake geometry

Figure 15.20
Models installed in (a) ONERA, (b) DLR and (c) RAE wind tunnels.
(d) Definition of pitot intake geometry used in all three wind-tunnel models.

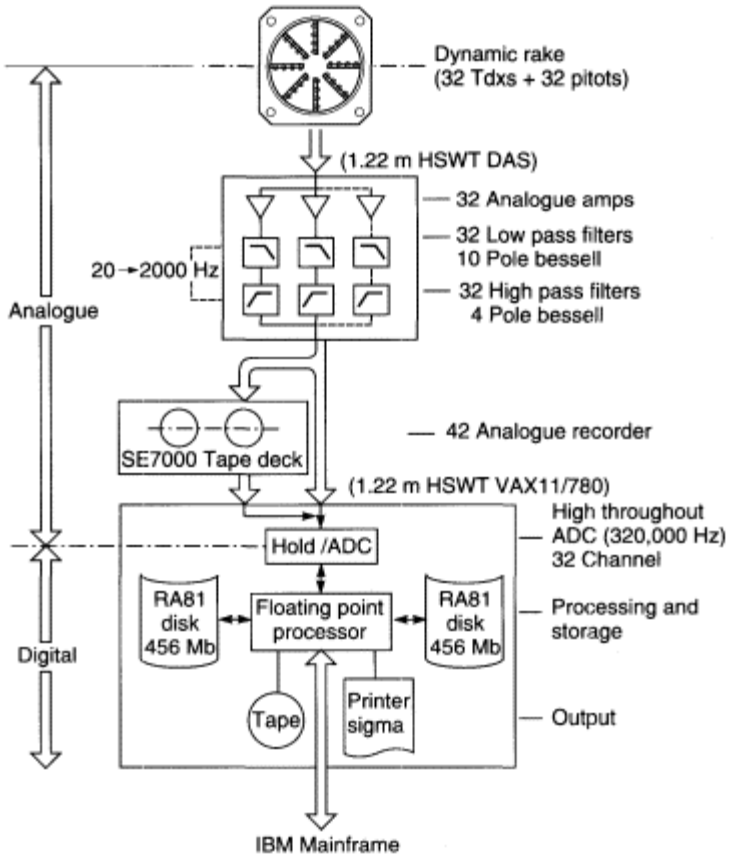

Figure 15.21
Dynamic distorsion instrumentation package
(British Aerospace).

computers or high-speed data acquisition systems, is detailed in AGARD Advisory Report 270 and in Chapter 2 of Goldsmith and Seddon (1993).

One other problem that has to be represented in wind-tunnel tests of an intake and duct is the simulation and measurements of pressure pulses caused by engine surge. With a relatively long duct two types of surge are of interest, 'pop' surge and cyclic or 'lock-in' surge. Pop surge is characterised by a single large-amplitude pressure pulse, usually called 'hammershock', which is then followed by one or two weaker pulses as the engine recovers, the whole process taking perhaps 0.1 seconds. In cyclic surge a repeatable pattern of pressure pulses is set up and to terminate the process in flight, the engine often has to be shut down.

A good simulation of cyclic surge for the Concorde intake was provided by the model shown in Fig. 15.23, where high-pressure air is pulsed upstream from a rotating butterfly valve. The success of such a device is shown by the comparison of model and flight pressure pulse times. A

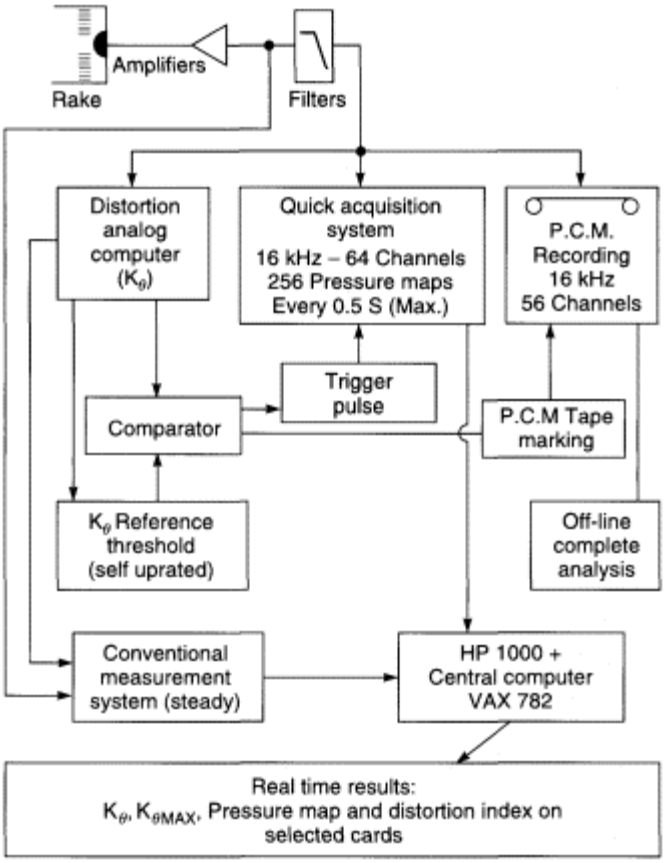

Figure 15.22
Unsteady distorsion measurement, with conditional real-time acquisition (ONERA).

similar type of device from Germany is the MBB surge wave generator shown in Fig. 15.24. This can also simulate a single pressure wave by the use of a bursting diaphragm in the supply pipe.

Before leaving internal flow measurements, attention should be drawn to the need for making detailed flow measurements so that checks can be made of the validity of calculation methods. Fig. 15.25 shows an internal probing system used and developed by ONERA. By combining the three movements of the support, the probe can explore the entire volume of the duct. The probe can be a pitot, a five-hole yawmeter or a hot wire for measuring unsteady pressures. For the validation of computer codes based on the Navier Stokes equations it is often necessary to be able to measure in duct flows not only the three mean velocity components U, V, W, but also the fluctuating velocity components and the shear stress and normal stress components.

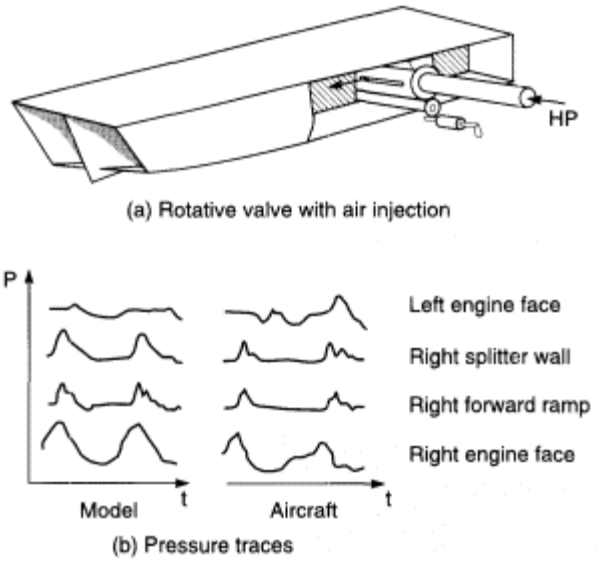

Figure 15.23
Engine surge simulation device (E.C. Carter).

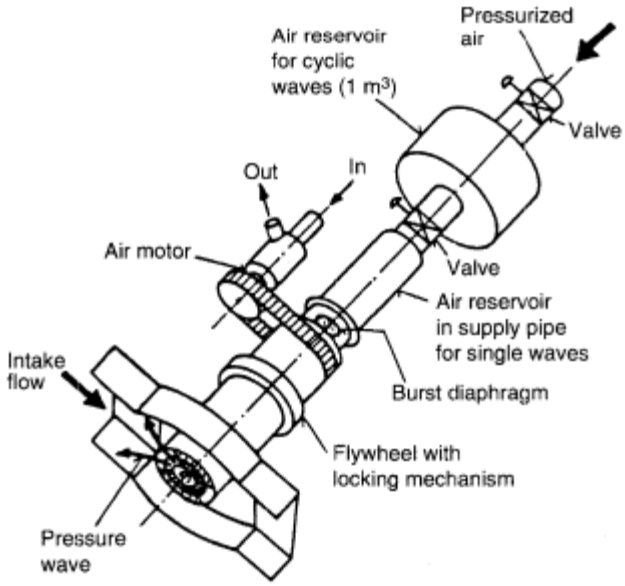

Figure 15.24
System display of MBB surge wave generator.

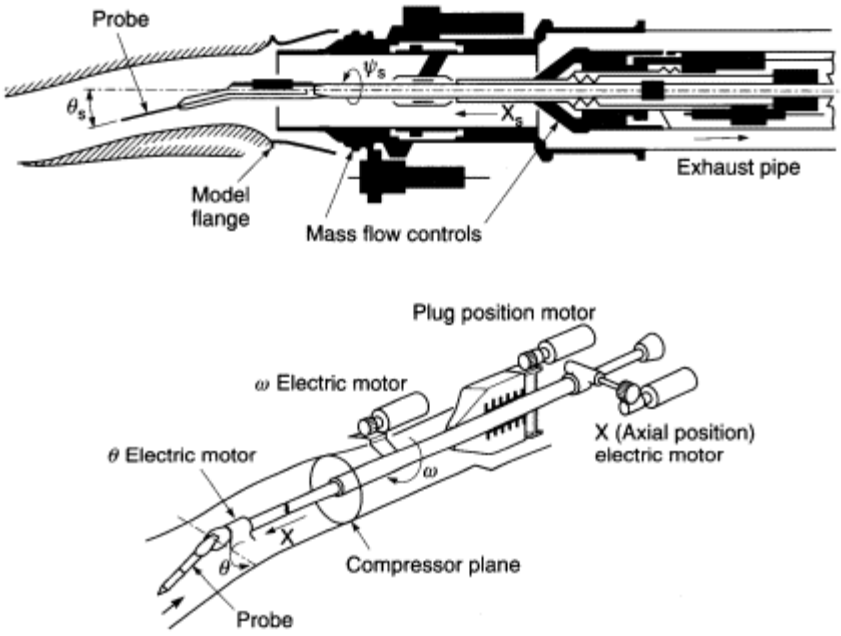

Figure 15.25
Internal probing device (ONERA).

15.4
External Forces and Moments

15.4.1
Corrections for the Effects of Internal Flow

In tests of an aircraft model embodying an intake duct, all the overall forces and moments will include components from the internal flow. For the most general case of a model at angle of incidence a and angle of sideslip b, if the duct axis is inclined at angles q and g to the body axis and the exit plane is canted at angles y and g in the incidence and yaw planes respectively (Fig. 15.26), the forces from the internal flow are the following:

$$\text{Drag } (D_{\text{int}}) = \rho_\infty V_\infty{}^2 A_\infty \cos\beta - A_e[p_e - p_\infty) \cos(\theta + \alpha - \psi) \cos(\lambda - \gamma) + \rho_e V_e{}^2 \cos\psi \cos(\theta + \alpha) \cos\gamma \cos\lambda] \quad (15.11)$$

$$\text{Lift } (L_{\text{int}}) = A_e [(p_e - p_\infty) \sin(\theta + \alpha - \psi) \cos(\lambda - \gamma) + \rho_e V_e{}^2 \cos\psi \sin(\theta + \alpha) \cos\gamma \cos\lambda] \quad (15.12)$$

$$\text{Pitching moment } (M_{\text{int}}) = -\rho_\infty V_\infty{}^2 A_\infty d_1 \cos\beta + A_e [(p_e - p_\infty) d_3 \cos(\lambda - \gamma) + \rho_e V_e{}^2 d_2 \cos\psi \cos\gamma] \quad (15.13)$$

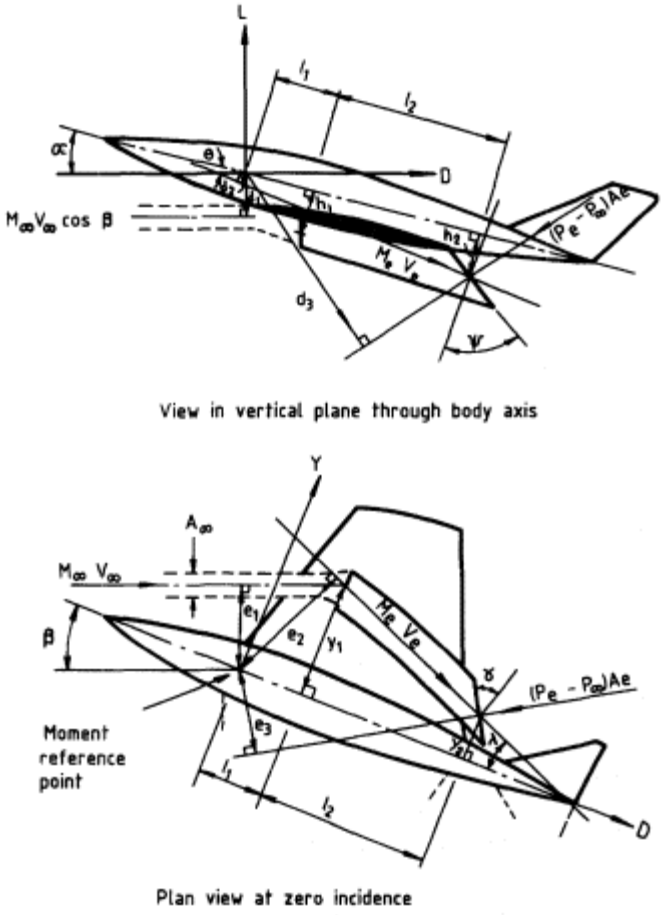

Figure 15.26
Model inclinations for general case.

$$\text{Sideforce } (Y_{\text{int}}) = -\rho_\infty {V_\infty}^2 A_\infty \sin\beta + A_e\,[(p_e - p_\infty)\sin(\lambda-\gamma) + \rho_e {V_e}^2 \cos\psi\cos\gamma\sin\lambda] \quad (15.14)$$

$$\text{Yawing moment } (N_{\text{int}}) = \rho_\infty {V_\infty}^2 A_\infty e_1 - A_e\,[(p_e - p_\infty)\,e_3\cos(\theta-\psi) + \rho_e {V_e}^2 e_2 \cos\psi\cos\gamma] \quad (15.15)$$

The moment arms $d1,2,3$ and $e1,2,3$ are shown in the diagram.

When the model is at zero sideslip and the exit plane is not canted, the equations reduce to:

$$D_{\text{int}} = \rho_\infty {V_\infty}^2 A_\infty - A_e \cos(\theta+\alpha)\,[(p_e - p_\infty) + \rho_e {V_e}^2] \quad (15.16)$$

$$L_{\text{int}} = A_e \sin(\theta+\alpha)\,[(p_e - p_\infty) + \rho_e {V_e}^2] \quad (15.17)$$

$$M_{int} = -\rho_\infty V_\infty{}^2 A_\infty d_1 + A_e \left[(p_e - p_\infty)\, d_3 + \rho_e V_e{}^2 d_2\right] \qquad (15.18)$$

$$Y_{int} = A_e \sin\lambda \left[(p_e - p_\infty) + \rho_e V_e{}^2\right] \qquad (15.19)$$

$$N_{int} = \rho_\infty V_\infty{}^2 A_\infty e_1 - A_e \left[(p_e - p_\infty)\, e_3 \cos\theta + \rho_e V_e{}^2 e_2\right] \qquad (15.20)$$

15.4.2
Drag by Force Measurement

Drag may be obtained by balance measurements on full or partial models. The primary choice in the design of a specialised drag model is whether the whole model or the intake part alone is to be metric, that is carried on the balance. For a research experiment, where the sum of cowl drag, pre-entry drag and possibly diverter drag and bleed drag in a uniform flow is required, the intake can be mounted on the tunnel wall as shown in Fig. 15.27. Struts emerging from the wall carry the model from a balance chamber. The restraint of bleed flow 'bellows', which should be minimal, is absorbed into calibration of the axial force link. All relevant pressures in the flow, on the base and in the balance chamber, are measured in a separate test and disconnected for the drag test.

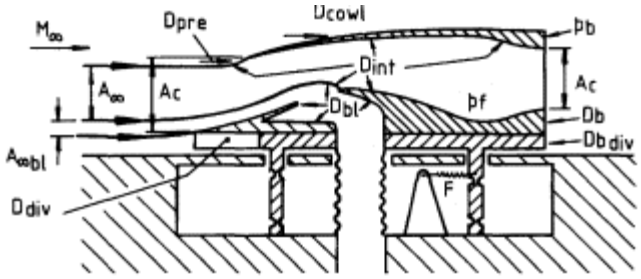

Figure 15.27
Intake mounted on tunnel wall for drag measurements.

Applying the same technique to a side intake carried on a fuselage brings in extra difficulty. There can be sealing problems between metric and non-metric portions, difficulties in the measurement of internal momentum flux at the break station, where flow uniformity may be poor, and problems of interpretation of forces measured on only part of the model. Interference drags can appear on both metric and non-metric parts, making the results of geometric changes inconclusive. Some of the problems can be minimised by the kind of careful design illustrated in Fig. 15.28, where the momentum-measuring station is taken well downstream to ensure reasonable flow distribution and the seals are located on surfaces parallel to the axis.

On the whole, the least difficult technique is to measure axial force on a fuselage or wing model, complete with intake, and again with the intake

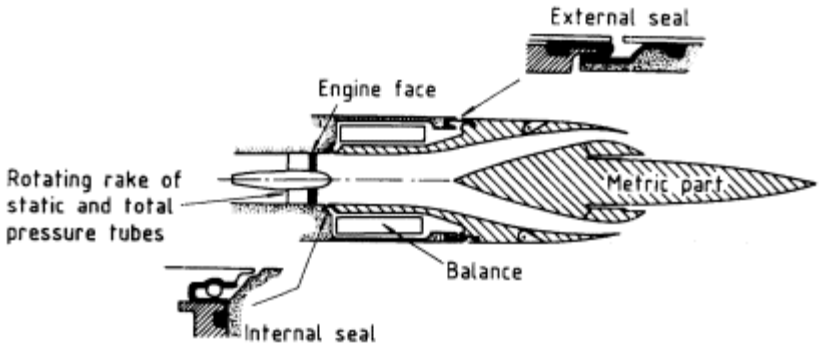

Figure 15.28
Arrangement for measurement of drag of front fuselage,
intakes and diverters in the presence of an aft fuselage.

removed (Fig. 15.29) and take the difference at constant incidence, or if possible at constant lift to exclude any change of induced drag. If the flow control plug and the instrumentation for momentum measurement are earthed, there are no sealing problems but care has to be taken to ensure that pitot tubes do not come into contact with the duct surface. If the model is large enough, base pressures can be measured by means of a transducer fitted into the nose of the fuselage. For smaller models, pitot tubes brought close up to, but not touching, the base area can be used. With a choked exit, uniformity of the base pressure may be improved by extending the duct a short way downstream by means of a thin-walled shroud (Fig. 15.10).

This method of drag assessment by difference is applicable in a number of ways, according to circumstances. Thus it may be used in supersonic, subsonic or low speed (i.e. incompressible flow) testing and may utilise either strain-gauge or mechanical-balance techniques. A problem liable to present itself, particularly with subsonic shapes, is an arbitrariness in defining the datum shape when the intake is removed.

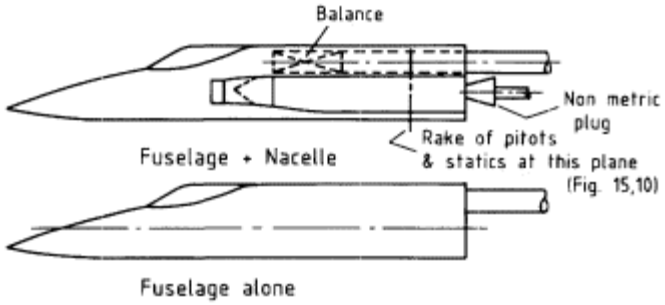

Figure 15.29
Measurement of fuselage drag
with and without intakes present.

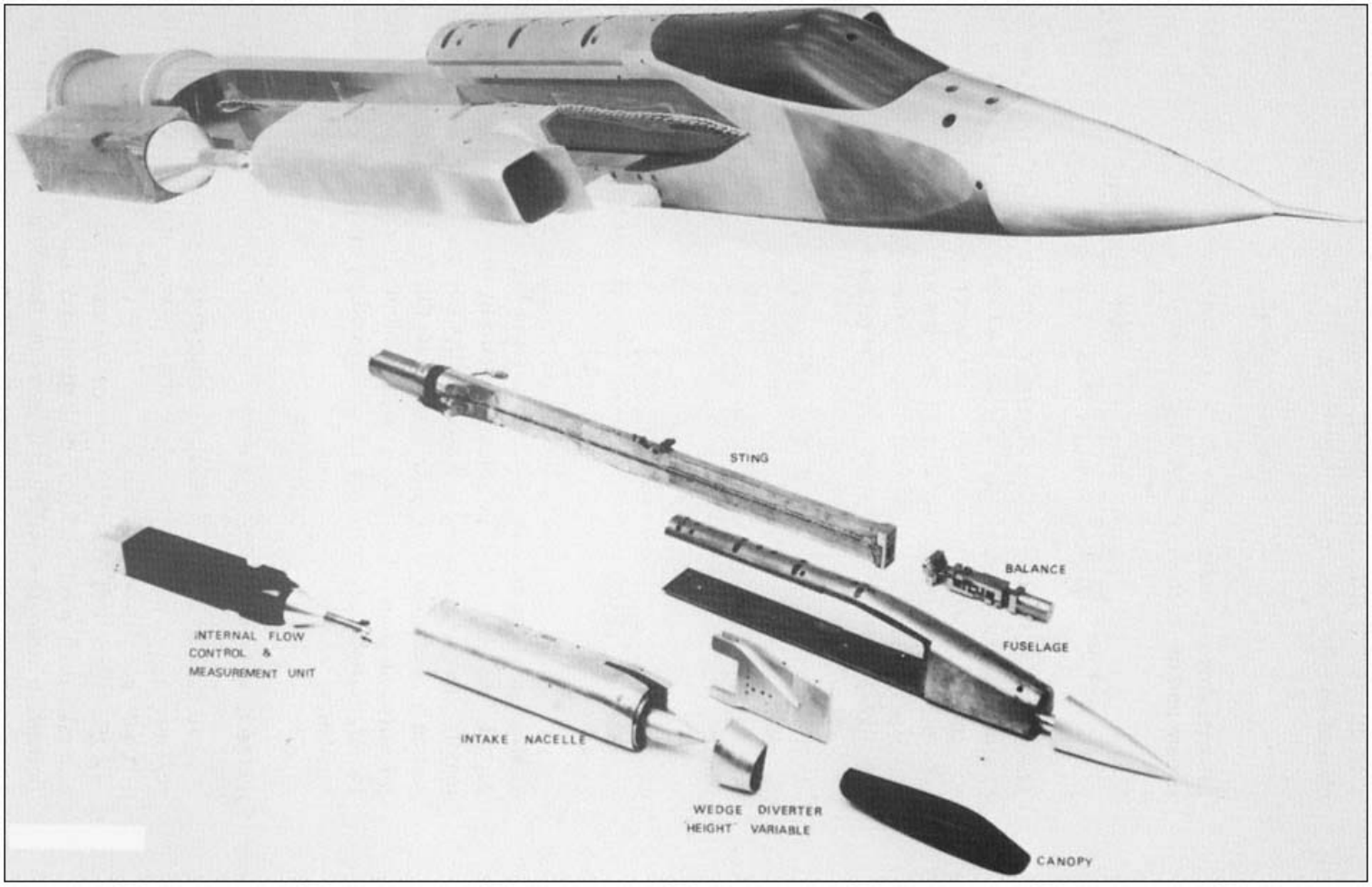

Figure 15.29
(*continued*)

In all the foregoing methods at supersonic speeds, the flow at exit is choked and the external drag is given by

$$D_{ext} = D_{balance} - D_{base} - D_{int} \qquad (15.21)$$

Internal drag *D*int is defined by the change in momentum flux between free stream and the duct measuring station, so that

$$(C_D)_{int} = \frac{D_{int}}{q_\infty A_{max}} = \frac{2A_\infty}{A_{max}} - \frac{A_f}{A_{max}} \cdot \frac{(p_f - p_\infty + 2q_f)}{q_\infty} \qquad (15.22)$$

The measuring station is arranged to be in a section of parallel duct and the internal drag needs to be corrected for a small amount of skin friction on the surface of the duct which is metric, downstream of the measuring station.

In tests on the Concorde aircraft (Britton 1965) where a particularly accurate value of cowl drag at full flow was required, use was made of the fact that the internal drag equation can be recast as

$$D_{int} = \int_{A_e} p_e f_1(M_e)\, dA + p_\infty A_e \qquad (15.23)$$

where

$$f_1(M_e) = \gamma M_e^2 \left[\frac{M_\infty \left(\frac{A}{A^*}\right)_\infty}{M_e \left(\frac{A}{A^*}\right)_e} - (1 + \gamma M_e^2) \right] \qquad (15.24)$$

Evaluation of the function *f*1(*M*e), shown in Fig. 15.30, indicates that for *M*e = 1.0 and *M*¥ = 2.2, the value is practically zero. Thus *D*int is approximately equal to *p*¥*A*e and is thereby independent of the measurements at station 'e'. Error curves (Fig. 15.31) indicate that for *M*e = 1, errors in static pressure *p*e have no effect but to similarly eliminate errors in total pressure *P*e, *M*e should vary from 0.4 to 1.0 depending upon free-stream Mach number.

15.4.3
Spillage Drag by Wake Traverse

A rig suitable for the assessment of spillage drag of an axisymmetric cowl by measurement of momentum defect in the flow was developed at the ARA and has been described by Carter and Pavitt (1976). The rig is pictured in Fig. 15.32. Pressures in the external flow are measured with a rotatable five-arm rake, each arm carrying 42 pitot tubes and eight static tubes. Rotation through 36° azimuth is sufficient to cover the flow field, provided that this is symmetrical about the incidence plane. Internal flow is measured simul-

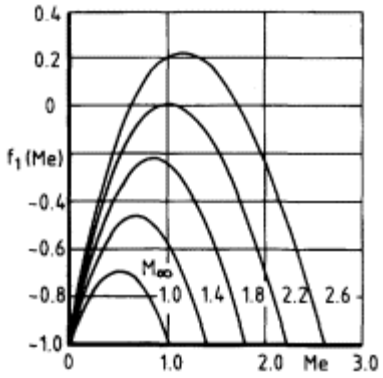

Figure 15.30
Dependence of exit Mach number function
on free stream and duct exit Mach numbers.

taneously on a rotating ten-arm rake together with wall statics: here five of the arms carry ten pitot tubes each and five carry four static tubes each.

Profile drag is calculated from the external rake measurements following the classical method of B.M. Jones (Cambridge University Aeronautical Laboratory 1936). In this, mass flow and total-pressure loss are determined for a particular streamtube at the rake and the data are used to calculate momentum deficit at 'infinity' downstream, assuming no further loss in total pressure. If *m*i and *V*i are the mass flow and downstream velocity associated with the i th pitot tube, we have

$$D = \sum_{1}^{n} m_i \cdot (V_\infty - V_i) \qquad (15.25)$$

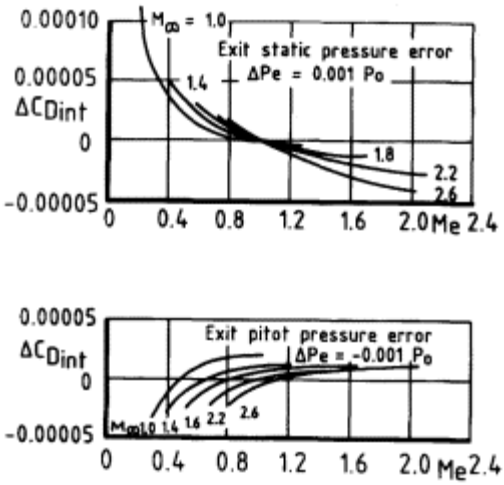

Figure 15.31
Influence of measurement errors in duct exit
Mach number, free stream Mach number and
static and total pressure on internal drag (Britton).

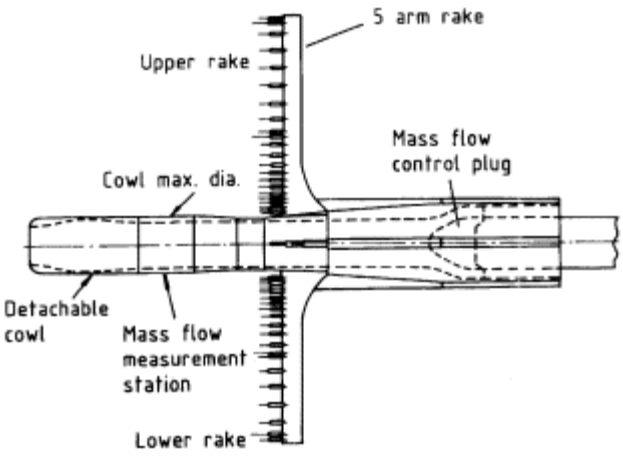

Figure 15.32
Axisymmetric cowl with
five-arm wake survey rake.

In terms of parameters $V/\ddot{O}T$ and a non-dimensional flow coefficient given by

$$Q = \frac{m\sqrt{T}}{AP} \qquad (15.26)$$

it is readily shown that

$$D = \sum_{1}^{n} Q_i P_i A_i \left[\frac{V_\infty}{\sqrt{T_\infty}} - \frac{V_i}{\sqrt{T_\infty}}\right] \qquad (15.27)$$

in which Ai is the area allocated to the i th streamtube.

15.4.4
Cowl Drag by Pressure Plotting.

For axisymmetric intakes at zero incidence, external drag on the cowl can be evaluated from a single line of surface pressure measurements, provided the model is made accurately and the tunnel flow is reasonably uniform. The net force is evaluated by resolving pressures from the stagnation point on the lip to a position of maximum area on the cowl. To locate the stagnation point accurately requires pressure holes to be positioned very close together in the highlight region and a significant variation of the stagnation position with intake flow ratio must be allowed for. A typical series of lip pressure distributions is shown in Fig. 15.33.

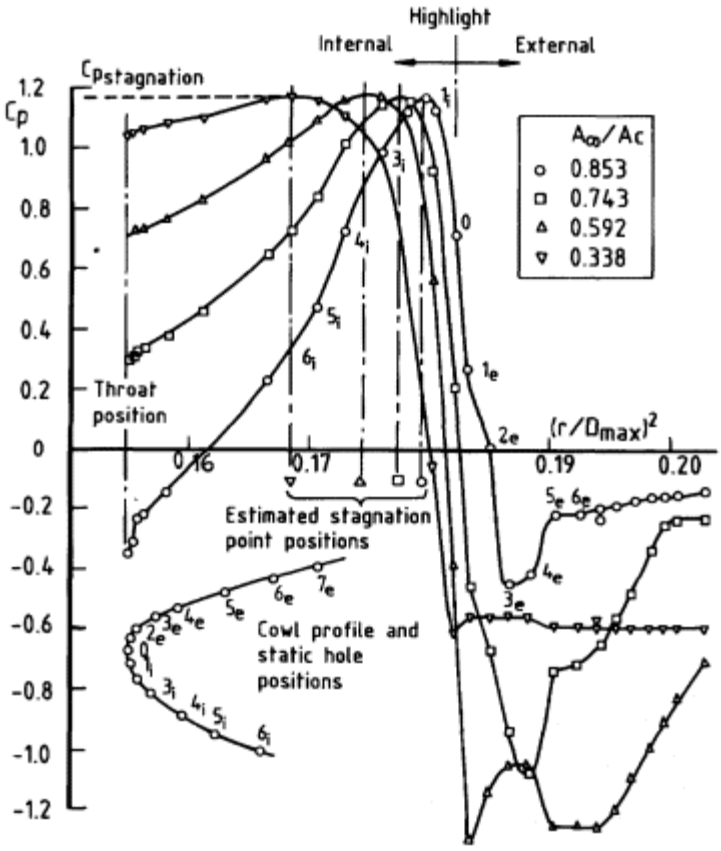

Figure 15.33
Typical pressure distribution on an axisymmetric cowl in vicinity of highlight position.

15.5
Local Flow Field at Intake Position

For accurate prediction of installed intake characteristics it is essential to measure the aircraft flow field in the intake locality. If the flow field is not excessively non-uniform, a combination of average flow quantities $\bar{M}_L$, $\bar{\alpha}_L$, $\bar{\beta}_L$ and $\bar{P}_L$, applied to the characteristics of the intake in isolation determined at *M*¥, a¥, b¥ and *P*¥, will adequately predict the intake performance *in situ.* If it does not, then the difference is a measure of interference effects from boundary layers and shock waves that is difficult to quantity by any other method.

The aircraft flow field, in terms of the above quantities, is measured by standard survey methods. It is often convenient to make total-pressure surveys in the boundary layer on one side of the fuselage (allowing for a considerably thickened boundary layer that will develop if the side is to

leeward), while at the same time surveying on the other side the flow field equivalent to the intake capture area. Standard five-hole yawmeters are often used but a four-facet head can reduce cross-flow interference. It is possible to measure variations as little at 0.02 in Mach number and angles accurate to ± 1/4° up to 10° inclination; for large angles of incidence and yaw combined, the accuracy is diminished. Evaluation of total pressure comes from a central pitot pressure coupled with Mach number.

References

Britton, J.W. (1965) 'Measurements of the internal drag of air breathing installations on slender wing body combinations at supersonic speeds'. RAE, TR 65275.

Calvert, W.J. and Merryweather, H. (1977) 'Data analysis facilities for unsteady pressure distributions within an annular duct'. NGTE, NT 968.

Carter, E.C. (1972) 'Experimental determination of inlet characteristics and inlet and airframe interference'. AGARD, LS 53.

Carter, E.C. and Pavitt, M. (1976) 'The operation and performance of the ARA cowl inlet test rig'. ARA, Memo 81.

Costakis, W.G. (1974) 'Analog computer implementation of four instantaneous distortion indices'. NASA, TM X-2993.

(1971): Engine-airplane interference and wall corrections in transonic wind tunnel tests'. AGARD, Advisory Report 36.

(1991) 'Air intakes for high speed vehicles'. AGARD Advisory Report 270.

Crites, R.C. (1970) 'The philosophy of analog techniques applied to the analysis and high speed screening of dynamic data'. AIAA, 70 595.

Fisher, S.A. and Street, P.G. (1967) 'The calibration of model air intake flow metering devices using nozzles of known discharge characteristics'. NGTE, NT 652.

Goldsmith, E.L. and Seddon, J. (eds.) (1993) *Practical Intake Aerodynamic Design.* Oxford: Blackwell Scientific.

Harris, A.E. and Carter, E.C. (1981) 'Wind tunnel test and analysis techniques using powered simulators for civil nacelle installation drag assessment'. AGARD, CP 301 Paper 24.

Herbert, M.V. and Pinker, R.A. (1964) 'The flow characteristics of some convergent nozzles'. NGTE, NT 542.

Jacocks, J.L. (1972) 'Statistical analysis of distortion factors'. AIAA, 72 1100.

Jacocks, J.L. and Kneile, K.R. (1975) 'Statistical prediction of maximum time variant inlet distortion levels'. AEDC, TR 74 121.

Jones, B.M., Cambridge University Aeronautics Laboratory (1936) 'The measure of profile drag by the pitot-traverse method'. ARC, R & 1688.

Livesey, J.L. (1982) 'Flow property averaging methods for compressible internal flows'. AIAA, 82 0135.

McGregor, I. (1971) 'The characteristics and calibration of two types of airflow metering device for investigating the performance of model air intakes'. RAE, TR 71212.

Pankhurst, R.C. and Holder, D.W. (1952) *Wind Tunnel Technique.* London: Pitman.

Pugh, G. and Harris, A.E. (1981) 'Establishment of an experimental technique to provide accurate measurement of the installed drag of a close coupled civil nacelle/airframe configuration using a full-span model with turbine-powered engine simulators'. AGARD, CP 301 Paper 25.

Ross, J.A. and Britton, J.W. (1973) 'Calibration of a shock plate for use in intake testing at supersonic speeds'. RAE, TM Aero 1530.

Seddon, J. and Haverty, L. (1953) 'Note on an application of the tilting-plate method of Mach number variation for wind tunnel tests at low supersonic speeds.' RAE, TN Aero 2238.

Wood, M.N. (1971) 'The use of injector units for engine simulation on wind tunnel models at high speeds'. RAE, TR 71215.

Index

(cont.)

(Cont.)